Transactions of the ASME®

Technical Editor, **T. H. OKIISHI (1998)**
Associate Technical Editors
Aeromechanical Interaction
R. E. KIELB (1999)
Gas Turbine (Review Chair)
A. KIDD (1997)
Heat Transfer
M. G. DUNN (1999)
Power
D. LOU (1998)
Turbomachinery
R. A. DELANEY (1998)
A. STRAZISAR (2000)

BOARD ON COMMUNICATIONS
Chairman and Vice-President
R. MATES

OFFICERS OF THE ASME
President, **KEITH B. THAYER**

Executive Director, **D. L. BELDEN**

Treasurer, **J. A. MASON**

PUBLISHING STAFF
Managing Director, Engineering
CHARLES W. BEARDSLEY

Director, Technical Publishing
PHILIP DI VIETRO

Managing Editor, Technical Publishing
CYNTHIA B. CLARK

Managing Editor, Transactions
CORNELIA MONAHAN

Production Coordinator
VALERIE WINTERS

Production Assistant
MARISOL ANDINO

Transactions of the ASME, Journal of Turbomachinery (ISSN 0889-504X) is published quarterly (Jan., Apr., July, Oct.) for $185.00 per year by The American Society of Mechanical Engineers, 345 East 47th Street, New York, NY 10017. Periodicals postage paid at New York, NY and additional mailing offices. POSTMASTER: Send address changes to Transactions of the ASME, Journal of Turbomachinery, c/o THE AMERICAN SOCIETY OF MECHANICAL ENGINEERS, 22 Law Drive, Box 2300. Fairfield, NJ 07007-2300.

CHANGES OF ADDRESS must be received at Society headquarters seven weeks before they are to be effective. Please send old label and new address.

PRICES: To members, $40.00, annually; to nonmembers, $185.00.
Add $40.00 for postage to countries outside the United States and Canada.

STATEMENT from By-Laws. The Society shall not be responsible for statements or opinions advanced in papers or . . . printed in its publications (B7.1, Par. 3).

COPYRIGHT © 1998 by The American Society of Mechanical Engineers. Authorization to photocopy material for internal or personal use under circumstances not falling within the fair use provisions of the Copyright Act is granted by ASME to libraries and other users registered with the Copyright Clearance Center (CCC) Transactional Reporting Service provided that the base fee of $3.00 per article is paid directly to CCC, 222 Rosewood Dr., Danvers, MA 01923. Request for special permission or bulk copying should be addressed to Reprints/Permission Department.

INDEXED by Applied Mechanics Reviews and Engineering Information, Inc.
Canadian Goods & Services
Tax Registration #126148048

Journal of Turbomachinery

Published Quarterly by The American Society of Mechanical Engineers

VOLUME 120 • NUMBER 1 • JANUARY 1998

TECHNICAL PAPERS

(Contents continued on p. 202)

This journal is printed on acid-free paper, which exceeds the ANSI Z39.48-1992 specification for permanence of paper and library materials. ∞™

♲ **85% recycled content, including 10% post-consumer fibers.**

Downloaded 01 Jun 2010 to 171.66.16.52. Redistribution subject to ASME license or copyright; see http://www.asme.org/terms/Terms_Use.cfm

(Contents continued)

ANNOUNCEMENTS

C. W. Haldeman, Jr.

M. G. Dunn

The Ohio State University
Gas Turbine Laboratory,
Columbus, OH 43235

High-Accuracy Turbine Performance Measurements in Short-Duration Facilities

This paper describes work done in preparation for the measurement of stage efficiency in a short-duration shock-tunnel facility. Efficiency measurements in this facility require knowledge of the flow path pressure and temperature, rotating system moment of inertia, and mass flow. This paper describes in detail an improved temperature compensation technique for the pressure transducers (Kulite) to reduce thermal drift problems, and measurements of the rotating system moment of inertia. The temperature compensation has shown that the conversion to pressure is accurate to within 0.689 kPa (0.1 psi) over the 40°C test range. The measurement of the moment of inertia is shown to be accurate to within 0.7 percent of the average value.

1.0 Introduction

For many years, short-duration facilities have been used to obtain time-averaged and time-resolved heat-flux and pressure data on the surface of the vanes and blades of full-scale rotating turbines, e.g., Dunn and Hause (1982); Dunn et al. (1984, 1986, 1992); Dunn and Haldeman (1994); and Rao et al. (1994). All of these measurement programs were performed at conditions that duplicated the flow function, the stage pressure ratio (total to static and total to total), the corrected speed, and the wall to free-stream temperature ratio. There are several major advantages in using short-duration facilities for experimental research: (*a*) Full-stage rotating engine hardware can be utilized, (*b*) the flow conditions (Reynolds number, Mach number, etc.) important to the turbine designer can be duplicated, and (*c*) cost is affordable and significantly less than that associated with long run time facilities. The next major step with the use of these facilities is to capitalize on experience with high-speed data acquisition and high-frequency response instrumentation to advance the capability by measuring turbine-stage performance both accurately and inexpensively.

Haldeman et al. (1991) presented an uncertainty analysis of turbine aerodynamic performance measurements in short-duration test facilities, which was an expansion on an earlier estimate presented by Epstein (1988) of the efficiency accuracy achievable in short-duration facilities. The goal of the Haldeman paper was to determine what had to be accomplished to achieve efficiency to within ±0.25 percent of the "true" value within a 95 percent confidence limit. It was argued in that paper that measurements with a ±0.25 percent precision should be obtainable, but to be sure that they were accurate to ±0.25 percent would be difficult, if not impossible. The desired efficiency accuracy of this value could easily be overshadowed when comparisons are made with data taken in other facilities because of differences in testing methods. Guenette et al. (1989) argue that the proper way of comparing efficiencies obtained in different facilities is to "correct" the indicated efficiency to account for losses and obtain an efficiency that is independent of the testing process. However, verification of these types of corrections becomes complicated.

The two independent techniques for measuring efficiency that are attractive to the shock-tunnel type facility (which are discussed by Haldeman et al., 1991) are the thermodynamic method and the mechanical method. The thermodynamic method requires accurate measurement of the upstream and downstream total pressure and total temperature in addition to the heat flux, which is used to correct for losses. The mechanical method replaces the downstream total temperature measurement with one of system rotational energy. Since accurate prediction of efficiency are extremely rare, and comparisons between facilities can be problematic (Haldeman et al. 1991), higher confidence in efficiency measurement can be obtained if the efficiency measured made by two separate techniques are in reasonable agreement.

Detailed analysis of the different efficiency measurement techniques and their relative uncertainties have been dealt with extensively by Haldeman et al. (1991) and will not be repeated here. The main conclusion of that work was that almost all major measurement techniques had to be improved in order to achieve the desired 0.25 percent accuracy calculation of efficiency. Specifically, a general number was that pressures needed to be accurate to about 0.1 percent and temperatures accurate to about 0.04 percent of their readings. For most types of short-duration facilities and turbine experiments, this is approximately 0.7 kPa (0.1 psia) and about 0.1°C. Different facilities require different improvements to realize these accuracies. For pressure transducers, this level of accuracy can generally be achieved in a static calibration at constant temperature. While shock-tunnel facilities generally have a relatively short test time, and thus the temperature increase of the transducer is relatively small, when used in medium-duration blowdown facilities, the pressure transducers heat up significantly, causing large changes in calibration. Because of the short test times in shock-tunnel facilities, the test turbine is allowed to spin-up during an experiment (speed changes of about 1 percent), which requires an accurate knowledge of the moment of inertia. Blowdown facilities generally employ some type of brake, which makes measurement of the torque critical. Since the goal of a good performance experiment would be to measure the efficiency using both techniques, an attempt has been made to improve the accuracy of the pressure, moment of inertia, and total temperature measurements in preparation for efficiency experiments.

This paper reviews the results achieved on the pressure and moment of inertia measurements resulting from work performed while the authors were working with CUBRC at Calspan Corp. in the 1994–1995 time period. Earlier thermocouple data were reported by Dunn et al. (1990). The remainder of the paper is divided into two main sections. Section 2 describes the technique used to measure the rotating system moment of inertia. Section 3 describes a temperature compensation technique used

---

Contributed by the International Gas Turbine Institute and presented at the 41st International Gas Turbine and Aeroengine Congress and Exhibition, Birmingham, United Kingdom, June 10–13, 1996. Manuscript received at ASME Headquarters February 1996. Paper No. 96-GT-210. Associate Technical Editor: J. N. Shinn.

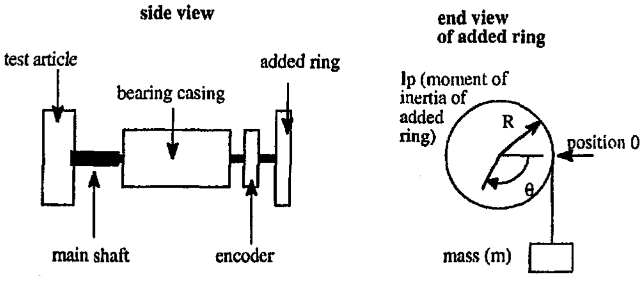

Fig. 1 Sketch of experimental setup

to reduce the thermal uncertainty of the flow path pressure measurements significantly.

2.0 Moment of Inertia

To utilize the mechanical method of measuring performance, measurements of both the mass flow and rotational energy are needed. In some blowdown facilities, the corrected speed is held constant using a brake, and the problem becomes one of measuring the power absorbed by the rotating component and accounting for inefficiencies in the braking system. The shock-tube-driven tunnel, because of its short test time, allows the rotor to spin up during a test. During the portion of the test time used to analyze data, the speed varies from the target speed by about ±1 percent. Because of the simplicity of the system, the total energy absorbed by the rotating system is equal to the moment of inertia multiplied by the acceleration rate.

The acceleration rate is a well determined quantity since the position of the rotor is recorded every $\frac{1}{500\text{th}}$ of a revolution using a 10 MHz clock. These data are used to calculate a speed history. As shown by Haldeman and Dunn (1995), the position can be expressed as a quadratic function in time. To within the resolution of the encoder, the quadratic model and the data are the same. Using the quadratic fit eliminates the need to perform a differentiation on a digital signal to calculate the velocity or an acceleration rate.

With the acceleration well characterized, the remaining problem is to measure the moment of inertia. This problem seems simple; however, modeling the effect of friction can be complicated because friction affects are far more important at low speeds than at high speeds.

2.1 Experimental Setup. Several different experimental procedures were tried while searching for a repeatable measurement that would agree both with a calculated value and an analytical model to within 1 percent accuracy. The experimental setup and geometry used for these experiments are shown in Fig. 1.

The system is simple with the turbine assembly (rotor, main shaft, and the bearing casing) attached to a second ring. A mass is attached to this ring via a string. By releasing the mass and recording the position of the entire assembly using a high-resolution encoder, the moment of inertia of the entire system (rotating assembly, second ring, and the mass) can be determined. Since the shape of the second ring can be controlled, the moment of inertia of that ring can be calculated in a straightforward manner, and the mass can be measured, leaving only the moment of inertia of the rotating assembly to be determined. Varying the masses provides an excellent check on the validity of the data because the inferred moment of inertia should be independent of the mass used to generate the motion.

2.2 Physical Model. The method settled upon uses the change in potential energy of the mass to increase the kinetic energy of the test article and then at a prescribed time disconnects the mass from the ring, while data continue to be acquired as the rotor slows down due only to frictional effects. Since the frictional effects are common to both sets of data, the difference is due only to the change in potential energy and the correct moment of inertia can be found. This system has provided highly repeatable measurements independent of the mass used.

The fundamental equation is:

$$\Delta E_{\text{mass}} = \Delta E_{\text{Rotating system}} + \Delta E_{\text{Friction}}, \tag{1}$$

which, for the geometry shown in Fig. 1, reduces to:

$$Rmg(\theta_j - \theta_i) = It\frac{\dot{\theta}_j^2 - \dot{\theta}_i^2}{2} + \oint_{x_i}^{x_j} Fr\delta\chi \tag{2}$$

The left-hand side is the change in potential energy, which is the force of the mass (mg) multiplied by the distance moved ($R\Delta\theta$). The right-hand side consists of two terms. The first is the change in kinetic energy of the system, which is the total moment of inertia of the system (It) multiplied by the change in the square of the velocity. In this case the total moment of inertia is:

$$It = Io + Ip + Is + mR^2 \tag{3}$$

where Io is the moment of inertia of the test article, Is is the moment of inertia of the shaft, Ip is the moment of inertia of the added ring, and mR^2 is the contribution to the measured moment of inertia due to the mass.

The second term in Eq. (1) is a frictional energy loss term. It is the integral of a frictional force F and the distance it is applied through. Since an analytical expression for the relationship of these terms is not available, the integral is taken over a set of dummy variables. The key problem in this experiment is accurately modeling this term so that the integral can be measured and thus the frictional effects determined.

To model the friction term, the decision was made to idealize the friction and replace the integral with an average value, which will be the same for any given test with a known mass when

Nomenclature

Moment of Inertia

a_i, b_i = regression coefficients
Fr = frictional force
g = gravitational constant
Io = moment of inertia of test turbine
Ip = moment of inertia of added plate
Is = moment of inertia of shaft
It = total moment of inertia of the rotating assembly
LCR = Linear Correlation Coefficient (quality of fit, R)
m = mass
R = radius of added ring
ΔE = change in energy of system
θ = angular position
$\dot{\theta}$ = angular velocity

Subscripts

j, i = different positions
A, B, C, D = different times

Temperature Compensation

R = resistance
Rn = modified leg resistance
Rs = span resistor
V = voltage
Vex = excitation voltage
$Vout$ = output voltage
Vs = power supply voltage

Subscripts

A, B = different temperatures
1, 2, 3, 4 = different bridge legs

evaluated over similar speed ranges. Mathematically this statement is expressed as:

$$\oint_{x_i}^{x_j} Fr\delta\chi = \overline{Fr}(\theta_j - \theta_i) \tag{4}$$

where it is claimed that $\overline{Fr}$ will be the same for two different tests if the data are examined over similar speed ranges.

Using this model, several different experiments were performed with different masses. Each experiment involved spinning the rotor with a mass attached and then separating the mass from the rotor and allowing the rotor to spin down. Combining Eqs. (2)–(4), the resulting equations can be solved for the moment of inertia of the rotating system. To aid in processing the data, the position notations of Eqs. (2)–(4) are replaced with a time-based notation:

$$Io + Is + Ip = \frac{Rm\left(g - \dfrac{1}{2}\dfrac{\dot{\theta}_B^2 - \dot{\theta}_A^2}{\theta_B - \theta_A}R\right)}{\dfrac{1}{2}\left(\dfrac{\dot{\theta}_B^2 - \dot{\theta}_A^2}{\theta_B - \theta_A} - \dfrac{\dot{\theta}_D^2 - \dot{\theta}_C^2}{\theta_D - \theta_C}\right)} \tag{5}$$

where the subscripts A and B are time indices for the data acquired when the mass is attached to the ring and C and D are time indices for when there is no mass attached to the ring. Equation (5) can be further simplified by noting that in these tests, position is a quadratic function of time and the coefficients can be calculated based on a simple regression of the acquired data. The coefficients would vary depending on which part of the experiment was being modeled:

$$\theta(t) = a_0 + a_1 t + a_2 t^2 \tag{6}$$

Doing the appropriate algebra, Eq. (5) can be reduced to:

$$Io + Is + Ip = \frac{Rm(g - 2a_2 R)}{2(a_2 - b_2)} \tag{7}$$

where a_2 is the quadratic coefficient for the data taken when both the mass and friction are acting, and b_2 is taken when just friction is acting.

Equation (7) has many advantages over Eq. (5) since (1) The quality of the data is immediately verified based on the quality of the data fits used to generate a_2 and b_2, (2) the only terms that matter in Eq. (7) are the quadratic terms, the data range is relatively unimportant since any change in ordinate axis does not affect the quadratic term, and (3) the quality of the fit can be compared directly to the instrument quality.

2.3 Verification Experiments and Analysis. This procedure was verified by measuring the moment of inertia of just the shaft and the added ring (no test article, $Io = 0$) since the moment of inertia of these items can be calculated relatively accurately.

Nine runs were performed using three different masses. A test consisted of hanging a mass from a length of line connected to the ring via a pin positioned in an open slot. The slot was machined such that when the pin was at position 0 (see Fig. 1) it would slide off the ring. The test was started by putting the pin in the slot and wrapping the line onto the ring about $\frac{3}{4}$ of a turn. The weight was released and data were taken for approximately 2–3 revolutions (depending upon the test). A once per revolution marker was aligned approximately with where the pin separated from the ring, and data immediately around this area (25 encoder points) on each side of the once/revolution marker were not used in the analysis.

The instrument accuracy in these experiments is limited by measurements of the mass, radius, and the encoder. The encoder and timer accuracies have already been stated (0.1 percent for the encoder, $\frac{1}{2}$ bit) and negligible inaccuracy on the clock (5e-6 percent). The masses were all weighed to within ±0.1 g, which as a conservative number yields an uncertainty in the mass of about 0.01 percent, and the radius was measured to within 0.007 percent. An example of the data is shown in Fig. 2 for run 8 (which has some of the largest deviations).

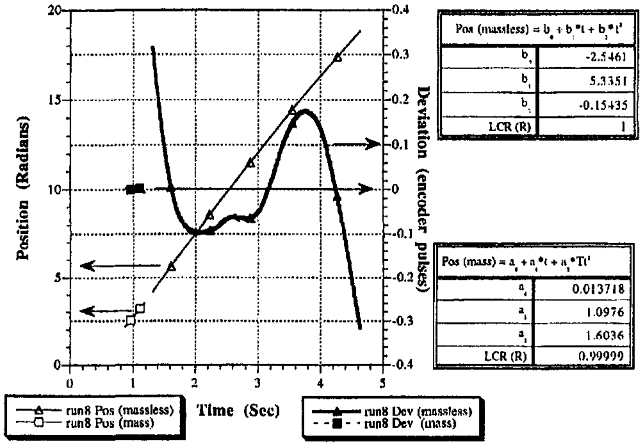

Fig. 2 Raw data and quadratic fits for run 8, with and without the mass attached

It is important to note that in the model of the friction used to derive Eq. (7), the velocities of the two experiments should be similar. This is done by evaluating the velocity of the system without any mass at its two endpoints and then only using the data in the mass section that correspond to the same velocity range. Because the effect of friction is relatively small (but not negligible) the rotor had a tendency to spin for quite some time after the weight was removed. Unfortunately, the experiment recorded only a few revolutions of data, so as shown in Fig. 2, the amount of data used in this model for when the mass was attached is relatively small. As a result, the data were analyzed both using a velocity matching technique (which may be more accurate mathematically, but has fewer data) and by using all the data available (which also includes the initial start-up, which has very high friction).

The calculated value of the moment of inertia of the shaft and plate is 2.5494 kg-M^2. This was obtained using hand calculations of the plate and measuring its density, and using a computer CAD model for the shaft and the nominal density of the shaft material. As a side note, the measured density of the plate was 0.5 percent larger than the reported value.

The uncertainty in the moment of inertia was determined by using a root-sum-square error propagation on the components of Eq. (7). The resulting equation is:

$$\frac{\Delta It}{It} = \left[\left(1 - \frac{2R}{\dfrac{g}{a_2} - 2R}\right)^2\left(\frac{\Delta R}{R}\right)^2 + \left(\frac{\Delta m}{m}\right)^2 + \left(-\frac{a_2}{a_2 - b_2} - \frac{2R}{\dfrac{g}{a_2} - 2R}\right)^2\left(\frac{\Delta a_2}{a_2}\right)^2 + \left(\frac{b_2}{a_2 - b_2}\right)^2\left(\frac{\Delta b_2}{b_2}\right)^2\right]^{1/2} \tag{8}$$

where $\Delta X/X$ represents the standard deviation of the relative uncertainty. The results of the analysis are shown in Table 1. The top rows of Table 1 show the statistics of a comparison of all nine runs when both the data is analyzed using a modified approach (i.e., velocity matching), and an unmodified (all data) approach. The first column is the average value of I. The second

Table 1 Results of verification experiments

	I average (kg-M^2)	Standard Deviation (kg-M^2)	Peak Positive Deviation (kg-M^2)	Peak Negative Deviation (kg-M^2)	(PP-PN)/(2Avg) (%)
Modified	2.5871	0.0103	2.6056	2.5701	0.69
Unmodified	2.5685	0.0071	2.5801	2.5550	0.49
Run	Mass (Kg)	I(mod) (Kg-m^2)	ΔI/I (mod)	I (unmod) (Kg-m^2)	ΔI/I (unmod)
Run 10	5.1405	2.5857	4.62E-04	2.5722	7.51E-05
Run 11	5.1405	2.6056	3.26E-04	2.5681	1.03E-04
Run 12	5.1405	2.5943	3.51E-04	2.5801	9.40E-05
Run 13	1.5099	2.5930	7.81E-05	2.5770	2.35E-04
Run 14	1.5099	2.5913	8.29E-05	2.5649	3.44E-04
Run 15	1.5099	2.5790	1.05E-04	2.5642	1.74E-04
Run 7	2.8715	2.5898	4.34E-04	2.5704	1.12E-04
Run 8	2.8715	2.5701	2.28E-04	2.5550	1.42E-04
Run 9	2.8715	2.5751	1.42E-04	2.5649	6.65E-05

represents a standard deviation (σ) of all measurements about the mean value. For the modified data this is about 0.39 percent and the unmodified data this is 0.28 percent. The next two columns provide the peak positive and peak negative values for the nine runs. The last column finds the maximum range from the average for the data. The lower part of the table shows the calculated moment of inertia and the uncertainty in I for each run. Figure 3 shows the moment of inertia for both cases plotted against the mass. The error bars shown are the ±95 percent uncertainty (or $\pm 2\Delta I/I$).

One of the more interesting points is the relative distribution of measured inertias for each mass. Low mass rates are not giving low moments of inertia. The variation is within acceptable limits for this experiment, but the randomness of the variation in Fig. 3 suggests that the range in the measurement could be reduced by increasing the test matrix (i.e., more masses and more repeat tests) and increasing the number of revolutions of the rotating system. While both systems are measuring a higher moment of inertia than the calculated value (0.7 and 1.4 percent), this could easily be accounted for by variations in the CAD model, the added inertia from the bearings (which were not modeled), or variations in the density of the materials from the nominal values used in the calculations. This system improves inertia measurements, a vital measurement needed for the mechanical system of measuring efficiency to the point where instrument uncertainties are below the variation due to multiple data runs.

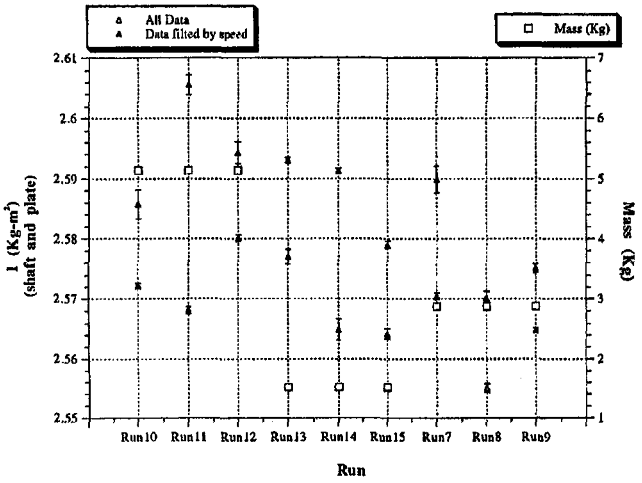

Fig. 3 Measured moment of inertia and its uncertainty for all data and for data filtered by speed

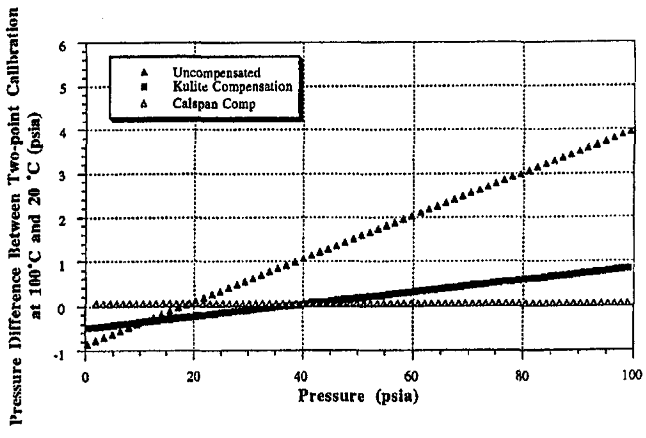

Fig. 4 Result of temperature compensation on semiconductor pressure transducer (Kulite)

3.0 Temperature Compensation of Semiconductor Pressure Transducer

One of the primary measurements needed for calculating efficiency is total pressure. The silicone wafer semiconductor pressure transducers (made by Kulite or Endevco) has become the pressure sensor of choice for many short-duration facility applications. These transducers have extremely high natural frequencies and thus can easily resolve fluctuations in the 0–100 kHz range without a significant decrease in signal quality. The units are available in many pressure ranges and styles, including a miniature version, which is easily installed in airfoils. These instruments have made it possible to obtain high-frequency pressure data on rotating components. However, they are known to be temperature sensitive, which can lead to an inaccurate measurement during an experiment, when temperatures vary, but still have high accuracy static calibrations at constant temperature.

Previous techniques for correcting this temperature sensitivity have taken many forms. The manufacturers generally have some form of passive compensation built into the sensors. Sometimes an insulator is applied (such as RTV or a black grease) to keep the diaphragm from heating up significantly during the test. Sometimes individuals will software compensate by recording the temperature of the diaphragm and then using a look-up table to correct the recorded data for the actual temperature. Whatever the technique, the results have generally been less than fully effective. This section models a Kulite transducer and shows how an improved passive temperature compensation scheme can be implemented to reduce the uncertainty due to temperature fluctuations significantly. This type of compensation allows the use of these transducers within a temperature range and with a verifiable calibration accuracy, without needing the temperature at every instance during a test. This can be extremely useful in situations where the recording of every diaphragm temperature could easily add 50 to 100 new channels of required data.

When reviewing the specifications for semiconductor transducers, it is difficult to translate the temperature sensitivity information provided (both span and gain) into numerical variations in pressure, because it is difficult to estimate the diaphragm temperature increase during testing. As shown by Haldeman and Dunn (1995), variations of 21 kPa (3 psi) due to temperature increases in a test are not uncommon during a medium duration test. Figure 4 shows a relative comparison of a Kulite transducer calibrated at 20°C and 100°C.

This transducer was run in three cases. The first was a completely uncompensated case, with a 28 kPa (4 psia) variation existing between high and low temperature calibrations. The second plot shows the transducer as supplied by Kulite with its compensation. The variation in this case is about ±7 kPa (±1 psia). The final plot shows a Calspan compensation technique (described later in this section). This type of performance is reflected in static calibration results as well. As shown by Haldeman and Dunn (1995), long-term (several week) calibrations

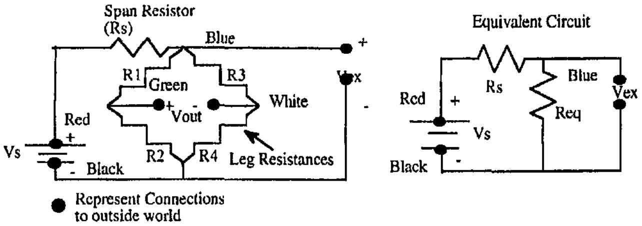

Fig. 5 Kulite model

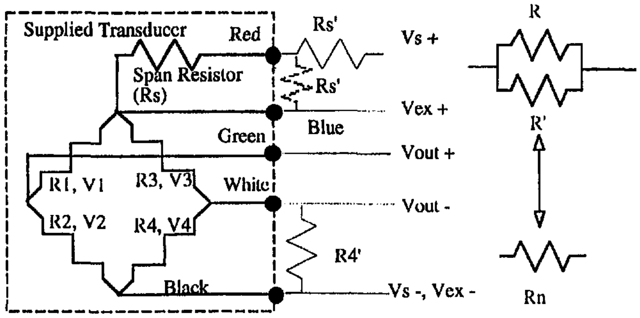

Fig. 6 Proposed correction for Kulite compensation

of Kulites show that those that are in a thermally stable environment traditional have calibration accuracies of ±0.7 kPa (±0.1 psi), and those which were not stable thermally generally had accuracies between two and four times worse.

3.1 Preliminary Experiments. It was observed that these pressure transducers have nearly linear output variation with temperature. The question arose as to whether the instrument could be modified so that the output would remain relatively constant with temperature variation, and that the only variation would be the intrinsic nonlinearities in the system. A Kulite transducer was used for this experiment, and with a great deal of help from Kulite, it was possible to compensate the transducer (this is shown as the third nearly flat line, in Fig. 4). This was done by making repeated transducer output measurements while varying the pressure and temperature ranges, and changing the span and leg resistances. After obtaining several matrices of data, some interpolation was done, and another set of data was taken. Within about three iterations the right combination of span resistor and leg shunt resistor was configured to generate the data shown in Fig. 4.

This technique is extremely tedious and time consuming and is not viable when contending with a large number of transducers. Clearly a simplified procedure was needed so that several transducers could be compensated at once. The next step was to develop a model with which the appropriate shunt resistors and span resistors could be calculated from a few simple measurements. The remainder of this section reviews this effort and the results of the initial experiments.

3.2 The Model. The Kulite transducers used in these experiments all have the same basic type of chip (100 psia, absolute sensor), which has five wires connected to it and is modeled as shown in Fig. 5

The chip is manufactured by "doping" certain areas of an etched silicon wafer, which forms the basis of the diaphragm. These areas form conductive regions, which can be modeled as resistors. The wafer is a complex shape, which has relieved areas upon which these "resistors" are deposited. They are deposited in a manner such that two of the "resistors" will increase in resistance and two will decrease in resistance when pressure is applied to the diaphragm, as a result of being mounted in either tension or compression. These resistors are paired such that $R1$ and $R4$ will behave in a similar manner and opposite of $R2$ and $R3$.

The output (*Vout*) of the sensor is the voltage difference between the green and the white leads. A constant voltage supply provides the power (*Vs*) across the red and the black leads, and the voltage measured between the blue and the black leads represents the voltage drop across the bridge (*Vex*), which is a function of the equivalent bridge resistance:

$$R_{eq} = \frac{(R_1 + R_2)(R_3 + R_4)}{(R_1 + R_2 + R_3 + R_4)}$$

$$R_{eq} = \frac{R_2\left(1 + \frac{R_1}{R_2}\right)\left(1 + \frac{R_3}{R_4}\right)}{\left(1 + \frac{R_1}{R_4} + \frac{R_2}{R_4} + \frac{R_3}{R_4}\right)} \tag{9}$$

and the resistors are as defined in Fig. 5. The output of the bridge (*Vout*) is given by:

$$Vout = Vex\frac{R_2R_3 - R_1R_4}{(R_2 + R_1)(R_4 + R_3)} \quad \text{or}$$

$$Vout = Vex\frac{BC - 1}{(B + 1)(C + 1)}, \quad B = \frac{R_2}{R_1}, \quad C = \frac{R_3}{R_4} \tag{10}$$

Vex (the voltage across the bridge) is a function of the equivalent bridge resistance, the span resistor (*Rs*), and the power supply voltage (*Vs*)

$$Vex = \frac{Vs}{\frac{Rs}{Req} + 1} \tag{11}$$

3.2.1 Model of Bridge Operation. The basic operation of this bridge is that two of the leg resistors increase with pressure (R_2 and R_3) and the other two decrease with pressure. As shown by Haldeman and Dunn (1995), an idealized bridge has two major characteristics:

1. The change in *Vout* is a function only of the change in resistance due to pressure and not temperature, and
2. *Req* will change only as a function of temperature and not pressure, thus from Eq. (11), *Vex* is a function only of temperature. For this reason, the voltage across the blue and black leads (*Vex*) is used by some as a measurement of the diaphragm temperature.

In reality, transducers, while displaying the macro characteristics described above, do not behave in an idealized way when one examines accuracies approaching 0.1 percent because:

1. All resistor legs are not the same value at the base conditions.
2. The resistor legs do not change by the same value at the same amount for an increase in pressure, even accounting for initial variations in the leg resistances (i.e., the percentage changes are not the same).
3. While all the resistors are deposited at the same time, their thermal coefficient of resistivity is not the same.

For these reasons, transducer output will change with temperature. Sometimes this is called a "drift," but "drift" is a poor choice of words since in general, the behavior is very repeatable and predictable. The change with temperature is due both to a change in the "zero" and a change in the gain of the transducer. The zero shift is defined as how much the output changes due to temperature when there is no stress on the diaphragm (i.e., under vacuum conditions for an absolute sensor). The gain shift is defined as how much the ratio of the change in voltage per unit change in pressure varies with temperature.

A model was derived (shown in Fig. 6) that allows measurements for an existing transducer to be extrapolated to the point where any inherent differences in the leg resistances can be compensated by external resistors.

The main idea is that there should be a set of resistors such that by adding them to one or more of the legs (an added resistor R_4' is shown) and adding them to the span resistor (Rs'), the transducer can be better compensated for temperature changes. The user has some choices regarding resistor addition. For instance, the final span resistor can be either less than or greater than the initial span resistor depending upon whether the shunt resistor (Rs') is added in series (shown in a solid line in Fig. 6) or in parallel (shown in the dashed line). However, for the leg resistance, the total leg resistance can only go down, because the resistors can only be added in parallel (as shown with R_4').

Any resistor added on the outside of the transducer can be: (1) precisely matched to the desired conditions, and (2) have a low temperature coefficient and be housed in an environmentally controlled box such that its resistance will not change with temperature. The addition of any resistor to a leg can be modeled as changing that leg resistance by a certain amount and changing the influence of temperature by a specific amount (Fig. 6), which changes both the effective resistance and temperature coefficient.

$$Rn(T) = \frac{R(T)}{1 + \dfrac{R(T)}{R'}} \tag{12}$$

3.2.2 Zero Shift Compensation. Combing Eqs. (9), (10) and (11), the output signal (*Vout*) can be derived in terms of the leg resistances, the power supply voltages, and the span resistor:

$$Vout = \frac{R_1\left(\dfrac{R_3}{R_4}\dfrac{R_2}{R_1} - 1\right)Vs}{\left(\dfrac{R_3}{R_4} + 1\right)\left(1 + \dfrac{R_1}{R_2}\right)R_2 + \left\{\dfrac{R_3}{R_4} + \left(1 + \dfrac{R_1}{R_2}\right)\dfrac{R_2}{R_4} + 1\right\}Rs} \tag{13}$$

If one assumes that these ratios exist at different temperatures (*A* and *B*), then a new resistor (R') positioned across a leg needs to be found such that:

$$Vout_A = Vout_B \tag{14}$$

In the simplest case (using only one resistor), there are four cases (corresponding to each of the legs) that need to be examined. Usually, only two of the legs will be able to be used (the other two would need a negative resistor). Consider the case for a change in leg 3. Equation (12) would be substituted into Eq. (13) where only R_3 is being changed. To simplify the notation, assume that the R' being sought is replaced by N. Then the equation being solved is:

$$\frac{\left. R_1\left(\dfrac{\dfrac{R_3}{1+\dfrac{R_3}{N}}}{R_4}\dfrac{R_2}{R_1} - 1\right)Vs\right|_A}{\left. R_1\left(\dfrac{\dfrac{R_3}{1+\dfrac{R_3}{N}}}{R_4}\dfrac{R_2}{R_1} - 1\right)Vs\right|_B} = \frac{\left.\left(\dfrac{\dfrac{R_3}{1+\dfrac{R_3}{N}}}{R_4} + 1\right)\left(1 + \dfrac{R_1}{R_2}\right)R_2 + \left\{\dfrac{\dfrac{R_3}{1+\dfrac{R_3}{N}}}{R_4} + \left(1 + \dfrac{R_1}{R_2}\right)\dfrac{R_2}{R_4} + 1\right\}Rs\right|_B}{\left.\left(\dfrac{\dfrac{R_3}{1+\dfrac{R_3}{N}}}{R_4} + 1\right)\left(1 + \dfrac{R_1}{R_2}\right)R_2 + \left\{\dfrac{\dfrac{R_3}{1+\dfrac{R_3}{N}}}{R_4} + \left(1 + \dfrac{R_1}{R_2}\right)\dfrac{R_2}{R_4} + 1\right\}Rs\right|_A} \tag{15}$$

Now the voltage supply will not change with temperature, and neither will the span resistor. Provided that the ratios in Eq. (15) are known, a value for N that will satisfy this relationship for at least one of the legs can be found implicitly.

3.2.3 Gain Shift Compensation. While the preceding section accounts for the zero shift, the gain shift is a separate problem. The reason for compensating for the gain shift is that the equivalent bridge resistance changes only with temperature. Given that the power supply is a constant voltage source, the excitation voltage across the bridge will change as the temperature changes (Eq. (11)). Since the output signal (*Vout*) depends upon the excitation voltage, the change in excitation voltage could be matched to compensate for any change in gain by selecting the proper span resistor.

The equation that governs this can be described in terms of a gain per unit voltage excitation (normalized gain), which should be constant at any given temperature and is defined as:

$$Gain' = \frac{Vout_{\text{High Pressure}} - Vout_{\text{Low Pressure}}}{\text{High pressure} - \text{Low Pressure}}\,\frac{1}{Vex} = \frac{\Delta Vout}{\Delta P\ Vex} \tag{16}$$

Now define two states: 1 represents the reference temperature and 2 represents the high temperature. One would fully expect that $Gain_1'$ would not be the same as $Gain_2'$ and the problem becomes one of finding a set of new excitation voltages (Vex_N) such that:

$$Vex_{N,1}\ Gain_1' = Vex_{,2}\ Gain_2' \tag{17}$$

Rearranging Eq. (11) to solve for *Rs* the correct span resistor will be given by:

$$Rs = \frac{\left(\dfrac{Gain_2'}{Gain_1'} - 1\right)Req_1}{\dfrac{Req_1}{Req_2} - \dfrac{Gain_2'}{Gain_1'}} \tag{18}$$

Equations (15) and (18) are the main ones that need to be solved to provide both zero and gain compensation.

3.3 Experimental Setup. The experimental setup is shown in Fig. 7 and is relatively simple. The setup consists of a small tank housed in an oven with its temperature monitored by an RTD. The tank in the oven is connected to the outside through $\frac{1}{2}''$ tubing. Outside of the oven is a HEISE 150 psia sensor, which is NIST traceable and is accurate to 0.5 percent of full scale and is temperature compensated over a range of room temperatures. On the other side of the HEISE sensor is another small volume and then a choke valve, which controls the bleed rate of the system. The system can be connected either

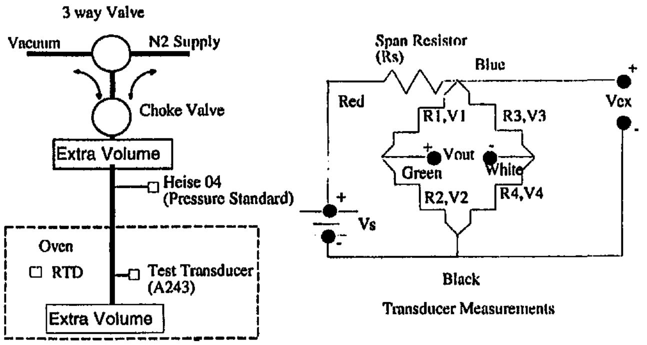

Measurement	Positive Lead	Negative lead
Vout	Green	White
Vsupply	Red	Black
Vspan	Red	Blue
Vex	Blue	Black
V1	Blue	Green
V2	Green	Black
V3	Blue	White
V4	White	Black

Fig. 7 Facility setup

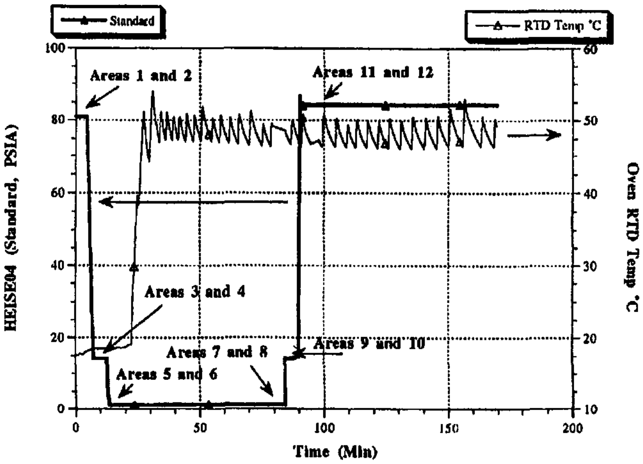

Fig. 8 Run 8 history of external test conditions

to a $N2$ supply or to vacuum through a three-way valve. All connections are made with $\frac{1}{2}''$ tubing, so the volumes are designed to provide enough extra space so as to keep gradients in the pipes to a minimum and to control the bleed rate more repeatably. Measurements are made on the Kulite transducer at the eight locations shown in Fig. 7, using the five leads that come standard with the transducer.

3.4 Measurements. There are many ways to make the measurements needed for the compensation equations. The leg resistors can be measured directly across the different leads, but this tends to be inaccurate. As a result, the leg resistors were inferred from a set of voltage measurements. As shown by Haldeman and Dunn (1995), two experiments were run that allowed the ratios of the resistances in Eq. (15) to be written as ratios of measured voltages. Experiment 1 applied power across the red and black leads and the measured resistance ratios can be found from the voltage ratios:

$$\frac{R_1}{R_2} = \frac{V_1}{V_2}, \quad \frac{R_3}{R_4} = \frac{V_3}{V_4} \tag{19}$$

The bridge equivalent resistance was derived by measuring the voltage drop across the span resistor and measuring the span resistor (a direct rearrangement of Eq. (11)). A second experiment at the same pressure and temperature was run were power was supplied to the green and the white wires. In this case the measured voltage ratios relate to different resistor ratios.

$$\frac{R_1}{R_3} = \frac{V_1}{V_3}, \quad \frac{R_2}{R_4} = \frac{V_2}{V_4} \tag{20}$$

These results can be substituted into Eq. (9) to derive an expression for R_2 in terms of measured values:

$$R_2 = \frac{Rs}{\dfrac{Vs}{Vex} - 1} \; \frac{\left[1 + \left(\left.\dfrac{V_1}{V_2}\right|_1 + 1\right)\left.\dfrac{V_2}{V_4}\right|_2 + \left.\dfrac{V_3}{V_4}\right|_1\right]}{\left(1 + \left.\dfrac{V_1}{V_2}\right|_1\right)\left(1 + \left.\dfrac{V_3}{V_4}\right|_1\right)} \tag{21}$$

where Rs, Vs, and Vex are not subscripted because their measurements are only applicable during experiment 1. At this point R_2 is known as a function of all measured variables and the other leg resistances can be calculated using this information. This particular set of experiments can be repeated at a higher temperature to find the leg resistances at high temperature. The benefit of this system is that the measurement can be made continuously, so that good statistical quantification can be done on the results.

The details of the data acquisition are given by Haldeman and Dunn (1995), but as a quick review the measurements were taken with two National Instruments AT-MIO-16X boards (16 bit, 8 channels each). The experiment would usually start at a low pressure and at room temperature and one would power both the red and black leads (acquire data for several samples) and then power the green and white leads. The pressure would be increased and the procedure would be repeated. Then the temperature would be increased and once stabilized, the entire procedure would be repeated.

Once the zero had been corrected, a separate set of experiments was performed where only the red and black leads were powered, and the main interest was in how the equivalent bridge resistance changed with temperature. For these experiments the system was brought up to pressure and slowly vented to vacuum. The resulting data would provide a set of calibration constants for the transducer at the test temperature. A second set of similar data would be taken at an elevated temperature. Having processed these data, the third set of experiments would be performed with the new shunt resistors installed, which would verify the performance of the new modified sensor.

3.5 Experimental Results. Three experiments were run with transducer reference number A243 over the temperature range of 15°C to 50°C (approximately the same range as the original specification of the transducer). The pressure range was vacuum to 594 kPa (85 psia).

Run 8 was the original, unmodified transducer test with the standard compensation supplied by Kulite installed. A plot of the pressure standard and the oven temperature is shown in Fig. 8.

During a test, a matrix of 12 separate points were investigated (each consisting of about 26 individual measurements). These were done in pairs with one set of measurements occurring when the red and black leads were powered, and a second set when the green and white leads were powered. The measurements occurred at full pressure, low pressure, and atmospheric pressure both at room temperature and at high temperature. These areas are marked on Fig. 8. The fluctuations in temperature at the high-temperature condition are a function of the oven, but as shown by Haldeman and Dunn (1995), this variation was attenuated at the transducer due to the mounting of the transducer.

The calculations used to determine the leg resistances at each of these conditions are shown in Table 2. The lower part of the table shows the percentage variation in the main measured val-

Table 2 Run 8 results

Area	Press (psia)	Req (Ω)	RTD 8 °C	V1/V2	V3/V4	V2/V4	R1	R2	R3	R4
1	81.015	665.96	17.84	0.975156	1.0211362		655.95	672.66	674.61	660.64
2	80.98		18.35			1.0181832				
3	14.23	666.38	18.49	0.99139086	1.0029327		662.08	667.83	668.79	666.84
4	14.3		18.53			1.001489				
5	1.282	666.74	18.63	0.99489248	0.99943861		663.38	666.79	668.22	668.59
6	1.279		18.66			0.997301				
7	1.318	696.78	47.55	0.9947592	0.99947222		693.15	696.81	698.41	698.77
8	1.317		47.38			0.99718215				
9	14.285	697.06	47.55	0.99157719	1.0029176		692.28	698.16	699.93	697.89
10	14.285		48.10			1.0003926				
11	84.2	696.58	48.04	0.97441329	1.0218972		685.54	703.54	706.19	691.06
12	84.2		48.43			1.0180615				

				% Variation over range [(Max-min)/min]*100		
Area	Press (psia)	Req (Ω)	RTD 8 °C	V1/V2	V3/V4	V2/V4
1	81.015	665.96	17.84	0.0067	0.0077	
2	80.98		18.35			0.0043
3	14.23	666.38	18.49	0.0086	0.0052	
4	14.3		18.53			0.0039
5	1.282	666.74	18.63	0.011	0.0073	
6	1.279		18.66			0.0049
7	1.318	696.78	47.55	0.024	0.0114	
8	1.317		47.38			0.0042
9	14.285	697.06	47.55	0.021	0.0119	
10	14.285		48.10			0.0037
11	84.2	696.58	48.04	0.0255	0.0135	
12	84.2		48.43			0.0041

ues (V_1/V_2, V_3/V_4, and V_2/V_4) for each of the areas. While only one set of measurements is required at a pressure level (instead of three), the extra data were used to verify the variation at different temperatures. Equations (19) and (20) were used to generate the leg resistances shown in Table 2.

Based upon the leg resistances at low pressure (areas 5–8), Eq. (15) was solved for each possible leg resistance. Only two were valid: A shunt across either R_2 or R_3 would work. A shunt of 161.97 ± 0.01 $K\Omega$ was applied across R_2 and the second series of tests (Run 9) was performed.

This particular set of tests was designed to look at the calibration of the sensor, so the two main areas of data were a quasistatic calibration of the transducer versus the pressure standard at room temperature and at high temperature. These data yielded a span resistor requirement of 434.136 Ω. Since an approximately 370 Ω span resistor was already installed, another resistor was added in series to bring the final measured value to 435.952 ± 0.002 Ω. One final run was performed. This time four quasi-static calibrations were performed. One set (both high and low temperature) was performed with the shunt resistors installed. The other set was done without the shunt resistors.

Figure 9 shows the difference (in psia) between a set of measured voltages evaluated with a set of low-temperature calibration constants versus a set of high-temperature calibration constants as a function of the low temperature pressure.

Three plots are shown: one with all the shunt resistors installed, one without any shunt resistors installed, and one with only the zero span resistor installed. One can see that for the calibrations with all the shunt resistors installed, the variation is about 0.1 psi maximum at the upper range of the test pressure. The other major finding is that the calibration constant with just the zero span resistors should start at about the same point that the fully compensated tests do, but they do not. This implies that there is an interconnection between the span compensation and the zero compensation. Clearly both of these cases are much better than the compensation that is the industrial standard.

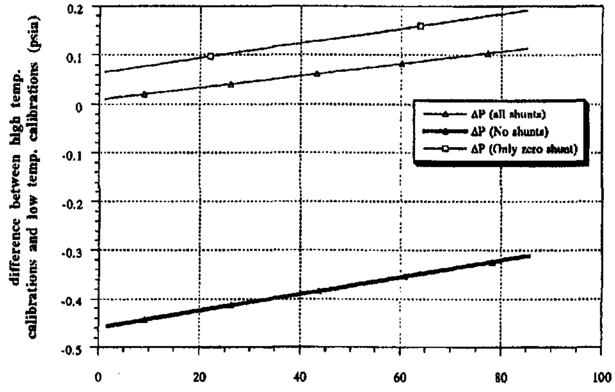

Fig. 9 Comparison of calibration constants over calibrated pressure range

While the compensation is not perfect, this was done with only one iteration. However, the overall result of the temperature compensation is that over this test range, the variations due to large fluctuations in temperature have been reduced to approximately the same variation observed in long-term static calibrations (Table 2). Work is continuing to incorporate these results into a system in which large number of transducers could be compensated simultaneously.

4.0 Conclusions

Both the moment of inertia measurements and the temperature compensation of the pressure sensors are important steps toward improving the overall measurements needed for high-accuracy efficiency experiments. It is demonstrated herein that the moment of inertia of the rotating system can be measured to an accuracy of about 0.5 percent. Transducer temperature compensation has been shown to reduce the uncertainty associated with pressure measurements from the 7 kPa (1 psi) level down to about 0.7 kPa (0.1 psi) (which for many transducers is within the static calibration accuracy). With the improvements that both of these techniques bring, higher inaccuracies in the main source of experimental problems for efficiency measurements, total temperature, can be tolerated. These techniques are presently being used in the measurement of turbine efficiency.

Acknowledgments

The authors would like to express their appreciation to Pratt and Whitney who supplied a portion of the funding for this effort via the Calspan–UB Research Center. In particular, we would like to acknowledge Mr. Dean Johnson and Mr. Bill Becker of Pratt and Whitney for their many suggestions and patience. We would also like to thank Mr. Jeff Barton, Mr. Bob Field, and Mr. Jim Weibel of Calspan, each of whom made significant contributions to the success of this project. Finally, we would like to acknowledge the many fruitful discussions and the insight provided to us by Dr. Tim Nunn of Kulite Semi-Conductor Company during the course of the temperature compensation effort.

References

Dunn, M. G., and Hause, A., 1982, "Measurement of Heat Flux and Pressure in a Turbine Stage," ASME *Journal of Engineering for Power*, Vol. 104, pp. 215–223.

Dunn, M. G., Rae, W. J., and Holt, J. L., 1984, "Measurement and Analysis of Heat Flux Data in a Turbine Stage: Part I—Description of Experimental Apparatus and Data Analysis, and Part II—Discussion of Results and Comparison With Predictions," ASME *Journal of Engineering for Gas Turbines and Power*, Vol. 106, pp. 229–240.

Dunn, M. G., George, W. K., Rae, W. J., Woodward, S. H., Moller, J. C., and Seymour, P. J., 1986, "Heat-Flux Measurements for the Rotor of a Full-Stage Turbine: Part II—Description of Analysis Technique and Typical Time-Resolved Measurements," ASME JOURNAL OF TURBOMACHINERY, Vol. 108, pp. 98–107.

Dunn, M. G., Bennett, W., Delaney, R., and Rao, K., 1992, "Investigation of Unsteady Flow Through a Transonic Turbine Stage: Part II—Data/Prediction Comparison for Time-Averaged and Phase-Resolved Pressure Data," ASME JOURNAL OF TURBOMACHINERY, Vol. 114, pp. 91–99.

Dunn, M. G., and Haldeman, C. H., 1994, "Phase-Resolved Surface Pressure and Heat-Transfer Measurements on the Blade of a Two-Stage Turbine," *Unsteady Flows in Aeropropulsion*, ASME AD-Vol. 40, Ng, W., Fant, D., and Povinelli, L., eds.

Epstein, A. H., 1988, "Short Duration Testing for Turbomachinery Research and Development," *Proc. Second International Symposium on Transport Phenomena, Dynamics, and Design of Rotating Machinery,* Honolulu, HI.

Guenette, G. R., Epstein, A. H., and Ito, E., 1989, "Turbine Aerodynamic Performance Measurements in Short Duration Facilities," Paper No. AIAA-89-2690.

Haldeman, C., Dunn, M., Lotsof, J., MacArthur, C., and Cohrs, B., 1991, "Uncertainty Analysis of Turbine Aerodynamic Performance Measurements in Short Duration Test Facilities," Paper No. AIAA-91-2131.

Rao, K. V., Delaney, R. A., and Dunn, M. G., 1994, "Vane-Blade Interaction in a Transonic Turbine, Part I—Aerodynamics and Part II—Heat Transfer," *AIAA J. of Propulsion and Power,* Vol. 10, No. 3, pp. 305–317.

T. C. Currie

W. E. Carscallen

Institute for Aerospace Research,
Aerodynamics Laboratory,
National Research Council of Canada,
Ottawa, Ontario, Canada, K1A 0R6

Simulation of Trailing Edge Vortex Shedding in a Transonic Turbine Cascade

Midspan losses in the NRC transonic turbine cascade peak at an exit Mach number (M_2) of ~1.0 and then decrease by ~40 percent as M_2 is increased to the design value of 1.16. Since recent experimental results suggest that the decrease may be related to a reduction in the intensity of trailing edge vortex shedding, both steady and unsteady quasi-three-dimensional Navier–Stokes simulations have been performed with a highly refined (unstructured) grid to determine the role of shedding. Predicted shedding frequencies are in good agreement with experiment, indicating the blade boundary layers and trailing edge separated free shear layers have been modeled satisfactorily, but the agreement for base pressures is relatively poor, probably due largely to false entropy created downstream of the trailing edge by numerical dissipation. The results nonetheless emphasize the importance of accounting for the effect of vortex shedding on base pressure and loss.

1 Introduction

Turbine airfoils in gas turbines typically have very thick, blunt trailing edges, both for stress reasons as well as to accommodate blade cooling passages and trailing edge coolant ejection in cooled designs. The static pressure in the region of separated flow just downstream of the trailing edge (i.e., the base region) is typically lower than that in the adjacent free stream, producing a component of the total loss known as the base loss. Since this loss can exceed 60 percent of the total in some cases (Nash et al., 1966), predicting and possibly reducing it are extremely important to the turbine designer. While it is generally accepted that the base pressure (p_b) at subsonic isentropic exit Mach numbers (M_2) is reduced below that which would be predicted in a steady-state analysis by periodic vortex shedding (Gostelow, 1984), although this effect is seldom taken into account, it is often assumed that vortex shedding is suppressed at supersonic exit Mach numbers and thus that the loss should be predictable with a steady-state approach. While this assumption is probably valid for M_2 exceeding ~1.3, experimental data obtained by Lawaczeck and Heinemann (1976), Heinemann et al. (1975), Sieverding (1977), Heinemann and Butefisch (1978), Motallebi and Norbury (1981), Bryanston-Cross and Camus (1982), Motallebi (1988), Carscallen et al. (1994, 1996), and Fleige (1994) show that vortex shedding is possible at lower M_2. For $M_2 > 1$, the effect of vortex shedding on base loss decreases as M_2 increases (Motallebi, 1988); however, because: (1) the vortex shedding becomes increasingly intermittent (Bryanston-Cross and Camus, 1982; Carscallen and Gostelow, 1994; Fleige, 1994; Carscallen et al., 1996), and (2) the vortices are shed downstream of the trailing edge at the confluence point of the pressure and suction surface separated shear layers (Motallebi and Norbury, 1981; Motallebi, 1988; Carscallen and Gostelow, 1994; Fleige, 1994; Carscallen et al., 1996). Motallebi (1988) has shown that base pressures predicted with the analytical models of Nash (1963) and Tanner (1978) for steady base flows become increasingly accurate as the distance from the trailing edge to the point of origin of the vortices increases, but that the effect of vortex shedding on base pressure and thus loss must be accounted for when the vortices are shed from the trailing edge. Computational results emphasizing the latter point will be given in this paper.

Just as analytical models for steady base flows are commonly used to predict base loss, it is also common practice to ignore vortex shedding in Navier–Stokes simulations. As speculated by Sieverding and Heinemann (1990), however, it is unlikely that blade losses can be predicted accurately with simulations that ignore trailing edge vortex shedding when shedding actually occurs, except possibly for the wrong reason, specifically numerical diffusion. The effect of excessive numerical diffusion of the pressure and suction side separated shear layers downstream of the trailing edge is to increase the lateral transport of momentum from the high-velocity free stream into the base region, thereby reducing the base pressure and increasing the base loss in a manner similar to vortex shedding (Dawes et al., 1987).

This paper will examine the effect of vortex shedding on blade loss by comparing the results of time-accurate unsteady and steady-state simulations of flow in a high turning transonic turbine cascade to experimental data. Experimental data for a large-scale cascade operated at the National Research Council of Canada (NRC), as reported by Moustapha et al. (1993), Carscallen and Gostelow (1994), Fleige (1994), and Carscallen et al. (1996) will be used for this purpose. Unlike most of the loss data reported in the literature for transonic cascades (e.g., Haller, 1980), which show a rapid increase in loss as M_2 is increased above 1.0, the midspan losses in the NRC cascade, which was designed by Pratt and Whitney Canada, peak at an exit Mach number of 1.0 and then drop by ~40 percent as M_2 is further increased to the design M_2 of 1.16. Since continuous vortex shedding occurs at or close to the trailing edge at $M_2 = 1.0$, while shedding at $M_2 = 1.16$ is intermittent and originates farther downstream, the reduction in loss between $M_2 = 1.0$ and 1.16 is believed to be due primarily to the corresponding reduction in the intensity of vortex shedding. Computational results supporting this theory are given in this paper.

Contributed by the International Gas Turbine Institute and presented at the 41st International Gas Turbine and Aeroengine Congress and Exhibition, Birmingham, United Kingdom, June 10–13, 1996. Manuscript received at ASME Headquarters February 1996. Paper No. 96-GT-483. Associate Technical Editor: J. N. Shinn.

2 Flow Solver

Governing Equations. Due to departures from two dimensionality produced by secondary flows and thinning and thickening of the endwall boundary layers, the axial velocity-density ratio (AVDR) in a turbine cascade is usually different from unity, where the AVDR is the ratio of the axial mass flux (ρu) at the downstream measurement plane to that at the upstream plane. Since it is well known that such departures from two dimensionality can be important (Gostelow, 1984), the simulations of vortex shedding were performed with a form of the Reynolds-averaged Navier–Stokes (RANS) equations that permits axial variations in streamtube thickness $h(x)$. The relevant conservative flux vector form of the "quasi-3D" RANS equations is (Vuillez and Veuillot, 1990)

$$\frac{\partial(h\mathbf{Q})}{\partial t} + \operatorname{div}(h\mathbf{F}(\mathbf{Q})) = \operatorname{div}(h\mathbf{F}_v(\mathbf{Q})) + \operatorname{div}(h\mathbf{F}'_v(\mathbf{Q})) + \mathbf{H} \qquad (1)$$

where the vector of conserved variables **Q** and the inviscid Euler flux vector **F** are given by

$$\mathbf{Q} = \begin{Bmatrix} \rho \\ \rho u \\ \rho v \\ e_o \end{Bmatrix} \quad \text{and} \quad \mathbf{F} = \begin{Bmatrix} \rho u \\ \rho u^2 + p \\ \rho u v \\ u(e_o + p) \end{Bmatrix} \mathbf{i} + \begin{Bmatrix} \rho v \\ \rho u v \\ \rho v^2 + p \\ v(e_o + p) \end{Bmatrix} \mathbf{j}$$

Variables ρ and u, v are the density and the velocity components in the x and y directions, respectively, while e_o is the total energy per unit volume and p is the static pressure ($= (\gamma - 1)\{e_o - \rho(u^2 + v^2)/2\}$). The source term **H** and the viscous flux vectors $\mathbf{F}'_v$ and $\mathbf{F}_v$ for an eddy-viscosity turbulence model are defined by the relations

$$\mathbf{H} = \begin{Bmatrix} 0 \\ (p - \tau'_{\theta\theta})\dfrac{dh}{dx} \\ 0 \\ 0 \end{Bmatrix}, \quad \mathbf{F}'_v = \begin{Bmatrix} 0 \\ \tau'_{xx} \\ 0 \\ u\tau'_{xx} \end{Bmatrix} \mathbf{i} + \begin{Bmatrix} 0 \\ 0 \\ \tau'_{yy} \\ v\tau'_{yy} \end{Bmatrix} \mathbf{j},$$

and

$$\mathbf{F}_v = \begin{Bmatrix} 0 \\ \tau_{xx} \\ \tau_{xy} \\ u\tau_{xx} + v\tau_{xy} - \dot{q}_x \end{Bmatrix} \mathbf{i} + \begin{Bmatrix} 0 \\ \tau_{xy} \\ \tau_{yy} \\ v\tau_{yy} + u\tau_{yx} - \dot{q}_y \end{Bmatrix} \mathbf{j}$$

where

$$\tau_{xx} = 2\mu(u_x - (u_x + v_y)/3), \quad \tau_{yy} = 2\mu(v_y - (u_x + v_y)/3)$$

$$\tau_{xy} = \tau_{yx} = \mu(u_y + v_x), \quad \tau'_{xx} = \tau'_{yy} = -\frac{2}{3}\mu\frac{u}{h}\frac{dh}{dx}$$

$$\tau'_{\theta\theta} = -\frac{2}{3}\mu\left(v_y + u_x - 2\frac{u}{h}\frac{dh}{dx}\right), \quad \dot{q}_x = -k_c T_x, \quad \dot{q}_y = -k_c T_y$$

and μ is the sum of the laminar and turbulent viscosities, μ_{lam} and μ_{turb}, respectively. Variables T and k_c are the static temperature and thermal conductivity, respectively, while terms with subscripts x and y are partial derivatives.

Spatial Discretization. The entries in **Q** are stored at the vertices of a triangular mesh. The Euler fluxes **F** in Eq. (1) are integrated over the boundaries of finite-volume cells formed from the median dual (Barth and Jesperson, 1989). The median dual is constructed by connecting the centroids of the triangular

Nomenclature

A_n = area of cell n
$\tilde{\mathbf{A}}$ = Roe matrix
$|\tilde{\mathbf{A}}|$ = diagonalized Roe matrix with absolute values in diagonal eigenvalue matrix
AMD$_k$ = area of median dual face bisecting edge k
AX, AY = projected areas of edge in x and y directions
$AXMD_k$ = x projection of AMD$_k$
$AYMD_k$ = y projection of AMD$_k$
B = flux Jacobian
CFL = Courant–Friedrichs–Lewy
C_{po} = local total pressure loss coefficient
$\bar{C}_{po}$ = pitchwise-averaged C_{po}
F = Euler flux vector
F_1 = blending function for k–ω/k–ϵ model (=1 for k–ω)
$\mathbf{F}_v$ = viscous flux vector
$\mathbf{F}'_v$ = vector of additional viscous terms associated with varying h
G_k = turbulent kinetic energy production term
H = vector of source terms
I = identity matrix
M = Mach number
N_{inner} = number of inner iterations
$\mathbf{P}_n$ = cell average value of **H** for cell n
Q = vector of conserved variables
R = residual vector
T = static temperature
X, Y = mixing analysis coordinates
U, V = velocity components in X and Y directions
c = chord
c_{ax} = axial chord
div = divergence
d_n = number of neighbouring nodes around node n
d_{te} = trailing edge diameter
e_o = total energy per unit volume
f_s = shedding frequency
h = streamtube height
i = unit vector in the x direction
j = unit vector in the y direction
k_c = thermal conductivity
p = static pressure
q = conserved variable
$\dot{q}_x$, $\dot{q}_y$ = x and y components of the heat flux vector $\dot{\mathbf{q}}$
Δr = distance from cell centroid to edge midpoint
t = time
Δt = time step
u = x component of velocity
v = y component of velocity
x = global Cartesian coordinate or distance from cascade leading edge
y = global Cartesian coordinate or distance from wall
y^+ = nondimensional wall coordinate
α = probe yaw angle
γ = ratio of specific heats
μ = viscosity
ρ = density
τ_{xx}, τ_{xy}, τ_{yy} = Reynolds stresses
τ'_{xx}, τ'_{yy}, $\tau'_{\theta\theta}$ = additional viscous stresses associated with varying h
τ_w = wall shear stress
ϕ = slope limiter ($0 \le \phi \le 1$)
ω = turbulent specific dissipation rate

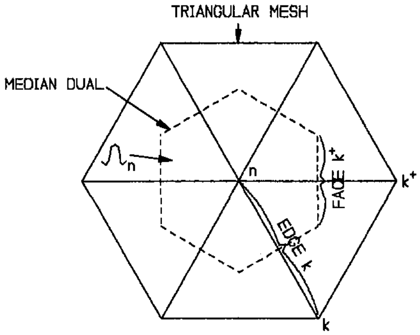

Fig. 1 Median dual control volume Ω_n for a triangular mesh

cells to the midpoints of their sides (Fig. 1). The resulting (nonoverlapping) cells, denoted Ω_n for vertex (node) n, are hexagonal in the case of a mesh of equilateral triangles.

The flux-difference splitting scheme of Roe (1981) is used to evaluate interfacial Euler fluxes. With a lumped representation of $\mathbf{Q}$ in cell n, the resulting conservation equation for the Euler fluxes alone is

$$\frac{d\mathbf{Q}_n}{dt} = -\frac{1}{h_n A_n} \sum_{k=1}^{d_n} \overline{h}_k \left[\frac{1}{2} (\mathbf{F_n} + \mathbf{F_k}) \cdot (AXMD_k \mathbf{i} + AYMD_k \mathbf{j}) - \frac{1}{2} |\tilde{\mathbf{A}}| (\mathbf{Q_R} - \mathbf{Q_L}) AMD_k - \mathbf{P_n} AXMD_k \right] \quad (2)$$

where d_n is the degree of vertex n (i.e., the number of incident edges and thus neighboring nodes) and $\mathbf{F_k}$ is the flux vector at the kth neighboring vertex (i.e., $\mathbf{F}(\mathbf{Q_k})$). The areas $AXMD_k$ and $AYMD_k$ are the (outward) directed projected areas of the median dual face bisecting edge k, in the x and y directions respectively, and $AMD_k = (AXMD_k^2 + AYMD_k^2)^{1/2}$. Vector $\mathbf{P_n}$ is the cell-averaged value of $\mathbf{H}$, with the factor dh/dx in the second entry omitted, while h_n and $\overline{h}_k$ are streamtube heights evaluated at node n and the center of face k, respectively. The parameter A_n is the area of cell n, while the 4×4 matrix $|\tilde{\mathbf{A}}|$ is the Roe matrix, defined by Gnoffo (1986). The entropy fix of Liou and van Leer (1988) is used to prevent the nonphysical expansion shocks that are otherwise possible with Roe's scheme.

The subscripts $\mathbf{L}$ and $\mathbf{R}$ in Eq. (2) refer to the states of the gas on the left and right-hand sides of the median dual face, where the left side is assumed to be the side on which node n is located. To obtain second-order accuracy, these states are determined by applying Van Leer's MUSCL (Monotone Upstream-Centered Schemes for Conservation Laws) technique (Van Leer, 1979), whereby a state variable q is linearly extrapolated from the cell centroid at x_o, y_o to the midpoint of edge k (i.e., a point midway between nodes n and k) at x_{kmid}, y_{kmid} by means of the equation

$$q(x_{\text{kmid}}, y_{\text{kmid}}) = q(x_o, y_o) + \phi_n \nabla \mathbf{q_n} \cdot \Delta \mathbf{r} \quad (3)$$

where $\Delta \mathbf{r} = (x_{\text{kmid}} - x_o)\mathbf{i} + (y_{\text{kmid}} - y_o)\mathbf{j}$ and $\nabla \mathbf{q_n}$ is the gradient in cell n. The gradient $\nabla \mathbf{q_n}$ is calculated using a least-squares reconstruction of q at node n and its d_n nearest neighbors (Barth, 1992).

The parameter ϕ_n is a slope limiter ($0 \le \phi_n \le 1$) needed to prevent oscillations in the solution near discontinuities (shocks). The limiter should have a value of unity in regions of the flow where the solution is smooth (e.g., subsonic regions) and a value of zero at extrema. The algorithm used to calculate ϕ_n is that given by Barth and Jesperson (1989), which requires that extrapolated values of q within Ω_n be bounded by the values at the centroids of Ω_m; $m \in \Gamma_n$, where Γ_n is the set of cells containing cell n itself and all of its neighbors. A common limiter, based on density, is applied to all entries of $\mathbf{Q}$. Since there are no discontinuities in regions where the flow is subsonic, the density-based limiter (ϕ_ρ) at node i is set equal to unity if the Mach number at node i and all of its nearest neighbors is <1.

The viscous terms in Eq. (1) are evaluated by assuming that u and v are piecewise linear functions in each triangle. The Green–Gauss formula is used to evaluate first derivatives (u_x, v_y, etc.) (Barth, 1991). If the finite-volume scheme described above is interpreted as a Galerkin finite-element discretization on linear triangles, as described by Barth (1991), Eq. (2) can be modified to include viscous terms by writing it as

$$\frac{d\mathbf{Q_n}}{dt} = -\frac{1}{2h_n A_n} \sum_{k=1}^{d_n} \overline{h}_k \left[(\mathbf{F_n} + \mathbf{F_k}) \cdot (\mathrm{AXMD_k}\mathbf{i} + \mathrm{AYMD_k}\mathbf{j}) - |\tilde{\mathbf{A}}| (\mathbf{Q_R} - \mathbf{Q_L}) AMD_k - 2\mathbf{P_n}\mathrm{AXMD_k} - \frac{\overline{h}_e}{\overline{h}_k} (\overline{\mathbf{F_v}} + \overline{\mathbf{F}'_\mathbf{v}}) \cdot (AX_{k \to k^+}\mathbf{i} + AY_{k \to k^+}\mathbf{j}) \right] \quad (4)$$

where $\overline{\mathbf{F}}_\mathbf{v}$ and $\overline{\mathbf{F}}'_\mathbf{v}$ are element-averaged viscous fluxes in the triangle (element) with outer edge $k \to k^+$ (Fig. 1). Areas $AX_{k \to k^+}$ and $AY_{k \to k^+}$ are the projected areas of edge $k \to k^+$ in the x and y directions, respectively, while $\overline{h}_e$ is h at the centroid of the triangle with edge $k \to k^+$.

Time Integration. If the right-hand side of Eq. (4) is denoted $\mathbf{R_n}$, that equation can be written as

$$\frac{d\mathbf{Q_n}}{dt} = \mathbf{R_n} \quad (5)$$

The same equation without the subscript n on $\mathbf{Q}$ and $\mathbf{R}$ applies to the full system of equations for all nodes.

Nomenclature (cont.)

Subscripts

Ω_n = median dual control volume for cell n
∇ = gradient
b = base
k = edge k or turbulent kinetic energy k
kmid = midpoint of edge k
lam = laminar
n = node n
nw = near-wall
o = total (stagnation)
turb = turbulent
x = partial derivative with respect to x or x component
y = partial derivative with respect to y or y component
uw = upwind
v = viscous
$\mathbf{L}$ = left side of median dual face
$\mathbf{R}$ = right side of median dual face
1 = cascade inlet
2 = cascade outlet
∞ = mixed-out

To avoid the restrictive (Courant) time step limit associated with an explicit time integration scheme, Eq. (5) is integrated implicitly with the three time-level, second-order accurate equation (Hirsch, 1990)

$$\frac{3\mathbf{Q}(t+\Delta t)-4\mathbf{Q}(t)+\mathbf{Q}(t-\Delta t)}{2\Delta t}=\mathbf{R}(t+\Delta t) \qquad (6)$$

where $\mathbf{Q}(t+\Delta t)$ and $\mathbf{R}(t+\Delta t)$ are $\mathbf{Q}$ and $\mathbf{R}$ evaluated at time $t+\Delta t$ respectively. Equation (6) is Newton-linearized to obtain the iterative equation

$$\left[\frac{3}{2}\frac{\mathbf{I}}{\Delta \mathbf{t}}-\mathbf{B}\right]\Delta\mathbf{Q}=\mathbf{R}(t+\Delta t)^n-\frac{1}{2\Delta t}[3\mathbf{Q}(t+\Delta t)^n - 4\mathbf{Q}(t)+Q(t-\Delta t)] \quad n=1, N_{\text{inner}} \qquad (7)$$

where $\Delta\mathbf{Q}=[\mathbf{Q}(t+\Delta t)^{n+1}-\mathbf{Q}(t+\Delta t)^n]$ and $\mathbf{Q}(t+\Delta t)^n$ is the nth estimate of $\mathbf{Q}(t+\Delta t)$. The parameter N_{inner} is the number of inner iterations required to reduce $\Delta\mathbf{Q}$ below a specified convergence tolerance, while $\mathbf{B}$ $(=\partial\mathbf{R}/\partial\mathbf{Q})$ is the flux Jacobian evaluated using $\mathbf{Q}(t+\Delta t)^n$. To minimize the memory required to store the Jacobian $\mathbf{B}$, the Euler fluxes are linearized with the Jacobian for a first-order accurate discretization. The only effect of this is to increase the number of inner iterations (N_{inner}) required to converge Eq. (7).

The implicit equation defined by Eq. (7) is solved with GMRES (*G*eneralized *M*inimal *Res*idual Method) (Saad and Schultz, 1986). Preconditioning is performed with block ILU(0) (incomplete lower-upper factorization with zero fill-in).

Grid Structure and Solution Adaptation. Grids for viscous simulations are obtained by first generating a thin structured mesh adjacent to solid surfaces and then filling the remainder of the solution domain with an unstructured grid consisting of roughly equilateral triangles. The initially quadrilateral cells in the thin structured mesh are bisected to form triangles. One set of grid lines in the structured mesh is constructed to be approximately normal to the solid surfaces to facilitate the calculation of wall coordinates (i.e., normal distances from the wall) and prevent the formation of highly obtuse triangles when the cells are subdivided during solution adaptation.

The grid is adapted to the solution in regions of high pressure gradient by quadrisecting the roughly equilateral cells and inserting additional wall normal grid lines in the initially structured layer (Fig. 2), as described in greater detail by Currie (1994). Adaptation of the grid to boundary layers is achieved by varying the stretching of the structured grid normal to the wall without changing the total thickness of the structured layer, which is typically 5 percent of blade chord. The stretching is prescribed according to a geometric stretching law so as to obtain a user-specified value of y_w^+ $(=\rho y_w\sqrt{(\tau_w/\rho)}/\mu_{\text{lam}}$ for wall coordinate y_w and wall shear stress $\tau_w)$ at the near-wall nodes (Currie, 1994).

Turbulence Modeling. Turbulence is modeled with the zonal $k-\omega/k-\epsilon$ "Shear Stress Transport" formulation of Menter (1993). This model uses the $k-\omega$ model of Wilcox (1988a, 1993) near walls and the high Reynolds number form of the $k-\epsilon$ model elsewhere. Transition from one model to the other is accomplished with "smart" blending functions derived and described by Menter.

The conservation equations for k and ω in Menter's zonal model can be written in conservative form as

$$\frac{\partial(h\mathbf{Q}_{\text{turb}})}{\partial t}+\text{div}\,(h\mathbf{F}_{\text{turb}})=\text{div}\,(h\mathbf{F}_{\text{v,turb}})+h\mathbf{H}_{\text{turb}} \qquad (8)$$

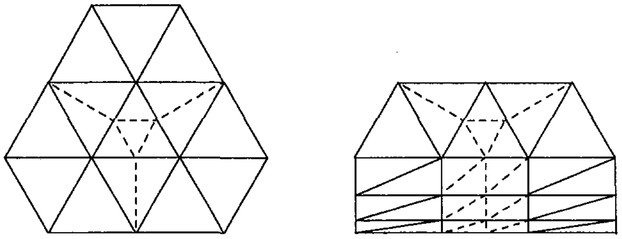

Fig. 2 Refinement strategies for cells in unstructured and (initially) structured regions

where

$$\mathbf{Q}_{\text{turb}}=\begin{Bmatrix}\rho k\\ \rho\omega\end{Bmatrix},\quad \mathbf{F}_{\text{turb}}=\begin{Bmatrix}\rho uk\\ \rho u\omega\end{Bmatrix}\mathbf{i}+\begin{Bmatrix}\rho vk\\ \rho v\omega\end{Bmatrix}\mathbf{j}$$

$$\mathbf{F}_{\text{v,turb}}=\begin{Bmatrix}\sigma_{xx}^k\\ \sigma_{xx}^\omega\end{Bmatrix}\mathbf{i}+\begin{Bmatrix}\sigma_{yy}^k\\ \sigma_{yy}^\omega\end{Bmatrix}\mathbf{j}$$

$$\mathbf{H}_{\text{turb}}=\begin{Bmatrix}G_k-\beta^*\rho\omega k\\ \dfrac{\rho\gamma}{\mu_{\text{turb}}}G_k-\beta\rho\omega^2+\dfrac{2(1-F_1)}{\omega}\rho s_{\omega 2}\left[\dfrac{\partial k}{\partial x}\dfrac{\partial\omega}{\partial x}+\dfrac{\partial k}{\partial y}\dfrac{\partial\omega}{\partial y}\right]\end{Bmatrix}$$

with $\beta^*=0.09$ and

$$\sigma_{xx}^k=(\mu_{\text{lam}}+s_k\mu_{\text{turb}})k_x,\quad \sigma_{xx}^\omega=(\mu_{\text{lam}}+s_\omega\mu_{\text{turb}})\omega_x$$

$$\sigma_{yy}^k=(\mu_{\text{lam}}+s_k\mu_{\text{turb}})k_y,\quad \sigma_{yy}^\omega=(\mu_{\text{lam}}+s_\omega\mu_{\text{turb}})\omega_y$$

$$G_k=\mu_{\text{turb}}\left\{2(u_x^2+v_y^2)+(u_y+v_x)^2+2\left(\frac{u}{h}\frac{dh}{dx}\right)^2\right\}$$

The parameter F_1 in the source term $\mathbf{H}_{\text{turb}}$ is a blending function, which equals unity for the $k-\omega$ model and zero for the $k-\epsilon$ model. Constants ϕ of the zonal model are calculated from constants ϕ_1 and ϕ_2 for the $k-\omega$ and $k-\epsilon$ models, respectively, by means of the expression $\phi=F_1\phi_1+(1-F_1)\phi_2$. The constants for the $k-\omega$ model (ϕ_1) are $s_{k1}=0.85$, $s_{\omega 1}=0.5$, $\beta_1=0.075$, and $\gamma_1=0.553$, while those for the $k-\epsilon$ model are $s_{k2}=1.0$, $s_{\omega 2}=0.856$, $\beta_2=0.0828$, and $\gamma_2=0.44$. Expressions for F_1 and μ_{turb} are given by Menter (1993).

Equation (8) is discretized on the median dual control volumes in the same manner as Eq. (1), although convective fluxes in the k and ω conservation equations are discretized with first-order upwind formulas for maximum robustness (Menter, 1993; Connell et al., 1993). The spatially discretized conservation equations for ρk and $\rho\omega$ at node n can be written in the form

$$\frac{d\mathbf{Q}_{\text{turb,n}}}{dt}=\mathbf{R}_{\text{turb,n}} \qquad (9)$$

where $\mathbf{R}_{\text{turb,n}}$ contains the convection, diffusion, and source terms. The same equation without the subscript n on $\mathbf{Q}_{\text{turb}}$ and $\mathbf{R}_{\text{turb}}$ applies to the full system of equations for all nodes.

To permit the turbulence model equations to be advanced in time with the same time step used to solve the flow equations, Eq. (9) is integrated with the first-order accurate backward Euler equation

$$\frac{\mathbf{Q}_{\text{turb}}(t+\Delta t)-\mathbf{Q}_{\text{turb}}(t)}{\Delta t}=\mathbf{R}_{\text{turb}}(t+\Delta t) \qquad (10)$$

Equation (10) is solved for $\mathbf{Q}_{\text{turb}}(t+\Delta t)$ using point Jacobi iteration after linearizing the source terms as described by Patankar (1987). Since $\mathbf{R}_{\text{turb}}(t+\Delta t)$ should strictly be evaluated with $\mathbf{Q}(t+\Delta t)$, just as $\mathbf{R}(t+\Delta t)$ in Eq. 6 should be evaluated using $\mathbf{Q}_{\mathrm{turb}}(t+\Delta t)$, Eq. (10) is solved after each inner iteration of Eq. (7) using the most recent estimate of $\mathbf{Q}(t+\Delta t)$. The resulting updated estimate of $\mathbf{Q}_{\mathrm{turb}}(t+\Delta t)$ is then used in the next inner iteration of Eq. (7).

The value of k is set to zero at no-slip boundaries (walls). Following the advice of Wilcox (1988a), the value of $\rho\omega$ at grid points where $y^+ \leq 2.5$ is obtained from the asymptotic relationship $\rho\omega \rightarrow 6\mu_{\mathrm{lam}}/\beta y_w^2$ as $y_w \rightarrow 0$. Although $\rho\omega \rightarrow \infty$ as $y_w \rightarrow 0$ according to this relationship, setting $(\rho\omega)_w \geq 60\mu_{\mathrm{lam}}/\beta y_{nw}^2$ at wall nodes yields a sufficiently large value in practice (Menter, 1993).

The modification of Zheng and Liu (1993), whereby ω is required to be greater than $3(G_k/\mu_{\mathrm{turb}})^{1/2}$, is used to improve the transition prediction capabilities of the $k-\omega$ model and avoid excessive values of μ_{turb} in regions where the production term (G_k) in the k equation is very large (Currie, 1994). Transition was allowed to occur at the locations predicted by the turbulence model.

Boundary Conditions. The no-penetration condition for walls is weakly enforced (i.e., enforced in an integral sense for each wall face). Walls are also assumed to be adiabatic. Periodic boundary conditions are applied by equating values of $\mathbf{Q}$, k, and ω at nodes on one periodic boundary to the values at matching nodes on the other. Total temperature, total pressure, and the experimental inlet flow angle are prescribed at the inlet, where the static pressure is obtained by zero-order extrapolation from the interior. The outlet static pressure (calculated from the experimental static pressure ratio) is specified at one point on the outflow boundary, where the axial velocity is subsonic. All other outflow boundary conditions are determined by first-order extrapolation from the interior. The values of k and ω at the outflow boundary are likewise determined by extrapolation from the interior while the values at inflow boundaries are specified. The inlet value of k (k_1) is given by $k_1 = 1.5*(Tu_1^* V_1)^2$, where Tu_1 and V_1 are the experimental inlet turbulence intensity and velocity, respectively. The inlet value of ω depends on the inlet turbulence length scale L_{turb} ($\omega = \sqrt{k}/(\beta^* L_{\mathrm{turb}})$, which is unknown. The results given below were found to be very insensitive to L_{turb} for the two values tried, however, which were $10^{-3}c$ and $0.1c$ (c = chord).

3 Results

Computational and experimental results have been obtained for vortex shedding in the NRC transonic turbine cascade. The blading in this cascade represents the midspan section of a nozzle tested both in an annular cascade and as part of a stage in the NRC highly loaded turbine (Williamson and Moustapha, 1986; Moustapha et al., 1987). Selected design parameters are included in the appendix, while more complete data, including blade coordinates, are given by Moustapha et al. (1993).

The cascade test rig is a continuously operating suction type facility with five nozzle passages (Moustapha et al., 1993). Photographic records of vortex shedding in the cascade were obtained with short ($\sim$1 μs) duration schlieren photographs, while quantitative measurements of shedding frequency (f_s) were obtained using high-frequency response pressure probes inserted into the path of the vortices, as well as with semiconductor (Kulite) transducers imbedded in the trailing edge. Base pressures were measured at the center of the trailing edge semicircle with conventional pneumatic taps. Tests were performed at M_2 of 0.84 to 1.28 (Fleige, 1994; Carscallen et al., 1996).

Vortex shedding was simulated at: (1) $M_2 = 1.16$ and the corresponding inlet total-to-outlet static pressure ratio (p_{o1}/p_2) of 2.3, and (2) $M_2 = 1.0$ and the corresponding total-to-static pressure ratio of 1.89. As mentioned in the introduction, the midspan losses peak at $M_2 = 1.0$ and then drop by $\sim$40 percent as M_2 is increased to 1.16. Vortex shedding is continuous at a frequency of $\sim$11 kHz at $M_2 = 1.0$ and intermittent at a frequency of $\sim$24–26.5 kHz at M_2= 1.16 (Fleige, 1994; Carscallen et al., 1996).

The streamtube thickness distribution ($h(x)$) at midspan required for the quasi-three-dimensional simulations was computed at $M_2 = 1.0$ and 1.16 by performing three-dimensional steady-state Navier–Stokes simulations, taking into account the (measured) inlet boundary layer. The resulting variations in streamtube thickness were found to be slight at both exit Mach numbers, with h ranging from a minimum of $0.98h_1$ ($h_1 = h$ at the inlet boundary) at the outlet boundary to a maximum of $1.006h_1$ at the trailing edge shock impingement point on the suction surface. The inlet and outlet boundaries were located $\sim 1.7c_{ax}$ (c_{ax} = axial chord) upstream of the leading edge and $\sim 2.9c_{ax}$ downstream of the trailing edge respectively in both the three-dimensional and subsequent quasi-three-dimensional simulations.

The computational grids for the quasi-three-dimensional simulations were obtained by first generating a structured grid around the blade and then meshing the region outside of the structured layer with triangles, as described previously. At this point, the grid contained 18,999 nodes and used 26 cells around the semicircular trailing edge. The flow solver was then run in solution-adaptive mode to refine the grid in the vicinity of shocks and vary the stretching of the nodes on the wall normals in the structured layer to achieve a uniform y^+ of $\sim$1 at all of the near-wall nodes outside of the base region. In addition, all of the triangles within a strip extending from the start of the trailing edge base circle to a location $\sim$2.1 axial chords downstream were quadrisected to improve the resolution of the vortex street. The width of the strip was $\sim 3d_{te}$ (d_{te} = trailing edge diameter = 6.35 mm). To further improve the resolution of the vortex street, all of the triangles within a slightly smaller strip $\sim 2d_{te}$ wide and extending $\sim$1.8 axial chords ($24d_{te}$) downstream of the trailing edge circle were quadrisected a second time. Finally, all of the cells within a small rectangle $\sim 1d_{te}$ wide and extending $\sim 2d_{te}$ downstream of the trailing edge circle were quadrisected yet again to improve the resolution of the pressure and suction surface separated shear layers, which were found to be excessively smeared without the last quadrisection. The trailing edge details of the final grid used in the simulation at M = 1.16, which contained 60,734 nodes, are shown in Fig. 3. The final grid for the simulation at $M_2 = 1$, which was obtained in the same way, contained 62,559 nodes. In the final grid, the size of the cells in the base region and the region where the pressure and suction surface separated shear layers merge (i.e., the confluence region) was $<\frac{1}{50}$th of d_{te}.

Steady-State Results. Initial conditions for all unsteady simulations were obtained from steady-state solutions at the same Mach number (i.e., back pressure). Vortex shedding was

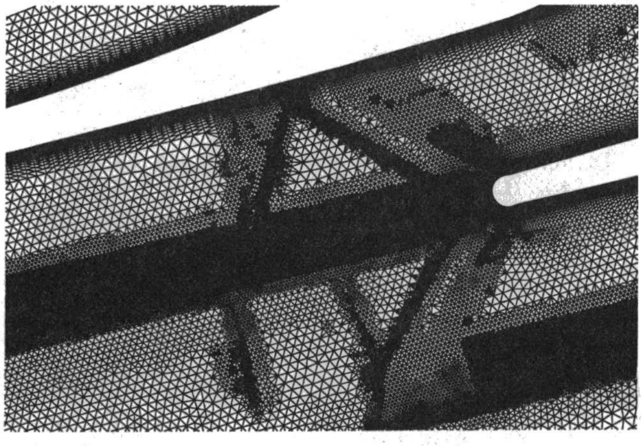

Fig. 3 Adapted grid at cascade trailing edge (M_2 = 1.16)

suppressed in these preliminary steady-state solutions by using a large time step.

Tables 1(*a*) and 1(*b*) compare steady-state results for base pressure (p_b), total pressure loss coefficient $\bar{C}_{po}$, and mixed-out total pressure loss coefficient $C_{po,\infty}$ to the corresponding experimental data for $M_2 = 1.16$ and 1.0 respectively. Predicted results are given for the initial (coarse) mesh, with 18,999 nodes, and the final (finest) mesh with ~60,000 nodes. The near-wall grid had been adapted in both cases to obtain a uniform y^+ of ~1 at all of the near-wall nodes outside of the base region, so the resolution of boundary layers would have been similar for the two grids.

To permit comparison with the experimental data, the base pressure figures in Tables 1(*a*) and 1(*b*) refer to the pressure at the midpoint of the trailing edge semicircle. The loss coefficient $C_{po,\infty}$ was obtained from the solution at the grid outlet boundary by assuming mixing of the flow at constant area.

The experimental loss coefficient $\bar{C}_{po}$ was calculated from total pressures measured with a nulled wedge probe at a traverse plane located 25 percent axial chord downstream of the trailing edge plane. The loss coefficient $\bar{C}_{po}$ is the pitchwise mean of C_{po}, where

$$C_{po} = \frac{p_{o1} - p_{o2}}{p_{o1} - p_2} \qquad (11)$$

is the local loss coefficient calculated with the cascade inlet (i.e., cell ambient) total pressure p_{o1}, pitchwise-average outlet static pressure p_2, and local total pressure p_{o2} at the traverse plane. The mixed-out loss coefficient is calculated from the same formula as C_{po} only with the mixed-out total and static pressures substituted for p_{o2} and p_2, respectively. It was not possible to calculate an experimental value of $C_{po,\infty}$ because the time-averaged probe data obtained in the unsteady blade wake did not provide all of the fluxes necessary to perform the mixing calculations.

At $M_2 = 1.16$ (Table 1(*a*)), the agreement between the experimental and computational values of $\bar{C}_{po}$ is better for the coarse grid than for the fine grid. The base pressure is lower for the coarse grid, however, so the higher loss was probably caused primarily by increased numerical diffusion of the trailing edge separated shear layers. These differences between the coarse and fine grid results are absent at $M_2 = 1.0$, when the trailing edge flow is subsonic, presumably because the classic triangular base region bounded by relatively long separated shear layers that exists for supersonic trailing edge flow is no longer present.

Table 1(*a*) Comparison of predicted (steady-state) and experimental base pressures and loss coefficients at $M_2 = 1.16$

	p_b/p_2	$\bar{C}_{po}$	$C_{po,\infty}$
Experiment	0.62±0.02	0.108	
Coarse mesh	0.67	0.113	0.149
Fine mesh	0.74	0.0845	0.110

Table 1(*b*) Comparison of predicted (steady-state) and experimental base pressures and loss coefficients at $M_2 = 1.0$

	p_b/p_2	$\bar{C}_{po}$	$C_{po,\infty}$
Experiment	0.61±0.07	0.174	
Coarse mesh	0.78	0.119	0.128
Fine mesh	0.78	0.113	0.126

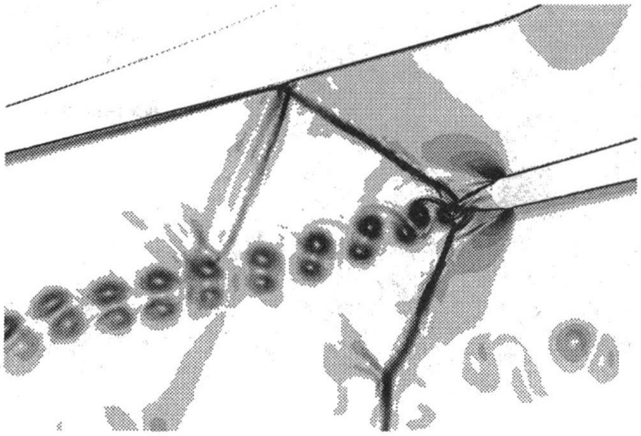

Fig. 4 Numerical schlieren of vortex street at $M_2 = 1.16$ after ~15 periods

Time-Accurate Results

$M_2 = 1.16$. It was not necessary to perturb the steady-state solutions to initiate vortex shedding. Figure 4 shows a numerical schlieren (gray-scale plot of the magnitude of the density gradient) of the trailing edge vortex street obtained ~0.55 ms after starting the simulation with the steady-state solution, while Fig. 5 shows a short-duration schlieren photograph obtained at the same conditions, as published by Carscallen and Gostelow (1994). The predicted f_s of ~26.1 kHz is in excellent agreement with the measured value of ~26.5 kHz (Fleige, 1994). Note that the vortices form downstream of the trailing edge at the confluence point of the suction and pressure surface separated shear layers.

At the experimental f_s of ~26.5 kHz, the 0.55 ms interval required to form the vortex sheet shown in Fig. 4 represents ~15 shedding periods. Figure 6 shows the appearance of the trailing edge wake after an additional 0.55 ms. At this point, the shear layers are no longer rolling up to form well-defined vortices, presumably because the mixing action of the vortices has entrained enough supersonic fluid from outside the wake (the flow downstream of the trailing edge shock system is supersonic at this M_2) to sufficiently reduce the length of the wake in which the flow is subsonic. It is assumed that the shear layers cannot roll up to form vortices unless a sufficient length of the wake (related to the vortex spacing) is subsonic, and the subsonic extent of the wake in Fig. 6 is similar to the vortex spacing in Fig. 4.

The simulation of vortex shedding was continued for a total time equivalent to several hundred shedding cycles (at 26.5 kHz). By that time, a repetitive pattern had emerged in which a burst of vortex shedding lasting less than ten cycles would be followed by a significantly longer period in which p_b would recover from its shedding value of $\sim 0.60 p_2$ to a peak value of $\sim 0.73 p_2$. The frequency of shedding, when it occurred, was always ~26 kHz.

Predicted and experimental values of p_b, $\bar{C}_{po}$ and $C_{po,\infty}$ are compared in Table 2, which includes the steady-state (fine grid) results from Table 1(*a*) for comparison purposes. The predicted values for the unsteady simulation represent time averages taken over a period spanning several cycles of shedding activity and inactivity. The relatively low value of $\bar{C}_{po}$ obtained in the unsteady simulation is believed to be due to an underestimation of the intermittency of vortex shedding, where the intermittency in this context is the fraction of time that shedding actually occurs, rather than to an underestimation of the loss sustained by the flow while shedding was actually occurring. While the intermittency was ~5 percent in the simulations, a statistical study of 170 schlierens indicates that it was ~50 percent in the experiments (Fleige, 1994).

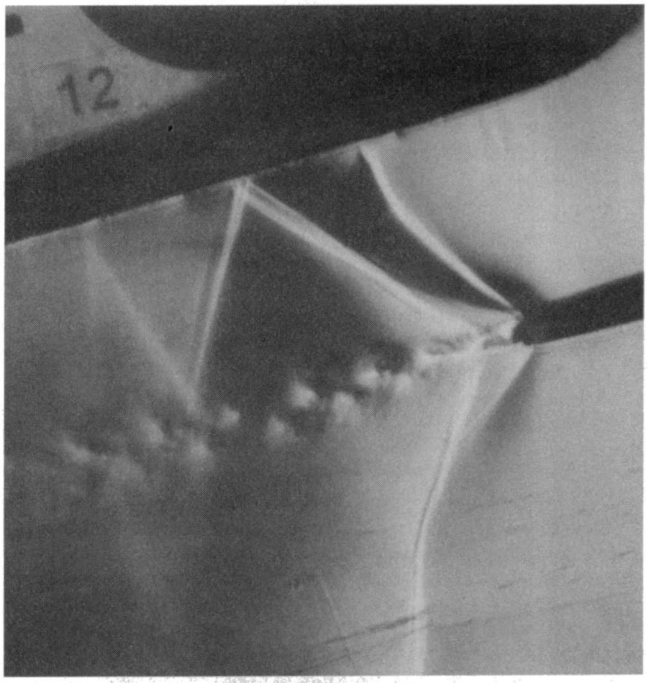

Fig. 5 Experimental schlieren of vortex street ($M_2 = 1.16$)

Table 2 Comparison of predicted and experimental base pressures and loss coefficients at $M_2 = 1.16$

	p_b	$\overline{C}_{po}$	$C_{po,\infty}$
Experiment	0.62±0.02	0.108	
Unsteady simulation	0.70	0.093	0.135
Steady simulation	0.74	0.0845	0.110

The manner in which p_{o2} in Eq. (11) was calculated from the results of the unsteady simulation requires explanation. To permit a meaningful comparison of the computed and experimental values of $\overline{C}_{po}$, it was necessary to evaluate p_{o2} in a manner that accounted, at least approximately, for the large high-frequency variations in both yaw angle (α) and Mach number that the wedge probe would have seen when it was positioned in the path of the vortices. Although it is known from calibration data that total pressures measured with the wedge probe used in the experiments do not require yaw angle correction for $\alpha < 10$ deg, it was necessary to estimate the yaw angle dependence for greater α. To that end, it was assumed that the dynamic component of the instantaneous total pressure (which was integrated with respect to time to obtain p_{o2}) should be computed with the component of the instantaneous velocity acting in the local time-averaged (i.e., nulled) flow direction. That component is designated V_{nd} (nd = *n*ulled *d*irection). For $M_{nd} > 1$, the total pressure thus calculated was further reduced by multiplying it by the stagnation pressure ratio ($p_{o,\text{downstream}}/p_{o,\text{upstream}}$) across a normal shock with $M_{\text{upstream}} = M_{nd}$. The result of this calculation was finally multiplied by the reciprocal stagnation pressure ratio ($p_{o,\text{upstream}}/p_{o,\text{downstream}}$) for a normal shock with an upstream Mach number equal to the local time-average value $\overline{M}$ (if $\overline{M} > 1$). The end result of this procedure was the instantaneous local total pressure, which was then integrated with respect to time to obtain p_{o2}. For steady flow, this procedure returns the true local total pressure for p_{o2}.

To check the predicted f_s for grid dependency, the unsteady simulation at $M_2 = 1.16$ was repeated with a grid in which the cells within a rectangle enclosing the separated shear layers and the confluence region were further quadrisected, thereby increasing the total number of nodes from 60734 to 86023. It was known from earlier simulations with coarser grids that the predicted f_s was very sensitive to the spatial resolution of the free shear layers. The f_s obtained after 0.55 ms in the repeat simulation, 25.3 kHz, was close to that obtained with the coarser grid, indicating that the latter was probably adequate, at least for predicting f_s. It is worth noting that the strong dependence of f_s on the state of the free shear layers has been noted in previous studies, both experimental (e.g., Sieverding and Heinemann, 1990) and theoretical, as summarized in a recent review of the literature on vortex shedding prepared by Cicatelli and Sieverding (1995).

$M_2 = 1.0$. Vortex shedding was continuous in the unsteady simulation at $M_2 = 1$, in accord with experiment. The flow is subsonic downstream of the trailing edge shock system at this Mach number, so entrainment of the fluid outside of the wake by vortex mixing does not cause the wake to become largely supersonic, as was the case at $M_2 = 1.16$. A well-developed vortex street had formed within 1.5 ms (~15 shedding periods at the measured f_s of ~10.6–11 kHz) after starting the simulation with the steady-state solution, while the losses had stabilized by ~10 ms (i.e., ~100 shedding periods). Figure 7 shows a numerical schlieren of the trailing edge vortex sheet at $t \approx 10$ ms, while Fig. 8 shows a short-duration schlieren photograph obtained at the same M_2, as published by Carscallen and Gostelow (1994). The predicted f_s of ~11 kHz is in very good agreement with the measured value of ~10.6–11 kHz (Fleige,

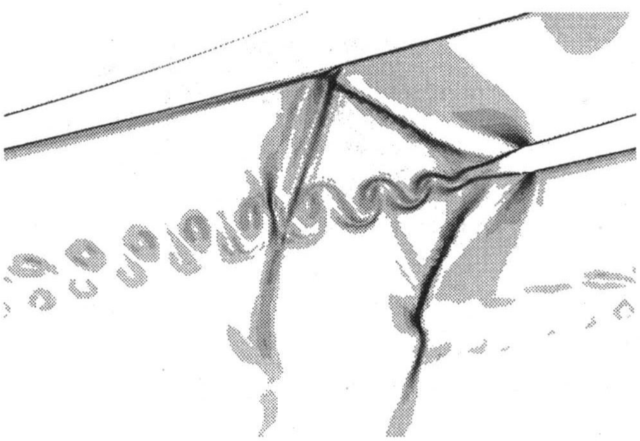

Fig. 6 Numerical schlieren of vortex street at $M_2 = 1.16$ after ~30 periods

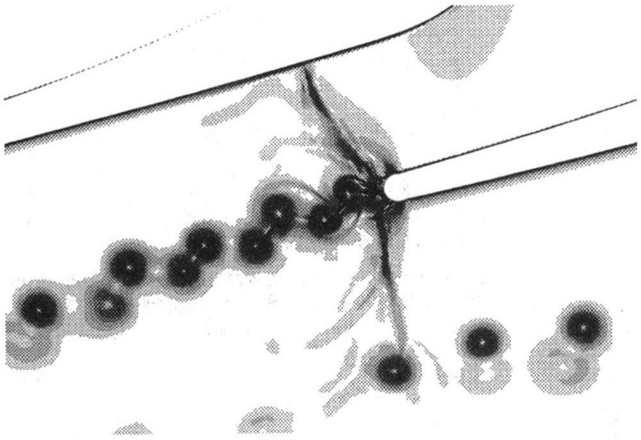

Fig. 7 Numerical schlieren of vortex street at $M_2 = 1.0$ after ~100 periods

Fig. 8 Experimental schlieren of vortex street at $M_2 = 1.0$

1994; Carscallen et al., 1996). Note that the vortices in Fig. 7 are larger and are shed closer to the trailing edge than those produced at the higher M_2 (Fig. 4), in accord with the experimental observations of Motallebi and Norbury (1981), Motallebi (1988), Carscallen and Gostelow (1994), Fleige (1994), and Carscallen et al. (1996).

Experimental values of p_b, $\bar{C}_{po}$, and $C_{po,\infty}$ are compared to the corresponding (time-average) computational results obtained at $t \approx 10$ ms in Table 3, which includes the steady-state predicted (fine grid) results from Table 1(*b*) for comparison purposes. It is believed that false entropy created by excessive numerical dissipation is largely responsible for the relatively low value of p_b predicted in the unsteady simulation, since the base drag is assumed to be directly related to the entropy generated during the formation and decay of the vortex street (Motallebi, 1988). Another possible explanation is that the pressure and suction surface boundary layers just upstream of the trailing edge were not modeled accurately, but this is considered less likely because significant errors in the boundary layer characteristics would have produced significant errors in f_s because of the above-mentioned sensitivity of f_s to the state of the separated free shear layers. The free shear layers are, of course, formed from the boundary layers. There is also experimental evidence (Sieverding and Heinemann, 1990) that p_b is insensitive to the state of the free shear layers, and thus also to the blade boundary layers prior to separation.

Three-dimensional effects and other experimental factors, such as acoustic interference from test cell and downstream noise sources (compressor, control valve, etc.), departures from the instantaneous periodicity assumed in the simulations (i.e., weaker coupling to the shedding from adjacent blades), etc., could also have contributed to the poor agreement for p_b.

Table 3 Comparison of predicted and experimental base pressures and loss coefficients at $M_2 = 1.0$

	p_b	$\bar{C}_{po}$	$C_{po,\infty}$
Experiment	0.61±0.07	0.174	
Unsteady simulation	0.42	0.168	0.231
Steady simulation	0.78	0.113	0.126

Mixing Analysis. When the NRC cascade is choked, as it is at $M_2 = 1.0$ and 1.16, the effect of variations in p_b on $C_{po,\infty}$ can be predicted from a simple mixing analysis. To demonstrate this, consider the dashed line control volume with boundary points a, b, c, d, e, f, and g shown in Fig. 9. Points b and g are located at the intersections of the trailing edge semicircle and the pressure and suction surfaces, respectively, while point a is positioned on the suction surface so that the straight line segment $a-b$ is perpendicular to a straight line joining points a and g. Lines $b-d$ and $f-e$ are parallel to the line joining a to g, while $e-d$ is parallel to $a-b$. Boundary curve $f-g$ coincides with the trailing edge semicircle, while curve $a-g$ follows the contour of the suction surface.

Boundary segments $f-e$ and $b-c$ are periodic, so all of the fluxes through them cancel. The flow through outlet boundaries $e-d$ and $c-d$ is assumed to be fully mixed out. If changes in the streamtube height h between the inlet and outlet boundaries are neglected, the mass and momentum conservation equations for the control volume are

Mass

$$\int_{a-b} \rho U dY = (\rho_\infty U_\infty)(Y_d - Y_e) + (\rho_\infty V_\infty)(X_d - X_c) \qquad (12)$$

X Momentum

$$\int_{a-b} (\rho U^2 + p) dY + \int_{a-g} p dY + \int_{f-g} p dY + \int_{a-g} \tau_w dX$$
$$= (\rho_\infty U_\infty^2 + p_\infty)(Y_d - Y_e) + (\rho_\infty U_\infty V_\infty)(X_d - X_c) \qquad (13)$$

Y Momentum

$$\int_{a-b} (\rho U V) dY + \int_{a-g} p dX + \int_{f-g} p dX$$
$$= (\rho_\infty U_\infty V_\infty)(Y_d - Y_e) + (\rho_\infty V_\infty^2 + p_\infty)(X_d - X_c) \qquad (14)$$

where the X axis is parallel to a straight line joining a to g and the Y axis is normal to it (Fig. 9). The velocities U and V are the components in the X and Y directions, respectively.

Since the curvature of the uncovered section of the suction surface is convex for the NRC cascade, point a is slightly upstream of the point of intersection of the throat with the suction surface, designated point h. The separation between points a and h is small, however, because the angle between tangents to the suction surface at points h and g (i.e., the suction surface curvature) is only 2.9 deg. Because line $a-b$ is slightly upstream of the throat, the fluxes of mass, momentum, and energy through $a-b$ will be the same with and without shedding when the cascade is choked. These fluxes can therefore be obtained from a steady-state calculation.

If it is assumed that the base pressure distribution around the trailing edge semicircle is approximately symmetric about the midpoint of the curve, the line integral of pressure over curve $f-g$ in Eq. (14) can be neglected. The line integral of pressure over curve $a-g$ in Eq. (13) can also be neglected if (1) the suction surface is almost flat, so that the maximum value of $(Y - Y_a)$ on curve $a-g$ is small compared to d_{te}, and/or (2) the pressure acting over the fraction of the directed curve with increasing Y roughly equals that over the fraction with decreasing Y. Both of these conditions are satisfied for the NRC cascade, where the maximum $(Y - Y_a)$ value of curve $a-g$ is $0.16 d_{te}$. If p_b is known, it is assumed that the line integral of pressure over curve $f-g$ in Eq. (13) can be approximated as $p_b d_{te}$.

Assuming constant total temperature T_o and using the appropriate form of the energy equation, Eqs. (12) and (13) can be solved simultaneously for specified values of p_b and p_∞ ($p_\infty \simeq$

p_2 in general) to obtain ρ_∞, U_∞, and V_∞. The mixed-out total pressure and thus loss can then be calculated. If required, the X integral of pressure over curve $a-g$ can be obtained from Eq. (14). Because $(X_g - X_a) \simeq (X_d - X_c)$ and the pressure integrals in Eq. (14) are much larger than the remaining terms, the average suction surface pressure over $a-g$ is $\sim p_\infty$.

With the fluxes across $a-b$ and the integrals of pressure over $f-g$ and τ_w over $a-g$ in Eq. (13) obtained from the results of the steady-state simulation at $M_2 = 1$, a mixing analysis gives $C_{po,\infty} = 0.126$, in perfect agreement with the fine grid computational result. When the integral of pressure over $f-g$ is then replaced by $p_b d_{te}$, with p_b set to the value of $0.42p_2$ computed in the unsteady simulation, $C_{po,\infty}$ increases to 0.246. The difference between this value and the corresponding numerical result of 0.231 can probably be attributed to the use of an approximate representation of the time-average integral of pressure over $f-g$ in Eq. (13). These results, and similar ones obtained at $M_2 = 1.16$, indicate that the base pressures predicted in the unsteady simulations are at least consistent with the predicted values of $C_{po,\infty}$, if not always with the measured values of p_b.

To illustrate the significant dependence of loss on p_b, it is worth noting that the value of $C_{po,\infty}$ predicted at $M_2 = 1.0$ with the measured p_b of $0.61p_2$ is 0.192. This figure is 52 percent higher than the $C_{po,\infty}$ of 0.126 obtained with what is believed to be a realistic estimate of the base pressure without shedding, $0.78p_2$.

The rate of entropy production associated with the formation and decay of the vortex street ($\dot{s}_v$) is assumed to equal the total rate of entropy production predicted in the mixing analysis (or unsteady Navier–Stokes simulation) from the inflow and outflow (mixed-out) entropies and mass flow rate, less the rate of entropy production in the blade boundary layers and trailing edge shocks. By calculating $\dot{s}_v$ using the results of the unsteady simulation at $M_2 = 1.0$ and using a similar procedure to calculate the rate of entropy production between the trailing edge and the downstream traverse plane, it has been determined that the latter is only ~20 percent of $\dot{s}_v$. This indicates that the rate of entropy production associated with the formation of the vortex street is significantly less than that associated with its decay and that the decay probably occurs over a distance significantly larger than typical spacings between blade rows. The mixed-out loss is still considered to be a meaningful measure of the effective loss in this case, however, because it is difficult to conceive how a significant fraction of the kinetic energy of the spinning fluid in the vortices could be recovered by a downstream blade row.

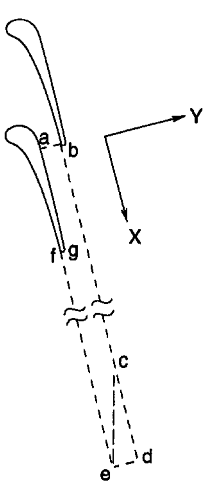

Fig. 9 Mixing analysis control volume

4 Conclusions

Vortex shedding in the NRC transonic turbine cascade has been simulated at exit Mach numbers of 1.0 and 1.16. Very good agreement between the computed and experimental vortex street configurations and shedding frequencies has been obtained in both cases. The accuracy of the shedding frequency predictions indicates that the blade boundary layers and trailing edge separated free shear layers were modeled satisfactorily. Although not described in the paper, virtually identical results to those obtained with the zonal $k-\omega/k-\epsilon$ turbulence model have been obtained with the Wilcox multiscale Reynolds stress formulation (Wilcox, 1988b). Although the differences between the two turbulence models may have been masked somewhat by numerical diffusion, these results suggest that the simpler eddy-viscosity type of model is probably adequate for shedding simulations similar to those presented.

At $M_2 = 1$, where vortex shedding is continuous, the mixed-out total pressure loss coefficient predicted with vortex shedding is 83 percent higher than the steady-state value. While this figure is undoubtedly inflated by the inevitable total pressure loss produced by numerical dissipation, the corresponding figure predicted using the measured base pressure in a mixing analysis is still 52 percent, providing strong evidence that vortex shedding is a major loss mechanism in this cascade at this Mach number. The simulation results also confirm that it is a reduction in the intensity of vortex shedding that causes the loss to decrease by ~40 percent as the exit Mach number is increased from 1.0 to 1.16.

References

Barth, T. J., 1987, "Analysis of Implicit Local Linearization Techniques for Upwind and TVD Algorithms," Paper No. AIAA-87-0595.

Barth, T. J., and Jespersen, D. C., 1989, "The Design and Application of Upwind Schemes on Unstructured Meshes," Paper No. AIAA-89-0366.

Barth, T. J., 1991, "Numerical Aspects of Computing Viscous High Reynolds Number Flows on Unstructured Meshes," Paper No. AIAA-91-0721.

Barth, T. J., 1992, "Aspects of Unstructured Grids and Finite-Volume Solvers for the Euler and Navier–Stokes Equations," in: *Unstructured Grid Methods for Advection Dominated Flows,* AGARD-R-787, Paper No. 6.

Bryanston-Cross, P. J., and Camus, J. J., 1982, "Auto and Cross-Correlation Measurements in a Turbine Cascade Using a Digital Correlator," ASME Paper No. 82-GT-132.

Carscallen, W. E., and Gostelow, J. P., 1994, "Observations of Vortex Shedding in the Wake From Transonic Nozzle Vanes," *Proc. ISROMAC 5* (Int. Symp. Rotating Machinery).

Carscallen, W. E., Fleige, H., and Gostelow, J. P., 1996, "Transonic Turbine Vane Wake Flows," ASME Paper No. 96-GT-419.

Cicatelli, G., and Sieverding, C. H., 1995, "A Review of the Research on Unsteady Turbine Blade Wake Characteristics," presented at the AGARD PEP Symposium on Loss Mechanisms and Unsteady Flows in Turbomachines, Derby, May 8–12.

Connell, S. D., Holmes, D. G., and Braaten, M. E., 1993, "Adaptive Unstructured 2D Navier–Stokes Solutions on Mixed Quadrilateral/Triangular Meshes," ASME Paper No. 93-GT-99.

Currie, T. C., 1994, "Navier–Stokes Simulation of Separated Flows in Transonic Compressor Cascades," *Proc. CFD 94,* Second Annual Conference of the CFD Society of Canada, 1–3 June, Toronto, Ontario, Canada.

Dawes, W. N., Camus, J. J., Xu, L. P., and Graham, C. G., 1987, "Measured and Predicted Loss Generation in Transonic Turbine Blading," in: *Transonic and Supersonic Phenomena in Turbomachines,* AGARD CP-401, Paper No. 8.

Fleige, H., 1994, "Investigation of Unsteady Wakes From Transonic Turbine Nozzle Vanes," Diploma-Thesis, Institute for Turbomachinery, University of Hannover, Nov.

Gnoffo, P. A., 1986, "Application of Program Laura to Three-Dimensional AOTV Flowfields," Paper No. AIAA-86-0565.

Gostelow, J. P., 1984, *Cascade Aerodynamics,* Pergamon Press.

Haller, B. R., 1980, "The Effects of Film Cooling on the Aerodynamic Performance of Transonic Turbine Blades," Ph.D. thesis, Cambridge University, United Kingdom.

Heinemann, H. J., Lawaczeck, O., and Butefisch, K. A., 1975, "Von Karman Vortices and Their Frequency Determination in the Wakes of Profiles in the Sub- and Transonic Regimes," IUTAM Symposium Transsonicum II, Sept. 8–13, Göttingen.

Heinemann, H. J., and Butefisch, K. A., 1978, "Determination of the Vortex Shedding Frequency of Cascades With Different Trailing Edge Thicknesses," AGARD CP-227.

Hirsch, C., 1990, *Numerical Computation of Internal and External Flows,* Vol. 2, Thomson Press.

Lawaczeck, O., and Heinemann, H. J., 1976, "Von Karman Vortex Streets in the Wakes of Subsonic and Transonic Cascades," AGARD CP-177.

Liou, M. S., and van Leer, B., 1988, "Choice of Implicit and Explicit Operators for the Upwind Differencing Scheme," Paper No. AIAA-88-0624.

Menter, F. R., 1993, "Zonal Two-Equation $k-\omega$ Turbulence Models for Aerodynamic Flows," Paper No. AIAA-93-2906.

Motallebi, F., and Norbury, J. F., 1981, "The Effect of Base Bleed on Vortex Shedding and Base Pressure in Compressible Flow," *Journal of Fluid Mechanics*, Vol. 110, p. 273.

Motallebi, F., 1988, "Base Pressure in Transonic Speeds—A Comparison Between Theory and Experiment," ASME Paper No. 88-GT-132.

Moustapha, S. H., Okapuu, U., and Williamson, R. G., 1987, "The Influence of Rotor Blade Aerodynamic Loading on the Performance of a Highly Loaded Turbine Stage," ASME JOURNAL OF TURBOMACHINERY, Vol. 109, pp. 155–162.

Moustapha, S. H., Carscallen, W. E., and McGeachy, J. D., 1993, "Aerodynamic Performance of a Transonic Low Aspect Ratio Turbine Nozzle," ASME JOURNAL OF TURBOMACHINERY, Vol. 115, pp. 400–408.

Nash, J. F., 1963, "An Analysis of Two-Dimensional Turbulent Base Flow Including the Effect of Approaching Boundary Layer," ARC R&M 3344.

Nash, J. F., Quincey, V. G., and Callinan, J., 1966, "Experiments on Two-Dimensional Base Flow at Subsonic and Transonic Speeds," ARC R&M 3427.

Patankar, S. V., 1987, "Elliptic Systems: Finite-Difference Method I," *Numerical Heat Transfer*, Vol. II, Chap. 6, Springer-Verlag.

Roe, P. L., 1981, "Approximate Riemann Solvers, Parameter Vectors, and Difference Schemes," *J. Comp. Phys.*, Vol. 43, No. 2, pp. 357–372.

Saad, Y., and Schultz, M. H., 1986, "GMRES: A Generalized Minimal Residual Algorithm for Solving Non-symmetric Linear Systems," *SIAM J. Sci. Stat. Comput.*, Vol. 7, No. 3.

Sieverding, C. H., 1977, "Unsteady Flow Measurements in Straight Cascades," *Proc. Symp. Measuring Techniques in Transonic and Supersonic Cascades and Turbomachines*, Lausanne.

Sieverding, C. H., and Heinemann, H., 1990, "The Influence of Boundary Layer State on Vortex Shedding From Flat Plates and Turbine Cascades," ASME JOURNAL OF TURBOMACHINERY, Vol. 112, pp. 181–187.

Tanner, M., 1978, "Two Different Theoretical Approaches to the Base Pressure in Two-Dimensional Supersonic Flow," *Aeronautical Quarterly*, Vol. XXIX, May.

Van Leer, B., 1979, "Towards the Ultimate Conservative Difference Scheme. V. A Second Order Sequel to Gudonov's Method," *Journal of Computational Physics*, Vol. 32, pp. 101–136.

Vuillez, C., and Veuillot, J. P., 1990, "Quasi-3D Viscous Flow Computations in Subsonic and Transonic Turbomachinery Bladings," Paper No. AIAA-90-2126.

Wilcox, D. C., 1988a, "Reassessment of the Scale-Determining Equation for Advanced Turbulence Models," *AIAA Journal*, Vol. 26, No. 11 (Nov.), pp. 1299–1310.

Wilcox, D. C., 1988b, "Multiscale Model for Turbulent Flows," *AIAA Journal*, Vol. 26, No. 11, Nov., pp. 1311–1320.

Wilcox, D. C., 1993, "A Two-Equation Turbulence Model for Wall-Bounded and Free-Shear Flows," Paper No. AIAA-93-2905.

Williamson, R. G., and Moustapha, S. H., 1986, "Annular Cascade Testing of Turbine Nozzles at High Exit Mach Numbers," ASME *Journal of Fluids Engineering*, Vol. 108, pp. 313–320.

Zheng, X., and Liu, F. 1993, "Numerical Solution of Navier–Stokes Equations and $k-\omega$ Turbulence Model Equations Using a Staggered Upwind Method," Paper No. AIAA-93-2968.

APPENDIX A

Cascade Design Parameters

Inlet total temperature, T_{o1}	293 K
Inlet total pressure, p_{o1}	1.013×10^5 Pa
Pressure ratio	2.3
Inlet Mach number, M_1	0.11
Inlet incidence	−10 deg
Isentropic exit Mach number, M_2	1.16
Blade chord, c	204 mm
Axial blade chord, c_{ax}	84.7 mm
Stagger angle	65.5 deg
Pitch	147.8 mm
Span	112.8 mm
Nozzle turning angle	76 deg
Nozzle throat opening	30.9 mm
Trailing edge diameter, d_{te}	6.35 mm

Measurements and Prediction of the Effects of Surface Roughness on Profile Losses and Deviation in a Turbine Cascade

R. J. Kind

P. J. Serjak

M. W. P. Abbott

Department of Mechanical and Aerospace Engineering,
Carleton University,
Ottawa, Ontario, Canada K1S 5B6

Measurements of pressure distributions, profile losses, and flow deviation were carried out on a planar turbine cascade in incompressible flow to assess the effects of partial roughness coverage of the blade surfaces. Spanwise-oriented bands of roughness were placed at various locations on the suction and pressure surfaces of the blades. Roughness height, spacing between roughness elements, and band width were varied. A computational method based on the inviscid/viscous interaction approach was also developed; its predictions were in good agreement with the experimental results. This indicates that good predictions can be expected for a variety of cascade and roughness configurations from any two-dimensional analysis that couples an inviscid method with a suitable rough surface boundary-layer analysis. The work also suggests that incorporation of the rough wall skin-friction law into a three-dimensional Navier–Stokes code would enable good predictions of roughness effects in three-dimensional situations. Roughness was found to have little effect on static pressure distribution around the blades and on deviation angle, provided that it does not precipitate substantial flow separation. Roughness on the suction surface can cause large increases in profile losses; roughness height and location of the leading edge of the roughness band are particularly important. Loss increments due to pressure-surface roughness are much smaller than those due to similar roughness on the suction surface.

Introduction

Turbine blades in gas turbine engines can become rough as a result of corrosion, erosion, and/or deposition during operation. Turbine and engine efficiencies can deteriorate significantly as a result. This paper describes experimental and computational work on the effects of roughness on turbine blade-row performance. It presents experimental results, shows how the effects of roughness can be predicted, and validates the prediction methodology.

Taylor (1990) and Tarada and Suzuki (1993) have measured roughness on turbine blades removed from aero and industrial engines. Tarada and Suzuki found some tendency for roughness to increase with in-service time, but roughness heights varied widely and no other distinct trends were identified. After a few thousand in-service hours roughness heights typically were in the range 20–150 μm centerline average (CLA). Roughness height generally varied greatly around the blade profiles, with the greatest roughness usually about midway along the pressure surface, but sometimes on the suction surface fairly near the leading edge. A correlation developed by Koch and Smith (1976) indicates that 20–150 μm CLA corresponds to standard Nikuradse (1950) sand roughness heights, k_s, from 125 to 950 μm or k_s/c from 0.0025 to 0.02 for a typical blade chord length, c, of about 50 mm. Bammert and Sandstede (1972, 1976) carried out experiments on a four-stage turbine with all blades uniformly covered with sand roughness. Four k_s/c values ranging from 0.001 to 0.01 were tested; best efficiency of the turbine dropped 7 to 14 percentage points due to the roughness. Boynton et al. (1992) found a stage efficiency increase of 2.1 percent when the rough coating, $k_s/c \approx 0.004$, of the turbine rotor blades of the Space Shuttle main engine high-pressure fuel turbopump was polished smooth. Clearly surface roughness can cause substantial deterioration of turbine efficiency.

The present paper focuses on the effects of roughness on the performance of an individual blade row. The main objective was to improve understanding and prediction capabilities for profile losses and flow turning for turbine cascades with partial roughness coverage of various types. The ultimate aim is to improve engine health monitoring capabilities by enabling prediction of roughness effects on turbine maps and engine operating parameters (e.g., Cue and Muir, 1991).

Experiments were carried out on a large-scale low-speed planar turbine cascade. Blade Reynolds numbers were comparable to those in small gas turbine engines. Smooth and roughened blades were tested. A three-hole pneumatic probe was traversed downstream of the central blade of the cascade to determine profile losses and flow exit angle for various incidence angles and roughness configurations. Static pressure distributions around the blade were also measured at midspan. Roughness consisted of sparsely distributed sand grains applied in spanwise-oriented bands of various widths and at various locations on the blades. Three sizes of sand grains were used, corresponding to k/c values 0.0021, 0.0045, and 0.0063, where k is the nominal grain diameter.

The work included development of a prediction method based on the viscous/inviscid interaction approach. Inviscid computations were done using a vortex panel method with source distributions to represent boundary-layer displacement effects. Dvorak's (1969) method and a modification of it were used to

---

Contributed by the International Gas Turbine Institute and presented at the 41st International Gas Turbine and Aeroengine Congress and Exhibition, Birmingham, United Kingdom, June 10–13, 1996. Manuscript received at ASME Headquarters February 1996. Paper No. 96-GT-203. Associate Technical Editor: J. N. Shinn.

calculate turbulent boundary layer development along the smooth or rough blade surfaces. This approach is appropriate for the two-dimensional incompressible flow of the experiments; it incorporates the effects of roughness at least as accurately and reliably as Navier–Stokes methods and is very much faster. Agreement between experiment and predictions was good.

Measurements on cascades of rough turbine blades have also been carried out by Speidel (1954) and by Bammert and Sandstede (1980). The entire surfaces of their blades were covered with closely spaced sand roughness; their highest value of k_s/c was only 0.003, which is at the lower end of the range of typical in-service values, mentioned earlier. Speidel presents pressure distribution, profile loss, and deviation angle data; Bammert and Sandstede present pressure distribution and boundary-layer development data. The present experiments were confined to cases with only partial roughness coverage and with most k_s/c values well above 0.003, because this is more typical of roughness that develops during engine operation and the work was directed at engine health monitoring. Bolcs and Sari (1988) did cascade measurements on turbine blades having a relatively thick rough deposit on the downstream portion of the pressure surface. Their tests were at transonic Mach numbers and they were mainly interested in the effects of the roughness and shape change on shock wave structure and stability.

Description of Experiments

A low-speed open circuit cascade wind tunnel was used for the experimental work. The linear cascade of five blades was mounted on a turntable, allowing measurements over a range of incidence angles. The tested cascade geometry corresponded to that at midheight of the power turbine rotor of a small aero engine of recent design. It had a space-to-chord ratio of 0.68, the blades were set at a stagger angle of 21.6 deg and blade inlet and exit metal angles were 25.5 and 57.5 deg, respectively, to the axial direction. The design incidence angle was 3.0 deg. Maximum and trailing-edge thickness-to-chord ratios were 0.20 and 0.026, respectively. The profile coordinates are available from Serjak (1995). The blade chord was 162.3 mm and the nominal inlet flow velocity was 30 m/s, giving a Reynolds number of 3×10^5 based on chord and inlet velocity. Turbulence intensity at inlet to the cascade was about 0.3 percent.

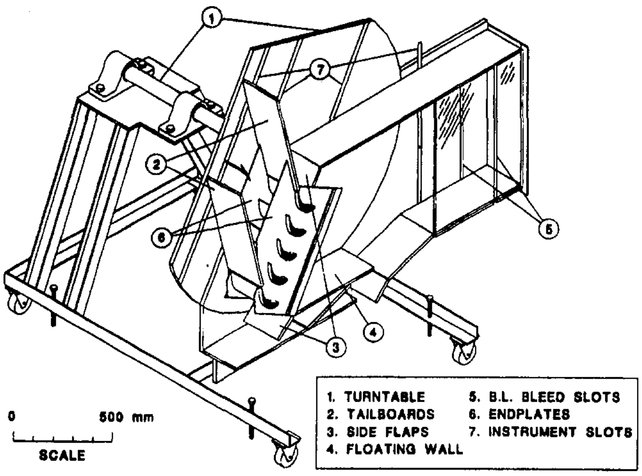

Fig. 1 Cascade tunnel test section

As shown in Fig. 1, the test section was fitted with top and bottom flaps, bypass flaps, and a floating lower wall to allow for adjustment of inlet-flow uniformity and exit-flow periodicity. The span of the cascade was only 200 mm. To assist in obtaining a core region of two-dimensional flow, it was fitted with endplates located about 2.5 cm inboard of the sidewalls to the test section. The small divergence angle between these endplates could be adjusted such that the ratio of inlet to exit mean axial velocity was unity at midspan, as required for two-dimensional incompressible flow. Uniformity, periodicity, and axial velocity ratio (AVR) were assessed by detailed traverses of the flow at midspan for each incidence angle and roughness configuration. The flaps and endplates were adjusted for each configuration using a trial and error process. Over the two central flow passages, inlet flow angle was maintained within ±0.5 deg of zero, axial velocity ratio within ±0.01 of unity, and exit flow angles within 0.5 deg of periodic for all test cases. Typical outlet flow angle and total pressure distributions are shown in Fig. 2. Traverses at a variety of spanwise positions showed nearly uniform profile loss over the central 20 percent of the overall blade span for incidence angles of 10 deg, with wider uniform regions for lower incidences. This suggests that the flow was indeed two dimensional in the midspan plane. This is supported by the good agreement between measured blade static pressure distributions and those predicted by a two-dimensional calculation method, as discussed later. Rodger et al. (1992)

Nomenclature

C_p = static pressure coefficient = $(p - p_1)/q_1$
C_{pt} = local total-pressure loss coefficient = $(P_{o1} - p_t)/q_1$
c = blade chord length
c_x = axial-chord length
i = incidence angle = (α_1 − inlet metal angle)
k = average height of roughness elements
k_s = height of standard-sand roughness
N = number of panels on each blade
P_o = mass-weighted mean total pressure in a blade-to-blade streamtube
p = static pressure
p_t = local total pressure
q = mass-weighted mean dynamic pressure in a blade-to-blade streamtube
S = spacing between blades
s = arc distance along blade surface
U = flow velocity
u^* = local friction velocity in boundary layer
x = chordwise distance from leading edge
Y = loss coefficient; see Eq. (1)
y = pitchwise position
α = mass-weighted mean flow angle in a blade-to-blade streamtube, with respect to axial
γ = local strength of vortex sheets
δ = flow deviation angle = (exit metal angle − α_2)
δ^* = boundary-layer displacement thickness
Δs = arc width of roughness band
θ = boundary-layer momentum-defect thickness
λ = roughness spacing parameter; see Eq. (2)
ν = kinematic viscosity

Subscripts and Abbreviations

AVR = axial velocity ratio
1 = cascade inlet
2 = cascade exit
des = design incidence
e = outer edge of boundary layer
l = lower or pressure surface of blades
m = junction-point index in the panel method
p = profile
rle = leading edge of roughness band
te = trailing edge of blades
tet = trailing-edge-thickness
u = upper or suction surface of blades

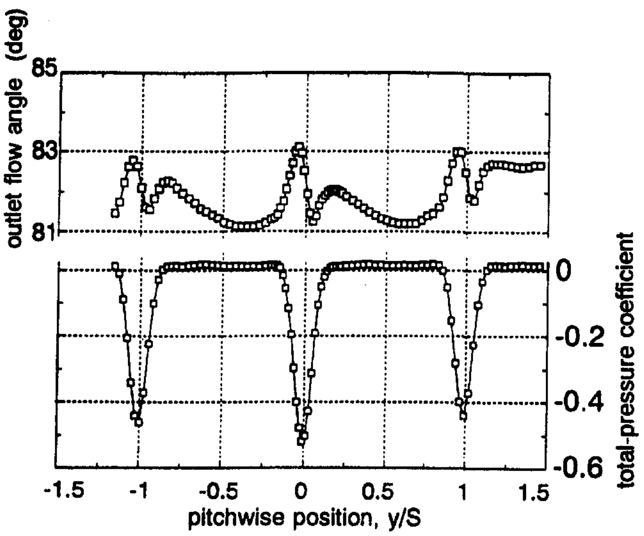

Fig. 2 Typical pitchwise distributions of flow angle and total pressure in outlet traverse plane at midspan (design incidence)

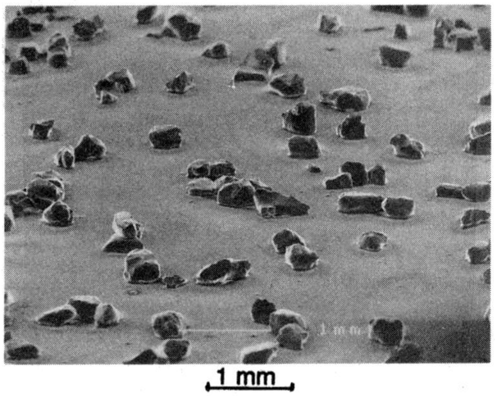

Fig. 3 Scanning electron microscope photograph of the roughness on a blade

discuss the methods for obtaining good flow quality in more detail.

The profile loss and flow angle data were obtained using a carefully calibrated three-hole pressure probe operated in the nonnulling mode. The probe tip was 2 mm high by 0.7 mm wide. The probe was aligned with the nominal flow direction and flow angles inferred from probe readings are accurate within ±0.5 deg while dynamic and total pressures are accurate within ±1 percent of the local dynamic pressure. Readings were found to be insensitive to out-of-plane flow angles less than 10 deg. The probe was traversed using a computer-controlled traverse gear and positioning accuracy was better than 0.01 mm. The traverse planes were 90 mm and 60 mm upstream and downstream of the cascade leading and trailing edges, respectively; this corresponds to 60 and 40 percent of axial chord, respectively.

Pressure instrumentation consisted of two transducers. One, 7 kPa (1 psid), was used to measure the reference dynamic pressure sensed by a Pitot probe in the inlet measurement plane, and the other, 3.5 kPa (0.5 psid), was used with a 48-port Scanivalve system to measure the three-hole probe pressures and the static pressures around the pressure tapped blade. Both transducers were referenced to the pressure sensed by a static tap in the test-section sidewall upstream of the cascade. Estimated accuracy is ±0.01 kPa for both transducers. The data were acquired and processed by a computer data acquisition system. Each reading consisted of the average of 110 samples taken over a period of 20 seconds. A 20 second pause was allowed between steps of the Scanivalve. The prevailing reference dynamic pressure was used in determining pressure coefficients to minimize the effects of any small drifts in tunnel operating conditions. These procedures were found to give stable repeatable results.

A stethoscope connected to a Pitot tube held on the blade surface was used to determine whether the flow in the blade boundary layer was laminar or turbulent.

The main experimental results are the deviation angle and profile-loss coefficient values for the tested configurations. The deviation angle is the difference between the exit metal angle and the mass-weighted mean flow exit angle in a blade-to-blade passage at midspan. The profile loss coefficient is defined as

$$Y_p = (P_{01} - P_{02})/q_2 \qquad (1)$$

where P_{02} and q_2 are the mass-weighted mean total pressure and dynamic pressure, respectively, in a blade-to-blade streamtube at midspan far downstream of the cascade. The actual losses measured at the downstream traverse plane have been converted to fully mixed-out losses by assuming constant area mixing.

The test cascade consisted of the same five blades for measurements with and without roughness, except when blade static pressure distributions were being measured. In the latter case a blade of identical shape, fitted with 43 static taps around its perimeter at midspan, was substituted for the central blade. Static taps in the roughened region were blocked. In all cases the roughness was statistically the same on all five blades of the test cascade. The blades were precisely positioned on a backing plate with the aid of locator pins; thus they could be readily removed for alteration of the roughness configuration and precisely re-installed.

The roughness consisted of sand grains distributed somewhat sparsely. The roughness height, k, is equal to the average size of the sand grains. Three grain sizes were used: 338, 722, and 1020 μm nominal diameter, corresponding to k/c values of 0.0021, 0.0045, and 0.0063. These grain sizes are the averages of the opening sizes of the passing and retaining sieves, 425–250, 850–594, and 1190–850 μm, respectively. These sizes will be referred to as "small," "medium," and "large." The sand grains were adhered to the blade surfaces by a strippable vinyl coating (CROWN Vinyl Strippable Coating #68040). Figure 3 is a scanning electron microscope photograph of typical adhered sand grains; clearly the adhesive has little effect on the shape of the roughness elements. The spacing between roughness elements, i.e., between sand grains, is characterized by the spacing parameter λ, defined as

$$\lambda = \frac{\text{(area of roughened blade surface)}}{\text{(total frontal area of roughness elements)}} \qquad (2)$$

In the present experiments λ ranged from 7 to 16 with most tests for a value near 10. The effective value of λ for standard Nikuradse (1950) sand roughness is about 3.0. As outlined by Kind and Lawrysyn (1992a), if k and λ are known for any roughness, an equivalent standard-sand roughness height, k_s, can easily be determined. This may be useful for comparisons with other experiments. Table 1 gives values of the ratio k_s/k

Table 1 Ratios k_s/k for various values of the spacing parameter λ

λ	k_s/k
7.	6.1
10.	4.
16.	2.4

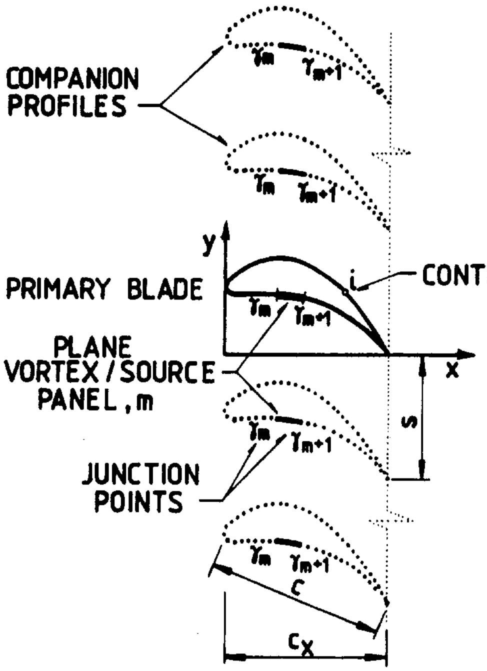

Fig. 4 Array of blades as used in inviscid part of computational method

for λ values in the range of interest. Note that the present roughness is "rougher" in an aerodynamic sense than standard (i.e., closely spaced) sand of the same height. This is because the individual grains are more exposed in the present case.

A special apparatus was developed to enable reasonably uniform and repeatable application of sand grains to the blade surfaces. The blades were placed onto a motor-driven cart, which passed under a slit from which sand was falling steadily. Sand grains would adhere to those areas of the blade that were coated with wet adhesive. The spacing parameter was subsequently determined for a number of sample areas on the blade either "manually" or by use of a digital image processing technique (see Abbott, 1993, and Serjak, 1995 for details). If λ values varied by more than ±1 from the mean value, the roughness was stripped and the application repeated.

An important feature of the roughness used in the present experiments is that it was readily quantifiable in the sense that k and λ could be determined for it by relatively straightforward geometric measurements. This enables an unambiguous assessment of the capabilities of calculation methods, which of course require characterization of the surface roughness as an input.

In addition to smooth blades, 17 different roughness configurations were tested, most at a number of incidence angles. Configurations included three roughness heights as already mentioned, three widths, $\Delta s/c = 0.24$, 0.47, and 0.71, of roughness band and five band locations with band leading edge at $x/c =$ 0.1, 0.25, 0.53, and 0.65 on the suction surface and 0.25 on the pressure surface. The choice of band widths and locations was guided by the observations of Taylor (1990) and of Tarada and Suzuki (1993) as well as by oral comments from engine-maintenance engineers.

Outline of Computational Method

The computational method was an inviscid/viscous interaction method based on a long used and well-validated computer code developed by the senior author for isolated airfoils.

A panel method (Kind, 1973) is used for the inviscid calculations. It solves for the potential flow over an array of blades as shown in Fig. 4. Each blade has identical panelling and identical distributions of vortex and source strength along the panels. Vortex and source strength vary linearly over the panels and are continuous at the junction points between panels. The source strengths are specified on the basis of separate boundary-layer calculations as outlined below. The vortex strengths, γ_m, at the junction points are the unknowns. The boundary condition of zero velocity normal to the blade contour is applied only at the control points on the central or "primary" blade of the array. There is a control point at the midpoint of each of the N panels of the primary blade. A Kutta condition is also applied on the primary blade. It requires equal and opposite values of vortex strength on the upper and lower surfaces at the trailing edge. That is

$$\gamma_1 = -\gamma_{N+1} \tag{3}$$

A set of $N + 1$ linear algebraic equations is thus obtained and solved for the unknowns γ_1 to γ_{N+1}. With thin trailing edges γ_1 and γ_{N+1} can take on unrealistically high numerical values because they tend to cancel one another. To avoid this they are subjected to the constraint

$$|\gamma_1| = |\gamma_{N+1}| = \tfrac{1}{2}(|\gamma_u| + |\gamma_l|)_{m=2} \tag{4}$$

The right-hand side of Eq. (4) represents the mean of the absolute values of the vortex strengths on the upper and lower surfaces one panel-length upstream of the trailing edge.

If there is a reasonably large number of blades in the array (41 in the present work) the solution will give the same vortex strength distribution around the central blade as if it were in an infinite cascade. Iteration is used to find the outflow angle for which the relations between angle of attack, mean flow velocity, circulation and blade lift coefficient (e.g., Dixon, 1978) are satisfied. Computed results are in excellent agreement with results given by other methods and with the exact potential flow solution of Gostelow (1984). Other panel methods could be similarly adapted to deal with cascades.

The actual blades had a blunt trailing edge of radius $0.013c$. The inviscid panel method would have given unrealistically high velocities due to the intense curvature of the potential flow around such a trailing edge. To avoid this difficulty the actual contour was modified slightly over about the last 15 percent of chord to give a sharp trailing edge, located at the end of the actual camber line. The computed results were insensitive to the details of the modification.

Boundary layer displacement effects are represented by using a source distribution around the trailing edge, as mentioned above. The flow from the sources displaces the external flow by an amount equal to the boundary-layer displacement thickness, δ^*. At each junction point in the panel method the source strength is set equal to the derivative $d(U_e\delta^*)/ds$, where U_e is the local inviscid flow velocity. The distribution of δ^* is obtained from boundary-layer development computations which use the U_e distribution given by the inviscid method as an input. The inviscid and boundary-layer calculations are coupled by using an iterative process. In the present work the following sequence was found to give satisfactory convergence: inviscid calculations with zero source strength, then boundary-layer calculations, then, finally, inviscid calculations with source strengths specified as noted above.

The boundary-layer calculations are crucial since that is where the direct effects of the surface roughness are represented. The only methods that use a direct physical description of the roughness (e.g., height and spacing of elements) as input appear to be those of Dvorak (1969) and Taylor et al. (1985). Both methods are for turbulent flow; of course laminar boundary-layer development and transition must be dealt with as well. In the present experiments the boundary layer was always either already turbulent at the leading edge of the roughness band or became turbulent very shortly thereafter. Therefore conventional methods could be used for the stagnation-point and laminar boundary-layer calculations; the

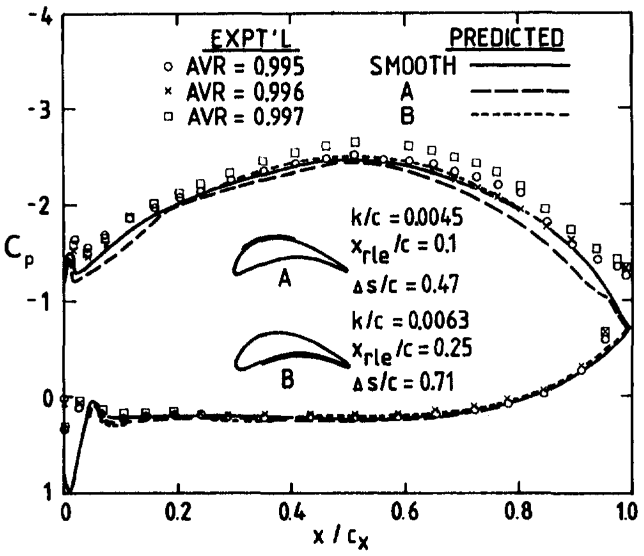

Fig. 5 Some measured and predicted blade static pressure distributions with and without roughness at design incidence

method given by Moran (1984) and Thwaites' method (see, e.g., Moran, 1984), respectively, were used. Transition on smooth surfaces was predicted using the H-R_{ex} method of Wazzan et al. (1981). For rough surfaces laminar flow was assumed to undergo transition when the roughness-height Reynolds number, u^*k/ν, exceeded 19. The latter is approximately equivalent to Braslow's (1960) criterion for roughness-induced transition. In the present application it predicted transition at the start of the roughness bands if the flow was not already turbulent there; this was consistent with the experimental observations. Instantaneous transition was assumed. The momentum thickness was assumed to remain constant through transition on smooth surfaces and to assume the value $10k/\lambda$ immediately after roughness-induced transition; the latter provides an ad hoc estimate of the momentum depletion during roughness induced transition at the beginning of a roughness band. The results were not sensitive to this assumption.

Dvorak's (1969) method and a modification of it were used for the turbulent boundary-layer calculations in the present work because this method uses a fast integral boundary-layer computation as opposed to the finite-difference method required for the Taylor et al. (1985) approach. Dvorak (1969) developed a skin-friction law for rough surfaces and coupled it with Head's (1958) entrainment method to compute boundary-layer development. Head's method is known to work well for airfoil-type pressure distributions but is not always reliable for nonequilibrium boundary layer flows (Kline et al., 1969). Head and Patel (1968) developed an improved entrainment method that dealt with these limitations; the improved method performed as well as the top-ranked methods in Kline et al. (1969). For the present work this improved entrainment method was coupled with Dvorak's (1969) skin-friction law for rough walls. As it happened, the results given by the improved method and the original Dvorak (1969) method were virtually identical in the present application.

To avoid an unduly abrupt change of roughness in the calculations, the roughness height was assumed to increase linearly from zero over a distance of about 0.1 c upstream of the nominal leading edge of the roughness bands.

Predicted deviation angles are given directly by the final inviscid computation. Predicted profile losses are obtained from the relation

$$Y_p = 2\theta_2/S \cos \alpha_2 + Y_{\text{tet}} \tag{5}$$

where

$$\theta_2 = (\theta_u + \theta_l)(U_{te}/U_2)^{3.2} \tag{6}$$

The momentum-defect thicknesses on the upper and lower surface at the trailing edge of the blades, θ_u and θ_l, are given by the boundary layer calculations. Equation (6) is the Squire and Young (1938) relation, which gives the corresponding momentum-defect thickness far downstream. The first term in Eq. (5) can be derived by a control volume analysis of a blade-to-blade streamtube. Y_{tet} is a trailing-edge-thickness loss; the correlation of Kacker and Okapuu (1982) is used for this; Y_{tet} had a value of 0.007 in the present application.

Results and Discussion

Figure 5 shows three pressure distributions measured at design incidence around the pressure-tapped blade, together with corresponding predictions. Focusing first on the experimental data, it can be seen that roughness has only small effects on the pressure distributions. This coincides with the findings of Speidel (1954) and Bammert and Sandstede (1980). The effects of the roughness appear almost entirely on the suction surface, even when it is located on the pressure surface. Roughness on the pressure surface thickens the boundary layer, causing higher velocity in the inviscid core flow due to blockage of the blade-to-blade passage. The effects of the velocity increase are most pronounced at the suction surface because the velocity is substantially higher there to begin with. Roughness on the suction surface would tend to produce the same effect, but the thickening of the suction-surface boundary layer would also tend to produce a de-cambering effect, which would tend to cause a compensatory slight decrease in loading over the rear portion of the blades.

At off-design incidences the effects of suction-surface roughness are similar to those seen in Fig. 5, while the effects of pressure-surface roughness are somewhat less. Figure 6 shows some measured pressure distributions at 15 deg above design incidence. In the case of the roughened blades there is a region of constant pressure near the trailing edge on the suction surface, clear evidence of flow separation. The separation evident in Fig. 6 causes more de-cambering than with attached flow and this effect happens almost exactly to compensate the effects of blockage due to the roughness-thickened boundary layer. As a result the pressure distributions and blade loading are almost unaffected by the roughness in the cases of Fig.

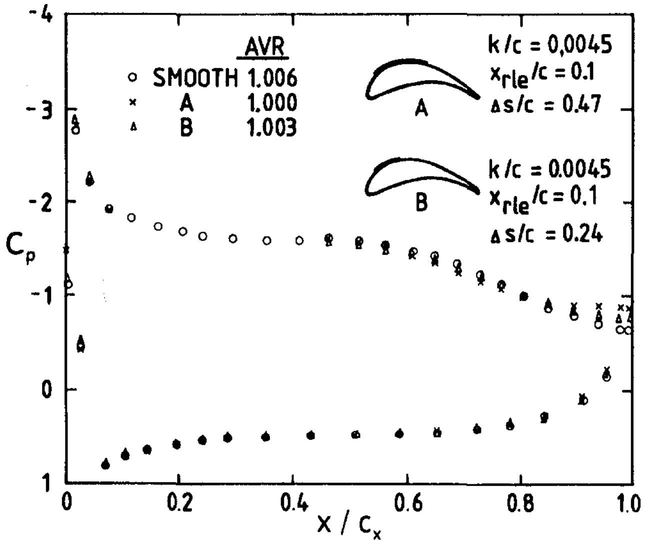

Fig. 6 Some measured blade static pressure distributions with and without roughness at 15 deg above design incidence

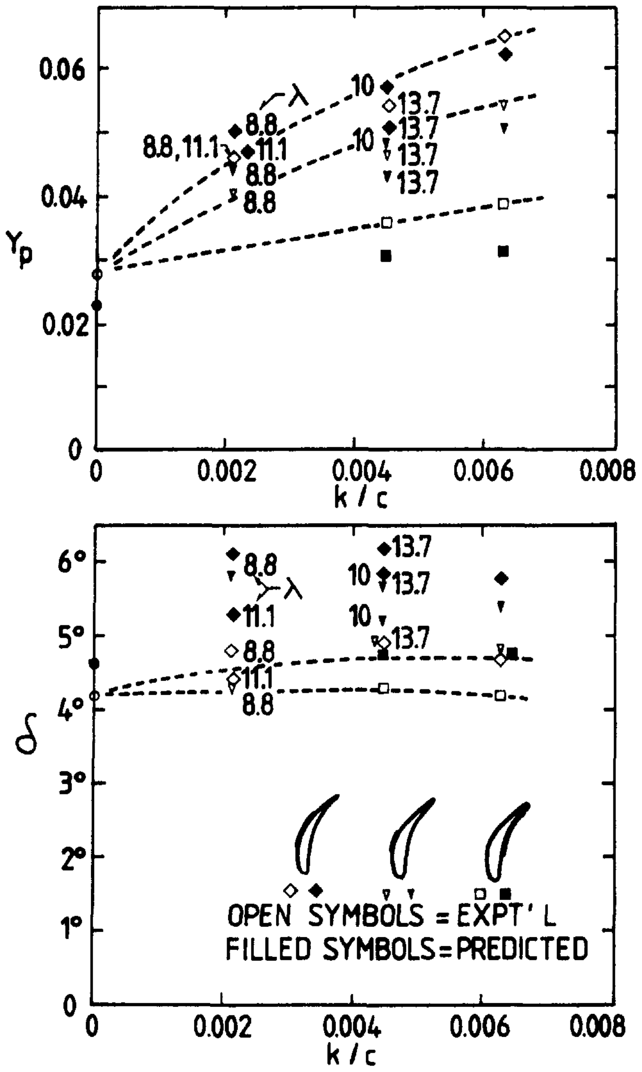

Fig. 7 Profile-loss coefficient and deviation angle versus roughness height at design incidence (x_{rle}/c = 0.25; $\Delta s/c$ = 0.24, 0.47, 0.71; $10 \le \lambda \le 10.5$ unless otherwise noted; i = 3 deg)

6. The deviation angle is therefore almost unaffected as well, although losses increase substantially, as can be seen in Fig. 9. Since significant flow separation was present for incidence angles of 15 deg or more above design, no predictions were computed for these cases because the computational model cannot deal with substantial separation in its present form.

The predicted pressure distributions compare reasonably well with the experimental ones, the agreement seen in Fig. 5 being typical. The experimental distributions exhibit somewhat higher than predicted suction levels on the upper surface of the blades; this is probably due mainly to deficiencies in the Kutta condition leading to slightly low values of predicted circulation around the blades. This is not serious since it is the *changes* due to roughness that are of most significance in the present work. The effects of roughness on the pressure distributions are predicted to be small and to occur almost entirely on the suction surface, consistent with the experimental findings. The slight decrease in aft loading due to roughness on the suction surface is well predicted although the slight increase in loading due to roughness on the pressure surface is sometimes underpredicted. Figure 7 and 8 present measured and predicted profile-loss coefficients and deviation angles as a function of roughness height, for design incidence, spacing parameter, λ, near 10 and various roughness locations and band widths. Both profile-loss coefficients and deviation angle are seen to be well predicted in general, agreement being within 0.01 and 1.5 deg, respectively. This is comparable with the experimental error, estimated at ±0.005 and ±0.5 deg, respectively for incidence angles of 10 deg or less.

The results in Fig. 7 show that roughness on the suction surface can cause large increases in profile losses while roughness on the pressure surface has relatively little effect. This is simply because velocity and adverse pressure gradient near the suction surface are much greater than those near the pressure surface. The height of the roughness is important, as would be expected. As seen from Fig. 8, roughness relatively close to the leading edge on the suction surface causes substantially greater loss increments than the same roughness located further aft. The roughness is relatively high compared to the boundary-layer thickness near the leading edge and it accordingly extracts more momentum from the flow; the effects of this are aggravated as the thickened boundary layer proceeds through the region of adverse pressure gradient further downstream on the blade. For the same reasons, loss increments increase less slowly than the width of the roughness strip, as can be seen in Fig. 7.

From Figs. 7 and 8 it is apparent that roughness has little effect on the flow deviation angle; δ increased no more than 1 deg for any case investigated and often did not increase at all. This is consistent with the small effect of roughness on static pressure distribution around the blades since, of course, flow deflection is directly dependent on blade load.

Figure 9 illustrates the effects of incidence angle. These are much the same for smooth and rough blades with roughness simply shifting the curves. Although premature stall did not occur for the cases shown in Fig. 9, it should be noted that roughness bands that begin near the leading edge on the suction surface could well precipitate extensive flow separation extensive flow separation (i.e., stall) at incidence angles much lower than for smooth blades. Extensive evidence of this has accumulated in recent years for isolated airfoils (e.g., Kind and Lawrysyn, 1992b; Valarezo et al., 1993) and the situation for cascades should be no different at incidence angles that produce a significant suction peak near the leading edge for attached flow. The present computational method is capable of predicting stall, but not post-stall performance.

Figure 10 gives an indication of the effect of the roughness-spacing parameter, λ. Its effect is not as large as might be expected in view of its substantial influence on the equivalent standard-sand roughness height; see Table 1.

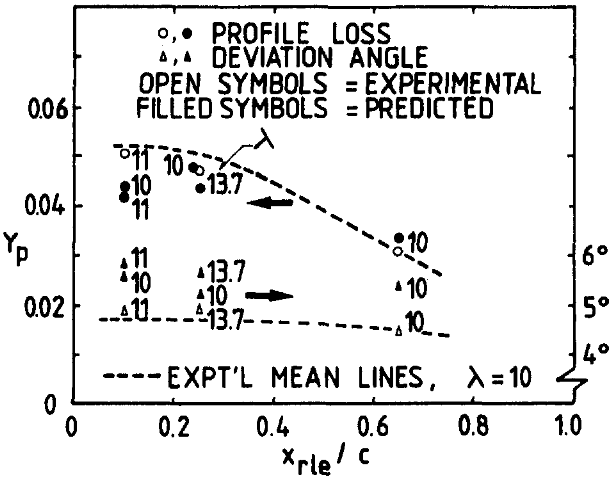

Fig. 8 Effect of suction-surface roughness band position on profile loss and deviation angle at design incidence (k/c = 0.0045; $\Delta s/c$ = 0.24; i = 3 deg)

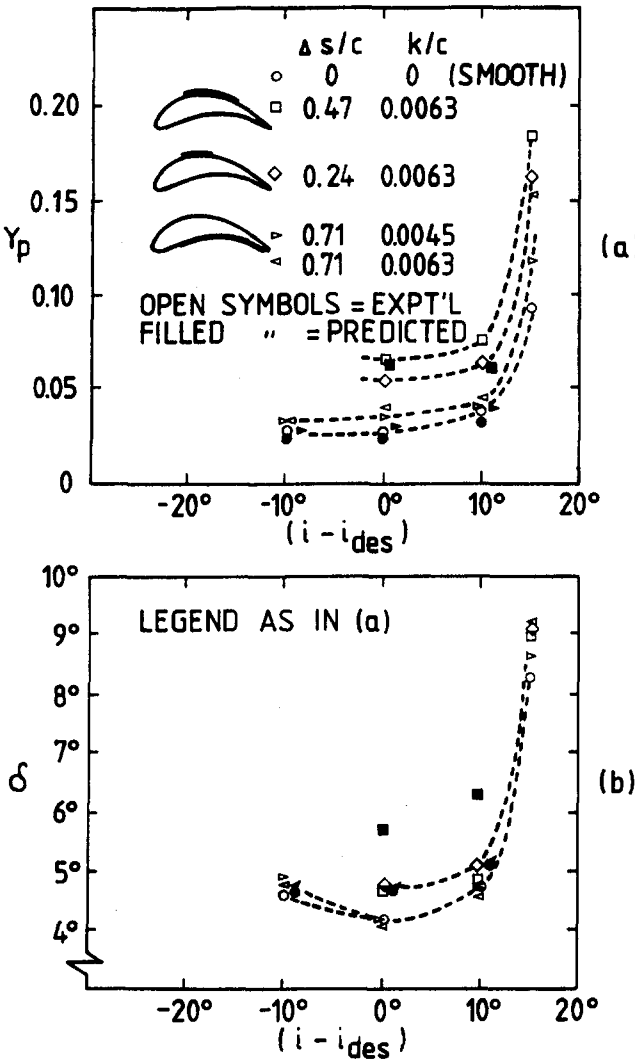

Fig. 9 Effect of incidence angle on profile loss and deviation angle for various roughness configurations (x_{rle}/c = 0.25; 10 ≤ λ ≤ 10.5)

Only qualitative comparison is possible between the present results for loss-coefficient and deviation angle and those of Speidel (1954). Speidel's Reynolds number and main cascade parameters were not greatly different from those of the present experiments. For his maximum k_s/c of 0.003, Speidel's deviation angles are within about 1 deg of those for his smooth blades. It is intriguing to note, however, that for a smaller k_s/c of 0.0009 his deviation angles are up to 3 deg higher than for $k_s/c = 0.003$. The reasons for this are not clear although $k_s/c = 0.0009$ was the critical roughness in the sense that it was the smallest height that caused a significant increase in profile losses. One can speculate that this roughness thickened the laminar boundary layer just enough to cause a laminar separation bubble near the leading edge of the blades where the smooth-surface pressure distributions exhibited two suction maxima, about $\Delta s/c = 0.3$ apart. Near design incidence Speidel's loss coefficients for $k_s/c = 0.003$ were about 400 percent larger than for his smooth blades. On the basis of the present experimental results (see Fig. 9 in which $k_s/c = 0.025$, and Fig. 7) one would expect a much smaller increase. Speidel's blades were entirely covered with roughness, but even allowing for the possibility that leading-edge roughness might be especially important, it is hard to explain the large increase in profile loss. The coordinates for Speidel's blades are not available but computations for the present cascade, uniformly covered with $k_s/c = 0.003$ roughness, predicted only about a 50 percent increase in profile loss. In these calculations the boundary layers were turbulent over almost the entire blade, but substantial separation did not occur. The sandpaper used by Speidel would have altered his blade profile shape, perhaps with especially deleterious effects in the highly curved leading-edge region. Substantial separation may have occurred from his roughened blades. Unfortunately he does not show pressure distributions that could help clarify this question. It appears probable that the effects of roughness reported by Speidel for the range $0.0009 \leq k_s/c \leq 0.003$ are atypically large.

The present computational method was not adjusted or "tuned" in any way to suit the particular cases of the experiments. Its success in predicting the effects of a wide variety of roughness configurations thus implies that it, or similar methods, should be capable of predicting profile losses and deviation for other cascade and roughness configurations, provided only that the flow is approximately incompressible and that the roughness can be quantified in terms of k, λ, or k_s. The results also imply that roughness effects in three-dimensional flows could be successfully predicted by incorporating the Dvorak (1969) skin-friction law, or the compressible extension of it (Dvorak, 1972), into a three-dimensional Navier–Stokes code.

Conclusions

Measurements of profile losses and flow deviation have been carried out on a planar turbine cascade to assess the effects of partial roughness coverage of the blade surfaces. Roughness was found to have little effect on static pressure distribution around the blades and on deviation angle, provided that it does not precipitate substantial flow separation. Roughness on the suction surface can cause large increases in profile losses; roughness height and location of the leading edge of the roughness band are particularly important. Loss increments due to pressure-surface roughness are much smaller than those due to similar roughness on the suction surface.

A computational method using the viscous/inviscid interaction approach was developed and was generally successful for cases without substantial flow separation. The method was not "tuned" in any way to the experimental cases. One can conclude that any two-dimensional viscous/inviscid interaction analysis that uses an inviscid method, coupled with a suitable rough surface boundary-layer analysis, should have similar capabilities. That is, it should give good predictions of blade pressure distributions, profile-loss coefficients, and

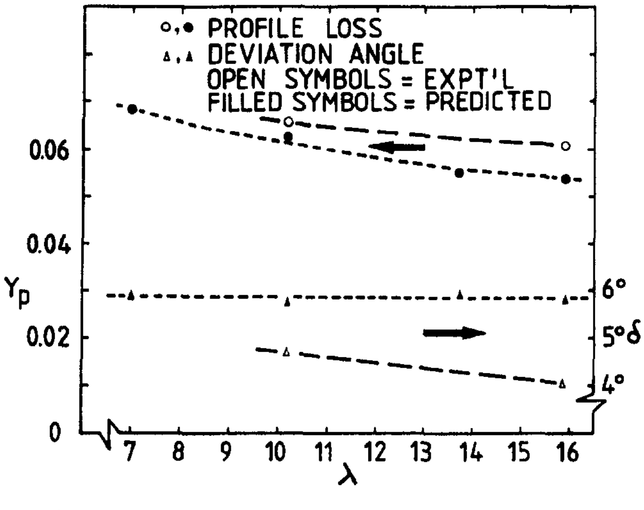

Fig. 10 Effect of roughness spacing parameter on profile losses and deviation angle (k/c = 0.0063; x_{rle}/c = 0.25; $\Delta s/c$ = 0.47; i = 3 deg; roughness band on suction surface)

deviation angles for a variety of cascade and roughness configurations, provided that substantial flow separation does not occur. The work also suggests that incorporation of the skin-friction law into a three-dimensional Navier–Stokes code would enable good predictions of roughness effects in three-dimensional situations.

Acknowledgments

The authors are grateful for financial support from GasTOPS Ltd., the Natural Sciences and Engineering Research Council and the Government of Ontario under its URIF Program. The cascade wind tunnel and measurement techniques were developed by S. A. Sjolander and his students; their contribution is also gratefully acknowledged.

References

Abbott, M. W. P., 1993, "The Aerodynamic Effect of Roughness on the Performance of a Turbine Cascade," M. Eng. Thesis, Carleton University, Ottawa, Ontario, Canada.

Bammert, K., and Sandstede, H., 1972, "Measurements Concerning the Influence of Surface Roughness and Profile Changes on the Performance of Gas Turbines," ASME *Journal of Engineering for Power,* Vol. 94, pp. 207–213.

Bammert, K., and Sandstede, H., 1976, "Influences of Manufacturing Tolerances and Surface Roughness of Blades on the Performance of Turbines," ASME *Journal of Engineering for Power,* Vol. 98, pp. 29–36.

Bammert, K., and Sandstede, H., 1980, "Measurements of the Boundary Layer Development Along a Turbine Blade With Rough Surfaces," ASME *Journal of Engineering for Power,* Vol. 102, pp. 978–983.

Bolcs, A., and Sari, O., 1988, "Influence of Deposit on the Flow in a Turbine Cascade," ASME JOURNAL OF TURBOMACHINERY, Vol. 110, pp. 512–519.

Boynton, J. L., Tabibzadeh, R., and Hudson, S. T., 1992, "Investigation of Rotor Blade Roughness Effects on Turbine Performance," ASME JOURNAL OF TURBOMACHINERY, Vol. 115, pp. 614–620.

Braslow, A. L., 1960, "Review of the Effect of Distributed Surface Roughness on Boundary-Layer Transition," AGARD Report 254.

Cue, R. W., and Muir, D. E., 1991, "Engine Performance Monitoring and Troubleshooting Techniques for the CF-18 Aircraft," ASME *Journal of Engineering for Gas Turbines and Power,* Vol. 113, pp. 11–19.

Dixon, S. L., 1978, *Fluid Mechanics, Thermodynamics of Turbomachinery,* 3rd ed., Pergamon Press, pp. 55–60.

Dvorak, F. A., 1969, "Calculation of Turbulent Boundary Layers on Rough Surfaces in Pressure Gradient," *AIAA Journal,* Vol. 7, pp. 1752–1759.

Dvorak, F. A., 1972, "Calculation of Compressible Turbulent Boundary Layers With Roughness and Heat Transfer," *AIAA Journal,* Vol. 10, pp. 1447–1451.

Gostelow, J. P., 1984, *Cascade Aerodynamics,* Pergamon Press Ltd., ch. 5.

Head, M. R., 1958, "Entrainment in the Turbulent Boundary Layer," Aeronautical Research Council (Great Britain) R & M 3152.

Head, M. R., and Patel, V. C., 1968, "Improved Entrainment Method for Calculating Turbulent Boundary Layer Development," Aeronautical Research Council (Great Britain) R & M 3643.

Kacker, S. C., and Okapuu, U., 1982, "A Mean Line Prediction Method for Axial Flow Turbine Efficiency," ASME *Journal of Engineering for Power,* Vol. 104, pp. 111–119.

Kind, R. J., 1973, "An Improved Surface-Vorticity Method of Solution for Potential Flow Over Arbitrary Airfoils," Dept. of Mech. and Aero. Eng. Report No. 73-1, Carleton University, Ottawa, Ontario, Canada.

Kind, R. J., and Lawrysyn, M. A., 1992a, "Aerodynamic Characteristics of Hoar Frost Roughness," *AIAA Journal,* Vol. 30, pp. 1703–1707.

Kind, R. J., and Lawrysyn, M. A., 1992b, "Performance Degradation Due to Hoar Frost on Lifting Surfaces," *Canadian Aeronautics and Space Journal,* Vol. 38, pp. 62–70.

Kline, S. J., Morkovin, M. V., Sovran, G. and Cockrell, D. J., eds., 1969, *Computation of Turbulent Boundary Layers,* Proc. 1968 AFOSR-IPP-Stanford Conference, Thermosciences Div., Dept. Mech. Eng., Stanford University, CA.

Koch, C. C., and Smith, L. H., Jr., 1976, "Loss Sources and Magnitudes in Axial-Flow Compressors," ASME *Journal of Engineering for Power,* Vol. 98, pp. 411–424.

Moran, J., 1984, *An Introduction to Theoretical and Computational Aerodynamics,* Wiley, pp. 206–209.

Nikuradse, J., 1950, "Laws of Flow in Rough Pipes," NACA TM 1292.

Rodger, P., Sjolander, S. A., and Moustapha, S. H., 1992, "Establishing Two-Dimensional Flow in a Large-Scale Planar Turbine Cascade," AIAA Paper No. 92-3066.

Serjak, P. J., 1995, "An Investigation of the Effects of Roughness on the Performance of a Turbine Cascade," M. Eng. Thesis, Carleton University, Ottawa, Ontario, Canada.

Speidel, L., 1954, "Einfluss der Oberflachenrauhigkeit auf die Stromungsverluste in Ebenen Schaufelgittern," *Forschung auf dem Gebiete des Ingenieurwesens,* Vol. 20, pp. 129–140.

Squire, H. B., and Young, A. D., 1938, "The Calculation of the Profile Drag of Aerofoils," Aeronautical Research Council (Great Britain) R & M 1838.

Tarada, F., and Suzuki, M., 1993, "External Heat Transfer Enhancement to Turbine Blading Due to Surface Roughness," ASME Paper No. 93-GT-74.

Taylor, R. P., Coleman, H. W., and Hodge, B. K., 1985, "Prediction of Rough-Wall Skin Friction Using a Discrete Element Approach," ASME *Journal of Fluids Engineering,* Vol. 107, pp. 251–257.

Taylor, R. P., 1990, "Surface Roughness Measurements on Gas Turbine Blades," ASME JOURNAL OF TURBOMACHINERY, Vol. 112, pp. 175–180.

Valarezo, W. O., Lynch, F. T., and McGhee, R. J., 1993, "Aerodynamic Performance Effects Due to Small Leading-Edge Ice (Roughness) on Wings and Tails," *Journal of Aircraft,* Vol. 30, pp. 807–812.

Wazzan, A. R., Gazely, C., Jr., and Smith, A. M. O., 1981, "H-R_x Method of Predicting Transition," *AIAA Journal,* Vol. 19, pp. 810–812.

Unsteady Wake-Induced Boundary Layer Transition in High Lift LP Turbines

V. Schulte[1]
Whittle Laboratory,
University of Cambridge,
Cambridge, United Kingdom

H. P. Hodson
Whittle Laboratory,
University of Cambridge,
Cambridge, United Kingdom

The development of the unsteady suction side boundary layer of a highly loaded LP turbine blade has been investigated in a rectilinear cascade experiment. Upstream rotor wakes were simulated with a moving-bar wake generator. A variety of cases with different wake-passing frequencies, different wake strength, and different Reynolds numbers were tested. Boundary layer surveys have been obtained with a single hot-wire probe. Wall shear stress has been investigated with surface-mounted hot-film gages. Losses have been measured. The suction surface boundary layer development of a modern highly loaded LP turbine blade is shown to be dominated by effects associated with unsteady wake-passing. Whereas without wakes the boundary layer features a large separation bubble at a typical cruise Reynolds number, the bubble was largely suppressed if subjected to unsteady wake-passing at a typical frequency and wake strength. Transitional patches and becalmed regions, induced by the wake, dominated the boundary layer development. The becalmed regions inhibited transition and separation and are shown to reduce the loss of the wake-affected boundary layer. An optimum wake-passing frequency exists at cruise Reynolds numbers. For a selected wake-passing frequency and wake strength, the profile loss is almost independent of Reynolds number. This demonstrates a potential to design highly loaded LP turbine profiles without suffering large losses at low Reynolds numbers.

Introduction

In a modern high-bypass-ratio civil engine, the LP turbine delivers the power for the fan. Today, increasing fan diameters result in a requirement for higher work output at lower rotational speed from the LP turbine. LP turbines usually consist of several stages and hence the associated weight is large. Furthermore, their efficiency strongly influences the specific fuel consumption. There is a significant incentive for improving this component.

Due to large aspect ratios in LP turbines, the profile loss is by far the largest portion of the total. The magnitude of profile loss depends upon the development of the airfoil boundary layers. Changes in the process of boundary layer transition and separation can alter the profile loss significantly for the same profile shape at different operating conditions. Consequently the search for further improvements in loading and efficiency of LP turbines should consider the details of the processes of boundary layer transition and separation.

For some time it has been recognized that the boundary layers on turbomachinery blades are by no means fully turbulent, nor are they steady (e.g., Walker, 1974; Hodson, 1984; Hodson et al., 1994; Halstead et al., 1997; Banhiegbal et al., 1995). The turbulence associated with the wakes shed by upstream blade rows is responsible for much of the unsteady nature of the transition process. The very low Reynolds numbers in LP turbines at design conditions result in laminar boundary layers for a large fraction of the blade surface and between the wake-passing. It is generally assumed that the profile loss in the turbine is higher than measured in a steady flow cascade test due to the effect of the wakes on the transition process. This is because the wakes trigger transition at a position located farther upstream of the position where natural transition would occur. The increased fraction of surface that is covered by turbulent flow is then responsible for the increased profile loss (Hodson, 1984). Parameters like the axial gap between blade rows, the strength of the wake, and the frequency of the wake-passing affect the profile loss (Hodson, 1984). These conclusions have, however, only been confirmed for attached boundary layers.

The performance targets of modern LP turbine blading concern not only efficiency, but also weight and manufacturing costs. It is desirable to use fewer blades per blade row, so that an individual blade has to carry a greater aerodynamic load. Increased lift coefficients can only be realized if the pressure distribution has regions of significant diffusion on the suction surface. This inevitably increases the risk of laminar separation. In order to avoid significant deterioration in efficiency due to large separation bubbles (or even non-reattached separation), the concept of controlled boundary layer design is widely used in industry (Hourmouziadis, 1989). It involves the design of either completely laminar blades with very low suction side diffusion, or of blades with a so-called roof-top pressure distribution, where transition or laminar separation and turbulent reattachment occur just after the suction peak. Both philosophies are meant to avoid large open separation and therefore yield reasonably low loss coefficients.

In the above-mentioned design procedures, no account is taken of the effects of wake-passing. For boundary layers that feature separation bubbles, loss reductions may be caused by increased turbulence levels generated by turbulence grids or stationary wakes (Hebbel, 1964; Ladwig, 1992). Only Schulte and Hodson (1994) investigated the effect of *moving* wakes on separated boundary layers in LP turbines. They show a loss reduction for some cases. In practice, we need to answer the question of how the profile loss of a highly loaded blade with a separation bubble on the suction surface is affected by the wake passing and associated parameters such as the wake-passing frequency and the wake strength (which is a function of the axial gap between blade rows and the loss of the previous blade row).

The aim of this paper is to describe the interaction of wakes shed by upstream blade rows with the separated suction surface

---

[1] Present address: BMW Rolls-Royce, Dahlewitz, Germany.

Contributed by the International Gas Turbine Institute and presented at the 41st International Gas Turbine and Aeroengine Congress and Exhibition, Birmingham, United Kingdom, June 10–13, 1996. Manuscript received at ASME Headquarters February 1996. Paper No. 96-GT-486. Associate Technical Editor: J. N. Shinn.

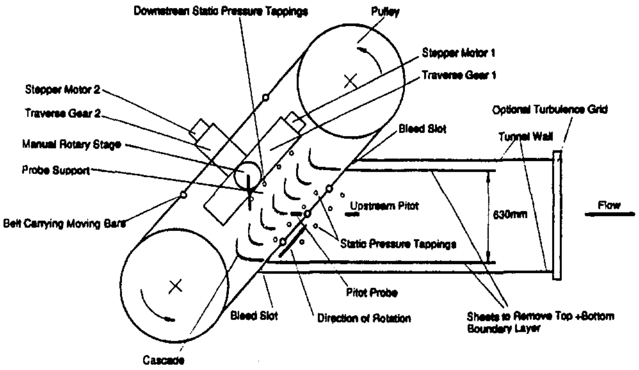

Fig. 1 Test section of low-speed moving bar cascade wind tunnel

Table 1 Cascade parameter

Number of Blades	7
Aspect Ratio	2.37
Chord	156mm
Axial Chord	127.8mm
Stagger	35.32 degrees from axial
Air Inlet Angle	-30.46 degrees
Design Exit Angle	62.86 degrees
Pitch/Chord Ratio	0.78

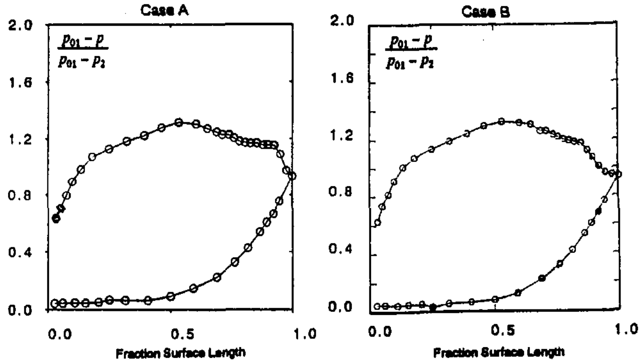

Fig. 2 Measured blade surface pressure distribution for case A ($Re_2 = 1.3 \times 10^5$, $Tu_{fs,1} = 0.5$ percent, no wakes) and case B ($Re_2 = 1.3 \times 10^5$, $\Phi = 0.7$, $\bar{f} = 0.78$, 2 mm bars, $Tu_{fs,1} = 0.5$ percent, $Tu_{w,1} = 10$ percent, $Y_{pw} = 0.03$)

boundary layer of a highly loaded LP turbine blade. The possibility of using a controlled boundary layer design philosophy that takes into consideration the effects of unsteady wake-passing is briefly examined.

Experimental Setup in Moving-Bar Low-Speed Cascade Wind Tunnel

A low-speed cascade wind tunnel in the Whittle Laboratory, Cambridge University, was used for this investigation. A schematic of the test section is shown in Fig. 1. The wake generator consists of nylon or steel bars that are fitted between two rubber belts on either side of the side-walls of the cascade. The belts are driven by a variable speed DC-motor. The moving bars are returned downstream of the cascade at a distance where they do not interfere with the exit flow field. Upstream of the cascade, the belts carrying the bars are moved through small gaps in the top and bottom walls of the tunnel. The flow in the midspan region can be considered to be two-dimensional. The test section has a rectangular cross section of 630 mm height and 370 mm width.

Two translational traverse gears (shown in Fig. 1) provide movement in the axial and pitchwise directions (cascade coordinate system). They are driven by stepper motors and offer a resolution of 5 μm. A manually driven rotary stage provides rotation around a spanwise axis.

Table 1 gives the parameters of the cascade used during this study. The pressure distribution is shown in Fig. 2. The inlet-to-exit velocity ratio is about 1.9. Curtis et al. (1996) describe the design of the profile, which is designated "Blade H" in their paper.

The wake-generating bars pass the blade leading edges at a distance of 0.6 axial chords upstream. During some tests a turbulence grid was located 1500 mm upstream of the leading edge of the center blade. It generated a turbulence intensity of $Tu_{fs,1} = 4.0$ percent at inlet to the center blade. Without the turbulence grid the turbulence intensity was $Tu_{fs,1} = 0.5$ percent. Further details can be found from Schulte (1995).

Measurement and Processing Techniques

Thermal Anemometry

Hot-Wire Boundary Layer Traverses. A DANTEC single-wire boundary layer probe of the type 55P15 and a DANTEC anemometer of the type 56C17 operated in the constant-temperature mode were used in this study.

The hot-wire probe was calibrated in a low-turbulence calibration wind tunnel using the general form of King's law

$$E^2 - E_0^2 = B \cdot V^n, \tag{1}$$

where E is the anemometer output voltage, B and n are calibration constants, and E_0 is the anemometer output voltage at zero flow conditions. Since the heat transfer from the hot-wire to the surroundings is also affected by the proximity of walls, E_0 has to be measured at each individual position, where measurements

Nomenclature

c_d = bar drag coefficient
d = bar diameter
$\bar{f}$ = reduced frequency (frequency*chord/exit velocity)
p = pressure
Re_2 = Reynolds number (based on chord and exit conditions)
s = bar spacing
%s = percentage surface distance
t = time
Tu = streamwise turbulence intensity, percent
V = free-stream velocity
w = relative velocity (in frame of moving bars)
Y_p = profile loss coefficient = $(p_{01} - p_{02})/(p_{01} - p_2)$
α = absolute flow angle against axial
β = relative flow angle against axial (in frame of moving bars)
ϕ = flow coefficient (ax. vel./bar speed)
ρ = density
τ_w = pseudo wall shear stress

Subscripts and Superscripts

0 = stagnation quantity
1 = inlet
2 = exit
x = axial
fs = free-stream
w = wake (peak value in cascade frame)
$\bar{\ }$ = time mean
$\sim$ = ensemble averaged
$\wedge$ = mixed-out
$'$ = turbulent fluctuation

are taken during the boundary layer traverse. Because the temperature at calibration could be different from the temperature during data acquisition (the temperature was taken with a thermocouple inside the tunnel), the temperature correction method of Bearman (1971) was used when processing the results.

For each probe position, 4096 samples were logged at a frequency of 20 kHz to acquire the raw velocity signal. The signal was conditioned using a low pass filter that was set to 10 kHz. In order to apply the ensemble-averaging technique (see below) 100 time traces were taken, each consisting of 96 samples that occupied three wake passing periods after a trigger signal (phase-locked logging). The once-per-revolution trigger signal was provided by a magnetic sensor that was placed in the belt carrying the moving bars.

Surface-mounted Hot-film Gages. The measurement of wall shear stress using surface-mounted hot-film gages is a well-established technique (Hodson, 1983). The gages are operated in the constant-temperature mode. The rate of heat transfer from a hot-film gage is proportional to the square of the output voltage of the anemometer bridge. The relationship for the wall shear stress is given by

$$E^2 - A^2 = k \cdot \tau_w^{1/3}, \tag{2}$$

where E is the anemometer output voltage and A and k are calibration constants. Calibration of hot-film sensors is, however, very elaborate and can be subject to errors. Therefore, the hot-films were used in a semi-quantitative manner (Hodson, 1983) using a relationship for the wall shear stress of the form

$$\tau_w \propto \left(\frac{E^2 - E_0^2}{E_0^2}\right)^3. \tag{3}$$

This relationship contains the measured output voltage E and the output voltage for zero flow condition E_0. This so-called zero-flow calibration provides a semi-quantitative measure for the shear stress at the surface. Hence the relative magnitude of the output signals of the individual gages can be compared, though the units associated with the quantity τ_w are arbitrary.

The hot-film sensors occupied a fraction of the blade suction surface ranging from 64 %s to the trailing edge. A total of 12 sensors were used in this region, which provides a spatial resolution of 3%s.

The upper frequency limit of the sensors is approximately 30 kHz. The same logging technique used for the hot-wire signals was used to acquire the hot-film data with the exception that the traces were acquired for six instead of three wake passing periods. As before, 100 phase-locked traces were obtained for ensemble averaging.

Pneumatic Measurements. Conventional pitot probes of 1 mm hole-diameter were used in order to measure stagnation pressure. The downstream pitot probe was aligned with the design exit flow angle.

The inlet stagnation pressure p_{01} (which is the reference stagnation pressure downstream of the moving bars) is calculated from the stagnation pressure upstream of the bars by performing a control volume analysis in the frame of the moving bars (Schulte, 1995). This circumvents the problem of probe-reading errors downstream of the moving bars (see appendix).

The variation of exit total pressure was found by traversing the three central blades of the cascade. Each pitch consisted of 30 measurement points, which were spaced closely inside the wake region. The loss coefficient $Y_p = (p_{01} - \bar{p}_{02})/(p_{01} - \bar{p}_2)$ was evaluated using the mixed-out exit stagnation pressure $\bar{p}_{02}$. The loss measurements were found to be repeatable with an error of $Y_p \pm 0.0015$.

Data Acquisition and Data Reduction. The data acquisition, stepper motor control, and processing are fully automated and software controlled.

Processing of the high-frequency data acquired by the thermal anemometry is carried out by using the well-established ensemble-averaging technique. The ensemble average of a quantity q is given by

$$\tilde{q}(t) = \frac{1}{N}\sum_{j=1}^{N} q_j(t), \tag{4}$$

where N is the number of ensembles. The ensemble-averaged rms (root mean square) is given by

$$\sqrt{\tilde{q}'^2(t)} = \sqrt{\frac{1}{N}\sum_{j=1}^{N}(q_j(t) - \tilde{q}(t))^2} \tag{5}$$

In order to obtain time-averaged values, the ensemble-averaged values are integrated with respect to time. Consequently the time-averaged value can be written

$$\bar{q} = \frac{1}{T}\int_{t=0}^{T} \tilde{q}(t))d\tau, \tag{6}$$

where T is the period time. In the case of the single hot-wire measurements, q will be substituted by the flow velocity u and in the case of the hot-film measurements by the psuedo-wall shear stress τ_w. The ensemble-averaged rms intensity measured with the hot-wire is given by

$$\tilde{T}u(t) = 100 \cdot \frac{\sqrt{\tilde{u}'^2(t)}}{\bar{u}}. \tag{7}$$

Here $\tilde{T}u(t)$ is not termed "turbulence intensity" because it not only contains high-frequency turbulent fluctuations, but also low-frequency mechanical fluctuations caused by the experimental facility and fluctuations caused by the intermittent switching of the boundary layer profile from laminar to turbulent.

Simulation Capabilities of the Moving Bar Rig

In order to achieve a realistic simulation of a rotor–stator interaction in a turbomachine by use of a moving bar rig, the kinematics of the interaction have to be simulated properly by matching the velocity triangles. This is achieved by adjusting the flow coefficient, which fixes the speed of the bars in the moving bar rig. Furthermore, the reduced frequency of the wake interaction has to be matched. This fixes the spacing between adjacent bars in the bar rig experiment.

Pfeil and Eifler (1976) showed that the structure of the far wake ($l/d > 80$) of an airfoil and that of a cylindrical body of the same drag are almost the same. Therefore, the wakes shed by turbomachinery blades can be simulated with cylindrical bars that produce an identical velocity wake and so produce the same loss. Here this is assumed to be valid also for smaller l/d. One can write the loss coefficient as

$$Y_P = \frac{c_d \cdot d}{s_{\text{bar}} \cdot \cos\beta}. \tag{8}$$

It is a function of the drag coefficient c_d of the bars. With $c_d = 1.0$ and the values for the spacing of the bars s_{bar} and the relative inlet flow angle β being given by the reduced frequency and the flow coefficient, one can determine the bar diameter d that is necessary to simulate a turbine blade with a certain loss coefficient. If then the ratio of the axial gap to the chord of the cascade matches this ratio in the real machine, then the wake velocity deficit and the wake width should be reasonably similar.

The simulation capabilities of this moving bar rig have been assessed by Schulte (1995) and Banieghbal et al. (1995). They show that the peak turbulence intensity in the wake matches the value in the turbine, if the velocity deficit matches. In contrast, Halstead et al. (1997) find that the bar-wake turbulence inten-

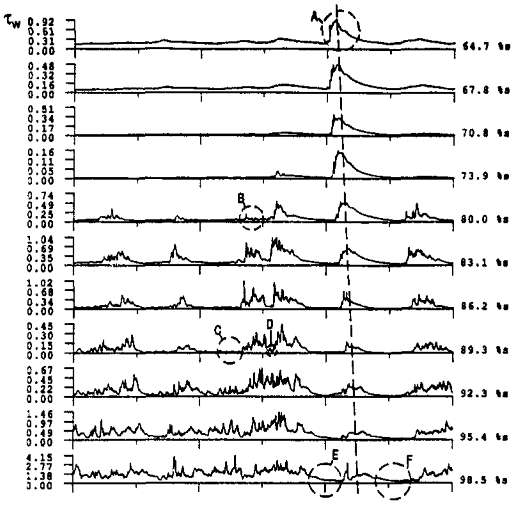

Fig. 3 Raw hot-film output (case B, $Re_2 = 1.3 \times 10^5$, $\Phi = 0.7$, $\bar{f} = 0.78$, 2 mm bars, $Tu_{fs,1} = 0.5$ percent, $Tu_{w,1} = 10$ percent, $Y_{pw} = 0.03$)

sity is higher than the turbulence intensity in the turbine blade wake with the same velocity deficit.

Case B (see below) is the simulation of a cruise condition in a modern LP turbine regarding wake frequency and wake strength.

Discussion of the Experimental Results

Surface Pressure Distributions

(Case A: $Re_2 = 1.3 \times 10^5$, $Tu_{fs,1} = 0.5$ percent, no wakes; Case B: $Re_2 = 1.3 \times 10^5$, $\Phi = 0.7$, $\bar{f} = 0.78$, 2 mm bars, $Tu_{fs,1} = 0.5\%$, $Tu_{w,1} = 10$ percent, $Y_{pw} = 0.03$). Figure 2 presents the measured surface pressure distribution for cases A and B. Strong diffusion on the suction surface leads to boundary layer separation at about 70 %s for case A and also for case B (time mean separation). A large separation bubble is visible for case A. The pressure recovery starts at approximately 90 %s. Reattachment occurs close to the trailing edge at 98 %s. For case B the separation bubble is smaller. The time mean effect of the wakes is to reduce the size of the separation bubble and promote much earlier reattachment. The reasons for this become clear when considering the time-resolved data below.

The pressure surface exhibits an almost constant velocity up to 40 %s. Afterward the acceleration rises gradually until the velocity reaches its exit value at the trailing edge. No sign of pressure surface separation is visible.

Two factors contribute to the high loading of this profile. These are the strong acceleration from the leading edge and the relatively high peak velocity. The latter produces a strong diffusion on the back surface, which leads to a separated boundary layer that only reattaches very close to the trailing edge.

Suction Surface Hot-Film Results

(Case B: $Re_2 = 1.3 \times 10^5$, $\Phi = 0.7$, $\bar{f} = 0.78$, 2 mm bars, $Tu_{fs,1} = 0.5$ percent, $Tu_{w,1} = 10$ percent, $Y_{pw} = 0.03$). Figure 3 presents the raw hot-film results. One individual wake triggered a turbulent event as far upstream as 64 %s (region A). This turbulent patch moves with an average velocity of 0.7 V_∞, as indicated by the dashed trajectory. It prevents the boundary layer from separating during its presence. This is indicated by the increased shear stress level in the hot-film signal and was also confirmed by hot-wire data (Schulte, 1995). The turbulent patch is followed by a distinct region with virtually no turbulent activity (becalmed region), for example region E. The shear stress falls from a turbulent level to a laminar level within this region. Region E is then terminated by the arrival of a new turbulent patch induced by the next wake. It can be seen that the becalmed region following the turbulent patch coming from A is even visible as far downstream as 98 %s (region F). There is evidence (supported by the hot-wire data below) that the becalmed region is also able to prevent the boundary layer from separating. This is due to its partly elevated shear stress level and its fuller velocity profile (Cumpsty, 1995; Halstead et al., 1997; Schulte, 1995).

The majority of wake-induced turbulent patches only emerge at 80 %s. Sometimes a wake-induced patch is slightly out of phase with the occurrence of the others, for example, region B. If the wakes were stronger, then the occurrence of wake-induced turbulent patches would be more deterministic (see for example case C/D). The patch at B does not cause the formation of a significant becalmed region. Rather, it merges quickly with the next wake-induced patch at D. The trace at 89 %s shows two more encircled regions. Regions C and D show transition between wake-induced patches. This indicates that for some periods the boundary layer separates slightly between the wake passing. This was also indicated by Fig. 2 that showed a small time mean separation for case B. However, the separation is at no time as large as in the no-wake case (case A). This was also shown by hot-wire boundary layer surveys in Schulte (1995) and will be demonstrated below.

By the trailing edge two large becalmed regions (E and F) are still visible. They are a special feature of the *unsteady* wake-induced transition process.

Suction Surface Hot-Wire Boundary Layer Traverse

(Case B: $Re_2 = 1.3 \times 10^5$, $\Phi = 0.7$, $\bar{f} = 0.78$, 2 mm bars, $Tu_{fs,1} = 0.5$ percent, $Tu_{w,1} = 10$ percent, $Y_{pw} = 0.03$). Figure 4 concentrates on the temporal variation of the momentum thickness at the trailing edge. Shown is the variation of the momentum thickness during three wake-passing cycles. The value of the momentum thickness measured in the case without wakes (case A) is indicated. So is the time mean value from this measurement. A hot-wire velocity trace and the ensemble-averaged rms from the outer part of the boundary layer are also shown (on an arbitrary scale). These show the position of the wake. It can be seen that during the wake-affected periods the momentum thickness is higher than between the wake-passing. At no instant is the momentum thickness as high as it is in the case without wakes. This again indicates that the wakes suppress the existence of the large separation that existed in the case

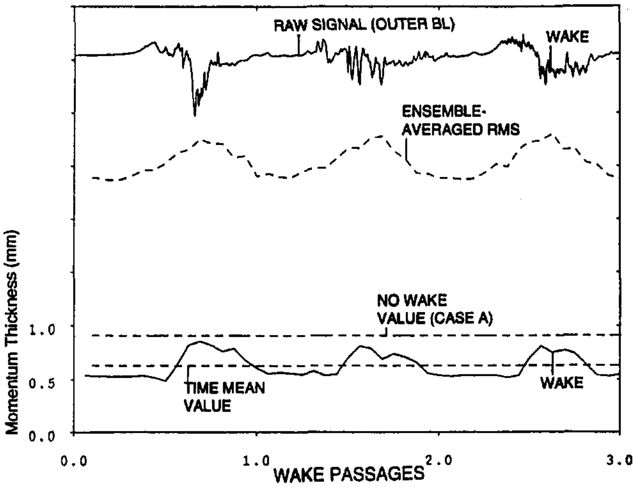

Fig. 4 Hot-wire momentum thickness at the trailing edge (case B, $Re_2 = 1.3 \times 10^5$, $\Phi = 0.7$, $\bar{f} = 0.78$, 2 mm bars, $Tu_{fs,1} = 0.5$ percent, $Tu_{w,1} = 10$ percent, $Y_{pw} = 0.03$)

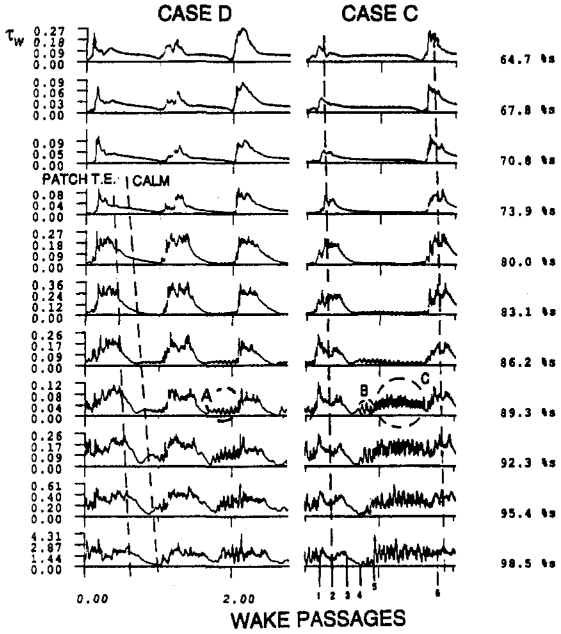

Fig. 5 Raw hot-film output (case C/D, $Re_2 = 1.3 \times 10^5$, $\Phi = 0.7$, $\bar{f} = 0.26/\bar{f} = 0.38$, 4 mm bars, $Tu_{fs,1} = 0.5$ percent, $Tu_{w,1} = 14$ percent, $Y_{pw} = 0.02/Y_{pw} = 0.03$)

without wakes. It also suggests that the wake passing the becalmed region and the process of the reappearing separation bubble are associated with low momentum thickness at the trailing edge. One can speculate that the separation bubble that would exist if no wakes were present only re-establishes if the time between consecutive wake-passings is long enough. Figure 4 also implies that the loss in case B is significantly reduced compared to the steady flow case A.

The Effect of Reduced Frequency and Wake Strength.[1] Figure 5 shows the raw hot-film signals for two different reduced frequencies in one plot. These are the cases C and D ($Re_2 = 1.3 \times 10^5$, $\Phi = 0.7$, $\bar{f} = 0.26/\bar{f} = 0.38$, 4 mm bars, $Tu_{fs,1} = 0.5$ percent, $Tu_{w,1} = 14$ percent, $Y_{pw} = 0.02/Y_{pw} = 0.03$). The time for case C is three times as long as in the datum case B (this corresponds to $\bar{f} = 0.26$). For case D the time between the wakes is twice that of case B (corresponding to $\bar{f} = 0.38$).

It can be seen from Fig. 5 that the onset of wake-induced transition is far upstream (64 %s or farther upstream) due to the increase in the strength of the wakes, which are now generated by 4 mm bars. The becalmed regions, as observed in Fig. 3, are very pronounced and persist until the trailing edge.

For case D ($\bar{f} = 0.38$) it is concluded, that as opposed to case B (Fig. 3) a separation occurs between the wake passing. This is illustrated, for example, at 89 %s (region A). This region is thought to be associated with the transition process in a separation bubble. The onset of separation between the wake-passing is at approximately 70 %s (also supported by hot-wire data in Schulte, 1995). In time, this region lies between a becalmed region and the following turbulent patch. The frequency content of region A is, however, not identical to that of a steady-flow separation bubble for this Reynolds number (Schulte, 1995). It is therefore concluded that this bubble is not fully developed in time. The bubble does not have enough time to re-establish until the next turbulent patch arrives.

Two more trajectories marked with "patch t.e." and "calm" are shown. These show the edge of the turbulent patch and the end of the becalmed region induced by the first wake. The most important observation is that in this case the temporal extent of the becalmed region is not reducing, but rather increasing toward the trailing edge. This only happens if the boundary layer separates without the presence of the wakes and if the wake-passing frequency is low enough to allow the becalmed region to develop. If the boundary layer were attached between the wake-passing, then spots coming from the position of natural transition onset would move into the becalmed region and reduce its temporal extent. This is illustrated in the schematic distance–time diagram in Fig. 6, which shows the general difference between becalmed regions in separated and attached boundary layers (see Schulte, 1995). The thick line indicates how the becalmed region would reduce in attached boundary layers. The propagation speeds associated with the trajectories "patch t.e." and "calm" are 0.46 U_∞ and 0.32 U_∞, respectively, in Fig. 5.

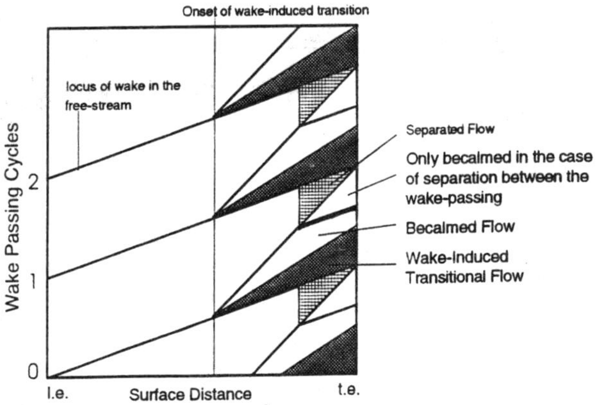

Fig. 6 Schematic distance–time diagram showing the effect of the wake-induced turbulent patch and becalmed region on attached and separated boundary layer

For case C ($\bar{f} = 0.26$) separation was inferred from the frequency content in region C and from Fig. 7 below. The regions B and C show that when the time between the wake-passing is long enough, the transition process is signified by two different distinct fluctuation frequencies. Whereas region B is similar to region A (signifying transition in a not yet fully developed separation bubble) of case D ($\bar{f} = 0.38$), the frequency in region C corresponds to that of no-wake flow

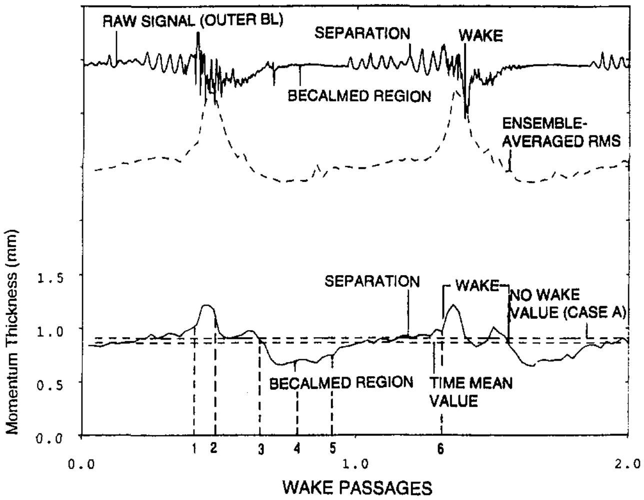

Fig. 7 Hot-wire momentum thickness at the trailing edge (case C, $Re_2 = 1.3 \times 10^5$, $\Phi = 0.7$, $\bar{f} = 0.26$, 4 mm bars, $Tu_{fs,1} = 0.5$ percent, $Tu_{w,1} = 14$ percent, $Y_{pw} = 0.02$)

---

[1] Wake strength refers to velocity defect and peak turbulence intensity. Both scale with bar diameter.

(Schulte, 1995). It follows that the separation bubble needs more time than in case D but less time than in case C to re-establish in time.

The process of re-establishment of the separation bubble after the wake-induced patch and its becalmed region have passed has more than a local impact. It is noticeable even close to the trailing edge at 98 %s. At this position the numbers 1–6 mark several times during the long wake-passing cycle ($\bar{f} = 0.26$). Point 1 marks the leading edge of the wake-induced patch and point 3 marks its trailing edge. It can be seen that the leading edge of the wake-induced turbulent patch is followed by a region of decreasing shear stress. The shear stress then rises again toward the trailing edge (point 3). Point 2 marks a local minimum of the shear stress. This point corresponds to the fluid that underwent transition farthest upstream. Therefore, the turbulent boundary layer has grown more than in the surrounding fluid and the shear stress is consequently lower (Cumpsty et al., 1995; Schulte, 1995) Point 4 marks the end of the becalmed region. Point 5 marks the position where the type of fluctuation (frequency and amplitude) changes and point 6 marks the arrival of the next turbulent patch.

Figure 7 presents hot-wire boundary layer traverse results from the trailing edge for case C ($Re_2 = 1.3 \times 10^5$, $\Phi = 0.7$, $\bar{f} = 0.26$, 4 mm bars). The variation of the momentum thickness during two wake-passing cycles is shown. A hot-wire velocity trace and the ensemble-averaged rms from the outer part of the boundary layer are also shown (on an arbitrary scale). These show the position of the wake. The marks 1–6 from the hot-film signal (Fig. 5) are transferred to this figure. The 1 position has been set at the leading side of the wake, and the other positions (2–5) are on the same relative scale as in Fig. 5.

It can be seen that the variation of momentum thickness correlates with changes in the nature of the hot-film output signal. After point 1 the momentum thickness has a peak value due to the turbulent patch that has grown for a long time. Point 2, which marked the low-shear valley in the middle of the wake-induced turbulent patch, occurs a short time after the momentum thickness has peaked. Before point 3, which marked the trailing edge of the turbulent patch in Fig. 5, another smaller peak in the momentum thickness occurs. The reason for the occurrence of this small peak is not known. Between point 3 and point 4, the low momentum thickness is a result of the becalmed region, which kept the boundary layer attached and laminar (becalmed). Between points 4 and 5 the momentum thickness rises slowly due to the slowly re-appearing separation bubble. Between points 5 and 6 the rise in momentum thickness continues until the value is equal to the value it would adopt in the case without wakes. At point 6 the next wake induces another peak in momentum thickness. The minimum value of momentum thickness during the cycle is about half of the maximum value.

Comparing Figs. 7 and 4 (case B, $Re_2 = 1.3 \times 10^5$, $\Phi = 0.7$, $\bar{f} = 0.78$, 2 mm bars) one notices that in Fig. 4 the phase of the reappearing separation bubble does not appear because of the higher reduced frequency. This caused the mean momentum thickness to be considerably lower than the steady flow value of case A, whereas in this case the mean momentum thickness is only slightly lower than the steady flow value of case A. The strong time-dependence of the momentum thickness at the trailing edge under the influence of the wake-passing gives rise to a significant dependence of its mean value on wake-passing frequency and wake strength.

Results of the Loss Measurements. Figure 8 presents a plot of the stagnation pressure loss coefficient versus Reynolds number. The plot shows data for the cases without wakes, with and without the turbulence grid. Data for the cases with wake passing for the datum reduced frequency of $\bar{f} = 0.78$ and two different bar diameters (2 mm and 4 mm) are also shown. The loss of the bars for the individual cases can be worked out using Eq. (4) (Re_2, Φ, and $\bar{f}$ determine s_{bar} and β).

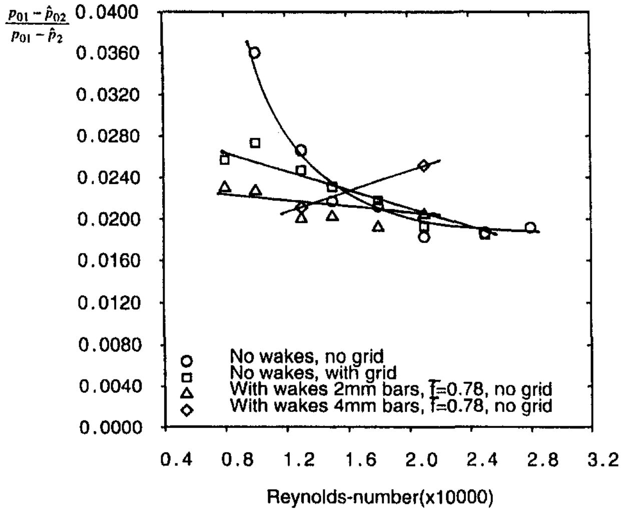

Fig. 8 Stagnation pressure loss versus Reynolds number

For steady flow (no wakes) and no turbulence grid the loss is almost constant for Reynolds numbers greater than 1.6×10^5. At lower Reynolds numbers the loss rises steeply. For steady flow with turbulence grid the loss at higher Reynolds numbers (above 1.6×10^5) is similar to the case without turbulence grid. In the low-Reynolds-number regime there is a reduction in profile loss when the turbulence grid is present compared to the case without the turbulence grid.

For the cases with wake-passing and 2 mm bars ($\bar{f} = 0.78$) the loss is almost at the same low level as in the case without wake-passing for Reynolds numbers above 1.6×10^5. For lower Reynolds numbers the loss rises only very slightly as the Reynolds number is reduced and is much lower than in the case without wakes and without the turbulence grid. It is also lower than in the case without wakes and with the turbulence grid. Overall the loss is weakly dependent on Reynolds number for this reduced frequency and bar diameter ($\bar{f} = 0.78$, 2 mm). It also has a low level. Curtis et al. (1997) show loss measurements for the same blade subjected to wakes produced by 1 mm bars at a higher frequency. At low Reynolds numbers the loss reduction compared to the steady case was not as large as for the case with 2 mm bars presented here.

For the case of 4 mm bars, only two data points are shown. At a Reynolds number of 2.1×10^5, the loss is significantly higher than for the case with 2 mm bars. This implies that for this Reynolds number, the detrimental effect (earlier wake-induced transition onset) outweighs the beneficial (stronger becalmed region) effect of the stronger wakes. At the lower Reynolds number (1.3×10^5), the loss is identical to the case with 2 mm bars. This implies that in the low-Reynolds-number regime, detrimental and beneficial effects of the stronger wakes cancel.

Figure 9 shows the stagnation pressure loss versus reduced frequency for different bar diameters at the datum Reynolds number (1.3×10^5). The data point at zero reduced frequency is the case with no wakes and no turbulence grid (case A). For 2 mm bars, the loss drops with increasing frequency up to the value of the datum reduced frequency ($\bar{f} = 0.78$). The point at higher frequency (filled symbol, $\bar{f} = 1.15$, $\Phi = 0.49$, 2 mm bars, no grid) could only be realized by increasing the speed of the bars, rather than increasing the numbers of bars, which led to a lower flow coefficient and hence a different wake strength. Therefore the changes in loss are not solely a result of the increased frequency.

The cases with 4 mm bars exhibit the same trend and almost the same loss values as the cases with 2 mm bars. Here again, the two cases with highest frequencies were only achieved at the expense of varying the flow coefficient (filled symbols).

Figure 10 shows loss versus reduced frequency for a higher Reynolds number (2.1×10^5) for different bar diameters. For 2 mm bars, the loss increases only slightly. The dependence on frequency is very weak. For the 4 mm cases the loss rises steeply with increasing frequency. At $\bar{f} = 0.78$ it is considerably higher than with no wakes present.

A similar trend of loss versus frequency as shown in Fig. 9 was shown by Schulte and Hodson (1994) for a different low-pressure turbine cascade. The interaction of the wakes with the boundary layer was in that case however shown to be dominated by the wake velocity effect (negative jet effect) rather than by wake-induced transition.

Further Discussion. A comparison of Figs. 8–10 shows that at low Reynolds numbers the unsteady wake-passing is beneficial, regardless of wake strength or frequency. However, the magnitude of loss reduction at low Reynolds numbers is a strong function of the reduced frequency. At high Reynolds numbers the loss is generally increased by unsteady wake-passing, though not as much as it is reduced at low Reynolds numbers. The magnitude of increase is a function of wake strength and wake frequency.

The results demonstrate a potential to design highly loaded LP turbine profiles without suffering large losses at low Reynolds numbers. This is because the large separation bubble (and associated loss) measured in steady-flow tests and predicted in steady-state calculations, in reality, can be suppressed successfully in the unsteady flow field of an actual turbomachine. This requires the adoption of a design method that accounts for unsteady boundary layer effects.

Conclusions

The suction surface boundary layer development of a modern highly loaded LP turbine blade is dominated by effects associated with unsteady wake-passing. The boundary layer with and without wake passing is very different. Whereas without wakes the boundary layer features a large separation bubble at a typical cruise Reynolds number, the bubble is largely suppressed if subjected to unsteady wake-passing at a typical frequency and wake strength. Wake-induced turbulent patches and becalmed regions dominate the boundary layer development.

The boundary layer behavior depends on the wake-passing frequency and the wake strength. Large variations in loss arise due to the different boundary layer characteristics comparing no-wake cases and wake cases and comparing different wake-passing configurations. This is especially true at low Reynolds numbers. The most important result seems to be that for a selected wake-passing frequency and wake-strength, the profile loss is very low and almost independent of the Reynolds-number.

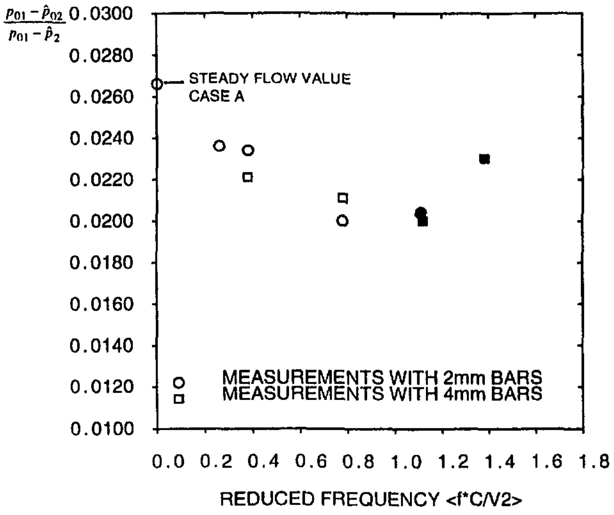

Fig. 9 Stagnation pressure loss versus reduced frequency at $Re_2 = 1.3 \times 10^5$

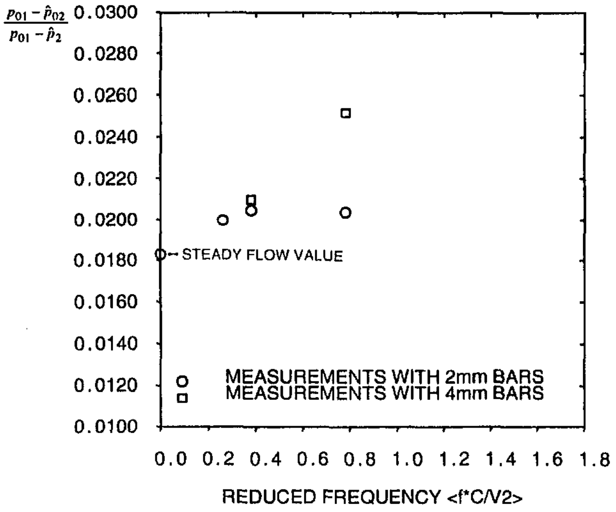

Fig. 10 Stagnation pressure loss versus reduced frequency at $Re_2 = 2.1 \times 10^5$

Acknowledgments

Thanks are due to Dr. R. Banieghbal and Mr. E. Curtis for designing and developing the experimental facility. Some of the measurements were carried out in collaboration with Mr. R. Howell. The technical assistance of Mr. J. Saunders is gratefully acknowledged. During the course of this research the first author was in receipt of grants from the Engineering and Physical Sciences and Research Council of the UK, the Cambridge University Engineering Department, and the Flughafen Frankfurt Main Stiftung.

References

Banieghbal, M. R., Curtis, E. M., Denton, J. D., Hodson, H. P., Huntsman, I., Schulte, V., Harvey, N. W., and Steele, A. B., 1995, "Wake Passing in LP Turbine Blades," presented at the AGARD conference, Derby, UK, 8.5–12.5.

Bearman, P. W., 1971, "Correction for the effect of ambient temperature drift on hot-wire measurements in incompressible flow," *DISA Information,* No. 11, pp. 25–30.

Cumpsty, N. A., Dong, Y., and Li, Y. S., 1995, "Compressor blade boundary layers in the presence of wakes," ASME Paper No. 95-GT-443.

Curtis, E. M., Hodson, H. P., Banieghbal, M. R., Denton, J. D., Howell, R. J., and Harvey, N. W., 1997, "Development of blade profiles for low-pressure turbine applications," ASME JOURNAL OF TURBOMACHINERY, Vol. 119, pp. 531–538.

Halstead, D. E., Wisler, D. C., Okiishi, T. H., Walker, G. J., Hodson, H. P., and Shin, H., 1997, "Boundary layer development in axial compressors and turbines: Part 1—Composite picture; Part 2—Compressors, Part 3—LP Turbines, Part 4—Computations and Analyses," ASME JOURNAL OF TURBOMACHINERY, Vol. 119, pp. 114–127; 426–444; 225–237; 128–139.

Hebbel, H., 1964, "Über den Einfluß der Machzahl und der Reynoldszahl auf die aerodynamischen Beiwerte von Turbinenschaufelgittern bei verschiedener Turbulenz der Strömung," *Forschung im Ingenieurwesen,* Vol. 30, No. 3, pp. 65–77.

Hodson, H. P., 1983, "The Detection of Boundary Layer Transition and Separation in High Speed Turbine Cascades," in: *Measurement Techniques for Transonic and Supersonic Flow—Proc. 7th Symposium,* Aachen, 21st–23rd Sept.

Hodson, H. P., 1984, "Boundary Layer and Loss Measurements on the Rotor of an Axial Flow Turbine," ASME *Journal of Engineering for Gas Turbines and Power,* Vol. 106, pp. 00–00.

Hodson, H. P., Huntsman, I., and Steele, A. B., 1994, "An investigation of boundary layer development in a multistage LP turbine," ASME JOURNAL OF TURBOMACHINERY, Vol. 116, pp. 375–383.

Hourmouziadis, J., 1989, "Aerodynamic Design of Low Pressure Turbines," AGARD Lecture Series, Vol. 167.

Ladwig, M., 1991, "Experimentelle Untersuchungen zum Einfluß einer inhomogenen Zuströmung auf die Entwicklung des Strömungsfeldes in Turbinenschaufelgittern," Dissertation Universität der Bundeswehr, München, Germany.

Pfeil, H., and Eifler, J., 1976, "Turbulenzverhältnisse hinter rotierenden Zylindergittern," *Forschung im Ingenieurwesen,* Vol. 42, pp. 27–32.

Schulte, V., and Hodson, H. P., 1994, "Wake-separation bubble interaction in low pressure turbines," presented at the 30th AIAA/ASME/SAE/ASEE Joint Propulsion Conference, June 27–29, Indianapolis, IN.

Schulte, V., 1995, "Unsteady Separated Boundary Layers in Axial-Flow Turbomachinery," PhD Dissertation, Cambridge University, United Kingdom.

Walker, G. J., 1974, "The Unsteady Nature of Boundary Layer Transition on an Axial-Flow Compressor Blade," ASME Paper No. 74-GT-135.

APPENDIX

Figure A1 shows the measured loss of stagnation pressure across the row of moving bars as a function of flow coefficient (axial velocity/bar speed) for different axial positions (x/d, axial distance/bar diameter) of the downstream pitot probe. If the downstream pitot probe reads a proper time mean stagnation pressure, then the measured loss should be almost independent of the position of the probe. Figure A1 shows that this is not so. The measurement of time mean stagnation pressure downstream of the moving bars is subject to significant errors due to the rapidly fluctuating stagnation pressure caused by the passing wakes.

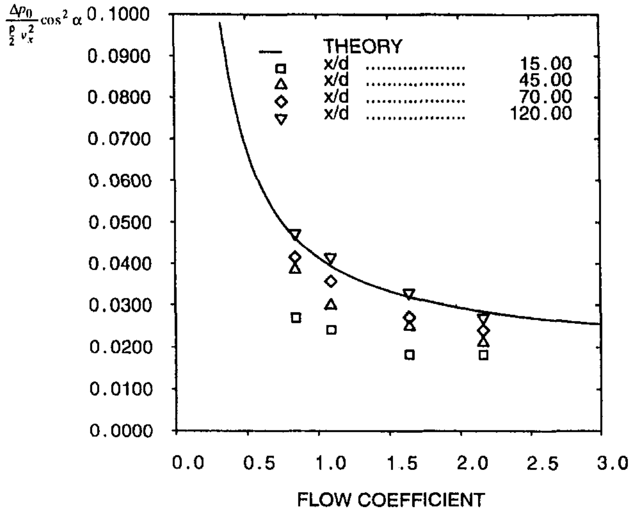

Fig. A1 Total pressure coefficient versus flow coefficient for flow across moving bars: comparison of theory with measurements from different axial probe positions (s/d = 67, c_d = 1.0, α_1 = −30.46 deg)

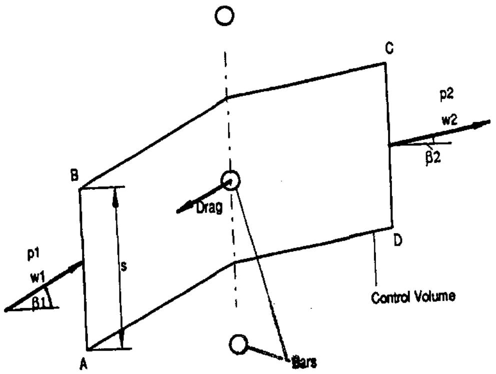

Fig. A2 Control volume for flow through bars in the relative frame (fixed to bars)

The solid line in Fig. A1 is calculated using

$$\frac{\Delta p_{0,\text{bar}}}{\frac{\rho}{2} v_x^2} = c_d \frac{d}{s} Z \cdot \left\{ 1 - \frac{c_d}{4} \frac{d}{s} Z \left(\tan^2 \alpha - \frac{2 \tan \alpha}{\Phi} + \frac{1}{\Phi^2} \right) + \frac{1}{\Phi^2} + \tan^2 \alpha - \frac{2 \tan \alpha}{\Phi} \right\}$$

with

$$Z = \sqrt{1 + \tan^2 \alpha - \frac{2 \tan \alpha}{\Phi} + \frac{1}{\Phi^2}}. \qquad \text{(A1)}$$

Equation (A1) is the result of a control volume analysis in the relative frame of reference (fixed to the bars) according to Fig. A2.

The calculated pressure loss agrees well with the measurements taken at the farthest downstream position where the measurement error is smallest (x/d = 120). Since a distance of x/d = 120 is not available in the cascade test, the theoretical solution is chosen to provide a reference inlet stagnation pressure to the cascade.

W. Sanz
Institute of Thermal Turbomachinery and
Machine Dynamics,
Graz University of Technology,
Graz, Austria

M. F. Platzer
Department of Aeronautics and
Astronautics,
Naval Postgraduate School,
Monterey, CA 93943

On the Navier–Stokes Calculation of Separation Bubbles With a New Transition Model

Laminar separation bubbles are commonly observed on turbomachinery blades and therefore require effective methods for their prediction. Therefore, a newly developed transition model by Gostelow et al. (1996) is incorporated into an upwind-biased Navier–Stokes code to simulate laminar–turbulent transition in the boundary layer. A study of the influence of the two adjustable parameters of the model, the transition onset location and the spot generation rate, is conducted and it is found that it can predict laminar separation bubbles, measured on a NACA 0012 airfoil. Additional results are presented for separation bubbles in an annular compressor cascade.

Introduction

Modern axial compressors are highly loaded to provide higher power output at reduced weight. Therefore, the viscous fluid flow along the blades is subject to high adverse pressure gradients, which increase the risk of boundary layer separation. Especially at off-design, the pressure losses in a compressor stage can rise dramatically as a result of massive flow separation.

Compressor blades usually have very thin leading edges, and therefore it is common to observe leading-edge separation bubbles. A strong adverse pressure gradient forces the laminar boundary layer to separate. The fluctuations in the separated shear layer cause rapid transition. The turbulent flow entrains more fluid and therefore the shear layer bends to the solid wall, causing the flow to reattach as a turbulent boundary layer. Because these short bubbles have only a small displacement effect, only a short region of almost uniform pressure can be observed. There is little effect on the overall pressure distribution. Sometimes they are considered as a means of flow control, because they force the flow to be turbulent. Small changes in either the Reynolds number or angle of attack can cause a short bubble to "burst" leading to a massively separated flow, which affects the pressure distribution along the whole blade and leads to high losses. This separation process is closely connected to laminar–turbulent transition. Therefore, the understanding of transition in adverse pressure gradients and in separated flows is necessary not only to improve the on-design performance but also the off-design behavior and therefore the off-design limits.

Transition in turbomachinery is still an active research topic. Mayle (1991) gives a detailed survey of the role of laminar–turbulent transition in gas turbine engines. Recently, Halstead et al. (1997) conducted an intensive study to investigate the boundary layer development on airfoil surfaces in multistage, axial-flow compressors and low-pressure turbines. Both experiments and computational analyses were made to study the unsteady boundary layer behavior. The occurrence of leading-edge bubbles was experimentally studied by Walraevens and Cumpsty (1995). They found that the free-stream turbulence level has a striking influence on the formation of the bubble. Roberts (1980) states that the main influencing factor on transition inside a separation bubble is the free-stream turbulence, whereas Mayle (1991) finds that transition is primarily controlled by the momentum thickness Reynolds number at separation.

Because of the bubbles' influence on turbomachinery performance, effective methods are required for their prediction. Recently, Platzer and collaborators (Van Dyken et al., 1994; Ekaterinaris et al., 1995; Ekaterinaris and Platzer, 1996) have succeeded in applying an upwind-biased thin-layer Navier–Stokes code to this problem by incorporating the Chen–Thyson transition model (1971) into this code. Transition onset in the separation bubble was estimated using an empirical criterion and the transition length was computed from the Chen–Thyson model. It could be shown that this type of modeling captures the essential physics of the flow problem, as documented by Ekaterinaris et al. (1995), provided the transition constant in the Chen–Thyson model is adjusted to achieve agreement with the available experiment by Chandrasekhara et al. (1992) for a NACA 0012 airfoil at a Reynolds number of 540,000. This adjustment was found to be necessary because the Chen–Thyson model is based on measurements of turbulent spots under zero pressure gradient conditions.

Very recently, Gostelow et al. (1996) presented data on the effect of the streamwise pressure gradient on turbulent spot development and developed a new model to calculate the transition length as a function of pressure gradient and free-stream turbulence level. Solomon et al. (1996) incorporated this model into a boundary layer code and applied it successfully. In the present paper the new model is incorporated into a Navier–Stokes code and it is found that it successfully predicts the NACA 0012 airfoil bubbles. Furthermore, additional results are presented for separation bubbles measured by Schulz and Gallus (1988) in an annular compressor cascade.

Numerical Approach

The thin-layer approximation of the compressible, Reynolds-averaged Navier–Stokes equations for a body-fitted coordinate system (ξ, η) is used to model the fluid flow. These equations are as follows:

$$\partial_t \hat{\mathbf{q}} + \partial_\xi \hat{\mathbf{F}} + \partial_\eta \hat{\mathbf{G}} = \mathrm{Re}^{-1} \partial_\eta \hat{\mathbf{S}} \qquad (1)$$

where $\hat{\mathbf{q}}$ is the conservative variable vector with the components ρ, ρu, ρv and e, $\hat{\mathbf{F}}$ and $\hat{\mathbf{G}}$ are the *inviscid flux vectors*, and $\hat{\mathbf{S}}$ represents the thin-layer approximation of the viscous terms in

---

Contributed by the International Gas Turbine Institute and presented at the 41st International Gas Turbine and Aeroengine Congress and Exhibition, Birmingham, United Kingdom, June 10–13. 1996. Manuscript received at ASME Headquarters February 1996. Paper No. 96-GT-487. Associate Technical Editor: J. N. Shinn.

the normal direction. In these equations all geometric dimensions are normalized with respect to airfoil chord; density, velocity, pressure, and total energy are normalized using free-stream density and speed of sound for single-airfoil calculations and the respective stagnation values for cascade calculations. The pressure is related to density and total energy through the equation of state for an ideal gas. A third-order, upwind-biased, factorized, iterative, implicit numerical scheme (Ekaterinaris and Platzer, 1996) is used to compute the mean flow:

$$\begin{aligned}[]&[\mathbf{I} + h_\xi(\nabla_\xi^b \tilde{\mathbf{A}}_{i,k}^+ + \Delta_\xi^f \tilde{\mathbf{A}}_{i,k}^-)]^p \times [\mathbf{I} + h_\eta(\nabla_\eta^b \tilde{\mathbf{B}}_{i,k}^+ + \Delta_\eta^f \tilde{\mathbf{B}}_{i,k}^- \\ &\quad - \mathrm{Re}^{-1}\delta_\eta \tilde{\mathbf{M}}_{i,k})]^p \times (\tilde{\mathbf{Q}}_{i,k}^{p+1} - \tilde{\mathbf{Q}}_{i,k}^p) = -[(\tilde{\mathbf{Q}}_{i,k}^p - \tilde{\mathbf{Q}}_{i,k}^n) \\ &\quad + h_\xi(\tilde{\mathbf{F}}_{i+1/2,k}^p - \tilde{\mathbf{F}}_{i-1/2,k}^p) + h_\eta(\tilde{\mathbf{G}}_{i,k+1/2}^p - \tilde{\mathbf{G}}_{i,k-1/2}^p) \\ &\qquad - \mathrm{Re}^{-1} h_\eta(\tilde{\mathbf{S}}_{i+1/2,k}^p - \tilde{\mathbf{S}}_{i-1/2,k}^p)] \end{aligned} \tag{2}$$

where $h_\xi = \Delta t/\Delta\xi$, etc., $\tilde{\mathbf{A}}^{\pm} = (\partial\tilde{\mathbf{F}}/\partial\tilde{\mathbf{Q}}^{\mp})$, etc., are the flux Jacobian matrices, and Δ, ∇, δ are the forward, backward, and central difference operators, respectively. The quantities $\tilde{\mathbf{F}}$, $\tilde{\mathbf{G}}$, and $\tilde{\mathbf{S}}$ are numerical fluxes. Time accuracy of the implicit scheme for the calculation of unsteady flow is improved by performing Newton iterations to convergence within each time step. The approximation to $\tilde{\mathbf{Q}}^{n+1}$ at each subiteration is the quantity $\tilde{\mathbf{Q}}^p$. The inviscid fluxes $\tilde{\mathbf{F}}$ and $\tilde{\mathbf{G}}$ are evaluated using Osher's upwind scheme (Osher and Solomon, 1982). For the linearization of the left-hand-side terms, the flux Jacobian matrices $\tilde{\mathbf{A}}$ and $\tilde{\mathbf{B}}$ are evaluated by the Steger–Warming flux-vector splitting (1981). The linearization errors are reduced by subiteration. The viscous fluxes are computed with central differences. The ability of the present method to predict boundary layer profiles accurately has been verified by comparison with conventional boundary layer computations.

Turbulence Modeling

The Baldwin–Barth turbulence model (1990) has been derived from the $k-\epsilon$ model equations by introducing some simplifying assumptions. An advantage of this model compared to algebraic ones (e.g., Baldwin and Lomax, 1978) is that it does not need evaluation of ambiguous length scales, and it describes more accurately the physics of the turbulent flow. It requires the numerical solution of one partial differential equation for a modified turbulent Reynolds number $\nu\tilde{R}_T$:

$$\begin{aligned}\frac{D(\nu\tilde{R}_T)}{Dt} &= (c_{\epsilon_2} f_2 - c_{\epsilon_1})\sqrt{\nu\tilde{R}_T P} + \left(\nu + \frac{\nu_t}{\sigma_\epsilon}\right)\nabla^2(\nu\tilde{R}_T) \\ &\qquad - \frac{1}{\sigma_\epsilon}(\nabla\nu_t)\cdot\nabla(\nu\tilde{R}_T)\end{aligned} \tag{3}$$

This field quantity is related to the $k-\epsilon$ quantities by $R_T = k^2/\nu\epsilon = \tilde{R}_T f_3(\tilde{R}_T)$, where $f_3(\tilde{R}_T)$ is a damping function, which depends on the wall distance. The eddy viscosity can be determined by $\nu_t = c_\mu f_\mu f_3 \nu\tilde{R}_T$ with f_μ as an additional damping function. All the terms and constants are evaluated according to Baldwin and Barth (1990). This turbulence equation is solved decoupled from the mean-flow equations using an implicit factored ADI solver. For the calculation of the flow around a single airfoil in free flow, a turbulent Reynolds number of 0.1 was chosen at the inflow boundaries as suggested by Baldwin and Barth (1990). For the turbomachinery calculation, a turbulent Reynolds number of 5 was applied at the inflow boundary according to a measured turbulence intensity of 1.25 percent.

An inherent feature of this turbulence model as well as of the $k-\epsilon$ turbulence model is that a kind of transition is simulated by the diffusion of turbulent kinetic energy from the main stream into the boundary layer. There is no flexibility in choosing the location of transition onset or the transition length, but in cases where transition occurs very close to the leading edge, a realistic flow behavior can be predicted (see results).

Transition Modeling

Very recently, Gostelow et al. (1996) presented data on the effect of the streamwise pressure gradient on turbulent spot development and developed a new model to calculate the transition length as a function of pressure gradient and free-stream turbulence level. This new method continuously adjusts the spot growth parameters in response to changes in the local pressure gradient and seems to be less sensitive to errors in predicting the start of the transition zone. Although this method was developed for transition in attached flows, it was incorporated in our Navier–Stokes code to predict laminar separation bubbles.

The intermittency distribution in the transitional region is given by

$$\gamma(x) = 1 - \exp\left[-n\int_{x_t}^{x}\frac{\sigma}{\tan\alpha}\left(\frac{dx}{U}\right)\int_{x_t}^{x}\tan\alpha dx\right] \tag{4}$$

where the correlations for the variation of σ and α as functions of the pressure gradient parameter λ_θ are:

$$\alpha = 4 + (22.14/(0.79 + 2.72\exp(47.63\lambda_\theta))) \tag{5}$$

$$\sigma = 0.03 + (0.37/(0.48 + 3.0\exp(52.9\lambda_\theta))) \tag{6}$$

The spot generation rate n is inferred from the dimensionless breakdown rate parameter N (Narasimha, 1985)

$$N = n\sigma\lambda_{\theta_t}^3/\nu \tag{7}$$

$$\begin{aligned}N = 0.86 \times 10^{-3}\exp(2.134\lambda_{\theta_t}\ln(q_t) \\ - 59.23\lambda_{\theta_t} - 0.564\ln(q_t)) \quad \text{for} \quad \lambda_{\theta_t} \le 0\end{aligned} \tag{8}$$

Nomenclature

c = chord length
c_f = local skin friction coefficient
c_l = lift coefficient
c_{ϵ_1}, c_{ϵ_2}, c_μ = constants of turbulence model
e = total energy per unit volume
f_2, f_3, f_μ = damping functions of the turbulence model
k = reduced frequency = $\pi fc/U_\infty$
N = nondimensional breakdown rate parameter = $n\sigma\theta_t^3/\nu$
n = spot generation rate
P = turbulence production term
q_t = free-stream turbulence at x_t, percent
Re = Reynolds number = cU/ν
R_T = turbulent Reynolds number = $k^2/\nu\epsilon$
U = local free-stream velocity
u, v = velocity components
x = streamwise distance from stagnation point
x_t = transition onset location
α = spot spreading half angle, angle of attack, flow angle
γ = intermittency factor
λ_θ = pressure gradient parameter = $(\theta^2/\nu)(dU/dx)$
$\lambda_{\theta t}$ = pressure gradient parameter at x_t
ν = kinematic viscosity
ν_t = turbulent viscosity
θ = boundary layer momentum thickness
ρ = density
σ = spot propagation parameter
σ_ϵ = constant of turbulence model

$$N = N(\lambda_{\theta_t} = 0) \times \exp(-10\sqrt{\lambda_{\theta_t}}) \quad \text{for} \quad \lambda_{\theta_t} > 0 \qquad (9)$$

These formulas imply a maximum value for σ and α for high negative values, but the spot generation rate is allowed to increase to infinity for high negative values of λ_{θ_t}.

The value of the intermittency $\gamma(x)$ is zero for $x \leq x_t$, and increases downstream from the transition point exponentially to a maximum value of one, which corresponds to fully turbulent flow. An effective eddy viscosity for the transitional region is obtained by scaling the turbulent eddy viscosity computed from the mean flow by $\gamma(x)$, i.e., $\mu_{\text{trans}} = \gamma(x)\mu_{\text{turb}}$.

The Gostelow model is based on measurements in attached flows, and in contrast to the Chen–Thyson model (1971), it does not need a second adjustable parameter besides the location of transition onset. But in separated flows the pressure gradient parameter λ_θ can assume high negative values, for which the model is not intended. The value of the spot generation rate n becomes very high for this case and instantaneous transition is predicted inside the bubble. Whereas Roberts (1980) assumes instantaneous transition, Mayle (1991) suggests a spot generation rate according to a zero pressure gradient and using the techniques adopted for attached flows. In our calculations we studied the influence of the spot generation rate on the separation bubble by either limiting the breakdown rate parameter N to a reasonable value of one, which also proved to predict instantaneous transition, or by assuming the value for a zero pressure gradient ($N = N(0) = 0.00315$).

The Gostelow model requires the evaluation of the momentum thickness in the boundary layer, which, unfortunately, is not defined for separated flow regions. Moreover, the intermittency function has only streamwise one-dimensional dependency; normal-to-wall effects are not considered for transition. But from an implementation point of view, the present transition model is quite easy to use; it can be combined with any turbulence model, and for attached flows it reduces the number of adjustable parameters to one.

In our investigation, the location of transition onset remains as a second adjustable parameter besides the breakdown rate parameter. There are several methods available for predicting the transition onset; most of them are based on empirical formulations for boundary layer flows, like the Michel criterion (Cebeci and Bradshaw, 1977) or the e^N method. A more promising procedure seems to be the parabolic stability equation by Herbert and Bertolotti (1987), which does not require empirical information. Mayle (1991) suggests an empirical formulation for the transition onset location in separation bubbles as a function of the momentum thickness Reynolds number at separation onset. His prediction differs between short and long bubbles by a factor of three. However, this is questionable, because our calculations predict a change from a short to a long bubble by slightly moving the transition onset inside the bubble. Therefore, for this investigation we specified the transition onset location as a second parameter and studied its influence on the flow prediction.

Results and Discussion

In this investigation numerical results were compared with the measurements of the flow over a NACA 0012 airfoil (Chandrasekhara et al., 1992) and of the three-dimensional flow through an annular compressor cascade (Schulz and Gallus, 1988).

Comparison With the Measurements of Chandrasekhara et al. (1992). In 1992 Chandrasekhara et al. conducted detailed measurements of the flow over a NACA 0012 airfoil in the NASA Ames Research Center. The measurements were obtained for steady flow at fixed angles of attack and for an oscillatory motion of the airfoil $\alpha(t) = 10$ deg + 2 deg sin (ωt) with a reduced frequency $k = 0.05$. Here the flow for a freestream Mach number of 0.3 and a Reynolds number of 540,000 based on the airfoil chord length (8500 based on leading edge radius) will be investigated. The maximum angle of attack is 12 deg, which is the static stall angle of attack. Laser-Doppler velocimetry (LDV) data and point diffraction interferometry (PDI) images were obtained for both steady and oscillatory flow. The key result of the experiments is that a leading-edge separation bubble forms on the airfoil. For steady flow at an angle of attack of 8 deg and 10 deg a separation bubble is formed, whereas at 12 deg the flow is fully stalled. For oscillatory motion the bubble grows in size during the upstroke. During the downstroke, the bubble decreases in size initially, but at an angle of 11.5 deg the vorticity in the bubble suddenly coalesces and is shed. At about half a degree later the flow reattaches. This behavior leads to a hysteresis in the pressure forces on the airfoil.

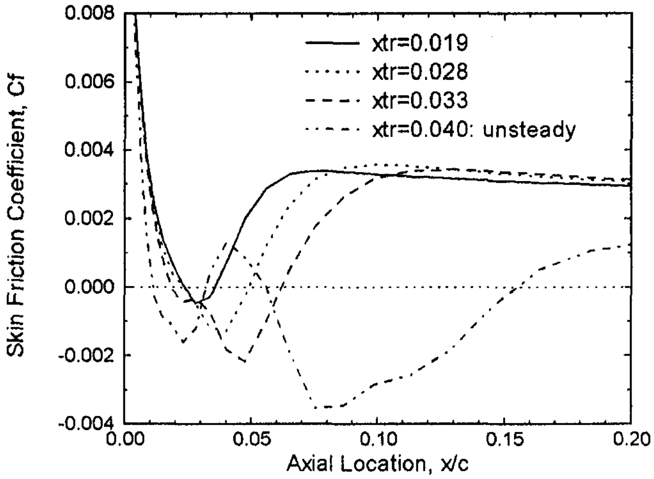

Fig. 1 Effect of transition onset location on skin friction distribution on the upper surface, $N = N(0) = 0.003$, $\alpha = 8$ deg

Computational results are presented at first for steady flow at 8, 10, and 12 deg angle of attack. Figure 1 shows the skin friction distribution c_f on the upper surface for the forward 20 percent of the airfoil at 8 deg angle of attack for a zero pressure gradient value of N. The negative value shows the region of reversed flow and hence the length of the separation bubble. Variation of the transition onset by 1.4 percent chord length from $x/c = 0.019$ to $x/c = 0.033$ increases the bubble length from about 1 percent chord length to about 4.5 percent. Moving the transition onset farther downstream results in an unsteady solution with high fluctuations.

In Fig. 2 the c_f value is compared for both values of the breakdown rate parameter N. The fully turbulent solution shows a minimum close to the leading edge, but does not predict separation. Nearly the same result is obtained for a transition onset at $x/c = 0.019$ and a breakdown rate parameter limit of one, but reverse flow occurs at one grid point. Choosing a zero pressure gradient value for N leads to a slightly longer separation bubble for the same transition onset. The longest predicted steady bubbles for both values of the breakdown rate parameter show that an instantaneous transition ($N < 1$) allows a more downstream transition onset and leads to two bubbles, as indicated by the positive c_f value within the separation zone with negative c_f values. Varying the transition onset and the breakdown rate parameter N can give results ranging from no bubble to a bubble length of about 5 percent chord length. It is interesting to note that in some cases, especially for very short bubbles, separation starts downstream of the transition onset. Figure 3 shows the intermittency function according to Fig. 2. A breakdown rate parameter limit of one leads to nearly instantaneous transition. In contrast, a zero pressure gradient value for N and

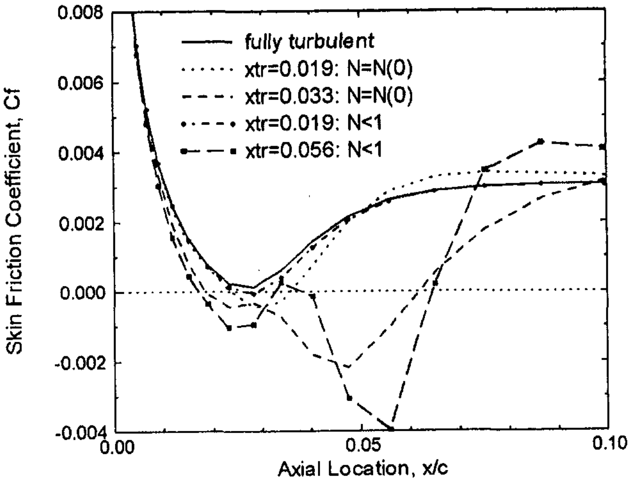

Fig. 2 Skin friction distribution on the upper surface, $\alpha = 8$ deg ($N(0) = 0.003$)

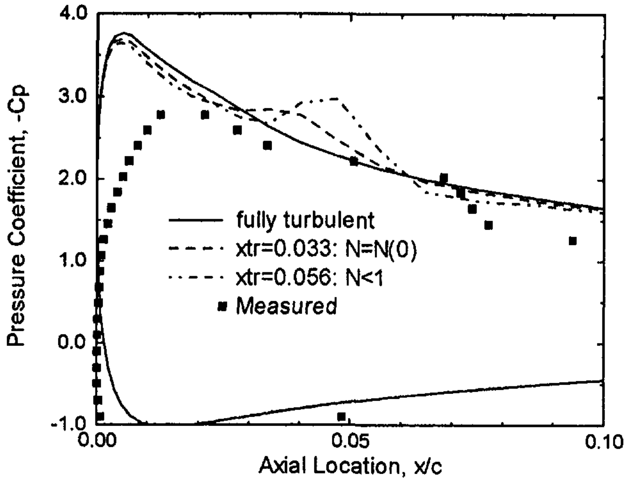

Fig. 4 Measured and calculated surface pressure distribution, $\alpha = 8$ deg ($N(0) = 0.003$)

a transition onset at $x/c = 0.033$ result in a transition length of about 15 percent. The computational result that the end of transition may lie downstream of the reattachment point was also observed by Walker et al. (1988). Using the momentum thickness Reynolds number at separation onset, Mayle's Eqs. (11), (12) (Mayle, 1991) predict a transition onset at $x/c = 0.034$ and a transition length of 1.3 percent chord. For the same case Walker (1993, Eq. (24)) predicts a transition length of 2.2 percent chord. The comparison of the measured pressure distribution with the computed solutions is shown in Fig. 4. The fully turbulent solution shows a continuous decrease in pressure after the suction peak, whereas the solutions with the longest steady bubbles for both values of N predict a region of constant or even increasing pressure. Both transitional solutions give a slightly smaller suction peak than the attached fully turbulent flow solution. In contrast, the measurements show a smaller suction peak and a longer region of constant pressure. The differences close to the leading edge can be partly explained by the measurement uncertainties of the experiment.

Figure 5 shows the comparison of the skin friction distribution between a fully turbulent solution and the smallest and longest separation bubbles predicted by a numerically stable solution for 10 deg angle of attack. The turbulent solution also predicts a separation bubble similar to the smallest bubbles obtained by the transitional solution. This can be explained by the inherent transitional feature of the Baldwin–Barth turbulence model. The bubble predicted by the zero pressure gradient value of N has a maximum length of about 4 percent and is nearly twice as long as that predicted by instantaneous transition ($N < 1$).

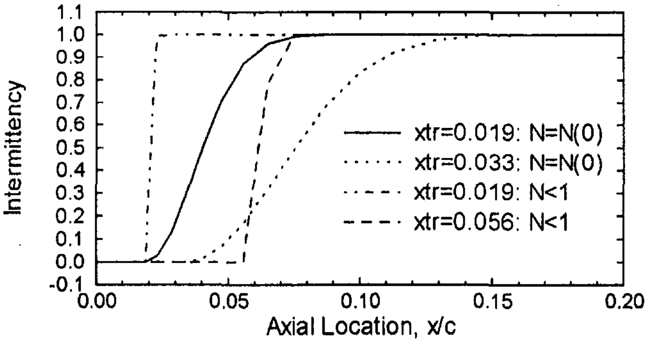

Fig. 3 Intermittency function versus axial location, $\alpha = 8$ deg ($N(0) = 0.003$)

The comparison of the calculated surface pressure for the longest bubbles with the measured values shows an earlier predicted separation start and much shorter predicted separation zone (Fig. 6). The difference in the suction peak is remarkable. Moving the transition onset location farther downstream leads to an unsteady shedding of the leading-edge separation bubble, as shown by the instantaneous streamline contours in Fig. 7. The suction peak is small and the pressure distribution is flat indicating stall where the flow is fully separated. Moving the transition onset downstream can lead to stall at an angle of attack 2 deg smaller than the measured static stall angle.

The experiment shows that static stall occurs at an angle of attack of 12 deg. Figure 8 shows the skin friction distribution for a fully turbulent solution and for transitional calculation just before and at stall. Again the fully turbulent solution is able to predict a separation bubble. Specifying the transition onset at $x/c = 0.009$ for a zero pressure gradient value of N or at $x/c = 0.019$ for N limited to one yields a stable separation bubble, but moving the transition onset one grid point downstream leads to stall. At stall a small laminar separation bubble occurs close to the leading edge, but the flow reattaches before it fully separates and becomes unsteady. The corresponding pressure distribution in Fig. 9 shows that the change in the location of the transition onset leads to a "burst" of the leading-edge bubble

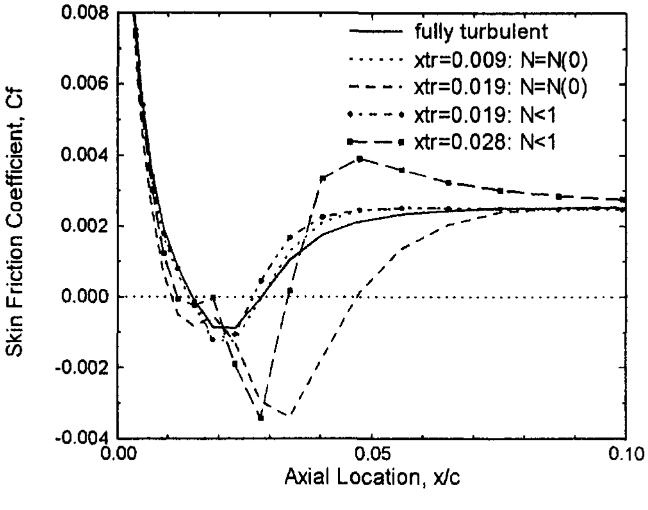

Fig. 5 Skin friction distribution on the upper surface, $\alpha = 10$ deg, ($N(0) = 0.003$)

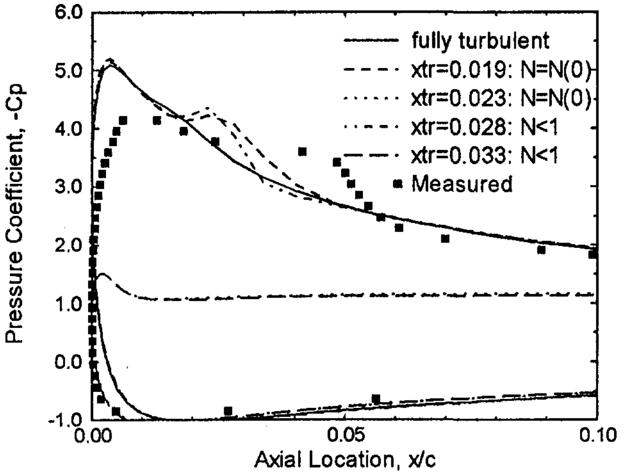

Fig. 6 Measured and calculated surface pressure distribution, α = 10 deg ($N(0)$ = 0.003)

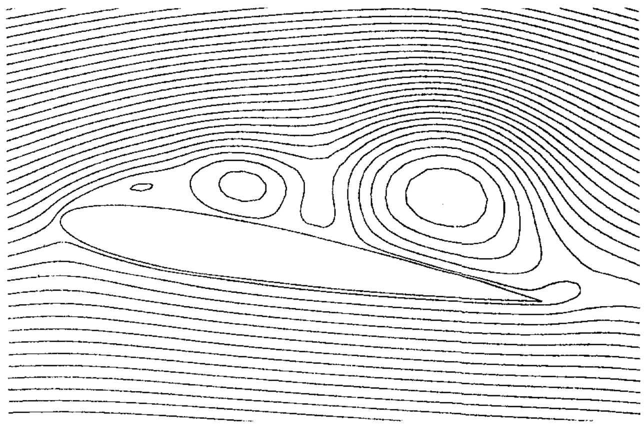

Fig. 7 Instantaneous streamline contours of the flow around a NACA 0012 airfoil, α = 10 deg, unsteady solution

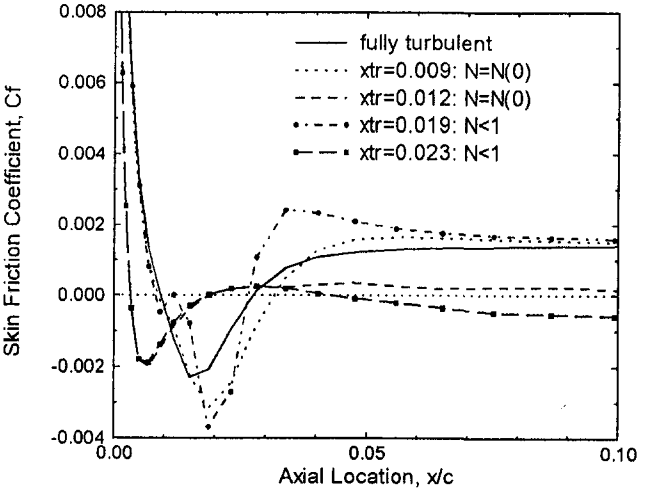

Fig. 8 Skin friction distribution on the upper surface, α = 12 deg ($N(0)$ = 0.003)

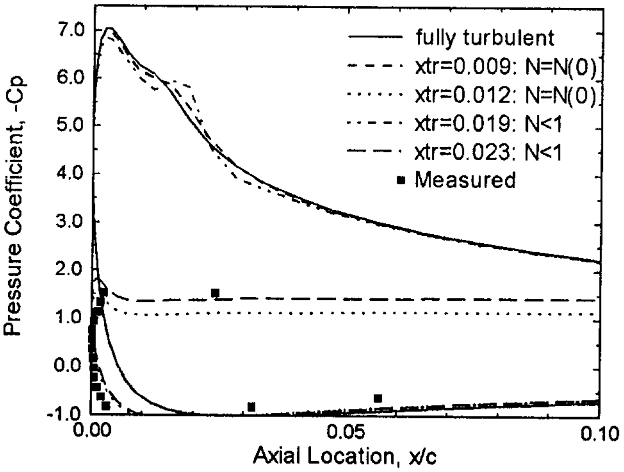

Fig. 9 Measured and calculated surface pressure distribution, α = 12 deg ($N(0)$ = 0.003)

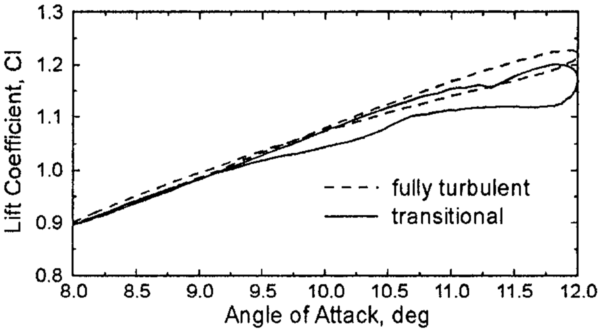

Fig. 10 Computed lift loop for oscillatory motion, $\alpha(t)$ = 10 deg + 2 deg sin (ωt), k = 0.05

and to fully separated flow indicated by the small suction peak and the flat pressure profile. In contrast to a fully turbulent solution, the transitional solution is capable of predicting the measured flow behavior of stall at this angle of attack.

The solution for the oscillating airfoil was obtained with 20,000 time steps for the entire cycle, corresponding to a nondimensional time step of Δt = 0.011 or a Courant number of approximately 1000, using two Newton iterations. The transitional solution was computed by limiting the breakdown rate parameter N to one and choosing the transition onset location according to the steady-state solution. Figure 10 shows the computed lift loop for a fully turbulent and a transitional solution. There is a significant hysteresis effect, which is not obtained by the fully turbulent solution. Vortex shedding was not observed at 12 deg angle of attack, nor for the downstroke as measured in the experiment. It seems that the turbulence model or the flow solver produces too much dissipation, which prevents the leading-edge bubble from shedding.

Comparison With the Measurements of Schulz and Gallus (1988). Schulz and Gallus (1988) conducted measurements of the flow through an annular compressor cascade with and without rotor for different flow angles. The flow without a rotor showed zones of laminar separation on the suction surface at midspan for flow angles of 40.0 and 44.2 deg. A three-dimensional flow analysis by Benetschik et al. (1995) using a low-Reynolds-number $k-\epsilon$ model could not predict this flow behavior. Therefore, a two-dimensional Navier–Stokes analysis with the Gostelow transition model was tried. The flow at midspan at a flow angle of 44.2 deg, which corresponds to an incidence

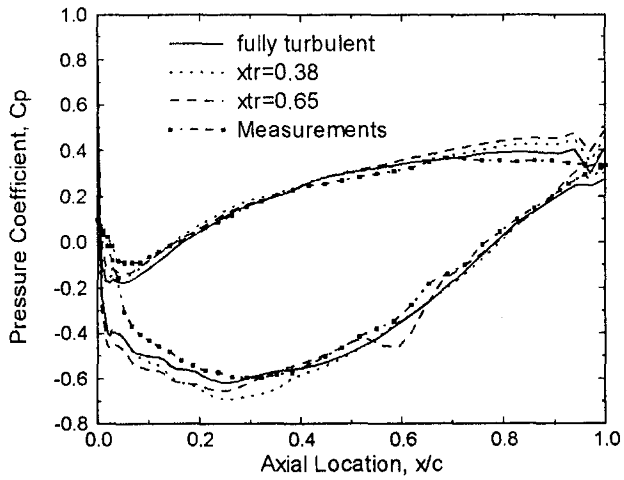

Fig. 11 Measured and calculated surface pressure distribution, annular compressor cascade, α = 44.2 deg

angle of 2 deg, was chosen, where a laminar separation bubble occurs, extending from 34 to 68 percent chord length (Schulz, 1989). The measured turbulence level is 1.25 percent. The breakdown rate parameter was again limited to one. Figure 11 shows the comparison of the predicted pressure distribution for the fully turbulent and the transitional solutions with the three-dimensional measurements. There are remarkable differences at the leading edge and the trailing edge due to three-dimensional effects. The wiggles in the predicted pressure distribution are caused by inaccuracies in the published blade coordinates. The fully turbulent and the transitional solutions also differ remarkably. A laminar separation bubble could not be found choosing a transition onset at the measured location x/c = 0.38, as shown in Fig. 12. But laminar separation occurs if a transition onset location is specified at x/c = 0.56 or farther downstream. The calculations remained steady up to a value of x/c = 0.65. The computations were conducted with both an inflow turbulence level of 0.1 and 1.25 percent, but no difference in the predicted solutions was found. This can be explained by the fact that the used intermittency function is only a streamwise one-dimensional function, which prevents diffusion of the turbulent kinetic energy from the main flow into the laminar boundary layer. Although the laminar separation zone predicted by this two-dimensional solution differs remarkably from the experiment, this study shows that the incorporation of laminar–turbulent transition is necessary to predict the measured flow behavior.

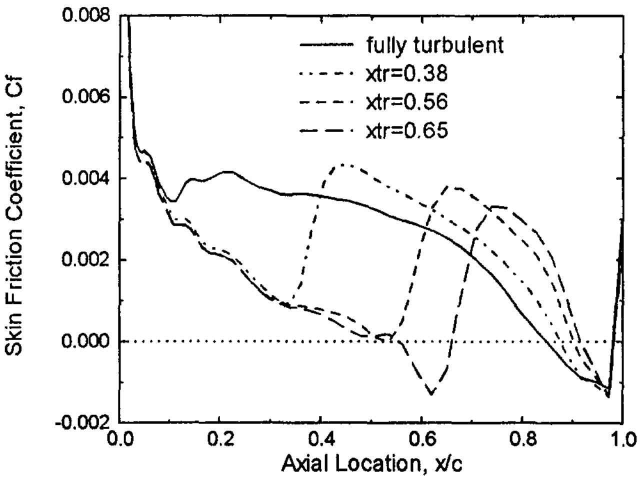

Fig. 12 Skin friction distribution on the blade suction surface, annular compressor cascade, α = 44.2 deg

Conclusion

A new transition model by Gostelow et al. (1996) was incorporated into a thin-layer, upwind-biased Navier–Stokes code to calculate laminar separation bubbles. Because the transition model was developed for attached flows, the spot generation rate was varied as a second adjustable parameter besides the transition onset location. If rapid transition is assumed, then the transition onset may be located farther downstream while still yielding steady solutions. Varying both spot generation rate and transition onset can give results ranging from no separation to bubbles of about 5 percent chord length to full stall, but it is found that for the cases investigated the incorporation of laminar–turbulent transition is necessary to predict the measured flow behavior. At present, there is no reliable method to choose the "correct" transition onset location and spot generation rate. Therefore, this information must be provided by detailed experimental measurements of the transition process (transition onset and transition length) inside separation bubbles.

Acknowledgments

The first author gratefully acknowledges the support of the Austrian Science Foundation (FWF) and of the California State University at Long Beach (Prof. Cebeci). The second author acknowledges the support of the Naval Air Warfare Center, China Lake, California. Furthermore, the authors are indebted to Prof. Gostelow of the University of Leicester, UK, and to Prof. Walker of the University of Tasmania, Australia, for their stimulating comments.

References

Baldwin, B. S., and Barth, T. J., 1990, "A One-Equation Turbulence Transport Model for High Reynolds Number Wall-Bounded Flows," NASA TM 102847.

Baldwin, B. S., and Lomax, H., 1978, "Thin-Layer Approximation and Algebraic Model for Separated Turbulent Flows," AIAA Paper No. 78-257.

Benetschik, H., Lohmann, A., Lücke, J. R., and Gallus, H. E., 1995, "Entwicklung eines Verfahrens zur Berechnung der reibungsbehafteten Strömung im Verdichtereinzelgitter," AG Turbo Forschungsvorhaben 1.1.2.6., Final Report, RWTH Aachen, Germany.

Cebeci, T., and Bradshaw, P., 1977, *Momentum Transfer in Boundary Layers*, Hemisphere Publishing Corporation, Washington, p. 153.

Chandrasekhara, M. S., Carr, L. W., and Ekaterinaris, J. A., 1992, "Interferometric and Computational Studies of an Oscillating Airfoil Compressible Dynamic Stall Flow Field," *Proc. 5th Asian Conference of Fluid Dynamics*, Vol. 2, pp. 1047–1050.

Chen, K. K., and Thyson, N. A., 1971, "Extension of Emmon's Spot Theory to Flows on Blunt Bodies," *AIAA Journal*, Vol. 9, No. 5.

Ekaterinaris, J. A., and Platzer, M. F., 1996, "Numerical Investigation of Stall Flutter," ASME JOURNAL OF TURBOMACHINERY, Vol. 118, pp. 197–203.

Ekaterinaris, J. A., Chandrasekhara, M. S., and Platzer, M. F., 1995, "Analysis of Low Reynolds Number Airfoil Flows," *Journal of Aircraft*, Vol. 32, No. 3.

Gostelow, J. P., Melwani, N., and Walker, G. J., 1996, "Effects of a Streamwise Pressure Gradient on Turbulent Spot Development," ASME JOURNAL OF TURBOMACHINERY, Vol. 118, pp. 737–743.

Halstead, D. E., Wisler, D. C., Okiishi, T. H., Walker, G. J., Hodson, H. P., and Shin, H.-W., 1997, "Boundary Layer Development in Axial Compressors and Turbines, Parts 1–4," ASME JOURNAL OF TURBOMACHINERY, Vol. 119, pp. 114–127; 426–444; 225–237; 128–139.

Herbert, T., and Bertolotti, F. P., 1987, "Stability Analysis of Nonparallel Boundary Layers," *Bulletin of the American Physical Society*, Vol. 32.

Mayle, R. E., 1991, "The Role of Laminar-Turbulent Transition in Gas Turbine Engines," ASME JOURNAL OF TURBOMACHINERY, Vol. 113, pp. 509–537.

Narasimha, R., 1985, "The Laminar-Turbulent Transition Zone in the Boundary Layer," *Progress in Aerospace Science*, Vol. 22, pp. 29–80.

Osher, S., and Solomon, F., 1982, "Upwind Difference Schemes for Hyperbolic Systems of Conservation Laws," *Mathematics of Computation*, Vol. 38, No. 158, pp. 339–374.

Roberts, W. B., 1980, "Calculation of Laminar Separation Bubbles and Their Effects on Airfoil Performance," *AIAA Journal*, Vol. 18, pp. 25–31.

Schulz, H. G., 1989, "Experimentelle Untersuchung der dreidimensionalen abgelösten Strömung in einem Axialverdichterringgitter," Dissertation, RWTH Aachen, Germany.

Schulz, H. D., and Gallus, H. E., 1988, "Experimental Investigation of the Three-Dimensional Flow in an Annular Compressor Cascade," ASME JOURNAL OF TURBOMACHINERY, Vol. 110, p. 467.

Solomon, W. J., Walker, G. J., and Gostelow, J. P., 1996, "Transition Length Prediction for Flows With Rapidly Changing Pressure Gradients," ASME JOURNAL OF TURBOMACHINERY, Vol. 118, pp. 744–751.

Steger, J. L., and Warming, R. F., 1981, "Flux Vector-Splitting of the Inviscid Gas Dynamic Equations With Applications to Finite-Difference Methods," *Journal of Computational Physics*, Vol. 40, pp. 263–293.

Van Dyken, R. D., Ekaterinaris, J. A., Chandrasekhara, M. S., and Platzer, M. F., 1994, "Analysis of Compressible Steady and Oscillatory Airfoil Flows at Transitional Reynolds Number," AIAA Paper No. AIAA-94-2255.

Walker, G. J., Subroto, P. H., and Platzer, M. F., 1988, "Transition Modeling Effects on Viscous/Inviscid Interaction Analysis of Low Reynolds Number Airfoil Flows Involving Laminar Separation Bubbles," ASME Paper No. 88-GT-32.

Walker, G. J., 1993, "The Role of Laminar–Turbulent Transition in Gas Turbine Engines: A Discussion," ASME JOURNAL OF TURBOMACHINERY, Vol. 115, p. 207–217

Walraevens, R. E., and Cumpsty, N. A., 1995, "Leading Edge Separation Bubbles on Turbomachine Blades," ASME JOURNAL OF TURBOMACHINERY, Vol. 117, pp. 115–125.

O. Popp

H. Zimmermann

J. Kutz

Daimler-Benz Aerospace
MTU München,
Munich, Federal Republic of Germany

CFD Analysis of Coverplate Receiver Flow

The flow field in a preswirled cooling air supply to a turbine rotor has been investigated by means of CFD simulations. Coefficients for system efficiency are derived. The influences of various geometric parameters for different configurations have been correlated with the help of appropriate coefficients. For some of the most important geometric parameters of the coverplate receiver, design recommendations have been made. For the preswirl nozzles, the potential of efficiency improvement by contour design is highlighted.

1 Introduction

In high-performance gas turbine engines, the blade cooling air is supplied through nozzles located on stationary components. Then either the air is fed directly to the blade roots, or coverplates are used to discharge the air at a convenient diameter with subsequent ducting to the turbine blades (see Fig. 1). In this case the air is collected by a series of rotating receiver holes in the coverplate. In order to reduce the temperature in the rotating frame of reference, preswirl is applied.

The characteristics of the preswirl nozzle and receiver flow have to be known in order to minimize temperatures in the rotating frame of reference and pressure losses. The receiver has to be designed for low pressure and acceptable swirl losses.

For this purpose there is little information available in the literature. Meierhofer and Franklin (1981) tested various preswirl geometries and it was found that the system efficiency was mainly dependent on the effective preswirl velocity ratio (see section 3.5). The investigation comprises many geometric parameters, and the striking result was that the geometry was mainly of little importance.

Zimmermann (1990) investigated the flow through an unbladed coverplate by CFD, but the analysis started behind the receiver. By a combined experimental and numerical study, El-Oun and Owen (1989) found that the efficiency of a preswirl system is mainly influenced by a boundary layer flow from the disk windage, which mixes with the preswirl flow and reduces the temperature drop. Kutz and Speer (1994) showed how the relevant pressure losses can be integrated into the complex cooling air system program of the whole engine. Wilson and Owen (1997) presented experimental and CFD analysis of the heat transfer in a preswirl system.

Engine development programs for the civil market are characterized by extremely short lead times. In many cases CFD analysis combined with existing model test results offers new opportunities to optimize the design without expensive and time consuming rig or engine tests.

In this paper the flow fields of preswirl nozzles and receivers are investigated by CFD and the influences on the design are highlighted. The objectives are the following:

- to understand the physics of the flow in the preswirl chamber and receiver;
- to determine the effects and importance of various geometric parameters;
- to obtain qualitative description of losses;
- to establish design rules on system geometry.

2 Methods

2.1 Methods of Investigation. In industry, CFD is used for flow optimization purposes and to find out the influence of various geometric parameters. For this analysis it was essential to have an effective CFD tool as many configurations were to be investigated. For most cases it can be stated that CFD modeling with the exact geometry provides results of higher accuracy than extrapolating from model test data.

2.2 Flow Field Computations. The flow fields were computed with a commercially available CFD code described in Raw et al. (1989). Relevant to this investigation is:

- turbulent eddy viscosity with the standard k–e model;
- range from subsonic to supersonic velocities;
- compressible and incompressible flow;
- logarithmic law of the wall used to account for wall friction;
- a high degree of numerical robustness is guaranteed by use of a fully coupled linear solver accelerated by a multigrid and a block correction scheme;
- accuracy is high due to a fully implicit, colocated finite volume method with a flux-element-based discretization of geometry and the availability of a second-order discretization;
- H-type grid. Walls are closely described by boundary fitted coordinates.

2.3 Simplifications

2.3.1 Modeling Simplifications. In order to obtain results applicable to a large variety of coverplate air supply systems, a prototype of a nozzle receiver system was designed for numerical analysis. The dimensions are similar to those of an MTU test rig for experimental flow analysis. Its geometry is described by Zimmermann (1990).

For simplification, only a circumferential sector of the annulus was investigated, assuming it to be the smallest periodic part of the system. Also, the number of receiver orifices was assumed to be an integer multiple of the number of preswirl nozzles (see Fig. 2). Furthermore, the annular arrangement was treated as a plane system in view of the small differences of inner and outer radii of the annulus. Orifices were squared with the edges having the length of the hydraulic diameter of the test rig orifices to keep the grid simple and to maintain numerical robustness of H-grid computations. The difference in discharge behavior between square and circular holes is negligible for this investigation, according to experiments performed by Callaghan and Bowden (1947).

For these reasons several simplifications are to be stated:

- neither Coriolis nor centrifugal forces are taken into account according to small radial differences;

Contributed by the International Gas Turbine Institute and presented at the 41st International Gas Turbine and Aeroengine Congress and Exhibition, Birmingham, United Kingdom, June 10–13, 1996. Manuscript received at ASME Headquarters February 1996. Paper No. 96-GT-357. Associate Technical Editor: J. N. Shinn.

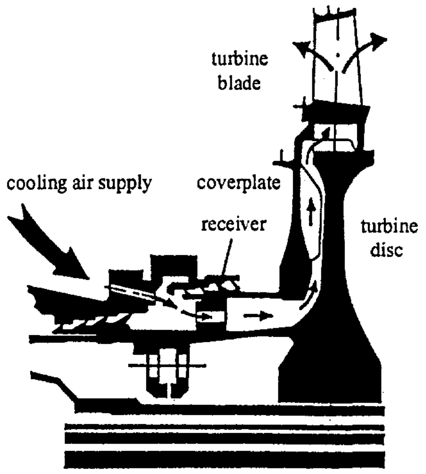

Fig. 1 Example of preswirled cooling air supply system

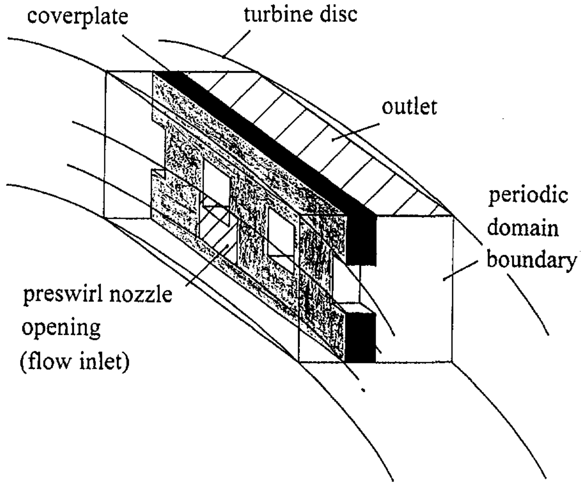

Fig. 2 Geometric model

- labyrinth leakage out of or into the coverplate prechamber is not simulated;
- effects of disk friction on temperature drop as investigated by El-Oun and Owen (1989) are not regarded.

The aerodynamic planes of reference and geometric parameters are shown in Fig. 3.

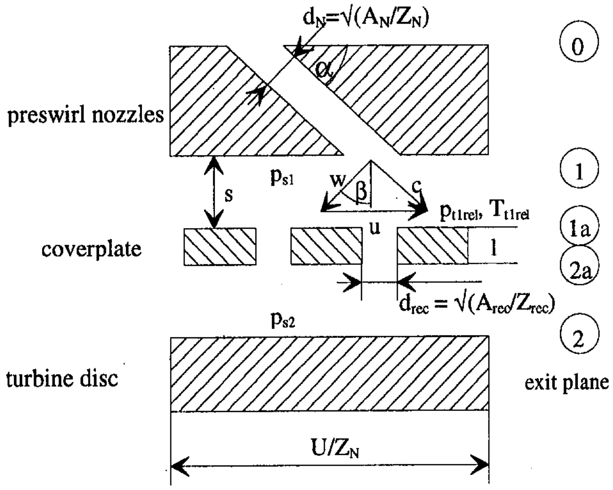

Fig. 3 Aerodynamic Planes and Geometric Parameters

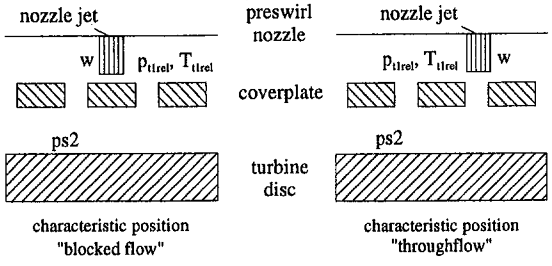

Fig. 4 Characteristic relative positions of nozzle and receiver orifices

2.3.2 Steady Treatment of Unsteady Problem. In order to keep the computing time within limits, allowing variation of many geometric parameters, the unsteady problem was treated as a steady one. It was decided to select two characteristic relative positions of nozzle and coverplate receiver and to consider the time-averaged values of system coefficients to be of similar magnitude as the arithmetic average of the coefficients observed with these two relative positions. Figure 4 shows these two positions as seen from the rotor frame of reference. The Strouhal number turns out to be about u/c_t. So for the lower range of this ratio unsteady effects can be neglected, whereas for very high rotational speeds they may appear to become more important. (A check by an unsteady computation of one particular geometry at one rotational speed showed that the assumptions made were acceptable.)

Nomenclature

A = cross-sectional area, m^2
c = absolute velocity, m/s
C_D, C_{DG}, C_{DN} = receiver, total, nozzle discharge coefficient
c_p = specific heat, m^2/s^2K
d = diameter, m
l = receiver orifice length, m
$\dot{m}$ = mass flow, kg/s
p = pressure, bar
R = gas constant, m^2/s^2K
s = spacing between nozzle and receiver, m
T = temperature, K
u = circumferential velocity of the rotor, m/s
w = relative velocity, m/s
Z = number of orifices
α = absolute jet inclination angle, deg
β = relative jet inclination angle, deg
κ = isentropic exponent
Π_{Loss} = pressure loss

Subscripts

av = averaged
i = counting index
ideal = ideal
is = isentropic
n = normal to receiver plane
max = maximal
N = nozzle
real = real
rec = receiver
rel = relative
s = static
t = total, tangential
theo = theoretical
0, 1, 2, = stage 1, 2, . .
limit = maximal or minimal value

2.3.3 Ideal Nozzle. As the main part of this investigation is concerned with the influence of coverplate receiver geometry, the influence of the nozzle on system efficiency was kept small by assuming an uniform total pressure and temperature profile over the entire nozzle exit area. So the influence of nozzle shape or throttling was disregarded but the effects of the receiver on the jet downstream of the nozzle were included.

2.4 Changing From Absolute to Relative Frame of Reference. In order to carry out investigations on the moving part of a stator–rotor system, it is convenient to change into the moving frame of reference. While physical properties of the air don't change in the absolute and relative frame of reference, total properties vary with relative motion:

$$\frac{T_{t\mathrm{rel}}}{T_{t0}} = 1 + \frac{u^2 - 2 \cdot u \cdot c_t}{2 \cdot c_p \cdot T_{t0}} \tag{1}$$

$$\frac{p_{t\mathrm{rel}}}{p_{t0}} = \left(1 + \frac{u^2 - 2 \cdot u \cdot c_t}{2 \cdot c_p \cdot T_{t0}}\right)^{\kappa/(\kappa-1)} \tag{2}$$

These correlations are graphically depicted in Fig. 5.

2.5 Definitions of System Coefficients

2.5.1 Aerodynamic Efficiency. The aerodynamic efficiency of the system can be described by the loss of total pressure. Thus the relative total pressure in outlet plane 2 is related to that of the nozzle entry $p_{t1\mathrm{rel}}$

$$\Pi_{\mathrm{Loss}} = \frac{p_{t1\mathrm{rel}} - p_{t2\mathrm{rel}}}{p_{t1\mathrm{rel}} - p_{s2}} \tag{3}$$

To characterize the flow field in the receiver holes a C_D value is used, and defined as follows. For every receiver hole, an ideal massflow is defined by the maximum relative total pressure in the orifice exit plane, the mass-averaged static pressure, and the geometric exit area. The total temperature is defined by inflow boundary conditions as explained in section 2.4. C_D is then defined as the ratio of the total real mass flow to the sum of the ideal mass flows of all receiver holes:

$$C_D = \frac{\sum_{i=1}^{Z_{\mathrm{rec}}} \dot{m}_{\mathrm{real}}}{\sum_{i=1}^{Z_{\mathrm{rec}}} \dot{m}_{\mathrm{ideal}}} = \frac{\sum_{i=1}^{Z_{\mathrm{rec}}} \dot{m}_{\mathrm{real}}}{\sum_{i=1}^{Z_{\mathrm{rec}}} \sqrt{\frac{2 \cdot \kappa}{\kappa - 1}} \cdot \frac{A_{\mathrm{rec}}}{Z_{\mathrm{rec}}} \cdot \frac{p_{t\_\mathrm{rel\_max\_}2a\_i}}{\sqrt{R \cdot T_{t\_\mathrm{rel}}}} \cdot \sqrt{\left(\frac{p_{s\_av\_2a}}{p_{t\_\mathrm{rel\_max\_}2a\_i}}\right)^{2/\kappa} - \left(\frac{p_{s\_av\_2a}}{p_{t\_\mathrm{rel\_max\_}2a\_i}}\right)^{(\kappa+1)/\kappa}}} \tag{4}$$

with the subscript i being the address of the receiver orifices.

2.5.2 Throttle Effects. The flow through the system is influenced by the flow resistance of the receiver. In order to describe this throttling effect of the receiver, the real mass flow is compared to the mass flow that would be observed if the receiver didn't have any throttling influence on the flow, i.e., the nozzle jet would expand freely from p_{t0} to p_{s2}. In real constellations the receiver's influence on the nozzle jet is to increase the static pressure at the nozzle exit and therefore decrease velocity and mass flow. The ratio of real to the hypothetical massflow is called C_{DG}. This definition is illustrated in Fig. 6.

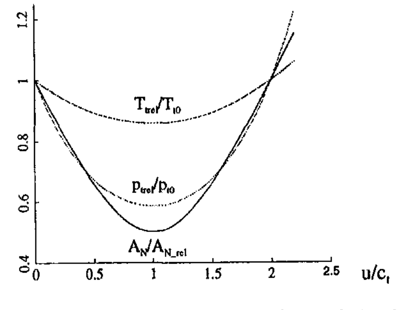

Fig. 5 Theoretical correlation between relative and absolute total properties for $c_t^2/(2c_pT_{t0}) = 0.135$

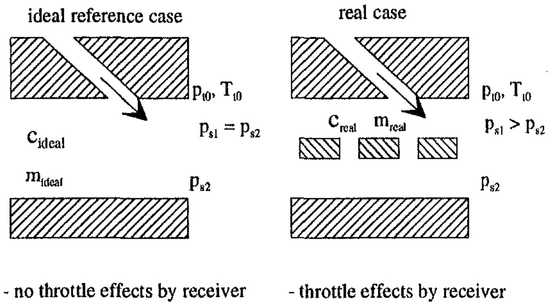

Fig. 6 Illustration of C_{DG} definition

C_{DG} then follows the equation:

$$C_{DG} = \frac{\dot{m}_{\mathrm{real}}}{\sqrt{\frac{2 \cdot \kappa}{\kappa - 1}} \cdot \frac{p_{t0}}{\sqrt{R \cdot T_{t0}}} \cdot A_N \cdot \sqrt{\left(\frac{p_{s2}}{p_{t0}}\right)^{2/\kappa} - \left(\frac{p_{s2}}{p_{t0}}\right)^{(\kappa+1)/\kappa}}} \tag{5}$$

where p_{s2} is a constant boundary condition in the exit area 2.

2.5.3 Nozzle Discharge Coefficient. The discharge coefficient describing the losses of the nozzle geometry is called C_{DN} and is defined as

$$C_{DN} = \frac{\dot{m}_{\mathrm{real}}}{\sqrt{\frac{2 \cdot \kappa}{\kappa - 1}} \cdot \frac{p_{t0}}{\sqrt{R \cdot T_{t0}}} \cdot A_N \cdot \sqrt{\left(\frac{p_{s1}}{p_{t0}}\right)^{2/\kappa} - \left(\frac{p_{s1}}{p_{t0}}\right)^{(\kappa+1)/\kappa}}} \tag{6}$$

2.5.4 Temperature Drop. The reason for applying preswirl air supply systems is to reduce the total temperature level in the rotating frame of reference. The highest temperature drop possible would be observed in the ideal reference case as described in section 2.5.2, Fig. 6. So when evaluating the simulations the real relative total temperature drop will be plotted together with the ideal temperature drop, in order to get a feeling for the effectiveness of the configuration.

2.6 Calculating System Coefficients. The calculations were carried out for constant absolute boundary conditions: $p_{t0}/p_{s2} = 2.0$, $T_{t0} = 333$ K, A_N, $\alpha = 30$ deg. Then the velocity ratios were varied so as to obtain relative inflow angles of $\beta = -45$, 0, 45 deg. In analyzing this three-dimensional periodic flow field, there is a need for averaging over a period and an area. As this investigation treated the unsteady problem in a quasi-steady manner, only averaging over an area was necessary. For this purpose the consistent space-averaging method proposed by Kreitmeier (1992) was applied on flat planes normal to the main flow direction.

2.7 Parameters Varied. In the table below all varied values of geometric parameters are listed.

Table 1 Parameters varied and range of variation

parameters	standard value	range of variation				
s	5 mm	3mm	5 mm			
Z_N	10	10	20			
Z_{rec}	30	30	60			
β	-	-45°	0°	45°		
l/d_{rec}	0.6	0.3	0.5	0.6	1.3	1.7
A_{rec}/A_N	7	1.1	2.1	7		

3 Results

3.1 Flow Characteristics

3.1.1 Characteristic Flow Patterns and Influence on C_D Values. The investigations showed that in the standard geometry there are actually three characteristic flow patterns to be observed, which vary in their total pressure profile over the receiver cross-sectional exit area. Figures 7–9 show these three characteristic flow patterns.

Regarding the varying values of C_D for the different flow patterns, the significance of this coefficient is demonstrated (Fig. 10). A high value of C_D occurs with big differences in flow pattern for different receiver holes, where a small part of the receiver orifices is strongly charged, while the greater part of them is not or only slightly charged. The strongly charged holes show an almost rectangular velocity profile. Therefore, a high C_D is characteristic for flow conditions with high local amplitudes and normal inflow.

The opposite case, i.e., a low value of C_D, shows up with rather similar flow conditions for the major part of the receiver holes. The velocity profiles show pronounced maxima. These flow characteristics occur in oblique inflow where the local amplitudes are small.

3.1.2 Prechamber Vortices. One of the most important three-dimensional effects was the formation of two vortex filaments in circumferential extension in the upper and the lower half of the prechamber due to oblique preswirl flow, as shown in Fig. 11. The flow through the receiver holes was strongly influenced by this vortex couple, especially with oblique inflow. By hampering the free throughflow of the preswirl jet through the receiver holes and instead charging the neighboring orifices with massflow of an almost equal amount, it creates a more uniform prechamber and receiver hole flow. Therefore the effect of different relative positions of preswirl nozzle and coverplate receiver is reduced.

The energy necessary to feed the vortex couple is delivered by the axial momentum of the nozzle jet. This is therefore dissipated and is no longer available for pressure recovery.

3.2 Influence of Geometric Parameters on System Efficiency

3.2.1 Influence of Gap Width s/d_N. The influence of s/d_N on the throttle characteristic and the thermal efficiency is indi-

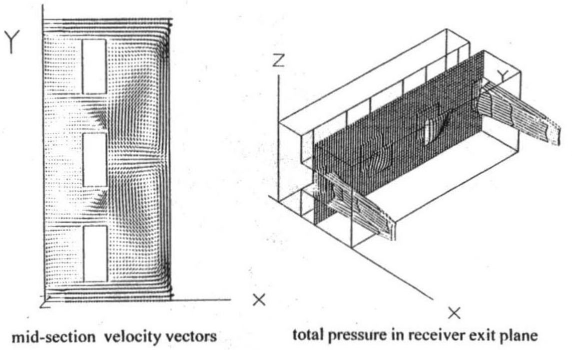

mid-section velocity vectors

total pressure in receiver exit plane

Fig. 7 Characteristic flow patterns with high C_D (normal throughflow)

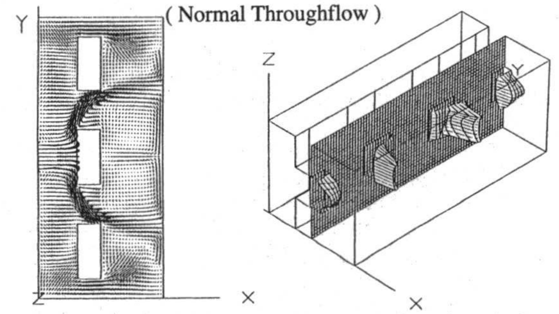

mid-section velocity vectors

total pressure in receiver exit plane

mid-section velocity vectors

total pressure in receiver exit plane

Fig. 8 Characteristic flow pattern with medium C_D (normal blocked flow)

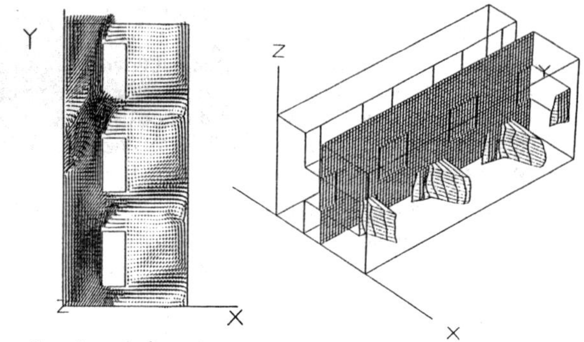

mid-section velocity vectors

total pressure in receiver exit plane

Fig. 9 Characteristic flow pattern low C_D (oblique inflow)

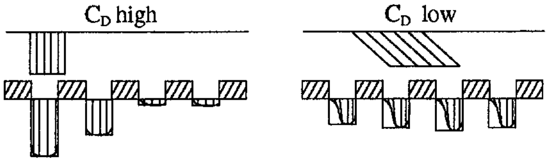

- normal inflow ($u / c_t = 1$)	- oblique inflow ($u / c_t \neq 1$)
- few orifices strongly streamed through with about rectangular velocity profile	- several orifices streamed through with nonuniform velocity profiles
- other orifices weakly streamed through	- other orifices weakly streamed through
- high local amplitudes	- small local amplitudes

Fig. 10 Significance of C_D coefficient

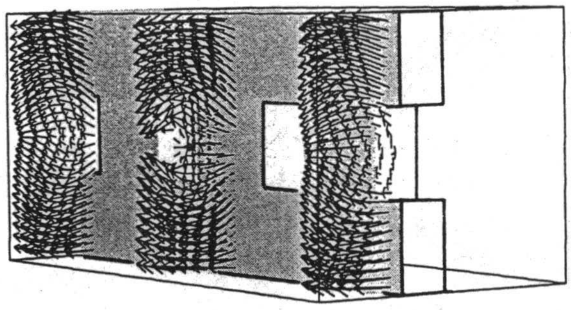

Fig. 11 Prechamber vortices

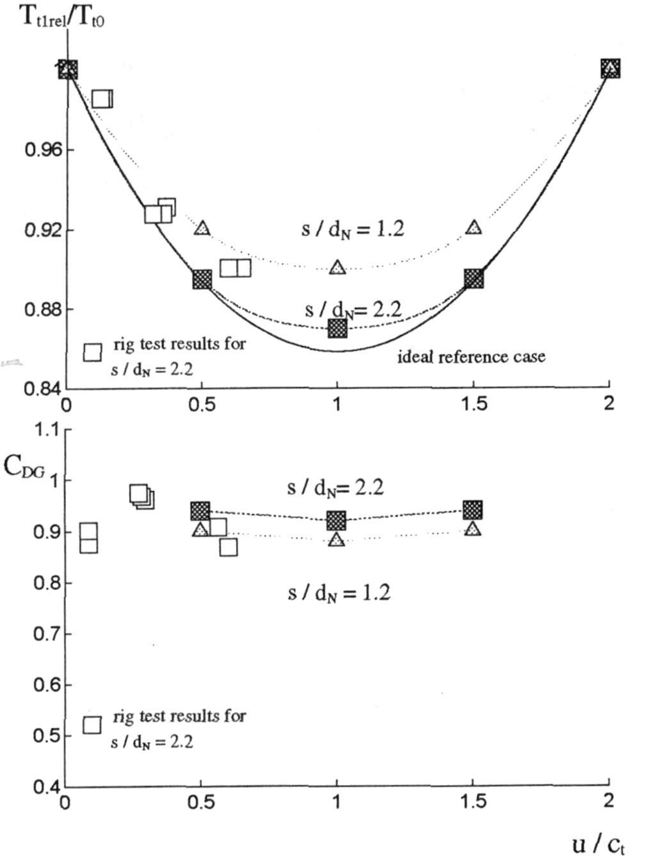

Fig. 12 Effect of gap width on C_{DG} and temperature ratio for p_{t0}/p_{s2} = 2, T_{t0} = 333, α = 30 deg

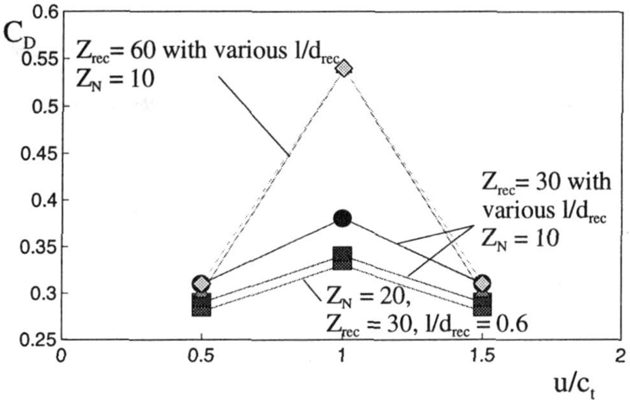

Fig. 13 Variation of $Z_{\rm rec}$, $l/d_{\rm rec}$, Z_N for p_{t0}/p_{s2} = 2, T_{t0} = 333, α = 30 deg

cated in Fig. 12. The ideal case is compared to CFD and unpublished rig test results. It shows that with smaller gap widths both mass flow and temperature drop are decreasing because inflow velocities are reduced by the stagnation pressure on the receiver surface. In an investigation of the impingement region in stagnation point flow, Giralt et al. (1977) stated that the influence of jet impingement on the free jet starts in a distance of $s = 1.2 \cdot d_N$. Within this range the static pressure differs significantly from the free jet static pressure.

It can be stated that this assumption is verified by the results shown in Fig. 12, as for the ratio $s/d_N = 1.2$ there is a significant influence on both C_{DG} and temperature drop.

The influence of the receiver gap width on the aerodynamic characteristic as expressed by C_D turned out to be negligible and is, therefore, not shown here. Even in configurations with very small gaps the prechamber vortices and characteristic orifice throughflow are similar. The circumferential velocity c_t of the test rig results was determined by measuring the total temperature in the rotating frame of reference and using Eq. (1).

3.2.2 Influence of Z_N, $Z_{\rm rec}$, $l/d_{\rm rec}$. From all variations of the number of preswirl nozzles and receiver holes, the conclusion was that there are no significant effects of these geometric parameters on the throttle characteristics C_{DG} and the temperature drop $T_{t\rm rel}/T_{t0}$ of the system with high (in general that means realistic) area ratios $A_{\rm rec}/A_N$ (see section 3.2.3). In a complete variation of $l/d_{\rm rec}$ and $Z_{\rm rec}$ there were no severe differences of the system efficiency coefficients as defined except for C_D, shown in Fig. 13.

With higher numbers of receiver orifices, these are blown through in a more axial and uniform way, especially in the stagnation point relative position at $u/c_t = 1$. Therefore the C_D value increases with the number of receiver holes during axial inflow. $l/d_{\rm rec}$ doesn't show a measurable effect on C_D. With oblique inflow the flow patterns don't change significantly with changing geometry parameters because of the leveling effect of the prechamber vortices.

3.2.3 Influence of Area Ratio A/A_N. The simulations showed that the axial velocity component w_n of the nozzle exit jet is largely dissipated in the prechamber so that the main velocity component in the prechamber is w_t. This doesn't change significantly from nozzle exit to receiver entry plane, as the only force in the tangential direction is wall friction of the nozzle plane boundary, which is small.

This circumferential velocity component implies a dynamic pressure, which doesn't support the orifice throughflow significantly. So the pressure that drives the orifice flow is mainly the static pressure in the prechamber p_{s1}.

With these assumptions, the equation of continuity yields

$$\frac{A_{\rm rec}}{A_N} = \frac{p_{t0}}{p_{s1}} \times \sqrt{\left(\left(\frac{p_{s1}}{p_{t0}}\right)^{2/\kappa} - \left(\frac{p_{s1}}{p_{t0}}\right)^{(\kappa+1)/\kappa}\right) \Big/ \left(\left(\frac{p_{s2}}{p_{s1}}\right)^{2/\kappa} - \left(\frac{p_{s2}}{p_{s1}}\right)^{(\kappa+1)/\kappa}\right)} \qquad (7)$$

This can be solved to supply a correlation between the pressure drop over the receiver orifices and the area ratio with the overall pressure drop as parameter, as shown in Fig. 14.

In this diagram there are also plotted the averaged prechamber pressures obtained from the CFD computations. They are closely adjacent to the curve derived from Eq. (7).

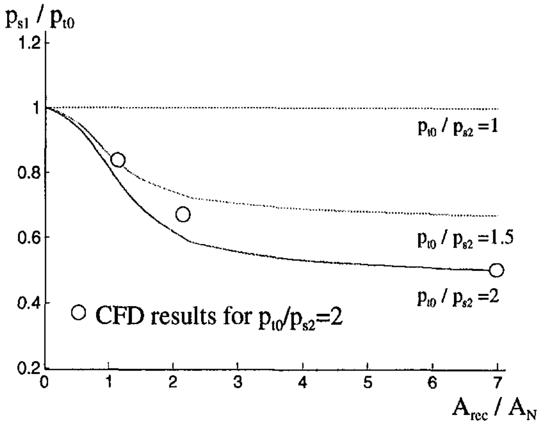

Fig. 14 Pressure drop with ideal throttling

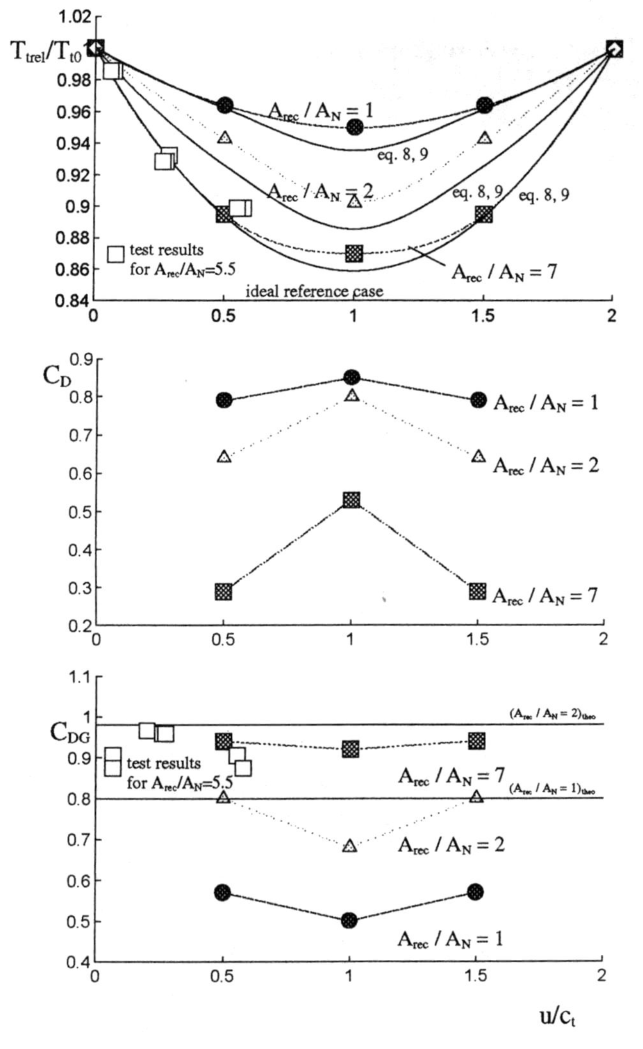

Fig. 15 Survey of effects of area ratio on system coefficients for $p_{t0}/p_{s2} = 2$, $T_{t0} = 333$, $\alpha = 30$ deg

The C_{DG} value expected with the described assumptions can be obtained as

$$C_{DG} = \sqrt{\left(\left(\frac{p_{s1}}{p_{t0}}\right)^{2/\kappa} - \left(\frac{p_{s1}}{p_{t0}}\right)^{(\kappa+1)/\kappa}\right) \Big/ \left(\left(\frac{p_{s2}}{p_{t0}}\right)^{2/\kappa} - \left(\frac{p_{s2}}{p_{t0}}\right)^{(\kappa+1)/\kappa}\right)} \tag{8}$$

The dependencies of C_{DG}, $T_{trel\,real}$, $T_{trel\,ideal}$, and C_D of the ideal reference case, the theoretical model, and the CFD results are plotted versus u/c_t in Fig. 15, which shows that the theoretical assumptions very closely describe the system behavior.

The diagrams indicate that the effects of the area ratio are of high significance toward all of the plotted system coefficients. The test results included in the diagrams support the reliability of the computations for velocity ratios below 0.66. For small area ratios most of the geometric parameters, which need not be regarded as significant for high area ratios, gain importance.

3.3 Pressure Losses. In all simulations one dynamic head loss was observed in the relative frame of reference independently from any varied geometric parameter (Fig. 16).

In the prechamber, the dynamic pressure resulting from the normal velocity component is dissipated by the swirl in all cases, except in the axial throughflow position. After deflection of most of the tangential velocity component into the axial direction by the receiver holes, its velocity head is dissipated due to sudden enlargements of the cross section downstream of the receiver holes. This result is in agreement with total pressure measurements in rig constellations, which yield values for pressure loss of more than 98 percent (Fig. 16).

3.4 Design Recommendations on Z_N, Z_{rec}, l/d_{rec}, *s*, *and Area Ratio.* Z_N, Z_{rec}, l/d_{rec}: These geometric parameters can be chosen rather freely within reasonable limits without severely affecting system effectiveness, as defined in this investigation provided the area ratio A_{rec}/A_N falls short of a certain minimum given below.

s/d_N: It has been shown that the gap width has an influence on inflow conditions and therefore on both temperature drop and C_{DG} value. According to Giralt et al. (1977) these effects become increasingly important for ratios of $s/d_N \leq 1.2$. Therefore, for design purposes higher s/d_N ratios than 1.2 are recommended.

A_{rec}/A_N: It has been stated that this is the most effective geometric parameter. From the simulations it has been shown that for massflow reductions of less than about 5 percent and for small reductions of temperature drop caused by the receiver geometry, the following value is recommended as a lower limit (see also Fig. 14):

$$\left(\frac{A_{rec}}{A_N}\right) \geq 4 \tag{9}$$

3.5 Comparison With Meierhofer's Results. Meierhofer and Franklin (1981) defined system efficiency as the ratio of absolute velocity computed from measured T_{t_rel} and the isentropic absolute velocity according to the pressure drop over the nozzle. The total temperature drop and this system coefficient are linked by:

$$\frac{T_{trel}}{T_{t0}} = 1 + \frac{c_{is}^2}{2\cdot c_p\cdot T_{t0}}\cdot\left(\frac{c}{c_{is}}\right)^2\cdot\left(\left(\frac{u}{c}\right)^2 - 2\cdot\cos\alpha\cdot\left(\frac{u}{c}\right)\right) \tag{10}$$

To derive a curve for T_{trel}/T_{t0} from Meierhofer's value for u/c and c/c_{is}, a value for $c_{is}^2/2\cdot c_p\cdot T_{t0}$ has to be chosen. The results are plotted versus u/c as it was done by Meierhofer and Franklin (1981) (Fig. 17).

With low velocity ratios, u/c, the measurements and the theoretical curves fit together very well. It is supposed that the measured reduction of temperature drop for $u/c \geq 0.6$ is due to frictional heat pick up of the boundary layer, which mixes according to Wilson and Owen (1997). This mixing effect is probably supported by the prechamber vortices described in section 3.1.2. The influence of windage heating is expected to increase with higher velocity ratios u/c just as the plotted curves show. For low values of u/c the overswirled boundary layer is cooled down by the work done on the rotating receiver. The balance of different effects, inefficiency of the swirl nozzle (see next chapter), work done, and small churning losses enable a good agreement between CFD and test rig results.

3.6 Influence of Preswirl Nozzles. As the comparison with Meierhofer's results suggests, the effects of the nozzle are of high importance. Therefore, some preliminary investigations

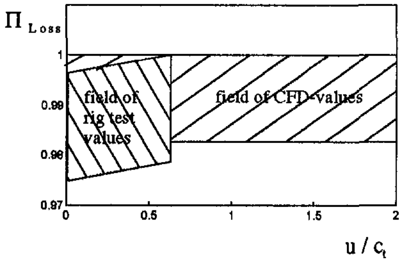

Fig. 16 Pressure losses

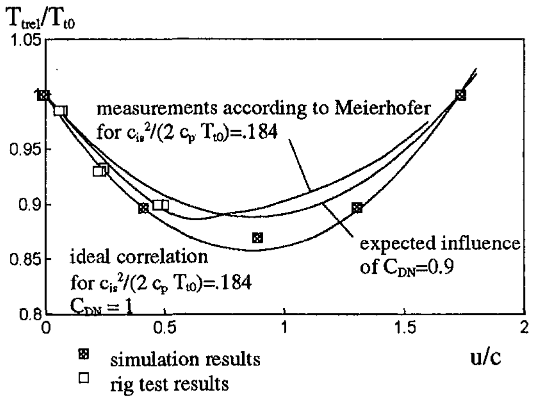

Fig. 17 Comparison with Meierhofer

on the nozzle geometry effect had become necessary. For these it was useful to go back into the absolute frame of reference. For simple orifices there are measurements available that can be compared to CFD results (see Fig. 18).

The CFD calculations yield a C_{DN} of 0.71 compared to the measurement of values between 0.72 and 0.78. It is thus assured that the simulation provides results of satisfying accuracy. Compared to the expected influence of a C_{DN} value of 0.9 (see Fig. 17) a nozzle discharge coefficient of about 0.7 is expected to have severe effects on temperature drop T_{trel}/T_{t0}. In order to reduce this effect an improved C_{DN} is required, which necessitates a better shaping of the nozzle. Comparison between a simple orifice nozzle and a nozzle of better shape is shown in Fig. 19.

The C_{DN} value of the well-shaped constellation rose up to 0.83 at a pressure drop of p_{t0}/p_{s2} = 1.5. According to these results system efficiency can be improved by nozzle shaping.

4 Conclusions

The most important geometric parameter for system efficiency is A_{rec}/A_N. The tendencies of area ratio effects on system efficiency are shown. A recommendation for the ratio s/d_N is given. With A_{rec}/A_N considered in the range of practical applications, the geometric parameters Z_N, Z_{rec}, and l/d_{rec} are of very little influence on system efficiency as defined in this investigation, i.e., the receiver holes are so large in most practical applications that there is one dynamic head loss of the preswirl flow and the receiver geometry is of little importance.

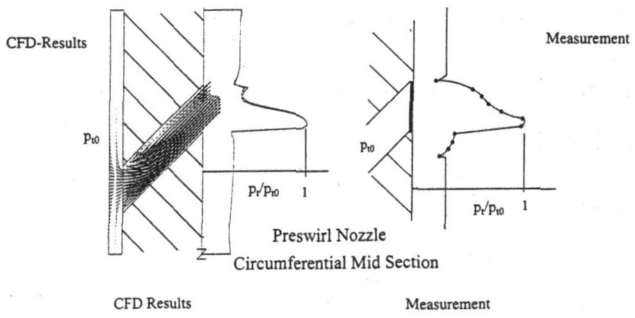

Fig. 18 Comparison of measured and computed orifice flow

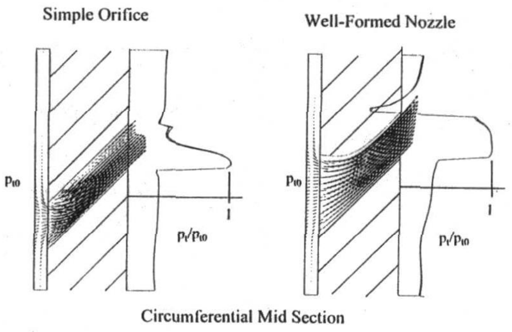

Fig. 19 Comparison of simple and well-shaped nozzle

The inflow process through the preswirl nozzles comes along with approximately one total head loss independent from any geometric parameters. A comparison between Meierhofer's test results, CFD calculations, and rig results shows a fair agreement for the range of practical applications. The negative influence of the preswirl nozzles on system efficiency can be reduced to a certain extent by giving the nozzles a well-shaped design.

References

Callaghan, E. E., and Bowden, D. T., 1947, "Investigation of Flow Coefficient of Circular, Square and Elliptical Orifices at High Pressure Ratios," NACA Technical Note.

El-Oun, J. B., and Owen, J. M., 1989, "Preswirl Blade Cooling Effectiveness in an Adiabatic Rotor-Stator System," ASME JOURNAL OF TURBOMACHINERY, Vol. 111, pp. 522–529.

Giralt, F., Chu-Jun, C., and Trass, O., 1977, "Characterization of the Impingement Region in an Axisymmetric Turbulent Jet," *Industrial Engineering Chemicals, Fundamentals,* Vol. 16.

Kreitmeier, F., 1992, "Space-Averaging 3D Flows Using Strictly Formulated Balance Equations in Turbomachinery," ASME IGTI Vol. 7.

Kutz, K. J., and Speer, T. M., 1994, "Simulation of the Secondary Air System of Aero Engines," ASME JOURNAL OF TURBOMACHINERY, Vol. 116, pp. 306–315.

Meierhofer, B., and Franklin, C. J., 1981, "An Investigation of a Preswirled Cooling Airflow to a Turbine Disc by Measuring the Air Temperature in the Rotating Channels" ASME Paper No. 81-GT-132.

Raw, M. J., Galpin, P. F., and Hutchinson B. R., 1989, "A Colocated Finite Volume Method for Solving the Navier–Stokes Equations for Incompressible and Compressible Flows in Turbomachinery," *Proc. Annual General Meeting of the Canadian Aeronautics and Space Institute.*

Wilson, M., and Owen, J. M., 1997, "Flow and Heat Transfer in a Preswirl Rotor–Stator System," ASME JOURNAL OF TURBOMACHINERY, Vol. 119, pp. 364–373.

Zimmermann, H., 1990, "Some Aerodynamic Aspects of Engine Secondary Air Systems," ASME *Journal of Engineering for Gas Turbines and Power,* Vol. 112, pp. 223–228.

An Experimental Study of Turbine Vane Heat Transfer With Water–Air Cooling

N. V. Nirmalan

J. A. Weaver

L. D. Hylton

Allison Engine Company,
SC W16, P.O. Box 420,
Indianapolis, IN 46206

This paper presents data showing the improvement in cooling effectiveness of turbine vanes through the application of water–air cooling technology in an industrial/utility engine application. The technique utilizes a finely dispersed water-in-air mixture that impinges on the internal surfaces of turbine airfoils to produce very high cooling rates. An airfoil was designed to contain a standard impingement tube, which distributes the water–air mixture over the inner surface of the airfoil. The water flash vaporizes off the airfoil inner wall. The resulting mixture of air–steam–water droplets is then routed through a pin fin array in the trailing edge region of the airfoil where additional water is vaporized. The mixture then exits the airfoil into the gas path through trailing edge slots. Experimental measurements were made in a three-vane, linear, two-dimensional cascade. The principal independent parameters—Mach number, Reynolds number, wall-to-gas temperature ratio, and coolant-to-gas mass flow ratio—were maintained over ranges consistent with typical engine conditions. Five impingement tubes were utilized to study geometry scaling, impingement tube-to-airfoil wall gap spacing, impingement tube hole diameter, and impingement tube hole patterns. The test matrix was structured to provide an assessment of the independent influence of parameters of interest, namely, exit Mach number, exit Reynolds number, gas-to-coolant temperature ratio, water- and air-coolant-to-gas mass flow ratios, and impingement tube geometry. Heat transfer effectiveness data obtained in this program demonstrated that overall cooling levels typical for air-cooled vanes could be achieved with the water–air cooling technique with reductions of cooling air flow of significantly more than 50 percent.

Introduction

The trend to improve overall efficiency of gas turbine engines traditionally leads to increases in turbine inlet temperature (TIT) and increases in compressor pressure ratio. Today's advanced gas turbine engines operate at temperatures much greater than the allowable metal temperatures of turbine airfoils, which in turn necessitates the cooling of airfoils. Some of the common methods of providing thermal protection to the airfoil are internal convective cooling and impingement cooling, external film cooling, and trailing edge ejection. Also, in today's high-pressure-ratio advanced engines, the cooling air temperatures are much higher. These increases in TIT and cooling air temperatures have made cooling the airfoil with compressor discharge air very challenging and have led to investigations of potential new techniques for cooling. One such candidate in a utility/industrial gas turbine engine is to use a water–air mixture as the cooling medium for turbine airfoils. Increases in thermal effectiveness will result in corresponding improvements in specific fuel consumption and output power through the reduced use of turbine cooling air flow. Further, today's low emission lean burn combustion systems require as much air as possible to be utilized in the combustion process. In addition, water–air cooling of turbine airfoils provides the capability of operating airfoils at much lower temperatures and thus the opportunity to use inexpensive materials and increase airfoil life in rugged turbine applications (Wenglarz et al., 1995).

The idea of using water cooling of gas turbine components is not new. The idea has been discussed for over 40 years (Schimdt, 1951). Some of these schemes have been experimentally tested and have been reviewed by Van Fossen and Stepka (1979). Dudley et al. (1984) and Sundell et al. (1984) conducted an experimental study of evaporative heat transfer of water in a gas turbine bucket. In this study, the authors indicated cooling capacity is limited by critical heat flux or boiling transition phenomena. They were also able to improve the heat transfer by flow spreaders in the cooling channels.

The concept of using water with the cooling air in a gas turbine airfoil cooling application has also been tried before. The simplest technique is to inject water into the cooling air upstream of the airfoil and allow it to evaporate, thus reducing the cooling air temperatures. A study conducted by Van Fossen (1983) on the aspects of gas turbine contingency power indicates that, by using this method, the engine power could be increased by 54.6 percent without detrimental effects on airfoil life. To expand on this study, Biesiadny et al. (1987) demonstrated higher power output of a turboshaft engine while maintaining turbine blade temperature by injecting water into the turbine cooling air. They concluded that there is the potential to increase the power by 17 percent while increasing TIT by 167°C (300°F). However, their concerns for other unprotected subcomponents of the hot section prevented demonstrating the technique's higher potential. This technique could be taken a step further by letting the water droplets evaporate in the cooling passages. This technique could lead to thermal failure of the airfoils due to the large temperature gradients possible during this cooling process. In case of small water droplets at low impact velocities, the Leidenfrost effects could prevent the water droplets from ever reaching the hot surfaces as shown experimentally by Pedersen (1970). Fiszdon et al. (1994) in their study simulated a turbine vane cooling application with a binary two-phase mixture of water and air as the cooling medium in a electrically heated tube. They concluded that by injection of water mist into the air flow immediately upstream of the coolant

---

Contributed by the International Gas Turbine Institute and presented at the 41st International Gas Turbine and Aeroengine Congress and Exhibition, Birmingham, United Kingdom, June 10–13, 1996. Manuscript received at ASME Headquarters February 1996. Paper No. 96-GT-381. Associate Technical Editor: J. N. Shinn.

entrance, they could achieve wall temperatures about 100°C (180°F) cooler than could be achieved with evaporatively cooled air.

The water–air cooling technique presented in this paper is an innovative concept for cooling turbine airfoils. The concept utilizes a two-phase mixture of air and water, where the water is vaporized by contact with the heated surface. This process provides a very large heat sink by taking advantage of both the sensible heat rise and the latent heat of vaporization of the liquid. The technique utilizes a finely dispersed liquid-in-air mixture, which impinges on the internal surfaces of high temperature turbine airfoils to produce very high heat transfer rates. This air–water impingement cooling technique is greatly dependent on the impingement characteristics such as water droplet velocity and size. If droplets are small and their velocity too low, they never reach the hot surface as they get entrained in vapor and air crossflow. If the droplets are too big and their velocity large, they tend to break up and rebound. If the droplets are large and their velocities small, the water droplets would not flash vaporize and hence the heat transfer would tend to be limited by the rules of pool boiling. However, if the water droplets are at the optimum size and velocity, the water droplets impinging on the surface become thin films and flash vaporize off the airfoil inner wall. The impinging and crossflow air further help in this technique by effectively removing the vapor.

The experimental measurements reported in this paper present overall heat transfer effectiveness data of a water–air cooled airfoil. The experiments were conducted in a moderate-temperature, three-vane, linear, two-dimensional cascade. The data were obtained at conditions that fully simulate engine conditions of a first-stage vane of an advanced turbine. The principal independent parameters—Mach number, Reynolds number, coolant-to-gas temperature ratio, and coolant-to-gas mass flow ratio—were maintained over ranges consistent with actual engine conditions, and the test matrix was structured to provide an assessment of the independent influence of parameters of interest, namely, exit Mach number, true chord exit Reynolds number, coolant-to-gas absolute temperature ratio, and coolant-to-gas mass flow ratio.

Experimental Apparatus and Procedure

Aerothermodynamic Cascade Facility. This experimental investigation was performed in the Allison Aerothermodynamic Cascade Facility (ACF). The purpose of this facility is to conduct experimental research in high-temperature turbine component models that embody advanced cooling techniques, aerodynamics, or materials. The experimental approach employs a two-dimensional model technique, with full dynamic similarity in free-stream Mach number (M) and boundary layer Reynolds number (Re) effects, and provides an experimental method to separate the effects on local heat transfer.

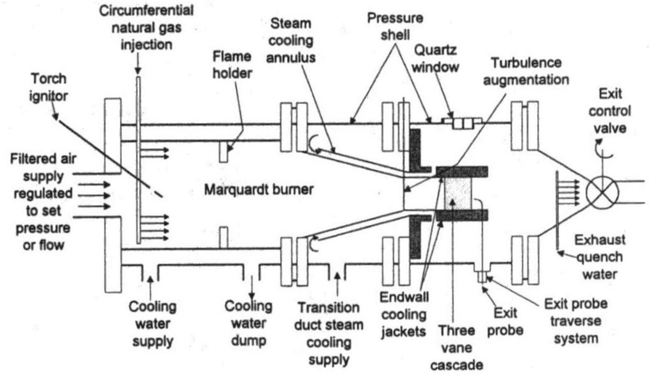

Fig. 1 Schematic of the aerothermodynamic cascade facility

The facility consists of a burner, a convergent section, a free-stream section with instrumentation and optical access, a test section with instrumentation, a quench zone with back pressure regulation, and an exhaust system. The facility is shown schematically in Fig. 1. The Mach number and Reynolds number modeling considerations necessitate a burner with a large temperature, flow, and pressure range. This burner capability, coupled with back pressure regulating valve, allows experimental separation of free-stream Mach number and boundary layer Reynolds number effects to simulate a wide range of engine designs and operating conditions accurately.

A constant cross section is provided downstream of the burner to establish uniform inlet velocity, temperature, and turbulence profiles into the test section. This section is provided with temperature-controlled cooled walls and isolates the test section from radiant heat transfer from the primary combustion zone. The walls of the test section are cooled with steam to keep them at, or close to, the vane surface temperature to prevent radiant exchange. The flow path upstream of the cascade in the ACF takes the burner discharge from a 31.5 cm (12.4 in.) diameter through a 50.8 cm (20. in.) long transition section to a 7.6 cm × 27.9 cm (3 in. × 11 in.) rectangular section. The rectangular section upstream of the cascade is 36.83 cm (14.50 in.) long and contains inlet instrumentation.

Facility operation and data acquisition are handled by a dedicated, state-of-the-art computer-controlled data acquisition system. Data input signals are multiplexed by Hewlett-Packard (HP) Model 3497 440-channel random access signal scanner, with analog to digital conversion performed by an HP 3456A integrating digital voltmeter. A Pentium™ based personal computer running under Microsoft® Windows™ operating system uses the National Instrument's Labview® software for data acquisition. A multitasking, facility-oriented software system was developed to do all routine control measurement tasks. The system is flexible and provides for real-time facility monitoring and diagnosis of instrumentation or control problems.

Cascade Description. The cascade configuration featured a three-vane cascade design. This design requires the addition of a tailboard and flow control devices to bleed air past the outer two vanes in order to insure the correct pressure distribution around the center airfoil. The exit plane static pressure taps provided information necessary to establish periodicity. In addition, this design requires that all instrumentation be located on the center airfoil. The three-vane design is beneficial in that it permits airfoils to be scaled to twice the size that could be

Nomenclature

ACF = aerothermodynamic cascade
m = mass flow
M = Mach number
Re = Reynolds number

T = temperature
TIT = turbine inlet temperature
var = varying
ϵ = effectiveness

Subscripts

air = coolant air
c = coolant
cascade = cascade
g = gas
w = wall
water = coolant water

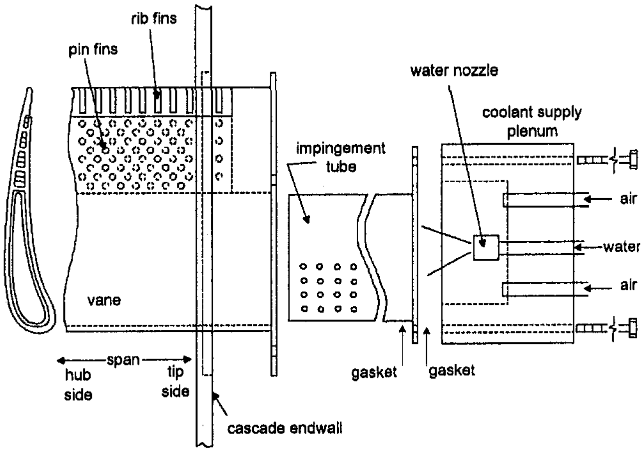

Fig. 2 Schematic showing the vane cross section with the impingement tube and coolant plenum assembly

installed in a five-vane cascade. This permits a closer match of engine and cascade Reynolds number as well a providing a larger airfoil for instrumenting, thereby increasing the density of instrumentation.

The cascade airfoil is 3.4 times engine size and is a two-dimensional profile of the midspan contour of an advanced turbine vane. The test vane, which has true chord of 14.16 cm (5.58 in.) and a span of 10.67 cm (4.2 in.), was cast as a single piece out of Inconel 625. A cross section of the design of this airfoil is shown in Fig. 2. It contains a capped impingement tube, which distributes the water–air mixture over the inner surface of the airfoil. The water–air coolant mixture is supplied to the impingement tube from a mixing plenum at the tip into which the water is sprayed with an atomizing nozzle. Crossflow cooling air is supplied to the cavity between the impingement tube and the vane inner wall from the hub. The resulting mixture of air–steam–water droplets flows axially in the passage between the impingement tube and vane inner wall, passes through the pin fin array, and exits the airfoil into the gas path through the trailing edge. A schematic of the vane, impingement tube, and coolant supply plenum prior to assembly is also shown in Fig. 2. A series of bolts passes through the plenum and impingement tube flange and screws into the vane flange to the hold the assembly together. This design facilitates the easy removal and replacement of the impingement tube.

Impingement Tube Description. A first-order heat transfer model was used to design the impingement tube hole patterns for the engine scale airfoil. Hence, the same pattern was going to be used for the cascade experiments with the scaled up airfoils. However, previous liquid–air cooling experiments conducted at Allison (Hylton et al., 1995) indicated that the impingement tube to airfoil wall gap spacing plays a very important role in this cooling concept. Hence, two impingement tubes, one having scaled-up geometry (hole diameter, hole spacing to diameter ratio), and the other with engine scale geometry, were designed. The first-order heat transfer model was also used to give some insight as to whether to use engine scale coolant geometries or scaled-up coolant geometries for the impingement tubes. Predicted vane surface temperatures show that the major difference in heat transfer between engine scale and scaled-up impingement tubes is on the pressure surface. This is mainly due to the difference in gap between impingement tube and vane inner surface. Since superior cooling performance was predicted on the pressure surface for the engine scale tube design, the majority of the impingement tubes studied in the experimental program contained the engine scale impingement tube design. One scaled-up design was tested to verify the predicted differences in cooling level. Five different impingement tubes were made and tested in the experiments.

Table 1 Impingement tube parameters

Imp. Tube No.	Scale	Hole Diameter mm (in.)	Pattern	Gap mm (in.)
1	Engine	0.406 (0.016)	Varying	0.508 (0.020)
2	Scaled up	1.372 (0.054)	Varying	1.702 (0.067)
3	Engine	0.508 (0.020)	Varying	0.508 (0.020)
4	Engine	0.406 (0.016)	Varying	0.762 (0.030)
6	Engine	0.406 (0.016)	Constant	0.508 (0.020)

Relevant factors in the design of the impingement tube that affect the thermal effectiveness were identified as impingement tube to airfoil wall gap spacing, impingement tube hole diameter, and impingement tube hole diameter to spacing ratio. Impingement tube 1 was designed with the hole pattern that was developed using the first-order heat transfer model. Tube 1 has a hole diameter of 0.406 mm (0.016 in.) with a tube-wall-to-vane-inner-surface gap of 0.508 mm (0.020 in.). Table 1 shows the pertinent dimensions of the impingement tube designs. Figure 3 shows the hole patterns on an unwrapped impingement tube surface with the leading edge region in the center. The hole pattern and hole diameter of impingement tube 2 are 3.34 times the scale of Tube 1. This tube was designed to study the effects of scaling. Tube 3 was designed to study the effects of hole diameter. In Tube 3, the impingement hole diameter is 0.508 mm (0.020 in.). However, the hole pattern pitch-to-diameter ratio and spacing-to-diameter ratio were kept constant; hence a different pattern is seen in Fig. 3. Tube 4 was designed with the tube-wall-to-vane-inner-surface gap of 0.762 mm (0.030 in.); hence it has the same hole pattern as Tube 1 except for minor differences to account for the changes in the impingement tube chord size. Decreasing hole density will decrease the number of holes in the impingement tube, thereby reducing cost of manufacture. Tube 6 was designed with a uniform hole pattern to obtain a baseline effect of impingement heat transfer.

The impingement tubes were cast in 625 Inconel. Spacers were welded onto the exterior of the tube to help maintain the specified gap between the impingement tube and the inner wall of the airfoil.

Atomization Facility. Prior to being installed in the airfoil in the ACF cascade, the impingement tubes were flowed in our Fuel Nozzle Research Lab to determine water droplet size for the different hole patterns and diameters and water–air ratios. The basic apparatus is comprised of a collection tank, which has an exhaust fan drawing air from the bottom of the tank to prevent any airborne liquid droplets from returning to the measurement area. A Malvern Instruments particle sizer and two-axis positioning mechanism (to which the impingement tube is attached) are located at the top of the tank to measure water droplet sizes as the water–air mixture leaves the impingement tube. The impingement tube is clamped to a plenum chamber where the water and air are supplied as in the ACF. Air and water flow rates were measured with mass flow meters. A pressure transducer was installed in the water supply line upstream of the water nozzle and in the water–air plenum to measure the pressure ratio across the tube. Photographs of the spray were taken with black and white film using a strobe light and a 35 mm camera.

Cascade Instrumentation. The airfoil gas side metal temperatures were measured using thermocouples installed in grooves on the exterior surface of the test vane. Figure 4 shows the distribution of the thermocouples at the midspan plane for the airfoil used in this testing. The airfoil surface was instru-

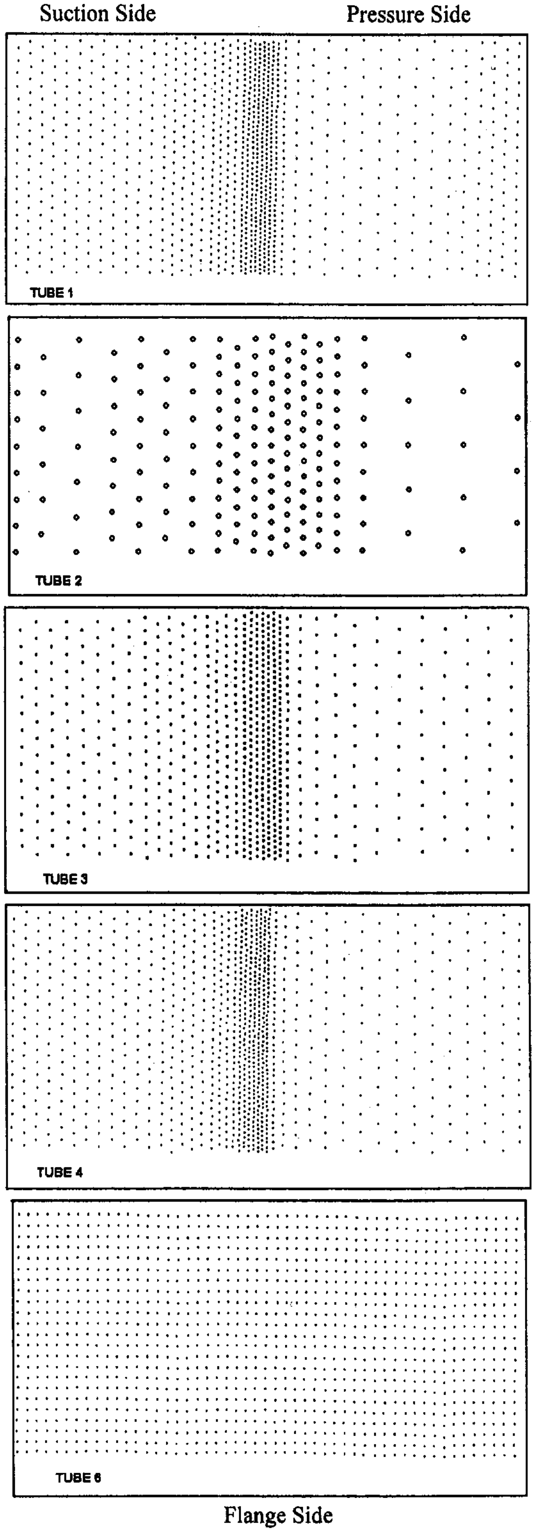

Fig. 3 Schematic of impingement tube hole patterns

mented with 103 0.51 mm (0.020 in.) diameter sheathed chromel-alumel thermocouples. The total number of thermocouples was distributed among the tip, midspan, and hub planes with 33, 35, and 35, respectively. The span of the airfoil in the gas path was 7.62 cm (3.0 in.). The midspan plane was 3.81 cm (1.5 in.) away from the endwall with the tip and hub planes 1.91 cm (0.75 in.) and 2.54 cm (1.0 in.), respectively, away from the midspan. In the chordwise direction, the thermocouple grooves were 0.183 cm (0.072 in.) apart. Thermocouples were brought off the vane (all to the hub end of the vane) in 0.58 mm (0.023 in.) deep radial grooves covered with cement, and blended by hand to provide a smooth surface. A grounded thermocouple (thermocouple bead attached to inside of the sheath tip) was used with the sheath end laser welded to the vane at the proper spanwise location in the groove.

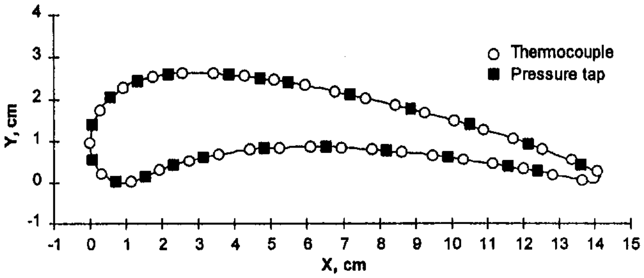

Fig. 4 Instrumentation locations for the airfoil

The test vane surface was instrumented with surface static pressure taps in addition to the heat transfer instrumentation. Data from these pressure taps provided verification that the cascade was properly simulating the engine flow conditions. Twenty-three taps were located around the airfoil outer surface at the midspan between thermocouple instrumentation. Figure 4 also illustrates the relative locations of the surface pressure taps on the airfoil. Stainless steel tubing, 0.81 mm (0.032 in.) OD, was laid in a spanwise surface groove to the midspan from the hub and laser welded periodically along the length. A normal hole, 0.46 mm diameter (0.018 in.), was drilled into the tube to create the static pressure tap. The tube was laser welded all around the hole to the vane with the area hand blended to the surrounding vane surface. The remainder of the groove was then filled with cement and hand blended smooth with the airfoil surface similar to the thermocouple installations.

Additional thermocouples and pressure taps were used to measure coolant water and air temperatures and pressures in the supply lines, impingement tube supply plenum (tip end) and crossflow supply plenum (hub end). The cascade inlet instrumentation consists of two inlet core total pressure rakes (each containing five total pressure probes), two inlet core temperature rakes (each containing five thermocouples), and eighteen endwall static pressure taps. The converging transition duct contains seven endwall static pressure taps. Thirty-seven endwall static pressure taps are located in the endwall of the cascade at the exit plane.

Standard sharp-edged orifices are used throughout to provide air flow-rate measurements. The orifices used to meter the secondary flow systems for the current tests were calibrated to provide flow measurement accuracy to ±2 percent. A mass flow meter was used to measure the water flow rate to the impingement tube.

Data Acquisition and Reduction Procedures. The heat transfer data were taken under the assumption that the nondimensional surface temperature of this geometrically scaled vane would be similar for the scaled condition as it would be for that condition in an engine. In order to determine this value, the surface temperature, the plenum coolant temperature, and the inlet total temperature were determined. In addition, overall cascade conditions such as inlet and exit Mach number, inlet and exit Reynolds number, coolant to cascade mass flow ratio, and the vane surface pressure distribution were determined.

The first phase of the data acquisition task was to set the cascade conditions to the required operating point. The software continuously monitors and displays the cascade operating condition as the desired run conditions are being established. Cascade inlet total pressure and temperature were based on readings of the upstream core flow rakes. The cascade inlet static pressure was defined as the average of readings at 18 endwall static pressure taps near the upstream core rakes. The average exit pressure was determined by obtaining an integrated average of the uniformly spaced endwall static pressure taps between the middle of the passage below the instrumented vane to the middle of the passage above the instrumented vane at the cascade exit plane. The operating conditions of the Mach number, the Reynolds number (based on true chord), and the coolant water and air flow conditions are displayed continuously on the monitor during the setup procedure until a satisfactory steady-state condition was achieved.

The change in temperature of the vane surface over a fixed period of time was then monitored until thermal equilibrium was established. In the second phase, after the desired steady-state operating conditions were achieved, the data acquisition software is requested to take a data point. In this mode, the data acquisition software samples, averages, and stores the raw voltage data and engineering data. All of the data were read in a single sweep that was repeated several times to provide time-averaged, steady-state values.

In the third phase, the data are tabulated, graphically presented, and printed. The final run conditions, such as cascade conditions, vane surface static pressure and temperature distributions, and coolant flow conditions are established. The changes in cascade conditions and coolant flow conditions between readings were checked to verify thermal stability during data acquisition.

Data Uncertainties. In order to assess the data uncertainties, the sources of error must first be outlined and their influence on the results described. The two measures of uncertainty that are useful to assess are the relative and absolute confidence intervals. The relative confidence interval provides a measure for assessing significant differences in data taken using a particular rig and sensors with a particular calibration. Relative errors are due to run to run variations and often result from unsteadiness in the rig or instrumentation. The absolute confidence interval provides a measure for assessing significant differences between two totally different rigs with different instrumentation. This value includes the relative error and also includes possible errors due to calibration, sensor location, and sensor installation.

Upon applying the technique of Kline and McClintock (1953) and using the uncertainties mentioned above, the following absolute uncertainty intervals were derived:

Reynolds number, Re	±2.7 percent
Mach number, M	±1.1 percent
Effectiveness, ϵ	±3.4 percent
Coolant air mass flow ratio, $m_{c,\mathrm{air}}/m_{\mathrm{cascade}}$	±2.5 percent
Coolant water mass flow ratio, $m_{c,\mathrm{water}}/m_{\mathrm{cascade}}$	±1.5 percent

The uncertainties presented in this subsection are intended to provide the analyst with an indication of the uncertainty in absolute levels in using the data for verification purposes. In comparing data runs for a given cascade (i.e., looking for Reynolds number trends, etc.), the uncertainty in the comparisons is considerably less than the values just described. This difference is due to the fact that several of the variables contributing to the uncertainty do not change from run to run. Thus comparisons of runs from a given cascade would not be affected. Reproducibility for a given cascade is on the order of ±2 percent.

Results

Impingement Tube Water Droplet Size. Atomization of the water and entrainment of water droplets in the impingement air flow are significant features of this cooling concept. Thus, it was important to characterize the size and distribution of water droplets within the cooling air as it leaves the impingement tube. In atomization experiments, several factors affect water droplet size in air assisted atomizers. In particular for this study, the relative velocity between the air and liquid and hole diameter are important. The relative velocity is varied by changing the air to liquid mass ratio. This parameter ranges between 0.11 and 0.26 in the atomization tests performed. Impingement tubes 1, 2, and 3 cover the range of hole diameters used in this study. The combination of these conditions will characterize the water drop size expected in the cascade tests.

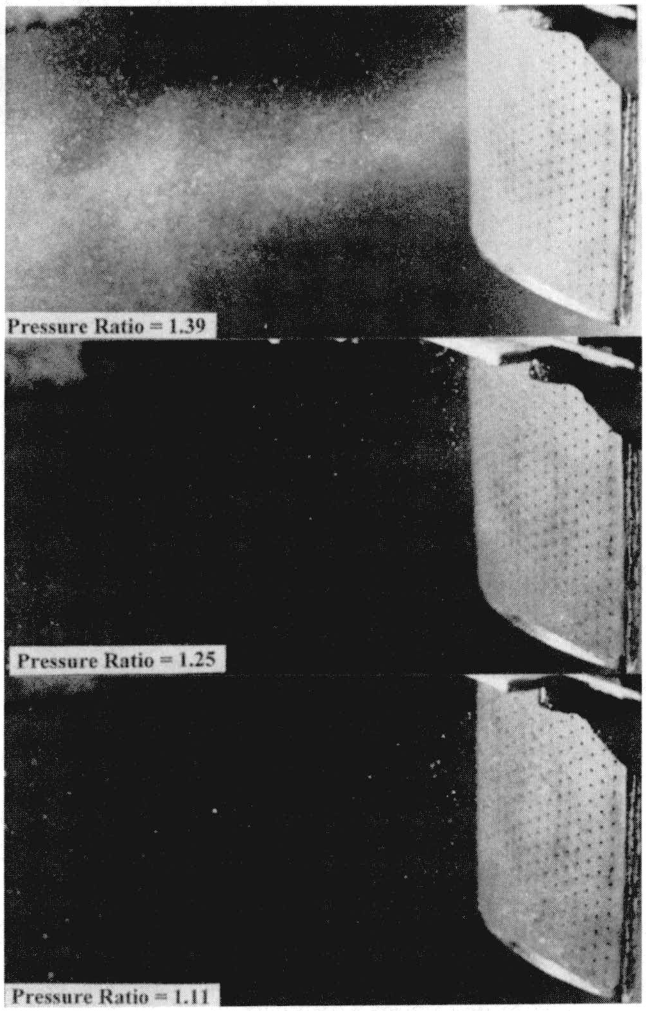

Fig. 5 Photograph of water spray from impingement tube 1

Table 1 gives the specifications for the three tubes tested (Nos. 1, 2, and 3). Qualitatively, the effect of the pressure ratio across the tube (i.e., air to liquid mass ratio) is illustrated in Fig. 5. The photographs show the drop size increases as the pressure ratio decreases. Basically, the relative velocity between the air and liquid decreases with decreasing pressure ratio. Correspondingly, there is less kinetic energy available to break the water into drops.

During measurements with the Malvern particle sizer, the tube surface was divided into three sections roughly characterized as the suction, pressure, and leading surfaces (the suction side of the tube is shown in Fig. 5). The distribution of water drop size with pressure ratio across the holes is shown in Fig. 6 for the suction side for all three tubes. Two runs were made with Tube 1 to check repeatability. The water flow rate was constant during the tests. The variation of drop size with the pressure ratio across the tube is typical of air-assisted atomizers.

A pressure ratio of 1.4 in the spray rig for Tubes 1 and 3 is expected to produce the same drop size (about 30 μm) as the operating conditions in the engine. Due to scaling considerations, a pressure ratio of 1.28 in the spray rig provides droplet sizes similar to what is expected in the engine for Tube 2.

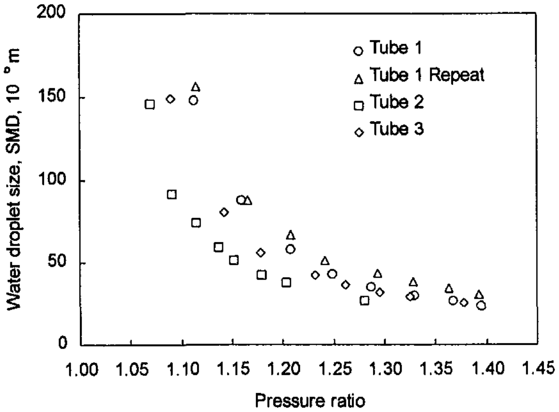

Fig. 6 Effect of pressure ratio on water drop size for the suction side of impingement tubes 1, 2, and 3

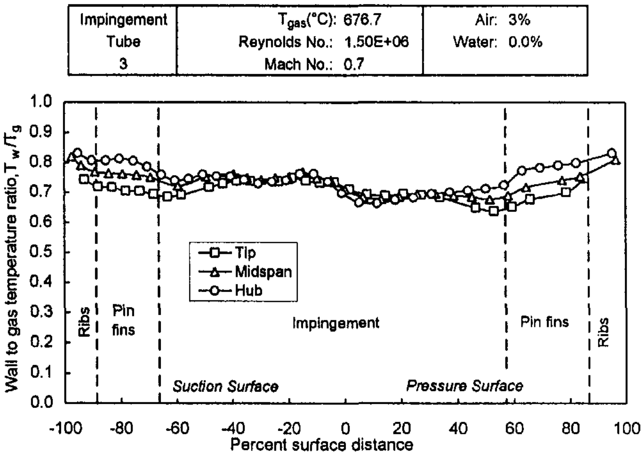

Fig. 8 Variation of the vane surface temperature with span for air cooling only

Previous proprietary studies have indicated that water droplets in this size range of 20–50 μm are required for the technique to function effectively. Referring to Fig. 6, mean water drop sizes of 36, 61, and 164 μm are measured for the pressure ratios illustrated in Fig. 5. Note, the largest drop size that can be measured by the Malvern Instrument used is 500 μm. As the mean diameter approaches 100 μm, the uncertainty in the measurement increases as more drops are out of the range the instrument can measure.

Cascade Operating Conditions and Test Matrix. The experimental results presented in this study were obtained at different test conditions with the variable parameters being exit Reynolds number, exit Mach number, coolant-to-gas absolute temperature ratio, and coolant-to-gas mass flow ratio as shown in Fig. 7. Exit Reynolds numbers referred to in the figures are based on airfoil true chord (not axial chord), and exit Mach numbers are based on measured inlet total pressure and midpassage to midpassage average measured exit plane static pressure. The cascade was run at three different nominal inlet gas temperatures of 538°C (1000°F), 677°C (1250°F), and 816°C (1500°F). The coolant air temperature was maintained at a typical engine T_g/T_c ratio of about 2.0. Water inlet temperature to the cascade was maintained at levels typical to what will be expected at an inlet to an industrial engine (approximately ambient temperature). The burner-generated turbulence intensity level is about 6.5 percent, based on LDA measurements taken previously at the cascade inlet plane as reported by Nealy et al. (1984). Figure 7 also shows the coolant air and water flows that were run at each cascade condition. These numbers are expressed as a percent of engine (or cascade) air mass flow. In addition, air only cooling was run as a baseline condition.

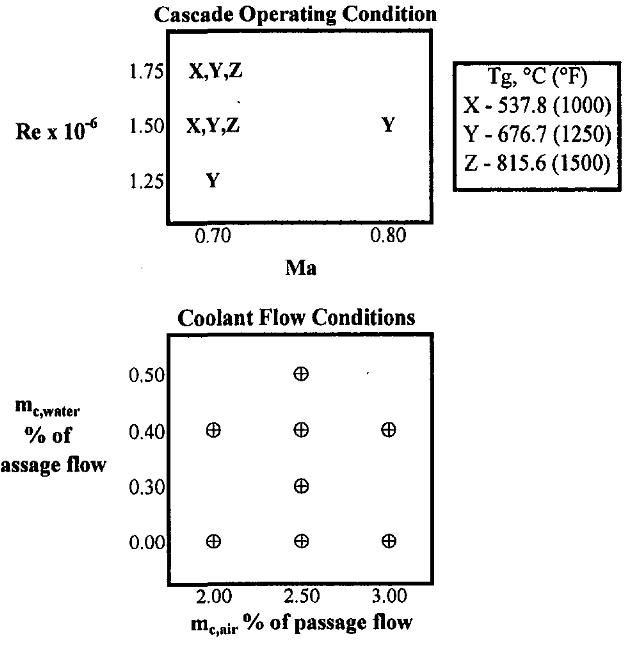

Fig. 7 Test matrix of relevant test variables

Aerothermodynamic Results. The data presented in this section include vane surface temperature and pressure distributions and overall effectiveness as functions of chordwise surface distance. The location of each measurement is expressed as a percent of suction or pressure surface length as measured from the geometric stagnation point. Negative values of distance indicate positions on the suction surface. To help in the discussions, the regions cooled by impingement, pin fins, and the ribbed fin slot are as follows: −66.3 to 57.1 percent of the percent surface distance is cooled by impingement; −88.7 to −66.3 percent and 57.1 to 86.6 percent of the surface are cooled by the pin fins; and −88.7 to 100 percent and 86.6 to 100 percent are cooled by the ribbed fin slot, as shown in Fig. 8.

Prior to obtaining water–air cooled heat transfer data, baseline data (i.e., air cooling only) were obtained at the four cascade conditions and cooling flow conditions described in Fig. 7. The variation of surface temperature along the chordwise direction for the three different spanwise locations are shown in Fig. 8 for the cascade conditions at a Reynolds number of 1.5×10^6, Mach number of 0.7, and a gas temperature of 676.7°C (1250°F). This is for the case of air only cooling with impingement tube 3. From the figure it is seen that the chordwise temperature distribution is relatively flat. Also the data show that in the impingement cooled region, the spanwise variation in temperature is minimal, while in the pin fin area, there is some amount of temperature variation.

Figure 9 shows the surface temperature distribution at the same cascade condition but with water cooling at 0.4 percent. In this case, there is a relatively large amount of temperature variation in the chordwise direction. In the spanwise direction the variation is somewhat smaller with the tip section being cooled better than the midspan and hub sections.

Typical measured surface static pressure distributions corresponding to the two cascade expansion ratios (Mach numbers) and three cascade mass flows (Reynolds numbers) tested are shown in Fig. 10. As observed before in previous cascade experiments (Nirmalan and Hylton, 1990), the primary effect of exit Mach number variations is to alter the suction surface pressure distribution downstream. There is very little variation in vane

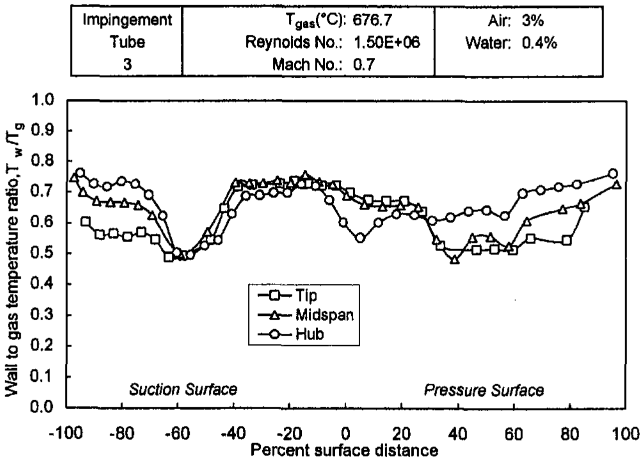

Fig. 9 Variation of the vane surface temperature with span for air–water cooling

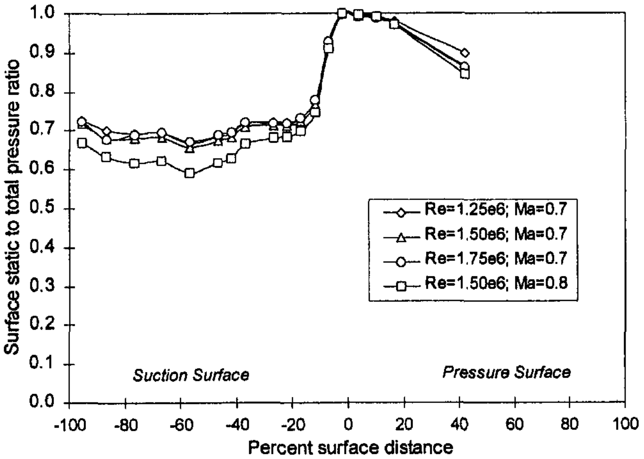

Fig. 10 Variation of the vane midspan static pressure distribution with Reynolds and Mach number

Impingement Tube 1	T_{gas}(°C): 676.7 Reynolds No.: 1.50E+06 Mach No.: 0.7	Air: 3% Water: Var

Average Effectiveness				
	Tip	Midspan	Hub	Overall
Water=0.0%	0.5596	0.4362	0.4586	0.4848
Water=0.3%	0.6725	0.5107	0.5168	0.5667
Water=0.4%	0.7172	0.5512	0.5518	0.6068
Water=0.5%	0.7463	0.5736	0.5838	0.6346

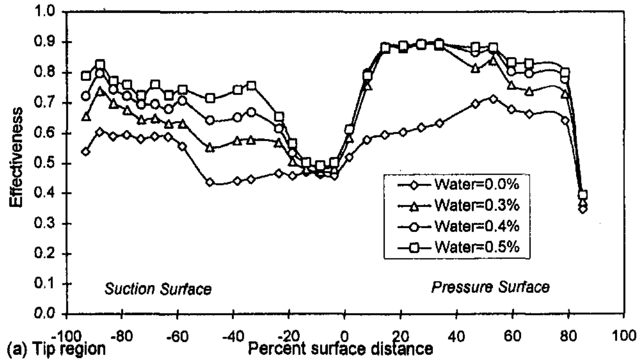

(a) Tip region

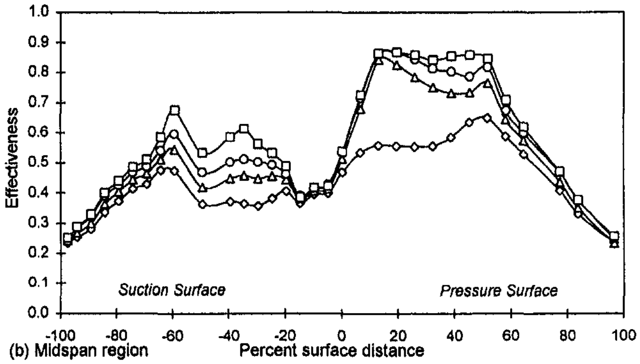

(b) Midspan region

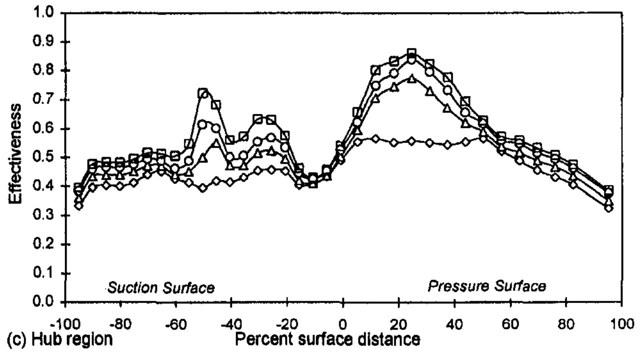

(c) Hub region

Fig. 11 Variation of the vane thermal effectiveness distribution with cooling water

surface pressure distribution with exit Reynolds number in the range of interest. These pressure profiles can be compared with those of other cascades run with the same airfoil. Similarity in pressure distribution for all cascades will ensure similarity in external heat transfer distribution, thus permitting direct comparison of different cooling techniques for this airfoil.

Since this experimental study was conducted at scaled conditions and in order to avoid variations due to slight differences in cascade conditions, the following discussion uses an overall heat transfer effectiveness instead of the wall temperature distributions. Overall effectiveness is defined as follows:

$$\epsilon = \frac{(T_g - T_w)}{(T_g - T_c)}$$

where T_g is the hot gas temperature, T_w is the vane outer wall temperature, and T_c is the coolant inlet temperature. The coolant temperature is measured by two thermocouples placed in the coolant plenum that feeds the air and water to the impingement tube. In the air only case, T_c is the average coolant air temperature entering the impingement tube. In the water–air cooling case, T_c is the average water–air mixture spray temperature.

Figure 11 shows the effect of increasing coolant water from no water to 0.5 percent at constant coolant air of 3.0 percent for impingement tube 1. In Fig. 11, the effectiveness values are shown for the tip, midspan, and hub region. For this run the cascade conditions were $T_g = 676.7$°C (1250°F), Re $= 1.5 \times 10^6$, and M $= 0.7$. The figure shows that there are considerable increases in effectiveness downstream of the leading edge on both the suction and pressure surfaces in the impingement area due to addition of water in the coolant air. Extremely high cooling effectiveness levels of 0.85–0.90 are reached in these areas.

In the leading edge region, the increase in effectiveness is very limited, indicating lack of water droplets reaching the leading edge region. Although the leading edge of the impingement tube was designed for the higher heat flux encountered in the region, it is believed that the droplet characteristics were not optimum. The water droplets did not effectively reach the airfoil inner surface of the leading edge region. In the pin fin region, as expected, the increase in the effectiveness is not as high as in the impingement region, since the main mode of heat transfer

Impingement Tube 1	T_{gas}(°C): 676.7 Reynolds No.: 1.25E+06 Mach No.: 0.7			Air: Var Water: 0.0%
Average Effectiveness				
	Tip	Midspan	Hub	Overall
Air=2%	0.4984	0.4088	0.3768	0.4280
Air=3%	0.5501	0.4579	0.4351	0.4810
Air=4%	0.5786	0.4888	0.4775	0.5149

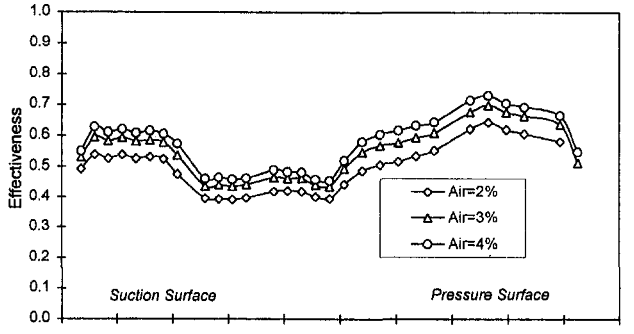

(a) Tip region

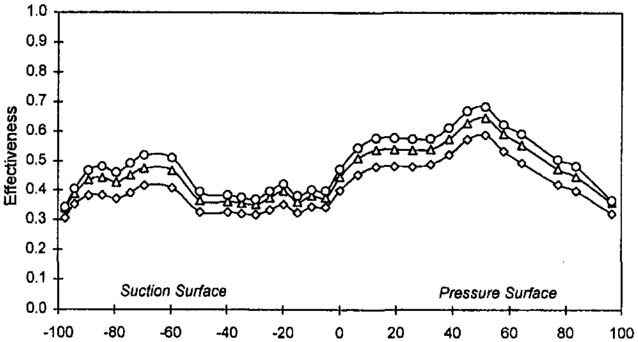

(b) Midspan region

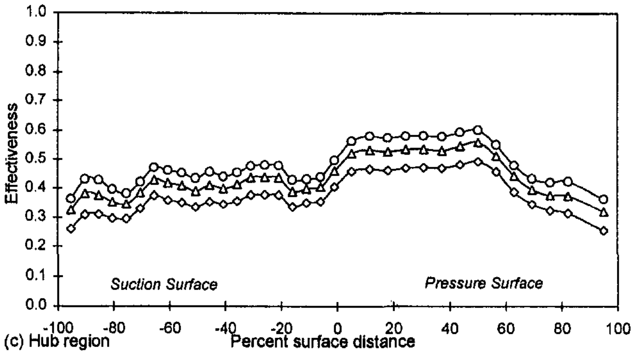

(c) Hub region

Fig. 12 Variation of the vane thermal effectiveness distribution with cooling air

Impingement Tube 1	T_{gas}(°C): 676.7 Reynolds No.: 1.25E+06 Mach No.: 0.7			Air: Var Water: 0.4%
Average Effectiveness				
	Tip	Midspan	Hub	Overall
Air=2%	0.6855	0.5061	0.4420	0.5446
Air=3%	0.7201	0.5618	0.5203	0.6007
Air=4%	0.7241	0.5920	0.5645	0.6269

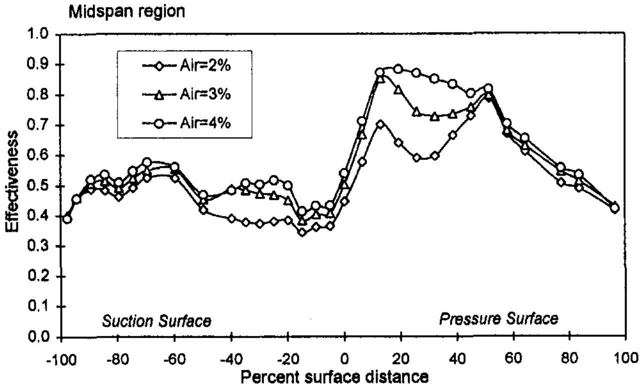

Fig. 13 Variation of the vane thermal effectiveness distribution with cooling air

is forced convection and some impingement of the remaining water droplets.

Also, from Fig. 11, it seen that the tip region is cooled better than the midspan and the hub region due in part to the tip side only introduction of the coolant mixture. This indicates that more work is necessary in designing the water distribution method, either by better spanwise distribution of the water or by varying the impingement tube hole diameter and spacing in the spanwise direction.

The average effectiveness values indicate that larger effectiveness increases are seen when the water flow is increased from 0.3 to 0.4 percent than from 0.4 to 0.5 percent. This indicates that there is an optimum water flow rate for this cooling technique.

The effect of increasing coolant air flow is shown in Fig. 12. In this particular case there is no water added to the coolant air and the cascade conditions are T_g = 676.7°C (1250°F), Re = 1.25×10^6, and M = 0.7. This figure indicates that effectiveness if reasonably uniform in chordwise direction with effectiveness levels decreasing slightly from the tip to the hub. Factors influencing the spanwise vane temperature distribution include inlet gas temperature profiles, conduction to the tip end flange of the vane, and that the impingement air enters the vane from the tip side only. Although ribs were added to the trailing edge slot, the trailing edge region is not cooled as effectively as would be required in an engine application.

The effect of varying the coolant air flow at a constant water flow of 0.4 percent is shown in Fig. 13 for the midspan region only. The data show that a larger increase in effectiveness is produced for an air flow increase from 2.0 to 3.0 percent than from 3.0 to 4.0 percent indicating, again, that there is an optimum air flow rate for this cooling technique.

The variation in heat transfer effectiveness with increasing gas temperatures, T_g is shown in Fig. 14 for impingement tube 3. In this case, the Reynolds number is 1.5×10^6, Mach number is 0.7, and the coolant air and water flow are maintained at 3.0 and 0.4 percent, respectively. Increasing T_g increases the heat flux to the vane. Since the coolant temperature remains relatively constant and the water–air flow is constant, the potential for removing energy on the coolant side is constant. Therefore, increasing gas temperature decreases the overall effectiveness. The gas temperature variation gives data at different T_g/T_c, which in turn can be used, by extrapolation, for a first order estimate of the effectiveness at engine conditions.

Figure 15 shows the effects of increasing Reynolds number for impingement tube 3 at cascade conditions of T_g = 676.7°C (1250°F) and M = 0.7. In both cases, the coolant air flow is maintained at 3.0 percent while in Fig. 15(*a*) there is no coolant water flow and Fig. 15(*b*) the coolant water flow is 0.4 percent. The data in Fig. 15(*a*) indicate that the increase in Reynolds number has negligible effect on heat transfer effectiveness. Increasing the Reynolds number increases the heat flux to the vane as well as the cascade mass flow, m_{cascade}. Thus, to maintain coolant air mass flow ratio, $m_{c,\text{air}}/m_{\text{cascade}}$, coolant air flow is increased, which results in negligible change in effectiveness. This indicates that Reynolds number effects are being well simulated by coolant air mass flow to cascade mass flow ratio, $m_{c,\text{air}}/m_{\text{cascade}}$ for air cooling with this type of cooling scheme. For the case of 3.0 percent air cooling with 0.4 percent water

Impingement Tube 3	T_{gas}(°C): Var *Reynolds No.:* *1.50E+06* Mach No.: 0.7		Air: 3% *Water:* *0.4%*	
Average Effectiveness				
	Tip	Midspan	Hub	Overall
Tgas=537.8°C	*0.7393*	*0.6831*	*0.6896*	*0.7040*
Tgas=676.7°C	0.6722	0.6080	0.5911	0.6238
Tgas=815.8°C	0.6253	0.5649	0.5816	0.5906

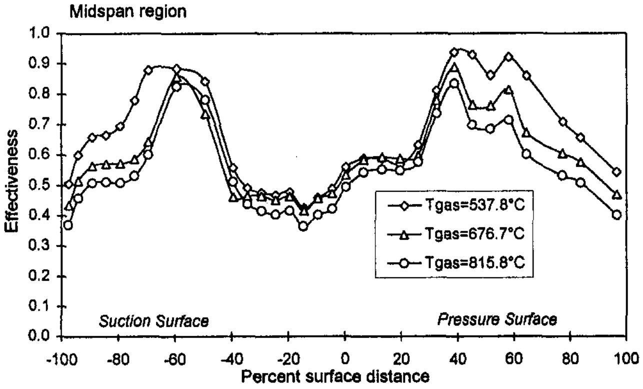

Fig. 14 Variation of the vane thermal effectiveness distribution with gas temperature

cooling, heat transfer effectiveness has some variations due to increasing Reynolds number. The simple ratios of $m_{c,\mathrm{air}}/m_{\mathrm{cascade}}$ and $m_{c,\mathrm{water}}/m_{\mathrm{cascade}}$ do not fully simulate the Reynolds number effects for the water–air cooling scheme. Mach number has very little effect on the heat transfer effectiveness for either air cooling or water–air cooling and hence no results are illustrated.

The effect of using a scaled-up impingement tube (Tube 2) and engine scale impingement tube (Tube 1) on heat transfer effectiveness is brought out in Fig. 16. In this case and in the following discussions on tube geometry effects, the cascade conditions were maintained at Re = 1.5×10^6, M = 0.7, and T_g = 676.7°C (1250°F). The coolant air flow was set at 3.0 percent. In Fig. 16 with a water coolant flow rate of 0.4 percent, the variation in effectiveness at the tip region is very minimal. In the hub and midspan region, just downstream of the leading edge on the pressure surface, the data with the engine scale geometry impingement tube (Tube 1) show a higher effectiveness. This may be due to the better water droplet distribution of the many more holes in the engine scale geometry impingement tube. However, on the suction surface, the trends are reversed.

Figure 17 shows the effect of different impingement hole diameter on heat transfer effectiveness. Tube 3 data show large chordwise variations in effectiveness. Also, Tube 3 shows a slightly higher overall average heat transfer effectiveness. Hence, increasing impingement hole diameter from 0.406 mm (0.016 in.) to 0.508 mm (0.020 in.) does increase the effectiveness; however, Tube 2, in Fig. 16, which has hole diameter of 1.372 mm (0.054 in.) did not show an increase in effectiveness over Tube 3, indicating that there may be an optimum impingement hole diameter, or an optimum combination of hole diameter and spacing.

The heat transfer effectiveness due to varying impingement-tube-to-vane-inner-surface gap from 0.508 mm (0.020 in.) to 0.762 mm (0.030 in.) is compared in Fig. 18. In this case the larger gap (Tube 4) has a considerably lower effectiveness at most locations. Average effectiveness of Tube 1 with a gap of 0.508 mm (0.020 in.) is about 10 percent higher than Tube 4, which has a gap of 0.762 mm (0.030 in.).

Impingement Tube 3	T_{gas}(°C): 676.7 *Reynolds No.:* *Var* Mach No.: 0.7		Air: 3% *Water:* *0.0%*	
Average Effectiveness				
	Tip	Midspan	Hub	Overall
Re=1.25e6	0.5507	0.4947	0.4695	0.5050
Re=1.50e6	0.5647	0.5072	0.4798	0.5172
Re=1.75e6	0.5520	0.4956	0.4742	0.5073

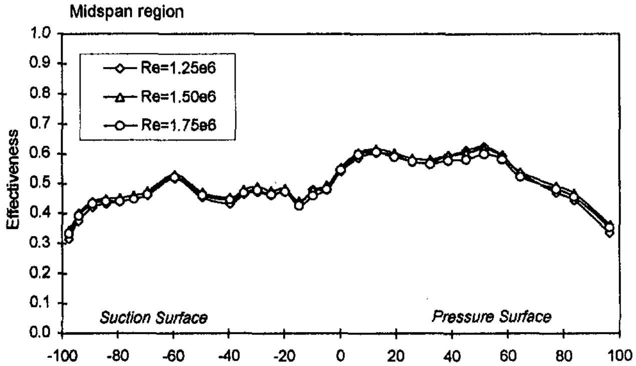

(a) Air cooling

Impingement Tube 3	T_{gas}(°C): 676.7 Reynolds No.: Var Mach No.: 0.7		Air: 3% Water: 0.4%	
Average Effectiveness				
	Tip	*Midspan*	*Hub*	*Overall*
Re=1.25e6	0.6894	0.6236	0.6293	0.6474
Re=1.50e6	0.6722	0.6080	0.5911	0.6238
Re=1.75e6	0.6779	0.6133	0.6087	0.6333

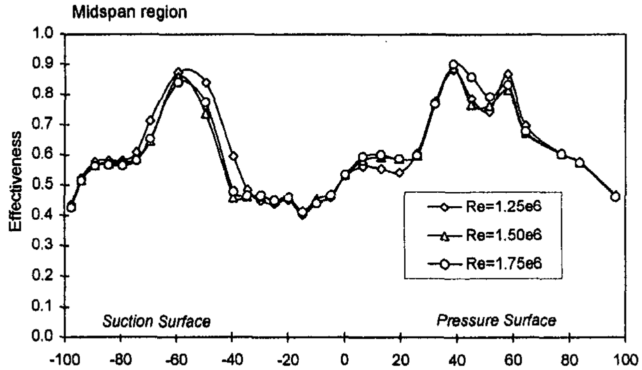

(b) Water-air cooling

Fig. 15 Variation of the vane thermal effectiveness distribution with Reynolds number

Figure 19 shows comparisons of results obtained using an impingement tube with a hole pattern (Tube 1) designed to match the heat flux variations on the vane surface with the results obtained using an impingement tube with a uniform hole pattern (Tube 6). In the case with air only cooling shown in Fig. 19(*a*), Tube 1 produces a slightly better effectiveness, especially in the leading edge region. Tube 1 shows a 3.3 percent better overall average effectiveness over Tube 6. In Fig. 19(*b*), results from Tubes 1 and 6 with water–air cooling are compared. In this case Tube 1, with the varying impingement tube hole pattern, shows a considerably better performance over the tube with a uniform hole pattern. Average effectiveness values for Tube 1 are 17 percent higher than Tube 6.

Due to concerns about the water atomization, Tube 3 was rerun with a different nozzle. Nozzle 2 had a flow rate of 37.86 cm^3/min (0.01 gal/min) and a spray angle of 80 deg. This compares to values of 75.72 cm^3/min (0.02 gal/min) and 65 deg for Nozzle 1. The flow rate is based on 2.76×10^5 N/m^2 (40 psi) drop across the nozzle. The nozzles are flat spray nozzles and the spray angle is the included angle of the fan portion of the spray. Figure 20 compares the heat transfer effectiveness obtained when using the different nozzles. Although Nozzle 2 shows better cooling effectiveness over more of the impingement cooled region, Nozzle 1 shows a higher overall

Impingement Tube Var	T_{gas}(°C): 676.7 Reynolds No.: 1.50E+06 Mach No.: 0.7	Air: 3% Water: 0.4%

Average Effectiveness				
	Tip	Midspan	Hub	Overall
Tube 1	0.7172	0.5512	0.5518	0.6068
Tube 2	0.7340	0.6118	0.5203	0.6221

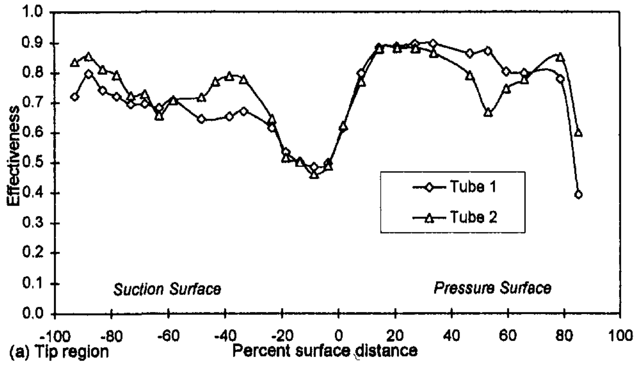

(a) Tip region

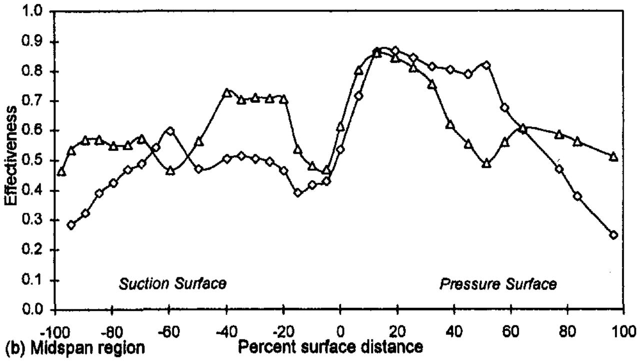

(b) Midspan region

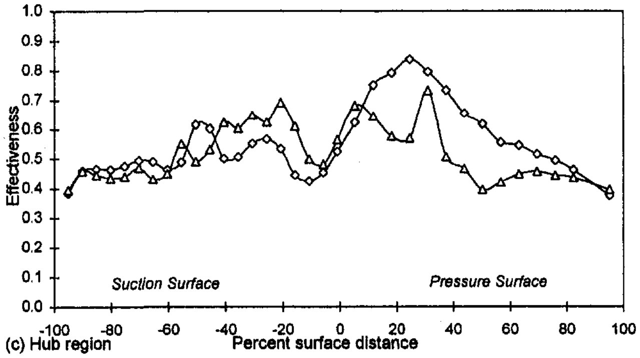

(c) Hub region

Fig. 16 Variation of the vane thermal effectiveness distribution with impingement tube geometric scaling

Impingement Tube Var	T_{gas}(°C): 676.7 Reynolds No.: 1.50E+06 Mach No.: 0.7	Air: 3% Water: 0.4%

Average Effectiveness				
	Tip	Midspan	Hub	Overall
Tube 1	0.7172	0.5512	0.5518	0.6068
Tube 3	0.6722	0.6080	0.5911	0.6238

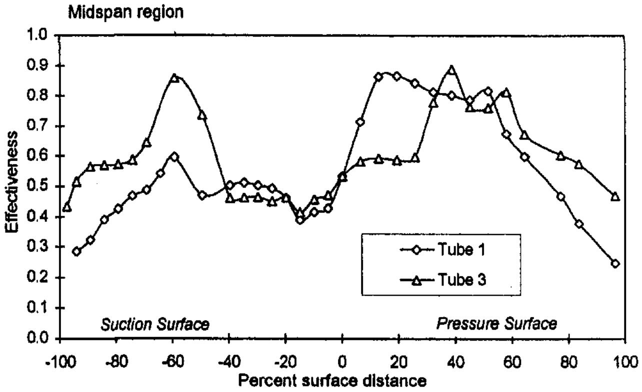

Fig. 17 Variation of the vane thermal effectiveness distribution with impingement tube hole diameter

Impingement Tube Var	T_{gas}(°C): 676.7 Reynolds No.: 1.50E+06 Mach No.: 0.7	Air: 3% Water: 0.4%

Average Effectiveness				
	Tip	Midspan	Hub	Overall
Tube 1	0.7172	0.5512	0.5518	0.6068
Tube 4	0.6418	0.5225	0.4804	0.5482

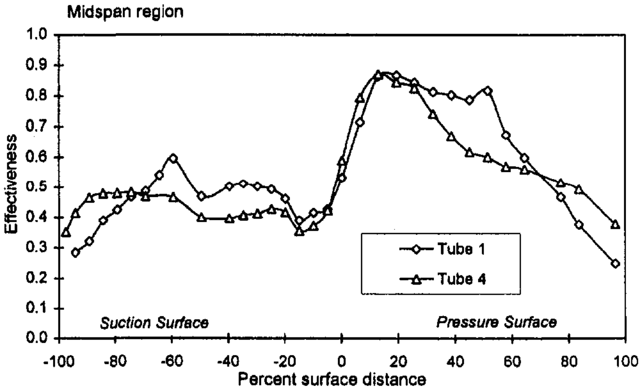

Fig. 18 Variation of the vane thermal effectiveness distribution with the gap between the impingement tube and vane

effectiveness. This indicates that the water nozzle also plays a role in designs for this water–air cooling technique.

Conclusions

The water-air cooling technique to cool turbine vanes was successfully demonstrated in a two-dimensional three-vane cascade. The cascade experiments have confirmed that water–air cooling of turbine vanes can achieve extremely high heat transfer cooling effectiveness: as high as 0.9 in some areas.

This cooling technique can achieve cooling effectiveness values comparable to traditional air cooled airfoil designs using cooling air flows less than 50 percent of those used by the air-cooled airfoils. Increasing coolant water and/or coolant air flow increases cooling effectiveness. However, results indicate that there is an optimum coolant flow rate above which the effectiveness increases are marginal.

Increasing gas to coolant temperature ratio, T_g/T_c, decreases effectiveness. Experiments were conducted at different gas temperatures to envelop the engine range of gas to coolant temperature ratio, T_g/T_c,. In the range of the experiments, the effects of varying Reynolds number are not fully accounted for by the coolant-to-cascade mass flow ratios, $m_{c,\text{air}}/m_{\text{cascade}}$ and $m_{c,\text{water}}/m_{\text{cascade}}$, for the air–water cooling technique. Varying Mach number has negligible effects on heat transfer effectiveness.

As predicted, using engine scale dimensions for the impingement tube geometry showed higher overall heat transfer effectiveness in the cascade experiments. Increasing impingement tube hole diameters from 0.406 mm (0.016 in.) to 0.508 mm (0.020 in.) increased overall effectiveness; however increasing hole diameters to 1.372 mm (0.054 in.), as in Tube 2, did not increase effectiveness, indicating that an optimum hole diameter or an optimum combination of hole diameter and spacing falls in this range. Increasing impingement-tube-to-vane-inner-surface gap from 0.508 mm (0.020 in.) to 0.762 mm (0.030) decreased

Impingement Tube Var	T_{gas}(°C): 676.7 Reynolds No.: 1.50E+06 Mach No.: 0.7		Air: 3% Water: 0.0%	
Average Effectiveness				
	Tip	Midspan	Hub	Overall
Tube 1	0.5596	0.4362	0.4586	0.4848
Tube 6	0.5105	0.4483	0.4475	0.4687

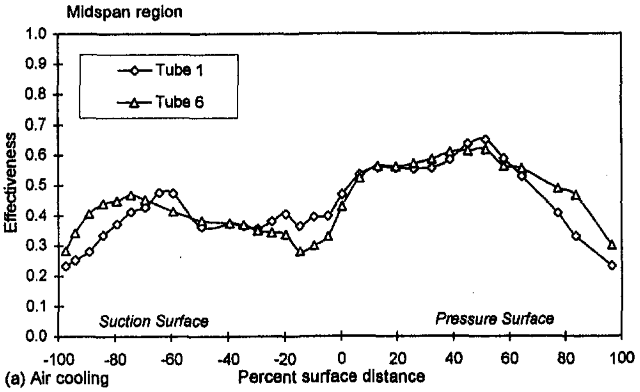

(a) Air cooling

Impingement Tube Var	T_{gas}(°C): 676.7 Reynolds No.: 1.50E+06 Mach No.: 0.7		Air: 3% Water: 0.4%	
Average Effectiveness				
	Tip	Midspan	Hub	Overall
Tube 1	0.7172	0.5512	0.5518	0.6068
Tube 6	0.5780	0.4896	0.4408	0.5028

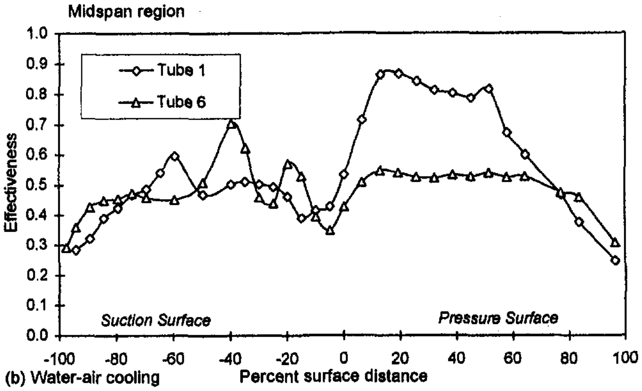

(b) Water-air cooling

Fig. 19 Variation of the vane thermal effectiveness distribution with impingement tube hole pattern

overall heat transfer effectiveness. A variable impingement tube hole pattern was shown to provide higher overall effectiveness values than were obtained with an impingement tube with a uniform hole pattern.

It was also determined that the spray nozzle used for the water atomization plays a major role in the distribution of the water droplets and thus affects the heat transfer cooling effectiveness.

Though very high heat transfer effectiveness was achieved by this water-air cooling technique, uniformly high effectiveness values were not attainable. Nonuniformity seems to be attributed to poor water droplet distribution by the nozzle and the flow characteristics of two-phase flow in the gap region between the impingement tube and the airfoil inner wall. This study has demonstrated the outstanding potential of this cooling technique, but has also demonstrated that more work will be required to develop a coolant delivery system that has an adequately uniform cooling distribution.

Acknowledgments

The investigations reported herein were performed by Allison Engine Company with funding provided by the U.S. Department of Energy, Morgantown Energy Technology Center under contract DE-AC21-93MC29257. The authors also acknowledge the U.S. Department of Energy, Morgantown Energy Technology Center for giving permission to publish this paper.

Impingement Tube 3	T_{gas}(°C): 676.7 Reynolds No.: 1.75E+06 Mach No.: 0.7		Air: 3% Water: 0.4%	
Average Effectiveness				
	Tip	Midspan	Hub	Overall
Nozzle 1	0.6779	0.6133	0.6087	0.6333
Nozzle 2	0.6915	0.5884	0.5736	0.6178

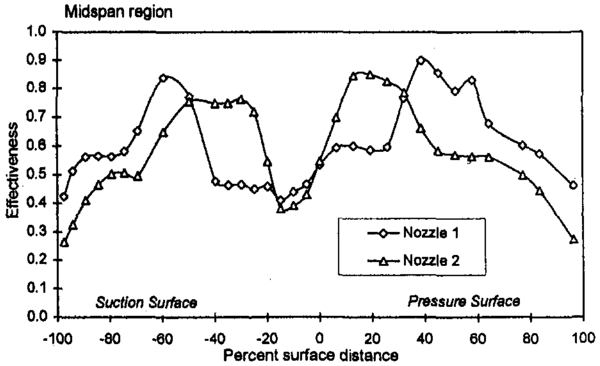

Fig. 20 Variation of the vane thermal effectiveness distribution with water nozzle

References

Biesiadny, T. J., Klann, G. A., Clark, D. A., and Berger, B. 1987. "Contingency Power for Turbo Small Turboshaft Engines Using Water Injection Into Turbine Cooling Air," NASA TM 89817, AIAA Paper No. 87-1906.

Dudley, J. C., Sundell, R. E., Goodwin, W. W., and Kercher, D. M., 1984, "Two-Phase Heat Transfer in Gas Turbine Bucket Cooling Passages: Part 1," in: *Heat and Mass Transfer in Rotating Machinery,* Metzer and Agfan, eds., Hemisphere Publishing Corporation, pp. 463–472.

Fiszdon, J. K., Florschuetz, L. W., and Janssen, J. M., 1994, "Heat Transfer to Two-Phase Air/Water Mixtures Flowing in Small Tubes With Inlet Disequilibrium," in: *Heat Transfer in Gas Turbines,* Chyu and Nirmalan, eds., ASME HTD-Vol. 300, pp. 165–171.

Hylton, L. D., Nirmalan, N. V., and Sweeney, P. C., 1995, "Advanced Cooling Concept," NASA Contractor Report, Preliminary Draft, Allison EDR 16666.

Kline, S. J., and McClintock, F. A., 1953. "Describing Uncertainties in Single-Sample Experiments," *Mechanical Engineering,* Jan., pp. 3–8.

Nealy, D. A., Mihelc, M. S., Hylton, L. D., and Gladden, H. J., 1984, "Measurements of Heat Transfer Distribution Over the Surfaces of Highly Loaded Turbine Nozzle Guide Vanes," ASME *Journal of Engineering for Gas Turbines and Power,* Vol. 106, pp. 149–158.

Nirmalan, N. V., and Hylton, L. D., 1990, "An Experimental Study of Turbine Vane Heat Transfer With Leading Edge and Downstream Film Cooling," ASME JOURNAL OF TURBOMACHINERY, Vol. 112, pp. 477–487.

Pedersen, C. O., 1970, "An Experimental Study of the Dynamic Behavior and Heat Transfer Characteristics of Water Droplets Impinging Upon a Heated Surface," *International Journal of Heat and Mass Transfer,* Vol. 13, pp. 369–381.

Schmidt, E., 1951, "Heat Transmission by Natural Convection at High Centrifugal Accelerations in Water-Cooled Gas Turbine Rotor Blades," *Institute of Mechanical Engineers Proceeding,* Vol. 185, pp. 219–222.

Sundell, R. E., Dudley, J. C., Grondhal, C. M., and Kercher, D. M., 1984, "Two-Phase Heat Transfer in Gas Turbine Bucket Cooling Passages: Part 2," in: *Heat and Mass Transfer in Rotating Machinery,* Metzer and Agfan, eds., Hemisphere Publishing Corporation, pp. 473–484.

Van Fossen, G. J., and Stepka, F. S., 1979, "Review and Status of Liquid Cooling Technology for Gas Turbines," NASA RP 1038.

Van Fossen, G. J., 1983, "The Feasibility of Water Injection Into the Turbine Coolant to Permit Gas Turbine Contingency Power for Helicopter Application," ASME *Journal of Engineering for Power,* Vol. 105, pp. 635–642.

Wenglarz, R. A., Nirmalan, N. V., and Daehler, T. G., 1995, "Rugged ATS Turbines for Alternate Fuels," ASME Paper No. 95-GT-73.

DISCUSSION

D. A. Nealy[1]

I commend the authors for their investigation of a rather novel approach to the high-temperature turbine cooling problem. The

---

[1] ABB Management Ltd., Corporate Research—CRBT1, CH-5405 Baden Dattwil, Switzerland.

Impingement Tube Var	T_{gas}(°C): 676.7 Reynolds No.: 1.50E+06 Mach No.: 0.7		Air: 3% Water: 0.0%	
Average Effectiveness				
	Tip	Midspan	Hub	Overall
Tube 1	0.5596	0.4362	0.4586	0.4848
Tube 6	0.5105	0.4483	0.4475	0.4687

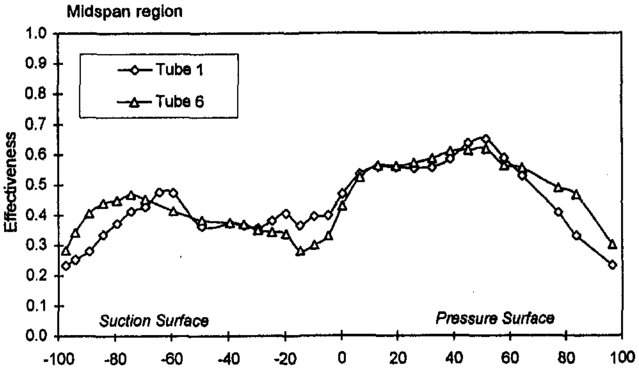

(a) Air cooling

Impingement Tube Var	T_{gas}(°C): 676.7 Reynolds No.: 1.50E+06 Mach No.: 0.7		Air: 3% Water: 0.4%	
Average Effectiveness				
	Tip	Midspan	Hub	Overall
Tube 1	0.7172	0.5512	0.5518	0.6068
Tube 6	0.5780	0.4896	0.4408	0.5028

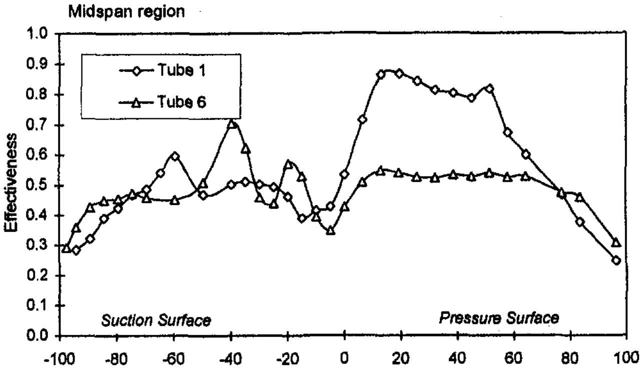

(b) Water-air cooling

Fig. 19 Variation of the vane thermal effectiveness distribution with impingement tube hole pattern

overall heat transfer effectiveness. A variable impingement tube hole pattern was shown to provide higher overall effectiveness values than were obtained with an impingement tube with a uniform hole pattern.

It was also determined that the spray nozzle used for the water atomization plays a major role in the distribution of the water droplets and thus affects the heat transfer cooling effectiveness.

Though very high heat transfer effectiveness was achieved by this water–air cooling technique, uniformly high effectiveness values were not attainable. Nonuniformity seems to be attributed to poor water droplet distribution by the nozzle and the flow characteristics of two-phase flow in the gap region between the impingement tube and the airfoil inner wall. This study has demonstrated the outstanding potential of this cooling technique, but has also demonstrated that more work will be required to develop a coolant delivery system that has an adequately uniform cooling distribution.

Acknowledgments

The investigations reported herein were performed by Allison Engine Company with funding provided by the U.S. Department of Energy, Morgantown Energy Technology Center under contract DE-AC21-93MC29257. The authors also acknowledge the U.S. Department of Energy, Morgantown Energy Technology Center for giving permission to publish this paper.

Impingement Tube 3	T_{gas}(°C): 676.7 Reynolds No.: 1.75E+06 Mach No.: 0.7		Air: 3% Water: 0.4%	
Average Effectiveness				
	Tip	Midspan	Hub	Overall
Nozzle 1	0.6779	0.6133	0.6087	0.6333
Nozzle 2	0.6915	0.5884	0.5736	0.6178

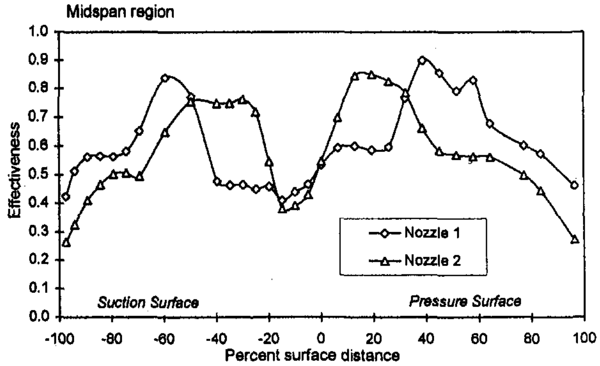

Fig. 20 Variation of the vane thermal effectiveness distribution with water nozzle

References

Biesiadny, T. J., Klann, G. A., Clark, D. A., and Berger, B. 1987. "Contingency Power for Turbo Small Turboshaft Engines Using Water Injection Into Turbine Cooling Air," NASA TM 89817, AIAA Paper No. 87-1906.

Dudley, J. C., Sundell, R. E., Goodwin, W. W., and Kercher, D. M., 1984, "Two-Phase Heat Transfer in Gas Turbine Bucket Cooling Passages: Part 1," in: *Heat and Mass Transfer in Rotating Machinery,* Metzer and Agfan, eds., Hemisphere Publishing Corporation, pp. 463–472.

Fiszdon, J. K., Florschuetz, L. W., and Janssen, J. M., 1994, "Heat Transfer to Two-Phase Air/Water Mixtures Flowing in Small Tubes With Inlet Disequilibrium," in: *Heat Transfer in Gas Turbines,* Chyu and Nirmalan, eds., ASME HTD-Vol. 300, pp. 165–171.

Hylton, L. D., Nirmalan, N. V., and Sweeney, P. C., 1995, "Advanced Cooling Concept," NASA Contractor Report, Preliminary Draft, Allison EDR 16666.

Kline, S. J., and McClintock, F. A., 1953. "Describing Uncertainties in Single-Sample Experiments," *Mechanical Engineering,* Jan., pp. 3–8.

Nealy, D. A., Mihelc, M. S., Hylton, L. D., and Gladden, H. J., 1984, "Measurements of Heat Transfer Distribution Over the Surfaces of Highly Loaded Turbine Nozzle Guide Vanes," ASME *Journal of Engineering for Gas Turbines and Power,* Vol. 106, pp. 149–158.

Nirmalan, N. V., and Hylton, L. D., 1990, "An Experimental Study of Turbine Vane Heat Transfer With Leading Edge and Downstream Film Cooling," ASME JOURNAL OF TURBOMACHINERY, Vol. 112, pp. 477–487.

Pedersen, C. O., 1970, "An Experimental Study of the Dynamic Behavior and Heat Transfer Characteristics of Water Droplets Impinging Upon a Heated Surface," *International Journal of Heat and Mass Transfer,* Vol. 13, pp. 369–381.

Schmidt, E., 1951, "Heat Transmission by Natural Convection at High Centrifugal Accelerations in Water-Cooled Gas Turbine Rotor Blades," *Institute of Mechanical Engineers Proceeding,* Vol. 185, pp. 219–222.

Sundell, R. E., Dudley, J. C., Grondhal, C. M., and Kercher, D. M., 1984, "Two-Phase Heat Transfer in Gas Turbine Bucket Cooling Passages: Part 2," in: *Heat and Mass Transfer in Rotating Machinery,* Metzer and Agfan, eds., Hemisphere Publishing Corporation, pp. 473–484.

Van Fossen, G. J., and Stepka, F. S., 1979, "Review and Status of Liquid Cooling Technology for Gas Turbines," NASA RP 1038.

Van Fossen, G. J., 1983, "The Feasibility of Water Injection Into the Turbine Coolant to Permit Gas Turbine Contingency Power for Helicopter Application," ASME *Journal of Engineering for Power,* Vol. 105, pp. 635–642.

Wenglarz, R. A., Nirmalan, N. V., and Daehler, T. G., 1995, "Rugged ATS Turbines for Alternate Fuels," ASME Paper No. 95-GT-73.

DISCUSSION

D. A. Nealy[1]

I commend the authors for their investigation of a rather novel approach to the high-temperature turbine cooling problem. The

---

[1] ABB Management Ltd., Corporate Research—CRBT1, CH-5405 Baden Dattwil, Switzerland.

method of suspended water droplets or "water mist" enhancement of air cooling would appear to offer some real promise once systematically characterized in terms of practical design variables. This work deserves high marks for originality, and several data trends in the paper are intriguing. However, little attempt is made to rationalize or systematically analyze those trends. Some specific comments follow:

1 A large amount of data is presented representing a considerable range of design and operational variables, but little attempt is made to interpret the data trends even in a first-order sense. The physical and geometric variables governing this cooling approach are undeniably complex and probably defy easy characterization. However, it is interesting to me that the broad trends with percent water injection (Fig. 11) almost behave as if latent heat of vaporization were not very important. If one would adopt the very simple-minded approach that the cooling effectiveness trends might be largely reconciled by defining a mass-average coolant mixture specific heat—ignoring latent heat of vaporization in the wall heat transfer process—the trends with increasing water content are surprisingly well predicted. If effectiveness, ϵ, is as defined in the paper, then one might argue from a simple energy balance perspective that, to first order,

$$R_m/R_a = (WCp)_m/(WCp)_a \tag{1}$$

where

$$R = \epsilon/(1-\epsilon)$$

and

W = coolant mass flow

Cp = coolant specific heat

The subscripts m and a denote air/water mixture and air, respectively. The mixture specific heat is simply defined as,

$$(Cp)_m = ((WCp)_w + (WCp)_a)/(W_w + W_a) \tag{2}$$

where the subscript w refers to water.

Evaluating Eqs. (1) and (2) for the relative proportions of air and water in the experiment, overall effectiveness trends with increasing water content can be evaluated and compared to the data in Fig. 11:

Water percent	Overall effectiveness (Fig. 11)	Overall effectiveness (Eq. (1))
0	0.485	0.485 (baseline)
0.3	0.567	0.569
0.4	0.607	0.591
0.5	0.635	0.611

While I do not suggest that such a simple procedure—implicitly neglecting direct latent heat of vaporization as well as cooling channel thermal efficiency effects—represents a viable design tool, there is the clear suggestion that the cooling process may be largely driven by mixture specific heat level. It would at least be interesting to determine if similar broad trends exist for the other impingement geometries as well.

2 The overall effectiveness trends with air cooling alone (Fig. 12) seem surprisingly modest for a variation in cooling flow of two to one. Assuming an internal heat transfer Nu/Re power law relationship with a slope of 0.70, I would estimate that to first order, the overall effectiveness at an airflow of 4 percent should be at least 0.565, taking the 2 percent airflow case as a baseline.

3 I confess that I do not understand the trends in Fig. 14 at all. I would expect overall effectiveness to be relatively insensitive to T_g (or T_g/T_c) alone. The data suggest that reducing T_g from 816°C to 538°C increases the ratio R (as defined above) by an astonishing 65 percent! This implies a 65 percent increase in mean coolant side heat transfer coefficient (relative to gas side heat transfer coefficient) as T_g is reduced. It is not at all clear how such a profound effect is produced. Comparing this change in overall effectiveness (with T_g) to that shown in Fig. 12 (effect of cooling flow variation), the indicated percentage change in the ratio R is 50 percent greater than that which occurs for a two to one increase in cooling air flow! Also, the increase in R ratio with reduced T_g (65 percent) is essentially equal to that shown in Fig. 11 for an increase in water injection from zero to 0.4 percent (64 percent increase). While independent changes in gas to coolant (or gas to wall) temperature ratio have been shown to have a second-order effect on overall cooling effectiveness, the dramatic results in Fig. 14 are difficult to reconcile, particularly in light of the comment that T_g/T_c was fixed at 2.0 throughout the testing (p. 7).

In fairness, it should be noted that the last arguments are strictly valid for nominally gaseous, single-phase coolants. Thus the trends in Fig. 14 may in fact reflect some fundamentally different behavior unique to the water mist cooling approach. If so, this is a very important trend and perhaps deserves more discussion than it receives in the paper.

4 Finally, I am a little confused by the various repeated contentions that some type of optimal configuration, flow split, etc., may exist. I don't know that the data really suggest that. For example, the conclusion that "results indicate that there is an optimum coolant flow rate above which effectiveness increases are marginal" is somewhat careless use of the word "optimum." All internally cooled systems show monotonic increases in effectiveness with cooling flow, trends that tend to become asymptotic at very high cooling flow levels. However, I am not aware of any data that suggest a change in the sign of the slope of such trends.

Authors' Closure

We appreciate Dr. Nealy's comments. His observation that the manuscript did not address any analytical approach to rationalizing the data trends is valid. An attempt was made to give a physical basis for the trends of the various perturbations in the experimental program. The authors felt an analytical approach was not warranted in the scope of this work. A one-dimensional model of the heat transfer and flow of an air–water mixture in a channel had been previously developed at Allison Engine Company and would be ideally suited for this task. A response for each of Dr. Nealy's specific comments follows:

1, 3 The authors feel both concerns are related to the dependence of water cooling on the difference between the wall temperature and saturation temperature of the water. It is an interesting observation by Dr. Nealy that the sensible energy rise of air and liquid water based on the temperature increase of the coolant mixture approximates the sensible and latent energy changes in the actual mixture. At the lower temperatures at which the experiments were conducted, the latent energy change of the water may be a relatively smaller portion of the overall and hence the trend cited by Dr. Nealy compares well with the data. At the elevated temperatures of engine conditions, the authors feel this would not be the case. Further investigation would be warranted to examine this and other possible explanations of the data trends. Additionally, T_g/T_c was not fixed at 2 as stated by Dr. Nealy, but "was maintained at a typical engine ratio of about 2." T_g/T_c does vary some. The variation of cooling effectiveness with T_g again points to the dependence of water cooling on the temperature difference between wall and coolant.

2 For an impingement arrangement, the slope on the Nu/Re power law relationship varies between 0.7 and 0.9 depending on the spacing and Re number (Kercher and Tabakoff, 1970).

method of suspended water droplets or ''water mist'' enhancement of air cooling would appear to offer some real promise once systematically characterized in terms of practical design variables. This work deserves high marks for originality, and several data trends in the paper are intriguing. However, little attempt is made to rationalize or systematically analyze those trends. Some specific comments follow:

1 A large amount of data is presented representing a considerable range of design and operational variables, but little attempt is made to interpret the data trends even in a first-order sense. The physical and geometric variables governing this cooling approach are undeniably complex and probably defy easy characterization. However, it is interesting to me that the broad trends with percent water injection (Fig. 11) almost behave as if latent heat of vaporization were not very important. If one would adopt the very simple-minded approach that the cooling effectiveness trends might be largely reconciled by defining a mass-average coolant mixture specific heat—ignoring latent heat of vaporization in the wall heat transfer process—the trends with increasing water content are surprisingly well predicted. If effectiveness, ϵ, is as defined in the paper, then one might argue from a simple energy balance perspective that, to first order,

$$R_m/R_a = (W\,Cp)_m/(W\,Cp)_a \qquad (1)$$

where

$$R = \epsilon/(1-\epsilon)$$

and

W = coolant mass flow

Cp = coolant specific heat

The subscripts m and a denote air/water mixture and air, respectively. The mixture specific heat is simply defined as,

$$(Cp)_m = ((W\,Cp)_w + (W\,Cp)_a)/(W_w + W_a) \qquad (2)$$

where the subscript w refers to water.

Evaluating Eqs. (1) and (2) for the relative proportions of air and water in the experiment, overall effectiveness trends with increasing water content can be evaluated and compared to the data in Fig. 11:

Water percent	Overall effectiveness (Fig. 11)	Overall effectiveness (Eq. (1))
0	0.485	0.485 (baseline)
0.3	0.567	0.569
0.4	0.607	0.591
0.5	0.635	0.611

While I do not suggest that such a simple procedure—implicitly neglecting direct latent heat of vaporization as well as cooling channel thermal efficiency effects—represents a viable design tool, there is the clear suggestion that the cooling process may be largely driven by mixture specific heat level. It would at least be interesting to determine if similar broad trends exist for the other impingement geometries as well.

2 The overall effectiveness trends with air cooling alone (Fig. 12) seem surprisingly modest for a variation in cooling flow of two to one. Assuming an internal heat transfer Nu/Re power law relationship with a slope of 0.70, I would estimate that to first order, the overall effectiveness at an airflow of 4 percent should be at least 0.565, taking the 2 percent airflow case as a baseline.

3 I confess that I do not understand the trends in Fig. 14 at all. I would expect overall effectiveness to be relatively insensitive to T_g (or T_g/T_c) alone. The data suggest that reducing T_g from 816°C to 538°C increases the ratio R (as defined above) by an astonishing 65 percent! This implies a 65 percent increase in mean coolant side heat transfer coefficient (relative to gas side heat transfer coefficient) as T_g is reduced. It is not at all clear how such a profound effect is produced. Comparing this change in overall effectiveness (with T_g) to that shown in Fig. 12 (effect of cooling flow variation), the indicated percentage change in the ratio R is 50 percent greater than that which occurs for a two to one increase in cooling air flow! Also, the increase in R ratio with reduced T_g (65 percent) is essentially equal to that shown in Fig. 11 for an increase in water injection from zero to 0.4 percent (64 percent increase). While independent changes in gas to coolant (or gas to wall) temperature ratio have been shown to have a second-order effect on overall cooling effectiveness, the dramatic results in Fig. 14 are difficult to reconcile, particularly in light of the comment that T_g/T_c was fixed at 2.0 throughout the testing (p. 7).

In fairness, it should be noted that the last arguments are strictly valid for nominally gaseous, single-phase coolants. Thus the trends in Fig. 14 may in fact reflect some fundamentally different behavior unique to the water mist cooling approach. If so, this is a very important trend and perhaps deserves more discussion than it receives in the paper.

4 Finally, I am a little confused by the various repeated contentions that some type of optimal configuration, flow split, etc., may exist. I don't know that the data really suggest that. For example, the conclusion that ''results indicate that there is an optimum coolant flow rate above which effectiveness increases are marginal'' is somewhat careless use of the word ''optimum.'' All internally cooled systems show monotonic increases in effectiveness with cooling flow, trends that tend to become asymptotic at very high cooling flow levels. However, I am not aware of any data that suggest a change in the sign of the slope of such trends.

Authors' Closure

We appreciate Dr. Nealy's comments. His observation that the manuscript did not address any analytical approach to rationalizing the data trends is valid. An attempt was made to give a physical basis for the trends of the various perturbations in the experimental program. The authors felt an analytical approach was not warranted in the scope of this work. A one-dimensional model of the heat transfer and flow of an air–water mixture in a channel had been previously developed at Allison Engine Company and would be ideally suited for this task. A response for each of Dr. Nealy's specific comments follows:

1, 3 The authors feel both concerns are related to the dependence of water cooling on the difference between the wall temperature and saturation temperature of the water. It is an interesting observation by Dr. Nealy that the sensible energy rise of air and liquid water based on the temperature increase of the coolant mixture approximates the sensible and latent energy changes in the actual mixture. At the lower temperatures at which the experiments were conducted, the latent energy change of the water may be a relatively smaller portion of the overall and hence the trend cited by Dr. Nealy compares well with the data. At the elevated temperatures of engine conditions, the authors feel this would not be the case. Further investigation would be warranted to examine this and other possible explanations of the data trends. Additionally, T_g/T_c was not fixed at 2 as stated by Dr. Nealy, but ''was maintained at a typical engine ratio of about 2.'' T_g/T_c does vary some. The variation of cooling effectiveness with T_g again points to the dependence of water cooling on the temperature difference between wall and coolant.

2 For an impingement arrangement, the slope on the Nu/Re power law relationship varies between 0.7 and 0.9 depending on the spacing and Re number (Kercher and Tabakoff, 1970).

As such, using a slope of 0.7 is reasonable. If a slope of 0.5 is assumed, then the effectiveness for an increase in airflow of 2 to 4 percent is 0.51, which closely matches the data of Fig. 12 (for comparison, using a slope of 0.7, the authors obtained an effectiveness of 0.55, which is slightly lower than Dr. Nealy's value of 0.57). However, crossflow effects do degrade the impingement heat transfer. For impingement tube 1, this effect would be important due to the large number of rows downstream of the leading edge. This could explain the trend for a smaller dependence than cited by Dr. Nealy. Also, a slope of 0.5 matches the 2 to 4 percent variation of air in Fig. 13.

4 Dr. Nealy makes a valid point. With reference to the effects of changing the cooling flow rates, optimum is inappropriately used. When discussing the different hole patterns of tubes 1, 2, and 3, preferred is possibly a better choice. Three data points do not make a basis for suggesting an optimum pattern or hole size that directly affects the overall atomization characteristics of the impingement tube supply system.

Reference

Kercher, D. M., and Tabakoff, W., 1970, "Heat Transfer by a Square Array of Round Air Jets Impinging Perpendicular to a Flat Surface Including the Effects of Spent Air," ASME *Journal of Engineering for Power*, Vol. 92, pp. 73–82.

Z. Wang
Ellison Surface Technologies, Inc.,
1780 Anderson Blvd.,
Hebron, KY 41048

P. T. Ireland
Department of Engineering Science,
University of Oxford, Parks Road,
Oxford, OX1 3PJ, United Kingdom

S. T. Kohler

J. W. Chew

Rolls Royce plc,
P.O. Box 3,
Filton, Bristol, BS12 7QE, United Kingdom

Heat Transfer Measurements to a Gas Turbine Cooling Passage With Inclined Ribs

The local heat transfer coefficient distribution over all four walls of a large-scale model of a gas turbine cooling passage have been measured in great detail. A new method of determining the heat transfer coefficient to the rib surface has been developed and the contribution of the rib, at 5 percent blockage, to the overall roughened heat transfer coefficient was found to be considerable. The vortex-dominated flow field was interpreted from the detailed form of the measured local heat transfer contours. Computational Fluid Dynamics calculations support this model of the flow and yield friction factors that agree with measured values. Advances in the heat transfer measuring technique and data analysis procedure that confirm the accuracy of the transient method are described in full.

Introduction

Countless different schemes have been adopted by engine manufacturers to cool the blades and vanes used in modern gas turbines. Sometimes, metallic inserts are used to partition the inside of hollow aerofoils to enable jets of coolant to be directed at the internal surface. Impingement cooling has received a great deal of research attention over the years and comprehensive reports by Florschuetz et al. (1981), Andrews et al. (1992), and, more recently, Van Treuren et al. (1996) number amongst those in the literature. Another frequently applied cooling strategy uses one or more cast passages, which snake back and forth inside the blade. In some cases, the external heat load is so high that the cooling performance of the internal passage needs to be improved by casting roughness elements into the walls. The boundary layers on the passage walls are interrupted by roughness elements, such as ribs, and the heat and momentum processes enhanced by additional turbulence and secondary flows. Over the past decade or so, J. C. Han and his co-workers have produced a large data set to be used for the prediction of heat transfer and pressure drop in ribbed passages; see for example Lau et al. (1991). Holographic interferometry was used by Lockett and Collins (1990) to investigate the temperature field around square and rounded ribs set orthogonal to the flow direction. They reported normalized Nusselt number distributions over the complete surface of ribs at 6.7 percent blockage. Liou and Hwang (1993) used holography to study the effect of rib shape on heat transfer. Taslim and Wadsworth (1997) measured the contribution of rib heat transfer to the overall heat transfer using separately heated ribs in steady-state experiments. They tested configurations in which the ribs were set at 90 deg to the flow direction and assessed the effect of rib pitch.

The present research has investigated a simple form of roughness element used in aeroengines. Inclined ribs have been added to two facing walls of a square section passage. The rib height is 5 percent of the passage hydraulic diameter and they are inclined at 45 deg to the passage major axis at a pitch of 10 rib sizes, Fig. 1. The ribs, on the opposite walls, are inline and hence the minimum passage space gap is 80 percent of the passage hydraulic diameter. This geometry and blockage were chosen for two reasons. First, they are typical of a configuration used in a particular aeroengine and the results were of direct interest to the designers. Second, data were available for the same geometry from the experiments of J. C. Han and his co-workers. The new means of determining the rib heat transfer coefficient, computing the flow field, using the heater mesh, and employing the adiabatic wall temperature in the analysis could then assessed by comparison to the results of these authors. Once the experimental steps were verified, as reported below, the complete technique was applied in a rib roughness optimizing program for Rolls-Royce plc. The present results are also significant in that the transient technique has been used to measure local heat transfer coefficients over the complete passage internal surface. This allows interpretation of the flow field in the light of complete surface data.

Experimental Apparatus

The experimental apparatus is shown in Fig. 2 and consists of a square cross section (50 mm × 50 mm) duct 2000 mm long. The first half of the duct is completely smooth walled and allows the hydrodynamic and thermal boundary layers to develop ahead of the second rib-roughened half. This is representative of a ribbed passage in a turbine blade fed from a smooth section through the blade root. The large scale (approximately 20×) enables engine Reynolds numbers to be achieved at low speed and atmospheric pressure. The heat transfer results referred to in the following were taken in a position of developed flow more than 15 d from the start of the ribbed section. The issue of modeling small cast passages at large scale with smooth materials has been addressed by the authors (Wang et al., 1991). Coatings of sand and copper, with scaled average roughness values R_a were used to measure the effect of engine representative roughness (R_a of order 1 μm) on heat transfer levels. The results showed that the roughness caused by the casting process could significantly affect the heat transfer and pressure drop in small cooling passages. However, for the engine passages modeled in the present work, which were of order 5 mm in hydraulic diameter, the casting roughness would have produced a second-order influence relative to the large ($\approx$250-μm-high) ribs.

Experimental Technique

Conventional Transient Heat Transfer Method. The transient heat transfer method has been applied by the authors to many different blade cooling problems. Its use was pioneered at Oxford by Jones (see Clifford et al., 1983), and recent devel-

---

Contributed by the International Gas Turbine Institute and presented at the 41st International Gas Turbine and Aeroengine Congress and Exhibition, Birmingham, United Kingdom, June 10–13, 1996. Manuscript received at ASME Headquarters February 1996. Paper No. 96-GT-542. Associate Technical Editor: J. N. Shinn.

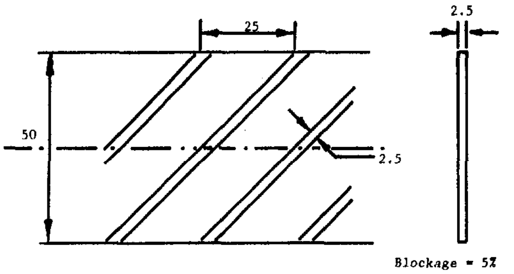

Fig. 1 Rib roughness geometry applied to two facing walls of the passage. Ribs extend continuously from smooth wall to smooth wall.

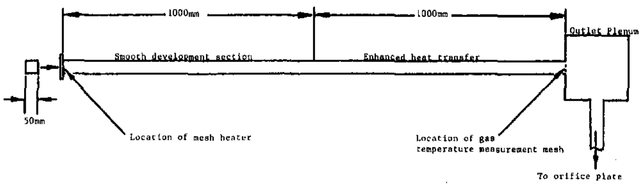

Fig. 2 Experimental apparatus

opments are discussed in detail by Ireland et al. (1995). It offers the significant advantage of yielding local heat transfer coefficients over complete test surfaces in a single experiment. The technique relies on interpreting the thermal response of an insulating model to a change in fluid to model temperature difference. In the present research, a new means of producing the air temperature change was employed. A fine, fast-response, mesh heater[1] was fitted to the duct inlet to produce the step change in gas temperature. This heater comprises a mesh of stainless steel wires, 40 μm in diameter, woven at a pitch of approximately 100 μm. The tiny heat transfer passages constitute a highly effective heat exchanger with a convective efficiency,[2] over the range of speeds used in these tests, of more than 50 percent. This means that the mesh can run comparatively cool when supplying air heated by approximately 50°C. The heater time response is a function of the flow velocity and has been quantified by Gillespie et al. (1998). In the present experiments, the time constant was always less than 0.030 s. In fact, the analysis of the crystal time response can be extended to account for the heater time constant (Gillespie et al., 1996), though this was not required in the present experiments.

The gas temperature was measured on the duct centerline at the axial location of the ribs. Conventional analysis that used the full gas temperature history was employed to determine the heat transfer coefficient at the site of a surface thermocouple applied to the perspex beneath the liquid crystal coating. It can be shown that, when the gas temperature change can be expressed as series of n summed step functions, the perspex surface temperature rise is

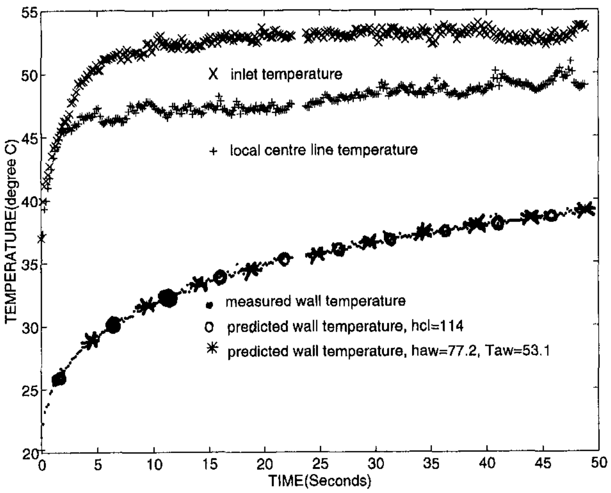

Fig. 3 Surface temperature calculated from the best fit values of h_{cl} and T_{aw} using Eq. (1)

$$T - T_o = \sum_{i=1}^{i=n} (T_i - T_{i-1}) U(t - t_i) \tag{1}$$

where

$$U(t - t_i) = 1 - \exp\left(\frac{h_{cl}^2 (t - t_i)}{\rho c k}\right) \operatorname{erfc}\left(\frac{h_{cl}\sqrt{t - t_i}}{\sqrt{\rho c k}}\right) \tag{2}$$

and T_i is the gas temperature at the ith step. An iterative procedure is used to determine the value of the heat transfer coefficient in Eq. (2) (the only unknown) that gives the best agreement to the measured perspex surface temperature. The success of the fitting approach is demonstrated in Fig. 3 where the values plotted as hollow circles are calculated using the best values of h_{cl} (114 W/m^{2}K) and T_{cl} was approximated using a series of steps. Measured inlet and local centerline gas temperatures are also included in this figure, together with a calculated surface temperature using adiabatic wall temperature and a different local heat transfer coefficient. The latter is discussed in the next section. The adiabatic wall temperature for the entire apparatus is the gas temperature at the inlet to the passage. The fast-response heater ensures that this undergoes a step change at the start of the test and the familiar analytical solution

$$\frac{(T_s - T_0)}{(T_{aw} - T_0)} = 1 - \exp\left(\frac{h_{aw}^2 t}{\rho c k}\right) \operatorname{erfc}\left(\frac{h_{aw}\sqrt{t}}{\sqrt{\rho c k}}\right) \tag{3}$$

for surface temperature, T_s, can be used in a regression procedure to determine *both* h_{aw} and adiabatic wall temperature from the measured surface temperature. The values of these two parameters that give the closest fit to the recorded wall temperature thermocouple signal are determined iteratively. The data points shown as the asterisks in Fig. 3 were calculated using this

---

[1] UK patent application 9517643.4.

[2] *Convective efficiency = actual heat transfer/ideal heat transferred.*

Nomenclature

a, b = constants in Eqs. (8) and (9)
c = specific heat capacity, J/kgK
d = passage dimension (0.05), m
f = friction factor
h = heat transfer coefficient, W/m^{2}K
l = coating thickness (equivalent to rib height), m
k = thermal conductivity, W/mK
p = pressure, N/m^2
q = heat flux, W/m^2
t = time, s
T = temperature, °C
U = response to delayed step or average velocity, m/s
x = distance in flow direction, m
β_c = coating capacity
ρ = density, kg/m^3

Subscripts

aw = adiabatic wall
c = conducting rib
cl = centerline
o = initial
r = rough wall
s = perspex surface
w = wall

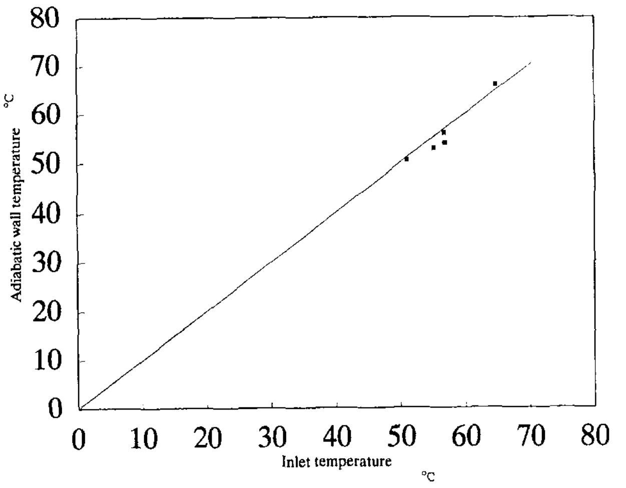

Fig. 4 Adiabatic wall temperature determined from the surface temperature variation compared to the gas temperature immediately downstream of the mesh perspex model initial temperature. The centerline temperature is then calculated from Eq. (4).

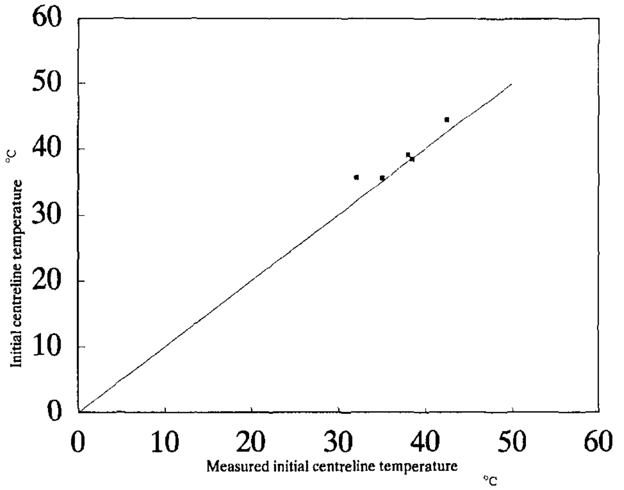

Fig. 5 Starting centerline gas temperature (at the instrumented rib location) determined from Eq. (5) compared to the measured value

approach. In all of the experiments considered here, the adiabatic wall temperature was calculated and found to be within 2°C of the gas temperature measured on the gas temperature immediately downstream of the mesh heater. The agreement between these temperatures for typical tests is demonstrated in Fig. 4.

The Use of Adiabatic Wall Temperature to Confirm Data Integrity. The local heat transfer coefficient based on the adiabatic wall temperature was also calculated and used as a check on the accuracy of the data. This heat transfer coefficient is significantly different from that based on the local centerline temperature (e.g., 77.2 and 114, respectively, in Fig. 3). As explained above, the latter was determined from the continuous record of the gas temperature using a regression procedure in which only h_{cl} was varied to produce the best fit for surface temperature calculated from the summed step change solution. Since the local heat flux at the thermocouple can be expressed in terms of either gas temperature,

$$q = h_{cl}(T_{cl} - T_w) = h_{aw}(T_{aw} - T_w) \qquad (4)$$

at a time when the wall temperature is known, the centerline temperature can be determined from the adiabatic wall temperature and heat transfer coefficient ratio. At the start of the test, the wall temperature is the perspex model initial temperature. The centerline temperature is then calculated from

$$T_{cl} = T_w\left(1 - \frac{h_{aw}}{h_{cl}}\right) + \frac{h_{aw}}{h_{cl}} T_{aw} \qquad (5)$$

The starting temperature measured at the gas thermocouple was then compared to that calculated from Eq. (5). Figure 5 is a plot of the starting gas temperature determined both ways. The agreement is further evidence that the experimental measurements of h_{cl} are accurate.

Image Processing. Conventional "hue scaling" as invented by Wang et al. (1994, 1995) was used to determine the local heat transfer values over the perspex surface between the ribs. In this method, the heat transfer coefficient divided by a reference heat transfer coefficient is calculated at each pixel. The uncertainty in measured heat transfer coefficient ratio is very small (less than 1 percent). The reference heat transfer coefficient is calculated from the full thermal transient measured using a surface thermocouple.

Rib Roughness Heat Transfer Measurement. A new approach to determining the rib heat transfer coefficients has been invented. Metallic ribs were glued to the encapsulated liquid crystal coated perspex inner surface and analysis that accounts for the rib heat capacity used to determine the effective heat transfer coefficient acting at the rib base. The high conductivity of the copper rib acts to keep the rib temperature uniform as the transient test proceeds. An assessment of the influence of variation in heat transfer coefficient along the rib length on the average h measured was made to confirm the accuracy of the approach. A numerical solution to the transient conduction equation in two dimensions was used to demonstrate that the average h, for realistic distributions of h, was achieved in the presence of conduction along the rib.

The effective heat transfer coefficient for the ribs was determined using the analysis developed at Oxford for grain roughness heat transfer measurements (Wang et al., 1991). The roughness surface temperature rise for a step change in gas temperature is related to the effective heat transfer coefficient, h, and the coating capacity, β_c, defined as

$$\beta_c = \rho_c c_c l\left(1 - \frac{hl}{2k_c}\right) \qquad (6)$$

by

$$\frac{T(0, t) - T_o}{T_g - T_o} = 1 - h\left(\frac{\exp(a^2 t)\ \mathrm{erfc}\ (a\sqrt{t})}{\beta a(a - b)} - \frac{\exp(b^2 t)\ \mathrm{erfc}\ (b\sqrt{t})}{\beta b(b - a)}\right) \qquad (7)$$

where

$$a = \frac{\sqrt{\rho c k}}{2\beta_c}\left(1 + \sqrt{1 - \frac{4\beta_c h}{\rho c k}}\right) \qquad (8)$$

and

$$b = \frac{\sqrt{\rho c k}}{2\beta_c}\left(1 - \sqrt{1 - \frac{4\beta_c h}{\rho c k}}\right) \qquad (9)$$

The contribution to the overall heat transfer of heat convected at the rib surface has been known to be important for some time and is referred to by Shen et al. (1996). It should be noted

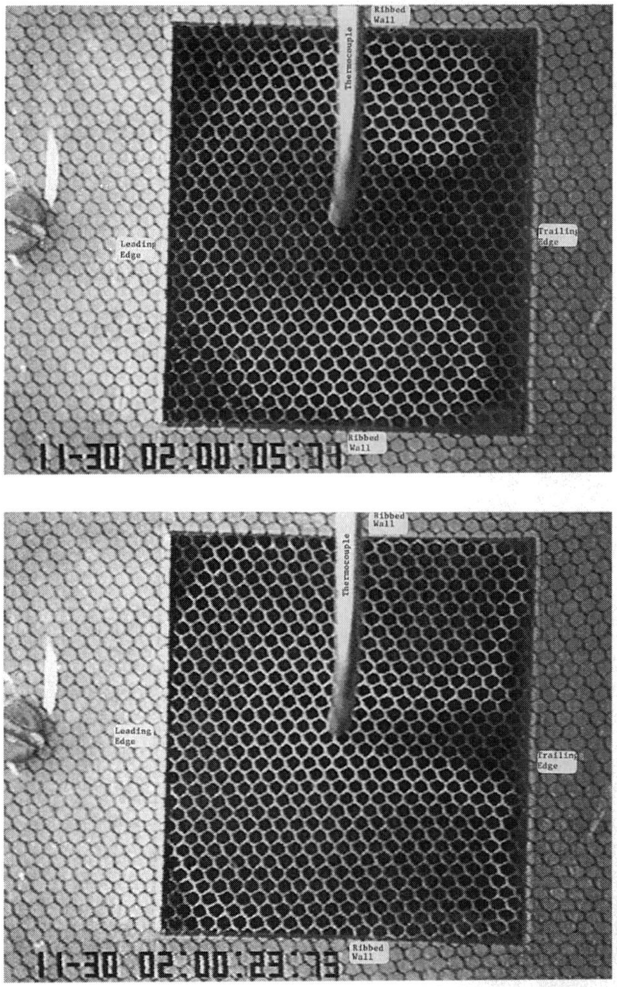

Fig. 6 The liquid crystal color play on the mesh fitted to the duct outlet at two instants during a transient experiment (sampled over the mesh fibers)

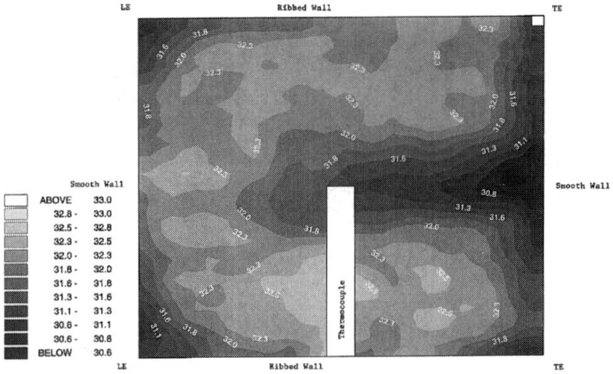

Fig. 7 Gas temperature distribution over the mesh at 46.6 seconds after switching power to the heater

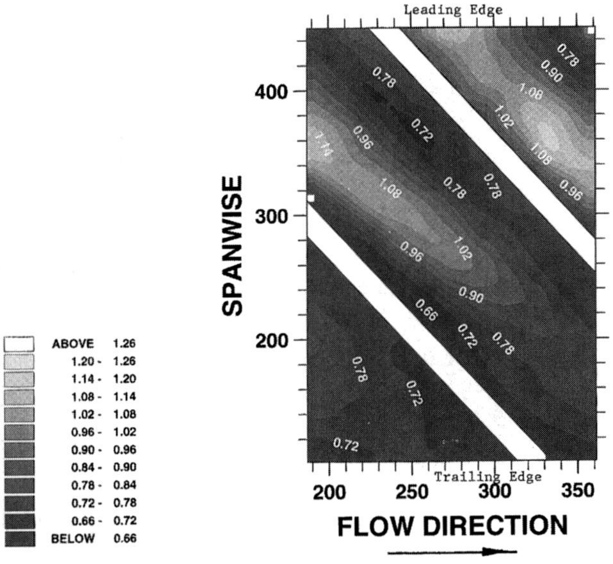

Fig. 8 Heat transfer coefficient distribution on the surface between the ribs

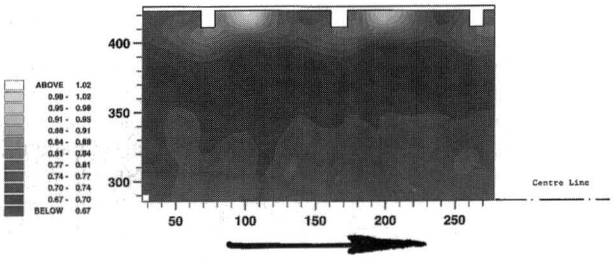

Fig. 9 Heat transfer coefficient distribution on the smooth wall adjacent to leading edge of the ribs. The arrow indicates flow direction.

that the ribs, as well as turbulating the flow, act as devices for extending the internal surface of the duct.

Outlet Gas Temperature Visualization. A nylon mesh, coated with temperature-sensitive liquid crystal, was fitted to the outlet of the duct to inspect the temperature field. The crystal color display on the mesh is shown at two times, during a transient heat transfer test, in Fig. 6. The use of these meshes is proving to be a very useful quantitative tool for investigating the temperature fields inside cooling passages; see Wang et al. (1996). The mesh used has a low porosity and produces a pressure drop of 8 percent of a dynamic head. For these experiments, it has been coated with encapsulated liquid crystals that show color in the range 25°C to 33°C. The temperature profile exhibits a narrow cooler zone (the gas is warmer than the perspex), which reaches from the smooth wall adjacent to the trailing edges of the inclined ribs, Fig. 7. In fact, the mesh shows that the centerline temperature is *less* than the temperature of the passage. The use of crystal-coated meshes to establish dimensionless temperature difference profiles is discussed in detail by Wang et al. (1996). The duct pressure loss measurements discussed below were performed without the crystal-coated mesh fitted.

Heat Transfer Measurements

The local heat transfer coefficient on the surface between the ribs is shown in Fig. 8. A predominant feature is the high heat transfer region between the ribs. Similar to 90 deg ribs, this high region is caused by the vortex structure between the ribs. It is interesting to note that in the direction parallel to the ribs the distribution is far from uniform, with a peak occurring toward the "leading edge" of the parallel ribs. Heat transfer levels are presented in this figure normalized with respect to the value at the thermocouple. The local heat transfer values on the smooth walls are shown in Figs. 9 and 10 where the considerable enhancement close to the rib tops can be seen. Other features in Figs. 8–10 are discussed later in conjunction with the result from a CFD computation. The averaged values of the smooth wall h are shown in Fig. 11 as a function of Reynolds number where comparison is also made to the level

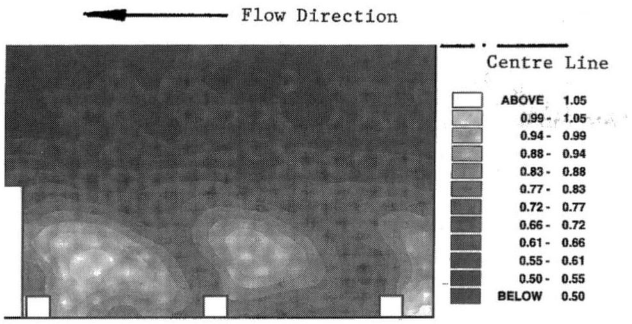

Fig. 10 Heat transfer coefficient distribution on the smooth wall adjacent to trailing edge of the ribs. The arrow indicates flow direction.

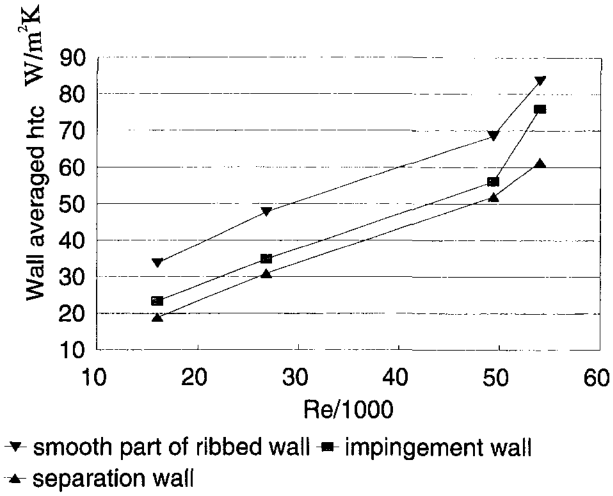

Fig. 11 Comparison of smooth surface heat transfer coefficients

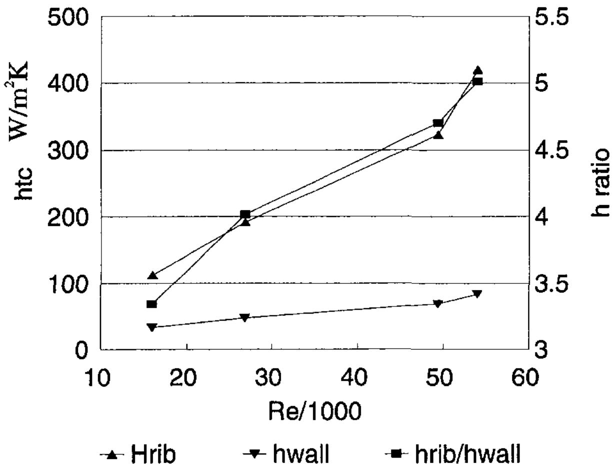

Fig. 12 Rib heat transfer coefficient compared to the value on the smooth wall between the ribs

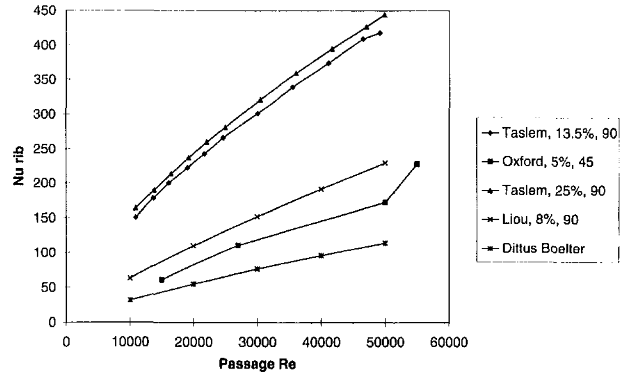

Fig. 13 Average Nusselt number over the rib surface compared to data from the literature

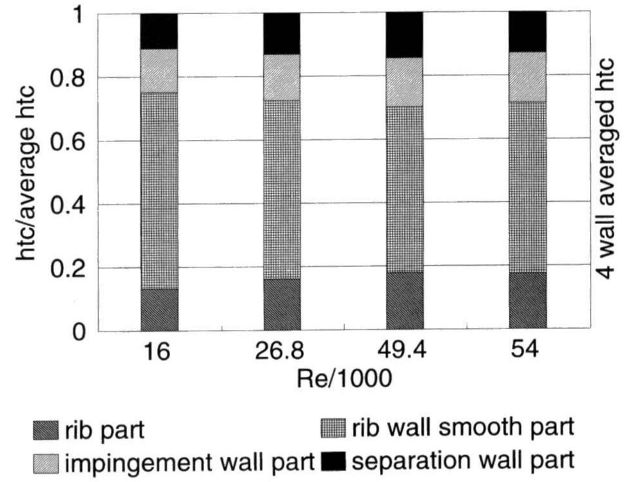

Fig. 14 Contributions of the different surfaces to the complete passage heat transfer

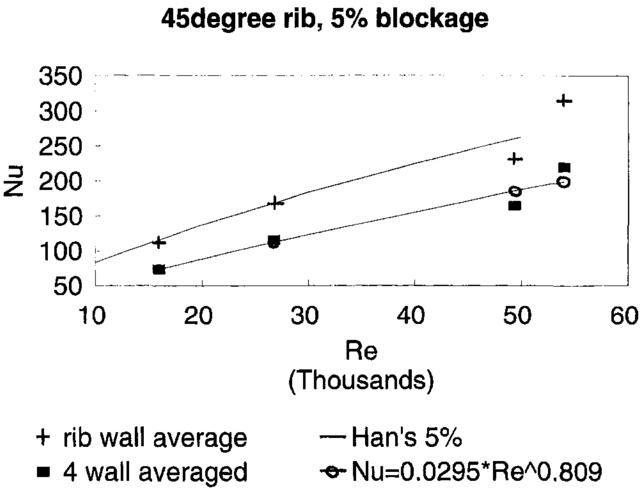

Fig. 15 Ribbed passage rough wall Nusselt number as a function of Reynolds number

between the ribs. The rib *h* values are, as expected, much higher than the smooth levels, and these are shown in Fig. 12. This figure includes the ratio of rib to smooth surface value on the ribbed wall. The average rib Nusselt number as a function of duct Reynolds number is presented in Fig. 13 where the length dimension is the passage diameter. The data from Taslim and Wadsworth, at relatively high blockage, were obtained in apparatus in which only the rib was heated. The thermal boundary conditions are thus different from the essentially isothermal wall state prevailing during the present transient tests. This difference would be expected to increase the former data compared to the transient results.

Insight can be gained into the relative contributions of the different surfaces to the overall heat transfer from Fig. 14. The appropriate surface areas have been used to determine this bar graph. The dimensionless, overall, rough-wall Nusselt number is plotted as a function of Reynolds number in Fig. 15 where

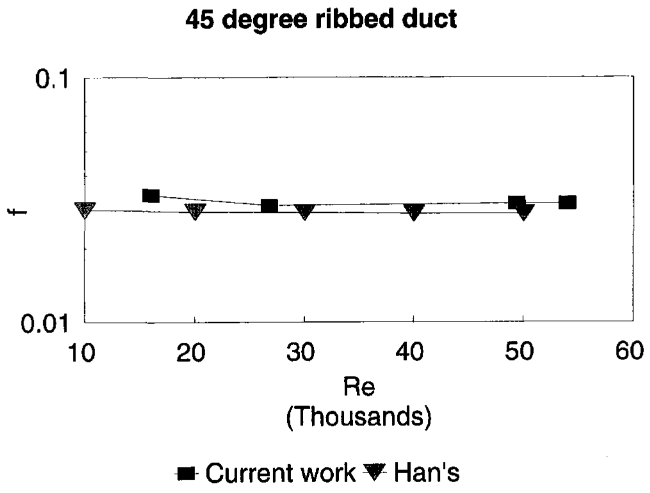

Fig. 16 Measured friction factor as a function of passage Reynolds number

comparison is made to the data from Texas A&M University. The data from Han et al. (1991) have been adjusted to yield values at the present blockage of 5 percent using the law of the wall roughness function (*R* and *G*) approach. Agreement with the present results is excellent, although it should be noted that the Texas heat transfer coefficients are based on the mixed bulk gas temperature and the present results are based on the local centerline temperature. Perhaps the similarity between the results is not surprising when account is taken of the uniformity of temperature distribution shown in Fig. 7. The analysis discussed by Wang et al. (1996) suggests that the Han data should be increased by approximately 8 percent to obtain Nusselt number values based on local centerline temperature.

Friction Factor Data

The static pressure was measured at different stations along the smooth passage wall for different Reynolds numbers. The friction factor, defined as

$$f = \frac{1}{\frac{1}{2}\rho U^2}\,\frac{d}{4}\,\frac{dp}{dx}, \qquad (10)$$

was calculated from the measurements and is plotted in Fig. 16. The results compare well with the line derived from the wall roughness functions after Han et al. (1991).

CFD Prediction

The flow field inside the passage was calculated using the simple drag coefficient model described by Chew et al. (1996). Here, the drag force due to the ribs is included in the momentum equations as a source (or body force) term averaged over the length of the ribbed section of the duct. This is assumed to act normal to the rib and is evaluated from the product of the rib area, the dynamic head of the local flow velocity, and an empirically determined coefficient. Secondary flows established by the angle forces are apparent from the vectors presented in Fig. 17. The values of friction factor derived were in good agreement with the measured data and will be reported later. The approach has been used successfully by Chew et al. (1996) to predict the variation of friction factor with rib inclination. CFD predictions of the flow temperature field are also given in Fig. 18.

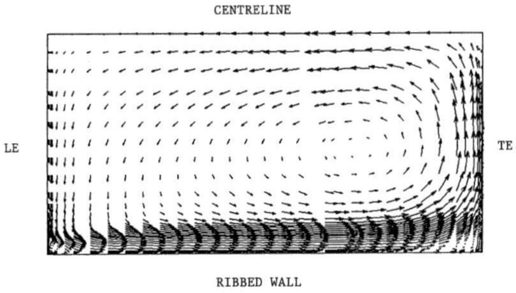

Fig. 17 Secondary flows calculated using the rib drag coefficient model reported by Chew et al. (1996)

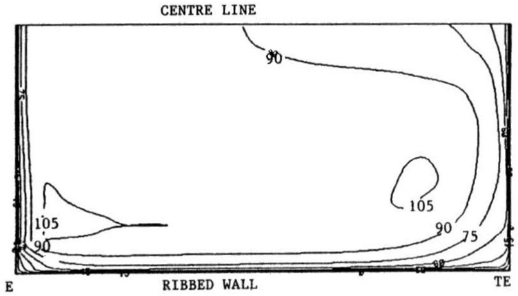

Fig. 18 Thermal field calculated using the rib drag coefficient model reported by Chew et al. (1996): $T_{avg} - T_w = 100$

Discussion of Results

The inclined ribs are expected to produce a pair of large counterrotating vortices as shown in the CFD results in Fig. 17. These vortices convey fluid from the center of the passage to the smooth wall adjacent to the leading edge of the ribs. The low cooling potential (temperature in the heat transfer experiment) at the core of the vortices is apparent from Fig. 17. It seems that the classical flow field behind parallel ribs is significantly influenced by the secondary flows as the heat transfer coefficient contours here do not run parallel to the ribs, Fig. 8. The reduction of the heat transfer level in the region close to the trailing edge is evident. This reduction may be explained, first, by the growth of the boundary layer in the secondary flow direction. The second possible reason for this reduction is the divergence and the "lift off" of the small vortex structure local to each rib. This phenomenon can be noted by comparing the size difference of the footprints of elevated heat transfer where the rib vortices interact with the smooth walls (Figs. 9 and 10). This trend can be explained by the counterrotating main vortices. On the leading edge smooth wall (Fig. 9), the secondary flow is predominantly in the direction from the centerline toward the ribbed wall. This tends to compress the rib vortex toward the ribbed wall. Also note the local high heat transfer level at the centerline, which is the consequence of the "impingement" of the twin large vortices. On the trailing edge smooth wall (Fig. 10) the secondary flow is from the ribbed wall toward the centerline. This has the effect of "lifting" and expanding the main rib vortex structure. The secondary flow is expected to change the flow conditions at which different flow phenomena occur, in particular, the condition for the onset of the classical "sealed" circulation between ribs at close spacing. Therefore the optimized rib pitch to height ratio for the inclined ribs is expected to differ from the established value of 10:1 for plain 90 deg ribs. This is clearly an important topic for future investigation.

Conclusions

1 The first local heat transfer coefficients over the complete surface of a typical inclined rib gas turbine cooling passage have been measured. The contours support a model of the flow field with two counterrotating major vortices.

2 Local values of h have been measured on the smooth surfaces. The highest heat transfer on these faces is observed close to the rib tops.
3 A new CFD prediction method has been used to calculate the flow field. The calculated secondary flows are consistent with the experimental data.
4 The transient heat transfer measuring technique has been advanced by introducing a hybrid model technique, which uses copper conducting, isothermal roughness elements in a perspex duct.
5 Sophisticated data analysis has been used to demonstrate the quality of the heat transfer data.

Acknowledgments

This work has been carried out with the support of the UK Ministry of Defence and DTI together with Rolls-Royce plc. The technical assistance of Mr. P. J. Timms was also much appreciated. The liquid crystals were supplied by Hallcrest L.C.T.[3]

References

Andrews, G. E., Asere, A. A., Hussain, C. I., Mkpadi, M. C., and Nazadi, A., 1992, "Impingement/Effusion Cooling," AGARD CP-527, Paper No. 30.

Chew, J. W., Taylor, I. J., and Bonsell, J. J., 1996, "CFD Developments for Turbine Blade Heat Transfer," presented at the 3rd International Conf. on Computers in Reciprocating Engines, I. Mech. E., London, 9–10 Jan., Paper No. C499-035.

Clifford, R. J., Jones, T. V., and Dunne, S. T., 1983, "Techniques for Obtaining Detailed Heat Transfer Coefficient Measurements Within Gas Turbine Blades and Vane Cooling Passages," ASME Paper No. 83-GT-58.

Florschuetz, L. W., Metzger, D. E., and Truman, C. R., 1981, "Jet Array Impingement With Crossflow-Correlation of Streamwise Resolved Flow and Heat Transfer Distributions," NASA CR 3373.

Gillespie, D. R. H., Wang, Z., Ireland, P. T., and Kohler, S. T., 1998," Full Surface Local Heat Transfer Coefficient Measurements in an Integrally Cast Impingement Cooling Geometry," ASME JOURNAL OF TURBOMACHINERY, Vol. 120, this issue, pp. 92–99.

Han, J. C., Zhang, Y. M., and Lee, C. P., 1991, "Augmented Heat Transfer in Square Channels With Parallel, Crossed and V-Shaped Angled Ribs," ASME *Journal of Heat Transfer,* Vol. 113, pp. 590–596.

Ireland, P. T., Wang, Z., and Jones, T. V., 1995, "Liquid Crystal Heat Transfer Measurements," VKI lecture series, *Measurement Techniques,* 1995-01.

Lau, S. C., McMillin, R. D., and Han, J. C., 1991, "Heat Transfer Characteristics of Turbulent Flow in a Square Channel With Angled Discrete Ribs," ASME JOURNAL OF TURBOMACHINERY, Vol. 113, pp. 367–374.

Liou, T. M., and Hwang, J. J., 1993, "Effects of Ridge Shapes on Turbulent Heat Transfer and Friction in a Rectangular Channel," *Int. Journal of Heat and Mass Transfer,* Vol. 36, pp. 931–940.

Lockett, J. F., and Collins, M. W., 1990, "Holographic Interferometry Applied to Rib-Roughness Heat Transfer in Turbulent Flow," *Int. Journal of Heat and Mass Transfer,* Vol. 33, No. 11, pp. 2439–2449.

Shen, J. R., Ireland, P. T., Wang, Z., Jones, T. V., and Byerley, A. R., 1996, "Heat Transfer Enhancement Within a Turbine Blade Cooling Passage Using Ribs and Combinations of Ribs With Film Cooling Holes," ASME JOURNAL OF TURBOMACHINERY, Vol. 118, pp. 428–434.

Taslim, M. E., and Wadsworth, C. M., 1997, "An Experimental Investigation of the Rib Surface-Averaged Heat Transfer Coefficient in a Rib-Roughened Square Passage," ASME JOURNAL OF TURBOMACHINERY, Vol. 119, pp. 381–389.

Van Treuren, K. V., Wang, Z., Ireland, P. T., Jones, T. V., and Kohler, S. T., 1996, "Comparison of Local and Average Heat Transfer Coefficients Under an Array of Inline and Staggered Impinging Jets," ASME Paper No. 96-GT-163.

Wang, Z., Ireland, P. T., and Kohler, S. T., 1996, "Gas Temperature Measurement in Internal Cooling Passages," ASME Paper No. 96-GT-534.

Wang, Z., Ireland, P. T., Jones, T. V., and Davenport, R., 1996, "A Color Image Processing System for Transient Liquid Crystal Heat Transfer Experiments," ASME JOURNAL OF TURBOMACHINERY, Vol. 118, pp. 421–427.

Wang, Z., Ireland, P. T., and Jones, T. V., 1995, "An Advanced Method of Processing Liquid Crystal Video Signal From Transient Heat Transfer Experiments," ASME JOURNAL OF TURBOMACHINERY, Vol. 117, pp. 184–189.

Wang, Z., Ireland, P. T., and Jones, T. V., 1991, "A Technique for Measuring Convective Heat Transfer at Rough Surfaces," *Trans. Inst. Measurement and Control,* Vol. 13, No. 3, pp. 145–154.

---

[3] Hallcrest L.C.T., Unit 9, Stepnell Reach, 541 Blandworthy Road, Hamworthy, Poole, Dorset. BH16 5BW.

Effect of Periodic Wake Passing on Film Effectiveness of Inclined Discrete Cooling Holes Around the Leading Edge of a Blunt Body

K. Funazaki

E. Koyabu

Department of Mechanical Engineering,
Iwate University,
Morioka, Japan

S. Yamawaki

Aero-Engine and Space Operation,
Ishikawajima-Harima Heavy Industries Co.,
Tokyo, Japan

Detailed studies are conducted on film effectiveness of inclined discrete cooling holes around the leading edge of a blunt body that is subjected to periodically incoming wakes as well as free-stream turbulence with various levels of intensity. The cooling holes have a configuration similar to that of a typical turbine blade and are angled at 30 and 90 deg to the surface in the spanwise and streamwise directions, respectively. A spoked-wheel-type wake generator is used in this study to simulate periodically incoming wakes to turbine blades. In addition, two types of turbulence grid are used to elevate a free-stream turbulence intensity. We adopt three blowing ratios of the secondary air to the mainstream. Most of the dominant flow conditions are reproduced in this study, except for the air density ratio of the secondary air and the main stream. For each of the blowing ratios, wall temperatures around the surface of the test model are measured by thermocouples situated inside the model. The temperature is visualized using liquid crystals to obtain traces of the injected secondary air on the test surface, which consequently helps us interpret the thermocouple data.

Introduction

To improve the performance of gas turbines, specifications for turbine inlet temperature have been increasing over the past several decades. Film cooling is an effective method for protecting blade surfaces from high-temperature combustion gas and there have been many investigations on the thermofluid characteristics of film cooling. The leading edge film cooling of turbine blades, which is our concern in this study, has been also attracting attentions from many researchers (Mick and Mayle, 1988; Mehendale and Han, 1992; Salcudean et al., 1994).

As Funazaki et al. (1995) pointed out, the heat load observed at the leading edge of turbine blades is greatly affected by free-stream turbulence as well as periodic wake passage, hence one can easily imagine that these flow disturbances have some influences on film cooling at the leading edge. Funazaki et al. (1997) accordingly studied the influence of periodic wake passing as well as free-stream turbulence on the film effectiveness of discrete cooling holes over the leading edge of a blunt body. Their test model had a realistic geometric configuration of cooling holes except for the injection angle. Their injection angle was normal to the surface. They found that the film effectiveness at lower blowing ratio greatly deteriorated due to the wake passing and the free-stream turbulence. Although their findings are useful for understanding how the film effectiveness of the leading edge cooling holes behaves under the realistic flow environment, they are not applicable to modern turbine cooling design in a straightforward manner because of the injection angle adopted in their study.

This study therefore focuses on the effect of periodic passing wakes on film effectiveness of spanwise inclined cooling holes on the leading edge under several free-stream turbulence conditions. The model used in this study has the same geometry as the previous study, consisting of a semicircular leading edge and two flat plates. The spanwise angle of each of the cooling holes is 30 deg, measured from the model surface, which is commonly used in modern turbine blades. The upstream periodic wake is produced by a spoked-wheel type wake generator. The free-stream turbulence is generated by turbulence grids. We adopt three blowing ratios of the secondary air to the mainstream. For each of the blowing ratios, adiabatic wall temperature around the test surface influenced by the wakes as well as the free-stream turbulence is measured by thermocouples.

The temperature distribution is visualized using a liquid crystal sheet in order to obtain traces of the injected secondary air on the test surface. These traces will be compared with the data of the surface thermocouples in order to clarify the relationship between the measured film effectiveness and the injected air.

Test Apparatus and Instruments

A schematic layout of the test apparatus is shown in Fig. 1. This apparatus is the same as that used in the previous study by Funazaki et al. (1997). Main flow rate is adjusted by the inlet valve of the blower. Air from the blower passes through the settling chamber to the contraction nozzle with the exit cross section of 240 mm × 350 mm. The test channel containing the test model is inserted into the transition duct, which is attached to the contraction nozzle. To remove the upstream boundary layer, the front portion of the test channel has a sharp edge and some amount of air is discharged from the clearance between the test channel and the transition duct. The transition duct has a slot through which the wake generating bars of the wake generator can pass. These wake-generating bars, 5 mm diameter and 250 mm length, are mounted on the disk rim. The rotational speed of the disk is controlled by transmission gear box connected to an induction motor. The rotational speed ranges from 900 through 1500 rpm. A turbulence grid is attached to the contraction nozzle exit, which is 300 mm upstream of the test

---

Contributed by the International Gas Turbine Institute and presented at the 41st International Gas Turbine and Aeroengine Congress and Exhibition, Birmingham, United Kingdom, June 10–13, 1996. Manuscript received at ASME Headquarters February 1996. Paper No. 96-GT-207. Associate Technical Editor: J. N. Shinn.

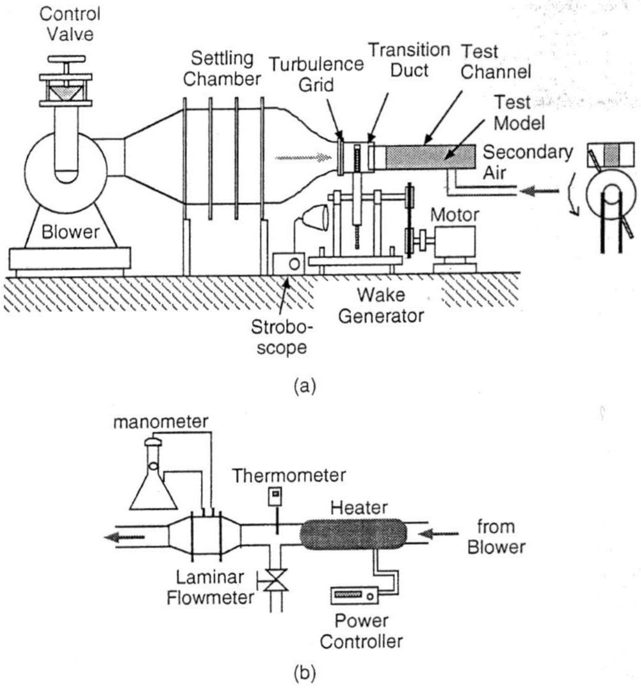

Fig. 1 Test apparatus: (*a*) wind tunnel; (*b*) secondary air supply system

Table 1 Configurations of turbulence grids and the characteristics of the turbulence generated by each grid

	Grid 1	Grid 3	No Grid
Wire Diameter (d_g)	0.8 mm	5.0 mm	-
Mesh Width (M)	5.0 mm	30.0 mm	-
Degree of Openness	0.7	0.69	-
M / d_g	6.25	6	-
Tu_b	1.50%	4.00%	0.80%
L_e	2.8 mm	7.8 mm	-

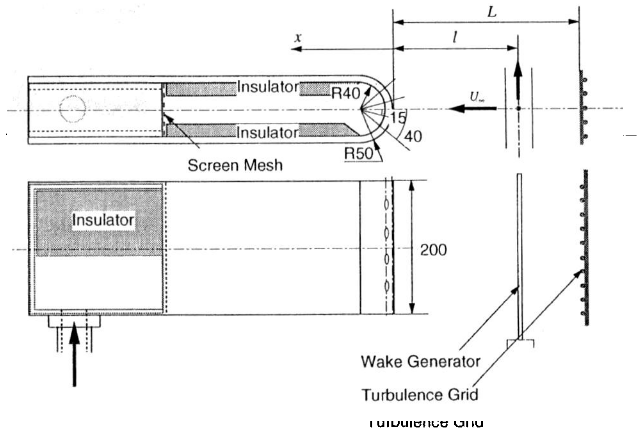

Fig. 2 Test model

model leading edge and 100 mm upstream of the wake generator. Two types of grid are used and details of the grid configurations are shown in Table 1. It is revealed that these "passive type" grids generate realistic turbulence intensity levels encountered in front of turbine rotor blades (Funazaki et al., 1997).

The secondary air supplied from the second blower to the film holes is heated before a laminar flowmeter. Accordingly, the film air temperature is higher than the free-stream temperature, which means we cannot simulate the density ratio of the secondary air to the mainstream air in an actual engine.

The cross section of the test channel is 200 mm high and 300 mm wide and its length is 1000 mm. The test model consists of a semicircular leading edge of 100 mm diameter and two flat plates, shown in Fig. 2. The test model is assembled with acrylic-resin parts of 10 mm thickness and 200 mm height. Two rows of cooling holes of $d = 10$ mm diameter and 40 mm $(4d)$ pitch are located at ±15 and ±40 deg from the model centerline. Axes of the holes are inclined spanwise by 30 deg. The ratio of the leading edge diameter and the cooling hole diameter D/d is 10. We will refer to the film holes at ±15 and ±40 deg as "the first row" and "the second row," respectively. The inner surface of the test model is covered with insulator except for the leading edge.

Figure 3 shows the location of the thermocouples and the film holes. The test model has 74 thermocouples embedded on the model surface to measure an adiabatic surface temperature distribution. The secondary air temperature is measured in the middle of the plenum chamber inside the model. A temperature on the inner surface of the model is also measured to check the adiabatic wall condition. Free-stream temperature is measured near the lower end of the leading edge stagnation line. All

Nomenclature

B = mean blowing ratio = $\rho_2 U_2 / \rho_\infty U_\infty$
B_{15}, B_{40} = local blowing ratio
D = leading edge diameter
d = cooling hole diameter
d_g = diameter of the turbulence grid wire
f = wake passing frequency = $nn_c/60$
h = heat transfer coefficient
L = axial gap between the turbulence grid and the model leading edge
l = axial gap between the wake generator and the model leading edge
L_e = streamwise dissipation length of free-stream turbulence and wake turbulence
M = grid mesh size of the turbulence grid
$\mathrm{Nu_D}$ = Nusselt number based on the leading edge diameter
n, n_c = rotating speed and the number of wake generating bars
R = radius of the leading edge
$\mathrm{Re_D}$ = Reynolds number based on the diameter of the leading edge and the inlet velocity = $U_\infty D/\upsilon$
S = Strouhal number = fD/U_∞
T, T_{aw} = temperature, adiabatic wall temperature
$Tu(t)$ = turbulence intensity
Tu_b = background turbulence intensity
U_{local} = local flow velocity around the model surface
U_∞ = inlet velocity
u' = streamwise velocity fluctuation
V_{out} = outlet velocity
v = velocity on the model surface
x = axial distance measured from the leading edge
x_{surf} = distance along the surface from the stagnation on the leading edge
η = film effectiveness = $(T_{aw} - T_\infty)/(T_2 - T_\infty)$

Subscripts

∞, 2 = mainstream, secondary air
15, 40 = first row, second row

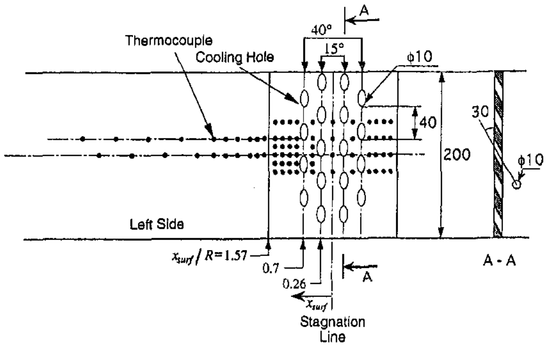

Fig. 3 Layout of the film holes and locations of thermocouples on unholded surface view

thermocouples are connected to a datalogger controlled by a personal computer. These temperature data are then averaged over 10 samples acquired within a minute to calculate time-averaged wall temperature distributions.

Pressure distributions around the test model are obtained using the test model of the same dimensions as the present one except for cooling holes, as had been employed by Funazaki (1994). Local flow velocity U_{local} is then determined from those data.

The temperature distribution is visualized using a liquid crystal sheet of 0.1 mm thickness (RW3040; Nippon Capsule Products). The sheet is pasted around the test model. The color changes in a temperature range of 30~40°C. Due to this broad range, it is difficult to get a sharp image of colored temperature distribution; however, the liquid crystal provides us a brief image about how the injected air spreads over the test model, which can be used for interpreting the temperature data of the surface thermocouples.

Experiment

In the present study, normalized parameters adopted in this study except for Mach number are comparable to those encountered in a real turbomachine. The inlet free-stream velocity was about 20 m/s and the Reynolds number Re_D based on the leading edge diameter was 120,000. The rotational speed of the wake generator was 900, 1260, and 1500 rpm. The corresponding Strouhal number S, defined as

$$S = fD/U_\infty, \quad f = nn_c/60 \tag{1}$$

was 0.24, 0.34, and 0.40.

Unsteady velocity measurements were already conducted using a hot-wire anemometer in the previous study (Funazaki et al., 1997) and those data, such as ensemble-averaged velocity or time-resolved turbulence intensity, were used to describe the unsteady flow field around the leading edge of the model.

The blowing ratio B, one of the most dominant parameters for film cooling, is defined as

$$B = \rho_2 U_2/\rho_\infty U_\infty. \tag{2}$$

All experiments were conducted at B = 0.4, 0.8, or 1.2. Although this blowing ratio is a convenient parameter for this type of experiment, local blowing ratio at each row is also an important quantity for understanding the local film cooling performance. The local blowing ratio is defined as

$$B_{15} = \frac{\rho_{2,15}U_{2,15}}{\rho_{\infty,15}U_{\infty,15}}, \quad B_{40} = \frac{\rho_{2,40}U_{2,40}}{\rho_{\infty,40}U_{\infty,40}}. \tag{2}$$

Figure 4 shows the analytical result of the relationship between the local and mean blowing ratios, indicating that these relationships differ for each row (for the detailed procedure to derive this result, refer to the appendix of Funazaki et al., 1997). The local blowing ratio B_{15} varies significantly with B, in contrast to the behavior of B_{40}.

Film effectiveness η is defined as

$$\eta = (T_{2w} - T_\infty)/(T_2 - T_\infty), \tag{4}$$

where T_{aw} is the adiabatic wall temperature, T_2 is the secondary air temperature, and T_∞ is the mainstream temperature. During the experiment, the temperature difference $T_2 - T_\infty$ was maintained about 20 K. It was actually difficult to achieve an adiabatic wall condition in this test model. Some correction had to be accordingly made on the results of Eq. (4), although a rigorous correction was almost impossible. The method used by Mick and Mayle (1988) was adopted in this study, which yielded the following modification of Eq. (4):

$$\eta = \frac{T_{aw} - T_\infty}{T_2 - T_\infty} = \frac{T_m - T_\infty - \Delta T}{T_2 - T_\infty} + \frac{q_{\text{rad}} + q_{\text{cond}}}{h(T_2 - T_\infty)}, \tag{5}$$

where T_m is the measured surface temperature, ΔT is the surface temperature correction, h is the heat transfer coefficient influenced by the injected air, q_{rad} and q_{cond} are the radiative and conduction heat flux from the surface, respectively. ΔT consists of two parts; one is the effect of back surface heating and the other is the effect of ill-positioning of the hot junctions of the thermocouples under the test surface. The magnitude of the latter effect was determined by the preliminary test. The former effect seems to depend on the temperature difference between the front and back sides of the test model ($T_2 - T_w$). In this study, on the basis of the finding by Mick and Mayle, it was assumed that the magnitude of ΔT was about 5 percent of ($T_2 - T_w$). For simplicity, we also assume that q_{rad} and q_{cond} cancel each other.

An uncertainty analysis based on the method of Kline and McClintock (1953) was carried out for the film effectiveness. The uncertainty of film effectiveness, including the effects of the above-mentioned assumptions, was about 6 percent over the leading edge region, except for the rim regions of the cooling holes and less than 12 percent for the far downstream of the holes.

Results and Discussion

Velocity Distribution. Figure 5 shows the experimental results of the velocity distribution as well as the heat transfer distribution ($\text{Nu}_D/\text{Re}_D^{0.5}$) around the leading edge of the test model, accompanied by the corresponding potential flow analysis by use of BEM (Boundary Element Method). These data show that there was a separation bubble around the junction of leading edge and flat plate. The separation began at $x_{\text{surf}}/R \cong 1$ and reattached at $x_{\text{surf}}/R \cong 2$.

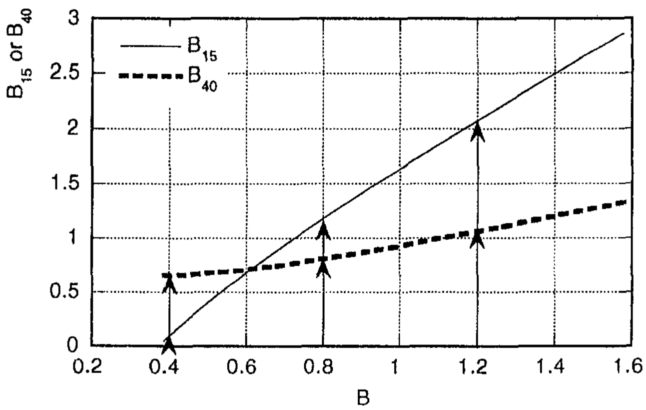

Fig. 4 Relationship of local and mean blowing ratio

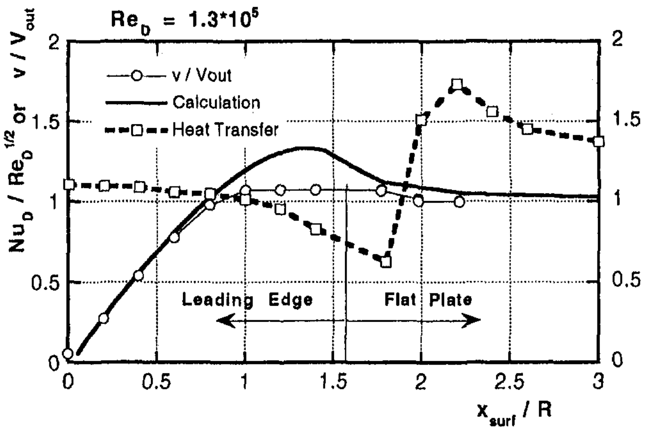

Fig. 5 Velocity and heat transfer distributions

It should be noted that these data were for the test model with no cooling holes. In fact, cooling holes or injected air have some influence on the boundary layer over the leading edge, which seems to affect the separation to some extent. To the author's best knowledge, however, little information is available on this point. Therefore the data in Fig. 5 can be used as an indicator of a separation bubble. Besides, detailed measurements on the behavior of separation bubble under several disturbances are under way to obtain some insight into this phenomenon (Koyabu, 1995).

Free-Stream Turbulence and Wake Turbulence. Characteristics of the free-stream turbulence as well as the wake turbulence obtained in this test facility were already determined by Funazaki et al. (1995), and a summary of those results is documented in the following.

Free-stream turbulence intensity Tu_b decreases along with the distance measured from the turbulence grid. It was found that this could be described by the following expression for each type of turbulence grid in this study:

$$Tu_b = 10.64((L - |x|)/M)^{-0.559}, \quad M/d_g \cong 6 \qquad (6)$$

where L is the distance between the turbulence grid and the test model. Equation (6) was modified in order to account for the blockage effect of the test model upon the turbulence intensity, which resulted in the following expression;

$$Tu_b(x) = 10.64((L - |x|)/M)^{-0.559}/(1 - (R/(x - R))^2). \qquad (7)$$

Conventionally a reference free-stream turbulence intensity is defined as the minimum value calculated from Eq. (7).

Wake turbulence was measured likewise in the free-stream turbulence case and the data were arranged in terms of peak turbulence intensity within the wake as follows:

$$Tu_{\max} = 73.58((l - |x|)/d)^{-0.67}, \qquad (8)$$

where l is the distance between the bar moving plane and test model. It is recently found that Eq. (9) yields almost the same results as the experimental data given by Halstead et al. (1997).

As for length scale of the free-stream turbulence, a streamwise turbulence dissipation scale L_e, defined as (Hancock and Bradshaw, 1983),

$$L_e = -(\overline{u'^2})^{3/2}/(U\overline{du'^2}/dx), \qquad (9)$$

can be calculated by use of Eq. (7).

In the nominal setting of the test model L is 300 mm and l is 200 mm and a reference free-stream turbulence and its dissipation length are accordingly determined as documented in Table 1.

Views of Temperature Distributions by Liquid Crystal. Figure 6 shows the front and side views of temperature distributions captured by the liquid crystal under no artificial flow disturbances for $B = 0.4$, 0.8, and 1.2, respectively. Note that white color regions appear in the side views due to the excessive lighting from above. For the lowest blowing ratio, as indicated in Fig. 4, a very small amount of the secondary air is injected from the cooling hole in the first row. Moreover, the injected air from the second row is convected almost horizontally along

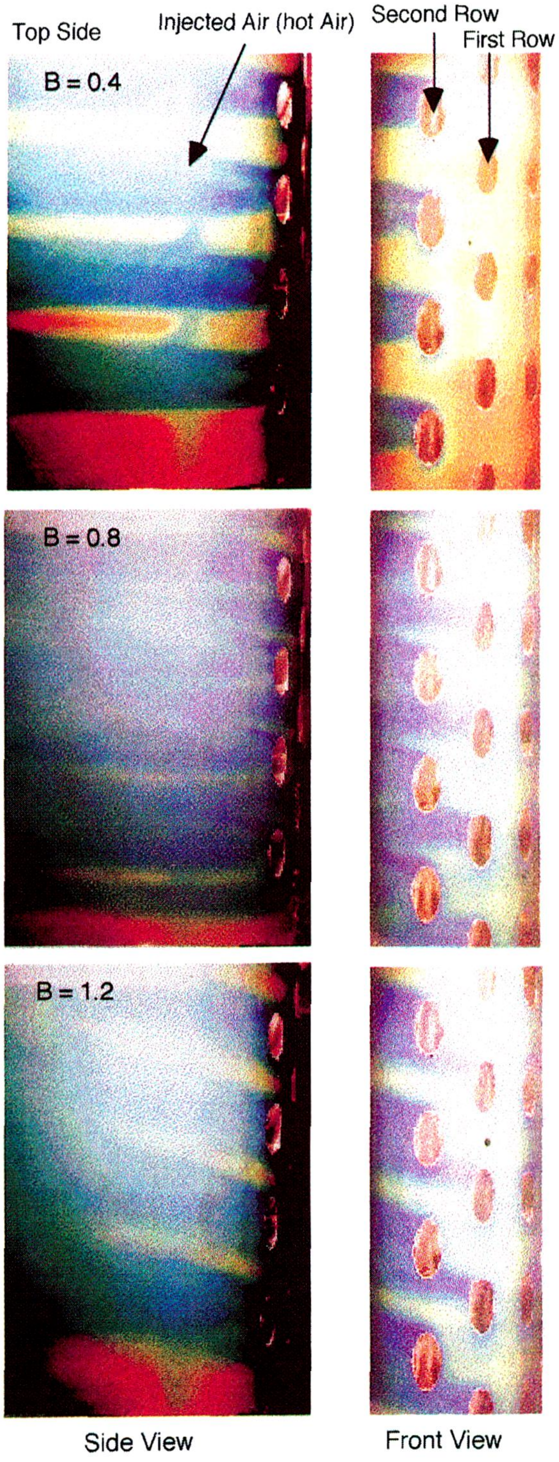

Fig. 6 Views of temperature distributions near the cooling holes obtained by the liquid crystal (No Grid/S = 0)

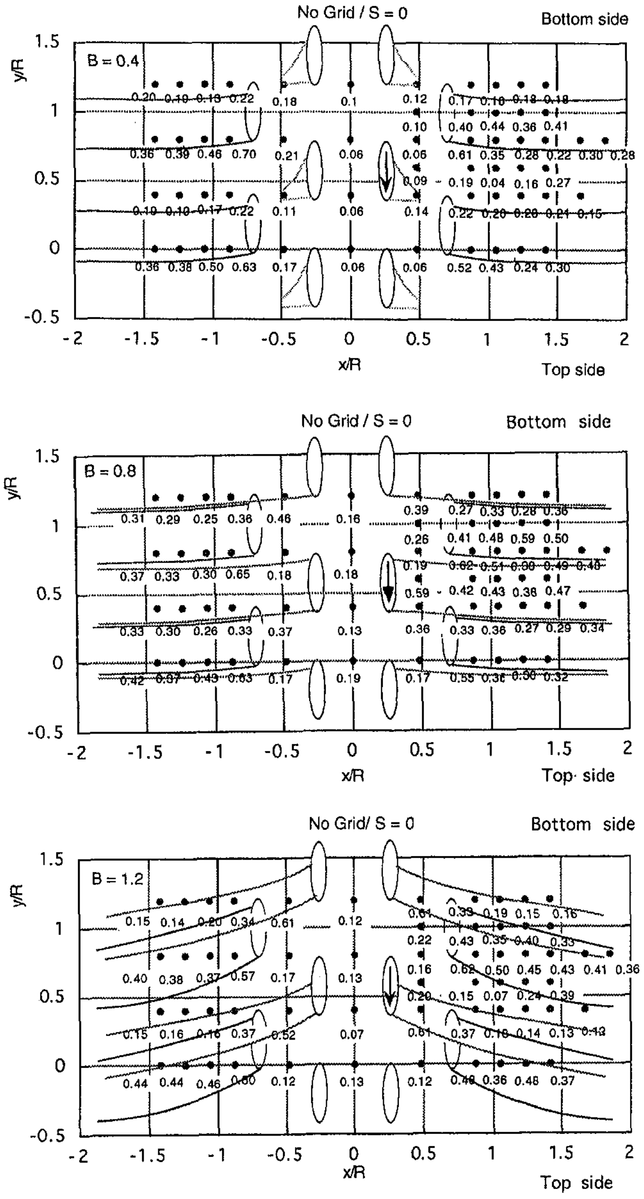

Fig. 7 Local film effectiveness distributions near the holes with sketches of the coverage of the injected air (No Grid/S = 0)

the model surface, covering a limited area on the entire model surface. For $B = 0.8$, injected air from the upper half of the cooling hole in the first row can be identified, which moves and spreads so as to cover the area between the neighboring cooling holes in the second row. Eventually the injected air, together with that from the second row, covers almost the entire surface after the second row so that the liquid crystal sheet becomes almost green. This suggests that the blowing ratio $B = 0.8$ will yield high values of spanwise averaged film effectiveness. For the highest blowing ratio $B = 1.2$, because of its high spanwise momentum flux, the injected air is gradually drifted in the spanwise direction along the model surface. One might notice that mergers happen between the injected airs from the first and the second rows, which ends up with the appearance of uncovered regions by the injected air.

Local Film Effectiveness Distribution

General Features. Figure 7 shows local film effectiveness distributions on the unfolded surface of the test model for three blowing ratios in the "no wake (S = 0)" condition with low free-stream turbulence (No Grid). Figure 7 also contains rough sketches of Fig. 6 indicating the coverage of the injected airs from the cooling holes. Note that the bottom line of the unfolded surface in Fig. 7 corresponds to the top line of Fig. 3. Therefore, y coordinate in Fig. 7 is directed toward the bottom of the test model.

Figure 7 reveals a clear relationship between the injected air and film effectiveness appearing at each measuring location. For $B = 0.4$, since only a small amount of secondary air comes from the cooling holes in the first row, the film effectiveness downstream of the first row is low. On the other hand, the film effectiveness downstream of the second row, especially at the upper side of the cooling hole, becomes considerably high, which results in large spanwise variation of the film effectiveness. For $B = 0.8$, the injected air covers almost the entire surface of the test model, so that we obtain relatively high values of film effectiveness over the surface. For $B = 1.2$, the injected air drifts toward the top side of the test model and eventually there appear regions behind the second row that are not covered by the injected air. This results in significant spanwise variation in film effectiveness downstream of the second row. Observations from the side view angle also show that the injected air tends to spread on the surface and those uncovered regions gradually disappear toward the aft portion of the test model.

Salcudean et al. (1994) have recently obtained contours of iso-film effectiveness near the cooling holes similar to those of the present study. However, dependencies of those results on the blowing ratio B slightly differ with each other, probably because of the difference in the location of the second row, e.g., ±40 deg for the present case, and ±44 deg for the case of Salcudean et al.

Effect of the Wake Passing. Figure 8 shows deviations of the film effectiveness of the cases of $S = 0.40$ measured from the cases of $S = 0.0$ (No Wake) for three blowing ratios under low free-stream turbulence. Note that the positive value stands for increase in film effectiveness from the corresponding base data (No Grid, $S = 0.0$), whereas the negative value stands for the decrease. For the blowing ratio $B = 0.4$, the wake-affected film effectiveness shows overall decrease, with some spots of slight increase. For the blowing ratio $B = 0.8$, which yields almost full coverage of the injected air over the model surface as shown above, significant decreases in film effectiveness occur behind the second row. One might notice that the effect of the wake passing does not appear in a symmetric manner with respect to the stagnation line $x_{\rm surf}/R = 0$. One possible explanation on this phenomenon is the effect of wake slip velocity (Kerrebrock and Mikolajczak, 1970), or a so-called negative jet of the wake. The other plausible explanation could be a contribution of wake-induced variation in local mass flux from each of the cooling holes to the film effectiveness. However, no information is available to verify these suppositions yet. For $B = 1.2$, meaningful and somewhat surprising increases in film effectiveness are observed after the second row. Actually Mehendale and Han (1992) reported similar findings in their study even under the influence of intense turbulence of about 10 percent. The authors think for $B = 1.2$ the wake passage effectively promotes spanwise mixing of the secondary air jets from the first and second rows that are overlapped with each other, so as to increase the area of film coverage.

Effect of Free-Stream Turbulence. Figure 9 shows deviations of the film effectiveness of the cases of Grid 3 measured from the cases of No Grid for three blowing ratios with no influence of the wake. For the blowing ratio $B = 0.4$, the film effectiveness surprisingly increases over almost the whole area of the measured test surface. Even for higher blowing ratio cases, a considerable number of spots with meaningful increase in film effectiveness appear; however, the effect of the enhanced-free-stream turbulence tends to weaken with the blow-

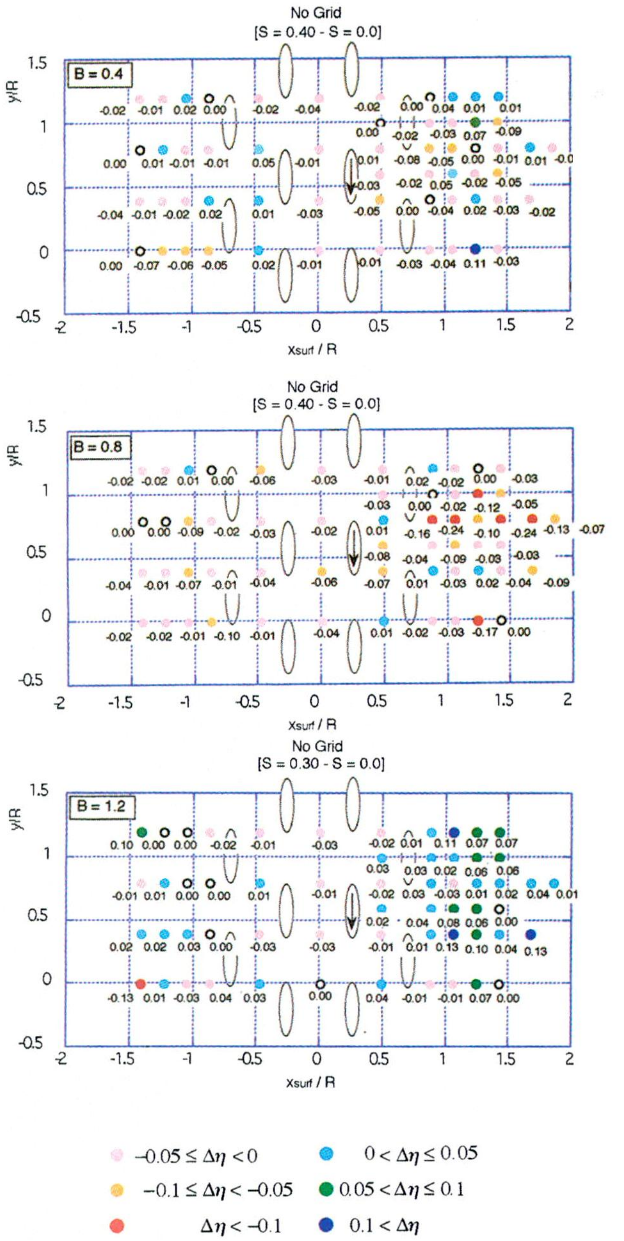

Fig. 8 Differences in film effectiveness between $S = 0.4$ and $S = 0$ with low free-stream turbulence

ing ration. Likewise in the above, this increase can be attributed to the effect of the enhanced spanwise mixing by the free-stream turbulence, similar to the findings by Mehendale and Han (1992), where the ratio of hole pitch to hole diameter was 3.

Spanwise mixing enhanced by the free-stream turbulence or by the wake passage is seemingly a plausible explanation for the local increase in film effectiveness; however, the authors feel great necessity to verify whether it is truly the case. Therefore temperature measurement of the flow field near the cooling holes is now under way.

Spanwise-Averaged Film Effectiveness

General Features. Figure 10 shows the plots of spanwise-averaged film effectiveness for three blowing ratios under the influence of the wake passing. As seen in the local film effectiveness, spanwise-averaged film effectiveness is not symmetric with respect to the stagnation line, $x_{surf}/R = 0$, especially for $B = 0.4$. In addition to the fact that sample numbers for averaging are different between both sides as shown in Fig. 3, it seems that mass flow rates from the holes at +15 and −15 deg are difference, especially in this lowest blowing ratio, which contributes to this asymmetry. Hereafter the discussion is focused on the data on the right-hand side $(x_{surf}/R \geq 0)$ of these plots.

Generally the maximum appears after the second row of film holes, followed by gradual decrease due to the dilution of the injected air. For $B = 0.8$, this decreasing rate is relatively slow compared to other cases, which results in the highest spanwise-averaged film effectiveness over the model surface among three blowing ratio cases, as can be expected from the local film effectiveness distributions. In the case of $B = 1.2$, there appears a small valley of the film effectiveness after the maximum, probably due to the spanwise variation of the local film effectiveness as identified above.

Effect of the Wake Passage. As the Strouhal number increases, the averaged film effectiveness tends to decrease for $B = 0.4$ and $B = 0.8$. However, for $B = 1.2$, the averaged film effectiveness rather exhibits a slight increase, as seen in the local film effectiveness distribution.

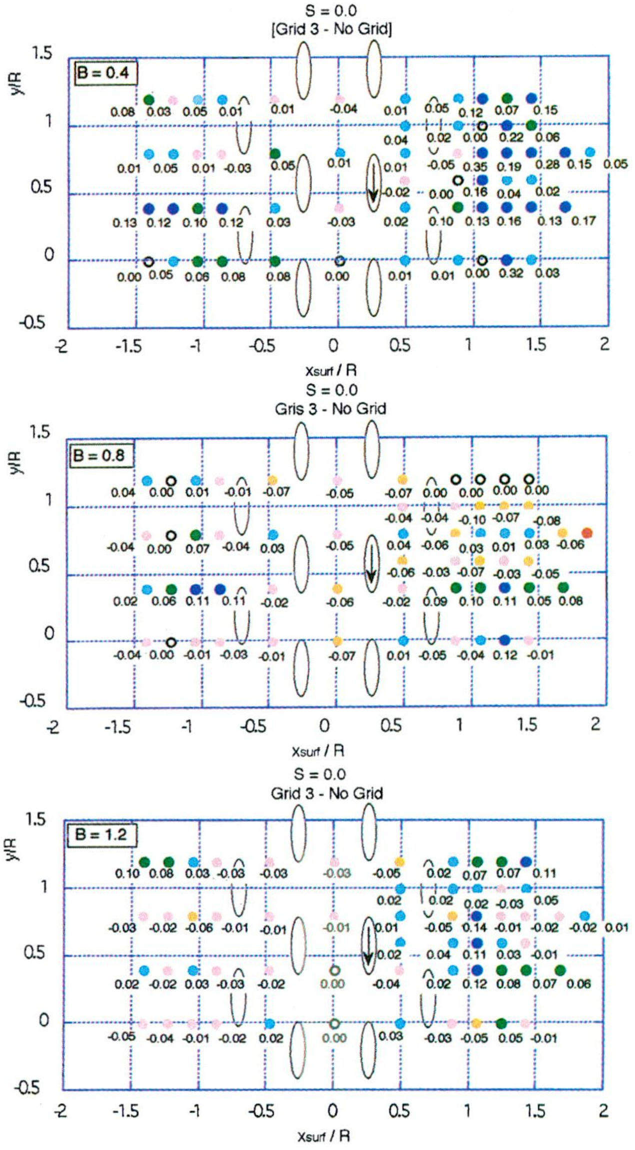

Fig. 9 Differences in film effectiveness between Grid 3 and No Grid with no wake effect

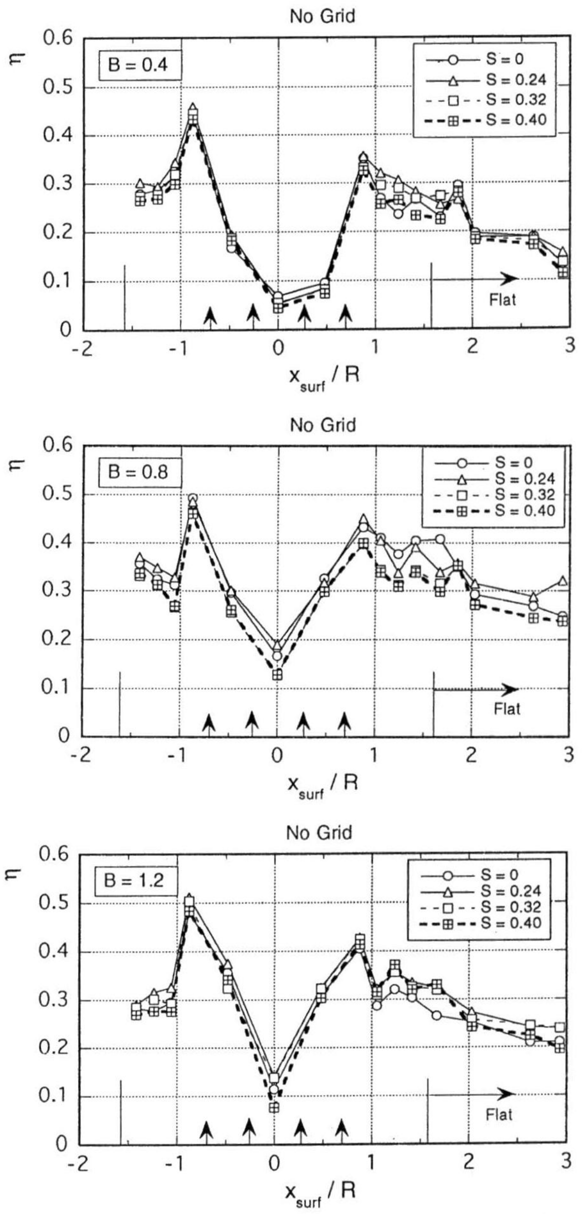

Fig. 10 Effect of wake passage upon the spanwise-averaged film effectiveness for three blowing ratios (No Grid)

Figure 11 shows spanwise-averaged film effectiveness under the influence of the wake passing as well as enhanced free-stream turbulence from Grid 3. Except for the case of $B = 0.4$ and the data obtained around the separation zone for $B = 0.8$, no discernible effect of the wake passage upon the average film effectiveness can be found. As for the case of $B = 0.4$, the reason for the notable decrease in the averaged film effectiveness with the increase of Strouhal number is not certain. However, it can be concluded that the wake passage over the test model reduces the film effectiveness in the case of low and moderate blowing ratios.

Effect of Free-Stream Turbulence. Figures 12 and 13 show the effect of free-stream turbulence on the spanwise-averaged film effectiveness for three blowing ratios without and with the influence of the periodic wakes. It follows from these data that, regardless of the influence of the wake passage, free-stream turbulence does not have any significant impact on the spanwise-averaged film effectiveness for $B = 1.2$. For the case of $B = 0.4$, augmented free-stream turbulence surprisingly increases the averaged film effectiveness over the region ranging from $x_{\mathrm{surf}}/R = 1 - 2$. Note that this region almost corresponds to the area where the separation occurs. This tendency does not change under the influence of the wake passing, although the effect of the free-stream turbulence becomes small (see Fig. 13). For a moderate blowing ratio $B = 0.8$, the enhanced free-stream turbulence appears to decrease the average film effectiveness to some extent. However, its effect almost diminishes under the influence of the wake passage.

Conclusions

Detailed studies were conducted on film effectiveness of inclined discrete film holes around the leading edge of a blunt test model of a turbine blade that was subjected to periodically incoming wakes as well as free-stream turbulence with various levels of intensity. Important findings, useful for designing film-

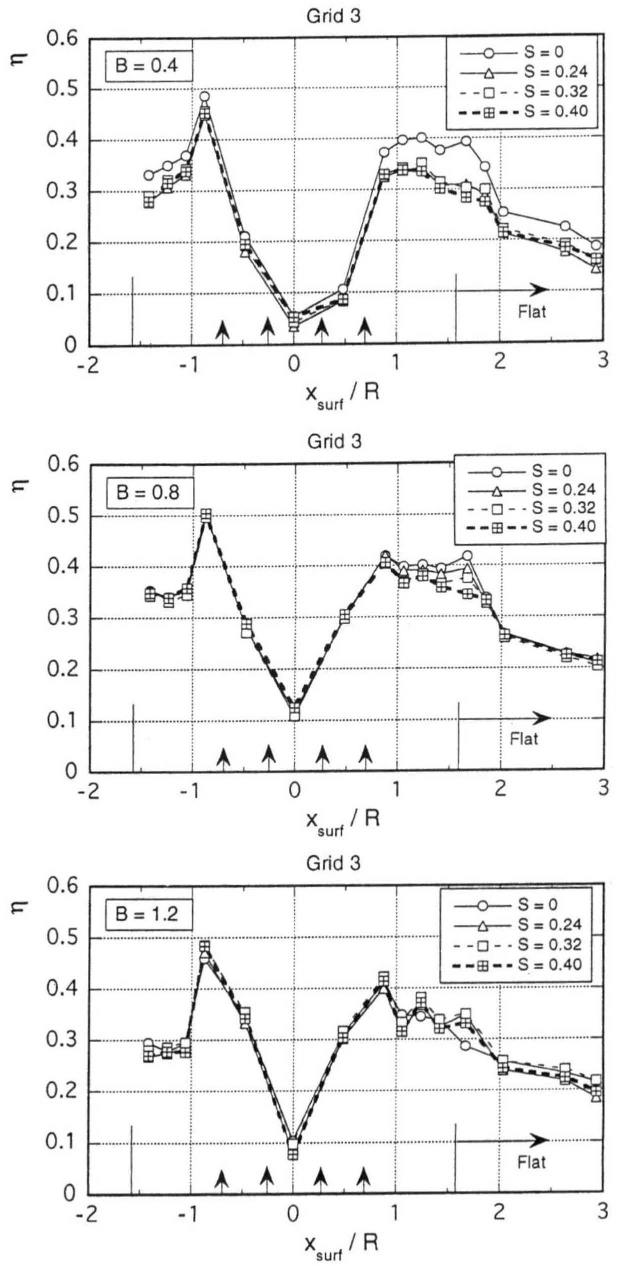

Fig. 11 Effect of wake passage upon the spanwise-averaged film effectiveness for three blowing ratios (Grid 3)

cooled turbine blades, were obtained in the studies. A summary of this paper is itemized as follows:

1 Observations by use of the liquid crystal revealed the extent of film coverage near the film holes at the leading edge. At the lowest blowing ratio $B = 0.4$, the secondary air from the film holes in the first row could not be identified and the air from the holes in the second row was convected almost horizontally. At the blowing ratio $B = 0.8$, the injected air from the holes in the first and second rows tended to cover almost the entire surface of the test model behind the second row. Further increase in blowing ratio caused spanwise drift of the injected air, which led to an appearance of uncovered region by the injected air.

2 From the local film effectiveness distributions, accompanied by the sketches of the injected air trajectories, it was found the blowing ratio $B = 0.8$ produced relatively small spanwise variation in film effectiveness compared to the other blowing ratio cases. This was because the injected secondary air achieved almost full coverage.

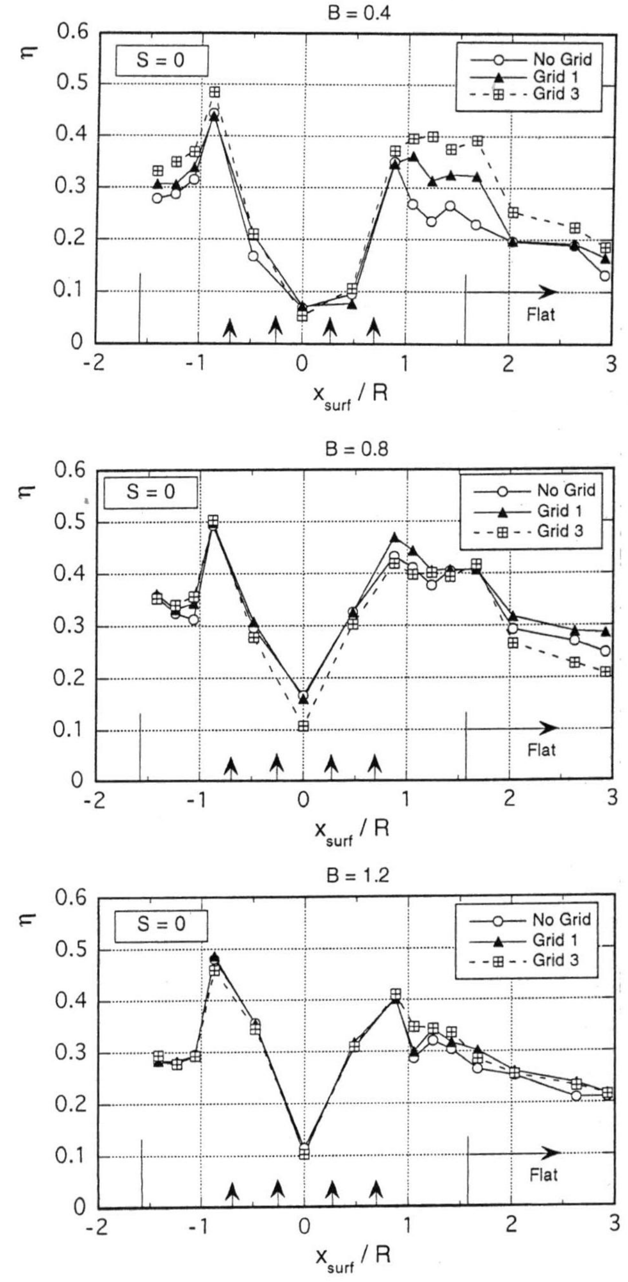

Fig. 12 Effect of enhanced free-stream turbulence on the spanwise-averaged film effectiveness for three blowing ratios (S = 0)

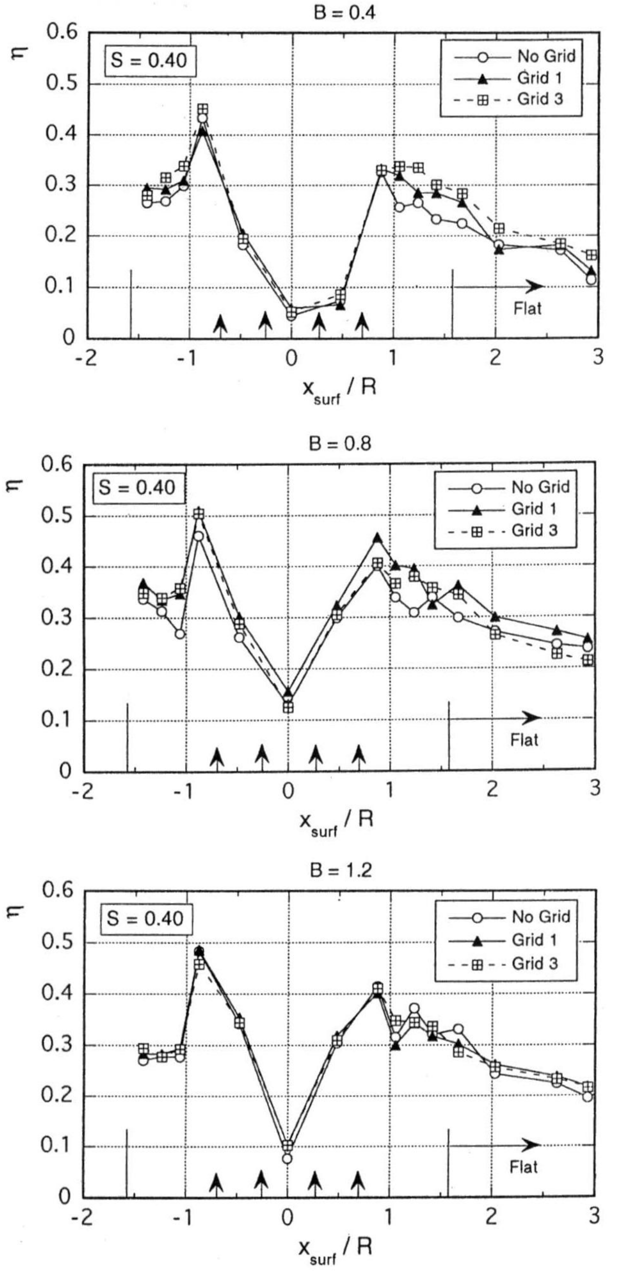

Fig. 13 Effect of enhanced free-stream turbulence on the spanwise-averaged film effectiveness for three blowing ratios (S = 0.40)

3 Generally, distributions of the spanwise-averaged film effectiveness exhibited the maximum just behind the second row, followed by gradual decrease toward the downstream. On the average, the blowing ratio $B = 0.8$ yielded relatively high film effectiveness. Periodic wake passage usually deteriorated the spanwise film effectiveness. On the other hand, enhanced free-stream turbulence did not always deteriorate the film effectiveness drastically; sometimes it caused a slight increase in the film effectiveness. The effect of the free-stream turbulence tended to diminish with the increase in Strouhal number.

Acknowledgments

The authors are greatly indebted to Mr. M. Yokota, a former graduate student at Iwate University, for his contribution to the present study.

References

Funazaki, K., 1996, ''Studies on Wake-Affected Heat Transfer Around the Circular Leading Edge of Blunt Body,'' ASME JOURNAL OF TURBOMACHINERY, Vol. 118, pp. 452–460.

Funazaki, K., Yamawaki, S., and Maya, T., 1995, ''Studies on Wake-Affected Heat Transfer Around the Leading Edge of a Blunt Body,'' *Proc. 3rd ASME/JSME Thermal Engineering Conference,* Vol. 1, pp. 343–350.

Funazaki, K., Yokota, M., and Yamawaki, S., 1997, ''The Effect of Periodic Wake Passing on Film Effectiveness of Discrete Cooling Holes Around the Leading Edge of a Blunt Body,'' ASME JOURNAL OF TURBOMACHINERY, Vol. 119, pp. 292–301.

Halstead, D. E., Wisler, D. C., Okiishi, T. H., Walker, G. J., Hodson, H. P. and Shin, H. W., 1997, ''Boundary Layer Development in Axial Compressor and Turbines: Part 4 of 4—Computations and Analysis,'' ASME JOURNAL OF TURBOMACHINERY, Vol. 119, pp. 128–139.

Hancock, P. E., and Bradshaw, P., 1983, ''The Effect of Free-Stream Turbulence on Turbulent Boundary Layers,'' ASME *Journal of Fluids Engineering,* Vol. 105, pp. 284–289.

Kerrebrock, J. L., and Mikolajczak, A. A., 1970, ''Inter-Stator Transport of Rotor Wakes and Its Effect on Compressor Performance,'' ASME *Journal of Engineering for Power,* Vol. 92, pp. 359–370.

Kline, S. J., and McClintock, F. A., 1953, ''Describing Uncertainties in Single Sample Experiments,'' *Mechanical Engineering,* Jan., pp. 3–8.

Koyabu, E., 1995, ''Studies on the Behavior of a Separation Bubble on a Blunt Body Under the Influence of the Wake Passage,'' Bachelor thesis, Iwate University, Japan.

Mehendale, A. B., and Han, J. C., 1992, ''Influence of High Mainstream Turbulence on Leading Edge Film Cooling Heat Transfer,'' ASME JOURNAL OF TURBOMACHINERY, Vol. 114, pp. 707–715.

Mick, W. J., and Mayle, R. E., 1988, ''Stagnation Film Cooling and Heat Transfer, Including Its Effect Within the Hole Pattern,'' ASME JOURNAL OF TURBOMACHINERY, Vol. 110, pp. 66–72.

Salcudean, M., Gartshore, I., Zhang, K., and McLean, I., 1994, ''An Experimental Study of Film Cooling Effectiveness Near the Leading Edge of a Turbine Blade,'' ASME JOURNAL OF TURBOMACHINERY, Vol. 116, pp. 71–79.

Rotation Effect on Jet Impingement Heat Transfer in Smooth Rectangular Channels With Four Heated Walls and Radially Outward Crossflow

J. A. Parsons[1]

J. C. Han

Turbine Heat Transfer Laboratory,
Department of Mechanical Engineering,
Texas A&M University,
College Station, TX 77843

C. P. Lee

GE Aircraft Engines,
Cincinnati, OH 45215

The effect of channel rotation on jet impingement cooling by arrays of circular jets in two channels was studied. Jet flow direction was in the direction of rotation in one channel and opposite to the rotation direction in the other channel. The jets impinged normally on two smooth target walls. Heat transfer results are presented for these two target walls, for the jet walls containing the jet producing orifices, and for side walls connecting the target and jet walls. The flow exited the channels in a single direction, radially outward, creating a crossflow on jets at larger radii. The mean test model radius-to-jet diameter ratio was 397. The jet rotation number was varied from 0.0 to 0.0028 and the isolated effects of jet Reynolds number (5000 and 10,000), and wall-to-coolant temperature difference ratio (0.0855 and 0.129) were measured. The results for nonrotating conditions show that the Nusselt numbers for the target and jet walls in both channels are about the same and are greater than those for the side walls of both channels. However, as rotation number increases, the heat transfer coefficients for all walls in both channels decrease up to 20 percent below those results that correspond to nonrotating conditions. As the wall-to-coolant temperature difference ratio increases, heat transfer coefficient decreases up to 10 percent with other parameters held constant.

Introduction

Many studies on jet impingement heat transfer have concentrated on *nonrotating* geometries for use in cooling combustor liners and turbine stator blades of gas turbine engines. For experimental investigations, the traditional steady-state, transient, and transient liquid crystal (Van Treuren et al., 1994) methods can obtain heat transfer characteristics for the target wall (the wall the jet flows are directed at and impinge on). Literature surveys on jet impingement heat transfer include, in addition to single isolated jets, studies for arrays of jets (Martin, 1977; Obot et al., 1980; Hrycak, 1981; Downs and James, 1987; Viskanta, 1993). An array of jets adds at least four parameters to describe the target wall surface heat transfer when compared with results for a single jet: streamwise, spanwise, relative (i.e., inline or staggered rows) jet spacing on the jet wall, and ratio of jet area to target wall surface area. Furthermore, turbine blade designers are challenged to cool the leading edges of the blades. Thus, Tabakoff and Clevenger (1972), Chupp et al. (1969), Metzger et al. (1969), and Bunker and Metzger (1990) have studied heat transfer on curved surfaces by a row of circular jets and an array of jets.

However, Epstein et al. (1985) investigated impingement cooling by a single row of circular jets (jet flow direction perpendicular to the direction of rotation) in the concave leading edge region of a *rotating* turbine blade with radially outward exiting crossflow. This and the associated MIT GTL reports may be the only data available in the open literature for rotating impingement heat transfer. They showed mean heat transfer decreased up to 30 percent compared with nonrotating results due to rotation induced buoyancy effects. Also, local heat transfer distribution near the blade root changed significantly due to jet deflection caused by rotation for their operating ranges. They concluded that rotation effects on heat transfer, if ignored, would cause large thermal stresses in turbine blades.

The goal of this investigation is to obtain heat transfer and flow distribution results for and thus extend the understanding of internal jet impingement cooling in channels under rotating conditions. Figure 1 shows cross-sectional sketches of the test model. Jets in one array flow in the direction of rotation and impinge on a target wall in the leading channel, while jets in the other array flow opposite to the rotation direction and impinge on another target wall in the trailing channel. The leading and trailing channel flows then exit radially outward, inducing crossflow on other jets in each array. Heat transfer results for all four walls of each channel will be presented. Actual turbine blades transfer heat by conduction from the external pressure and suction surfaces to all walls of the internal coolant channels via the web structure of the turbine blade. Thus, this information is important for turbine blade coolant passage designers. Specifically, the objective is to determine the effect of rotation (rotation-induced Coriolis, centrifugal, and buoyancy forces) on pressure distributions (to determine flow distributions) in and regional surface convective heat transfer on smooth target, jet and side walls in rectangular cross-sectioned, orthogonally rotating, twin channels with impingement cooling by square arrays of circular jets. Nonrotating data also will be taken for a baseline and to compare with previous investigations.

Test Stand and Model

Figure 2 shows a test rig schematic. Regulated compressed air (coolant), throttled by a flow control valve, flows through

---

[1] Present address: Westinghouse Electric Corp., Orlando, FL.

Contributed by the International Gas Turbine Institute and presented at the 41st International Gas Turbine and Aeroengine Congress and Exhibition, Birmingham, United Kingdom, June 10–13, 1996. Manuscript received at ASME Headquarters February 1996. Paper No. 96-GT-387. Associate Technical Editor: J. N. Shinn.

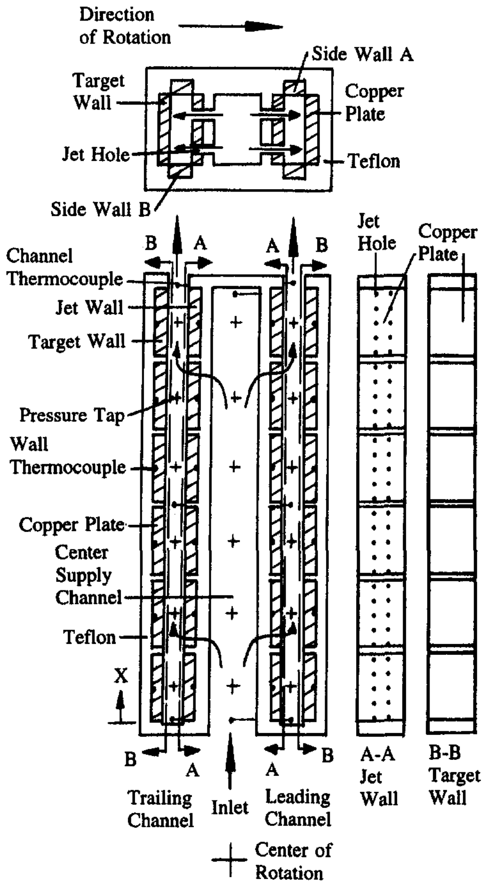

Fig. 1 Test model schematic

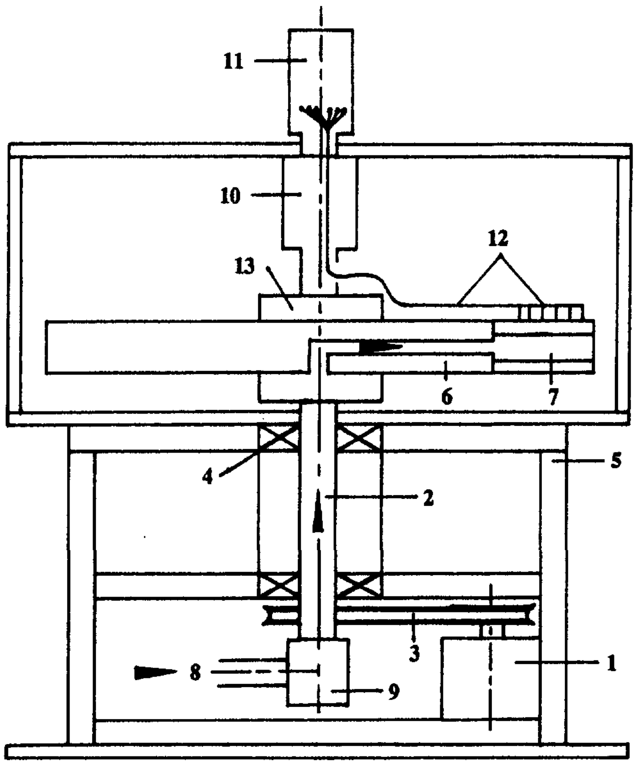

1. Motor
2. Rotating Shaft
3. Belt Drive-Pulley System
4. Bearing Support System
5. Steel Table
6. Rotating Arm
7. Test Model
8. Compressed, Regulated Air
9. Rotating Union
10. Slip Ring Unit
11. Scanivalve Unit
12. Pressure Taps & Tubing
13. Hub

Fig. 2 Test stand schematic

a sharp-edged orifice flowmeter, through tubing, and through a rotating union at the bottom of a rotating shaft. The air then passes through the hollow, rotating shaft and an aluminum, hollow rotating arm mounted perpendicularly onto the shaft. Finally, the coolant passes through the test model and exits into the lab. The test model slips into one end of the arm and the other end serves as a counterbalance. An electric motor with an adjustable frequency controller turns the shaft, arm, test model, a slip ring unit and a Scanivalve unit via a toothed belt. A digital photo tachometer measures the rotating shaft speed.

Figure 1 shows that the channel walls of the test model are parallel or perpendicular to the axes of the rotating shaft and

Nomenclature

A_w = exposed heated plate surface area
D = impingement jet orifice diameter = 1.59 mm (0.0625 in.)
F = fluid body forces due to rotation
G = mass flux based on cross-sectional area of flow
h = heat transfer coefficient
k = thermal conductivity of coolant (air)
Nu = local Nusselt number ($=hD/k$) for rotating conditions
Nu_o = nonrotating local Nusselt number at corresponding location
q_{loss} = heat transfer rate from heated wall to test model
q_{total} = total heat transfer rate to heated wall
Re_{jet} = average jet hole Reynolds number = $\rho \bar{V}_j D/\mu$
Ro = average jet rotation number = $\Omega D/\bar{V}_j$
r_m = radial distance from axis of rotation to mean radius of test model
T = local temperature
T_b = calculated bulk mean coolant temperature in the channels
T_c = measured (and interpolated) coolant temperature in the channels
T_j = inlet or jet temperature ≈ 21 to 27°C
V = local velocity
$\bar{V}$ = average velocity
V_v = local vortical velocity
X = radially outward distance from test model inlet (see Fig. 1)
$(T_w - T_j)/T_w$ = wall-to-coolant temperature difference ratio based on jet inlet temperature, R
μ = air dynamic viscosity
ρ = coolant density
Ω = rotational speed; rad/s in Ro and forces, rpm in figures

Subscripts

AW = side wall A
BW = side wall B
c = channel
COR = due to Coriolis force
CEN = due to centrifugal force
j = jet
JW = jet wall
TW = target wall
w = wall (or plate)

the arm, while a symmetry plane exists that passes through these axes. The test model consists of twin channels of rectangular cross sections (2.18 cm × 0.64 cm) flanking (in and opposite to the direction of rotation) the square cross section supply channel (1.91 cm × 1.91 cm) at a mean rotating radius-to-jet diameter ratio of 397 and has a test model length-to-jet diameter ratio of 151.0. Circular jet orifice holes of length-to-jet diameter ratio of 5.2 are through the jet walls and connect the supply channel to each twin channel. The diameter of the jet holes is 1.59 mm. The jet orifice holes create jets that impinge perpendicularly on the target walls with the distance between the jet hole exit and the target wall to the jet diameter ratio of 4.0. The jet arrays for both twin channels are square with 30 rows in the radial direction with only two jets in each row for 60 jets per channel, 120 impinging jets in total. The distance between jet centers to jet diameter ratio is 5.0. In the test model, air first enters the supply channel, and flows through the 120 orifice holes, impinging on the target wall in the trailing channel and on the target wall in the leading channel. It finally exits the test model radially outward through one of two rectangular holes.

Figure 1 also shows that the channel walls are each made of six isolated copper plates to obtain regionally averaged heat transfer measurements. For each target wall plate, the face is 3.81 cm × 1.91 cm and the thickness is 3.2 mm. Ten jets are directly opposite each plate with jet area to target wall area ratio of 0.027. The exposed face of each jet wall plate is 3.81 cm × 1.91 cm and it is also 3.2 mm thick. Each jet wall plate contains 10 holes for creating the impinging jets. The plates for A and B side walls are 3.81 cm × 6.4 mm and are 3.2 mm thick. Each wall is separately heated by wire resistance heaters uniformly cemented in grooves on the backside of the wall's six copper plates. The jet wall copper plates in each channel are backed by Teflon insulation material of 5.1 mm to reduce heat loss while all of the other plates are backed by Teflon of at least 2.5 cm. Thin 1.59-mm-wide Teflon partitions separate and insulate the copper plates. Thermocouples (T type, copper-constantan with Teflon-Neoflon PFA duplex insulation) in the plates measure wall temperatures, while thermocouples in the center of all three channels measure local coolant temperatures. The thermocouples in the channels are at the ends of wires protruding from one jet wall in the supply channel and from selected Teflon partitions of the jet walls in the heated channels (see Fig. 1). These wires remain perpendicular to the walls with coolant flow and rotation. An air passage of circular cross section (2.06 cm diameter) immediately upstream of the heated test model is made of Teflon for insulation. A slip ring unit mounts directly atop a hub that connects the shaft to the arm. This 100-channel slip ring unit transfers thermocouple outputs to a data logger interfaced to a personal computer and variable transformer outputs to the wire resistance heaters.

Flow distribution measurements are obtained from six wall static pressure taps in each of the three channels. A nineteenth tap is at the inlet to the supply channel. Tubes from the taps are routed through the center of and connected to a Scanivalve unit mounted atop the slip ring unit. The Scanivalve unit contains a multiport fluid switch, a stepper motor, a differential type pressure transducer, and an encoder. The multiport fluid switch connects only one pressure tap-port combination at a time to the transducer for pressure measurement. The motor moves the switch to different ports and the encoder indicates the selected tapport. One additional port is connected to a u-tube manometer for transducer calibration. The scanivalve motor control, input to and output from the pressure transducer, and output of the encoder are also via slip ring channels. The Scanivalve motor controller, the pressure transducer power supply and amplifier, a decoder that interprets the encoder output, the adjustable variac transformers that supply electrical power to the heaters, the data logger, and voltage and amperage meters for measurements, are all located on a table next to the test rig.

Heat Transfer Data Reduction

For heat transfer results, the regional convective heat transfer coefficient h is:

$$h = (q_{\text{total}} - q_{\text{loss}})/[A_w(T_w - T_c)] \qquad (1)$$

where q_{total} is the heat generated in a copper plate for heat transfer tests, q_{loss} is the heat loss for a plate, A_w is the heated plate exposed surface area, T_w is a plate temperature, and T_c is a temperature for the coolant adjacent to the centers of the heated plates, which is obtained by spatial interpolation between measured local air temperatures. For heat transfer tests, the rotating speed and overall coolant flow rate are set and the transformers adjusted until the desired heated wall temperatures are reached. The plate and coolant temperatures, voltages, and currents for each heater, and overall flow rate are recorded at steady-state conditions. Then q_{total} (per plate) = voltage × current/6.0. The heat loss per plate (q_{loss}) is the amount of heat conducted into the test model and test stand but not convected directly to the coolant. Tests for heat loss are performed at the same rotating speed, with no coolant flow, and with the exit end cap holes covered with tape to prevent forced convection induced by rotation. Several input power levels are used to determine the heat loss per plate as a function of their corresponding temperature differences between each plate and the surroundings (room conditions) for all of the plates.

The uncertainty of the local heat transfer depends on the net heat input ($q_{\text{total}} - q_{\text{loss}}$) to the coolant and the local wall-to-coolant temperature difference. This uncertainty increases with decreasing temperature difference and decreasing net heat input. Considering the method by Kline and McClintock (1953), the typical uncertainty in the Nusselt number is estimated to be less than 8 percent for $\text{Re}_{\text{jet}} = 10{,}000$. However, the maximum uncertainty could be up to 13 percent for $\text{Re}_{\text{jet}} = 5000$ at the largest radial location ($X/D = 138$). The heat conduction among a plate and its neighbors is estimated to be less than 2 percent of the net heat input for each plate at $\text{Re}_{\text{jet}} = 5000$. However, this percentage decreases to 0.8 percent at $\text{Re}_{\text{jet}} = 10{,}000$. For $\text{Re}_{\text{jet}} = 5000$, as rotation rate increases from 0 to 800 rpm, the average ratios of heat loss to the total plate power increase from 0.06, 0.15, and 0.29 to 0.07, 0.16, and 0.37 for the jet, target, and side walls, respectively. These ratios decrease for $\text{Re}_{\text{jet}} = 10{,}000$.

Experimental Results and Discussion

When considering test model geometry, the Nusselt number for jet impingement in rotating channels depends on: (1) the ratio of the test model's mean radius to jet diameter, (2) the ratio of local radial distance to jet diameter, (3) average jet Reynolds number, (4) Prandtl number, (5) jet rotation number, (6) wall-to-coolant temperature difference ratio, (7) jet flow direction with respect to rotation direction, and (8) channel geometry (wall, cross section and orientation). The functional relationship is expressed as:

$$\text{Nu} = f(r_m/D,\ X/D,\ \text{Re}_{\text{jet}},\ \text{Pr},\ Ro,\ (T_w - T_j)/T_w,\ \text{jet direction, channel geometry}) \qquad (2)$$

where Pr = 0.72 and $r_m/D = 397$. Operating conditions are: $\text{Re}_{\text{jet}} = 5000$, and 10,000, and $\Omega = 0$, 400, and 800 rpm, combining to produce $Ro = 0.0$, 0.0008, 0.0015, and 0.0028. For all four walls held at a uniform temperature, the wall-to-coolant temperature difference ratio is 0.129 for 0 rpm, 0.129 for 400 rpm, and 0.0855 and 0.129 for 800 rpm. Air properties are at the film temperature ($=(T_c + T_w)/2$).

Flow Distribution. Figures 3(a) and 3(b) show distributions for channel static pressures and calculated mass fluxes ($G = \rho\bar{V}$), respectively. For nonrotation and both Reynolds numbers, Fig. 3(a) shows the supply channel pressure increases

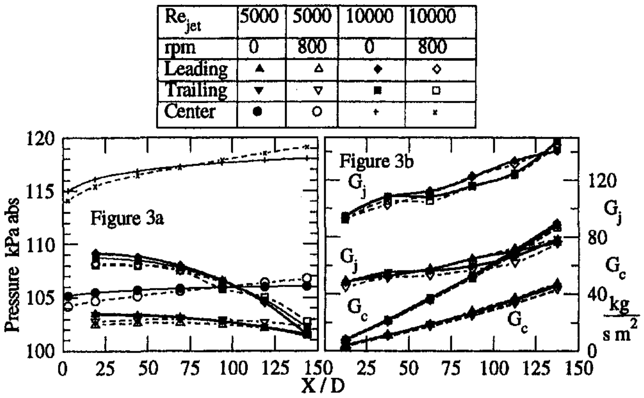

Fig. 3(*a*) and 3(*b*) Pressure and mass flux distributions at Re_{jet} = 5000 and 10,000, Ω = 0 and 800 rpm

with channel location since the air comes to a stop at the end of this channel. The leading and trailing channel pressures decrease as X/D increases. Thus the pressure differences across the jet holes and the jet mass fluxes increase with X/D. Also as the channel location increases, the channel crossflow (in the X direction) increases with channel location. As Re_{jet} increases, these flows and mass fluxes increase and are the same for the leading and trailing channels. Finally, from comparing jet parameters from film cooling studies to those for the present data, the jets bend in the flow direction but do not attach to the jet walls.

Figures 3(*a*) and 3(*b*) also show that the effect of rotation on the flow distributions is relatively small. Thus the jet and channel crossflows for rotation are nearly the same as those results for nonrotation. However, rotation creates complicated secondary flows in both the leading and trailing channels. Figure 4 shows the directions for induced Coriolis and centrifugal forces and the resulting the secondary flows. Also buoyancy forces develop that depend on local air density/temperature variations. It is these secondary flows that alter the wall heat transfer as compared to those results for nonrotating conditions. Parsons and Han (1998) fully describe the nonrotating and rotating flow distribution results for these test conditions.

Heat Transfer

Nonrotating Results. Figure 5 shows nonrotating Nusselt number versus channel location (X/D) for two Reynolds numbers at $(T_w - T_j)/T_w = 0.129$ for the target wall, jet wall, and side walls A and B of each channel. First for a jet Reynolds number, the nonrotating leading channel Nusselt numbers for all four walls are nearly the same as those for the corresponding trailing channel walls. This confirms that the test model operates symmetrically for flow and heat transfer under nonrotating conditions. Second, as Re_{jet} increases, so do nonrotating Nusselt numbers. This is because heat transfer increases as the jet and channel crossflow increase that thin boundary layers.

Figure 5 shows that as X/D increases for the target walls in the leading and trailing channels, Nu_{oTW} initially decreases and then remains constant. This is explained as follows. Local convection heat transfer at the point of impingement is high and decreases as the distance from this point increases. This is due to decreasing target surface velocity gradients as the jet fluid spreads on the target walls away from the point of impingement. However, as X/D increases, the magnitude of crossflow velocity V_c increases and bends jet flow away from the target walls toward the radially outward direction. This reduces locally high heat transfer at the point of impingement. Also, as the crossflow develops, the heat transfer initially decreases at small X/D as for developing flow at a channel entrance. Unlike channel flow, however, the heat transfer increases further downstream since the amount of crossflow increases as the result of added jet flow. This produces increasing velocity gradients at the channel walls that increase surface heat transfer. Thus, as X/D increases, regional heat transfer is initially high due to jet impingement, and decreases due to developing crossflow conditions and jet deflection. It remains nearly constant at larger X/D due to the combined effects of jet deflection, and added crossflow.

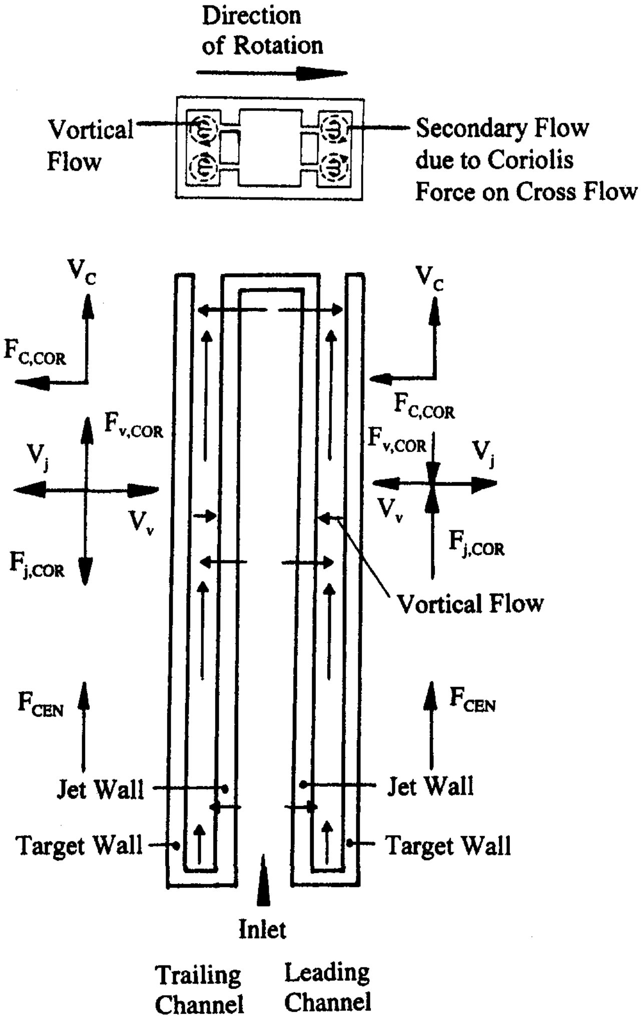

Fig. 4 Schematic including velocities and forces

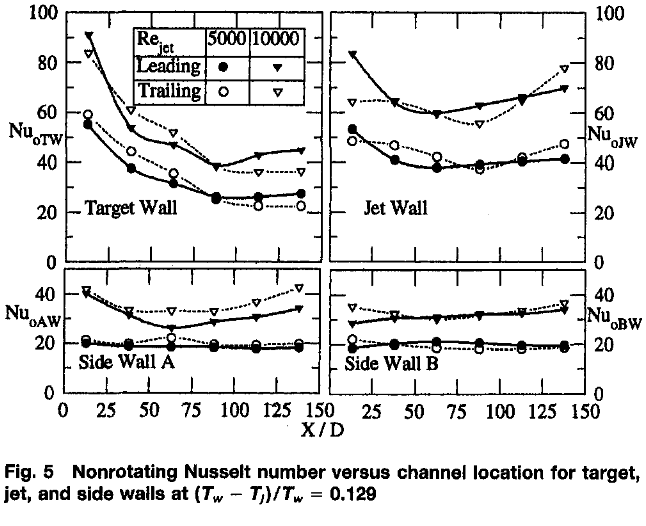

Fig. 5 Nonrotating Nusselt number versus channel location for target, jet, and side walls at $(T_w - T_j)/T_w = 0.129$

For the jet walls, as X/D increases, Nu_{oJW} initially decreases and then increases again at surprisingly enhanced levels when compared with those levels for target wall nonrotating results. This is explained as follows. First, as described above for the target wall, as X/D increases, the jet wall heat transfer initially decreases due to developing channel flow conditions, but it increases due to added crossflow. In addition, when flow from a jet impinges and spreads on the target wall surface, it turns away from the target wall because this flow opposes target wall surface flow from other surrounding jets. Likewise, the side walls also turn target wall surface flow away from the target wall. This creates vortical flows (additional secondary flows) along the target, jet, and side walls (see Fig. 4). This vortical flow, whose strength increases with jet Reynolds number and thus X/D, further disturbs the jet wall boundary layers and therefore increases jet wall heat transfer as X/D increases. Furthermore, jet flow through the orifice holes in the copper plates of the jet walls produces locally high heat transfer regions around each hole. This hole heat transfer, which is part of the total plate heat transfer, increases with jet Reynolds number and thus as X/D increases. The jet wall A_w value is for the exposed plate (flat) surface and does not include the cylindrical walls of the jet holes. In summary, as X/D increases, the jet wall heat transfer coefficient initially decreases due to developing channel flow. It increases at larger X/D due to the added channel crossflow, vortical flow, and orifice hole flow.

For the leading and trailing side walls A and B, Fig. 5 shows that as X/D increases Nu_{oAW} and Nu_{oBW} initially decrease slightly and then increase slightly or remain constant. However, the levels of these heat transfer coefficients for nonrotation are lower than those corresponding to the target and jet walls for both channels. As explained for the jet walls, as channel location increases, the side wall heat transfer coefficients vary due to interactions of developing channel flow conditions, of vortical flow and of added channel crossflow. However, these lower levels are because the boundary layers of the target, jet, and side walls all combine to create low velocity and relatively large boundary layers adjacent to these narrow side walls.

To show the integrity of the experimental method and test model, calculated bulk mean coolant temperature rises from overall energy balances are within 10 and 35 percent of the measured local air temperature rises for $Re_{jet} = 5000$ and 10,000, respectively. Figure 6 shows values of wall-averaged (the 12-plate average for corresponding walls of the leading and trailing channels) Nusselt numbers for the target wall, jet wall, side wall A, and side wall B versus Re_{jet} under nonrotating conditions. Figure 6 also shows nonrotating target wall Nusselt numbers from two types of similar investigations. The first type (Lucas et al., 1992) employs the transient liquid crystal method with isothermal channel walls, which is the same channel wall thermal boundary condition as the present data. For the second type (Chance, 1974; Kercher and Tabakoff, 1970; Parsons and Han, 1998) only the target wall is heated in the channel with the other three walls unheated. In general, for impingement heat transfer, the target wall Nusselt number is proportional to Re_{jet}^{m} where $0.5 < m < 0.85$. The present data follows the same trend with the jet wall the highest, and the target wall greater than the approximately equal side walls A and B. It is interesting to note that the target wall results for the four heated walls are greater than those for only the target wall heated.

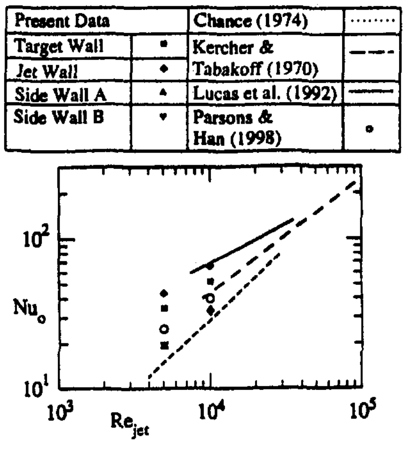

Fig. 6 Nonrotating Nusselt number versus Re_{jet} for present data and comparison with other investigations

Rotating Results. Effect of rotation relative to nonrotation. Figure 7 shows the effect of rotation on the local Nusselt number ratios Nu_{TW}/Nu_{oTW}, Nu_{JW}/Nu_{oJW}, Nu_{AW}/Nu_{oAW}, and Nu_{BW}/Nu_{oBW}. Note that the Nusselt number ratio is the local Nusselt number with rotation divided by its corresponding measured local Nusselt number for nonrotation (see Fig. 5). These results show leading and trailing channel target, jet, and side wall Nusselt number ratios are at 1.0 (the nonrotating value) or below for all channel locations. Figure 7 shows results for $Re_{jet} = 5000$ while rotation number $Ro = 0.0$ and 0.0028 ($\Omega = 0$ and 800 rpm, respectively). In addition to the flow structures discussed above for nonrotating results, new secondary flows grow as rotation rate (Ω) increases due to centrifugal forces ($\rho\Omega^2 r$), Coriolis forces ($\rho\Omega V_{local}$), and buoyancy forces ($\Delta\rho \cdot (\Omega^2 r + \Omega V_{local})$). For the leading channel, Fig. 4 shows the secondary flow due to Coriolis force on the channel crossflow. At the jet hole exit, this force deflects the jets away from the leading channel target wall. In addition, the centrifugal force adds to the Coriolis force for jets toward the leading channel target wall to further bend jet flow away from the leading channel target wall. Also, the Coriolis force for leading channel crossflow is directed away from and thus pulls air away from the leading channel target wall. But as crossflow velocity increases with channel location, these Coriolis forces and secondary flows increase. Thus these produce larger jet deflections and greater pulls on the air flow. These rotational effects combine to thicken the leading channel target wall boundary layer and decrease its heat transfer by up to 15 percent as compared to those results for nonrotating conditions. For the trailing channel, the secondary flow due to Coriolis force on the channel crossflow and the centrifugal force also combine to deflect the jets away from the trailing channel target wall. However, the trailing channel Coriolis force is directed toward the trailing channel target wall and tries to thin the boundary layer of this wall. But the net effect is to reduce locally the high heat transfer under the impinging jets on the trailing channel target wall and to decrease its Nusselt number ratio by up to 20 percent as compared with nonrotating results.

Figure 7 also shows similar results for rotation for the leading and trailing channel jet walls. This is because identical secondary flow relationships exist for jet walls as those for target walls. Whereas the trailing channel Coriolis force is toward the trailing channel target wall, the channel Coriolis force for the leading channel is toward the leading channel jet wall. And where the Coriolis force for jet flow toward the trailing channel target wall opposes channel crossflow, the Coriolis force for vortical flow toward the leading channel jet wall also opposes channel crossflow. Furthermore, the centrifugal force is radially outward for all conditions. Thus, as for the trailing channel target wall, the leading channel jet wall Nusselt number ratios are at or up to 15 percent below 1.0. Correspondingly, as for the leading channel target wall, the trailing channel jet wall Nusselt number ratios are at or up to 20 percent below 1.0. Note once again that jet wall Nusselt number ratios for the trailing channel are lower than those for the leading channel.

The greater decrease of 20 percent for the trailing channel as compared to the decrease of 15 percent for the leading channel is explained as follows. For the leading channel, the secondary

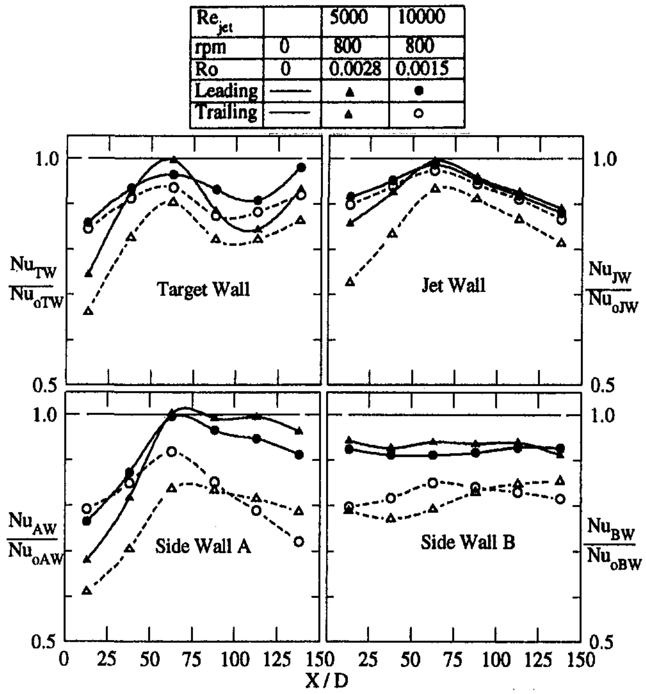

Fig. 7 Effect of rotation on Nusselt number ratio for target, jet, and side walls at $(T_w - T_j)/T_w = 0.129$

flow due to Coriolis force on the channel crossflow combines with the vortical flow from the jets in the center of the channel to carry relatively cooler center channel air toward the walls of the channel. On the other hand, for the trailing channel, the secondary flow due to Coriolis force on the channel crossflow opposes the jet vortical flow in the center of the channel. This creates a stagnant region, which reduces the circulation of cooler center channel air to the walls of the trailing channel. Thus the Nusselt number ratios for the leading channel are slightly greater than those for the trailing channel.

Figure 7 also shows the Nusselt number ratios for side walls A and B versus channel location. All Nusselt number ratios are at or up to 25 percent below 1.0. The differences between these Nusselt number ratios and 1.0 for side walls A and B increase as rotation number (or Ω) increases at constant jet Reynolds number. Furthermore, the Nusselt number ratios for side walls A and B in the trailing channel are slightly smaller than those results corresponding for the leading channel side walls A and B (which are nearly 1.0 for the full length of the walls). This is because for the leading channel, the secondary flow due to the Coriolis force on the channel crossflow opposes the vortical jet flow adjacent to the side walls in the leading channel. This creates relatively more turbulence at these sidewalls as compared to the side walls in the trailing channel. There the secondary flow due to Coriolis force on the channel crossflow is in the same direction as the vortical flow and this produces relatively lower turbulence levels. The higher turbulence levels in the side wall boundary layers of the leading channel enhance heat transfer (Nusselt number ratios) as compared to those corresponding for the trailing channel side walls.

This discussion pertains to results for $\mathrm{Re}_{\mathrm{jet}} = 5000$ and $Ro = 0.0$ and 0.0028. Figure 7 also shows the results for $\mathrm{Re}_{\mathrm{jet}} = 10{,}000$ and $Ro = 0.0$ and 0.0015 ($\Omega = 0$ and 800 rpm, respectively). The trends for $\mathrm{Re}_{\mathrm{jet}} = 10{,}000$ (at lower rotation numbers) are the same as discussed above but with reduced differences between the rotating Nusselt number ratios and 1.0 as compared with those corresponding differences for $\mathrm{Re}_{\mathrm{jet}} = 5000$ (at higher rotation numbers). Thus, the effect of rotation is reduced as the rotation number is reduced.

Effect of wall-to-coolant temperature difference ratio. Figure 8 shows the effect of the wall-to-coolant temperature difference ratio $(T_w - T_j)/T_w$ on Nusselt number ratio for $\mathrm{Re}_{\mathrm{jet}} = 5000$, $Ro = 0.0028$. In Fig. 8 the Nusselt number ratios are generally below or within 20–30 percent of 1.0 for all walls in both channels. The reasons for this are discussed above. In addition, for the target, jet, and side walls in both channels as $(T_w - T_j)/T_w$ increases from 0.0855 to 0.129, Nusselt number ratios decrease up to 10 percent while other parameters are held constant. Differences between Nusselt number ratios for $(T_w - T_j)/T_w = 0.0855$ and 0.129 in the trailing channel are larger than those differences for the leading channel. For jet impingement on target walls with a crossflow exit condition, flow structures that include spreading surface flow and vortical flow develop that have flow in many directions. Even the jet flow and channel crossflow are deflected due to rotational effects. Thus, the effects due to Coriolis forces are in many directions and not cohesive. This greatly diminishes the effect of Coriolis forces when compared with those results for throughflow in rotating serpentine channels (Wagner et al., 1991). Since the flow structures are mixed, the local temperature and therefore density variations are small. With the centrifugal and Coriolis body forces acting on small density variations in the flow, only small buoyancy forces develop.

Summary

The main conclusions are as follows:

1 Jet and channel crossflow velocities (and mass fluxes) increase as channel location increases for a square array of jets impinging normally on target walls in a rectangular channel with crossflow in one direction (radially outward) as the exit condition, At jet Reynolds numbers of 5000 and 10,000, pressure and thus flow distributions are nearly the same with rotation as those distributions without rotation.

2 At a constant jet Reynolds number and stationary conditions, as channel location increases, the leading and trailing target wall Nusselt numbers initially decrease and then remain constant while the leading and trailing jet wall Nusselt numbers initially decrease and then increase. However, the wall-averaged Nusselt numbers for the jet walls are highest and those for the target walls are higher than those for the side walls.

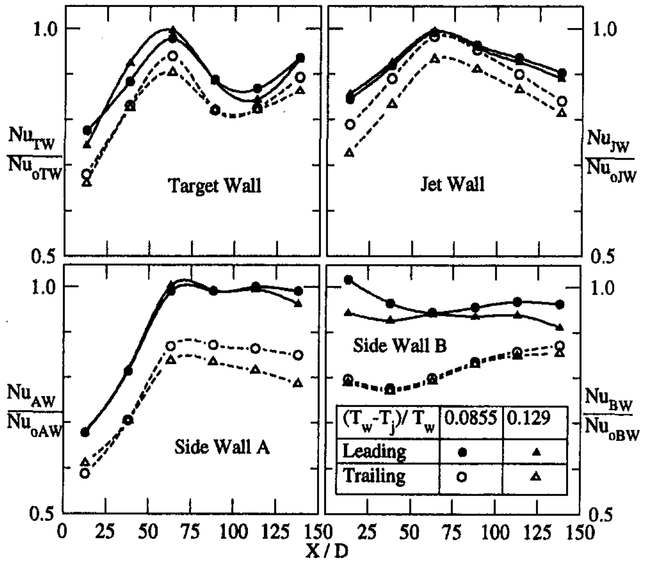

Fig. 8 Effect of wall-to-coolant temperature difference ratio on Nusselt number ratio for target, jet, and side walls at $\mathrm{Re}_{\mathrm{jet}} = 5000$, $Ro = 0.0028$, and rpm = 800

3 For nonrotating conditions, the present results agree with trends of previous researchers for impingement heat transfer by an array of jets with crossflow in one direction (radially outward) as the channel exit flow condition. As rotation number increases, the Nusselt number ratios for the leading channel target and jet walls decrease up to 15 percent and for the trailing channel target and jet walls decrease up to 20 percent below 1.0 (the nonrotating value). The Nusselt number ratios for side walls A and B of both channels decrease up to 25 percent below 1.0 as Ro increases.

4 As the wall-to-coolant temperature difference ratio increases, Nusselt number ratios decrease up to 10 percent for all walls in both channels with other parameters held constant.

Acknowledgments

This investigation was supported by GE Aircraft Engines.

References

Bunker, R. S., and Metzger, D. E., 1990, "Local Heat Transfer in Internally Cooled Turbine Airfoil Leading Edge Regions: Part I—Impingement Cooling Without Film Coolant Extraction," ASME JOURNAL OF TURBOMACHINERY, Vol. 112, pp. 451–458.

Chance, J. L., 1974, "Experimental Investigation of Air Impingement Heat Transfer Under an Array of Round Jets," *TAPPI*, Vol. 57, No. 6, pp. 108–112.

Chupp, R. E., Helms, H. E., McFadden, P. W., and Brown, T. R., 1969, "Evaluation of Internal Heat Transfer Coefficients for Impingement Cooled Turbine Blades," *AIAA Journal of Aircraft*, Vol. 6, pp. 203–208, also AIAA Paper No. 68-564.

Downs, S. J., and James, E. H., 1987, "Jet Impingement Heat Transfer—A Literature Survey," ASME Paper No. 87-HT-35.

Epstein, A. H., Kerrebrock, J. L., Koo, J. J., and Preiser, U. Z., 1985, "Rotational Effects on Impingement Cooling," *Proc. Symposium on Transport Phenomena in Rotating Machinery*, Apr. 28–May 3, Honolulu, HI.

Hrycak, P., 1981, "Heat Transfer From Impinging Jets, A Literature Review," AFWAL-TR-81-3054.

Kercher, D. M., and Tabakoff, W., 1970, "Heat Transfer by a Square Array of Round Air Jets Impinging Perpendicular to a Flat Surface Including the Effect of Spent Air," ASME *Journal of Engineering for Power*, Vol. 92, pp. 73–82.

Kline, S. J., and McClintock, F. A., 1953, "Describing Uncertainties in Single-Sample Experiments," *Mechanical Engineering*, Vol. 75, Jan., pp. 3–8.

Lucas, M. L., Ireland, P. T., Wang, Z., and Jones, T. V., 1992, "Fundamental Studies of Impingement Cooling Thermal Boundary Conditions," AGARD 80th PEP Symposium, Paper No. 14.

Martin, H., 1977, "Heat and Mass Transfer Between Impinging Gas Jets and Solid Surfaces," *Advances in Heat Transfer*, Harnett, J. P., and Irvine Jr., T. F., eds., Academic Press, NY, Vol. 13, pp. 1–60.

Metzger, D. E., Yamashita, T., and Jenkins, C. W., 1969, "Impingement Cooling of Concave Surfaces With Lines of Circular Air Jets," ASME *Journal of Engineering for Power*, Vol. 91, No. 3, pp. 149–158.

Obot, N. T., Mujumdar, A. S., and Douglas, W. J. M., 1980, "Design Correlations for Heat and Mass Transfer Under Various Turbulent Impinging Jet Configurations," *Drying '80*, Hemisphere, Vol. 1, pp. 388–402.

Parsons, J. A., and Han, J. C., 1998, "Rotation Effect on Jet Impingement Heat Transfer in Smooth Rectangular Channels With Heated Target Walls and Radially Outward Cross Flow," accepted for publication in the *International Journal of Heat and Mass Transfer.*

Tabakoff, W., and Clevenger, W., 1972, "Gas Turbine Blade Heat Transfer Augmentation by Impingement of Air Jets Having Various Configuration," ASME *Journal of Engineering for Power*, Vol. 94, pp. 51–60.

Van Treuren, K. W., Wang, Z., Ireland, P. T., and Jones, T. V., 1994, "Detailed Measurements of Local Heat Transfer Coefficient and Adiabatic Wall Temperature Beneath an Array of Impinging Jets," ASME JOURNAL OF TURBOMACHINERY, Vol. 116, pp. 369–374.

Viskanta, R., 1993, "Heat Transfer to Impinging Isothermal Gas and Flame Jets," *Experimental Thermal and Fluid Science*, Vol. 6, pp. 111–134.

Wagner, J. H., Johnson, B. V., and Kopper, F. C., 1991, "Heat Transfer in Rotating Serpentine Passages With Smooth Walls," ASME JOURNAL OF TURBOMACHINERY, Vol. 113, pp. 321–330.

Fluctuating Thermal Field in the Near-Hole Region for Film Cooling Flows

A. Kohli

D. G. Bogard

Mechanical Engineering Department,
University of Texas at Austin,
Austin, TX 78712

The film cooling flow field is the result of a highly complex interaction between the film cooling jets and the mainstream. Understanding this interaction is important in order to explain the physical mechanisms involved in the rapid decrease of effectiveness, which occurs close to the hole exit. Not surprisingly, it is this region that is not modeled satisfactorily with current film cooling models. This study uses a high-frequency-response temperature sensor, which provides new information about the film cooling flow in terms of actual turbulence levels and probability density functions of the thermal field. Mean and rms temperature results are presented for 35 deg round holes at a momentum flux ratio of $I = 0.16$, at a density ratio of $DR = 1.05$. Probability density functions of the temperature indicate penetration of the mainstream into the coolant core, and ejection of coolant into the mainstream. Extreme excursions in the fluctuating temperature measurements suggest existence of strong intermittent flow structures responsible for dilution and dispersion of the coolant jets.

Introduction

Film cooling of turbine blades has been studied for more than 20 years. Many of these studies have evaluated the performance of film cooling in terms of adiabatic effectiveness, i.e., mean surface temperature with an adiabatic wall. While these results provide information regarding the net effect of film cooling in lowering the thermal driving potential and thereby lowering heat transfer to the wall, they do not provide information about the interactions between the coolant jet and the mainstream. A few studies have measured the mean thermal field and turbulent velocity field in film cooling flows, and these studies do provide some information about the jet–mainstream interaction, but lack details on the mechanisms causing the dilution and dispersion of the coolant jet. Understanding this complex interaction is critical for improving the predictive capabilities of existing film cooling models, especially close to the hole. A primary goal of this study was to find the mechanisms causing rapid reduction in effectiveness of film cooling jets close to the hole exit.

A well-documented characteristic of film cooling using discrete holes is the rapid decrease in film cooling adiabatic effectiveness (η) immediately downstream of the hole. For example, Sinha et al. (1991) showed that even for blowing rates that gave the maximum effectiveness along the centerline near the hole, the centerline effectiveness reduces to $\eta \approx 0.8$ by $x/D = 1$, and further reduces to $\eta \approx 0.5$ by $x/D = 6$. (note that $\eta = 1$ would correspond to a wall temperature equal to the jet exit temperature). This dramatic loss in adiabatic effectiveness near the holes suggests that the coolant jet is being rapidly diluted or dispersed near the hole. A more direct measure of the dilution of the film cooling jet was provided by Thole et al. (1992) who measured the mean temperature field for a typical film cooling geometry using a wide range of operating conditions. The trajectory of the coolant jet, and the dilution of the jet with downstream distance were clearly evident in this study. But the physical mechanisms causing the jet dilution are not evident from mean temperature measurements such as these.

The present study focuses on temperature measurements in a film cooling flow field using a high-frequency-response temperature sensor. The fluctuating temperature measurements are statistically quantified in terms of rms levels and probability density functions (pdf's). While the rms temperature data are particularly useful in showing where the major interaction between the coolant jet and the mainstream occurs, the pdf's provide details indicating penetration of mainstream fluid within the jet core and ejection of coolant fluid into the mainstream. Such information is vital to understanding the complex interaction between the jet and mainstream flow, and how the effectiveness reduces rapidly near the injection location.

Experimental Facilities and Techniques

The film cooling geometry used in this study was a row of round holes inclined in the streamwise direction at an angle of 35 deg. All experiments were carried out in a closed-loop wind tunnel with a free-stream turbulence level of 0.6 percent, and a test section that was 0.15 m high, 0.6 m wide, and 1.8 m long. Detailed descriptions of this wind tunnel are presented by Thole (1992) and Thole et al. (1994). A secondary flow loop used for film cooling simulations similar to that described by Pietrzyk et al. (1990) was added to this facility (a detailed description of the facility modification is given by Schmidt, 1995). For this study, the mainstream velocity was maintained at $U_\infty = 10.0$ m/s. An approach turbulent boundary layer was obtained by tripping the flow using a 0.8 mm trip wire, $9D$ from the leading edge. At the leading edge of the holes, the boundary layer was relatively thin with a displacement thickness of $\delta^*/D = 0.1$ and a Reynolds number of $\mathrm{Re}_\theta = 420$. These values are representative of typical turbine airfoil conditions. Note that for boundary layer displacement thicknesses of $\delta^*/D < 0.15$, the boundary layer has negligible effect on film cooling effectiveness. The shape factor for the approach boundary layer was $H = 1.66$, consistent with a fully turbulent boundary layer flow.

For this study, the jet was cooled to obtain a density ratio of $DR = 1.05$. Although this density ratio is not representative of that in the actual turbine environment, Thole et al. (1992) showed that, for film cooling flows, similar thermal fields occur for a wide range of density ratios ($1.2 \leq DR \leq 2$) when the jet-to-mainstream momentum flux ratio (I) is matched. This

---

Contributed by the International Gas Turbine Institute and presented at the 41st International Gas Turbine and Aeroengine Congress and Exhibition, Birmingham, United Kingdom, June 10–13, 1996. Manuscript received at ASME Headquarters February 1996. Paper No. 96-GT-209. Associate Technical Editor: J. N. Shinn.

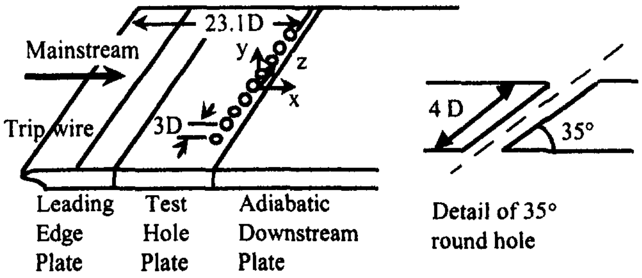

Fig. 1 Schematic of test section geometry

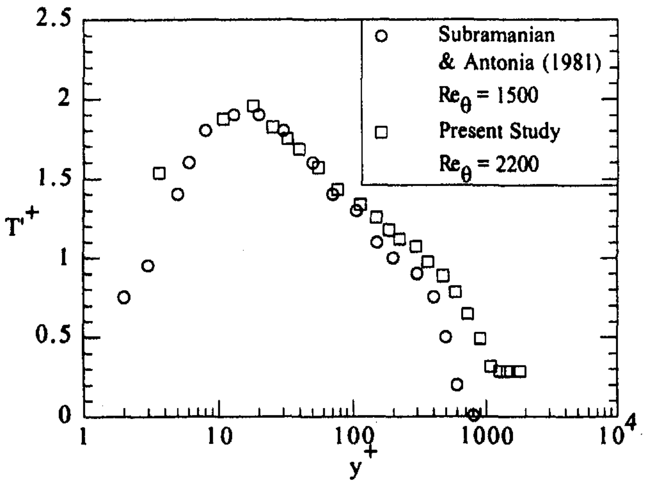

Fig. 2 Comparison of rms temperature profiles with literature

was further confirmed in the present study by comparing the mean thermal field at $DR = 1.05$ with previous measurements at $DR = 1.6$ (discussed in the results section). All measurements were made using a momentum flux ratio of $I = 0.16$ for the film cooling jets, with corresponding mass flux ratio of $M = 0.40$ and velocity ratio of $VR = 0.38$. This momentum flux ratio is in the range that provides maximum centerline adiabatic effectiveness (Sinha et al., 1991).

The test section (see Fig. 1) consisted of three separate sections: an elliptical leading edge plate, followed by a film cooling hole plate, downstream of which was an adiabatic plate. For this study a single row of nine round holes inclined at 35 deg was used. The holes had a diameter of $D = 11.1$ mm ($\mathrm{Re_D} = 7050$), were spaced $P/D = 3$ apart and had a length, $L/D = 4$, representative of actual gas turbines. The hole inlets and exits were sharp edged, and the interiors were aerodynamically smooth. To minimize conduction losses, the film cooling hole plate was made out of extruded polystyrene foam, which had a thickness of 2.54 cm. The adiabatic plate comprised a 1.27-cm-thick polystyrene foam glued to a 1.27 cm fiberglass composite (EXTREN) sheet for structural rigidity. A 15 cm layer of Corning fiberglass insulation was installed below the adiabatic plate to reduce backside conduction losses. Sinha et al. (1991) used a three-dimensional conduction heat transfer code to determine that the conduction errors were minimal for this configuration.

Note that an adiabatic plate was used in these experiments so that the thermal field measurements would be indicative of the interaction of the coolant jet with the mainstream without a confounding effect of conduction to the wall. Of course, in actual turbine airfoil film cooling, conduction to the wall will result in an additional thermal boundary layer; however, close to the hole ($x/D < 10$), this thermal boundary layer is estimated to be small relative to the coolant jet thickness.

An integral part of this study was the use of a high-frequency-response cold-wire. The Wollaston wire used for these sensors was bent into a U-shape and only the flat part of the U-shape was etched to give a sensing length of $l = 0.6$ mm. With a diameter of $d = 1.5$ μm, the sensor had a length-to-diameter ratio of $l/d = 400$. Note that this value is twice as large as that recommended by Ligrani and Bradshaw (1987) for hot-wire measurements in order to have negligible end effects. The frequency response of this sensor, obtained by an electronic test outlined by Thole and Bogard (1994), was 2.6 kHz. One of the problems associated with cold-wire measurements is that of velocity sensitivity caused by heat generation within the wire. A current of 0.25 mA was used in this study and tests were done to confirm that the sensor had negligible sensitivity to velocity.

Validation of the cold-wire measurements of fluctuating temperatures could not be done by direct comparison with previous measurements in a film cooling flow since no such measurements exist in the literature. There have been a small number of studies in which fluctuating temperatures were measured for turbulent wall flows. Therefore, our cold-wire measurements were validated by making fluctuating temperature measurements in a flat plate thermal boundary layer on a constant heat flux surface, and comparing to results available in literature. For these measurements, the flow was tripped to obtain turbulent thermal and momentum boundary layers which were of equal thickness to ensure "equilibrium" boundary layer conditions. These data were compared to the experimental measurements of Subramanian and Antonia (1981) who used a similar submicron diameter cold-wire and took care to ensure equilibrium thermal and momentum boundary layers. Figure 2 shows that our mea-

Nomenclature

D = diameter of film cooling hole
d = diameter of cold wire
DR = density ratio of jet to mainstream $= \rho_j/\rho_\infty$
H = shape factor = δ^*/θ
I = momentum flux ratio = $\rho_j U_j^2/\rho_\infty U_\infty^2$
l = length of cold wire
L = hole length
M = mass flux (blowing) ratio = $\rho_j U_j/\rho_\infty U_\infty$
P = hole spacing
pdf = probability density function
rms = root mean square
$\mathrm{Re_D}$ = Reynolds number based on hole diameter = $U_\infty D/\nu$
Re_θ = Reynolds number = $U_\infty \theta/\nu$
St = Stanton number
T = temperature
T'^+ = normalized rms temperature = $\mathrm{St}\,(T_w - T_\infty)(U_\infty/u_\tau)$
U_∞ = mainstream velocity
u_τ = friction velocity
x = streamwise distance from downstream edge of holes
y = wall normal distance
y^+ = normalized boundary layer distance = yu_τ/ν
z = spanwise distance from the centerline of holes
δ = boundary layer thickness
δ^* = displacement thickness
θ = momentum thickness
ρ = density
Θ = normalized temperature = $(T - T_\infty)/(T_j - T_\infty)$
Θ' =normalized rms temperature = $T'/(T_j - T_\infty)$

Subscripts

j = jet
w = wall
∞ = mainstream

Superscripts

$'$ = root mean square
$-$ = mean

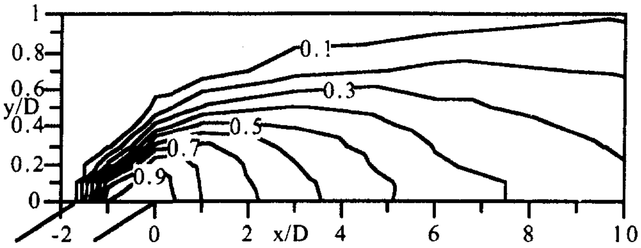

Fig. 3(*a*) **Mean temperature contours (Θ) on jet centerline; *M* = 0.4, *DR* = 1.05, *I* = 0.156**

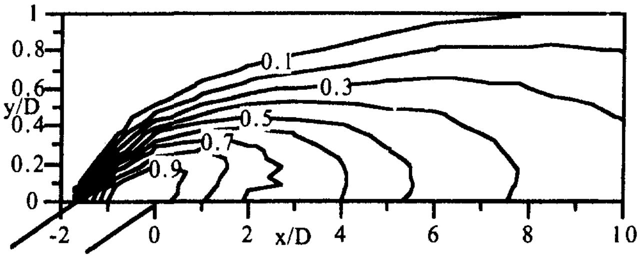

Fig. 3(*b*) Mean temperature contours (Θ) on jet centerline from Schmidt et al.; *M* = 0.5, *DR* = 1.6, *I* = 0.16

surements of the rms temperature profile compared well with experimental measurements of Subramanian and Antonia, supporting the accuracy of our cold-wire fluctuating temperature measurements.

Thermal field measurements were made on the jet centerline at $x/D = -1.75, -1, -0.5, 0, 1, 3, 6,$ and 10. Vertical measurement locations were typically, $y/D = 0.1, 0.2, 0.3, 0.4, 0.5, 0.7,$ 1, 1.5, 2, 2.5, and 3. In addition to the profiles on the jet centerline, measurements were made typically at $z/D = 0.2, 0.4, 0.7,$ 1, and 1.5 at $x/D = -0.5, 0, 1$ and 3. The wall temperatures for the mean temperature results presented in this study were extrapolated from measurements close to the wall. Typically the extrapolated wall temperatures were less than 0.3°C ($\Theta = 0.02$) different from the temperatures measured at $y/D = 0.1$. At each measurement location 81,920 data points were acquired over a duration of 16.4 s, which gave a mean temperature within ±0.1°C. For the experiments done in this study, the mainstream and jet temperatures were maintained within ±0.1°C of their nominal values. The mass flux ratio for the injection flow loop was held constant within $\delta M = \pm 1.8$ percent. The uncertainty in the thermal field results at a nominal value of $\Theta = 0.5$ due to variation in the mainstream and jet temperatures, and the uncertainty in the temperature measurement was $\delta\Theta = \pm 1.6$ percent.

Results and Discussion

As stated earlier, the motivation behind this study was not to do surface effectiveness measurements or study the performance of the 35 deg round holes over a range of momentum flux ratio. It was to understand how the effectiveness of a film cooling jet reduced so rapidly close to the hole exit, for a momentum flux ratio that was known to give optimum performance.

Figures 3(*a*) and 3(*b*) show the normalized mean temperature contours, Θ, for the 35 deg round hole with $I = 0.16$ from this study using $DR = 1.05$ and that by Schmidt et al. (1995) using $DR = 1.6$. There is very good agreement between the two, in terms of the streamwise and wall normal position of the contour levels. The $\Theta = 0.7$ and 0.8 contours for the $DR = 1.6$ case suggest slight separation of the jet, which is not seen in the results from this study. Except for this slight difference, which could be attributed to the vastly different density ratios used in the two studies, the general behavior of the jet is similar. Note that the jet loses 50 percent of its effectiveness by $x/D = 5$, clearly seen by looking at the contour level of $\Theta = 0.5$. The temperature contours over the hole indicate that the maximum mean thermal gradients occur at the leading edge of the jet, and the core of the coolant jet is pushed toward the trailing edge of the hole.

Temperature contours of the film cooling jet in lateral planes at $x/D = -0.5, 0, 1,$ and 3 are shown in Fig. 4. Over the hole and at the downstream edge of the hole, $x/D = -0.5$ and 0, the interface between the jet and the mainstream is not sharp but instead rather broad. This broad interface may be attributed to the highly turbulent mixing expected to occur at this interface. Note that in the lateral direction, the mean temperature contours extend well beyond the edge of the hole at $z/D = 0.5$. However, the core of the coolant jet (which can best be identified with the Θ pdf distributions, which are discussed later) is actually still within $z/D = 0.5$. The mean temperature contours farther downstream, at $x/D = 1$ and 3, indicate that the coolant jet is well attached to the surface. From $x/D = 0$ to 3 the mean thermal gradients around the jet decrease substantially, and the cross section of the jet becomes more rounded in shape by expanding in the vertical direction but maintaining a relatively constant width.

The rms temperature results on the jet centerline shown in Fig. 5 give information about the highly turbulent nature of the film cooling flow field. Levels as high as $\Theta' = 0.25$ exist in the flow, which indicated strong fluctuations in the temperature field. For comparison, the highest rms levels in a boundary layer flow are of the order of $\Theta' = 0.1$. Maximum rms temperature levels will tend to be generated at the interface between the jet and the mainstream where the mean temperature gradient and turbulence levels are greatest (Pietrzyk et al., 1990, showed high turbulence levels are generated at the edge of the film cooling jet). The outer boundary of the cooling jet is probably best identified by the locus line for the maximum Θ' as shown in Fig. 5. The rms temperature levels decrease downstream, consistent with decreases in mean temperature gradients and decay of turbulence levels. Figure 6 shows the lateral rms contours at $x/D = -0.5, 0, 1,$ and 3. At every streamwise position, the highest rms levels are consistently at the top interaction region between the jet and the mainstream, with distinctly lower maximum rms levels on the sides. The maximum Θ' level at the top of the jet increases in height with flow downstream, but the lateral position of maximum Θ' to the sides of the jet remains relatively constant. These results again suggest that the coolant jet is expanding in the vertical direction, but is maintaining a constant width.

The results from the rms temperature statistics established that there are very large fluctuations in the thermal field, but determining the mechanisms responsible for these large rms levels requires examination of the probability density function (pdf) for the fluctuating temperature data. The pdf of Θ at a point was obtained from

$$\mathrm{pdf}(\Theta_i) = N_i/(N\Delta\Theta) \quad i = 1, 2, \ldots \tag{1}$$

where, N_i = number of occurrences of a Θ value in the interval $\Theta_i + \Delta\Theta$, and N = total number of Θ data points. The pdf gives more insight into the nature of the turbulent transport process by indicating the fraction of time that fluid of a certain temperature is passing through a point in the flow.

The jet dispersion and dilution process at the exit of the hole is evident from the series of pdf distributions taken across the jet at $z/D = 0$ and $x/D = 0$ as shown in Fig. 7. The highest position shown is essentially the mainstream with $\bar{\Theta} = 0.01$. Here the sharp peak in the pdf distribution indicates a very narrow range for Θ, which is merely an indication of the uniform temperature of the mainstream. At heights from $y/D = 0.7$ down to $y/D = 0.4$, $\bar{\Theta}$ increases from 0.02 to 0.33. This region may be regarded as the outer edge of the coolant jet. In this region there is consistently a sharp "spike" in the pdf at

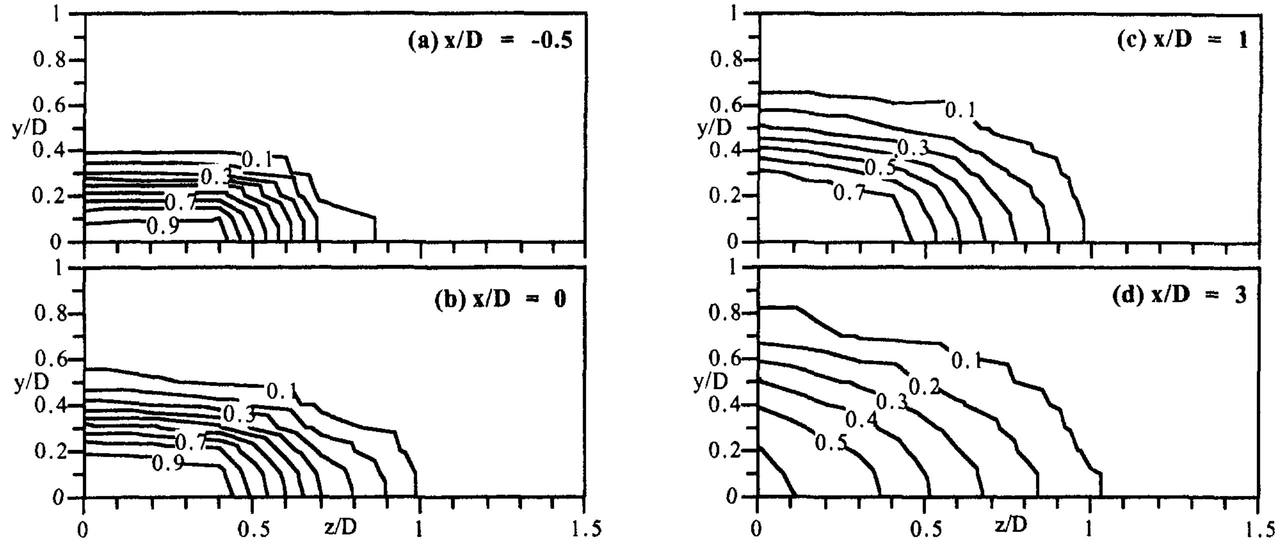

Fig. 4 Lateral mean temperature (Q) contours at various streamwise positions: (*a*) $x/D = -0.5$, (*b*) $x/D = 0$, (*c*) $x/D = 1$, and (*d*) $x/D = 3$; $M = 0.4$, $DR = 1.05$, $I = 0.156$

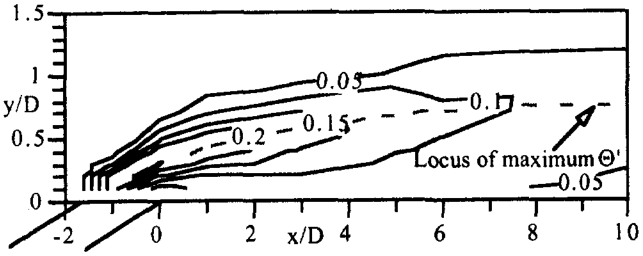

Fig. 5 The rms temperature contours (Θ') on jet centerline; $M = 0.4$, $DR = 1.05$, $I = 0.156$

low Θ with a "tail" in the pdf extending toward higher Θ values. The spikes in the pdf distributions indicate that most of the time the fluid temperature in this outer region is nominally mainstream temperature; whereas the tails indicate that there are short periods when much colder fluid passes through this region. Physically this may be interpreted as a region that is generally occupied by mainstream flow, but intermittently small elements of coolant are ejected into the region by turbulent motions.

Near the wall at $y/D = 0.1$ the pdf again has a narrow spike centered about $\Theta = 0.95$, indicating that the coolant jet is essentially undisturbed at this position. Moving away from the wall, the pdf spike reduces in magnitude and there is a tail extending to lower values of Θ. The shape of the pdf at $y/D = 0.3$ is shown in more detail in Fig. 8(*a*). As an aid in interpreting this pdf distribution, a sample time trace of the fluid temperature is shown in Fig. 8(*b*). The large spike in the pdf distribution centered at $\Theta \approx 0.9$ is associated with relatively long periods of time when the fluid temperature holds steady at $\Theta \approx 0.9$, evident in Fig. 8(*b*). The pdf has a long tail, and the magnitude of the pdf slightly increases from $\Theta = 0.6$ to 0.2, then sharply drops off at $\Theta = 0.15$. This characteristic is associated with the negative spikes in the Θ time trace, which more often than not extend to $\Theta \approx 0.2$. Since the peaks of these

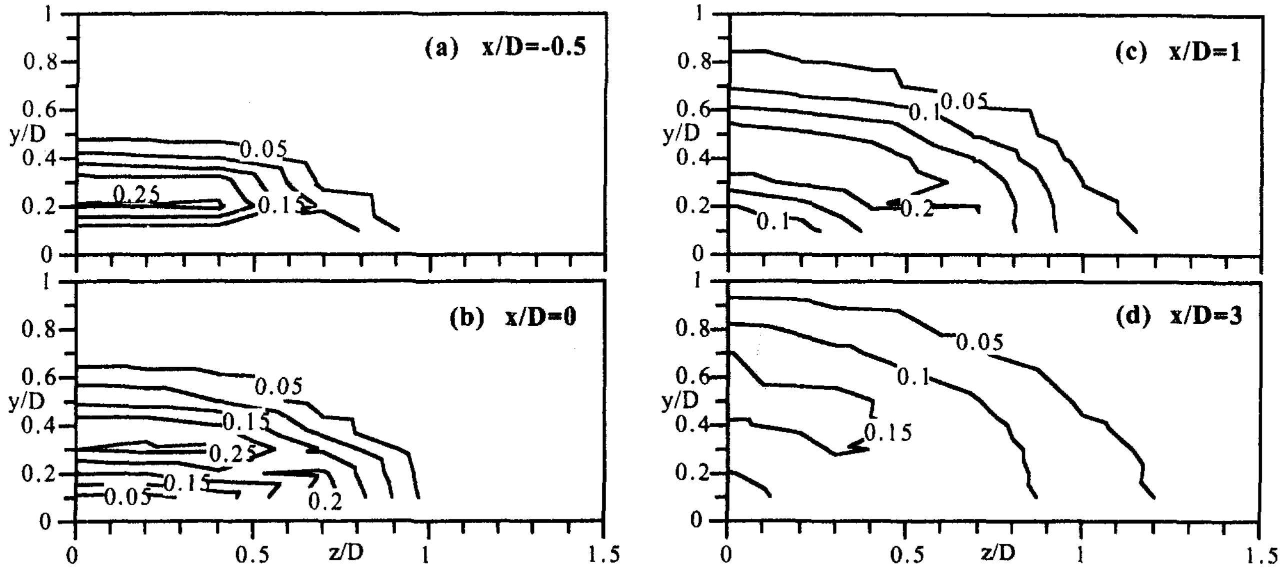

Fig. 6 Lateral rms temperature (Θ') contours at various streamwise positions: (*a*) $x/D = -0.5$, (*b*) $x/D = 0$, (*c*) $x/D = 1$, and (*d*) $x/D = 3$; $M = 0.4$, $DR = 1.05$, $I = 0.156$

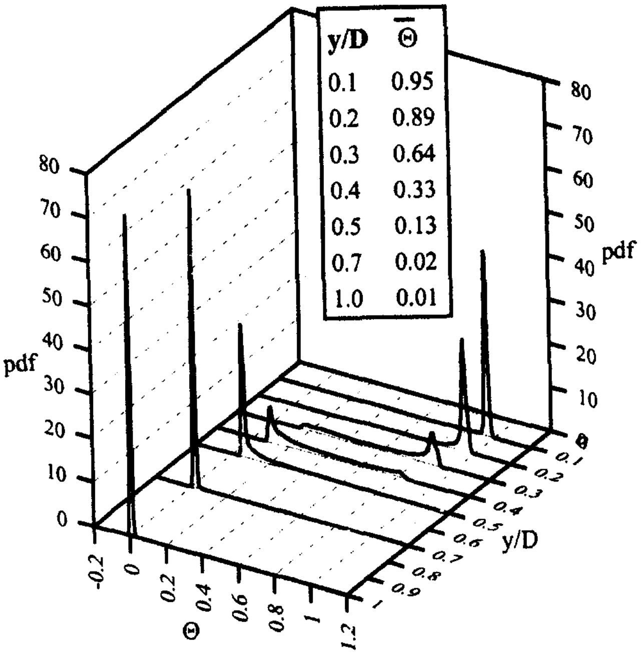

y/D	$\bar{\Theta}$
0.1	0.95
0.2	0.89
0.3	0.64
0.4	0.33
0.5	0.13
0.7	0.02
1.0	0.01

Fig. 7 Variation of pdf with height on the jet centerline at x/D = 0; table shows mean temperature at each height

spikes tend to be at $\Theta \approx 0.2$, there is a slightly higher pdf value here. Physically, these large spikes are due to turbulent mixing causing elements of warm mainstream fluid to penetrate into the coolant jet, and the relatively steady periods at $\Theta \approx 0.9$ represent the undisturbed core of the coolant jet. Note that at this position previous upstream penetrations have warmed the core of the coolant jet to $\Theta \approx 0.9$ and cooled the mainstream fluid to $\Theta \approx 0.15$.

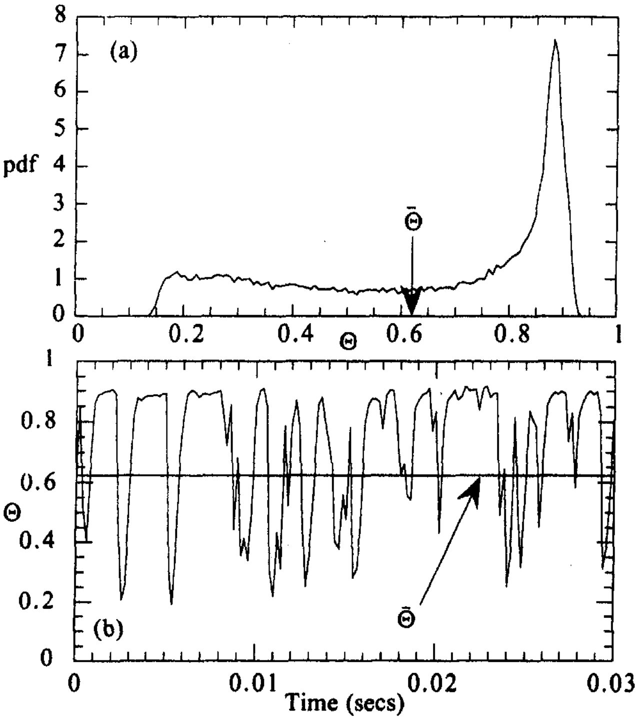

Fig. 8 Detail of (*a*) pdf and (*b*) time history at x/D = 0 and y/D = 0.3; $\bar{\Theta}$ = 0.64

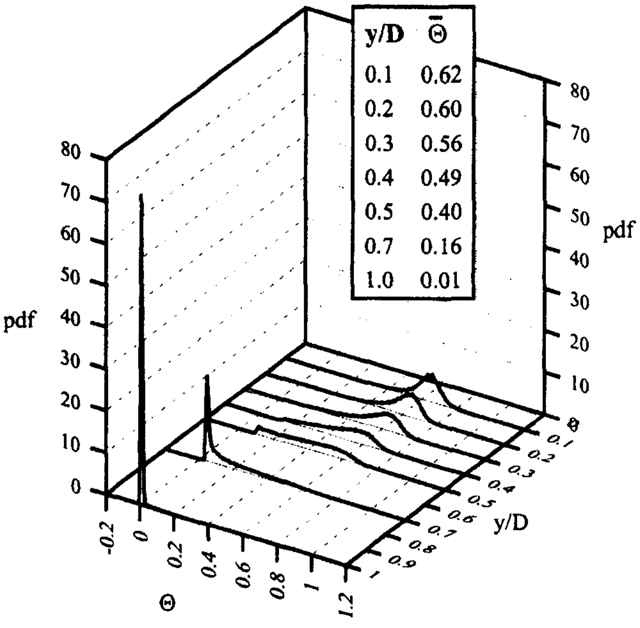

y/D	$\bar{\Theta}$
0.1	0.62
0.2	0.60
0.3	0.56
0.4	0.49
0.5	0.40
0.7	0.16
1.0	0.01

Fig. 9 Variation of pdf with height on the jet centerline at x/D = 3; table shows mean temperature at each height

A similar series of pdf distributions from farther downstream at $z/D = 0$ and $x/D = 3$, presented in Fig. 9, show a distinctly different character. The outer region is similar in showing dominance of mainstream fluid interspersed with elements of cooler fluid. However, near the wall there is no distinct spike indicating an undisturbed coolant core, and the core of the coolant jet has significantly increased in temperature. The broad pdf distributions at $y/D = 0.5$ and 0.6, and the tails for the pdf distributions at $y/D = 0.3$ and 0.2, indicate that there are still significant incursions of mainstream fluid into the coolant jet.

Conclusions

The focus of this study was on the thermal field in the near-hole region of a film cooling flow with the motivation to understand better the mechanisms responsible for the rapid dilution of the coolant jet when it exits the hole. Measurements were made using a momentum flux ratio, which gave the best adiabatic effectiveness near the injection location. It was shown that matching the momentum flux ratio captures the general characteristics of the thermal field, even for widely different density ratios. Although the mean temperature field indicates the extent to which the coolant has been diluted, the rms and probability density function (pdf) for the fluctuating temperature measurements reveal details of the physical mechanisms causing the dilution, and provide a more thorough statistical description of the thermal field, which is useful for evaluating time resolved computational models. The rms fluctuating temperatures were found to be extremely large along the top interface between the jet and the mainstream. Turbulent interaction at the jet interface causes dispersion of the coolant jet by ejecting elements of coolant into the mainstream, and dilution of the coolant jet occurs due to incursions of elements of the mainstream fluid deep within the core of the coolant jet. The strong intermittent flow structures that occur at the jet interface suggest that there is a shear layer instability generating these dominant eddy structures. The large-scale turbulent eddies generated at the interface are primarily responsible for the rapid dilution of the coolant jet.

Acknowledgments

The authors gratefully acknowledge AlliedSignal Aerospace Company for partial support of this research.

References

Ligrani, P. M., and Bradshaw, P., 1987, "Spatial Resolution and Measurements of Turbulence in the Viscous Sublayer Using Subminiature Hot-Wire Probes," *Experiments in Fluids,* Vol. 5, pp. 407–417.

Pietrzyk, J. R., Bogard, D. G., and Crawford, M. E., 1990, "Effects of Density Ratio on the Hydrodynamics of Film Cooling," ASME JOURNAL OF TURBOMACHINERY, Vol. 112, pp. 437–443.

Schmidt, D. L., 1995, "Effects of Injection Hole Geometry, Surface Roughness, and Freestream Condition on Film Cooling," Ph.D. Dissertation, The University of Texas at Austin.

Schmidt, D. L., Sen, B., Bogard, D. G., and Crawford, M. E., 1995, "Effects of Hole Geometry and Pressure Gradient on Film Cooling," Report TTCRL 95-1, prepared with support from Garrett Engine Division of the AlliedSignal Aerospace Company.

Sinha, A. K., Bogard, D. G., and Crawford, M. E., 1991, "Film Cooling Effectiveness Downstream of a Single Row of Holes With Variable Density Ratio," ASME JOURNAL OF TURBOMACHINERY, Vol. 113, pp. 442–449.

Subramanian, C. S., and Antonia, R. A., 1981, "Effect of Reynolds Number on a Slightly Heated Turbulent Boundary Layer," *International Journal of Heat and Mass Transfer,* Vol. 24, No. 11, pp. 1833–1846.

Thole, K. A., 1992, "High Freestream Turbulence Effects on the Transport of Heat and Momentum," Ph.D. Dissertation, The University of Texas at Austin.

Thole, K. A., Sinha, A. K., Bogard, D. G., and Crawford, M. E., 1992, "Mean Temperature Measurements of Jets With a Crossflow for Gas Turbine Film Cooling Application," *Rotating Machinery Transport Phenomena,* J. H. Kim and W. J. Yang, eds., Hemisphere Pub. Corp., New York.

Thole, K. A., and Bogard, D. G., 1994, "Simultaneous Temperature and Velocity Measurements," *Meas. Sci. Technol.,* Vol. 5, pp. 435–439.

Thole, K. A., Bogard, D. G., and Whan-Tong, J. L., 1994, "Generating High Freestream Turbulence Levels," *Experiments in Fluids,* Vol. 17, pp. 375–380.

Full Surface Local Heat Transfer Coefficient Measurements in a Model of an Integrally Cast Impingement Cooling Geometry

D. R. H. Gillespie

Z. Wang

P. T. Ireland

Dept. of Engineering Science,
University of Oxford,
Oxford, United Kingdom

S. T. Kohler

Rolls Royce,
Bristol, United Kingdom

Cast impingement cooling geometries offer the gas turbine designer higher structural integrity and improved convective cooling when compared to traditional impingement cooling systems, which rely on plate inserts. In this paper, it is shown that the surface that forms the jets contributes significantly to the total cooling. Local heat transfer coefficient distributions have been measured in a model of an engine wall cooling geometry using the transient heat transfer technique. The method employs temperature-sensitive liquid crystals to measure the surface temperature of large-scale perspex models during transient experiments. Full distributions of local Nusselt number on both surfaces of the impingement plate, and on the impingement target plate, are presented at engine representative Reynolds numbers. The relative effects of the impingement plate thermal boundary condition and the coolant supply temperature on the target plate heat transfer have been determined by maintaining an isothermal boundary condition at the impingement plate during the transient tests. The results are discussed in terms of the interpreted flow field.

Introduction

The drive toward higher turbine entry temperatures coupled with the requirement for longer engine component life means that the turbine aerofoil designer must be able to predict component temperature fields accurately. A precise thermal model requires detailed specification of the convective boundary condition on all heat transfer surfaces of the blading. Impingement cooling has been widely used in nozzle guide vane applications, but limited structural integrity of impingement plate inserts has curtailed use in rotating stages. The integral casting of the holed impingement surface into a rotor blade investigated in this study has two advantages. First, the impingement plate is cast into the structure of the blade and not subject to vibrational problems. Second, the design provides additional heat transfer surface in good thermal contact with the heated sections of the blade, Fig. 1. The thermal stresses are likely to be highest in the highly cooled region around the hole and it is thus necessary to obtain the convective boundary condition (heat transfer coefficient distribution) on these surfaces in addition to over the impingement target surface. The current work has succeeded in measuring the detailed local heat transfer coefficient distribution on the impingement target surface and over the upstream and downstream surfaces of the impingement hole surface of a typical geometry. This planar, integrally cast, impingement cooling arrangement with film cooling extraction has been experimentally investigated over a range of engine representative Reynolds numbers.

Previous Work

Impingement cooling performance is known to be a function of many different parameters. The cooling system geometry is clearly important and experiments have previously been performed to investigate the effects of plate to target spacing, hole diameter, and hole spacing in a multihole array and plate curvature. The influence of flow parameters such as jet Reynolds number and crossflow to jet mass velocity[1] ratio have been studied. Many workers (for example, Florschuetz et al., 1980) have carried out steady-state tests to yield spanwise-averaged results and have correlated Nusselt number to these parameters for specific geometries. Lucas et al. (1992) and Van Treuren (1994) produced full surface local Nusselt numbers for a single confined jet and for in-line and staggered arrays, respectively, which impinged on a flat target surface using steady-state and transient liquid crystal techniques.

Bunker and Metzger (1990) first used transient tests to investigate leading edge impingement. They found that the heat transfer coefficient increases as the jet nozzle diameter to pitch ratio is decreased, but is severely degraded for a slot jet. Furthermore, they concluded that close nozzle to internal apex spacings are desirable for improved leading edge heat transfer. Van Treuren et al. (1993) have shown that for both an in-line and staggered array of holes, with z/d in the range 1 to 4, the Nusselt number at the jet stagnation point is proportional to $\mathrm{Re}_{\mathrm{jet}}^{1/2}$. This implies that, where the jet core impinges on the target surface, a laminar boundary layer results. An initial peak in heat transfer (Gillespie, 1996) is seen $0.5-1d$ from the axis of an isolated jet. This is thought to be caused by the velocity variation as the flow first accelerates and then decelerates away from the stagnation point. Gillespie (1996) was able to predict this peak without reference to the jet turbulence profile where it would be expected to strike the surface. A second peak in heat transfer at 2–3 hole diameters (Lucas et al., 1992; Van Treuren, 1994; Gillespie, 1996) from the center of the jet core is thought to be caused by boundary layer transition. Despite the many earlier investigations there are no data for impingement into strongly confined passages representative of a cast passage design. Metzger and Bunker (1990) found that average Nusselt number enhancement on the impingement target surface through the addition of film-cooling extraction was dependent on the relative position of impingement and film-cooling holes, with local

Contributed by the International Gas Turbine Institute and presented at the 41st International Gas Turbine and Aeroengine Congress and Exhibition, Birmingham, United Kingdom, June 10–13, 1996. Manuscript received at ASME Headquarters February 1996. Paper No. 96-GT-200. Associate Technical Editor: J. N. Shinn.

---

[1] Jet mass velocity = ρu_{jet}.

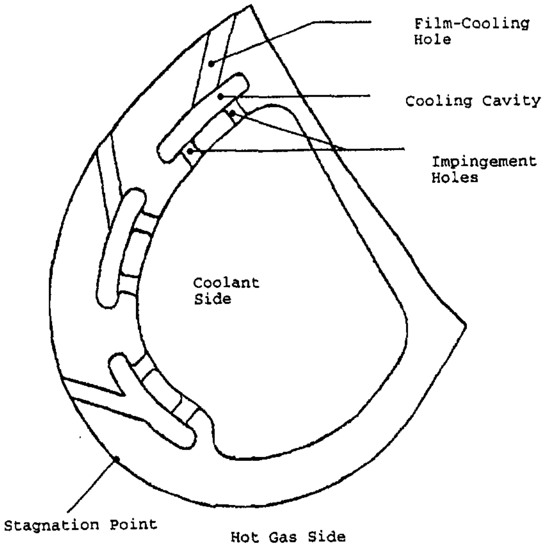

Fig. 1 Integrally cast cooling passage

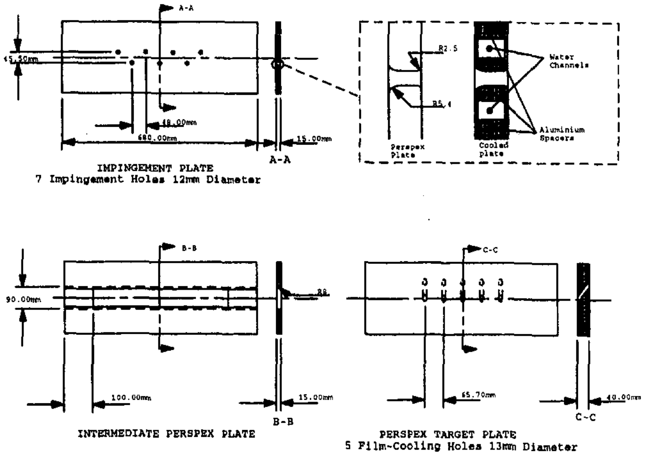

Fig. 2 Working section

heat transfer coefficients increased by up to 50 percent. Interestingly, Huber and Viskanta (1994) have shown that the addition of spent air outlets increases the heat transfer coefficient distribution under an array of semi-confined jets. Byerley (1988) studied a related problem and showed that film cooling extraction produces a local increase in heat transfer downstream of a single film cooling hole where the boundary layer is removed by the outflow.

Experimental Apparatus

A staggered double row of seven impingement holes exhausting through a single row of five inclined film cooling holes was chosen to represent part of a typical cast impingement passage. The impingement hole surface (equivalent to the impingement plate in conventional designs) has thickness to impingement hole diameter ratio, l/d, equal to 1.25. This is the same as the space between the target plate and this holed surface. The spanwise pitch of the impingement holes is $4d$ and the array is offset from the spanwise passage centre line by $\pm 1.90d$. The film-cooling holes are $1.08d$ diameter, and pass through a $3.33d$ thick target plate inclined to its surface at 30 deg. The spanwise pitch of these holes is $5.475d$. The entrance and exit of the impingement holes are radiused ($R0.45d$ and $R0.2d$, respectively) to represent cast features, while the film-cooling holes are sharp edged to represent machined holes. Air enters the impingement holes from a fiber-board inlet plenum of dimensions $40d \times 24d \times 20d$ and passes into a cavity $7.5d$ wide, with radiused comers, Fig. 2. Two impingement plates were manufactured with 12-mm-dia impingement holes, representing a 20:1 scale model of an engine configuration. The first was machined from solid perspex, an optically clear acrylic material, and the second has a hollow construction fabricated from aluminum plates and it includes internal water channels. The latter kept the plate at constant temperature throughout the transient experiments. In all cases the target plate and cavity end walls were manufactured from perspex. A compact planar heater[2] was mounted across the inlet $15d$ upstream of the working section. This comprised a mesh of fine (40-μm-dia stainless steel) wires in a woven arrangement yielding 38 percent open area. The heater provides a rapid increase in gas temperature at the start and a steady gas temperature throughout the experiment. Power was fed to the mesh from a high current, low voltage power supply through carefully designed brass bus-bars.

The mass flow rate through the rig was measured using a B.S.1042[3] orifice plate installed between the exit plenum and the suction pump. A coating of thermochromic encapsulated liquid crystal applied to three different surfaces of the model, as shown on Fig. 3, was used to measure the perspex surface temperature, and a thermally thin layer of black ink was applied to the exposed surface of the liquid crystal to eliminate transmitted light and improve visibility. Several T-type foil thermocouples were mounted on the surface in this region to allow the crystal color play to be calibrated. The crystal-coated surfaces were illuminated using fluorescent tubes mounted on the exit plenum. The color play from the liquid crystal was recorded using a video camera outside the tunnel, which viewed through the exit plenum perspex wall and the 40-mm-thick target plate. Both the target plate and the downstream side of the impingement plate were viewed from this position. Color play on areas obscured by the inclined film-cooling holes was not recorded. A schematic diagram of the test rig is shown in Fig. 3. The recorded video data were digitized at a frame rate of 50 frames per second and with a spatial resolution of approximately 3 pixels per millimetre on the model surface using a frame grabber and software developed by Wang et al. (1996).

Experimental Technique

The full surface heat transfer distribution in internal cooling geometries has been measured using the transient liquid crystal

---

[2] UK patent application 9517643.4.

[3] British Standard 1042, "Fluid Flow in Closed Conduits."

Nomenclature

d = impingement hole diameter, m
h = heat transfer coefficient, W/m^{2}K
h_{jet} = jet heat transfer coefficient, W/m^{2}K
h_{plate} = plate heat transfer coefficient, W/m^{2}K
Nu = Nusselt number
R = nozzle inlet radius, m
Re = Reynolds number based on impingement hole diameter
T_{aw} = adiabatic wall temperature, °C
T_{jet} = driving gas jet temperature, °C
T_{plate} = isothermal impingement plate temperature, °C
T_{surface} = local surface temperature, °C
t = time, s
x, y = distance from the working section origin, m
z = distance from the impingement plate to the target plate, m
τ = time constant of heater mesh, s

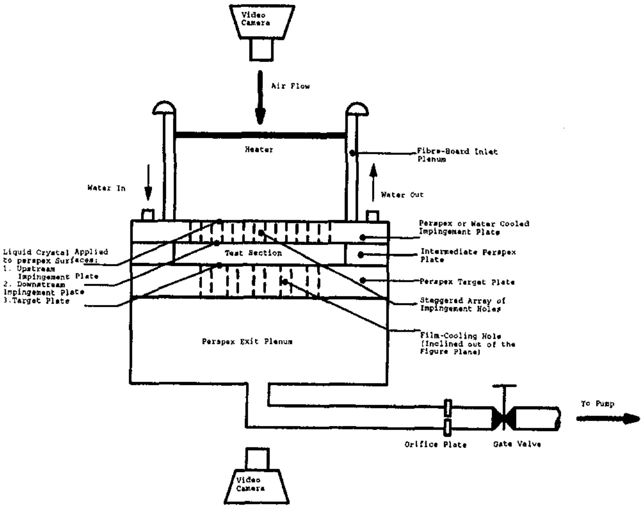

Fig. 3 Rig schematic

technique by many other workers (see for example Ireland and Jones, 1985; Van Treuren, 1994). In cases when the local adiabatic temperature is known and a single crystal color change event is recorded, it has been shown that the method yields h with an uncertainty of less than 7 percent. Wang et al. (1996) showed that color processing, used in this investigation, allows the method to be extended to obtain both h and T_{aw} with an uncertainty of 7.5–8.5 percent and 1.5–2.1 percent, respectively. It is the uncertainty in the measured value of the thermal product of perspex, $\sqrt{\rho c k} = 569 \pm 29$ Ws$^{1/2}$/m^{2}K (Ireland, 1987), and the 50 Hz video frame recording rate that predominantly account for these uncertainties. Their technique uses a full temperature history derived from the liquid crystal color play. Both of these techniques have been used by the present authors to obtain the heat transfer distributions in the current series of experiments.

Prior to the start of each test, the model temperature is uniform and equal to the room temperature. Air from atmosphere passes, unheated, through the rig, and the mass flow rate is adjusted to obtain the desired jet Reynolds number. The experiment begins when electrical power is switched to the heating mesh. The mesh temperature then increases, with a first-order lag, to a steady value determined by the air velocity, atmospheric temperature, and flow speed. The time constant, τ, has been measured by the authors using a hot-wire anemometer and the results for atmospheric air are presented in Fig. 4. The gas transport time through the 40-μm-thick mesh is negligible and so the heated air temperature and the mesh temperature increase with the same time constant. In experiments where the aluminum impingement plate was used, the flow of water inside the plate ensured that the temperature of the plate did not change by more than 0.5°C from its initial temperature. Maximum test times were limited to approximately 120 seconds since this corresponds to the time taken for the thermal pulse to penetrate the thinnest section of the model wall. The mass flow rate remained steady throughout the test and the value determined from an average of continuously logged signal is used to calculate jet Reynolds number. A temperature survey across the inlet plenum downstream of the heater showed that the flow temperature was uniform to within 1°C apart from within a narrow region 1d from the plenum wall (Fig. 5).

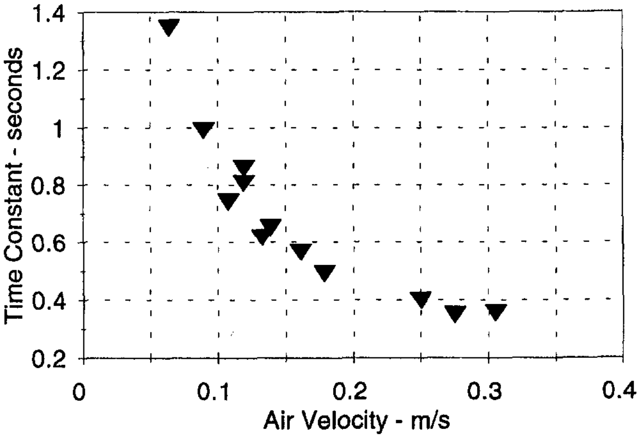

Fig. 4 Heater transient time constant

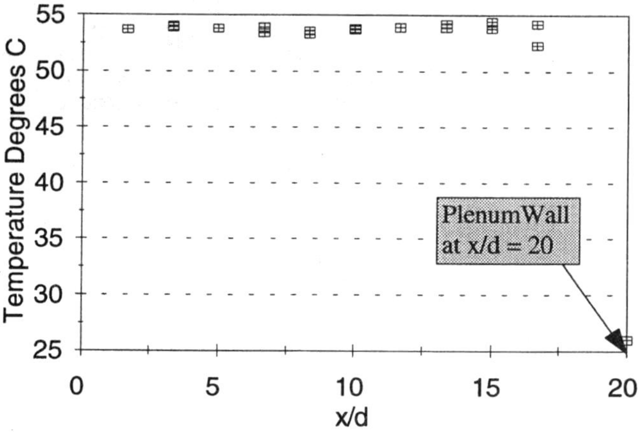

Fig. 5 Temperature uniformity in inlet plenum

Data Analysis

In transient heat transfer experiments in which the gas temperature follows a simple step function, the local heat transfer coefficient can be found from the surface temperature rise using the solution to the one-dimensional Fourier equation. In the following solution, the adiabatic wall temperature, T_{aw}, and the initial model temperature, T_{init}, are measured and the heat transfer coefficient, h, is determined from the time taken, t, for the liquid crystal to reach its calibrated temperature, T_w.

$$\frac{T_w - T_{\text{init}}}{T_{aw} - T_{\text{init}}} = 1 - e^{\beta^2}\operatorname{erfc}\beta \qquad (1)$$

ere:

$$\beta = \frac{h\sqrt{t}}{\sqrt{\rho c k}} \qquad (2)$$

When the gas temperature change follows an exponential increase, $T_{jet} = T_{\text{init}} + (T_{aw} - T_{\text{init}})\cdot(1 - e^{-(t/\tau)})$, the authors were able to show that the solution for the surface temperature is:

$$\frac{T_w - T_{\text{init}}}{T_{aw} - T_{\text{init}}} = 1 - \frac{\rho c k/h^2\tau}{(1 + \rho c k/h^2\tau)} \times e^{\beta^2}\operatorname{erfc}(\beta) - e^{-t/\tau}\frac{1}{(1 + \rho c k/h^2\tau)} \times \left(1 + \frac{\sqrt{\rho c k}}{h\sqrt{\tau}}\left(\frac{1}{\pi}\sqrt{\frac{t}{\tau}} + \frac{2}{\pi}\sum_{n=1}^{\infty}\frac{1}{n}e^{-n^2/4}\,\mathrm{Sinh}\,n\sqrt{\frac{t}{\tau}}\right)\right) \qquad (3)$$

A single wide band liquid crystal (Hallcrest BM/R20C20W/S-40) nominally displaying color between 20°C and 40°C was used in the investigation of the impingement target surface and

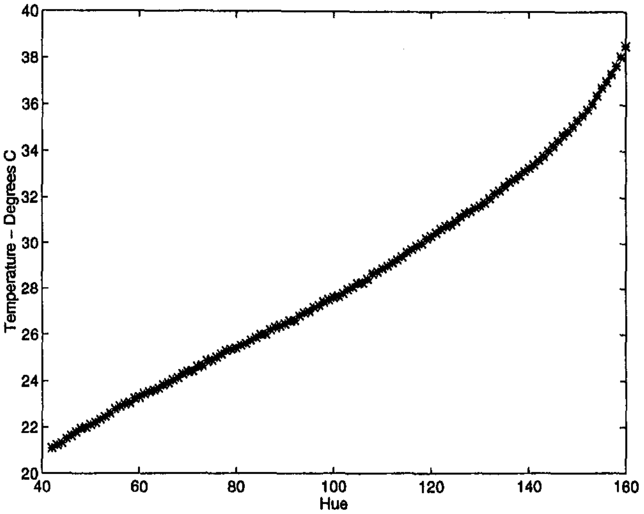

Fig. 6 Liquid crystal calibration

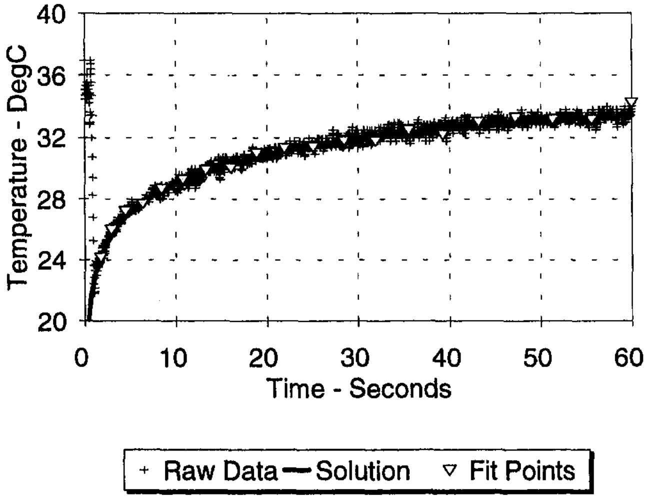

Fig. 8 Typical solution fitted to 20 data points

the downstream surface of the holed impingement surface. In each case an in-situ calibration (Fig. 6) relating the hue component of the video signal to the surface temperature was made under experimental lighting conditions. It was found that the hue could be accurately and repeatedly mapped to temperature over a range of 15°C (23°C–38°C) with an uncertainty of less than 0.3°C. The hue history of any point (Fig. 7) on the model surface was obtained from the digitized video data, and the temperature history found from the calibration.

In the case of the impingement target surface, the temperature of the water-cooled aluminum impingement plate was held constant throughout each test. This allowed the *jet effectiveness*, the relative contribution to heat transfer of the plenum temperature and the impingement plate temperature as defined by Eq. (7), to be determined by consideration of the calculated local adiabatic wall temperature. Van Treuren et al. (1996) have shown that the ratio between the impingement surface to target surface temperature difference and the impinging jet to target surface temperature difference, i.e., $(T_{\text{target surface}} - T_{\text{impingement plate}})/(T_{\text{target surface}} - T_{\text{jet}})$ lies between 0.7–0.72 at engine representative Reynolds number in a midspan array. Since the plate temperature is different from the gas temperature, the importance of the impingement surface temperature contribution to overall heat transfer can be seen. Due to the linearity of the energy equation, superposition may be used to determine temperature fields and heat transfer to the target surface. It can be shown that, for any three-temperature problem, the heat flux can be expressed as the summation of two heat transfer coefficient by temperature difference products. In this case, at the target surface we can write

$$\dot{q} = h_{\text{jet}}(T_{\text{jet}} - T_w) + h_{\text{plate}}(T_{\text{plate}} - T_w) \tag{4}$$

where h_{jet} and h_{plate} are the jet and plate heat transfer coefficients, respectively. This equation can be rearranged to

$$\dot{q} = (h_{\text{jet}} + h_{\text{plate}})\left[\frac{h_{\text{jet}}T_{\text{jet}} + h_{\text{plate}}T_{\text{plate}}}{h_{\text{jet}} + h_{\text{plate}}} - T_w\right] \tag{5}$$

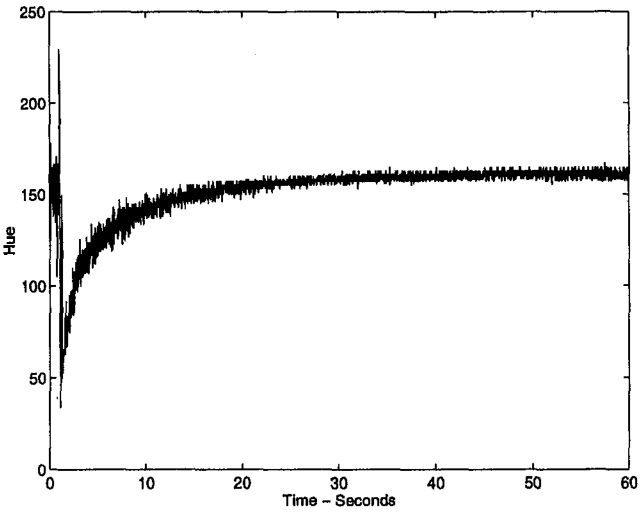

Fig. 7 Typical hue history

The local heat flux at the surface may also be written in terms of a heat transfer coefficient and the local adiabatic wall temperature:

$$\dot{q} = h(T_{aw} - T_w) \tag{6}$$

In the following, dimensionless adiabatic wall temperature is presented as effectiveness, defined as

$$\text{Jet Effectiveness} = \frac{h_{\text{jet}}}{h_{\text{jet}} + h_{\text{plate}}} = \frac{T_{aw} - T_{\text{plate}}}{T_{\text{jet}} - T_{\text{plate}}} \tag{7}$$

For each location on the target surface the one-dimensional Fourier equation was solved for both heat transfer coefficient and local adiabatic wall temperature. This was achieved by selecting values of h and T_{aw} to minimize the sum of the squared difference between the measured surface temperature signal and values calculated from Eq. (3). For each location the crystal color play occurred between 5 seconds (250 temperature measurements) and 120 seconds (6000 measurements). It was found that fitting a solution to 20 data points at each pixel location resulted in an insignificant loss in accuracy while greatly reducing processing time. A typical result of the fitting process is shown in Fig. 8.

The heat transfer coefficient distribution on the downstream face of the holed impingement surface was similarly determined; however, as in this case the entire working section was constructed from perspex, the adiabatic wall temperature at all points on the model surface was the measured inlet gas temperature. The regression procedure described above was then used to determine h.

A single event narrow band liquid crystal with peak intensity calibrated to 35.6°C was used to determine the heat transfer coefficient distribution on the upstream face of the holed im-

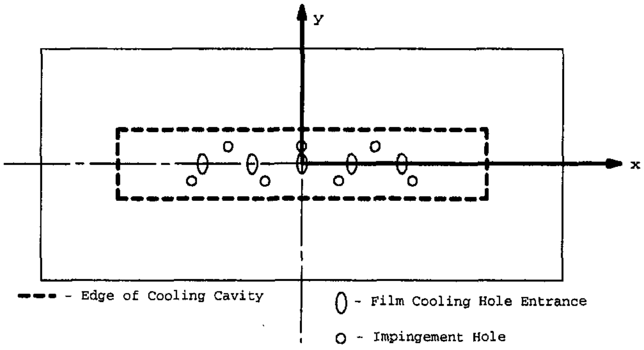

Fig. 9 Coordinate system

pingement surface. A development of the method allowed the temperature to be measured in spite of restricted visibility. The surface was viewed *through* the heater mesh, and this allowed the liquid crystal color change to be observed in the entrance to the impingement hole where the surface slopes away from the camera. As the adiabatic wall temperature was equal to the inlet gas temperature, the recording of a single temperature event was sufficient to determine the heat transfer coefficient distribution, using Eq. (3). The inlet gas temperature was chosen so that the time for the single temperature event to occur was maximized, within the requirement that semi-infinite boundary condition remained valid.

Results

Local Heat Transfer Distribution. The local heat transfer coefficient (based on adiabatic wall temperature) distribution on each surface is presented as Nusselt number, based on hole diameter and conductivity of air at the adiabatic wall temperature. The coordinate system for all results is that shown on Fig. 9.

Impingement Target Surface. The Nusselt number, adiabatic wall temperature, and jet effectiveness distributions on the target plate surface are presented in Figs. 10–12. Approximately 200 data points have been used to construct each contour plot, and each data point location is marked. The coordinate system measures from the passage center line in the y direction and, in the x direction, from a line that passes through a coincident impingement hole and film-cooling hole. The form of the pattern of heat transfer remains constant with Reynolds number and the overall level increases with Reynolds number. Under each jet there is an area of high heat transfer in the impingement zone and additional high heat transfer areas where the flow is accelerated out to the film-cooling holes. The stagnation point heat transfer coefficient is compared to other workers' results in Fig. 13. The present results are ~10 percent higher than the result of Obot et al. (1979) for a single contoured nozzle, but are in good agreement with the results and correlation of Van Treuren (1994) for an array of sharp-edged holes with $z/d = 1$. The plate temperature, as expected, has no effect directly under the jet, nor where the impinging air passes directly into a film-cooling hole without recirculating in the cavity. The jet effectiveness in these regions is close to unity. Remembering that the spanwise pitch of the impingement holes differs from that of the film-cooling holes, the extent of each region of high heat transfer can be explained by the proximity of the jet impinging on the target surface to the entrance of a film-cooling hole. Where these are close, the jet is dragged toward the film-cooling hole, and the effectiveness values suggest a weak recirculation in the cooling cavity around the jet. This creates a region of low heat transfer (e.g., at $y/d < 0$ & $x/d = 0$) where the influence of the impingement plate temperature is stronger. This is indicated by the drop in jet effectiveness to values as low as 0.70 in this region. From a design point of view, it is interesting to note that the Nusselt number can vary by a factor of three between the highest and lowest heat transfer zones.

Impingement Plate Downstream Surface. Figure 14 shows the Nusselt number distribution on the downstream (inside the cooling cavity) face of the impingement plate. 250 data points have been used to produce each contour plot. Since the jet is directed away from the impingement plate, the levels of heat transfer are determined by the strength of the local recirculation inside the closed cooling passage. On this surface, the highest heat transfer position is found far away from the closely spaced jets and film-cooling holes on the target surface. There is also a ring of heightened heat transfer around the exit of each impingement hole. This is probably due to locally high velocities in the entrained air in this region adjacent to the shear layers bounding the jets.

Impingement Plate Upstream Surface. The local Nusselt number on the upstream surface of the impingement plate (Fig. 15) is significantly lower than on the other heat transfer surfaces. 500 data points along the heat transfer coefficient contours have been used to produce each plot. The distribution can be explained if, in the inlet plenum, the pressure and velocity distributions are approximately radially symmetric around each hole. Under these conditions the level of heat transfer is deter-

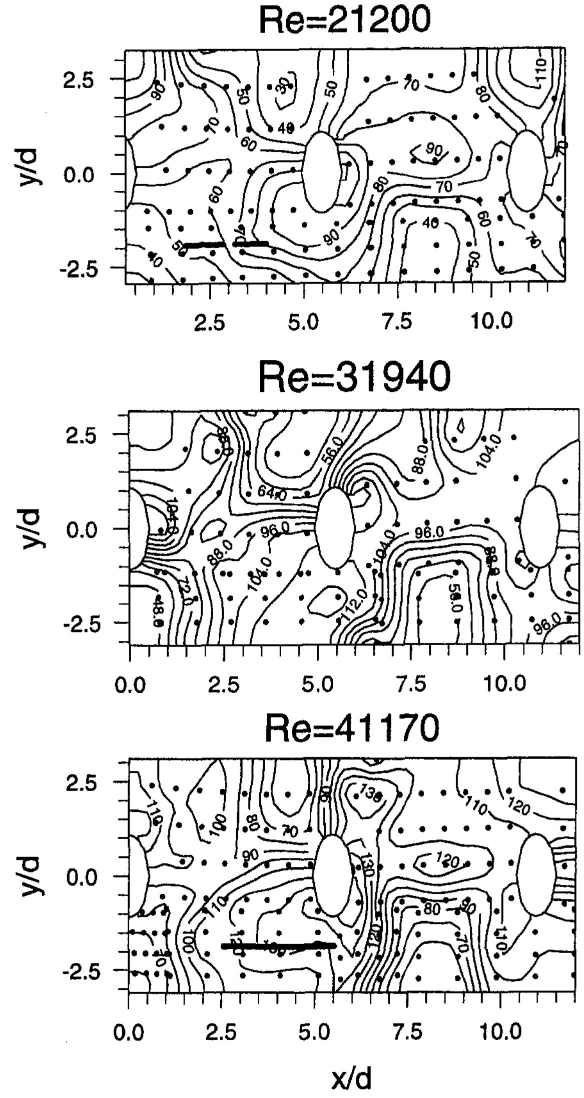

Fig. 10 Impingement target plate local Nusselt number distribution

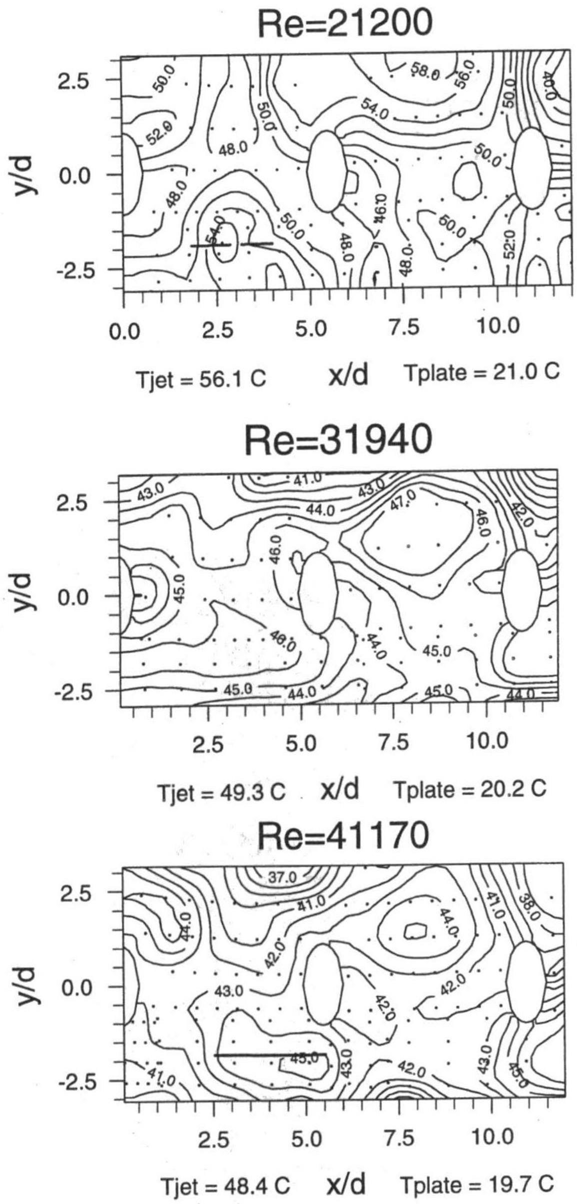

Fig. 11 Impingement target plate local adiabatic wall temperature distribution (temperature in °C)

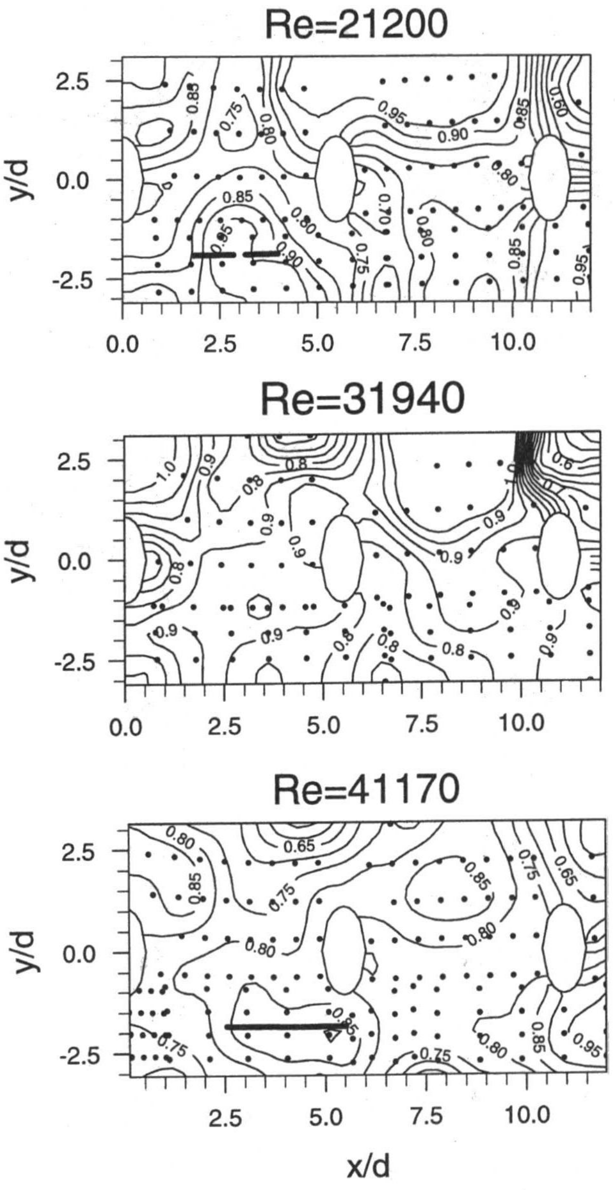

Fig. 12 Impingement target surface local jet effectiveness distribution

mined by the axially symmetric velocity and by the thickness of the boundary layer. In positions where the boundary layer at the entrance of the hole grows from the edge of the inlet plenum, it is expected to be of greatest thickness, and the heat transfer coefficient around the hole is lowest. Between neighboring impingement holes, there is a dividing streamline, and the boundary layer that develops from this point at the entrance to the impingement hole is much thinner. As the flow accelerates into the hole from the dividing streamline, the heat transfer is highest at this point despite the growing boundary layer. It is along the zig-zag strip connecting the staggered double row of impingement holes that all the significant heat transfer occurs. The level of heat transfer outside this strip is determined by the distance to the perimeter of the inlet plenum, which would be equivalent to the distance to the dividing streamline between adjacent cast cooling passages in a turbine blade. The levels of local Nusselt number are proportional to the square root of the Reynolds number, and this suggests that the boundary layer is laminar on the impingement plate upstream surface.

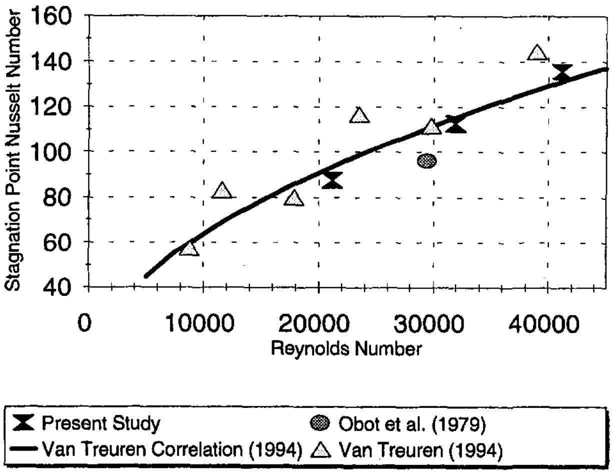

Fig. 13 Impingement target plate stagnation point Nusselt number

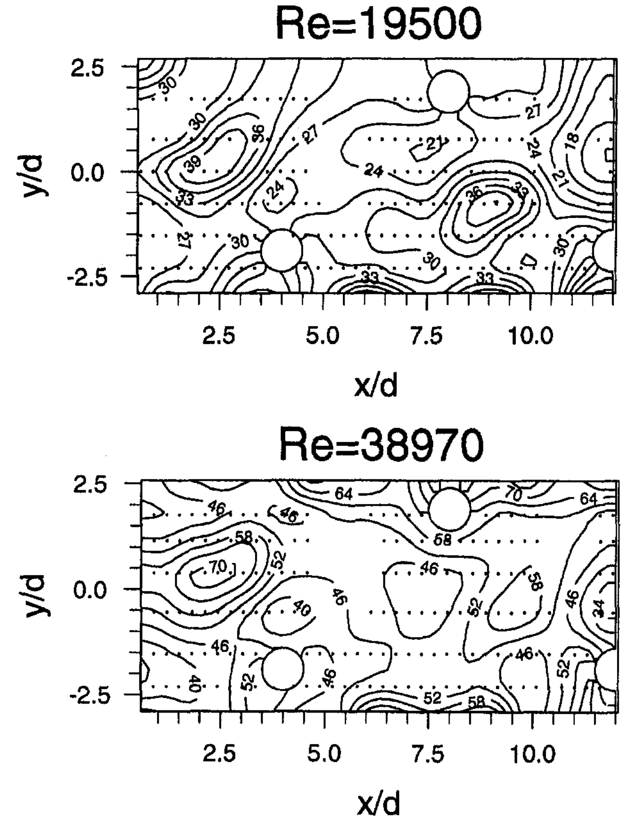

Fig. 14 Impingement plate downstream face local Nusselt number distribution

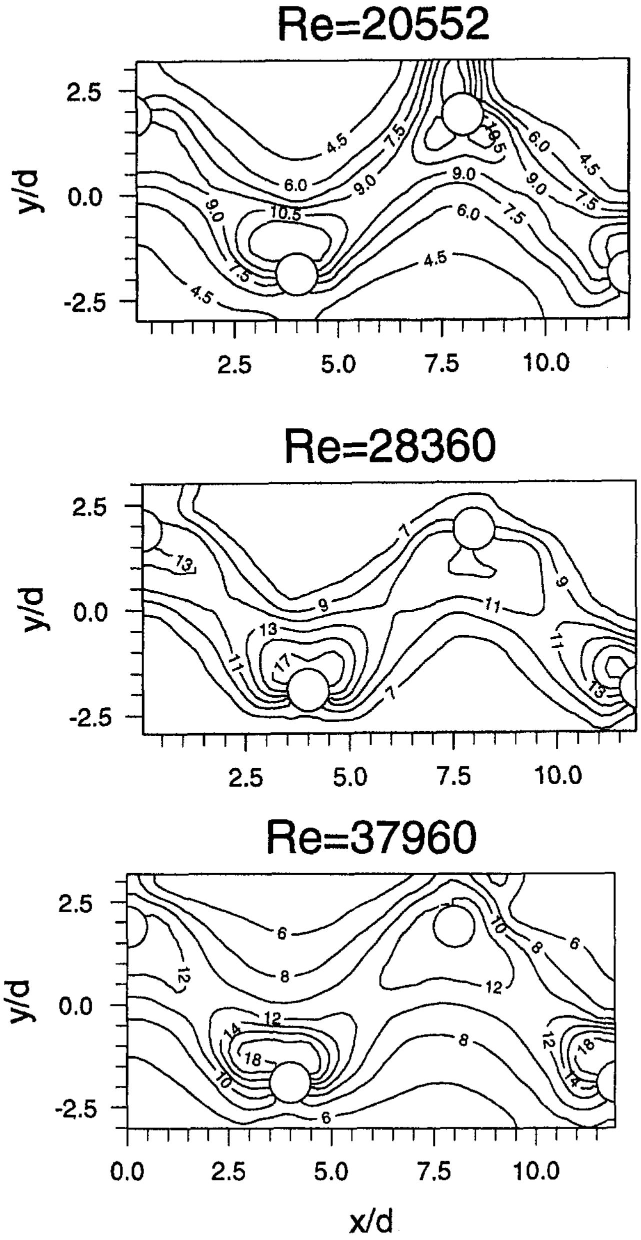

Fig. 15 Impingement plate upstream face local Nusselt number distribution

Average Heat Transfer. The local heat transfer coefficient distribution over each of the surfaces at the Reynolds numbers tested has been averaged to give an indication of the relative contribution of each surface to the overall performance of the cooling device (Fig. 16). In each case a strip between 0 and $8d$ in the x direction and $\pm 3.1d$ in the y direction is averaged. This strip represents the width of the planar portion of the cooling cavity in the y direction, and the portion of the test section where flow representative of that expected in a real engine had been established in the x direction. As with conventional designs, the highest heat transfer occurs on the impingement target surface. A significant contribution to heat transfer is made by the downstream face of the holed impingement surface where the average Nusselt number is ~50 percent of that on the impingement target surface, while on the upstream face the average Nusselt number is only ~10 percent of the target plate value.

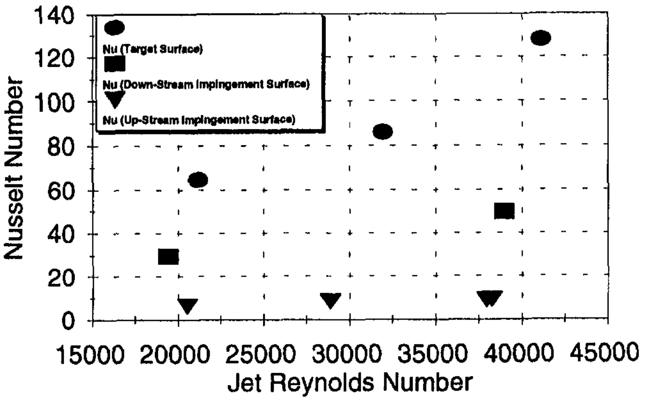

Fig. 16 Average Nusselt number

Summary

The heat transfer coefficient distribution on all surfaces of a novel impingement cooling device have been experimentally measured. The heat transfer on the impingement target plate was found to be comparable to that of conventional designs. The additional surfaces around the impingement holes were seen to be important regions contributing to heat transfer from the coolant to the wall in turbine blades. A completely new means of producing the thermal transient in the heat transfer experiments has been tested and validated by the authors. The heater mesh used enables the problems associated with switching low-speed flows to be overcome. Inspection of the adiabatic wall temperature distributions on the target surface, for experiments in which the impingement plate temperature was held constant, provides considerable insight into flow behavior. These values also enable the influence of nonisothermal conditions in the engine to be accounted for. Stagnation point heat transfer levels on the target surface are comparable to values under other confined jets in the literature. The efflux through the film cooling holes has been shown to increase heat transfer levels locally. Heat transfer levels on the upstream face have been explained in terms of a simple laminar boundary layer model.

Acknowledgments

The authors gratefully acknowledge the support of the M.O.D. (U.K.) and Rolls-Royce for the work reported here. The Department of Education for Northern Ireland financially supported David Gillespie, and this is greatly appreciated. The experimental apparatus was built by P. J. Timms whose technical expertise is much appreciated. The liquid crystals were supplied by Hallcrest LCT.[4]

References

Bunker, R. S., and Metzger, D. E., 1990, "Local Heat Transfer in Internally Cooled Turbine Airfoil Leading Edge Regions—Part 1: Impingement Cooling Without Film Coolant Extraction," ASME JOURNAL OF TURBOMACHINERY, Vol. 112, pp. 451–458.

Byerley, A. R., 1988, "Heat Transfer Near the Entrance to a Film Cooling Hole in a Gas Turbine Blade," D. Phil Thesis, Department of Engineering Science, University of Oxford, United Kingdom.

Florschuetz, L. W., Metzger, D. E., Takeuichi, D. I., and Berry, R. A., 1980, "Multiple Jet Impingement Heat Transfer Characteristic—Experimental Investigation of In-Line and Staggered Arrays With Crossflow," NASA Contractor Report 3217.

Gillespie, D. R. H., 1996, "Intricate Internal Cooling Systems for Gas Turbine Blading," D. Phil Thesis, Department of Engineering Science, University of Oxford, United Kingdom.

Huber, A. M., and Viskanta, R., 1994, "Convective Heat Transfer to a Confined Impinging Array of Air-Jets With Spent Air Exits," ASME JOURNAL OF HEAT TRANSFER, Vol. 116, pp. 570–576.

Ireland, P. T., and Jones, T. V., 1985, "The Measurement of Local Heat Transfer Coefficients in Blade Cooling Geometries," AGARD Conference on Heat Transfer and Cooling in Gas Turbines, CP 390 Paper 28, Bergen.

Ireland, P. T., 1987, "Internal Cooling of Turbine Blades," D. Phil Thesis, Department of Engineering Science, University of Oxford, United Kingdom.

Lucas, M. G., Ireland, P. T., Wang, Z., Jones, T. V., and Pearce, W. J., 1992, "Fundamental Studies of Impingement Cooling Thermal Boundary Conditions," AGARD Turkey 1992, Paper No. 14.

Metzger, D. E., and Bunker, R. S., 1990, "Local Heat Transfer in Internally Cooled Turbine Airfoil Leading-Edge Regions. 2. Impingement Cooling With Film Coolant Extraction," ASME JOURNAL OF TURBOMACHINERY, Vol. 112, pp. 459–466.

Obot, N. T., Majumdar, A. S., and Douglas, W. J. M., 1979, "The Effect of Nozzle Geometry on Impingement Heat Transfer Under a Round Turbulent Jet," ASME Paper No. 79-WA/HT-53.

Van Treuren, K., V., Wang, Z., Ireland, P. T., Jones, T. V., and Kohler, S. J., 1993, "Detailed Measurements of Local Heat Transfer Coefficient and Adiabatic Wall Temperature Beneath an Array of Impinging Jets," ASME JOURNAL OF TURBOMACHINERY, Vol. 116, pp. 369–374.

Van Treuren, K. V., 1994, "Impingement Flow Heat Transfer Measurements of Turbine Blades Using a Jet Array," D. Phil Thesis, Department of Engineering Science, University of Oxford, United Kingdom.

Van Treuren, K. V., Wang, Z., Ireland, P. T., and Kohler, S. T., 1996, "The Role of the Impingement Plate in Impinging Jet Array Heat Transfer," ASME Paper No. 96-GT-162.

Wang, Z., Ireland, P. T., Jones, T. V., and Davenport, R., 1996, "A Color Image Processing System for Transient Liquid Crystal Heat Transfer Experiments," ASME JOURNAL OF TURBOMACHINERY, Vol. 118, pp. 421–427.

---

[4] Hallcrest Liquid Crystal Technology Ltd., Unit 9, 541 Blanford Road, Poole, BH16 5BW, UK.

C. Camci
Department of Aerospace Engineering,
The Pennsylvania State University,
University Park, PA 16802

B. Glezer
Solar Turbines, Inc.,
San Diego, CA 92101

J. M. Owen

R. G. Pilbrow

B. J. Syson

School of Mechanical Engineering,
University of Bath,
Bath, United Kingdom

Application of Thermochromic Liquid Crystal to Rotating Surfaces

Encapsulated thermochromic liquid crystal (TLC) can be used to measure the surface temperature of stationary or rotating bodies. However, some research workers have reported a "rotational shift": When the temperature of a rotating body is measured by thermocouples and TLC, there is a difference between the two sets of temperatures, and this difference increases with increasing rotational speed. Two research groups (Camci and Glezer in the USA, and Owen, Pilbrow, and Syson in the UK) have independently examined the effect of speed on TLC applied to the surfaces of rotating disks. The USA group used narrow-band TLC on a disk of 305 mm diameter rotating up to 7500 rpm measuring the surface temperature using an infrared (IR) sensor. The UK group used wide-band TLC on a disk of 580 mm diameter rotating up to 7000 rpm, measuring the temperature with an IR thermal imager. Both groups used the so-called hue technique to evaluate the temperature of the TLC and concluded that, even for centripetal accelerations in excess of 10^4 g, there is no significant effect of rotational speed on either narrow-band or wide-band TLC. It is suggested that the "rotational shift" observed by some researchers was probably caused by thermal-disturbance errors, which affected the thermocouples, rather than by changes in the TLC.

1 Introduction

Encapsulated thermochromic liquid crystal (TLC) is used extensively for surface-temperature measurements in heat transfer experiments. Originally, most research workers used narrow-band TLC, where the colors change from red to blue over a small change in temperature, typically 1°C. Using a single color (say yellow), the surface temperature can be determined with an uncertainty of around 0.1°C. More recently, wide-band TLC (with a bandwidth around 10°C), and the so-called hue technique has been used to determine the temperature. The hue technique uses hue, saturation, and intensity (HSI) instead of the more conventional red, green, and blue (RGB) system of color processing, and this can result in an order-of-magnitude improvement in accuracy. Details are given by Kim (1991), Camci et al. (1992, 1993), Wilson et al. (1993), Farina et al. (1993), and Rizzo and Camci (1994).

Most of the applications of TLC have been on stationary objects, but the technique has also been applied to rotating bodies. Metzger et al. (1991) used narrow-band TLC applied to an acrylic rotating disk to determine the local heat transfer coefficients. Blair et al. (1991) made measurements using thermocouples and narrow-band TLC on a large-scale low-speed turbine rig. These authors observed a "rotational shift" in which the TLC output at 400 rpm changed by 2°C, compared with the thermocouple measurements. They also made measurements in a rotating cooling passage and reported a 3° to 4°C "rotational shift" at 525 rpm, corresponding to a centripetal acceleration of around 280 g.

Camci and Glezer in the USA and Owen, Pilbrow, and Syson in the UK carried out independent research work on rotating-disk systems, in which the disk temperatures were measured by TLC, thermocouples, and infrared (IR) thermography. Both groups found that, when thermocouples were used, there was evidence of the "rotational shift"; but, as described below, when IR measurements were used a different picture emerged. When Camci and Glezer presented their preliminary findings at the 1995 ASME Gas Turbine and Aeroengine Congress in Houston, it became apparent that both groups were proceeding along parallel lines. They agreed to collaborate: Each group would submit its detailed findings to an engineering journal for publication (Camci and Glezer, 1997; Syson et al., 1996), and a joint account of their work would be submitted to the 1996 ASME Gas Turbine Congress.

This paper contains the joint account of that research. The apparatus used by each group is described in Section 2, the experimental results in Section 3, and the conclusions in Section 4.

2 Experimental Apparatus

2.1 Tests With Narrow-Band TLC. The rotating disk used by Camci and Glezer was 0.305 m in diameter and was made from aluminum. It could be rotated up to 7500 rpm by means of an ac electric motor, and its speed was measured with an uncertainty of ±1 rpm.

One surface of the disk was first painted black and then coated with narrow-band TLC. Separate tests were conducted with two narrow-band crystals: R30C1W and R45C1W (manufactured by Hallcrest, Inc.), which were activated at 30°C and 45°C, respectively. A color video recording of the TLC was made for each test, and the hue was determined using an image-processing system incorporating a 24-bit image processor, a video decoder/encoder, and an array processor; further details of the hue technique are given by Camci et al. (1992).

The surface temperature of the disk was measured using an infra-red (IR) point sensor (manufactured by Raytek Thermalert). The sensor head was located normal to the disk, an axial distance of 76 mm from it, and the effective circular target area had a diameter of 2.5 mm. The spectral response of the detector was between 8 and 14 μm, which made it insensitive to the lighting used to illuminate the TLC. For this illumination, a 250 W incandescent light source was located at an angle of 45 deg to the target area and 1.5 m from it. Although the emissivity

---

Contributed by the International Gas Turbine Institute and presented at the 41st International Gas Turbine and Aeroengine Congress and Exhibition, Birmingham, United Kingdom, June 10–13, 1996. Manuscript received at ASME Headquarters February 1996. Paper No. 96-GT-138. Associate Technical Editor: J. N. Shinn.

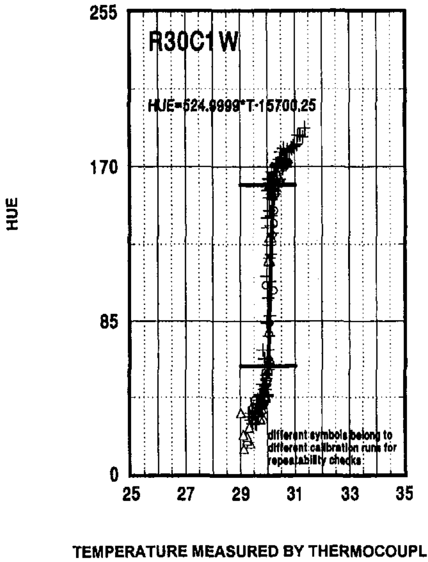

Fig. 1 Variation of hue for narrow-band TLC with temperature measured by thermocouple in stationary plate

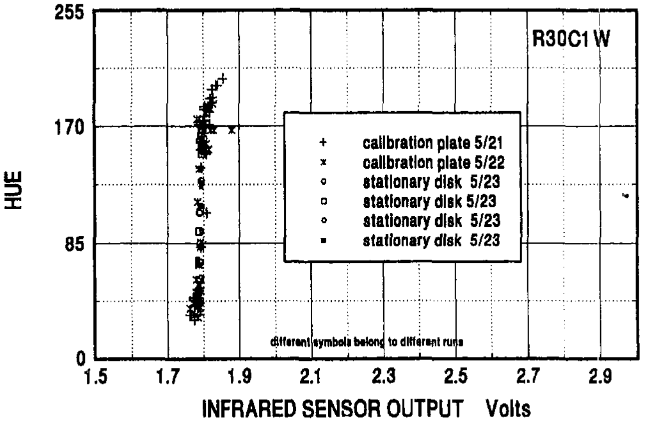

Fig. 3 Variation of hue for narrow-band TLC with voltage output of infrared sensor (stationary measurement)

of the surface of the TLC was not required for these tests, it was estimated to be $\epsilon = 0.96$.

A stationary calibration plate, made from aluminum and coated with black paint and TLC, was used for the calibration. A thin-foil (10 μm thickness) K-type thermocouple was attached to the black surface, which was then coated with TLC. The plate was heated to 60°C by a hot-air gun and allowed to cool slowly (around 0.1°C/min). The IR sensor was focused on the thermocouple, and a video recording was made during the thermal transient.

Figures 1 and 2 show the respective variations of hue, from the 30°C (R30C1W) crystal, and voltage, from the IR sensor, with the temperature of the aluminum plate measured by the thermocouple; the different symbols refer to different tests used to determine repeatability. Using a cross-plot of these results, it was possible to obtain the variation of hue with IR voltage shown in Fig. 3. The hue–temperature calibration tests were also successfully repeated on the surface of the aluminum disk when it was stationary. This calibration was used for subsequent tests on the rotating disk, thus avoiding the need to use thermocouples and sliprings with their associated errors.

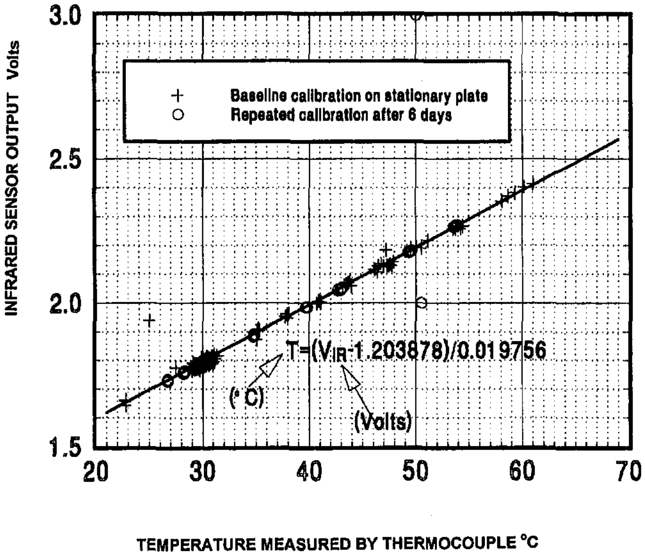

Fig. 2 Variation of voltage output of infrared sensor with temperature measured by thermocouple in stationary plate

2.2 Tests With Wide-Band TLC. The rotating disk used by Syson et al. was 0.580 m in diameter and was made from steel. It could be rotated up to 7000 rpm by a dc electric motor, and its speed was measured with an uncertainty of ± 1 rpm. The disk could be heated up to 150°C by thyristor-controlled stationary radiant heaters.

One surface of the disk was sprayed with black paint, and an annular area ($220 < r < 290$ mm) was then coated with wideband TLC (Hallcrest, R45C 10W) with an effective range of 45 to 55°C. A video recording was made of the heated surface, and an image-processing system, similar to that described by Wilson al. (1993), was used to determine the hue of the TLC.

The surface temperature was measured using an Agema IR thermal imager, featuring a thermal scanner and associated hardware and software to convert the electrical signal to a temperature output. The scanner, which is sensitive to radiation with wavelengths between 2 and 5 μm, uses oscillating and rotating mirrors to scan a 70-line field at 25 fields/second, and the software generates a 140 × 140 pixel image of the viewed surface. The manufacturer's specified accuracy is 2 percent or ±2°C, whichever is the larger, and the resolution at 60°C (which is at the top end of the TLC range) is 0.07°C. Improved accuracy was obtained by averaging 20 consecutive frames.

For the tests, the back face of the disk was radiantly heated and the front face, coated with TLC, was viewed using the IR imager and a video camera. The scanner was positioned to be normal to the disk at a distance of 0.5 m from it, and the video camera and tungsten-filament lamp, used to illuminate the TLC, were located a distance of 0.4 m from the disk at respective angles to the axial direction of 30 and 60 deg.

Before conducting the rotating-disk tests, the IR imager and TLC were calibrated using a copper-block rig. A copper block (67 × 67 × 5 mm) was embedded in insulating material, with one surface of the block exposed. A calibrated T-type thermocouple, embedded in the block, was used to measure its temperature, and the exposed surface was coated with black paint and TLC. Ten values of the measured temperatures were compared over the range 47.5 to 58.3°C. Using an emissivity setting of $\epsilon = 0.96$, the IR and thermocouple readings agreed within 0.1°C for eight of these readings; the differences between the other two readings were 0.2 and 0.3°C.

3 Experimental Results

3.1 Narrow-Band Tests. Using the apparatus described in Section 2.1, tests were conducted on the rotating aluminum

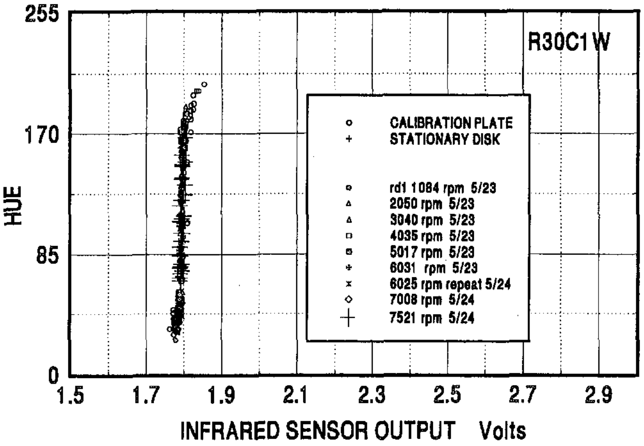

Fig. 4 Effect of rotation on variation of hue for narrow-band TLC with voltage output of infrared sensor

disk. Figure 3 shows the variation of hue, from the 30°C (R30C1W) crystal, with "IR voltage" (that is, the voltage from the IR sensor) for the stationary disk. The results, which were obtained from four individual cooling tests, give confidence in the accuracy and repeatability of the experimental technique.

Tests were carried out on the disk at a radius of $r = 0.135$ m for rotational speeds up to 7500 rpm, corresponding to centripetal accelerations up to $8500g$. Figure 4 shows the variation of hue, from the 30°C crystal, with "IR voltage" for various speeds. Several hundred data points on the figure confirm that there is no significant effect of rotational speed on the output of the TLC. Similar results were obtained from the 45°C crystal.

Figure 5 shows the variation of hue, from both crystals, with the temperature measured by the IR sensor. Again, it can be concluded that, for speeds up to 7500 rpm, there is no significant effect of rotational speed on the TLC.

3.2 Wide-Band Tests. Tests were conducted on the rotating steel disk, using the apparatus described in Section 2.2, for rotational speeds between 1000 and 7000 rpm. For the coated ring on the disk, which extended radially from 225 to 285 mm, these speeds corresponded to centripetal accelerations between $250g$ and $15{,}600g$.

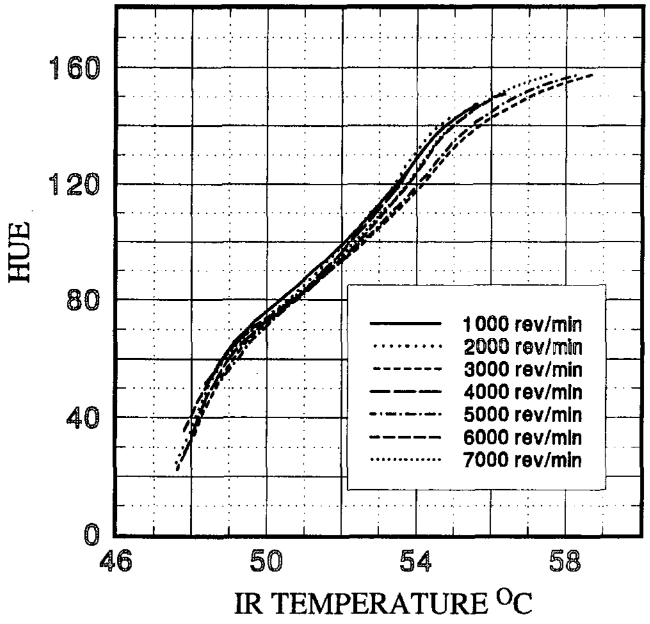

Fig. 6 Effect of rotation on variation of hue for wide-band TLC with temperature measured by infrared imager

Figure 6 shows the variation of hue (obtained from the video recording of the TLC) with the temperature of the disk measured by the IR imager. Despite the scatter in the experimental results, there appear to be no *obvious* effects of rotational speed. For speeds between 1000 and 7000 rpm and for a fixed value of hue in the range 80 to 120, the temperature variation with speed may be around 0.5°C, but the temperature variations for the results at the extremes of 1000 and 7000 rpm are smaller than this. If there is an effect of rotational speed then it is not progressive: The effect does not increase monotonically as the speed increases.

Figure 7 shows the variation of the temperature measured by the TLC (obtained using the copper-block hue–temperature calibration) with the temperature of the disk measured by the IR imager. The calibration line, obtained from the copper block for a *stationary* frame of reference, is also shown on the figure. The measurements show both scatter and an "oscillatory bias" around the calibration line: There appears to be some effect of

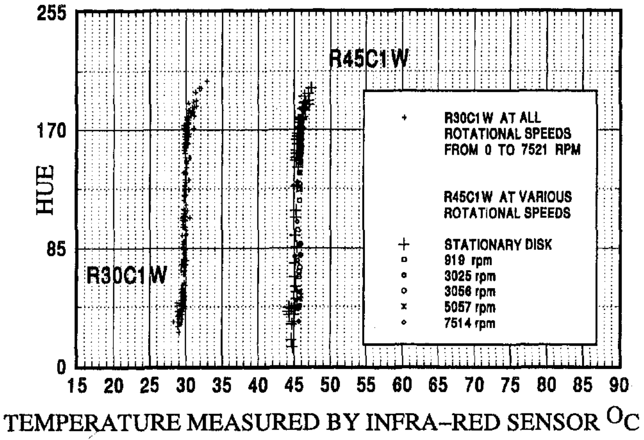

Fig. 5 Effect of rotation on variation of hue for narrow-band TLC with temperature measured by infrared sensor

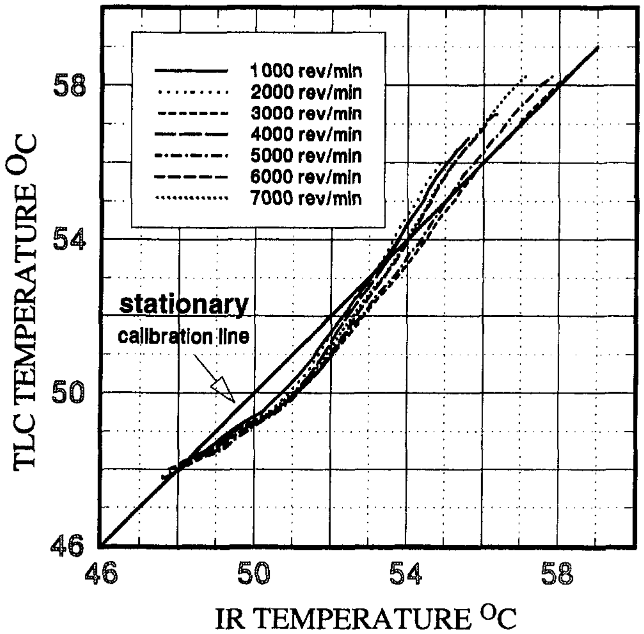

Fig. 7 Effect of rotation on variation of temperature measured by wide-band TLC (using copper-block calibration) with temperature measured by infrared imager

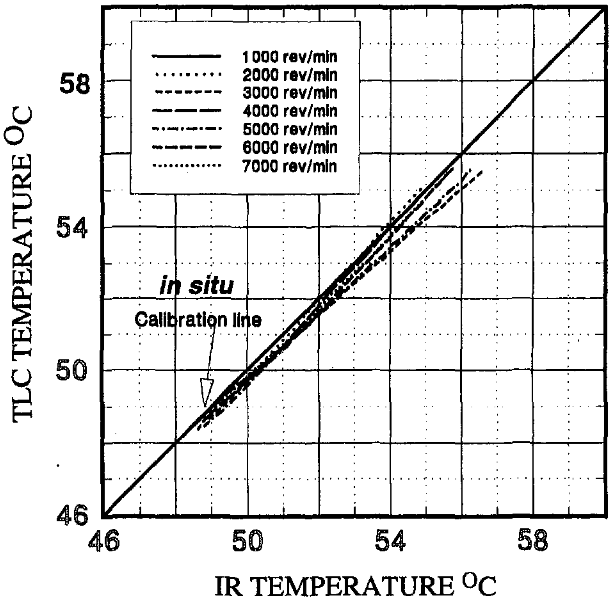

Fig. 8 Effect of rotation on variation of temperature measured by wide-band TLC (using in situ calibration) with temperature measured by infrared imager

rotational speed, but the scatter is relatively small and the bias is not a monotonic function of speed.

The "oscillatory bias" was *originally* thought to be caused not by moving from a stationary to a rotating frame *per se* but by moving from the *surface* of the copper block to that of the disk. The two surfaces could have different emissivities and reflectivities, and this would affect the optical and IR signals in different ways. To test this hypothesis, an *in situ* calibration was performed on the disk when it was rotating at 1000 rpm; owing to the way the disk was heated, tests on a stationary disk were impracticable. For the *in situ* calibration, the hue values for the TLC were calibrated using the IR measurements obtained from the surface of the heated disk; the emissivity setting of the IR imager was kept at $\epsilon = 0.96$, the value used for the original copper-block calibration.

Figure 8 shows the variation of the temperature measured by the TLC (using the *in situ* calibration) with the temperature measured by the IR imager. There is still scatter in the measurements, but the oscillatory bias has been reduced significantly. The departure of the measurements made at 7000 rpm from the calibration at 1000 rpm is typically less than 0.3°C, although the departure of measurements at intermediate speeds (for example, 3000 rpm) is up to 0.5°C. While the departure from the calibration line is relatively small, and it does not increase monotonically with speed, the effect does appear to be speed related.

The bias referred to above appears to be caused by the color-balance circuits in the video hardware. In the experiments, it was not possible to keep the radial temperature distribution on the disk the same for all tests; consequently there was a variation in the distribution of hue, from the TLC, from speed to speed. The apparent speed-related bias in the results was believed to be caused by the varying temperature distributions and not by any intrinsic effect of speed on the TLC.

3.3 The "Rotational Shift." A thermocouple, which will be a different material from that of the body in which it is embedded, will cause a local disturbance of the temperature distribution in the body. This creates a thermal-disturbance error in which there is a difference between the true (undisturbed) temperature and the measured temperature. The magnitude of the error depends, among other things, on the size of the thermocouple, the thermal properties of the materials, and the local heat flux.

For a rotating body at a constant temperature, the heat transfer coefficient, and hence the surface heat flux, increases as the rotational speed increases. Consequently, the thermal-disturbance error created by an embedded thermocouple will increase with rotational speed. If thermocouples and TLC are used to measure the temperature of a rotating body, then the difference between the two measurements will also increase with speed.

This phenomenon has been observed independently in experiments carried out by the two groups of authors. It is believed to be the reason why other research workers have observed what they (wrongly) believed to be the "rotational shift" in TLC output referred to in Section 1.

4 Conclusions

Experiments have been conducted on narrow-band (1°C bandwidth) and wide-band (10°C bandwidth) TLC, by two groups of research workers in the USA and the UK, to determine if there is an effect of rotational speed on the output of TLC. The narrow-band tests were conducted on a disk of 0.305 m diameter rotating up to 7500 rpm (corresponding to centripetal accelerations up to $8500g$). The wide-band tests were carried out on a disk of 0.580 m diameter rotating up to 7000 rpm ($15{,}600g$). In both cases, the so-called hue technique was used to determine the output of the TLC, and infrared thermography was used to measure the surface temperature of the rotating disk: For the narrow-band tests, an IR point sensor was used; for the wide-band tests, an IR imager was employed.

Within the uncertainty of the experimental measurements, it was concluded that there is no significant effect of rotational speed on the output of TLC. The "rotational shift" observed by other research workers is believed to be caused by thermal-disturbance errors in their thermocouples and not by the TLC itself.

References

Blair, M. F., Wagner, J. H., and Steuber, G. D., 1991, "New Applications of Liquid Crystal Thermography in Rotating Turbomachinery Heat Transfer Research," ASME Paper No. 91-GT-354.

Camci, C., Kim, K., and Hippensteele, S. A., 1992, "A New Hue Capturing Technique for the Quantitative Interpretation of Liquid-Crystal Images Used in Convective Heat Transfer Studies," ASME JOURNAL OF TURBOMACHINERY, Vol. 114, pp. 765–775.

Camci, C., Kim, K., Hippensteele, S. A., and Poinsatte, P. E., 1993, "Evaluation of a Hue Capturing Based Transient Liquid Crystal Method for High Resolution Mapping of Convective Heat-Transfer on Curved Surfaces," ASME *Journal of Heat Transfer*, Vol. 115, pp. 311–318.

Camci, C., and Glezer, B., 1997, "Liquid Crystal Thermography on the Fluid Solid Interface of Rotating Systems," ASME *Journal of Heat Transfer*, Vol. 119, pp. 20–29.

Farina, D. J., Hacker, J. M., Moffat, R. J., and Eaton, J., 1993, "Illuminant Invariant Calibration of Thermochromic Liquid Crystals," ASME HTD-Vol. 252, *Visualization of Heat Transfer Processes*.

Kim, K., 1991, "A New Hue Capturing Technique for the Quantitative Interpretation of Liquid Crystal Images Used in Convective Heat Transfer Studies," PhD Thesis, The Pennsylvania State University, USA.

Metzger, D. E., Bunker, R. S., and Bosch, G., 1991, "Transient Liquid-Crystal Measurement of Local Heat Transfer on a Rotating Disk With Jet Impingement," ASME JOURNAL OF TURBOMACHINERY, Vol. 113, pp. 52–59.

Rizzo, D., and Camci, C., 1994, "The Effects of a Boundary Layer Fence on the Aerodynamic Flowfield and Endwall Heat Transfer in a 90° Turning Square Duct," presented at ASME Winter Annual Meeting, Session: Heat Transfer In Gas Turbines, Chicago, IL.

Syson, B. J., Pilbrow, R. G., and Owen, J. M., 1996, "Effect of Rotation on Temperature Response of Thermochromic Liquid Crystal," *Int. J. Heat Fluid Flow*, Vol. 17, No. 5, pp. 491–499.

Wilson, M., Syson, B. J., and Owen, J. M., 1993, "Image Processing Techniques Applied to Wide-Band Thermochromic Liquid Crystals," presented at Eurotherm 32: Heat Transfer in Single Phase Flows, Oxford, UK, July.

Computation of the Unsteady Transonic Flow in Harmonically Oscillating Turbine Cascades Taking Into Account Viscous Effects

B. Grüber

V. Carstens

Institute of Aeroelasticity,
DLR,
Göttingen, Federal Republic of Germany

This paper presents the numerical results of a code for computing the unsteady transonic viscous flow in a two-dimensional cascade of harmonically oscillating blades. The flow field is calculated by a Navier–Stokes code, the basic features of which are the use of an upwind flux vector splitting scheme for the convective terms (Advection Upstream Splitting Method), an implicit time integration, and the implementation of a mixing length turbulence model. For the present investigations, two experimentally investigated test cases have been selected, in which the blades had performed tuned harmonic bending vibrations. The results obtained by the Navier–Stokes code are compared with experimental data, as well as with the results of an Euler method. The first test case, which is a steam turbine cascade with entirely subsonic flow at nominal operating conditions, is the fourth standard configuration of the "Workshop on Aeroelasticity in Turbomachines." Here the application of an Euler method already leads to acceptable results for unsteady pressure and damping coefficients and hence this cascade is very appropriate for a first validation of any Navier–Stokes code. The second test case is a highly loaded gas turbine cascade operating in transonic flow at design and off-design conditions. This case is characterized by a normal shock appearing on the rear part of the blades's suction surface, and is very sensitive to small changes in flow conditions. When comparing experimental and Euler results, differences are observed in the steady and unsteady pressure coefficients. The computation of this test case with the Navier–Stokes method improves to some extent the agreement between the experiment and numerical simulation.

Introduction

For aeroelastic investigations on highly loaded and oscillating transonic turbomachine blade rows, the first essential is the exact knowledge of the unsteady airloads. For this reason much theoretical work has been done in the last decade to develop methods that accurately predict the unsteady pressure, lift, and moment coefficients of turbomachinery bladings vibrating in transonic flow.

Until recently, linearized aerodynamic methods have been developed and used as standard tools for routine aeroelastic design studies (Whitehead and Grant, 1980; Verdon and Caspar, 1984; Hall and Crawley, 1989; Kahl and Klose, 1993). Although they meet the requirement of computational efficiency and in many cases produce reasonable results, their range of application is limited to unsteady flows in which strong compressibility and viscosity effects, such as large amplitude shock movement and flow separation, do not play an essential role.

Further improvement has been gained by the development of nonlinear Euler methods, which may be regarded as a first step toward the solution of the Navier–Stokes equations. Fransson (1986) and Gerolymos (1988) were among the first to present a two-dimensional time-marching analysis for solving the nonlinearized Euler equations, followed by similar publications of He (1990), Huff (1991), Peitsch et al. (1991), and Carstens (1991). Recently, Gerolymos and Vallet (1994), Peitsch et al. (1994), and Carstens (1994) presented extensions of their methods to three-dimensional flow.

The steadily growing capability of computers to perform arithmetic operations at an increasingly higher speed has stimulated the development of numerical methods for solving the complete set equations for unsteady viscous flow. Since the direct simulation of turbulence lies far beyond the computer capabilities available today, the Reynolds-averaged Navier–Stokes equations are solved together with an appropriate turbulence model. One of the first to provide a code for calculating the unsteady transonic viscous flow in turbomachinery bladings was Rai (1985), who investigated stator–rotor interaction with this method. Further contributions considering the problem of an isolated oscillating blade row have been published by Sidén (1991), Giles and Haimes (1993), He and Denton (1994), Dorney and Verdon (1994), and Abhari and Giles (1997).

The aim of this paper is to provide an insight into the capability of a Navier–Stokes code to predict unsteady aerodynamic coefficients required for flutter investigations. In former calculations of harmonically oscillating subsonic and transonic turbine cascades with Euler methods, it was demonstrated that the measured unsteady pressure and damping coefficients were in some cases well predicted by the computed results, whereas in other cases significant differences were observed (Carstens et al., 1993). These differences obviously are due to dropping the viscous terms in the governing flow equations, i.e., phenomena such as flow separation and shock-boundary layer interaction cannot be taken into account.

Contributed by the International Gas Turbine Institute and presented at the 41st International Gas Turbine and Aeroengine Congress and Exhibition, Birmingham, United Kingdom, June 10–13, 1996. Manuscript received at ASME Headquarters February 1996. Paper No. 96-GT-338. Associate Technical Editor: J. N. Shinn.

Numerical Method

Basic Equations. The strong conservation law form of the unsteady compressible two-dimensional Reynolds-averaged Navier–Stokes equations in transformed coordinates can be written in a nondimensional form as:

$$\partial_\tau Q + \partial_\xi F + \partial_\eta G = \partial_\xi R + \partial_\eta S \tag{1}$$

with the transformed state vector

$$Q = \frac{1}{J}\begin{bmatrix} \rho \\ \rho u \\ \rho v \\ \rho E \end{bmatrix}, \tag{2}$$

the transformed inviscid fluxes

$$F = \frac{1}{J}\begin{bmatrix} \rho U \\ \rho u U + \xi_x p \\ \rho v U + \xi_y p \\ \rho H U - \xi_t p \end{bmatrix} G = \frac{1}{J}\begin{bmatrix} \rho V \\ \rho u V + \eta_x P \\ \rho v V + \eta_y p \\ \rho H V - \eta_t p \end{bmatrix}, \tag{3}$$

and the transformed viscous fluxes

$$R = \frac{1}{\mathrm{Re}J}(\xi_x R_c + \xi_y S_c)$$

$$S = \frac{1}{\mathrm{Re}J}(\eta_x R_c + \eta_y S_c), \tag{4}$$

where the Cartesian fluxes R_c and S_c are given by

$$R_c = \begin{bmatrix} 0 \\ \tau_{xx} \\ \tau_{xy} \\ u\tau_{xx} + v\tau_{xy} + \dfrac{\mu}{P_r(\kappa - 1)}\dfrac{\partial T}{\partial x} \end{bmatrix};$$

$$S_c = \begin{bmatrix} 0 \\ \tau_{xy} \\ \tau_{yy} \\ u\tau_{xy} + v\tau_{yy} + \dfrac{\mu}{P_r(\kappa - 1)}\dfrac{\partial T}{\partial y} \end{bmatrix} \tag{5}$$

with

$$\tau_{xx} = \frac{\mu}{3}\{4(\xi_x u_\xi + \eta_x u_\eta) - 2(\xi_y v_\xi + \eta_y v_\eta)\}$$

$$\tau_{xy} = \mu\{(\xi_y u_\xi + \eta_y u_\eta) - (\xi_x v_\xi + \eta_x v_\eta)\}$$

$$\tau_{yy} = \frac{\mu}{3}\{-2(\xi_x u_\xi + \eta_x u_\eta) + 4(\xi_y v_\xi + \eta_y v_\eta)\}$$

$$\frac{\partial T}{\partial x} = \xi_x T_\xi + \eta_x T_\eta$$

$$\frac{\partial T}{\partial y} = \xi_y T_\xi + \eta_y T_\eta \tag{6}$$

The density, the Cartesian velocity components, the static pressure, and the temperature are denoted by ρ, u, v, p and T, while $\kappa = 1.4$ is the ratio of specific heats and μ, Re, Pr are symbols for the dynamic viscosity, the Reynolds number, and the Prandtl number. The Jacobian of the transformation is defined as $J = (\xi_x\eta_y - \xi_y\eta_x)$ and U, V are the contravariant velocity components, given as follows:

$$U = \xi_t + \xi_x u + \xi_y v$$

$$V = \eta_t + \eta_x u + \eta_y v \tag{7}$$

Assuming a thermally and calorically perfect gas, the pressure, p, and the temperature, T, are related to the conservative variables Q by the equations

$$p = (\kappa - 1)\rho(E - \tfrac{1}{2}(u^2 + v^2)); \quad T = \kappa\frac{p}{\rho} \tag{8}$$

and the specific total energy, E, and specific total enthalpy, H, are then given by

$$E = \frac{p}{\rho(\kappa - 1)} + \tfrac{1}{2}(u^2 + v^2); \quad H = E + \frac{p}{\rho} \tag{9}$$

By designating physical quantities with a tilde, the nondimensional variables of Eq. (1) are obtained by referring all geometric dimensions to the blade-chord length L, introducing a nondimensional time by $t = \tilde{t}\tilde{a}_0/L$ and scaling the flow variables $\tilde{\rho}$, $\tilde{u}$, $\tilde{v}$, and $\tilde{E}$ as

$$\rho = \frac{\tilde{\rho}}{\tilde{\rho}_0}; \quad u = \frac{\tilde{u}}{\tilde{a}_0}: \quad v = \frac{\tilde{v}}{\tilde{a}_0}: \quad E = \frac{\tilde{E}}{\tilde{a}_0^2}, \tag{10}$$

where the index 0 refers to the stagnation quantities and the speed of sound $\tilde{a}$ is related to the pressure and density by $\tilde{a}^2 = \kappa\tilde{p}/\tilde{\rho}$. The viscous coefficients are scaled according to

$$\mu = \frac{\tilde{\mu}}{\tilde{\mu}_0}; \quad \mathrm{Re} = \frac{\tilde{\rho}_0 L\tilde{a}_0}{\tilde{\mu}_0}, \tag{11}$$

where the laminar viscosity μ is calculated by Sutherland's law. For turbulent flows, the algebraic turbulence model of Baldwin–Lomax (1978) is used, i.e., μ is replaced by $\mu + \mu_t$ and μ/Pr is replaced by $\mu/\mathrm{Pr} + \mu_t/\mathrm{Pr}_t$, with $\mathrm{Pr} = 0.72$ and $\mathrm{Pr}_t = 0.9$.

Flux Vector Splitting of the Inviscid Fluxes. The numerical scheme has been written in a cell-centered finite-volume formulation where the inviscid fluxes are differentiated according to the so-called AUSM-scheme (Advection Upstream Splitting Method) of Liou/Steffen (1993) described below, while the viscous fluxes are computed with central differences. In contrast to the flux vector splitting methods of Steger/Warming (1981) and Leer (1982), the AUSM scheme is characterized by a separate splitting of the convective and pressure terms of the inviscid fluxes. The numerical flux vector F^*, e.g., is computed at a cell interface $i + \frac{1}{2}$ as

$$\begin{aligned} &F^*_{i+1/2}(Q_L, Q_R) \\ &= \sqrt{\xi_x^2 + \xi_y^2}\left\{\tfrac{1}{2}\mathrm{M}_{i+1/2}\left(\begin{bmatrix} \rho a \\ \rho a u \\ \rho a v \\ \rho a H \end{bmatrix}_L + \begin{bmatrix} \rho a \\ \rho a u \\ \rho a v \\ \rho a H \end{bmatrix}_R\right)\right. \\ &\qquad \left. - \tfrac{1}{2}|\mathrm{M}_{i+1/2}|\left(\begin{bmatrix} \rho a \\ \rho a u \\ \rho a v \\ \rho a H \end{bmatrix}_R - \begin{bmatrix} \rho a \\ \rho a u \\ \rho a v \\ \rho a H \end{bmatrix}_L\right)\right\} \\ &\qquad + \begin{bmatrix} 0 \\ \xi_x(p_L^+ + p_R^-) \\ \xi_y(p_L^+ + p_R^-) \\ 0 \end{bmatrix}, \end{aligned} \tag{12}$$

where L and R designate the left and right values of the state vector with respect to a cell interface. $\mathrm{M}_{i+1/2}$, the cell interface Mach number, is obtained by summing up the contributions from the left and right states

$$\mathrm{M}_{i+1/2} = \mathrm{M}_L^+ + \mathrm{M}_R^- \tag{13}$$

with the split Mach numbers M^+ and M^- defined by

$$\mathrm{M}^{\pm} = \begin{cases} \pm\frac{1}{4}(\mathrm{M} \pm 1)^2 & \text{if} \quad |\mathrm{M}| \leq 1 \\ \frac{1}{2}(\mathrm{M} \pm |\mathrm{M}|) & \text{otherwise} \end{cases} \tag{14}$$

where M from Eq. (14) is the contravariant Mach number $\mathrm{M} = U/a$.

The pressure p is calculated in a similar way as

$$p = p_L^+ + p_R^-, \tag{15}$$

where p^+ and p^- are obtained by

$$p^{\pm} = \begin{cases} \frac{1}{4}p(\mathrm{M} \pm 1)^2(2 \mp \mathrm{M}) & \text{if} \quad |\mathrm{M}| \leq 1 \\ \frac{1}{2}p(\mathrm{M} \pm |\mathrm{M}|)/\mathrm{M} & \text{otherwise} \end{cases} \tag{16}$$

As the dissipative term of the flux balance is given by the second term of Eq. (12), the dissipation vanishes for zero Mach numbers, which leads to accurate results in boundary layers, where the physical viscosity must not be falsified by an overly high amount of numerical viscosity.

Time Integration and Spatial Discretization. The method of time integration is the approximately factored implicit algorithm of Beam and Warming (1976). In order to make feasible the application of an approximate factorization scheme, the viscous fluxes are split into two parts:

$$R = R_1 + R_2, \quad S = S_1 + S_2, \tag{17}$$

with R_1 and S_1 consisting of velocity and temperature derivatives merely in the ξ direction and R_2 and S_2 containing the corresponding terms in the η direction. A first-order time-accurate algorithm in delta form is then given by

$$\begin{aligned} &\left\{I + \Delta\tau\left(\delta_\xi\left[\frac{\partial F^*}{\partial Q_{L_\xi}}\Delta Q_{L_\xi}\right] + \delta_\xi\left[\frac{\partial F^*}{\partial Q_{R_\xi}}\Delta Q_{R_\xi}\right]\right.\right. \\ &\quad \left.\left. - \delta_\xi\left[\frac{\partial R_1}{\partial Q_{A_\xi}}\Delta Q_{A_\xi}\right]\right)\right\}\cdot\left\{I + \Delta\tau\left(\delta_\eta\left[\frac{\partial G^*}{\partial Q_{L_\eta}}\Delta Q_{L_\eta}\right]\right.\right. \\ &\quad \left.\left. + \delta_\eta\left[\frac{\partial G^*}{\partial Q_{R_\eta}}\Delta Q_{R_\eta}\right] - \delta_\eta\left[\frac{\partial S_2}{\partial Q_{A_\eta}}\Delta Q_{A_\eta}\right]\right)\right\} \\ &= -\Delta\tau\{\delta_\xi(F^* - R_1 - R_2 - \Delta R_2) \\ &\qquad + \delta_\eta(G^* - S_1 - \Delta S_1 - S_2)\}, \end{aligned} \tag{18}$$

where F^* and G^* are the inviscid numerical fluxes according to Eq. (12). $\Delta Q = Q^{n+1} - Q^n$ is the difference of the state vector between time steps $n + 1$ and n, while the indices L_ξ, R_ξ, $A_\xi L_\eta$, R_η, A_η indicate whether Q is updated at the cell interface from left (L), right (R) or averaged (A) state vectors in the ξ or η direction. Since the fluxes R_2 and S_1 contain derivatives in η and ξ directions, respectively, they cannot be included in the factorization algorithm and thus have to be calculated from the previous time step:

$$\Delta R_2 = R_2^n - R_2^{n-1} \quad \Delta S_1 = S_1^n - S_1^{n-1} \tag{19}$$

Since the time integration for the harmonic blade motion has been performed with at least 800 (Euler) or 10,000 (Navier–Stokes) time steps per period, a first-order scheme is sufficient to guarantee time accuracy. It was found that a second-order accurate time integration does not change the pressure amplitudes or phases for the selected test cases.

The special method for determining Q_L and Q_R is the MUSCL approach (van Leer, 1979) where the state vector at the cell interface is obtained by upwind extrapolation between neighboring cell-centered values. The spatial discretization scheme used for the present investigations is the fully one-sided first/second-order scheme (here in ξ-direction at cell interface $i + \frac{1}{2}$):

$$\begin{aligned} Q_{L_\xi} &= Q_i + \frac{\epsilon}{2}(Q_i - Q_{i-1}) \\ Q_{R_\xi} &= Q_{i+1} + \frac{\epsilon}{2}(Q_{i+1} - Q_{i+2}) \end{aligned} \tag{20}$$

which is of first- or second-order accuracy for $\epsilon = 0$ or $\epsilon = 1$, respectively. Finally, the averaged cell interface values Q_A required to update the viscous fluxes are computed as

$$Q_{A_\epsilon} = \tfrac{1}{2}(Q_i + Q_{i+1}) \tag{21}$$

In order to simplify the solution of Eq. (18), the right-hand side of this equation is computed with second-order differences ($\epsilon = 1$), whereas the left-hand side is computed with first-order spatial accuracy ($\epsilon = 0$). This procedure yields a block-tridiagonal structure of the discretized implicit equations. It is easy to show that this manipulation does not alter the overall spatial accuracy of the scheme, which is of second order.

Boundary Conditions. On the blade's surface the flow velocity is equal to the blade velocity. This means that

$$\begin{aligned} &u = 0 && v = 0 && \text{for steady flow} \\ &u = \tfrac{1}{J}(\eta_t\xi_y - \xi_t\eta_y) && v = \tfrac{1}{J}(\xi_t\eta_x - \eta_t\xi_x) && \text{for unsteady flow} \end{aligned} \tag{22}$$

Furthermore, adiabatic walls are assumed, which requires a vanishing temperature gradient, and the pressure gradient at the wall is set to zero:

$$\left(\frac{\partial T}{\partial n}\right)_{\text{Wall}} = 0; \quad \left(\frac{\partial p}{\partial n}\right)_{\text{Wall}} = 0 \tag{23}$$

Smooth walls are assumed and consequently, the turbulent viscosity $(\mu_t)_{\text{Wall}}$ is set to zero.

The implementation of inlet and outlet boundary conditions is accomplished by the method of Chakravarthy (1982), who proposed a quasi-two-dimensional approach. Assuming that the in- and outlet boundaries are ξ = const lines, only the wave transport along the characteristics in the $\xi - \tau$ plane is taken into account, whereas the flux in the η direction is regarded as a source term. A description of the special application of this technique to steady and unsteady turbomachinery flow is given by Carstens (1991).

Assuming that the axial flow component is entirely subsonic at the in- and outlet plane of the cascade, boundary conditions for steady flow are established by replacing incoming waves with fixed flow values, i.e., total pressure, total temperature, and flow angle are prescribed at the inlet boundary while static pressure is kept constant at the outlet boundary.

Nonreflecting boundary conditions are used for unsteady flow, i.e., incoming waves (three at the inlet, one at the outlet boundary) have to be suppressed, which is accomplished by setting their time derivative to zero.

The application of periodic boundary conditions is self-evident with a line-periodic H-grid (see next section), the type of computational mesh used here.

Grid Generation for Moving Blades

The grid generation needed to compute the solution of the Navier–Stokes algorithm in a boundary-fitted coordinate sys-

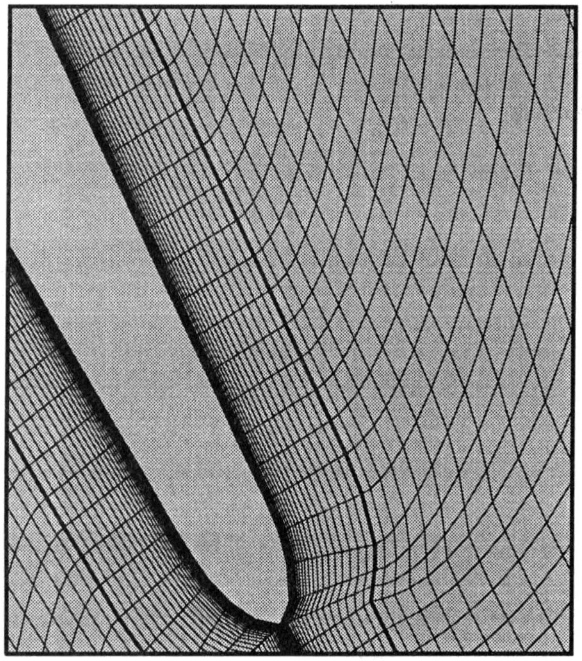

Fig. 1 Close-up of the grid at the trailing edge

tem is obtained by a method presented by Carstens (1988). The procedure used is an elliptic grid-generation code based on the solution of Poisson equations, the basic feature of which is the possibility to control the line spacing and intersection angle of the grid lines at the physical boundaries.

The type of grid used for the cascade flow calculation is a line-periodic H-grid, where each grid point on the lower channel boundary has its counterpart on the upper channel boundary in the pitchwise direction. Hence an implicit code is easily introduced on the grid and the periodic boundary conditions can be imposed in an implicit manner.

Due to the strong velocity gradient normal to the wall, a viscous flow computation requires a sufficient density of those grid lines that run parallel to solid boundaries. Additionally, the calculation of the outer eddy viscosity coefficient in the Baldwin–Lomax turbulence model is simplified if the grid lines intersecting the wall are orthogonal to the other family of mesh lines. For this reason, a separate "boundary-layer grid," which matches the elliptic grid at its outer boundary has been generated algebraically (Fig. 1).

The grid point displacement must be carefully organized for unsteady flow, i.e., for oscillating blades. As the blades are in relative motion to each other, the total grid has to be deformed to enable it to conform to the new position of the vibrating blades after each time step. An important feature of any unsteady grid generation is the control of the grid point speed in the interior field. For harmonic motions the time-dependent grid is computed by harmonic interpolation (with respect to time) of a set of steady-state grids with different blade amplitudes. An interactive grid generation procedure is used for nonharmonic blade motions. In this case a new grid is calculated with the original grid generation algorithm after each time step, regarding the old mesh as an initial solution and the new position of the blades as changed boundary conditions. Since in the present method the unsteady cascade flow is computed according to the so-called multichannel method, the number of blade channels in which the flow has to be calculated depends on the oscillation mode of the cascade. Tuned modes with constant amplitude and constant interblade phase angle result in a pitchwise spatially periodic flow where the spatial periodic length is determined by the interblade phase angle Θ. Consequently, an interblade phase angle of $\Theta = 180$ deg requires two blade channels to compute the unsteady flow; four channels are sufficient for $\Theta = \pm 90$ deg, etc.

In any other case of vibration mode forcing a nonperiodic behavior of flow quantities in the pitchwise direction, the computational domain has to include the complete cascade.

Presentation and Discussion of Results

The results for unsteady cascade flow were calculated for two different turbine cascades, namely a steam turbine cascade, which has become the Fourth Standard Configuration (STC4) of the "Workshop on Aeroelasticity in Turbomachines" (Bölcs and Fransson, 1986), and a transonic gas turbine cascade known as the TCT3 cascade. Both cascades have been experimentally investigated in the nonrotating annular cascade tunnel of the Swiss Federal Institute of Technology, Lausanne, where the first cascade was run in high subsonic flow at design conditions while the second cascade was investigated in transonic flow at design and off-design conditions.

Unsteady pressure distributions were measured in both cascades for tuned bending modes, i.e., heaving oscillations with the same frequency and amplitude but with a constant controlled interblade phase angle Θ. The reduced frequency ω^* is given by

$$\omega^* = \frac{2\pi f(L/2)}{V_2}, \tag{24}$$

where f, L, and V_2 are the vibration frequency, the blade chord length, and the cascade outlet velocity, respectively. The interblade phase angle in both cascade configurations is defined as such that it is positive if the phase of the pressure side blade advances to the phase of the regarded blade. The computational mesh for both cascades consisted of a (205×91) grid for Navier–Stokes computations with 27 points in the viscous region and of a coarser (115×27) grid for Euler calculations, which have been performed with the AUSM scheme as well as with van Leer flux vector splitting and yield almost identical results. The results presented for inviscid flow are computed with van Leer flux vector splitting. The minimum grid line spacing in the η direction was chosen as 4×10^{-5} at the blade's surface, which leads to maximum values of 2.0 (STC4) and 1.2 (TCT3) for the nondimensional wall distance $y^+ = (y/\mu_w)\sqrt{\rho_w \tau_w}$, where τ_w is the wall shear stress.

Since no information about transition was available from the experimental data, no transition model was incorporated into the code, i.e., the boundary layers along the blade walls were assumed to be fully turbulent. This assumption is supported by several test calculations, which were performed a priori with either laminar–turbulent or fully turbulent flow. For the STC4 cascade a change from a laminar–turbulent (prescribed transition at 30 percent of chord length) to a fully turbulent flow does not lead to any differences in the computed pressure distributions. Calculating the design flow through the TCT3 cascade with a laminar–turbulent boundary layer (prescribed transition at 40 percent of chord length) laminar separation is obtained at the leading edge of the blade, which indicates that the flow must have been fully turbulent. The off-design flow of this cascade is characterized by a measured separation bubble at the leading edge justifying again the assumption of fully turbulent flow. The geometric data, the in- and outlet flow values and the vibration data of both cascades are listed in Table 1.

Fourth Standard Configuration. Before comparing the results for unsteady flow, the computed data for steady flow must be validated because they are the starting point for unsteady flow calculations. The steady pressure coefficient is defined here with respect to the inlet flow values

Table 1 Geometry and operating data of cascades STC4 and TCT3

	STC4	TCT3 design	TCT3 off-design
chord length L	74 mm	78.5 mm	78.5mm
stagger angle γ	56.6°	41.0°	41.0°
pitch cord ratio τ/L	0.76	0.72	0.72
inflow Mach number M_1	0.28	0.34	0.40
inflow angle β_1	−45°	15°	33°
outflow Mach number M_2	0.90	1.00	0.99
outflow angle β_2	−72°	−58°	−58°
inflow Reynolds number Re_1	$4.2 \cdot 10^5$	$5.7 \cdot 10^5$	$5.7 \cdot 10^5$
bending angle δ (against chord)	60°	90°	90°
vibration amplitude y_0/L	0.0030	0.0050	0.0035
vibration frequency f	150 Hz	210 Hz	212 Hz
reduced frequency ω^*	0.1153	0.1558	0.1545
interblade phase angle Θ	0°, ±90°, 180°	0°, ±18°, ... 180°	0°, ±36°, ... 180°

$$c_{p_s} = \frac{p - p_1}{p_{t_1} - p_1}, \tag{25}$$

where p_1 and p_{t_1} denote the measured static and total inlet pressure. Figure 2 shows the comparison between the experimental and theoretical steady pressure distribution. The agreement is generally good; only small deviations are noticeable at approximately 30 percent of the chord length on the suction side and on the aft portion of the blade's pressure side. It was found that the Navier–Stokes results are sensitive to the grid cell length at the trailing edge of the blade. For this reason the results have been computed with decreasing TECL values (TECL = Trailing Edge Cell Length), two of which are presented here. The typical overprediction of the acceleration on the front part of the suction side, which is confirmed by the computed results of Abhari and Giles (1997), is less pronounced with the smaller cell length of 0.2 percent, a value below which no further changes in the pressure coefficient are observable. A possible explanation for this behavior is that the coarser grids produce a larger separation region on the pressure side of the trailing edge, which on the other hand, causes a displacement of mass flow to the suction side of the adjacent blade and therefore effect a stronger flow acceleration on this part of the blade.

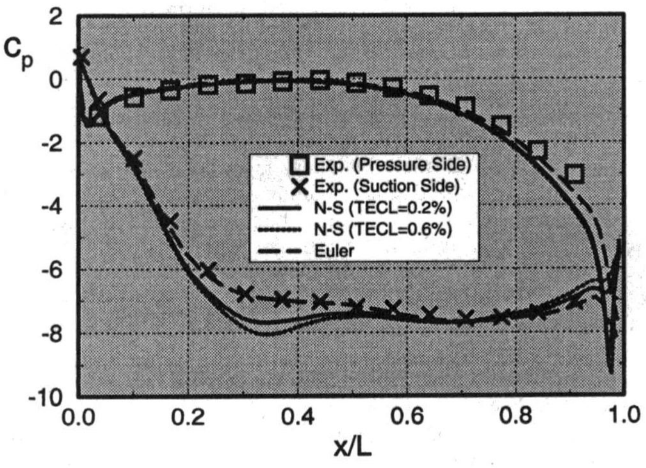

Fig. 2 Theoretical and experimental steady pressure distribution, cascade STC4 (TECL = Trailing Edge Cell Length)

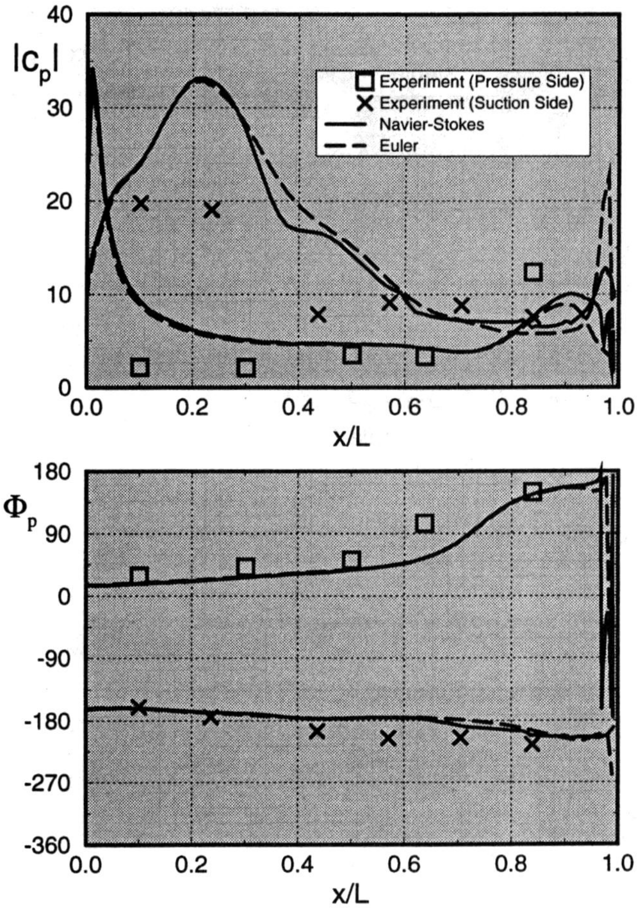

Fig. 3 Theoretical and experimental unsteady pressure distribution, cascade STC4, bending motion, Θ = 180 deg; upper figure: modulus, lower figure: phase

The calculation of the unsteady flow variables for the tuned modes mentioned above has always been performed with the same technique. At rest in steady flow, the blades are started with the prescribed oscillation mode. The calculation is stopped when the peak values of the unsteady lift coefficient for two succesive periods of blade motion do not differ from each other more than 0.1 percent. Since the reduced frequencies for the regarded test cases are low, three or four cycles of blade motion were enough to drive the solution to the desired convergence. By applying a Fourier analysis to the time-dependent values of the last calculated period, the first harmonic of the unsteady pressure and lift coefficients were obtained and compared with the corresponding measured data. Denoting the nondimensional amplitude of a harmonic bending vibration by y_0/L, the unsteady pressure coefficient is defined as the complex number

$$c_{p_{us}} = \frac{\tilde{p}e^{i\phi}}{(y_0/L)(p_{t_1} - p_1)}, \tag{26}$$

where $\tilde{p}$ and ϕ are the unsteady pressure amplitude and the phase angle with respect to the blade motion.

Figure 3 shows the comparison of the computed with the measured unsteady pressure distributions for the interblade phase angle Θ = 180 deg. The results of the first harmonics are presented in a module phase diagram. The unsteady pressure data predicted by the Navier–Stokes and Euler code are in reasonable agreement with each other and with the measured ones, except for the peak region of the suction side. Although large discrepancies occur in the front portion of the suction surface, the phase lead or lag of the pressure coefficient with respect to the blade motion is in agreement with the experiment. An important quantity easily obtained by integration of the out-of-phase part of the unsteady pressure coefficient is the aerodynamic damping. In Fig. 4 this damping coefficient is presented as function of the interblade phase angle. Figure 4 demonstrates the strong influence of Θ on the aerodynamic

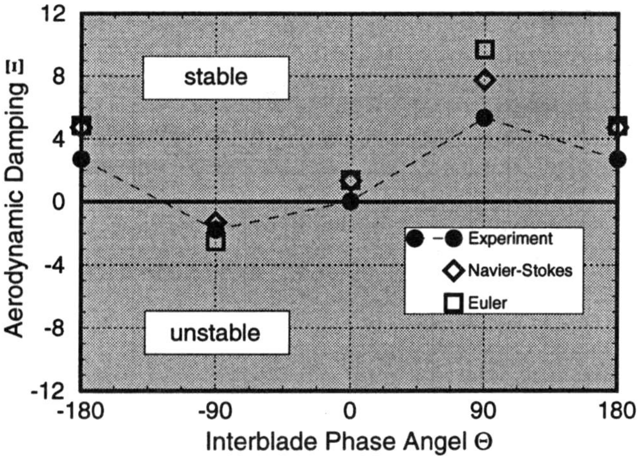

Fig. 4 Aerodynamic damping versus interblade phase angel, cascade STC4, bending motion

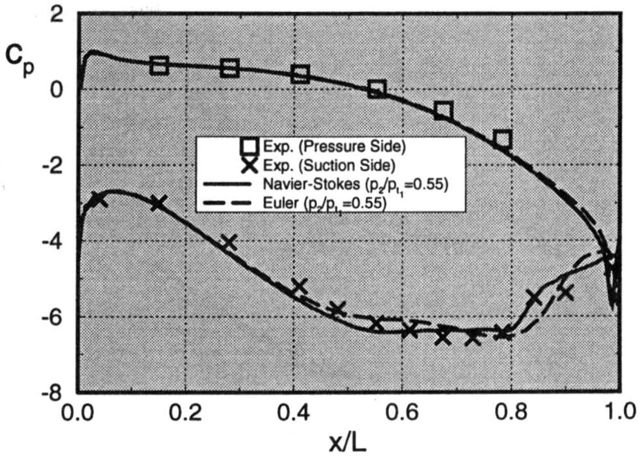

Fig. 6 Theoretical and experimental steady pressure distribution, cascade TCT3, design flow, increased exit pressure

stability of tuned modes. Vibrations with interblade phase angles in the domain of +90 deg are clearly damped, whereas significant excitation occurs for Θ values in the area of −90 deg. The agreement between predicted and measured damping coefficients is good, although the damping at Θ = +90 deg is overpredicted.

Transonic Gas Turbine Cascade, Design Flow. This test case is characterized by transonic flow on the suction side of the blade where the supersonic region is terminated by a normal shock at approximately 80 percent of the chord length. The steady pressure distribution is depicted in Fig. 5. The pressure coefficient on the pressure side is well predicted by the Navier–Stokes and Euler codes. As in the previous case, the pressure distribution on the suction side again significantly depends on the fineness of the grid at the trailing edge. Coarser grids effect an upstream movement of the shock due to the displacement of mass flow to the suction side of the blades. Again, for TECL values below 0.25 percent no further changes of the flow values are observable.

In contrast to the Euler results, which reproduce the shock position too far behind the measured location, the Navier–Stokes computation predicts a shock position, which is markedly closer to the experimental value. Due to the shock-induced separation bubble, which effects a sudden thickening of the boundary layer, the shock moves upstream, since the pressure gradient in front of the shock is fairly small.

In order to investigate the influence of the shock position on the unsteady pressure and lift coefficients, the exit pressure ratio was increased until the predicted shock position was almost identical to the measured one. To achieve this, the exit pressure ratio p_2/p_{t_1} has to be raised from 0.53 to 0.55 (4 percent of its original value). Figure 6 shows the corresponding steady pressure coefficients of the Navier–Stokes and the Euler calculations. Again, the shock position predicted by the Euler code is located too far downstream.

In Fig. 7 the unsteady pressure distributions are plotted for Θ = 180 deg and both exit pressure values. On the blade's

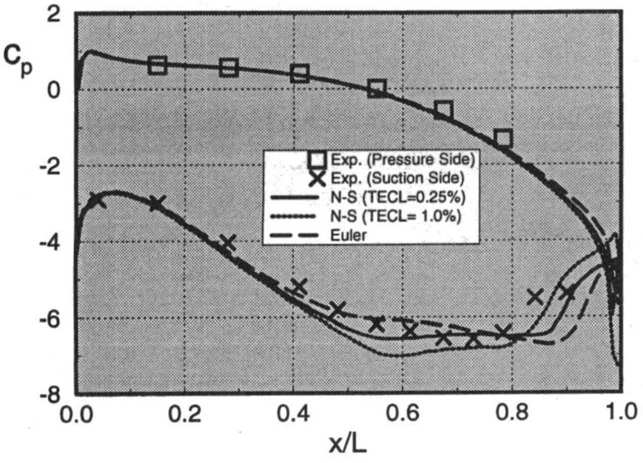

Fig. 5 Theoretical and experimental steady pressure distribution, cascade TCT3, design flow, (TECL = Trailing Edge Cell Length)

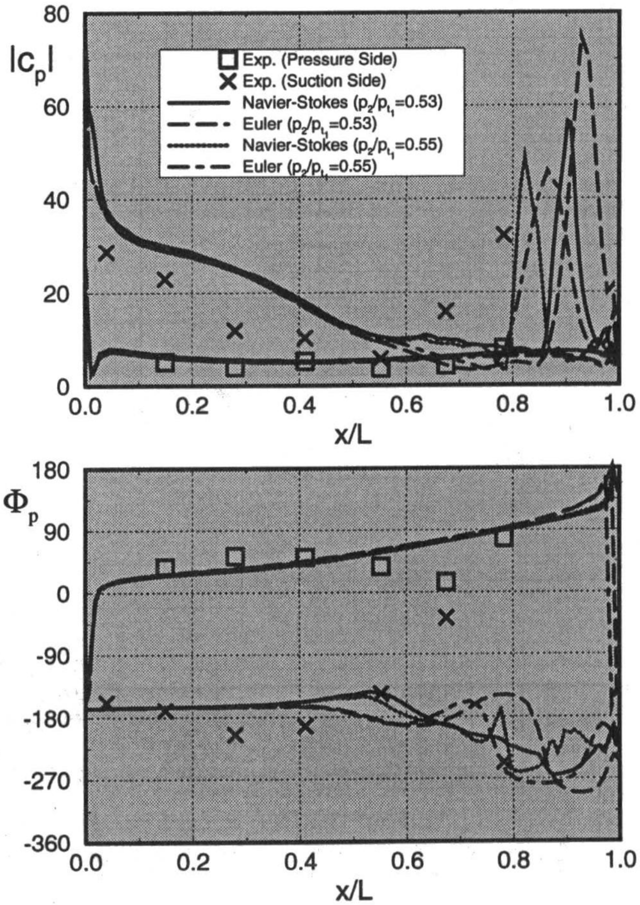

Fig. 7 Theoretical and experimental unsteady pressure distribution, cascade TCT3, design flow, bending motion, Θ = 180 deg, upper figure: modulus, lower figure: phase

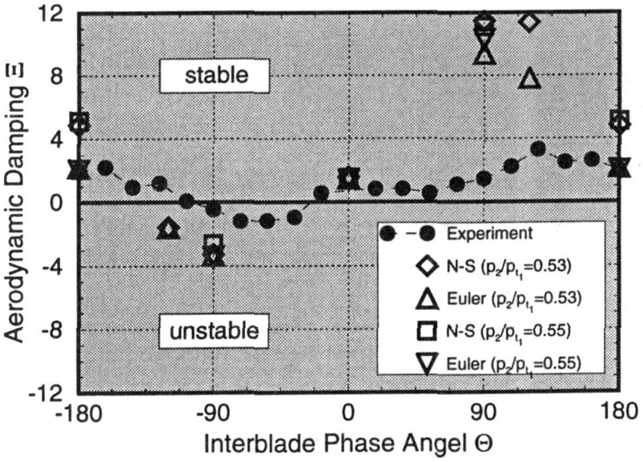

Fig. 8 Aerodynamic damping versus interblade phase angel, cascade TCT3, design flow, bending motion

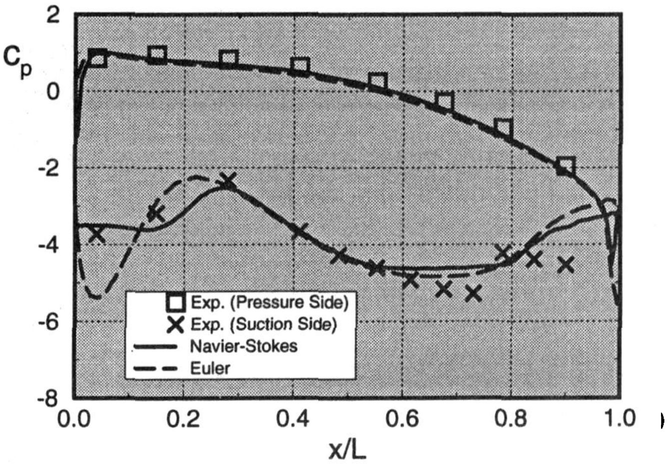

Fig. 9 Theoretical and experimental steady pressure distribution, cascade TCT3, off-design flow

pressure side the Navier–Stokes and Euler results are in good agreement with the experimental data. Furthermore, the unsteady pressure modulus and phase on the suction side are fairly well reproduced in the region in front of the shock, whereas the shock position as well as absolute pressure and phase in the region of the shock are not met satisfactorily by the theoretical results. When comparing Navier–Stokes and Euler results, the Navier–Stokes code produces the more accurate data with respect to the shock position where the best agreement is obtained with the higher exit pressure ratio $p_2/p_{t_1} = 0.55$.

The aerodynamic damping of the measured and computed results is depicted in Fig. 8, where the experimental damping coefficients have been calculated from the measured pressure data. Since the unsteady pressure has been measured with only seven transducers on the suction side (only one transducer in the shock region) and six on the pressure side, the aerodynamic damping can be integrated only with some inaccuracy. The agreement between experiment and theory is satisfactory, although the absolute values of damping in the stable and unstable domains are overpredicted by the computed results. A further important result is obtained by comparing the theoretical results obtained for the two different values of p_2/p_{t_1}. Both codes yield approximately the same damping coefficients, the consequence of which is that the shock position in this test case does not essentially influence aerodynamic damping.

Transonic Gas Turbine Cascade, Off-Design Flow. The experiments for this test case were performed at an off-design inflow angle of $\beta_1 = 33$ deg, which differs widely from the nominal inlet angle, which is given as 15 deg. From surface paint flow visualization, it can be concluded that a separation bubble exists from the leading edge to approximately 30 percent of the chord length on the suction side. After the separation bubble, the flow is accelerated to supersonic values and is recompressed by a normal shock at three quarters of the chord length.

The steady pressure coefficients depicted in Fig. 9 show that the separation bubble is correctly predicted by the Navier–Stokes code, whereas the Euler code, having reached the limit of its performance, produces a large nonphysical suction peak. In comparison to the experiment, both methods predict the shock too far downstream and produce an overly high pressure level in front of the shock. Since this pressure level is slightly higher in the Euler results, which supports an upstream movement of the shock, there exists no observable difference between the Navier–Stokes and Euler data with respect to the shock location. On the pressure side of the blade the computed pressure coefficients are, as in the previous cases, in agreement with the measured data.

Unsteady pressure coefficients for an interblade phase angle of $\Theta = 180$ deg are depicted in Fig. 10. Here, the modulus, as well as the phase, of the computed unsteady pressure is in good agreement with the experimental values on the pressure side. The same is valid for the region on the suction side ahead of the shock, with the exception that the absolute pressure is overpredicted at the position of the separation bubble, whereby the peak value of the Navier–Stokes results is 10 percent of the chord length behind the corresponding peak of the Euler result. At the shock the computed results of absolute pressure

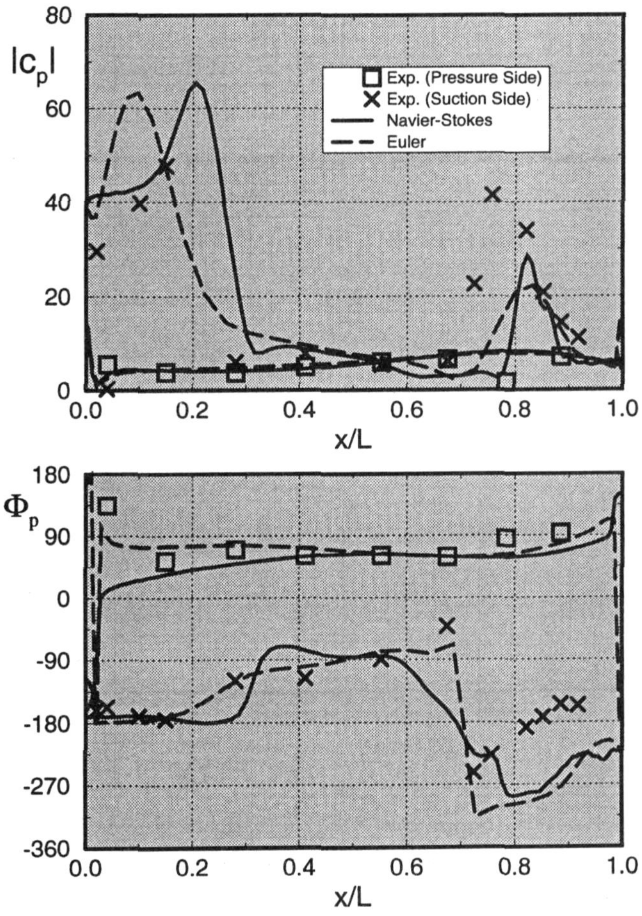

Fig. 10 Theoretical and experimental unsteady pressure distribution, cascade TCT3, off-design flow, bending motion, $\Theta = 180$ deg, upper figure: modulus, lower figure: phase

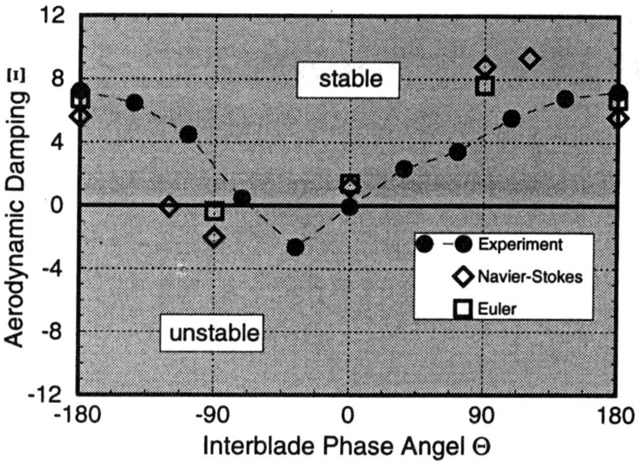

Fig. 11 Aerodynamic damping versus interblade phase angel, cascade TCT3, off-design flow, bending motion

are significantly lower than the experimentally determined values, a fact that is explained by the higher calculated steady pressure coefficient in front of the shock.

Finally, the aerodynamic damping is presented as function of the interblade phase angle Θ in Fig. 11. The agreement between theoretical and experimental damping is better than in the case of design flow. Since both codes correctly predict the pressure phase by $\Phi_p \approx 180$ deg in the region of the separation bubble, i.e., the unsteady pressure at this position does not contribute to the aerodynamic damping, no larger differences are noticeable when comparing the Navier–Stokes and Euler results. Hence, the separation bubble in this test case does not influence the aerodynamic damping.

Concluding Remarks

A two-dimensional Navier–Stokes method for computing the unsteady transonic flow through vibrating blade rows has been presented here. The basic features of the existing code are the use of an appropriate upwind discretization of the inviscid fluxes (AUSM scheme), an implicit time integration of the transformed Navier–Stokes equations, which are solved on deforming grids, and of an algebraic turbulence model (Baldwin–Lomax). Steady and unsteady pressure and damping coefficients have been presented for two different turbine cascade configurations, which were experimentally investigated for tuned bending modes.

The first configuration investigated, the STC4 cascade of the "Workshop on Aeroelasticity in Turbomachines," was merely used for code validation. Comparison between the experimental data of this turbine configuration with the theoretical values clearly shows the capability of the newly developed viscous method to predict unsteady pressure and damping coefficients correctly for nonseparated shock-free flow. Additionally, it was shown that the fineness of the grid at the trailing edge considerably influences the steady and unsteady flow on the suction side.

The results of the second test case, the transonic gas turbine cascade TCT3, demonstrate the capability of the new code to simulate flow separation as well as shock boundary layer interaction. This conclusion may be drawn from the Navier–Stokes results for steady flow where the shock position for design flow is predicted markedly closer to the measured location by the viscous method than by the Euler code. Furthermore, the large separation bubble at the leading edge for off-design flow is well reproduced by the Navier–Stokes method. The unsteady pressure and damping coefficients predicted by the new code are in satisfactory agreement with the experimental data for design as well as for off-design flow, but are closer to the Euler results than to the measured data. Finally, it was found that the leading edge flow separation (off-design flow), as well as the shock position, has only little influence on the aerodynamic damping of the blades.

References

Abhari, R. S., and Giles, M., 1997, "A Navier–Stokes Analysis of Airfoils in Oscillating Transonic Cascades for the Prediction of Aerodynamic Damping," ASME JOURNAL OF TURBOMACHINERY, Vol. 119, pp. 77–84.

Baldwin, B. S., and Lomax, H., 1978, "Thin Layer Approximation and Algebraic Model for Separated Turbulent Flows," AIAA Paper No. 78-257.

Beam, R. M., and Warming, R. F., 1976, "An Implicit Finite-Difference Algorithm for Hyperbolic Systems in Conservation-Law Form," *J. Comp. Phys.*, Vol. 22, pp. 87–110.

Bölcs, A., and Fransson, T. H., 1986, "Aeroelasticity in Turbomachines—Comparison of Theoretical and Experimental Results," *Communications du Laboratoire de Thermique Appliquée et de Turbomachines,* Vol. 13, EPFL, Lausanne.

Carstens, V., 1988, "Two Dimensional Elliptic Grid Generation for Airfoils and Cascades," *DLR-FB,* pp. 88–52.

Carstens, V., 1991, "Computation of the Unsteady Transonic 2D Cascade Flow by an Euler Algorithm With Interactive Grid Generation," AGARD CP 507, Transonic Unsteady Aerodynamics and Aeroelasticity, San Diego, USA, Oct. 7–11.

Carstens, V., Bölcs, A., and Körbächer, H., 1993, "Comparison of Experimental and Theoretical Results for Unsteady Transonic Cascade Flow at Design and Off-Design Conditions," ASME Paper No. 93-GT-100.

Carstens, V., 1994, "Computation of Unsteady Transonic 3D-Flow in Oscillating Turbomachinery Bladings by an Euler Algorithm With Deforming Grids," *Proc. 7th International Symposium on Unsteady Arodynamics and Aeroelasticity of Turbomachines,* Fukuoka, Japan, Sept. 25–29.

Chakravarthy, S. R., 1982, "Euler Equations—Implicit Schemes and Boundary Conditions," AIAA Paper No. 82-0228.

Dorney, D. J., and Verdon, J. M., 1994, "Numerical Simulations of Unsteady Cascade Flows," ASME JOURNAL OF TURBOMACHINERY, Vol. 116, pp. 665–675.

Fransson, T. H., 1986, "Numerical Investigation of Unsteady Subsonic Compressible Flows Through Vibrating Cascades," Thesis, Communication du Laboratoire de Thermique Appliquée et de Turbomachines, 12, EPFL, Lausanne.

Gerolymos, G. A., 1988, "Numerical Integration of the Blade-to-Blade Surface Euler Equations in Vibrating Cascades," *AIAA J.,* Vol. 26, pp. 1483–1492.

Gerolymos, G. A., and Vallet, I., 1994, "Validation of Three-Dimensional Euler Methods for Vibrating Cascade Aerodynamics," ASME JOURNAL OF TURBOMACHINERY, Vol. 118, pp. 771–782.

Giles, M., and Haimes, R., 1993, "Validation of a Numerical Method for Unsteady flow Calculations," ASME JOURNAL OF TURBOMACHINERY, Vol. 115, pp. 110–117.

Hall, K. C., and Crawley, E. F., 1989, "Calculation of Unsteady Flows in Turbomachinery Using the Linearized Euler Equations," *AIAA J.,* Vol. 27, pp. 777–787.

He, L., 1990, "An Euler Solution for Unsteady Flows Around Oscillating Blades," ASME JOURNAL OF TURBOMACHINERY, Vol. 112, pp. 714–722.

He, L., and Denton, J. D., 1994, "Three-Dimensional Time-Marching Inviscid and Viscous Solutions for Unsteady Flows Around Vibrating Blades," ASME JOURNAL OF TURBOMACHINERY, Vol. 116, pp. 469–476.

Huff, D. L., 1991, "Unsteady Flow Field Predictions for Oscillating Cascades," *Proc. 6th International Symposium on Unsteady Aerodynamics, Aeroacoustics and Aeroelasticity of Turbomachines and Propellers,* University of Notre Dame, USA, Sept. 15–19.

Kahl, G., and Klose, A., 1993, "Computation of the Linearized Transonic Flow in Oscillating Cascades," ASME Paper No. 93-GT-269.

Liou, M. S., and Steffen, C. J., Jr., 1993, "A New Flux Splitting Scheme," *J. Comp. Phys.,* Vol. 107, pp. 23–39.

Peitsch, D., Gallus, H. E., and Kau, H. P., 1991, "Prediction of Unsteady 2D Flow in Turbomachinery Bladings," *Proc. 6th International Symposium on Unsteady Aerodynamics, Aeroacoustics and Aeroelasticity of Turbomachines and Propellers,* University of Notre Dame, USA, Sept. 15–19.

Peitsch, D., Gallus, H. E., and Weber, S., 1994, "Computation of Unsteady Transonic 3D-Flow in Turbomachine Bladings," *Proc. 7th International Symposium on Unsteady Aerodynamics and Aeroelasticity of Turbomachines,* Fukuoka, Japan, Sept. 25–29.

Rai, M. M., 1985, "Navier–Stokes Simulations of Rotor–Stator Interaction Using Patched and Overlaid Grids," AIAA Paper No. 85-1519.

Sidén, L. D. G., 1991, "Numerical Simulation of Unsteady Viscous Compressible Flows Applied to Blade Flutter Analysis," ASME No. Paper 91-GT-203.

Steger, J. L., and Warming, R. F., 1981, "Flux Vector Splitting of the Inviscid Gasdynamic Equations With Application to Finite-Difference Methods," *J. Comp. Phys.,* Vol. 40, pp. 263–293.

van Leer, B., 1979, "Towards the Ultimate Conservative Difference Scheme, V. A Second Order Sequel to Godunov's Method," *J. Comp. Phys.,* Vol. 32, pp. 101–136.

van Leer, B., 1982, "Flux Vector Splitting for the Euler Equations," ICASE Report No. 82-30.

Verdon, J. M., and Caspar, J. K., 1984, "A Linear Aerodynamic Analysis for Unsteady Transonic Cascades," NASA-CR 3833.

Whitehead, D. S., and Grant, R. J., 1980, "Force and Moment Coefficients for High-Deflection Cascades," *Proc. 2nd Symposium for Aeroelasticity of Turbomachines,* EPFL, Lausanne.

Validation of a Nonlinear Unsteady Aerodynamic Simulator for Vibrating Blade Rows

T. C. Ayer

J. M. Verdon

United Technologies Research Center,
Theoretical & Computational
Fluid Dynamics,
East Hartford, CT 06108

A time-accurate Euler/Navier–Stokes analysis is applied to predict unsteady subsonic and transonic flows through a vibrating cascade. The intent is to validate this nonlinear analysis along with an existing linearized inviscid analysis via result comparisons for unsteady flows that are representative of those associated with blade flutter. The time-accurate analysis has also been applied to determine the relative importance of nonlinear and viscous effects on blade response. The subsonic results reveal a close agreement between inviscid and viscous unsteady blade loadings. Also, the unsteady surface pressure responses are essentially linear, and predicted quite accurately using a linearized inviscid analysis. For unsteady transonic flows, shocks and their motions cause significant nonlinear contributions to the local unsteady response. Viscous displacement effects tend to diminish shock strength and impulsive unsteady shock loads. For both subsonic and transonic flows, the energy transfer between the fluid and the structure is essentially captured by the first-harmonic component of the nonlinear unsteady solutions, but in transonic flows, the nonlinear first-harmonic and the linearized inviscid responses differ significantly in the vicinity of shocks.

Introduction

For the most part, the unsteady aerodynamic analyses that are being used in turbomachinery aeroelastic and aeroacoustic design studies are based on linearized inviscid flow theory. Such analyses meet the need for efficient unsteady aerodynamic response predictions, but, of necessity, they ignore potentially important physical properties of the flow, including the effects of moderate to large amplitude unsteady excitation and the effects of viscous-layer displacement and separation. A time-accurate, nonlinear, Euler/Navier–Stokes analysis, or numerical unsteady aerodynamic simulator, is therefore needed to understand the relative importance of nonlinear and viscous effects on the unsteady flows associated with turbomachinery blade vibration and blade-row noise generation.

Since the mid-1980's, a number of Euler and Navier–Stokes procedures have been developed. These have been applied to predict flows through single blade rows in which the unsteadiness is caused by prescribed blade vibrations (Huff and Reddy, 1989; He, 1990; Siden, 1991) or by prescribed aerodynamic disturbances at the inflow or outflow boundaries (Giles, 1988), and flows through aerodynamically coupled arrays in which the unsteadiness is caused by the relative motions of adjacent blade rows (Rai, 1987, 1989).

Because of these recent and important advances in the numerical simulation of unsteady flows, it has become appropriate to carefully validate and, if necessary, extend Euler/Navier–Stokes procedures for the prediction of turbomachinery aeroelastic and aeroacoustic response phenomena. A validated analysis for turbomachinery unsteady flows can provide engineers with useful insights into the nonlinear and viscous effects associated with blade vibration and discrete-tone noise generation. It could also provide a test bed for evaluating and improving the asymptotic, i.e., the linearized inviscid and high Reynolds number, inviscid/viscid interaction, models that are being used in aeroelastic and aeroacoustic design prediction systems.

Usually, numerical procedures are verified via result comparisons with experimental data (e.g., see Manwaring and Wisler, 1993), but because of the numerous controlling parameters and uncertainties involved in turbomachinery unsteady flows, it is often difficult to ascertain causes for the differences between the numerical and experimental results. Thus, we are taking an alternative approach, one in which solutions based upon very different analytical procedures are compared, both to validate the procedures and to understand the relevant unsteady flow phenomena.

In a previous investigation (Dorney and Verdon, 1994), the multi-blade-row Navier–Stokes analysis, ROTOR2, developed by Rai (1987), was modified and applied to predict unsteady subsonic flows, excited by prescribed external aerodynamic disturbances, through isolated, two-dimensional blade rows (the gust response problem). Numerical simulations were performed for inviscid and viscous unsteady flows, and the predicted results were compared with those based on linearized inviscid flow theory. For small-amplitude excitations, the unsteady pressure responses predicted by the nonlinear and linearized analyses showed very good agreement, both in the field and along the blade surfaces. Based upon a limited range of parametric studies, it was also observed that the unsteady surface pressure responses to inlet vortical and acoustic excitations were linear over a surprisingly wide range of excitation amplitudes, but acoustic excitations from downstream produced responses with significant nonlinear content.

In the present study we have applied a numerical simulator to gain insight into the importance of nonlinear and viscous effects on the unsteady aerodynamic responses to prescribed blade motions (the flutter problem). Euler and Navier–Stokes solutions have been determined for subsonic and transonic unsteady cascade flows, using the NPHASE analysis (Swafford et al., 1994). NPHASE is a multiblock, finite-volume analysis, that was constructed by Huff et al. (1991) for the time-accurate resolution of two-dimensional, nonlinear, unsteady flows through vibrating cascades.

In the present paper, numerical results will be presented for unsteady flows through a high-speed compressor cascade; namely, the Tenth Standard Cascade of Fransson and Verdon (1993). We will consider unsteady subsonic and transonic flows

---

Contributed by the International Gas Turbine Institute and presented at the 41st International Gas Turbine and Aeroengine Congress and Exhibition, Birmingham, United Kingdom, June 10–13, 1996. Manuscript received at ASME Headquarters February 1996. Paper No. 96-GT-340. Associate Technical Editor: J. N. Shinn.

driven by blade torsional and bending vibrations. NPHASE results will be compared with those obtained from the linearized inviscid analysis LINFLO (Verdon, 1993) to help demonstrate and validate this Euler/Navier–Stokes prediction capability, and to determine the relative importance of nonlinear and viscous effects on unsteady aerodynamic response.

Flow Through a Vibrating Cascade

We consider time-dependent flow, at high Reynolds number (Re) and with negligible body forces, of a perfect gas with constant specific heats through a two-dimensional cascade, such as the one shown in Fig. 1. We assume that the unsteady fluctuations in the flow are due to prescribed blade motions, and the flows far upstream and far downstream from the blade row are at most small perturbations of uniform free streams.

In the following discussion, all physical variables are dimensionless. Lengths have been scaled with respect to blade chord, time with respect to the ratio of blade chord to upstream free-stream flow speed, density and velocity with respect to their upstream free-stream values and stress, and therefore, pressure, with respect to the product of the upstream free-stream density and the square of the upstream free-stream speed. The scalings for the remaining variables can be determined from the equations given below, which have the same forms as their dimensional counterparts.

We will analyze the unsteady flow in a blade-row fixed coordinate frame in terms of the independent variables, $\mathbf{x}$ and t, where $\mathbf{x}(\bar{\mathbf{x}}, t) = \bar{\mathbf{x}} + \mathscr{R}(\bar{\mathbf{x}}, t)$ is a position vector that describes the instantaneous location of a moving field or boundary point, say $\mathcal{P}$, and t is time. The vector $\bar{\mathbf{x}}$ refers to the mean or steady-state position of $\mathcal{P}$, and $\mathscr{R}(\bar{\mathbf{x}}, t)$ describes the displacement of $\mathcal{P}$ from its mean position. $\mathscr{R}$ is prescribed such that the solution domain moves with solid boundaries and is stationary far from the blade row.

The mean or steady-state positions of the blade chord lines coincide with the line segments $\bar{\eta} = \bar{\xi} \tan \Theta + mG$, $0 \leq \bar{\xi} \leq \cos \Theta$, $m = 0, \pm 1, \pm 2, \ldots$, where $\bar{\xi}$ and $\bar{\eta}$ are Cartesian coordinates in the axial flow and cascade tangential directions, respectively, m is a blade number index, Θ is the cascade stagger angle, and $G = |\mathbf{G}|$, where $\mathbf{G}$ is the cascade gap vector (see Fig. 1). The blade motions are defined by

$$\mathbf{x}_{\mathcal{B}_m} = \bar{\mathbf{x}}_{B_m} + \mathscr{R}_{B_m}(\bar{\mathbf{x}}_{B_m}, t), \quad m = 0, \pm 1, \pm 2, \ldots . \tag{1}$$

These motions exhibit phase-lagged, blade-to-blade, periodicity, i.e., $\mathscr{R}_{B_m}(\bar{\mathbf{x}} + m\mathbf{G}, t - m\sigma/\omega) = \mathscr{R}_B(\bar{\mathbf{x}}, t)$ for $\bar{\mathbf{x}} \in B$, where the vector, $\mathscr{R}_B$, describes the motion of a point on the moving reference ($m = 0$) blade, $\mathcal{B}$, relative to its mean position on B.

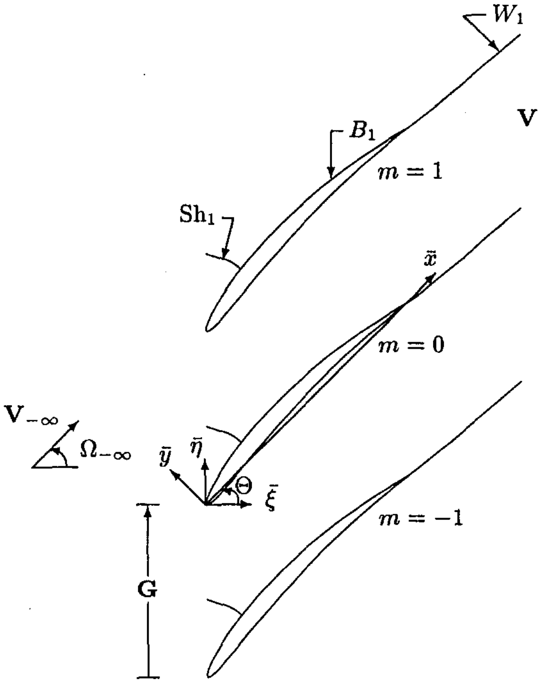

Fig. 1 **Two-dimensional transonic compressor cascade**

Fluid Dynamic Equations

The field equations for the flow, i.e., the Reynolds-averaged Navier–Stokes equations, are determined from the conservation laws for mass, momentum, and energy, the thermodynamic relations for a perfect gas, and the constitutive relations for a Newtonian fluid. It is useful to write these equations in terms of curvilinear spatial coordinates (α_1, α_2) and the time $\tau = t$, i.e.,

$$\left.\frac{\partial \hat{\mathbf{U}}}{\partial \tau}\right|_{\alpha} + \frac{\partial}{\partial \alpha_j}(\hat{\mathbf{F}}_j + \hat{\mathbf{G}}_j) = 0, \tag{2}$$

where the α_1 and α_2 coordinate curves generally lie parallel and normal to the blade surfaces,

$$\hat{\mathbf{U}} = J^{-1}\mathbf{U}, \quad \hat{\mathbf{F}}_j = J^{-1}\left(\frac{\partial \alpha_j}{\partial t}\mathbf{U} + \frac{\partial \alpha_j}{\partial x_k}\mathbf{F}_k\right),$$

$$\hat{\mathbf{G}}_j = J^{-1}\left(\frac{\partial \alpha_j}{\partial x_k}\mathbf{G}_k\right), \tag{3}$$

J is the Jacobian of the transformation $(\mathbf{x}, t) \rightarrow (\boldsymbol{\alpha}, \tau)$, and a summation over repeated indices is implied.

The physical state vector $\mathbf{U}$, and the physical flux vectors $\mathbf{F}_j$ and $\mathbf{G}_j$, $j = 1, 2$, in Eq. (2), are given by

$$\mathbf{U}^T = [\rho \quad \rho V_{x_1} \quad \rho V_{x_2} \quad \rho E_T],$$

$$\mathbf{F}_j = \begin{bmatrix} \rho V_{x_j} \\ \rho V_{x_1} V_{x_j} + P\delta_{1j} \\ \rho V_{x_2} V_{x_j} + P\delta_{2j} \\ \rho(E_T + P/\rho)V_{x_j} \end{bmatrix},$$

$$\mathbf{G}_j = \begin{bmatrix} 0 \\ -\Pi_{x_1 x_j} \\ -\Pi_{x_2 x_j} \\ -\Pi_{x_j x_i} V_{x_i} + Q_{x_j} \end{bmatrix}. \tag{4}$$

where ρ, $\mathbf{V}$, $E_T = E + V^2/2$, and $P = (\gamma - 1)\rho(E_T - V^2/2)$ are the fluid density, velocity, specific total internal energy, and pressure, respectively, γ is the fluid specific heat ratio, and $\Pi_{x_i x_j}$ and Q_{x_i} are the components of the viscous stress tensor and the heat flux vector, respectively. The heat flux is related to the fluid temperature, $T = \gamma(E_T - V^2/2)$, by Fourier's law.

The effects of random turbulent fluctuations are accommodated by incorporating turbulent correlations into the relations for the stress tensor and the heat flux vector. These correlations are related to gradients in the ensemble-averaged or mean-flow variables using algebraic eddy viscosity models.

For turbomachinery applications the field Eqs. (2) must be supplemented by conditions at the vibrating blade surfaces and at the cascade inflow and outflow boundaries. Since transient unsteady aerodynamic behavior will not be considered, a precise knowledge of the initial state of the fluid is not required. The no-slip condition, i.e., $\mathbf{V} = \dot{\mathscr{R}}_{\mathcal{B}_m}$ for $\mathbf{x} \in \mathcal{B}_m$, applies at blade surfaces. In addition, either the heat flux $\mathbf{Q} \cdot \mathbf{n}_{\mathcal{B}_m}$ or the temperature T must be prescribed at such surfaces. Averaged values of the total pressure, total temperature and flow angle are specified at inlet, i.e., at $\xi = \xi_-$ and the averaged value of the static pressure is specified at the exit boundary, $\xi = \xi_+$. Total pressure and total temperature fluctuations at exit and outgoing pressure disturbances at inlet and exit must be determined as part of the unsteady solution.

High-Reynolds-Number Flow. For most flows of practical interest, the Reynolds number (Re) is sufficiently high so that the viscous effects are concentrated within thin layers that lie along the blade surfaces (boundary layers), and extend downstream from the blade trailing edges (wakes). Such flows can be described by approximate field equations, known as the thin-layer equations, leading to a substantial reduction in the computational resources needed to determine viscous unsteady solutions. The thin-layer equations are derived from Eq. (2) by assuming that gradients in the viscous flux terms parallel to a blade or wake, i.e., $\partial\hat{\mathbf{G}}_1/\partial\alpha_1$, and velocity and temperature gradients in the α_1 direction are negligible.

The field equations resulting from the foregoing approximations are

$$\left.\frac{\partial\hat{\mathbf{U}}}{\partial\tau}\right|_{\boldsymbol{\alpha}} + \frac{\partial}{\partial\alpha_j}\hat{\mathbf{F}}_j + \frac{\partial}{\partial\alpha_2}\hat{\mathbf{G}}_2 = 0, \tag{5}$$

where

$$\hat{\mathbf{G}}_2 \approx -(J\,\mathrm{Re})^{-1} \times \begin{bmatrix} 0 \\ \mu_{\mathrm{eff}}\left(K_1\dfrac{\partial V_{x_1}}{\partial\alpha_2} + K_2\dfrac{\partial\alpha_2}{\partial x_1}\right) \\ \mu_{\mathrm{eff}}\left(K_1\dfrac{\partial V_{x_2}}{\partial\alpha_2} + K_2\dfrac{\partial\alpha_2}{\partial x_2}\right) \\ K_1\left[\mu_{\mathrm{eff}}\dfrac{\partial(V^2/2)}{\partial\alpha_2} + k_{\mathrm{eff}}\,\mathrm{Pr}^{-1}\dfrac{\partial T}{\partial\alpha_2}\right] + K_2K_3 \end{bmatrix}, \tag{6}$$

with

$$K_1 = \left(\frac{\partial\alpha_2}{\partial x_1}\right)^2 + \left(\frac{\partial\alpha_2}{\partial x_2}\right)^2,$$

$$K_2 = (1/3)\left(\frac{\partial\alpha_2}{\partial x_1}\frac{\partial V_{x_1}}{\partial\alpha_2} + \frac{\partial\alpha_2}{\partial x_2}\frac{\partial V_{x_2}}{\partial\alpha_2}\right), \tag{7}$$

and

$$K_3 = V_{x_1}\frac{\partial\alpha_2}{\partial x_1} + V_{x_2}\frac{\partial\alpha_2}{\partial x_2}.$$

In Eq. (6), Pr is the Prandtl number of the flow, and $\mu_{\mathrm{eff}} = \mu + \epsilon$ and $k_{\mathrm{eff}} = k + (\mathrm{Pr}/\mathrm{Pr}_T)\epsilon$, where Pr_T is the turbulent Prandtl number, are the effective viscosity and the effective thermal conductivity, respectively. In the present study, we set Pr = 0.72 and $\mathrm{Pr}_T = 0.9$. The coefficients of shear viscosity, μ, and thermal conductivity, k, are related to the temperature using Sutherland's Law, and the turbulent eddy viscosity ϵ is determined using the Baldwin and Lomax (1978) turbulence model for blade boundary layers and the Thomas (1979) model for blade wakes.

Inviscid Flow. The field equations that govern the fluid motion in the inviscid limit ($\mathrm{Re} \to \infty$), i.e., the Euler equations, are obtained from Eq. (5) by setting $\hat{\mathbf{G}}_2 \equiv 0$. In principle, the inviscid field equations must be supplemented by jump conditions that apply at vortex-sheet wakes, W_m, and at shocks, Sh_m (see Fig. 1). However, the usual practice is to solve the inviscid field equations over the entire fluid domain, in an attempt to capture discontinuous wake and shock phenomena. The inviscid flow is then determined as a solution of the Euler equations subject to flow tangency conditions, i.e., $(\mathbf{V} - \dot{\mathcal{R}}_{B_m})\cdot\mathbf{n} = 0$, at the moving blade surfaces. The far-field conditions used in the inviscid approximation are the same as those indicated previously for Navier–Stokes simulations.

NPHASE Analysis

An implicit, flux-split, finite-volume analysis for nonlinear unsteady flows has been developed by Whitfield et al. (1988). This analysis was subsequently extended and implemented into the turbomachinery unsteady flow code, NPHASE, by Huff et al. (1991). NPHASE is a multiblock, cell-centered, finite-volume code, that can be used for predicting two-dimensional, nonlinear, viscous, at high Reynolds number, and inviscid unsteady flows through vibrating cascades. A brief description of the NPHASE analysis is given below. A detailed description can be found in Swafford et al. (1994) and the references cited therein.

The computational mesh used in NPHASE is a sheared, moving **H**-mesh, typically generated using the IGB grid generation package of Beach and Hoffman (1992). A coordinate transformation, $(\mathbf{x}, t) \to (\boldsymbol{\alpha}, \tau)$, where $\mathbf{x} = \bar{\mathbf{x}} + \mathcal{R}(\bar{\mathbf{x}}, t)$, from the physical domain, in which the grid deforms with the blade motion, to a computational domain, in which the grid is stationary, uniform, and orthogonal, is applied to simplify the implementation of numerical differencing and flow boundary conditions. The prescribed displacement field, $\mathcal{R}(\bar{\mathbf{x}}, t)$, is determined here as a solution of Laplace's equation, subject to the conditions $\mathcal{R} = \mathcal{R}_{B_m}$ at blade surfaces, $\mathcal{R} = 0$ in the far field and to the requirement of phase-lagged, passage-to-passage periodicity.

For a finite volume discretization, the time-dependent geometric properties of the mesh cells in physical space are required. These include the cell volume, $\vartheta = J^{-1}$, the volume swept out per unit time by a constant α_j face as the cell moves, $\dot{\vartheta}_j = J^{-1}\partial\alpha_j/\partial t$, and the area of a constant α_j face projected in the x_k direction, $A_{jk} = J^{-1}\partial\alpha_j/\partial x_k$. These properties are determined from the instantaneous locations of the cell vertices in physical space.

Finite Volume Equations. We can write the finite volume spatial discretization of Eq. (5) as

$$\partial\hat{\mathbf{U}}/\partial\tau|_{\boldsymbol{\alpha}} = -\delta_j\hat{\mathbf{F}}_j - \delta_2\hat{\mathbf{G}}_2 = -\hat{\mathbf{R}} \tag{8}$$

where $\hat{\mathbf{U}} = \vartheta\mathbf{U}$, $\hat{\mathbf{F}}_j = -\dot{\vartheta}_j\mathbf{U} + A_{jk}\mathbf{F}_k$ and $\hat{\mathbf{G}}_2 = A_{2k}\mathbf{G}_k$. Here, $\mathbf{U}$ represents an average over the cell volume; $\hat{\mathbf{F}}_j$ is the inviscid flux across a constant α_j cell face; $\hat{\mathbf{G}}_2$ is the viscous flux across a constant α_2 cell face; $\hat{\mathbf{R}}$ is the residual; and the symbol δ denotes the difference across adjacent cell interfaces; so that the sum $\delta_j\hat{\mathbf{F}}_j$ is the net inviscid flux through the cell.

The time-derivative in Eq. (8) is approximated using a second-order, implicit, three-point, backward, difference approximation. After applying this scheme and separating the time dependence of the state vector and the cell volume, we find that

$$\begin{aligned}\hat{\vartheta}\Delta\mathbf{U}^n + \hat{\mathbf{R}}^{n+1} &= \vartheta^{n-1}\Delta\mathbf{U}^{n-1}/2\Delta\tau \\ &-\mathbf{U}^n(3\vartheta^{n+1} - 4\vartheta^n + \vartheta^{n-1})/2\Delta\tau = \mathscr{G}^{n+1},\end{aligned} \tag{9}$$

where $\Delta\mathbf{U}^n = \mathbf{U}^{n+1} - \mathbf{U}^n$, $\hat{\vartheta} = 3\vartheta^{n+1}/2\Delta\tau$, and the superscript n refers to the nth time level. The nonlinear Eq. (9) is solved at each time step using a Newton iteration, i.e.,

$$\begin{aligned}\hat{\vartheta}\Delta\mathbf{U}^p &+ \delta_j(\partial\hat{\mathbf{F}}_j/\partial\mathbf{U}|_{\mathbf{U}^{p-1}}\Delta\mathbf{U}^p) \\ &= \hat{\vartheta}(\mathbf{U}^{p-1} - \mathbf{U}^n) - \hat{\mathbf{R}}^{p-1} + \mathscr{G}^{n+1}\end{aligned} \tag{10}$$

in which the viscous flux term is treated explicitly. Here $p = 1, 2, \ldots,$ is the iteration index, $\mathbf{U}^0 = \mathbf{U}^n$, $\Delta\mathbf{U}^p = \mathbf{U}^p - \mathbf{U}^{p-1}$, and $\mathbf{U}^p$ is the update to the state vector. Once the Newton iteration converges $\Delta\mathbf{U}^p \equiv 0$, and $\mathbf{U}^p \equiv \mathbf{U}^{n+1}$.

Spatial Discretization. Flux splitting is used in NPHASE to evaluate the inviscid flux terms in Eq. (10). The flux terms appearing on the left-hand side are evaluated using a first-order accurate, flux-vector splitting approximation (Steger and Warming, 1981) as a convenience in defining the approximate factorization that is used to facilitate the iterative solution. Although this approximation results in first order spatial accuracy, it is only used in the approximate factorization, and therefore, does not appear in the converged solution.

The inviscid flux vectors that appear in the residual on the right-hand side of Eq. (10) are evaluated using a flux-difference splitting approximation (Roe, 1981), with corrective fluxes included to obtain second-order spatial accuracy. The viscous flux vector, $\hat{\mathbf{G}}_2$, is evaluated at a cell interface in terms of the values of the relevant flow variables in the cell volumes to the left and right of the interface. The individual terms that make up this vector [cf. Eq. (6)] are considered separately, and derivatives of the fluid properties are evaluated using central difference approximations. Once the inviscid and viscous fluxes at the cell interfaces have been evaluated, they are spatially differenced to compute the net flux $\delta_j\hat{\mathbf{F}}_j + \delta_2\hat{\mathbf{G}}_2 = \hat{\mathbf{R}}$ through the cell.

Approximate Factorization. Flux-vector splitting leads to an approximate factorization of Eq. (10) of the form

$$\begin{aligned}\hat{\mathbf{D}}\Delta\mathbf{U}^p - \hat{\mathbf{M}}^{+}_{j-1}\Delta\mathbf{U}^p_{j-1} + \hat{\mathbf{M}}^{-}_{j+1}\Delta\mathbf{U}^p_{j+1}\\ = -\hat{\vartheta}(\mathbf{U}^{p-1} - \mathbf{U}^n) - \hat{\mathbf{R}}^{p-1} + \mathscr{G}^{n+1}, \quad (11)\end{aligned}$$

where j is a grid point index corresponding to the jth computational coordinate direction and the $\hat{\mathbf{D}}$ and $\hat{\mathbf{M}}$ matrices are evaluated based on the state vector $\mathbf{U}^{p-1}$. The $\hat{\mathbf{D}}$ matrix contains the diagonal elements of the iteration matrix, and the $\hat{\mathbf{M}}^+$ and $\hat{\mathbf{M}}^-$ matrices contain the off-diagonal elements in the negative and positive computational coordinate directions, respectively.

To reduce the error introduced by the approximate factorization, Eq. (11) is solved for $\Delta\mathbf{U}^p$ using a symmetric Gauss–Seidel subiteration procedure. The first subiteration is over positive grid indices; the second, over negative grid indices. The subiteration procedure thus involves an *LU* decomposition of the Newton iteration matrix, with forward and backward substitution. Once it converges, Eq. (10) is satisfied. As the overall solution converges, any errors introduced by the Newton iteration or the approximate factorization vanish. Only the errors in the residual calculation remain.

The field Eq. (8) is solved subject to the appropriate surface and far-field conditions. The flow tangency condition used in the inviscid version of the NPHASE analysis is based on a two phantom-cell, pressure-symmetry, implementation to lower the generation of spurious numerical entropy and vorticity at blade surfaces. At present, the far-field conditions, used in NPHASE, are based on one-dimensional characteristic theory and the computational mesh is stretched in the axial direction to dissipate oblique outgoing waves.

Unsteady Excitation and Response

We are restricting our consideration to unsteady flows driven by prescribed rigid-body blade motions of the form

$$\begin{aligned}\mathscr{R}_{B_m} = \tilde{\mathbf{h}}_m(t) + (\mathbf{e}_z \times \mathbf{R}_P)\sin\tilde{\alpha}_m(t)\\ - \mathbf{R}_P[1 - \cos\tilde{\alpha}_m(t)]. \quad (12)\end{aligned}$$

Here, $\tilde{\mathbf{h}}_m(t)$ and $\tilde{\boldsymbol{\alpha}}_m(t) = \tilde{\alpha}_m(t)\mathbf{e}_z$ are the translational and rotational displacement vectors, respectively, for the mth blade, $\mathbf{R}_P$ is the distance from the mean position of the mth blade axis of rotation at $\overline{\mathbf{x}}_{P_m} = \overline{\mathbf{x}}_P + m\mathbf{G}$ to the point $\overline{\mathbf{x}}_{B_m} = \overline{\mathbf{x}}_B + m\mathbf{G}$, and the unit vector $\mathbf{e}_z$ points out from the page. We assume that $\tilde{\mathbf{h}}_m = \mathrm{Re}\{\mathbf{h}\exp[i(\omega t + m\sigma)]\}$ and $\tilde{\boldsymbol{\alpha}}_m = \mathrm{Re}\{\boldsymbol{\alpha}\exp[i(\omega t + m\sigma)]\}$ where $\mathbf{h}$ and $\boldsymbol{\alpha}$ are the complex amplitudes of the reference ($m = 0$) blade displacements, ω is the frequency of the blade motion, σ is the phase angle between the motions of adjacent blades, and Re{ } denotes the real part of { }.

After expanding Eq. (12) into a power series in $\tilde{\alpha}_m$, we find that

$$\mathscr{R}_{B_m}(\overline{\mathbf{x}}_{B_m}, t) \approx \tilde{\mathbf{r}}_{B_m} - \mathbf{R}_P\tilde{\alpha}_m^2/2 + \ldots, \quad (13)$$

where $\tilde{\mathbf{r}}_{B_m} = \mathrm{Re}\{\mathbf{r}_B\exp[i(\omega t + m\sigma)]\}$ is the linearized approximation to a rigid-body blade motion, and $\mathbf{r}_B = (\mathbf{h} + \boldsymbol{\alpha} \times \mathbf{R}_P)$.

Unsteady Aerodynamic Response. It is usually assumed that a periodic unsteady excitation with temporal period $2\pi/\omega$ will produce an unsteady surface pressure response that is also periodic in time, with period $2\pi/\omega$. In this case we can express the pressure, P_B, acting at the moving reference blade surface, $\mathcal{B}$, in the form

$$P_B(\overline{\mathbf{x}}_B, t) = P_0(\overline{\mathbf{x}}_B) + \sum_{n=1}^{\infty}\mathrm{Re}\{p_n(\overline{\mathbf{x}}_B)\exp(in\omega t)\}, \quad (14)$$

where P_0 is the temporal mean value and $p_n(\overline{\mathbf{x}}_B)$, $n = 1, 2, \ldots$, is the complex amplitude of the nth-harmonic component of the unsteady pressure.

Two surface response parameters that are useful in blade aeroelastic studies are the aerodynamic global, W_C, and local, $w_C(\overline{\mathbf{x}}_B)$, works per cycle (Verdon, 1993). The global work per cycle,

$$W_C = -\omega^{-1}\int_{\phi}^{\phi+2\pi}\oint_{\mathcal{B}} P_B\frac{\partial\mathscr{R}_B}{\partial t}\cdot\mathbf{n}_B d\tau_B d(\omega t), \quad (15)$$

where $\mathbf{n}_B$ is a unit normal vector pointing out from the moving blade surface, $\mathcal{B}$, and τ_B measures distance in the counterclockwise direction along this surface, is the work done by the fluid on a given blade over one cycle of its motion. A prescribed blade motion is classified as stable, neutrally stable, or unstable depending upon whether the aerodynamic work per cycle is less than, equal to, or greater than zero, respectively.

If the reference blade displacement, $\mathscr{R}_B$, and hence, the unit normal, $\mathbf{n}_B$, and the surface pressure, P_B, are expressed as functions of $\overline{\mathbf{x}}_B$ and t, we can write

$$W_C = \oint_B w_C(\tau_B)d\tau_B. \quad (16)$$

The function

$$w_C(\tau_B) = -\omega^{-1}\int_{\phi}^{\phi+2\pi} P_B\frac{\partial\mathscr{R}_B}{\partial t}\cdot\mathbf{n}_B d(\omega t) \quad (17)$$

is the local work per cycle or pressure-displacement function. It describes the distribution of the W_C over a blade surface.

If we consider rigid-body blade motions of small-amplitude, introduce the series expansions Eqs. (13) and (14) into Eq. (17), and carry out the integration, we find that

$$\begin{aligned}w_C = -\pi\,\mathrm{Im}\{P_0\alpha\mathbf{r}_B^* \cdot \boldsymbol{\tau}_B + p_1\mathbf{r}_B^* \cdot \mathbf{n}_B\\ + p_2(\alpha^*\mathbf{r}_B^* \cdot \boldsymbol{\tau}_B - \alpha^{*2}\mathbf{R}_P \cdot \mathbf{n}_B)/2\} + \ldots, \quad (18)\end{aligned}$$

where Im{ } indicates the imaginary part of { } and the superscript * denotes the complex conjugate. If, as is assumed in linearized unsteady aerodynamic theory, the time-mean or steady pressure is of $\mathcal{O}(1)$; the first harmonic of the unsteady pressure is of $\mathcal{O}(|\mathscr{R}_B|)$; and the second and higher harmonics of the unsteady pressure are at most of $\mathcal{O}(|\mathscr{R}_B|^2)$; then

$$w_C = -\pi\,\mathrm{Im}\{P_0\alpha\mathbf{r}_B^* \cdot \boldsymbol{\tau}_B + p_1\mathbf{r}_B^* \cdot \mathbf{n}_B\} + \mathcal{O}(|\mathscr{R}_B|^4). \quad (19)$$

Thus, the higher harmonic content of the unsteady pressure response would have a negligible impact on the transfer of energy from the fluid to the structural motion. Also, for single-degree-of-freedom (SDOF) blade motions, or coupled blade motions in which $\tilde{\mathbf{h}}(t)$ and $\tilde{\alpha}(t)$ are in phase, the lead

$[\mathscr{O}(|\mathscr{B}_B|^2)]$ term in Eq. (19) depends only on the first-harmonic unsteady pressure; in particular, on the component of p_1 that is out-of-phase with the blade displacement. Finally, for pure translations ($\tilde{\alpha} = 0$), the transfer of energy depends only on the out-of-phase first-harmonic unsteady pressure. These are important analytical results that can be used to guide the interpretation and validation of nonlinear unsteady aerodynamic predictions.

Numerical Results

NPHASE, nonlinear, unsteady aerodynamic response predictions will be presented below for two-dimensional, inviscid and viscous (at $\mathrm{Re} = 10^6$), flows through the Tenth Standard Cascade. For purposes of comparison, we will also present linear response predictions based on the LINFLO analysis (Usab and Verdon, 1991; Verdon, 1993). In the latter, the unsteady flow is regarded as a small inviscid perturbation of a potential steady background flow. The potential analysis of Caspar (1983) is used to provide steady background flow information needed for the LINFLO calculations. Additional results from this study can be found in Ayer and Verdon (1994).

The Tenth Standard Cascade (Fransson and Verdon, 1993) consists of modified NACA 5506 airfoils. It has a stagger angle, Θ, of 45 deg and a gap/chord ratio, G, of unity, and operates under uniform subsonic inflow conditions. We will consider unsteady subsonic flows occurring at an inlet free-stream Mach number $\mathrm{M}_{-\infty}$ and flow angle, $\Omega_{-\infty}$, of 0.7 and 55 deg, respectively, and unsteady transonic flows occurring at $\mathrm{M}_{-\infty} = 0.8$ and $\Omega_{-\infty} = 58$ deg.

The unsteady flows are excited by prescribed SDOF, harmonic, blade motions. The latter occur at unit frequency ($\omega = 1$) and with constant phase angle σ between the motions of adjacent blades. The blade motions considered are pure translations normal to the blade chords (bending) and pure rotations about axes at the blade midchords (torsion). These motions are termed subresonant if all acoustic response disturbances attenuate with increasing axial distance from the blade row; superresonant (m, n) if m and n such disturbances persist in the far upstream and far downstream flow regions, respectively, and carry energy away from the blade row; and resonant if at least one acoustic response disturbance persists in either the far upstream or far downstream regions of the flow and carries energy along the blade row (Verdon, 1989).

The NPHASE solutions have been determined on H-type meshes. An H-mesh consisting of 141 axial and 41 tangential lines was used for the inviscid subsonic calculations. For inviscid transonic flows, the 161×41 H-mesh, shown in Fig. 2, was applied. The viscous subsonic and transonic calculations were performed on 141×81 and 161×81 meshes, respectively. In each case, the mesh extended 5 axial chords upstream and 9 axial chords downstream from the blade row. The normal mesh spacings for the viscous calculations were defined such that the law-of-the-wall coordinate, Y^+, had an average value of approximately 2.0 at a blade surface.

The full potential steady and the linearized inviscid unsteady solutions were determined on composite meshes consisting of local C-meshes embedded in global H-meshes. The H- and C-meshes used with LINFLO consisted of 155 axial and 41 tangential lines and 101 radial and 11 circumferential lines, respectively. Coarser meshes were used for the CASPOF calculations. Since analytic, two-dimensional, far-field conditions are applied, the H-meshes extended only one axial chord upstream and downstream from the blade row.

The numerical solutions, reported herein, were determined on an IBM-370 Workstation. NPHASE steady subsonic inviscid and viscous solutions required 21 and 52 CPU minutes, respectively; the corresponding transonic solutions, 25 and 61 CPU minutes. The NPHASE unsteady calculations were started from the appropriate steady solution, and performed using 1000 time steps per cycle of blade motion, 3 Newton iterations per time step and 3 symmetric Gauss–Siedel iterations per Newton iteration. Four cycles of motion were needed to converge the nonlinear inviscid and viscous solutions to a periodic state. The subsonic inviscid and viscous calculations required, on average, 48 and 128 CPU min, respectively, per blade passage. The corresponding transonic calculations required 57 and 153 CPU min per passage. The number of blade passages included in a nonlinear unsteady calculation depends upon the interblade phase angle. For example, if $\sigma = 60$ deg, six passages are needed. The steady potential solutions were obtained within 10 CPU seconds, and the LINFLO unsteady solutions required about 90 CPU seconds per case.

Fig. 2 H-mesh used for the NPHASE, steady and unsteady, inviscid, transonic simulations

Steady Background Flows. Predicted surface pressure, P, and wall shear stress, $\tau_w = (\mathrm{Re})^{-1}\mu\partial V_T/\partial n|_w$, distributions for the subsonic and transonic steady background flows are shown in Figs. 3 and 4, respectively. The two subsonic inviscid predictions for the blade surface pressures (Fig. 3(a)) are in very close agreement. The thin-layer Navier–Stokes predictions indicate that viscous-displacement effects cause a slight reduction in the steady pressure loading over the rear half of each blade. The surface shear stress distributions (Fig. 3(b)) indicate that the viscous flow separates ($\tau_w < 0$) from the suction surface of each blade and reattaches just upstream of the trailing edge. The separation region extends from 88 to 98 percent of blade chord.

The predicted exit conditions, i.e., the exit free-stream (isentropic) Mach number, $\mathrm{M}_{+\infty}$, and flow angle, $\Omega_{+\infty}$, and steady lift acting on each blade, F_y, for the subsonic steady flow are as follows: the potential analysis indicates that $\mathrm{M}_{+\infty} = 0.446$, $\Omega_{+\infty} = 40.2$ deg, and $F_y = 0.348$; the Euler analysis, that $\mathrm{M}_{+\infty} = 0.446$, $\Omega_{+\infty} = 39.8$ deg, and $F_y = 0.348$; and the Navier–Stokes analysis yields $\mathrm{M}_{+\infty} = 0.461$, $\Omega_{+\infty} = 41.2$ deg, and $F_y = 0.324$. Thus, viscous-displacement effects cause a 7 percent reduction in the steady lift force that acts on each blade.

The inviscid surface pressure distributions for the steady transonic flow (Fig. 4(a)) are also in good agreement, but differences occur in the vicinity of the shock and in the supersonic region upstream of the shock. Viscous effects reduce the pressure rise across the shock and the pressure-difference loading over most of the blade. The transonic flow separates downstream of the shock and is more or less separated from the

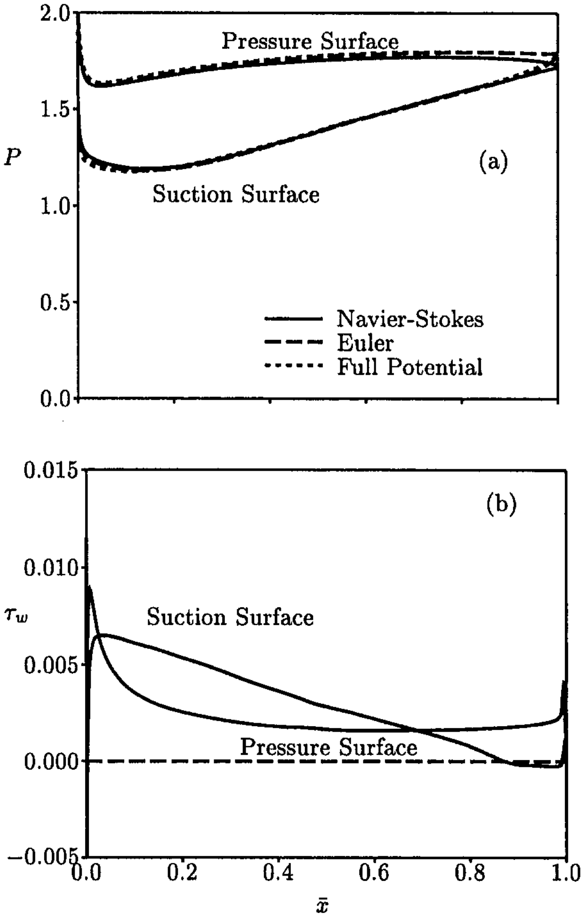

Fig. 3 Predicted steady surface pressure (*a*) and shear stress (*b*) distributions for inviscid and viscous (Re = 10^6) subsonic flows through the 10th Standard Cascade

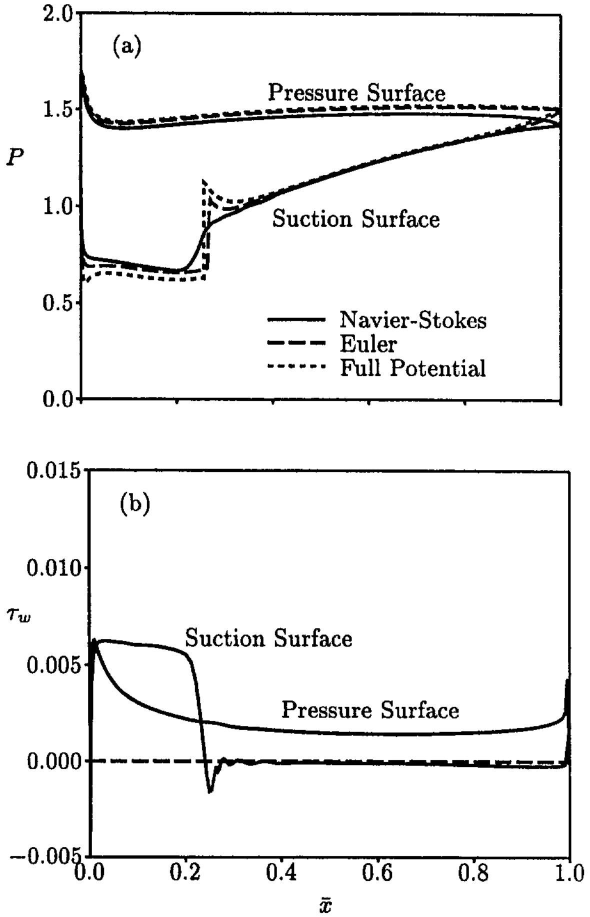

Fig. 4 Predicted steady surface pressure (*a*) and shear stress (*b*) distributions for inviscid and viscous (Re = 10^6) transonic flows through the 10th Standard Cascade

suction surface from just aft of the shock to a point just upstream of the trailing edge.

For this transonic flow, the potential analysis indicates that $M_{+\infty} = 0.432$, $\Omega_{+\infty} = 40.3$ deg, $F_y = 0.412$, and the Mach numbers at the base of each shock are 1.292 on the upstream side and 0.794 on the downstream side. The Euler analysis yields $M_{+\infty} = 0.432$, $\Omega_{+\infty} = 40.0$ deg, $F_y = 0.408$, and isentropic Mach numbers at the base of a shock of 1.22 and 0.871. The Navier–Stokes results are $M_{+\infty} = 0.461$, $\Omega_{+\infty} = 42.6$ deg, and $F_y = 0.372$, and the Mach number is continuous through the shock. The predictions indicate that viscous effects cause a reduction of approximately 9 percent in the steady lift force acting on each blade.

Unsteady Subsonic Flows. We proceed to consider unsteady subsonic flows, at $\omega = 1$, that are excited by in-phase ($\sigma = 0$ deg) torsional blade motions about midchord at $|\alpha| = 2$ deg, and by out-of phase ($\sigma = 180$ deg), bending vibrations at $|h_y| = 0.01$. In particular, we set $\alpha = (2 \text{ deg}, 0)$ and $\mathbf{h} = h_y\mathbf{e}_y$ with $h_y = (0.01, 0)$ to define these blade vibrations. Thus, for both motions, $w_c \approx -\pi \operatorname{Im}\{p_1\}\mathbf{r}_B \cdot \mathbf{n} + \ldots$ [cf. Eq. (19)]. The in-phase motion is superresonant (1, 1); the out-of-phase motion is subresonant.

Instantaneous surface pressure distributions have been determined using the nonlinear inviscid and viscous analyses. The viscous results for the torsional vibration are shown in Fig. 5. The inviscid and viscous unsteady surface pressure predictions are very similar indicating that, although viscous effects cause a small reduction in the time-averaged or mean pressure loading over the latter half of a blade, they have a negligible impact on the unsteady surface pressure fluctuations.

We have processed the NPHASE instantaneous subsonic, inviscid and viscous, surface pressure responses to provide results for the harmonic components, p_n, of the unsteady surface pressure (Ayer and Verdon, 1994), and the local, w_C, and global, W_C, works per cycle. The NPHASE first-harmonic, inviscid and viscous, surface pressure predictions are nearly identical, and they are in very good agreement with LINFLO predictions. Differences occur, however, between the NPHASE and LIN-

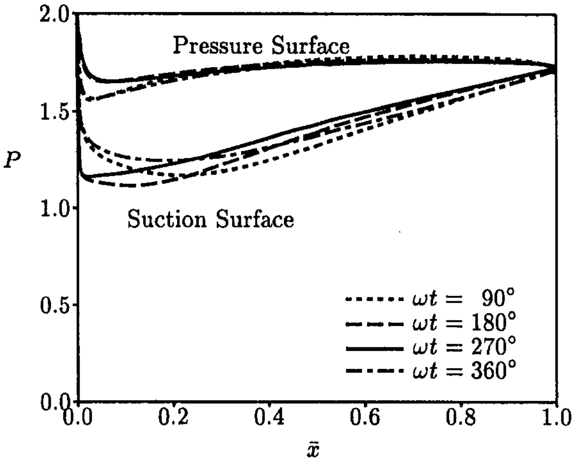

Fig. 5 Instantaneous surface pressure distributions for subsonic viscous flow at Re = 10^6 through the 10th Standard Cascade undergoing an in-phase torsional vibration

FLO results for $\mathrm{Re}\{p_1\}$, i.e., the pressure in phase with the blade displacement, in the vicinity of a blade leading edge. These may be caused by a breakdown in the linearized inviscid approximation at rounded blade leading edges. The nonlinear and the linearized inviscid results for the out-of-phase, first-harmonic pressure, i.e., $\mathrm{Im}\{p_1\}$, and therefore, those for the local work per cycle, are in close agreement. Finally, the second (and higher) harmonics of both the inviscid and viscous nonlinear unsteady surface pressures are quite small.

Thus, for the unsteady subsonic flows considered, the effects of viscous displacement on the unsteady surface pressure responses are small; these responses are essentially captured by the first-harmonic components of the nonlinear solutions for the unsteady pressure; and, for the most part, these first harmonic components are accurately predicted by a linearized inviscid analysis.

The predicted local work-per-cycle distributions and the corresponding global works per cycle for the in-phase torsional and out-of-phase bending vibrations are shown in Figs. 6 and 7, respectively. Since the NPHASE inviscid and viscous predictions for the local work per cycle are nearly identical, only the inviscid results are presented. The NPHASE results in Figs. 6(*a*) and 7 are based on the Euler predictions for the nonlinear unsteady surface pressure; those in Fig. 6(*b*) on the Euler predictions for the first-harmonic component of this pressure. Since the bending vibration has a linear harmonic form, there is no difference between the NPHASE nonlinear and first-harmonic predictions for the local and global works per cycle.

The agreement among the NPHASE nonlinear, the NPHASE first-harmonic, and the LINFLO predictions for w_C and W_C is excellent, again indicating that the unsteady fluctuations in this subsonic flow are essentially linear perturbations of the underlying steady background flow. The Navier–Stokes solutions for the unsteady viscous flows at $\mathrm{Re} = 10^6$ provide curves for w_C versus $\bar{x}$ that are closely aligned with those given in Figs. 6 and 7. For the torsional vibration, the viscous nonlinear and first-harmonic predictions for the global work per cycle are $|\alpha^{-2}|W_C = -0.61$ and -0.60, respectively; for the bending vibration, both give $|h_y^{-2}|W_C = -8.06$. Thus, the effects of viscous displacement on the local and global work per cycle responses are small, and for subsonic flows, these responses are captured accurately by the first-harmonic component of the unsteady viscous solution for the pressure.

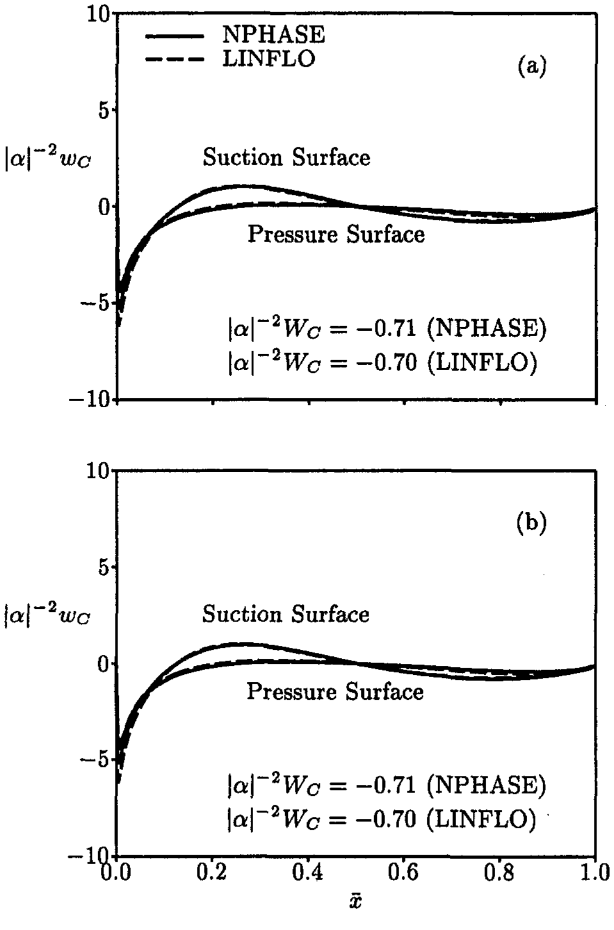

Fig. 6 Work per cycle predictions for inviscid subsonic flow through the 10th Standard Cascade for an in-phase torsional vibration about midchord: (*a*) NPHASE nonlinear prediction; (*b*) NPHASE first-harmonic prediction

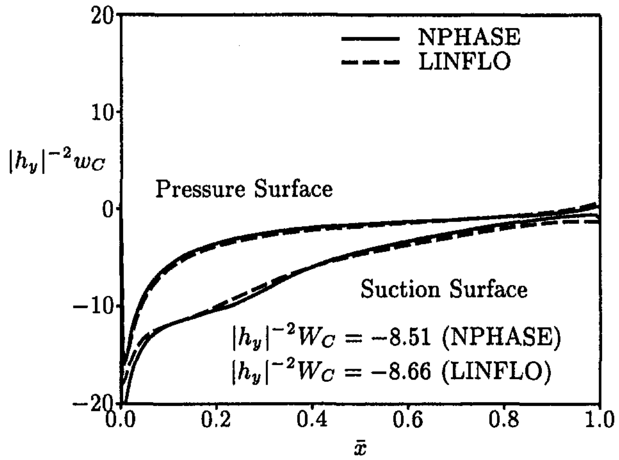

Fig. 7 Work per cycle predictions for inviscid subsonic flow through the 10th Standard Cascade undergoing an out-of-phase bending vibration

The behavior of the global work-per-cycle versus interblade phase angle is shown in Fig. 8 for pure torsional and pure bending vibrations at unit frequency. The vertical lines above each curve indicate the resonant interblade phase angles, i.e., $\sigma = \sigma^{\mp}_{\mp\infty}$, for a unit frequency excitation. Here, the subscripts refer to the far upstream ($-\infty$) and far downstream ($+\infty$) regions of the flow, and the superscripts indicate that there are two resonances, one at $\sigma^- < 0$, the other at $\sigma^+ > 0$, associated with each region.

The results in Fig. 8 reveal that the SDOF blade motions are stable ($W_C < 0$) and that the torsional vibrations generally have the lower stability margin. The NPHASE results in Fig. 8 are based upon the nonlinear viscous and inviscid solutions for the unsteady pressure. Corresponding predictions, based on the first harmonic components of the pressure, are almost identical to the results shown. Also, the NPHASE and LINFLO global response predictions are in good agreement. The greatest deviation occurs at $\sigma = 120$ deg, which is near an upstream resonance condition.

The result agreement indicated in Fig. 8 demonstrates the accuracy of both analyses, NPHASE and LINFLO, over the entire range of interblade phase angles. The relatively small differences between the LINFLO and the NPHASE inviscid and viscous solutions indicate that, for the flows considered, nonlinear and viscous effects have only a small impact on aeroelastic stability margin.

Unsteady Transonic Flows. Next, we consider unsteady transonic flows through the 10th Standard Cascade, and again examine the responses to SDOF torsional (at $|\alpha| = 1$ deg) and bending ($|h_y| = 0.01$) vibrations at unit frequency. Here, the torsional amplitude is set at 1 deg so that the shocks that occur persist throughout the unsteady motion. The nonlinear calculations have shown that, for $|\alpha| = 2$ deg, shocks disappear when blades are near their mean positions and rotating clockwise.

Detailed results from the inviscid and viscous versions of NPHASE have been determined for in-phase torsional and out-

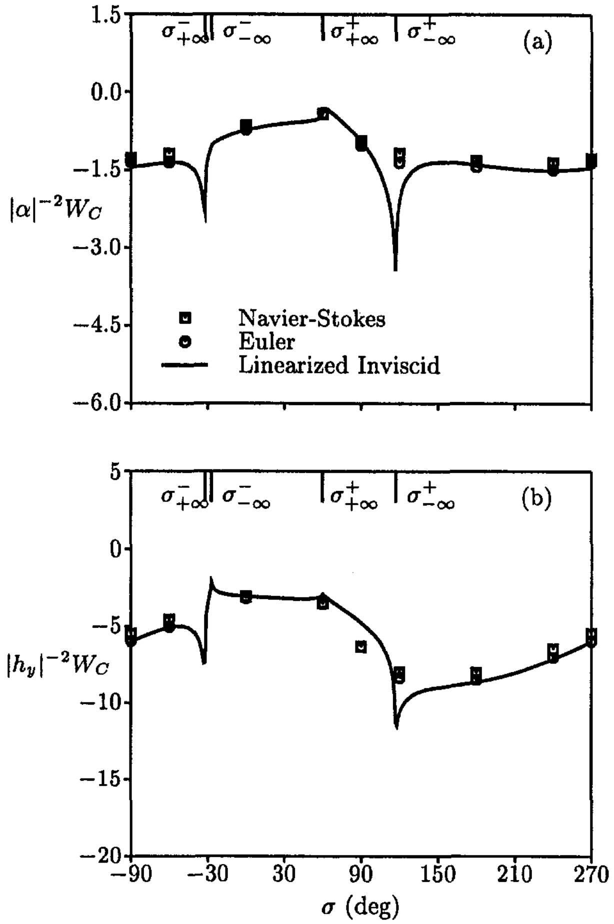

Fig. 8 Work per cycle versus interblade phase angle for inviscid and viscous (Re = 10^6) subsonic flows through the 10th Standard Cascade undergoing prescribed blade motions at unit frequency: (*a*) torsional vibrations, about midchord, $|\alpha|$ = 2 deg; (*b*) bending vibrations, $|h_y|$ = 0.01

of-phase bending motions. For the transonic operating condition, in-phase blade motions are superresonant (1, 1) and the out-of-phase motions are superresonant (1, 0). Inviscid and viscous (at Re = 10^6) instantaneous surface pressure distributions for the in-phase torsional blade vibration are shown in Fig. 9. These results, along with similar ones for the bending motion, indicate that the unsteady pressure fluctuations on the suction surface are considerably stronger than those on the pressure surface, particularly in the vicinity of the shock. Also, an observer stationed between the extreme shock positions will experience large changes in pressure as the shock passes by. Viscous effects tend to smear shocks and reduce the impulsive unsteady loads associated with shock motion.

For the two blade motions considered, the first harmonics of the nonlinear inviscid and viscous surface pressure predictions are in close agreement and the second and higher harmonics are quite small, except in regions traversed by the shocks. In these regions, the inviscid and viscous first harmonics differ substantially and relatively large second and higher harmonics of the unsteady pressure occur. The NPHASE predictions for the first-harmonic pressure differ substantially from those of the linearized inviscid analysis near a blade leading edge, in the vicinity of a shock, and in the supersonic region upstream of the shock. However, the nonlinear and the linearized solutions for the first-harmonic pressure response are in very good agreement in the subsonic regions of the flow.

Work-per-cycle predictions for the in-phase torsional and the out-of-phase bending blade motions are presented in Figs. 10 and 11, respectively. The NPHASE results in Figs. 10(*a*) and 11 are based on the nonlinear unsteady pressure; those in Fig. 10(*b*), on the first-harmonic component of this pressure. Although NPHASE provides sharp shock resolutions at each instant of time, the integrations used to determine the local work per cycle [cf. Eq. (17)] tend to distribute the unsteady shock loads. Shocks are "fitted" in the LINFLO analysis by imposing jump conditions at the mean shock positions. This fitting provides concentrated shock loads, represented by the Dirac delta function, δ, in Figs. 10 and 11, that depend on the product of the steady pressure jump across the shock and the shock displacement, and first-harmonic unsteady surface pressures that are discontinuous at mean shock locations.

The transonic local work per cycle predictions indicate that the nonlinear viscous and inviscid solutions are in very close agreement, except in regions traversed by moving shocks. Viscous displacement affects shift mean shock positions slightly upstream and weaken impulsive unsteady shock loads. The first-harmonic local and global work per cycle predictions shown in Fig. 10(*b*) are in excellent agreement with those based on the full nonlinear pressure, indicating that the energy transfer between the fluid and the torsional blade motion is almost entirely due to the first-harmonic response of the fluid. Thus, due to the shock, viscous-displacement effects have some impact on the stability of a blade motion, but the higher harmonics of the unsteady surface pressure have a negligible impact.

The NPHASE inviscid and the LINFLO results for w_C differ substantially in the vicinity of a shock and in the supersonic regions upstream of the shocks, but they are in close agreement in subsonic regions, i.e., along the blade suction surface down-

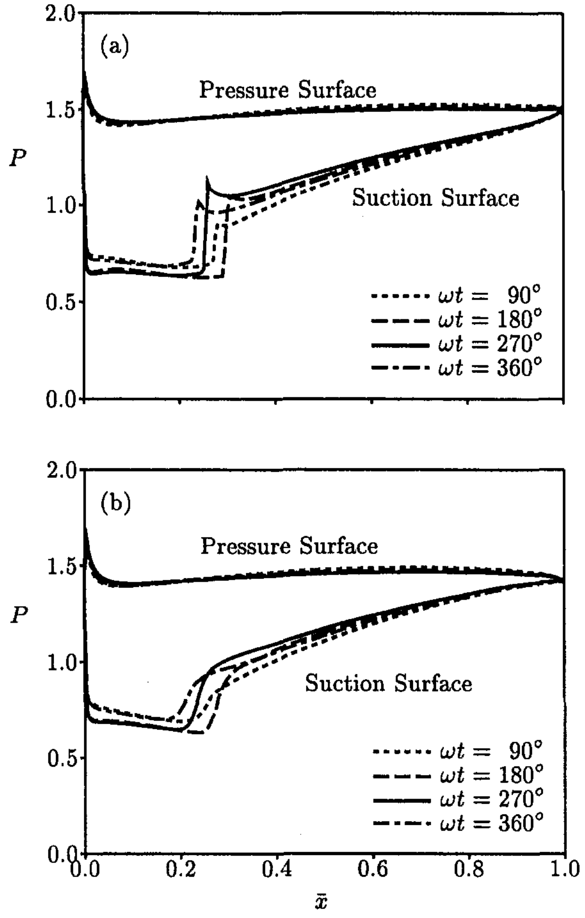

Fig. 9 Instantaneous surface pressure distributions for transonic flows through the 10th Standard Cascade undergoing in-phase torsional blade vibrations: (*a*) inviscid flow; (*b*) viscous flow at Re = 10^6

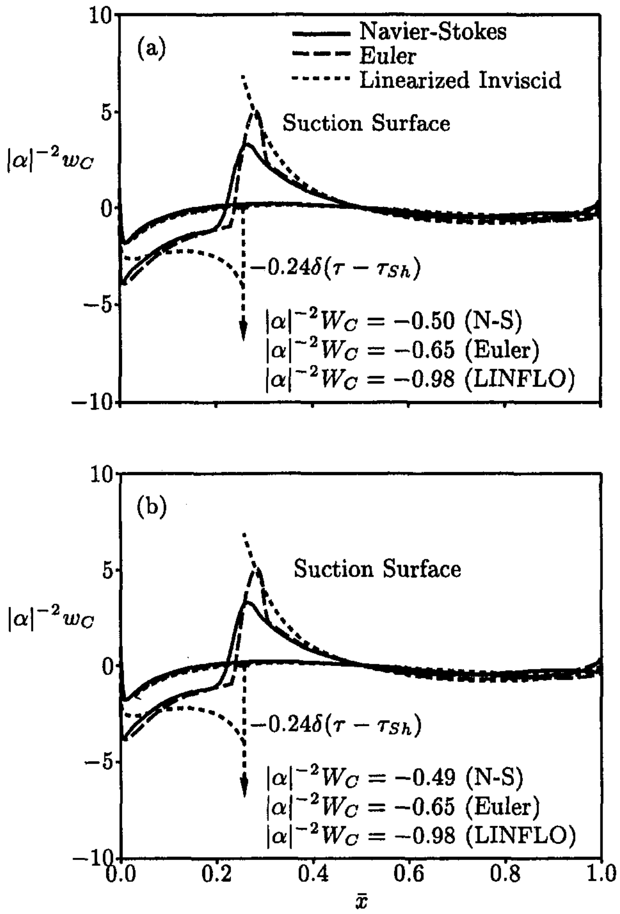

Fig. 10 Work per cycle predictions for viscous (at Re = 10^6) and inviscid transonic flows through the 10th Standard Cascade undergoing an in-phase torsional vibration about midchord: (*a*) NPHASE nonlinear predictions; (*b*) NPHASE first-harmonic predictions

stream of the shock and over the entire pressure surface. To some extent the differences at the shock arise because of the different methods used to resolve shock phenomena. Those in the supersonic region upstream of the shock are not well understood at this time, but could be associated with the use of stretched grids with the NPHASE analysis. These may fail to accurately capture near-field unsteady pressure waves that travel away from the blades.

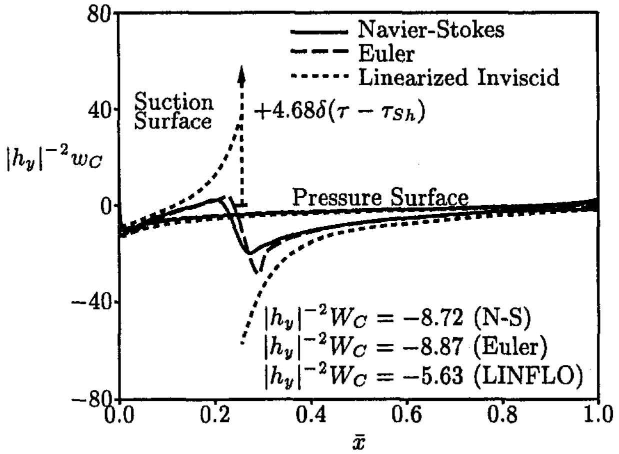

Fig. 11 Work per cycle predictions for viscous (at Re = 10^6) and inviscid transonic flows through the 10th Standard Cascade undergoing an out-of-phase bending vibration

Global work per cycle predictions for unit-frequency torsional and bending vibrations of the transonic 10th Standard Cascade are shown in Fig. 12. The NPHASE viscous and inviscid results are in fairly close agreement. The NPHASE and LINFLO results show similar trends, but significant quantitative differences. The latter are due to the discrepancies between the local response predictions of the two analyses in supersonic regions and at shocks. Work per cycle predictions, based on the NPHASE viscous and inviscid predictions for the first-harmonic components of the unsteady pressure, are in close agreement with the nonlinear results shown in Fig. 12, indicating that, even for transonic flows, the stability margin for a given blade motion is essentially determined by the first-harmonic component of the unsteady pressure response.

Concluding Remarks

The implicit, wave-split, Euler/Navier–Stokes analysis, NPHASE, has been applied to predict subsonic and transonic, unsteady flows through a vibrating cascade. Linearized inviscid unsteady aerodynamic response predictions have also been determined to help validate and illustrate the Euler/Navier–Stokes prediction capability. The NPHASE results have also been interrogated to assess the importance of nonlinear and viscous effects on the unsteady aerodynamic responses to blades vibrating at a frequency representative of flutter in modern fans and compressors.

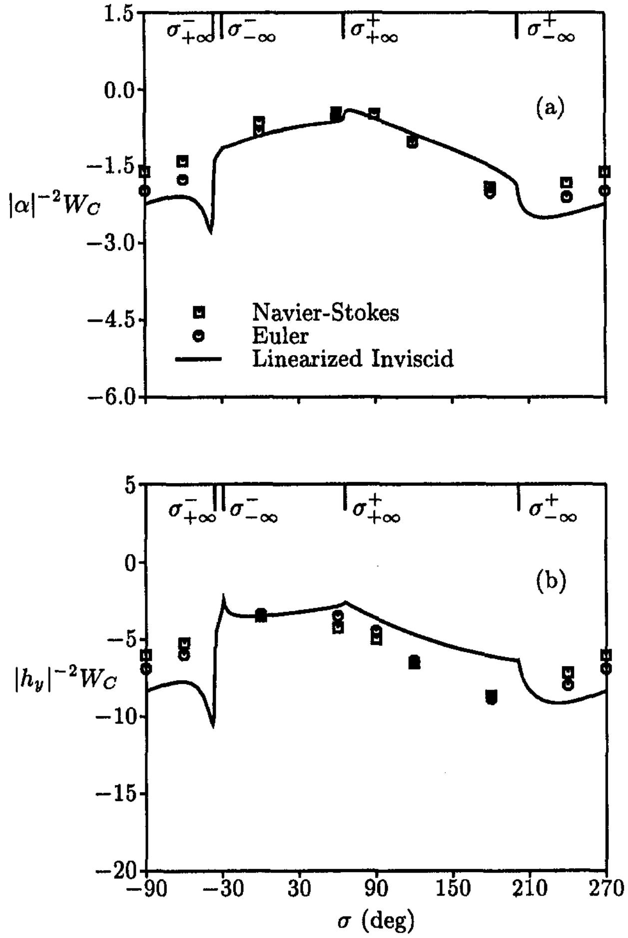

Fig. 12 Work per cycle versus interblade phase angle for inviscid and viscous (Re = 10^6) transonic flows through the 10th Standard Cascade undergoing prescribed blade motions at unit frequency: (*a*) torsional vibrations at about midchord, $|\alpha|$ = 1 deg; (*b*) bending vibrations, $|h_y|$ = 0.01

The numerical results for subsonic flows indicate that viscous effects have only a small impact on steady and unsteady blade loadings, and that unsteady surface pressure responses are essentially linear. In particular, viscous effects cause a small decrease in steady pressure loading over the rear half of a blade and a suction-surface flow separation just upstream of a blade trailing edge. The nonlinear unsteady simulations show a close agreement between the inviscid and viscous predictions for the unsteady surface pressure and, hence, the local and global works per cycle. In addition, the unsteady surface pressure responses are essentially first-harmonic responses, as the second- and higher-harmonic components of the pressure are quite small. Finally, the linearized inviscid response predictions are in excellent agreement with the nonlinear Euler and Navier–Stokes predictions. Thus, for the subsonic flows considered, aeroelastic stability margins could be determined accurately using linearized inviscid methods.

The numerical results for transonic flows indicate that nonlinear and viscous effects can be important in regions traversed by moving shocks. The Euler and Navier–Stokes steady-flow predictions indicate that viscous displacement effects tend to weaken and distribute shock effects, reduce blade pressure-difference loadings away from the shock, and promote flow separation downstream of the shock.

The unsteady transonic predictions indicate that viscous effects diminish the impulsive unsteady loads associated with shock motion. Also, nonlinear and viscous-displacement effects have a significant impact on the unsteady surface pressure response in the vicinity of a shock, but only a small impact elsewhere. In particular, relatively large second- and higher-harmonic pressure variations occur in the region traversed by a moving shock, but, away from this region, the higher-harmonic content of the unsteady surface pressure response is small. The local and global work per cycle responses, and hence, the stability margins for the blade motions, are again essentially determined by the first-harmonic component of the nonlinear unsteady surface pressure. Unfortunately, at present, the nonlinear, first-harmonic and the linearized inviscid results are not in good agreement at shocks and in the supersonic regions upstream of shocks.

In future work, two-dimensional, nonreflecting, far-field conditions should be incorporated into NPHASE to avoid the use of axially stretched meshes. Such conditions should lead to improved predictions in the supersonic regions of transonic flows and improved global unsteady aerodynamic response predictions for superresonant and near-resonant blade motions. Also, the differences between the shock loads predicted by nonlinear and linearized unsteady aerodynamic analyses must be clearly understood. We might find that a linearized analysis that accounts for viscous displacement effects in the vicinity of a shock will provide useful transonic, aeroelastic, design predictions. Unsteady flows in which shocks appear and disappear over a cycle of blade motion should be studied to gain insight into the importance of large shock excursions on aeroelastic stability. Also, the effects of large-scale viscous separations and the use of different turbulence and transition models on unsteady aerodynamic response predictions, should be investigated.

Acknowledgments

This work was supported through the GUIde Consortium under Air Force Contract F33615-92-C-2212. The authors gratefully acknowledge this support.

References

Ayer, T. C., and Verdon, J. M., 1994, "Numerical Unsteady Aerodynamic Simulator for Blade Forced Response Phenomena," Air Force CR WL-TR-95-2011.

Baldwin, B. S., and Lomax, H., 1978, "Thin-Layer Approximation and Algebraic Model for Separated Turbulent Flow," AIAA Paper No. 78-257.

Beach, T. A., and Hoffman, G., 1992, "IGB Grid: User's Manual (A Turbomachinery Grid Generation Code)," NASA CR 189104.

Caspar, J. R., 1983, "Unconditionally Stable Calculation of Transonic Potential Flow Through Cascades Using an Adaptive Mesh for Shock Capture," ASME *Journal of Engineering for Power*, Vol. 105, pp. 504–513.

Dorney, D. J., and Verdon, J. M., 1994, "Numerical Simulations of Unsteady Cascade Flows," ASME JOURNAL OF TURBOMACHINERY, Vol. 116, pp. 665–675.

Fransson, T. H., and Verdon, J. M., 1993, "Standard Configurations for Unsteady Flow Through Vibrating Axial-Flow Turbomachine Cascades," in: *Unsteady Aerodynamics, Aeroacoustics and Aeroelasticity of Turbomachines and Propellers*, H. M. Atassi, ed., Springer-Verlag, New York, pp. 859–889.

Giles, M. B., 1988, "Calculation of Unsteady Wake Rotor Interaction," *AIAA Journal of Propulsion and Power*, Vol. 4, No. 4, pp. 356–362.

He, L., 1990, "An Euler Solution for Unsteady Flows Around Oscillating Blades," ASME JOURNAL OF TURBOMACHINERY, Vol. 112, pp. 714–722.

Huff, D. L., and Reddy, T. S. R., 1989, "Numerical Analysis of Supersonic Flow Through Oscillating Cascade Sections by Using a Deforming Grid," AIAA Paper No. 89-2805.

Huff, D. L., Swafford, T. W., and Reddy, T. S. R., 1991, "Euler Flow Predictions for an Oscillating Cascade Using a High Resolution Wave-Split Scheme," ASME Paper No. 91-GT-198.

Manwaring, S. R., and Wisler, D. C., 1993, "Unsteady Aerodynamics and Gust Response in Compressors and Turbines," ASME JOURNAL OF TURBOMACHINERY, Vol. 115, pp. 724–740.

Rai, M. M., 1987, "Navier–Stokes Simulations of Rotor–Stator Interaction Using Patched and Overlaid Grids," *AIAA Journal of Propulsion and Power*, Vol. 3, No. 5, pp. 387–396.

Rai, M. M., 1989, "Three-Dimensional Navier–Stokes Simulations of Turbine Rotor–Stator Interaction," *AIAA Journal of Propulsion and Power*, Vol. 5, No. 3, pp. 305–319.

Roe, P. L., 1981, "Approximate Riemann Solvers, Parameter Vectors and Difference Schemes," *Journal of Computational Physics*, Vol. 43, pp. 357–372.

Siden, L. D. G., 1991, "Numerical Simulation of Unsteady Viscous Compressible Flows Applied to Blade Flutter Analysis," ASME Paper No. 91-GT-203.

Steger, J. L., and Warming, R. F., 1981, "Flux Vector Splitting of the Inviscid Gasdynamic Equations With Application to Finite Difference Methods," *Journal of Computational Physics*, Vol. 40, No. 2, pp. 263–293.

Swafford, T. W., Loe, D. H., Huff, D. L., Huddleston, D. H., and Reddy, T. S. R., 1994, "The Evolution of NPHASE: Euler/Navier–Stokes Computations of Unsteady Two-Dimensional Cascade Flow Fields," AIAA Paper No. 94-1834.

Thomas, P. D., 1979, "Numerical Method for Predicting Flow Characteristics and Performance of Nonaxisymmetric Nozzles," NASA CR 3147.

Usab, W. J., and Verdon, J. M., 1991, "Advances in the Numerical Analysis of Linearized Unsteady Cascade Flows," ASME JOURNAL OF TURBOMACHINERY, Vol. 113, pp. 633–643.

Verdon, J. M., 1989, "The Unsteady Flow in the Far Field of an Isolated Blade Row," *Journal of Fluids and Structures*, Vol. 3, No. 2, pp. 123–149.

Verdon, J. M., 1993, "Unsteady Aerodynamic Methods for Turbomachinery Aeroelastic and Aeroacoustic Applications," *AIAA Journal*, Vol. 31, No. 2, pp. 235–250.

Whitfield, D. L., Janus, J. M., and Simpson, L. B., 1988, "Implicit Finite Volume High Resolution Wave Split Scheme for Solving the Unsteady Three-Dimensional Euler and Navier-Stokes Equations on Stationary or Dynamic Grids," Mississippi State Univ. Report No. MSSU-EIRS-ASE-88-2.

D. H. Buffum
NASA Lewis Research Center
Cleveland, OH 44135

V. R. Capece

A. J. King

Department of Mechanical &
Aeronautical Engineering,
University of California,
Davis, CA 95616

Y. M. EL-Aini
Pratt & Whitney,
West Palm Beach, FL 33410

Oscillating Cascade Aerodynamics at Large Mean Incidence

The aerodynamics of a cascade of airfoils oscillating in torsion about the midchord is investigated experimentally at a large mean incidence angle and, for reference, at a low mean incidence angle. The airfoil section is representative of a modern, low-aspect-ratio, fan blade tip section. Time-dependent airfoil surface pressure measurements were made for reduced frequencies of up to 1.2 for out-of-phase oscillations at a Mach number of 0.5 and chordal incidence angles of 0 and 10 deg; the Reynolds number was 0.9×10^6*. For the 10 deg chordal incidence angle, a separation bubble formed at the leading edge of the suction surface. The separated flow field was found to have a dramatic effect on the chordwise distribution of the unsteady pressure. In this region, substantial deviations from the attached flow data were found, with the deviations becoming less apparent in the aft region of the airfoil for all reduced frequencies. In particular, near the leading edge the separated flow had a strong destabilizing influence while the attached flow had a strong stabilizing influence.*

Introduction

Subsonic/transonic stall flutter continues to be a problem in the development of fan and compressor blades for advanced military and commercial aircraft gas turbine engines. As schematically depicted in Fig. 1, this type of flutter occurs at part speed where the blade incidence angle is quite large and the inlet relative Mach number is transonic; this type of flutter typically occurs in the first torsion mode. Due to the large incidence angles, viscous effects are significant for this type of flutter. While considerable effort has been devoted to the development of unsteady aerodynamic models for flutter, accurate predictions of stall flutter have remained elusive. As a result, current stall flutter prediction systems rely on purely empirical correlations of flutter boundaries based on previous rig and engine testing, simplified separation models, or semi-empirical methods (EL-Aini and Capece, 1995).

To improve stall flutter predictions, experimental data are required. Unfortunately, only a very limited quantity of unsteady aerodynamic data exist at large mean incidence angles to verify and direct refinements to these models. In fact, the significant effects of unsteady separated flow at realistic reduced frequency values have not been adequately addressed experimentally for turbomachinery.

Previous investigations have, at best, been only partially successful at obtaining the data necessary to improve stall flutter prediction capabilities. For example, Carta and St. Hilaire (1979) and Carta (1983), using a linear compressor cascade in which NACA 65 series airfoils were harmonically oscillated in torsion, measured the resulting unsteady surface pressure distributions along the chord of the airfoils. These studies, at reduced frequencies (based on chord) less than 0.4, investigated the effects of steady blade loading and interblade phase angle on the unsteady aerodynamics. This investigation showed a decrease in aerodynamic damping (stability) with increasing incidence angle even though steady flow suction surface separation was not apparent. While the interblade phase angle values were within the range of interest for turbomachines, the reduced frequency values and Mach number were low for advanced fan and compressor stall flutter.

Széchényi and Finas (1981a) and Széchényi and Girault (1981b) (the fifth standard configuration in Bölcs and Fransson (1986)) harmonically oscillated in torsion a symmetric airfoil in a linear compressor cascade. They obtained unsteady aerodynamic data over a range of Mach numbers, reduced frequencies, and incidence angles, including partially and fully separated flow. Experimental results for 0.5 Mach number have indicated negative aerodynamic damping (instability) for incidence angles greater than 8 deg for a reduced frequency of 0.74. In this experiment only one blade was oscillated. Hence, the experimental data does not explicitly account for the effects of interblade phase angle. Instead, the unsteady aerodynamic coefficients correspond to the influence of the oscillation of the reference blade on itself when all other blades in the cascade are fixed.

These investigations point to the basic difficulty of cascade stall flutter investigations: It is extremely difficult to obtain experimental data with all of the relevant parameters simultaneously having appropriate values. Appropriate values are: (1) high subsonic or transonic mean flow, (2) large mean incidence angles that include separated flow, and (3) reduced frequency of one or greater. In addition, data for simultaneous oscillation of the airfoils at a number of different interblade phase angles is desirable.

The objective of this experimental investigation is to obtain data that are, in all respects, appropriate for advancing the state of turbomachinery stall flutter prediction capabilities. Experiments are performed that use the unique capability of the NASA Lewis Research Center Transonic Oscillating Cascade to simultaneously obtain appropriate parameter values. These experiments quantify the effects of separation and reduced frequency on the airfoil unsteady aerodynamic response.

In this paper, the aerodynamics of a cascade of airfoils executing torsion mode oscillations is investigated. The airfoil cross section was similar to that found in the tip region of low-aspect-ratio fan blades. For an inlet Mach number of 0.5, results will be presented for a low mean incidence, attached flow condition, and a high mean incidence condition with leading edge separation. Reduced frequencies as high as 1.2 were attained. The low incidence data are correlated with predictions from a linearized cascade unsteady aerodynamics code.

Contributed by the International Gas Turbine Institute and presented at the 41st International Gas Turbine and Aeroengine Congress and Exhibition, Birmingham, United Kingdom, June 10–13, 1996. Manuscript received at ASME Headquarters February 1996. Paper No. 96-GT-339. Associate Technical Editor: J. N. Shinn.

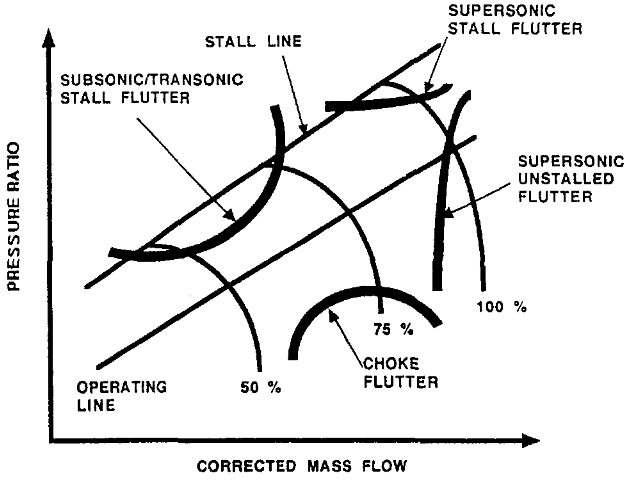

Fig. 1 Compressor performance map showing flutter boundaries

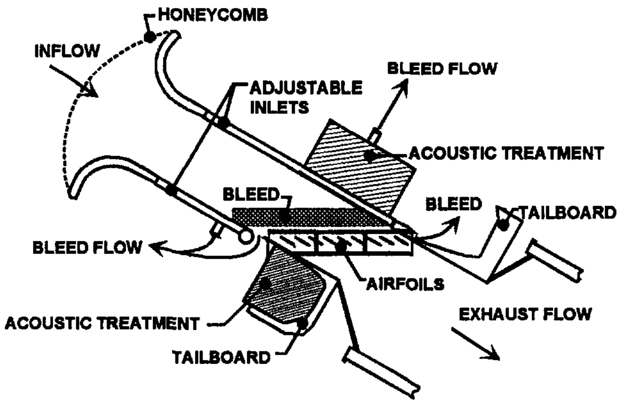

Fig. 2 NASA Lewis oscillating cascade

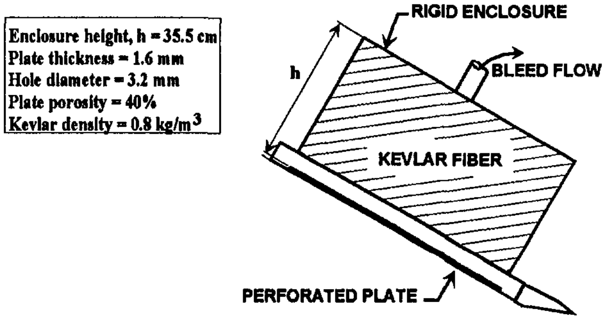

Fig. 3 Upper wall acoustic treatment

Facility and Instrumentation

Oscillating Cascade. The NASA Lewis Oscillating Cascade, Fig. 2, combines a linear cascade wind tunnel capable of inlet flow approaching Mach 1 with a high-speed airfoil drive system. The drive system imparts torsional oscillations to the cascaded airfoils at specified interblade phase angles and realistic values of reduced frequency. For facility details not discussed below, see Buffum and Fleeter (1990).

Air drawn from the atmosphere passes through honeycomb into a smooth contraction inlet section then into a constant area rectangular duct. For an inlet Mach number of 0.2, turbulence intensity in the test section was 0.3 percent. The duct measures 9.78 cm in span and 58.6 cm along the stagger line. Upstream of the test section, suction is applied through perforated sidewalls to reduce the boundary layer thickness. Tailboards are used to adjust the cascade exit region static pressure and also form bleed scoops, which further reduce upper and lower wall boundary layer effects. Downstream of the test section, the air is expanded through a diffuser into an exhaust header. The cascade inlet may be adjusted to obtain a wide range of incidence angles.

The facility features a high-speed mechanism, which may drive any or all of the airfoils in controlled torsional oscillations. For this investigation, all the airfoils were oscillated simultaneously, and the maximum reduced frequency was 1.2 (based on chord) at an inlet Mach number of 0.5, which corresponds to a 370 Hz oscillation frequency. Stainless steel barrel cams, each having a six-cycle sinusoidal groove machined into its periphery, are mounted on a common rotating shaft driven by a 74.6 kW electric motor. A cam follower assembly, consisting of a titanium alloy connecting arm with a stainless steel button on one end, is joined on the other end to an airfoil trunnion. The button fits into the cam groove, thus coupling the airfoil with the camshaft. The drive system geometry fixes the pitching amplitude to 1.2 deg. Lubrication of the cam/follower assembly is provided by an oil bath. The interblade phase angle is fixed by the relative positions of the cams on the drive shaft.

External to the oil bath, on the same shaft as the airfoil drive cams, is a cam used to indicate the shaft position. A proximity probe facing this reference cam produced a time-dependent voltage indicating the position of the airfoils.

The upper wall and the lower tailboard are acoustically treated. Experiments performed before acoustic treatment was installed (Buffum and Fleeter, 1993, 1994) indicated that reflections of acoustic waves by the solid walls were compromising the blade-to-blade periodicity of the unsteady flow field. Thus the walls were modified to reduce acoustic wave reflections. Portions of the solid boundaries were replaced by perforated plates backed by enclosures filled with Kevlar fiber as depicted in Fig. 3. Rice (1992) provided the design parameters (plate thickness and porosity, hole diameter, enclosure depth

Nomenclature

C = blade chord length
C_m = first harmonic unsteady aerodynamic moment coefficient, Eq. (4)
$\bar{C}_p$ = steady pressure coefficient = $(p_{in} - p)/(\rho V^2)$
C_p = first harmonic unsteady pressure coefficient = $p_1/\rho V^2 \alpha_1$
Im = imaginary part
k = reduced frequency = $\omega C/V$
M = inlet Mach number
n = airfoil number = 0, ±1, . . . ±4
p_{in} = cascade mean inlet pressure
p_{ex} = cascade mean exit pressure
p = mean pressure (zeroth harmonic)
p_1 = first harmonic unsteady pressure
Re = real part
Re_C = Reynolds number = $\rho VC/\mu$
R_p = cascade pressure ratio = p_{ex}/p_{in}
S = blade spacing
$t_{\max}$ = maximum blade thickness
V = inlet velocity
x = chordal distance
$x_{\max}$ = position of maximum blade thickness
x_p = pitching axis locations
α = mean incidence relative to the airfoil chord line
α_1 = amplitude of torsional oscillation = 0.0209 rad
β = interblade phase angle
γ = stagger angle
θ^* = leading edge camber angle
μ = dynamic viscosity at cascade inlet
ρ = density at cascade inlet
ω = frequency of oscillation

Table 1 Airfoil and cascade parameters

Chord, C	8.89 cm
Maximum thickness, t_{max}	0.048 chord
Location of maximum thickness, x_{max}	0.625 chord
Leading edge camber angle, $\theta*$	-9.5 degrees
Number of airfoils	9
Stagger angle, γ	30 degrees
Solidity, C/S	1.52
Pitching axis	0.5 chord

and Kevlar density). Bleed lines were attached to the cavities to allow boundary layer suction through the perforated walls.

Airfoils. The airfoils used in this study have a cross section similar to that found in the tip region of current low-aspect-ratio fan blades. The airfoil section was designed using the Pratt & Whitney fan and compressor aerodynamic design system, which is for flow in circular ducts. Hence, to simulate the two-dimensional conditions to be encountered in the linear cascade, the airfoils were designed using a radius ratio of 0.99. The loading levels, losses, solidity, and stagger angle are consistent with current design practice for fan blades. The airfoil cascade parameters are given in Table 1; refer to Fig. 4 for definitions of the geometry.

Instrumentation. Wall static pressure taps were used to measure the inlet and exit pressures. From these measurements, mean values were determined to provide the cascade pressure rise.

Four airfoils were instrumented with static pressure taps. Two airfoils were instrumented with taps very near the midspan, one on the suction surface, the other on the pressure surface. As shown in Fig. 5(*a*), taps were clustered near the leading edge to capture the large pressure gradients there. Taps were also clustered in the 50 to 70 percent chord region in anticipation of shock wave impingement on the pressure surface when operating near choked flow conditions. Two additional airfoils were instrumented with pressure taps, Fig. 5(*b*), some of which are redundant to the midspan instrumentation shown in part (*a*) and others that indicate the spanwise variations in the pressure. The redundant midspan taps were used to indicate blade-to-blade periodicity of the cascade steady flow field. The spanwise taps supply information on the three dimensionality of the flow field.

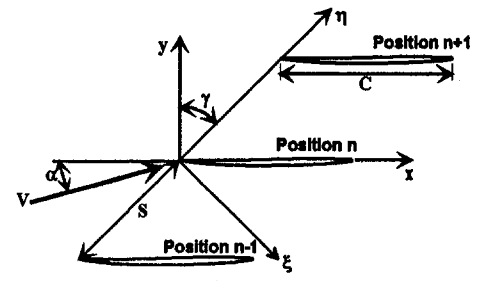

Cascade geometry

Airfoil geometry

Fig. 4 Airfoil and cascade geometry

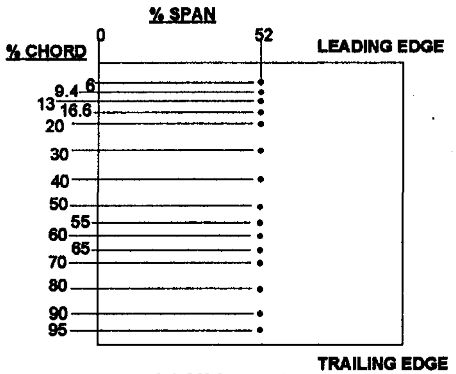

(a) Midspan taps

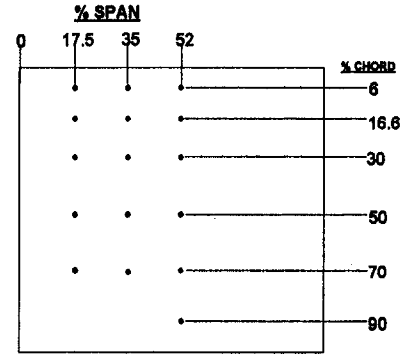

(b) Spanwise and redundant taps

Fig. 5 Airfoil surface pressure taps

Two airfoils were instrumented with flush-mounted miniature pressure transducers. The transducers were chosen for having the following desirable characteristics: small dimensions, high frequency response, and invariance of dynamic response with change in temperature. Static and dynamic calibrations were made.

Kulite Semiconductor Products miniature pressure transducers were used, each of which consists of a silicon diaphragm containing a four-arm strain gage bridge mounted over a cylindrical cavity. Slots were machined into the airfoil surfaces to allow the transducer diaphragms to be mounted flush with the airfoil surface and to serve as passages for the wire leads. Once the transducers were installed, each slot was filled and smoothed to the airfoil contour, and each transducer was coated with RTV (room-temperature-vulcanizing rubber) for improved durability and conformance with the airfoil profile. To provide isolation from airfoil strain, each transducer was potted in RTV. The pressure sensitive diameter was 0.7 mm (0.8 percent of the airfoil chord).

The transducers were located on the upper surface of one airfoil and the lower surface of another airfoil. There were 15 transducers per surface. The locations, the same as those of the midspan pressure taps (Fig. 5(*a*)), vary from 6 to 95 percent of chord. The transducer thickness relative to the airfoil thickness was the limiting factor in placing the transducers closest to the leading and trailing edges; at these locations, the airfoil thickness was chosen to be at least twice the transducer thickness.

Static calibration of the transducers was performed at NASA Lewis Research Center. Each blade was installed in a calibration chamber, the ambient pressure of which was controlled using a vacuum pump. The transducer electronics and the data acquisition system were identical to those used during all of the calibrations and the unsteady experiments. The response for each transducer was linear. The calibrations were repeatable: Changes in sensitivities were typically less than 0.25 percent between calibrations.

Although the transducer specifications state that the frequency response is in excess of 100 kHz, the RTV coating is expected to reduce it. To verify the response, a resonant tube assembly similar to that used by Capece and Fleeter (1987) was used to excite the transducers with acoustic waves. The assembly consists of a 20.3-cm-dia, 4.6-m-long plastic tube with a speaker mounted at one end. An instrumented airfoil was mounted at the opposite end of the tube, which was open to atmosphere. Amplified sine waves were used to drive the speaker, which in turn created acoustic waves in the tube for excitation of the transducers. The resulting pressure transducer responses were flat to frequencies in excess of 1000 Hz within ±2 percent in magnitude and ±3 deg in phase.

During the experiments, the pressure transducers are subject to maximum accelerations in excess of 300 times that due to gravity. Acceleration deflects the transducer diaphragm and thus produces apparent pressure signals. Calibration was used to correct for this effect. Each blade was oscillated in a chamber with low ambient pressure (1.2 kPa) over the range of frequencies encountered in the experiments. The mode of oscillation was identical to that used in the cascade. Through Fourier analysis of the resulting signals, the transducer responses as a function of oscillation frequency were determined. Second degree polynomial curves were found to fit the calibration data well; the calibration coefficients were used to correct the experimental data. For example, at 370 Hz, the correction for the upper surface leading edge transducer was 2.6 kPa.

Data Acquisition and Analysis

Unsteady signals from the pressure transducers and the proximity probe were recorded using a Teac XR-7000 VHS tape recorder. During tape playback, the signals were simultaneously digitized at rates typically 10 times the oscillation frequency, with 16,384 samples taken per channel. Each channel of data was divided into blocks with 1024 samples, windowed using a Hanning window, then Fourier transformed to determine the first harmonic of each block. The first harmonic of each block was referenced to the airfoil motion by subtracting from it the phase of the first harmonic motion signal of the corresponding block. Once all of the blocks from a channel were decomposed in this manner, the first harmonic block results were averaged and the complex-valued acceleration response was subtracted vectorally.

The motion of the nth airfoil is defined by the change in the incidence angle with time:

$$\alpha^n(t) = \alpha + \alpha_1 Re[\exp(i(\omega t + n\beta))] \quad (1)$$

The first harmonic unsteady pressure coefficient is defined as

$$C_p(x) = \frac{p_1(x)}{\rho V^2 \alpha_1} \quad (2)$$

The pressure difference coefficient is defined to be the difference between the lower and upper surface unsteady pressure coefficients:

$$\Delta C_p = (C_p)_{\text{lower}} - (C_p)_{\text{upper}} \quad (3)$$

The unsteady aerodynamic moment coefficient for a flat plate airfoil is defined as

$$C_M = \int_0^1 \left(\frac{x_p}{C} - \frac{x}{C}\right) \Delta C_p\left(\frac{x}{C}\right) d\,\frac{x}{C} \quad (4)$$

where $x_p/C = 0.5$. The work done on the airfoil by the fluid per cycle of oscillation is proportional to $Im(C_M)$, thus the sign of $Im(C_M)$ determines the airfoil stability with $Im(C_M) > 0$ indicating instability.

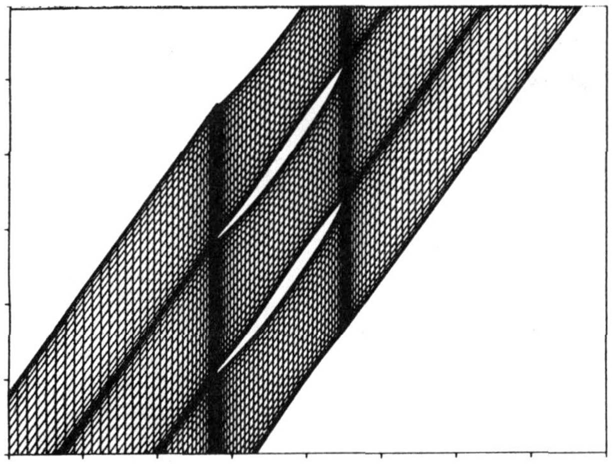

Fig. 6 SFLOW/LINFLO grid

Results

Results will be presented for 0 and 10 deg of incidence at an inlet Mach number of 0.5. These incidence angles are based on the cascade inlet angles relative to the airfoil chord line; upstream flow angle measurements were not made. Unsteady data will be presented for a 180 deg interblade phase angle and reduced frequencies of 0.4, 0.8, and 1.2.

For $\alpha = 0$ deg, the steady and unsteady data are correlated with two-dimensional potential flow predictions; the influence of stream tube contractions was not considered in the analyses. For $\alpha = 10$ deg, solutions were not obtainable due to the extremely large flow gradients created by the sharp leading edge of the airfoils. The steady flow surface pressure distribution is correlated with the nonlinear full potential solver SFLOW (Hoyniak and Verdon, 1993), and the first harmonic surface pressure distribution is correlated with the linearized analysis LINFLO (Verdon and Hall, 1990). The predictions from SFLOW are used by LINFLO as the nonlinear background steady flow around which the harmonic unsteady flow solutions are formed.

The airfoil trailing edge was modified by inserting a wedge in place of the finite radius trailing edge for enforcement of the Kutta condition. This gave a trailing edge that was not a true cusp configuration. This was found to challenge the steady and unsteady computational implementations of the Kutta condition.

A 120 by 21 H-Grid was used in the computations. A localized region of the grid is illustrated in Fig. 6. This cosine-distributed grid yields a large number of grid points in the leading and trailing edge regions where the flow gradients are the highest. The cascade inlet flow angle was varied until the best match was found between the steady chordwise pressure coefficient data and the predictions. This resulted in a 0.5 deg chordal incidence angle being used in all of the predictions.

Steady Aerodynamics. For a linear cascade to be a valid simulation of a turbomachine blade row, the cascade must exhibit good passage-to-passage periodicity for the steady flow field. To verify that the cascade was periodic, airfoil surface pressure distributions were obtained at the center airfoil position (position 0) and the two adjacent positions (positions −1 and 1) in the nine-airfoil cascade. The resulting airfoil surface pressure distributions for M = 0.5 and $\alpha = 0$ deg are shown in Fig. 7. The periodicity is good. Additionally, there is excellent agreement between the data and the SFLOW predictions up to about 85 percent chord. Aft of this location the predictions show a steep

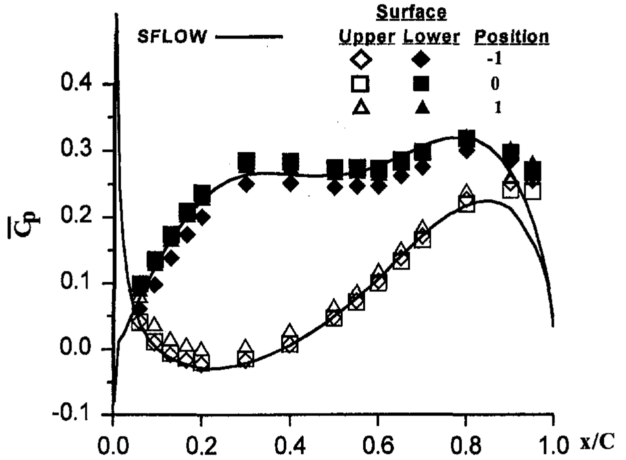

Fig. 7 Airfoil surface pressure coefficient distribution, M = 0.5, α = 0 deg

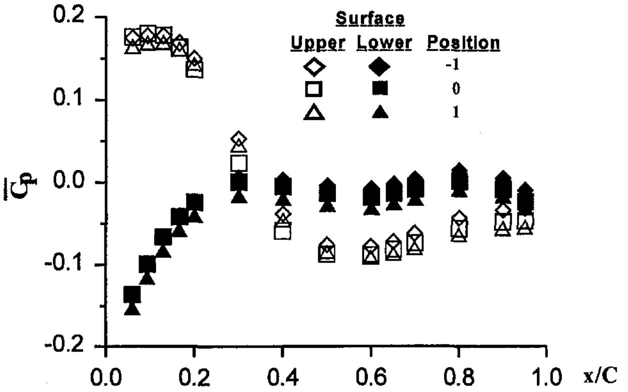

Fig. 8 Airfoil surface pressure coefficient distribution, M = 0.5, α = 10 deg

pressure gradient as the trailing edge is approached, whereas the upper surface data do not have this trend and the lower surface data have a more gradual pressure gradient. The discrepancy in the data-theory correlation in this region is attributed to the airfoil modification and viscous effects.

The α = 10 deg data are shown in Fig. 8. The periodicity is again good. Comparison of the pressure distributions in Figs. 7 and 8 shows the large differences in the mean flow fields due to incidence. At the lower incidence angle, the flow was attached and accelerating through the passage. At the higher incidence angle, the flow separated from the upper surface at the leading edge.

Cascade pressure ratio and Reynolds number for the two steady flow conditions are given in Table 2. The predicted pressure ratio for the low incidence flow was 0.924.

To visualize the flow, the airfoil surface was coated with an oil–pigment mixture. At 10 deg incidence, separation from the upper surface was evident. The largest separated region was found at midspan; there, the flow was separated from the leading edge to about 40 percent of chord. Near the endwalls, the separation bubble extended to about 7 percent of chord. Between midspan and the endwalls, the reattachment region was defined by a smooth arc.

Table 2 Cascade pressure ratio and Reynolds number

Mach no.	Incidence	Pressure ratio	Reynolds number
0.5	0°	0.93	0.9×10^6
0.5	10°	1.03	0.9×10^6

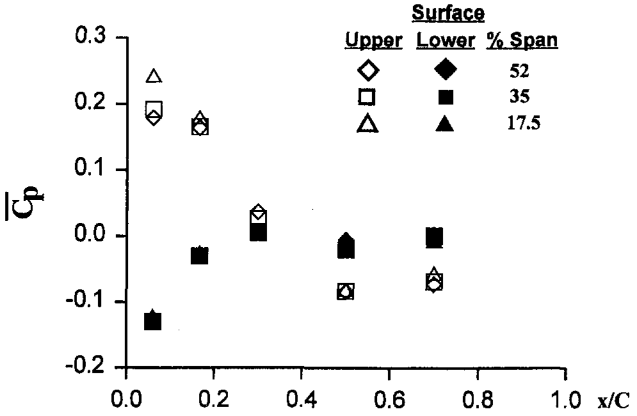

Fig. 9 Spanwise variation of airfoil surface pressure coefficient distribution, M = 0.5, α = 10 deg

To quantify three-dimensional effects in the steady flow, pressure taps were placed at several different spanwise locations of the blade upper surface. Despite the three-dimensional nature of the separation bubble, Fig. 9 shows that the spanwise pressure distributions are nearly constant, except very near the upper surface leading edge. There, the 17.5 percent span value of C_p is larger than the 35 and 52 percent of span values even though visualization showed that the flow was separated at each of those locations.

Unsteady Aerodynamics. Unsteady pressure data will be presented for $\alpha = 0$ and $\alpha = 10$ deg for out-of-phase oscillations (β = 180 deg). The α = 0 deg data will be correlated with linearized flow analysis predictions. Comparisons between the α = 0 deg and the α = 10 deg data will be used to isolate effects of the mean flow on the unsteady aerodynamics. The effect of reduced frequency on the unsteady separated flow will also be investigated. Cascade dynamic periodicity was a primary concern; to quantify periodicity, unsteady data were obtained at the center airfoil position and the two adjacent positions in the nine-airfoil cascade.

Starting with the α = 0 deg data, first harmonic unsteady pressure coefficients for β = 180 deg, k = 0.8 are shown in Fig. 10. Data were taken for two passages. Referring to the schematic in Fig. 10, the lower surface data were taken at positions 0 (the center airfoil position) and 1; the upper surface data were taken at positions −1 and 0. For the C_p values, 95 percent confidence intervals of ±5 percent are estimated. For both surfaces, the data are highly periodic. The lower surface response is dominated by $Re(C_p)$ forward of midchord. Gaps in the lower surface data at 60 and 65 percent of chord, along with several other missing data points, are due to transducer failures. In contrast, the upper surface response on the forward half of the airfoil is rather flat outside of an abrupt increase in both the real and imaginary parts very near the leading edge. On the aft half of the upper surface, potentially interesting trends in $Re(C_p)$ are obscured by faulty transducers at 65 and 70 percent of chord.

Predictions of the chordwise distribution of C_p are in good agreement with the α = 0 deg data in terms of magnitude and trend. The upper surface predictions illustrate exceptional agreement with the data, whereas the lower surface predictions show some deviation near the leading edge for the imaginary part and near the trailing edge for the real part starting at about 80 percent chord.

Changing the mean incidence angle to 10 deg has a dramatic effect on the unsteady pressure coefficient distributions. In Fig.

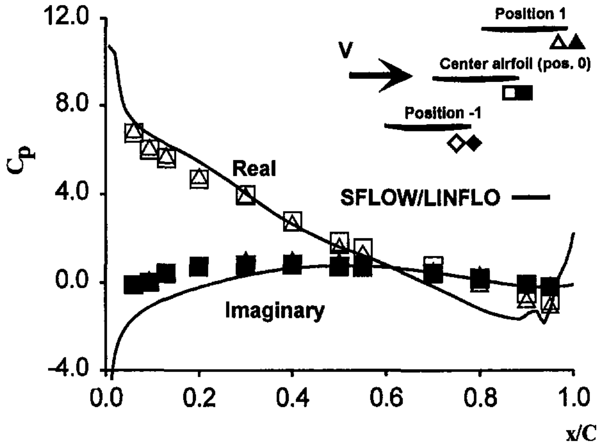

(a) Lower surface

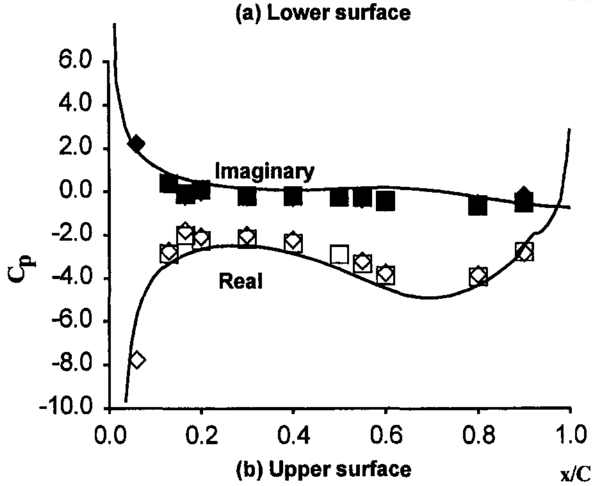

(b) Upper surface

Fig. 10 First harmonic airfoil surface pressure coefficients, M = 0.5, α = 0 deg, β = 180 deg, k = 0.8

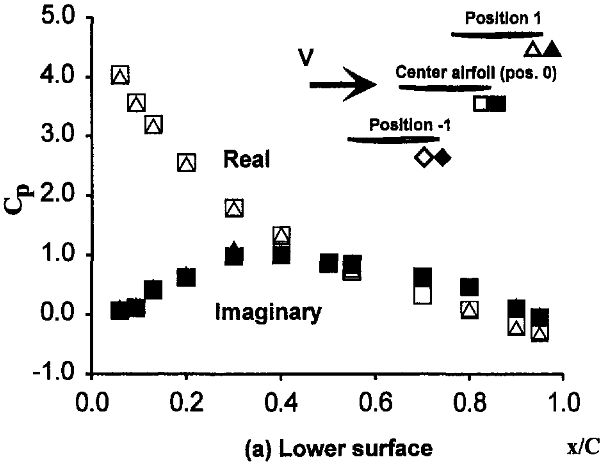

(a) Lower surface

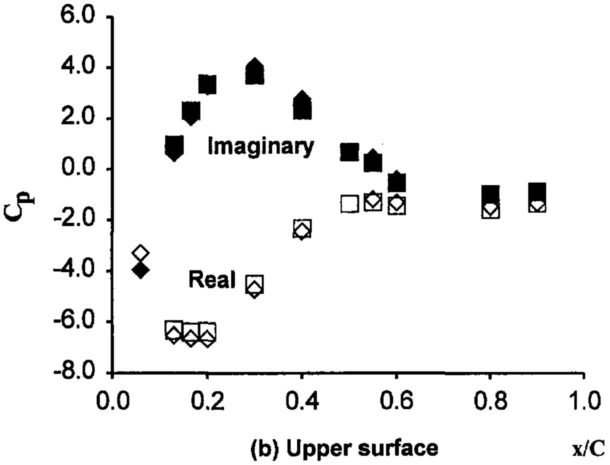

(b) Upper surface

Fig. 11 First harmonic airfoil surface pressure coefficients, M = 0.5, α = 10 deg, β = 180 deg, k = 0.8

11(a), while the distribution of the lower surface $Im(C_p)$ data is quite similar to the $\alpha = 0$ deg data, the $Re(C_p)$ data reach a much smaller peak near the leading edge. It is no surprise that the upper surface pressure coefficients shown in Fig. 11(b) are greatly affected by the separation; relative to the $\alpha = 0$ deg data, much larger pressure fluctuations are evident over the first half of the blade with the exception of $x/C = 0.06$. Despite the severely separated flow, the unsteady pressure data are highly periodic.

Airfoil upper surface pressure spectra for these two conditions are shown in Fig. 12. At low incidence, Fig. 12(a), the spectra are dominated by the response at the oscillation frequency, and only in the measurement nearest the leading edge is there a significant higher harmonic response. In contrast, the high incidence spectra, Fig. 12(b), show higher harmonic responses at all locations encompassed by the steady flow separation bubble with the first harmonic responses still dominant.

To further illustrate the mean flow effects, ΔC_p distributions for $\beta = 180$ deg, $k = 0.8$ are shown in Fig. 13 for $\alpha = 0$ deg and $\alpha = 10$ deg. The ΔC_p values were calculated using the available center airfoil data; where center airfoil data were incomplete, i.e., $x/C = 0.06$, data from the neighboring airfoils were used. The trends in the unsteady loading for the two different values of mean incidence are quite different. Near the leading edge, $Re(\Delta C_p)_{\alpha=0^\circ}$ exhibits a large negative slope. $Re(\Delta C_p)_{\alpha=10^\circ}$ starts with positive slope near there then, moving aft, changes to negative slope. $Im(\Delta C_p)_{\alpha=0^\circ}$ is negative-valued near the leading edge and has positive slope, while $Im(\Delta C_p)_{\alpha=10^\circ}$ starts out positive-valued and has negative slope. On the aft half of the airfoil, the unsteady loading is relatively small except for $Re(\Delta C_p)_{\alpha=0^\circ}$. It is also seen that there is good agreement between the predictions and the data for the attached flow case. However, there are some "wiggles" in the predicted $Re(\Delta C_p)$ in the trailing edge region of this figure and in C_p in Fig. 10. This is believed to be caused by the airfoil modification and the high pressure gradients in the steady flow solution. This will be found in all the presented unsteady surface pressure predictions.

For $k = 0.4$ and $\alpha = 10$ deg, the cascade dynamic periodicity, presented in Fig. 14, is also good. In Fig. 15, the center airfoil ΔC_p data are plotted along with the corresponding data for $\alpha = 0$ deg and analysis predictions. Periodicity of the low mean incidence data (not shown) was comparable to that of the high mean incidence data. Qualitatively, the differences between the $\alpha = 0$ deg and $\alpha = 10$ deg data are similar to the differences seen between the corresponding $k = 0.8$ data. The predictions show good agreement with the attached flow data.

Analogous results for $k = 1.2$ are shown in Figs. 16 and 17. There are some differences in the blade-to-blade lower surface $Im(C_p)$ data. Otherwise the periodicity is good. Differences in ΔC_p due to the incidence angle are qualitatively similar to the differences found for $k = 0.4$ and $k = 0.8$. However, a comparison of Figs. 17, 15, and 13 shows that the magnitude of the differences in $Im(\Delta C_p)$ due to the incidence angle increase with frequency in the separated flow region. Once again, the predictions are in good agreement with the low incidence data.

The C_p data for the three reduced frequencies are cross-plotted in Fig. 18. The lower surface C_p data, Fig. 18(a), increase with reduced frequency. Increasing k causes relatively small changes in $Re(C_p)_{\text{lower}}$ near the leading edge, but the relative

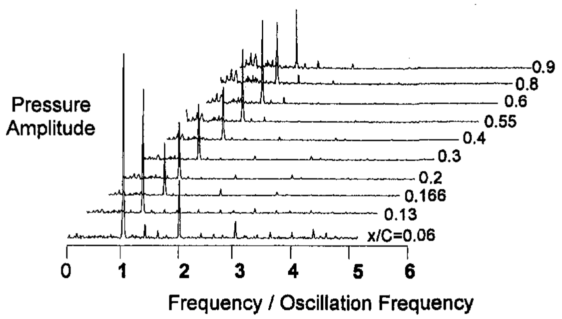

(a) α=0°

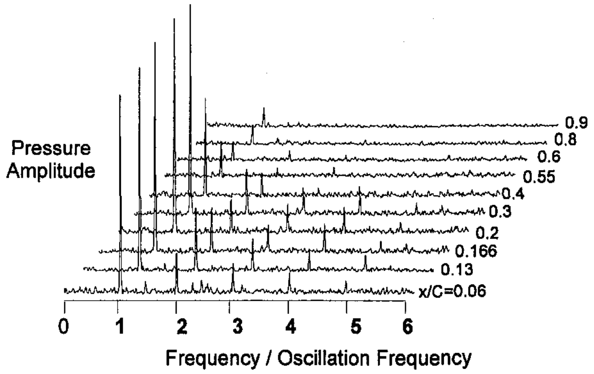

(b) α=10°

Fig. 12 Airfoil upper surface pressure spectra, M = 0.5, β = 180 deg, k = 0.8

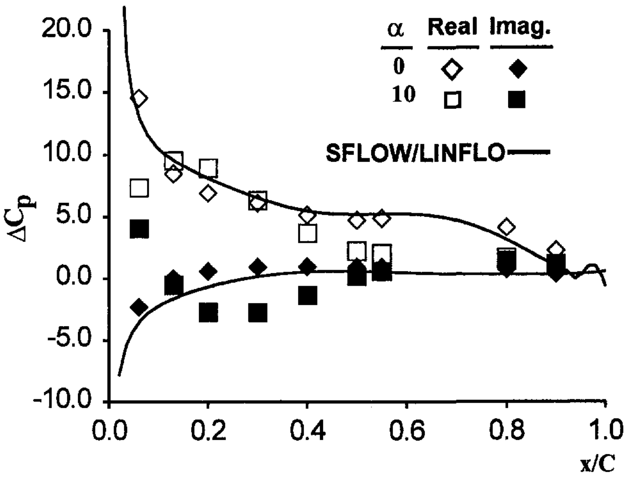

Fig. 13 Unsteady pressure difference coefficient distribution, M = 0.5, β = 180 deg, k = 0.8

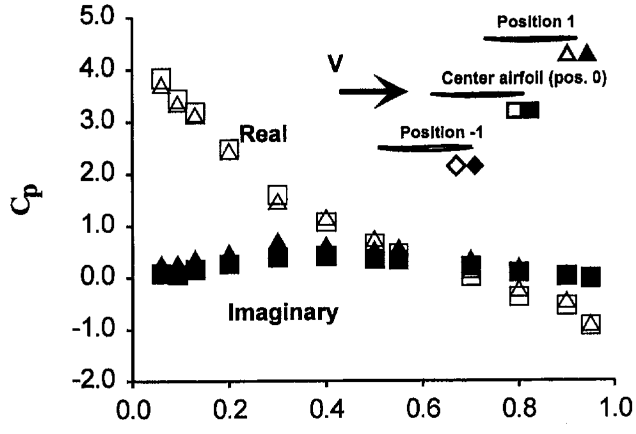

(a) Lower surface

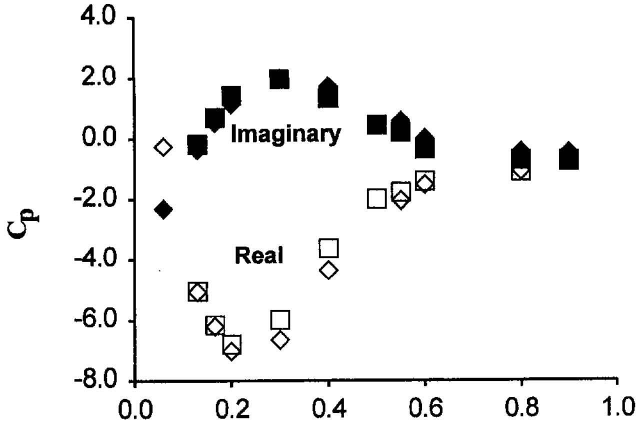

(b) Upper surface

Fig. 14 First harmonic airfoil surface pressure coefficients, M = 0.5, α = 10 deg, β = 180 deg, k = 0.4

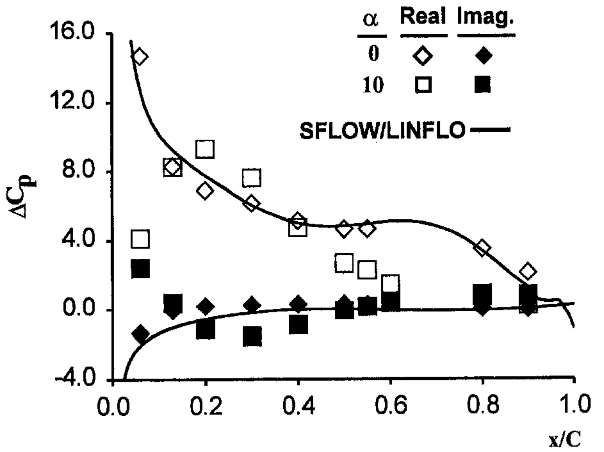

Fig. 15 Unsteady pressure difference coefficient distribution, M = 0.5, β = 180 deg, k = 0.4

changes become progressively larger as the trailing edge is approached. Changes in the imaginary part are more significant. At the lowest reduced frequency, $Im(C_p)_{\text{lower}}$ is near zero in value at all positions. As k is increased, $Im(C_p)_{\text{lower}}$ increases dramatically along the first 50 percent of chord.

The upper surface unsteady pressure distributions, Fig. 18(b), are dominated by the unsteady separated flow, the effects of which are confined to the front half of the airfoil. Changing the reduced frequency has a profound effect on the upper surface data in the separated flow region. The low-frequency $k = 0.4$ data are characterized by smooth, relatively gradual changes in C_p with chordwise position. The high-frequency $k = 1.2$ data are prone to much more abrupt changes and peak at larger values than the low frequency data. Changes in the intermediate $k = 0.8$ data are less pronounced than the $k = 1.2$ data, but more so than the $k = 0.4$ data.

The chordwise extent of the separation bubble appears to fall somewhere between 35 and 50 percent of chord depending upon the reduced frequency. At 50 percent of chord, the C_p distributions for the three frequencies are nearly converged and have relatively small magnitudes. This suggests that the flow at this point is attached throughout the cycle of oscillation. At 40 percent of chord, the imaginary parts are approximately

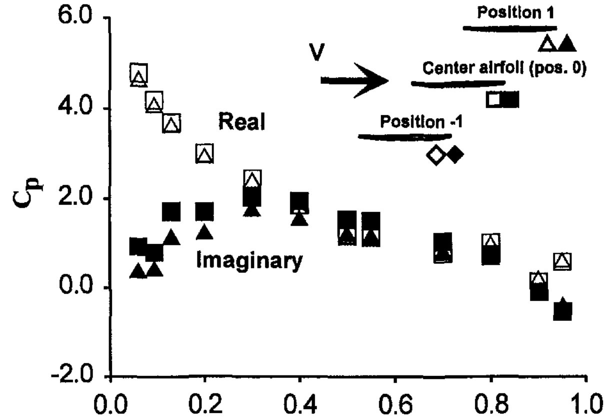

(a) Lower surface

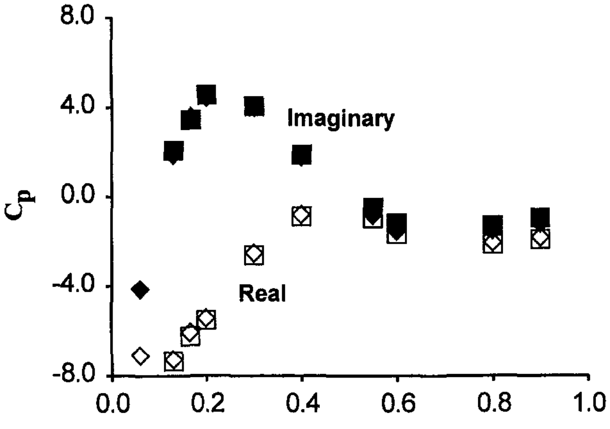

(b) Upper surface

Fig. 16 First harmonic airfoil surface pressure coefficients, M = 0.5, α = 10 deg, β = 180 deg, k = 1.2

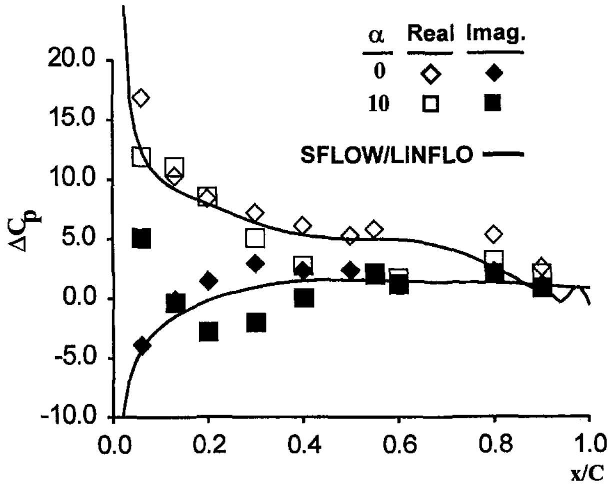

Fig. 17 Unsteady pressure difference coefficient distribution, M = 0.5, β = 180 deg, k = 1.2

equal, but the real parts decrease in magnitude with increasing reduced frequency. This behavior is consistent with the expectation that the reattachment point will move less as the frequency is increased.

Due to its influence on the unsteady aerodynamic work per cycle, the imaginary part of ΔC_p warrants further attention. From Eq. (4), the contribution of the pressure difference at a point x, $\Delta C_p(x)$, to the unsteady aerodynamic moment coefficient is proportional to $(0.5 - x)$, the distance from the pitching axis. Thus, to understand better the consequences of the data shown in Fig. 18, $C'_w \equiv (0.5 - x/C)\ Im(\Delta C_p(x/C))$ versus x/C, the chordwise distribution of the work per cycle, is plotted in Fig. 19. From this figure it is clear that the cascade stability

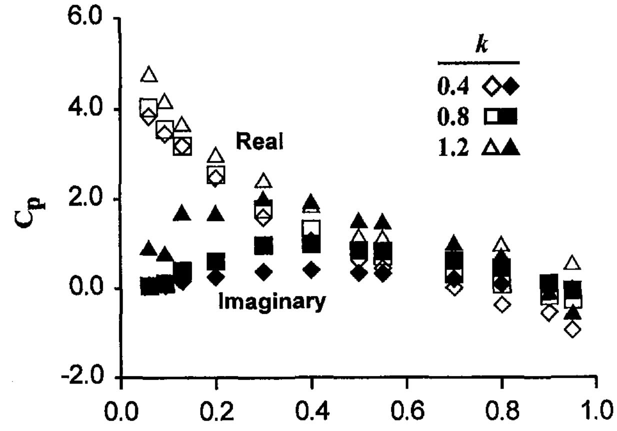

(a) Lower surface

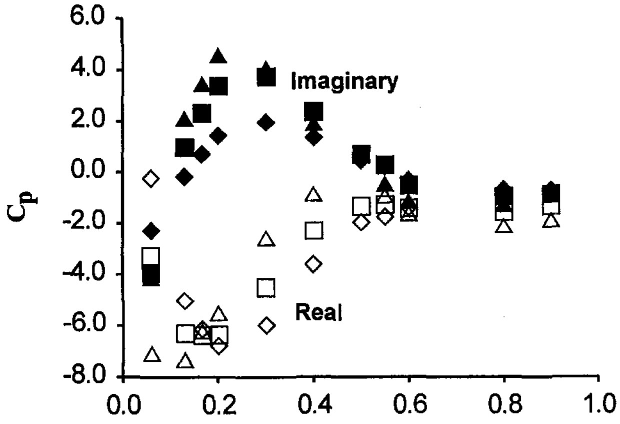

(b) Upper surface

Fig. 18 First harmonic airfoil surface pressure coefficients, M = 0.5, α = 10 deg, β = 180 deg

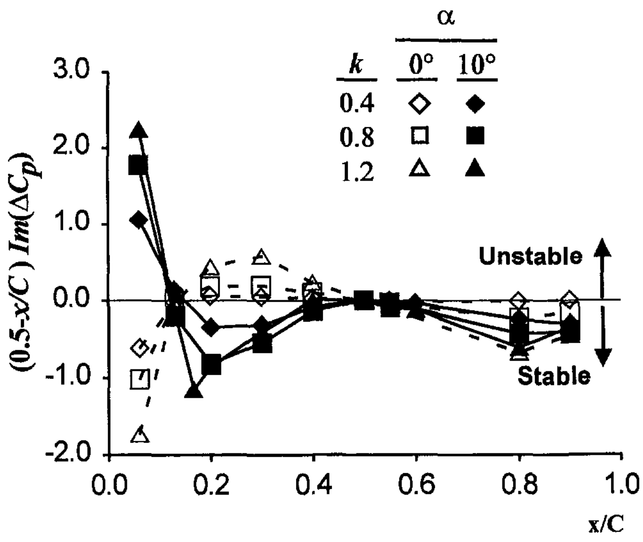

Fig. 19 Chordwise distributions of unsteady aerodynamic work per cycle, M = 0.5, β = 180 deg

is highly dependent on the behavior of ΔC_p near the leading edge. In that region, the $\alpha = 0$ deg ΔC_p distribution has a strong stabilizing effect, while the $\alpha = 10$ deg ΔC_p distribution has a strong destabilizing effect. For the data points nearest the leading edge, the absolute value of C'_w increases with increasing k: The destabilizing influence of the separated flow increases with k. Beyond that, the data cross over into regions of destabilizing influence for the low mean incidence and stabilizing influence for the high mean incidence before coalescing at the pitching point. Although the data are too sparse in the aft airfoil section to conclude much, the data at 80 and 90 percent of chord are all stabilizing. Although more data, particularly data closer to the leading edge, are needed to draw firm conclusions, these data suggest the perhaps surprising result that increasing the reduced frequency destabilizes the cascade.

Summary and Conclusion

A fundamental series of experiments have been conducted in the NASA Lewis Oscillating Cascade to investigate torsion mode oscillating aerodynamics for both attached and separated flow at realistic values of the reduced frequency. The airfoil cross section was typical of those found in advanced low-aspect-ratio fan blades. For an inlet Mach number of 0.5, steady and unsteady aerodynamic data were presented for low incidence attached flow and high mean incidence flow with leading edge separation. The surface unsteady pressure distributions were quantified for reduced frequencies of 0.4, 0.8, and 1.2 for an interblade phase angle of 180 deg. The steady and unsteady aerodynamic data were correlated with potential flow analysis predictions for the attached flow cases.

The analysis of these unique data and correlation with the predictions from the potential flow analyses revealed the following:

1 For $\alpha = 10$ deg the flow was found to separate from the suction surface (upper surface) at the leading edge and reattach in the 40 percent chord region. The separation zone was found to diminish in the endwall region. However, the flow was shown to be two dimensional in the midspan region where steady and unsteady aerodynamic response of the airfoil was quantified.

2 The steady flow exhibited good passage-to-passage periodicity for both $\alpha = 0$ deg and $\alpha = 10$ deg, thus providing a valid simulation of a turbomachine blade row.

3 Cascade dynamic periodicity was also found to be good for both the attached and separated flow conditions, thus providing a valid simulation of a turbomachine blade row undergoing torsion mode oscillations at a constant interblade phase angle.

4 Increasing the incidence angle was found to have a significant influence on the unsteady pressure distributions, particularly in the separated flow regions. In these regions, substantial deviations from the attached flow, low incidence data were found with the deviations becoming less apparent in the aft region of the airfoil.

5 Comparing the chordwise distribution of the work-per-cycle forward of midchord for separated and attached flows showed opposite trends. Near the leading edge, the separated flows had strongly destabilizing influences, while the attached flows had strongly stabilizing influences. In particular, the destabilizing influence of the separated flow near the leading edge increased with reduced frequency. Before reaching 20 percent of chord, the separated flows became stabilizing while the attached flows became destabilizing. Aft of midchord, the differences were small.

6 Correlation of the steady, attached flow experimental data with the predictions from a nonlinear two-dimensional potential flow code was good except in the trailing edge region. The discrepancy between the data and the predictions are attributed to viscous effects that are not included in the computational model and the replacement of the finite radius trailing edge with a wedge.

7 Correlation of the attached flow experimental data with the linearized potential code first harmonic predictions was good over most of the airfoil chord for both the individual surface pressure distributions and the pressure difference distributions. The predictions captured the trend and magnitude of the unsteady pressure distributions. Differences between the data and the predictions were most prominent in the trailing edge region where the deviations in the steady flow were also influencing the unsteady predictions.

Acknowledgments

Support of this research program by the NASA Lewis Research Center and Pratt & Whitney, Government Engines & Space Propulsion, is gratefully acknowledged. Dr. Daniel Hoyniak of Westinghouse Electric Corp. provided many helpful suggestions to improve the computational predictions. The successful completion of the experiments was enabled by excellent engineering and technical support. The engineers were W. Camperchioli, T. Jett, H. La, J. Little, and V. Verhoff. The technicians were D. Costello, M. Lupica, and R. Torres. Of particular importance were improvements made by Thomas Jett and Ricardo Torres, which greatly reduced the down time for the frequent cascade configuration changes.

References

Bölcs, A., and Fransson, T. H., 1986, "Aeroelasticity in Turbomachines: Comparison of Theoretical and Experimental Cascade Results," *Communication du Laboratoire de Thermique Appliquée et de Turbomachines*, EPF—Lausanne, Switzerland, No. 13.

Buffum, D. H., and Fleeter, S., 1990, "Aerodynamics of a Linear Oscillating Cascade," NASA TM 103250.

Buffum, D. H., and Fleeter, S., 1993, "Wind Tunnel Wall Effects in a Linear Oscillating Cascade," ASME JOURNAL OF TURBOMACHINERY, Vol. 115, pp. 147–156.

Buffum, D. H., and Fleeter, S., 1994, "Effect of Wind Tunnel Acoustic Modes on Linear Oscillating Cascade Aerodynamics," ASME JOURNAL OF TURBOMACHINERY, Vol. 116, pp. 513–524.

Capece, V. R., and Fleeter, S., 1987, "Forced Response Unsteady Aerodynamics in a Multistage Compressor," Purdue University Report ME-TSPC-TR-87-12.

Carta, F. O., and St. Hilaire, A. O., 1979, "Effect of Interblade Phase Angle and Incidence Angle on Cascade Pitching Stability," ASME Paper No. 79-GT-153.

Carta, F. O., 1983, "Unsteady Aerodynamics and Gapwise Periodicity of Oscillating Cascaded Airfoils," ASME *Journal of Engineering for Power*, Vol. 105, pp. 565–574.

EL-Aini, Y. M., and Capece, V. R., 1995, "Stall Flutter Prediction Techniques for Fan and Compressor Blades," AIAA Paper No. AIAA-95-2652.

Hoyniak, D., and Verdon J. M., 1993, "Development of a Steady Potential Solver for Use With Linearized Unsteady Aerodynamic Analyses," *Unsteady Aerodynamics, Aeroacoustics, and Aeroelasticity of Turbomachines and Propellers*, H. M. Atassi, ed., Springer-Verlag.

Rice, E. J., 1992, private communication, NASA Lewis Research Center, Cleveland, OH.

Széchényi, E., and Finas, R., 1981a, "Aeroelastic Testing in a Straight Cascade Wind Tunnel," *Aeroelasticity in Turbomachines*, Suter, ed., Juris-Verlag, pp. 143–149.

Széchényi, E., and Girault, J. Ph., 1981b, "A Study of Compressor Blade Stall Flutter in a Straight Cascade Wind Tunnel," *Aeroelasticity in Turbomachines*, P. Suter, ed., Juris-Verlag, pp. 163–169.

Verdon, J. M., and Hall, K. C., 1990, "Development of a Linearized Unsteady Aerodynamic Analysis for Cascade Gust Response Predictions," NASA Contractor Report NAS3-25425.

Calculation of Tip Clearance Effects in a Transonic Compressor Rotor

R. V. Chima
NASA Lewis Research Center,
Cleveland, OH 44135

The flow through the tip clearance region of a transonic compressor rotor (NASA rotor 37) was computed and compared to aerodynamic probe and laser anemometer data. Tip clearance effects were modeled both by gridding the clearance gap and by using a simple periodicity model across the ungridded gap. The simple model was run with both the full gap height, and with half the gap height to simulate a vena-contracta effect. Comparisons between computed and measured performance maps and downstream profiles were used to validate the models and to assess the effects of gap height on the simple clearance model. Recommendations were made concerning the use of the simple clearance model. Detailed comparisons were made between the gridded clearance gap solution and the laser anemometer data near the tip at two operating points. The computed results agreed fairly well with the data but overpredicted the extent of the casing separation and underpredicted the wake decay rate. The computations were then used to describe the interaction of the tip vortex, the passage shock, and the casing boundary layer.

Introduction

It is well known that tip clearance flows can reduce the pressure rise, flow range, and efficiency of turbomachinery. Smith and Cumpsty [16] have shown a 23 percent drop in maximum pressure rise and a 15 percent increase in flow coefficient at stall in a large, low-speed compressor as the tip clearance was increased from 1 to 6 percent of chord. Wisler [23] has shown a 1.5 point drop in efficiency of a low-speed compressor when the tip clearance was doubled. Yet the details of tip clearance flows are not well understood. Storer and Cumpsty, for example, suggest that most of the loss often attributed to tip clearance effects is probably due to other causes [19].

Several analytic models of tip clearance flows have been developed. Chen et al. [4] developed a model that predicts the trajectory of the clearance vortex. Denton [10] and Storer and Cumpsty [19] have developed models that estimate tip clearance losses based on mixing of the clearance jet with the free-stream flow. The analytical models all assume inviscid, incompressible flow, infinitely thin blades, and that the pressure difference across the blade tip drives the flow. They also assume that a vena-contracta effect causes separation at the edge of the blade that must be modeled with an empirical discharge coefficient. None of the models consider the effects of the clearance flow on the endwall boundary layers or on the stall point.

Tip clearance flows have also been studied computationally. Dawes [9] computed clearance flows in a transonic compressor by rounding the blade tip such that an H-type grid could be distorted to fill in the gap over the blade. Kirtley et al. [12] proposed a simple clearance model that assumes that the flow is tangentially periodic across a nongridded region above the blade. The model is exact for infinitely thin blades. Adamczyk et al. [2] used Kirtley's model to examine the role of tip clearance flows in high-speed fan stall. They calibrated the model to simulate the vena-contracta effect by reducing the size of the gap until the calculations matched an experimentally measured stall point. Suder and Celestina [21] examined tip clearance flows in a transonic compressor rotor at several operating points. They compared calculations made using Kirtley's clearance model with laser anemometer data made near the tip of the rotor. Ameri and Steinthorsson [1] used a fine multiblock grid in the clearance gap over a low-speed turbine rotor to compute the edge separation in detail.

In the present work the flow through the tip clearance region of a transonic compressor rotor, designated NASA rotor 37, was computed using three clearance models. The first clearance model used a fine O-type grid in the clearance region and the author's SWIFT multiblock turbomachinery analysis code to resolve the details of the clearance flow. These computations were originally made for the ASME code assessment "blind" test case presented at the ASME/IGTI 39th International Gas Turbine Conference held in The Hague in June of 1994. The results of the blind test case have not yet been published, but a brief overview was given in [20]. Details of the SWIFT code and the predictions required for the test case will be published elsewhere. The other two models applied Kirtley's simple periodicity model over either the full gap height or a reduced gap height to simulate a vena-contract effect. The three models were compared to each other and to experimental performance maps and aerodynamic probe data to assess the effects of the reduced gap height on the predicted performance.

There were three objectives to the present work:

1. To determine the accuracy of the simple periodicity clearance model for overall performance calculations by comparing it to the more detailed multiblock model. The effects of reducing the gap height to simulate a vena-contracta effect were also studied.
2. To validate the multiblock model in the clearance region through detailed comparisons to experimental data and to the analytic clearance model described in [4]. The blind test case did not require comparisons in the clearance region.
3. To investigate the interaction of the shock, the clearance vortex, and the casing boundary layer at operating points near peak efficiency and near stall using the multiblock calculations.

Test Compressor and Experimental Measurements

A low-aspect-ratio transonic inlet rotor for a core compressor, designated NASA rotor 37, was used for the present study.

Contributed by the International Gas Turbine Institute and presented at the 41st International Gas Turbine and Aeroengine Congress and Exhibition, Birmingham, United Kingdom, June 10–13, 1996. Manuscript received at ASME Headquarters February 1996. Paper No. 96-GT-114. Associate Technical Editor: J. N. Shinn.

The rotor was originally designed and tested at NASA Lewis Research Center in the late 1970's by Reid and Moore [14, 15]. The rotor has a design pressure ratio of 2.106 at a mass flow of 20.19 kg/s, with a measured choking mass flow of 20.93 kg/s. The rotor has 36 multiple-circular-arc blades with a hub–tip ratio of 0.7, an aspect ratio of 1.19, and a tip solidity of 1.288. The running tip clearance was estimated to be 0.0356 cm (0.45 percent span) for the blind test case using both touch probe and rub probe measurements. It has since been revised to 0.0400 cm [21]. The design wheel speed is 17,188.7 rpm, giving a nominal tip speed of 454 m/s.

For the blind test case the isolated rotor was tested in a single-stage compressor facility at NASA Lewis. A brief description of the test facility and laser anemometer system was given by Suder et al. [21, 22]. Mass flow was measured using a calibrated orifice plate far upstream of the rotor. Radial distributions of static and total pressure, total temperature, and flow angle were measured at two axial stations designated stations 1 and 4. Using the blade hub leading edge as the origin, station 1 was at $z = -4.19$ cm and station 4 was at $z = 10.19$ cm. In the present work the inlet and exit of the computational grid were chosen to coincide with stations 1 and 4. Data at two other axial stations are also referenced here. Station 2 was located inside the passage 0.2 chords downstream of the leading edge, and station 3 was just downstream of the trailing edge at $z = 4.57$ cm.

A laser fringe anemometer system was used to obtain detailed velocity measurements throughout the flow field. A two-color system gave simultaneous measurements of the axial and tangential components. Velocity measurements were made in 184 windows across each of the 36 passages as the blades passed by. Approximately 300–400 measurements were made at each (x, r) location and then ensemble-averaged to give results for an average passage. Measurements were made at 30, 50, 70, 90, and 95 percent span, and at axial intervals of about 5 percent chord. In the present work comparisons were only made at 95 percent span.

SWIFT Multiblock Analysis Code

Calculations were made using the SWIFT turbomachinery analysis code, which is a multiblock version of the single block RVC3D code described in [5, 7]. The SWIFT code solves the Navier–Stokes and energy equations on body-fitted grids using an explicit finite-difference scheme. It includes viscous terms in the blade-to-blade and hub-to-tip directions, but neglects them in the streamwise direction using the thin-layer approximation.

The turbulent viscosity was modeled using the Baldwin–Lomax turbulence model [3], implemented as described in [6]. The standard model constants were replaced by $C_{cp} = 1.216$ and $C_{Kleb} = 0.646$, which were shown in [6] to give better agreement with the standard Cebeci–Smith model. Hub and casing profiles were assumed to be fully turbulent, but the blade boundary layer was allowed to transition using the model proposed by Baldwin and Lomax. The effects of transition on this rotor are discussed in [22].

Storer and Cumpsty have noted that tip clearance effects seem to be calculated fairly accurately with Navier–Stokes codes using coarse grids and unsophisticated turbulence models in the clearance region [18]. In the present work, however, some early calculations were made using a turbulent viscosity model for fully developed duct flow across the clearance gap. Stall was predicted at a very high flow rate using this model. The model was replaced with the Baldwin–Lomax model adapted to the clearance region. The inner formulation was used near the blade tip and the casing, and a constant outer turbulent viscosity was used across the rest of the gap. For the outer formulation $f_{\max}$ was taken as the maximum of the function f across the entire gap, and $y_{\max}$ was taken as the distance to the nearest of the tip or casing walls. As will be shown later the new model predicted the stall point fairly accurately, suggesting that some aspects of the clearance flow may be strongly affected by the turbulence model. Unfortunately, the original results were discarded and the reasons for its poor performance were not determined.

Boundary conditions were specified as follows: At the inlet, T_0 was set to a constant and P_0 profiles were specified to match equilibrium turbulent velocity profiles. Inlet boundary layer thickness were set to 10 percent span at both the hub and the tip based on limited experimental data. Note that the inlet casing boundary layer was 45 times larger than the clearance gap. At the exit the hub static pressure ratio was specified and simple radial equilibrium was solved. At the walls, no-slip boundary conditions were used and pressure and temperature gradients were set to zero (adiabatic walls.)

An explicit, multistage Runge–Kutta scheme [11] was used to solve the flow equations. Physical and artificial dissipation terms were computed only at the first stage for efficiency. Conservative second and fourth-difference artificial dissipation terms were added to capture shocks and to control point decoupling. Eigenvalue scaling as described in [13] was used to scale the artificial dissipation directionally on the highly stretched grids. The artificial dissipation was also reduced linearly with grid index near solid surfaces (typically by a factor of 0.04 at the wall) to minimize effects on boundary layers. A spatially varying time step and implicit residual smoothing were used to accelerate convergence to a steady state, and Eigenvalue scaling was used to minimize the implicit smoothing coefficients at each point in each direction. All calculations were run with a four-stage Runge–Kutta scheme at a Courant number of 5.6.

Computational Grids

A multiblock grid was generated using the TCGRID turbomachinery grid code, which is described briefly in [7]. The code generates C-type blade-to-blade grids at a few spanwise locations using an elliptic grid generator developed by Sorenson [17]. The C-grids are reclustered spanwise using a hyperbolic tangent clustering function. Transfinite interpolation is used to generate an H-grid ahead of the blade, and an algebraic O-grid is generated to fill the hole in the C-grid in the tip clearance region above the blade. Each grid overlaps its neighbor by one point. Grid generation takes about 30 seconds on a Cray C-90.

The C-grid had 319 points around the blade, with 60 points along each side of the wake and 199 points on the blade surface. Grid spacing at the blade and endwalls was 4×10^{-4} cm, giving $y^+ = 2$ to 4 at the surface. There were 46 points from the blade to the periodic boundary, or effectively 89 points blade-to-blade. There were 63 points spanwise with 13 points across the clearance gap. The C-grid had a total of 924,462 points.

The H-grid ahead of the blade had 45 points streamwise, 35 points blade-to-blade, and 63 points spanwise, for a total of 99,225 points. The blade-to-blade H-C grid at 70 percent span is shown in Fig. 1, where points have been omitted for clarity.

The O-grid in the tip clearance region is shown in Fig. 2. It had 199 points in the O-direction, 13 points from the mean camber line to the blade surface, and 13 points across the gap, for a total of 33,631 points. The gap was specified as 0.0356 cm as measured experimentally. Although the gap was only 0.45 percent of the span, it was 89 times the grid spacing at the casing, so the O-grid was highly stretched across the clearance gap. There were 1,057,318 points in the full multiblock grid.

A single-block C-type grid was also generated using TCGRID for use with the simple tip clearance model. The single-block grid was identical to the C-part of the multiblock grid except that the number of spanwise points was reduced from 63 to 51 by deleting the points in the clearance gap and reclustering the remaining points to the casing. This left nine points across the gap. The single-block C-grid was also stretched about

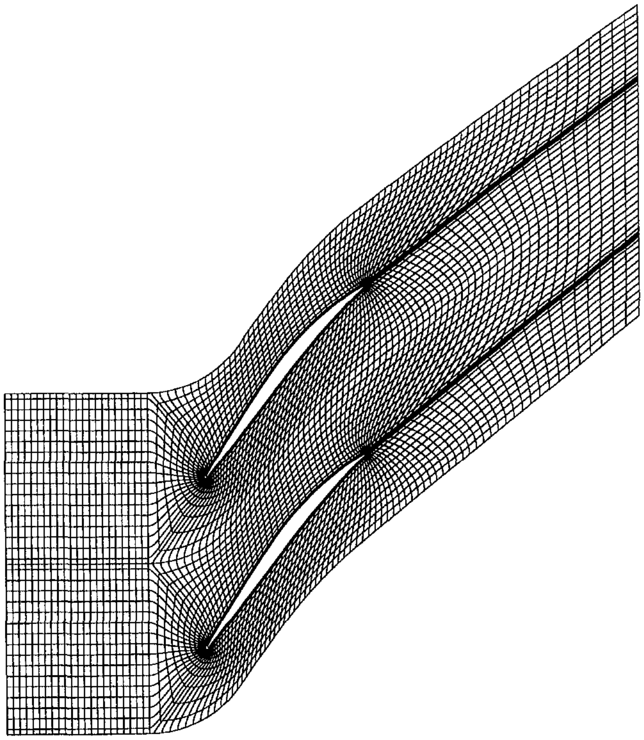

Fig. 1 H-C grid at 70 percent span. Grid lines have been omitted for clarity

one-half pitch further upstream than the C-part of the multiblock grid, but not as far upstream as the H-grid. There were 748,374 points in the single block grid.

Computational Details

Multiblock calculations were run on the Cray C-90 computer *von-neuman* at NASA Ames Research Center, under support of the Numerical Aerodynamic Simulation (NAS) Project Office. A few calculations were also run on the Cray Y-MP at NASA Lewis Research Center. The C-90 was approximately 2.2 times faster than the Y-MP.

All grid and solution arrays were stored on the Cray solid state storage device (SSD). The code was dimensioned to hold the largest grid, here the C-grid, in core memory. Asynchronous I/O was used on the Cray to move the grid and solution arrays between the core memory used by the solver and the SSD. The total storage required was about 24 MWords core memory and 18 MWords of SSD. I/O time was less than 5 percent of the total solution time.

Each operating point was typically run for 2,000 iterations. On the C-90 multiblock solutions required 7.42 seconds per iteration for 1,057,318 points, or about 7.02×10^{-6} seconds per iteration per grid point, and took about 4.1 hours per case.

Single block calculations were run on the C-90 *eagle* at NASA Ames, entirely in core. Single block solutions required 4.55 seconds per iteration for 748,374 points, or about 6.07×10^{-6} seconds per iteration per grid point, and took about 2.5 hours per case.

Results

Operating maps for the rotor at the design rotational speed were computed by running many cases with different back pressures. Choked flow points were run by imposing a low back pressure. They converged in about 1500 iterations. Intermediate flow points were computed by increasing the back pressure and restarting from a previous solution at a higher flow. Most intermediate points were run 2000 iterations. Near stall the back pressure was increased in very small increments. Cases were considered to be stalled if the flow rate and integrated exit properties were still decreasing continuously after 8000 iterations. Three operating maps were computed. One was computed using the multiblock grid with a gridded clearance gap. The other two were computed using the single-block grid and the simple periodicity clearance model, one using the measured gap, and one using half the measured gap.

For the blind test case, calculated mass flows were normalized by the choking flow rate calculated by the respective code. Similarly, the experimental mass flows were normalized by the experimental choking flow rate. This procedure normalized all mass flows to one at choke, thereby hiding differences in the computed choking flow rates and distorting the relative shapes of the curves. To avoid confusion, all curves on a given plot should be normalized by the same value. Here the experimental choking flow rate was used to normalize all flow rates because it was given with the initial specifications of the blind test case. A computed value could have been used as well, but the best procedure is probably to leave the flow rate in dimensional terms.

The multiblock grid started 0.63 chords farther upstream than the single block grid, and the multiblock solutions included endwall boundary layer losses and shock losses in that region. These losses were evaluated by averaging the multiblock solutions at the inlet of the single block grid. Then each single-block solution was adjusted to have the same corrected massflow and inlet total pressure as its respective multiblock solution.

Figure 3 compares characteristics of pressure ratio versus mass flow calculated with the three clearance models to experimental data. The calculations were energy-averaged over the entire exit grid, not at just the experimental spanwise measurement points as recommended for the blind test case. The experimental characteristic is not vertical at choke because the rotor-only tests (shown) choked prematurely in the facility diffuser. Tests of a complete stage choked in the rotor at the quoted flow rate [22]. Two of the computed characteristics are not perfectly vertical at choke because the extra operating points were not run. It is felt that these two curves are choked at their lowest points for all practical purposes.

The calculated pressure ratios are all higher than the experimental data. The multiblock results (dots) match the slope of the measured characteristic slightly better than the modeled gap results. Modeled-gap results using the full gap height (triangles) match the multiblock results closely. The half-gap model results (squares) have a very low stall point and show an abrupt fall-off to choke with a higher choking flow. The stall point was determined to four significant digits in back pressure for the

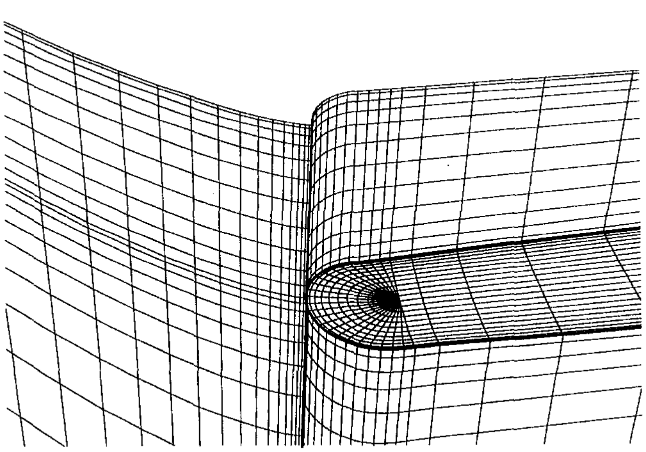

Fig. 2 Tip clearance grid near the leading edge

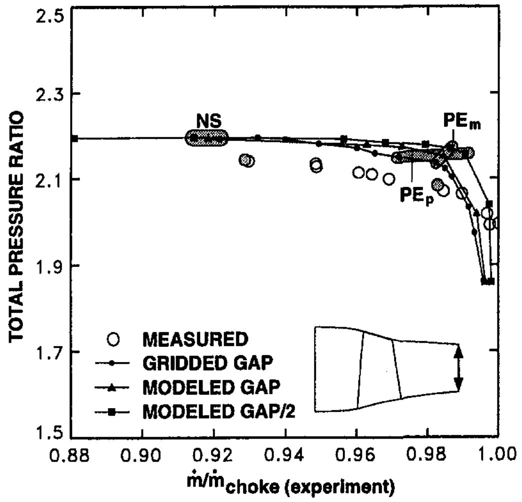

Fig. 3 Measured and computed pressure ratio characteristics

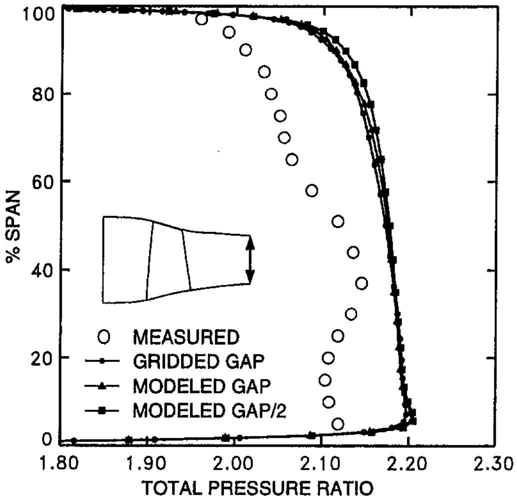

Fig. 5 Total pressure ratio profiles, station 4, peak η, calculations at same back pressure

multiblock calculations, but slightly less accurately for the single-block calculations.

Spanwise profiles of pressure ratio or efficiency computed with the three clearance models are compared to probe data measured at station 4 at the nominal peak efficiency point in Figs. 4–6. Results are usually compared at a constant mass flow, found iteratively by varying the back pressure. Total pressure profiles at 98 percent flow (the three circled points labeled "$\mathrm{PE_m}$" and shaded experimental point in Fig. 3) are shown in Fig. 4. All computed pressure ratios are higher than the data and fail to match the shape of the measured profile. This discrepancy was common to most of the codes entered in the blind test case and has yet to be explained. Profiles from the three models are very different over the entire span, and not just at the tip, as might be expected. This is because the three models required different back pressures to produce the same nominal mass flow, apparently because the models produce different amounts of endwall blockage. The exit hub static pressure ratio required for 98 percent flow was 1.225 for the gridded gap model, 1.24 for the full-gap model, and 1.25 for the half-gap model. Exit static pressure profiles (not shown) vary almost linearly from hub to tip, and the total pressure profiles vary in proportion to the static pressure.

The three models were also compared at a constant back pressure ratio of 1.24 (the three circled points labeled "$\mathrm{PE_p}$" in Fig. 3). Although comparing results at constant back pressure is not standard practice, several arguments can be made for doing so.

1 Mathematically, back pressure is an independent variable while mass flow is a dependent variable. The results are mathematically similar if they have the same independent variables.
2 Physically, back pressure (throttle setting) is also an independent variable while mass flow is a dependent variable.
3 At choke, mass flow is constant and cannot be used to compare results.
4 In a two-dimensional blade element calculation, e.g., [8, 22], mass flow is a meaningless quantity but back pressure can still be used to compare results.

At constant back pressure, the total pressure profiles collapse neatly except near the tip, as shown in Fig. 5. It is felt that this comparison separates the effects of the clearance model from the effects of varying back pressure. Here total pressure distributions computed using the full-height modeled gap agree closely with the multiblock results, but total pressures computed using the half-height gap are somewhat high at the tip.

Adiabatic efficiency profiles at the same back pressure are shown in Fig. 6. All models are in fairly good agreement with

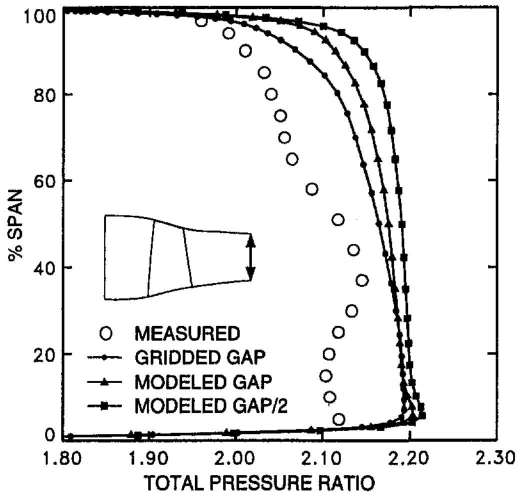

Fig. 4 Total pressure ratio profiles, station 4, peak η, calculations at same mass flow

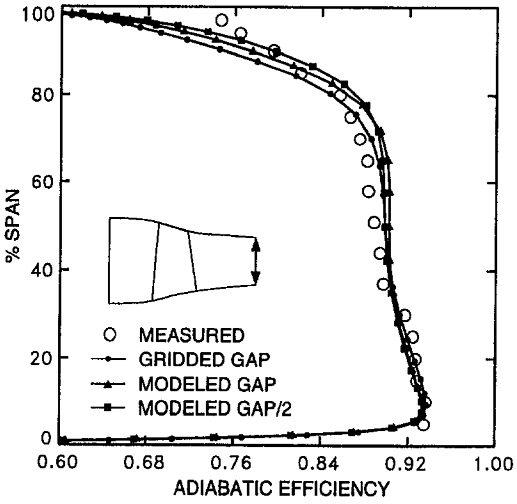

Fig. 6 Adiabatic efficiency profiles, station 4, peak η, calculations at same back pressure

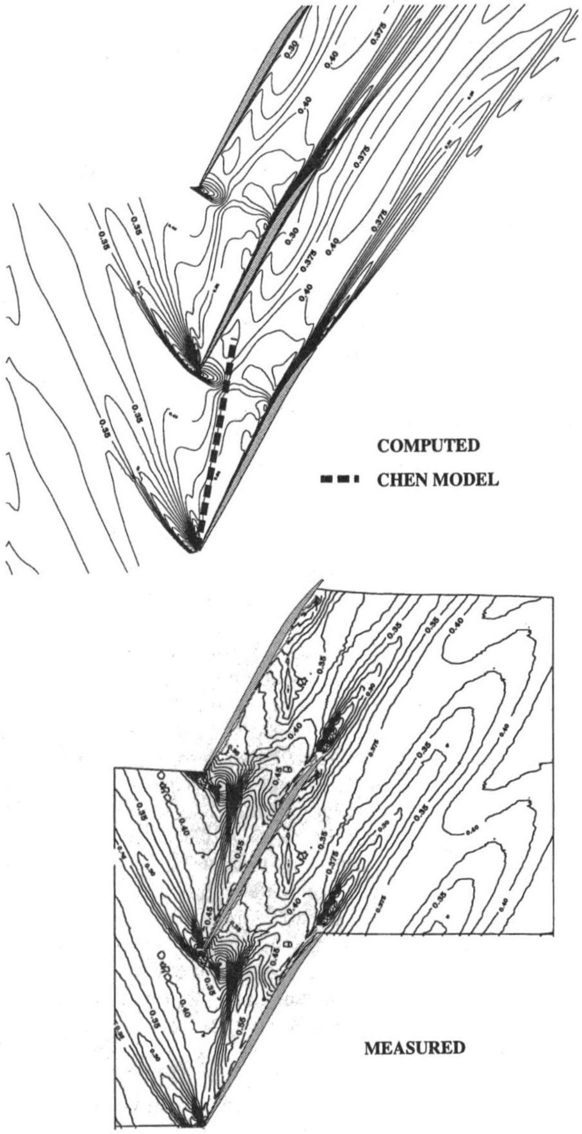

Fig. 7 Contours of normalized axial velocity component at 95 percent span, peak η

the data except near the tip. The three models give nearly identical results up to about 70 percent span. Near the tip, the full-height modeled gap gives the better agreement with the multiblock results.

From the results shown in Figs. 3–6 it is concluded that the simple clearance model using the full gap height gives reasonable agreement with a more detailed multiblock model. Later discussion will suggest a physical explanation for this conclusion. However, the conclusion does contradict the work of Adamczyk et al., who found that using one-half the gap height gave the best match with the experimental stall point for a transonic fan [2]. The reasons for this disagreement are unknown.

The remaining results make some detailed comparisons between the multiblock computations and the experimental data near the tip to validate the multiblock code. The physics of the clearance flow is then discussed.

Results at an operating point near peak efficiency (highlighted point labeled "PE" in Fig. 3) are shown in Figs. 7–11. Computed and measured contours of normalized axial velocity (normalized by $U_{\text{tip}} = 454.14$ m/s) at 95 percent span are compared in Fig. 7. Axial velocity contours are measurable, independent of frame of reference, and show many flow features surprisingly well. The contours show a shock standing ahead of the leading edge of each blade that runs obliquely downward to the suction side of the neighboring blade where it hits at about 70 percent chord. The tip vortex core leaves the leading edge of each blade and runs diagonally upward across the pas-

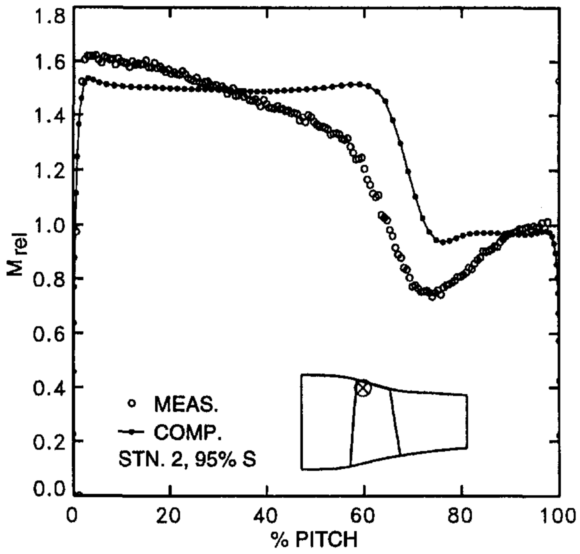

Fig. 8(*a*) Blade-to-blade Mach number, station 2, 95 percent span, peak η

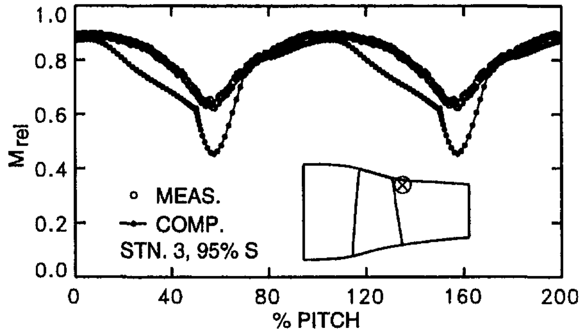

Fig. 8(*b*) Blade-to-blade Mach number, station 3, 95 percent span, peak η

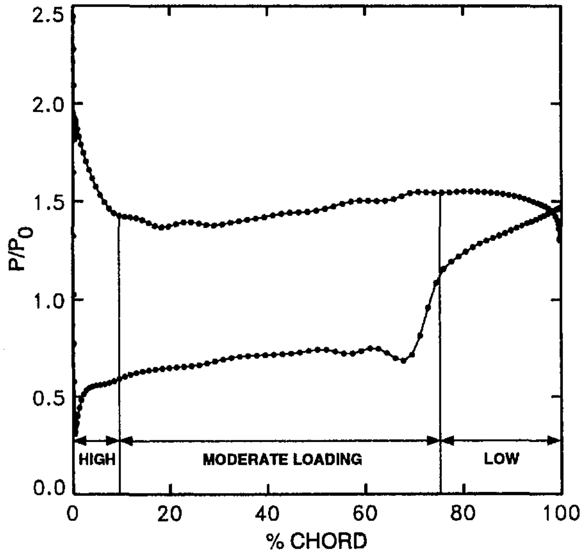

Fig. 9 Static pressure distribution at 95 percent span, peak η

sage and through the shock. Above the shock–vortex interaction is a region of low-momentum fluid with no evidence of a vortex in the contours. The computed contours match the measured contours quite well except in the low-momentum region near midchord, and in the wakes.

The path of the vortex core was estimated using the analytic model of Chen et al. [4] and is shown by the dashed line in the figure. This model maps the three-dimensional steady vortex trajectory problem to a two-dimensional unsteady vortex growth problem on a cross-channel plane. The model is inviscid and incompressible, neglects blade thickness, and assumes that the pressure difference across the clearance gap drives the flow. It shows that the center of the tip vortex should move linearly away from the blade with an angle of 16.7 deg between the blade surface and the vortex core. Figure 7 shows an angle of about 17 deg for computations and about 18 deg for the measurements. The excellent agreement between the computations, measurements, and Chen's model tends to verify that the clearance vortex is driven by the pressure difference across the clearance gap.

Computed blade-to-blade profiles of relative Mach number at 95 percent span are compared to laser data at two axial locations in Figs. 8(*a*) and 8(*b*). These figures help to quantify the more qualitative comparison made with the contour plots in Fig. 7. Figure 8(*a*) compares profiles at station 2, showing some disagreement in profile shape and shock location. At 95 percent span this profile is well within the casing boundary layer where the computations are probably strongly influenced by the turbulence model. Figure 8(*b*) compares profiles at station 3, showing that the measured wake has mixed out more than the computed wake. Many of the codes entered in the blind test case failed to predict the measured wake mixing unless a highly stretched grid was used downstream; then inadequate resolution of the wakes gave better agreement with the data. Other turbulence models do not appear to improve the wake predictions. In [8], quasi-three-dimensional calculations of this rotor with a $\kappa-\omega$ turbulence model gave wake profiles only marginally better than those calculated with the Baldwin–Lomax model. It is also possible that the rapid mixing of the measured wakes is due to unsteady vortex shedding not modeled with the steady calculations.

Based on the relatively good agreement between the calculations, Chen's model, and the measurements shown in Figs. 7 and 8, it is concluded that the multiblock calculations are sufficiently accurate for investigating the interaction of the shock, the clearance flow, and the casing boundary layer. Figure 9 begins by showing the computed static pressure distribution along the blade at 95 percent span. Three regions with different blade loadings can be seen: a highly loaded region near the leading edge, a moderately loaded region ahead of the shock, and a lightly loaded region downstream of the shock. In conjunction with Fig. 10, it will be shown that the clearance flow behaves differently in these three regions.

Figure 10 shows the interaction of the shock and clearance flow. The shock location is approximated by contours of $p/p_0 = 0.84$ ($M_{\text{rel}} \approx 1.35$), shown at 95 percent span and at midgap. At 95 percent span the shock passes continuously across the passage. The shock at midgap bends where it intersects the clearance vortex. This phenomenon will be discussed later. The clearance flow is shown by particle traces released at midgap and followed in both directions in time. The clearance flow originates upstream of the blade within the endwall boundary layer. It moves toward the pressure side of the advancing blade, climbs the blade surface, then turns abruptly around the edge of the blade and enters the gap. The clearance flow leaving the gap is discussed separately for the three regions of blade loading.

1 Highly loaded region (less than about 10 percent chord.) Near the tip, the first 10 percent of the blade is highly

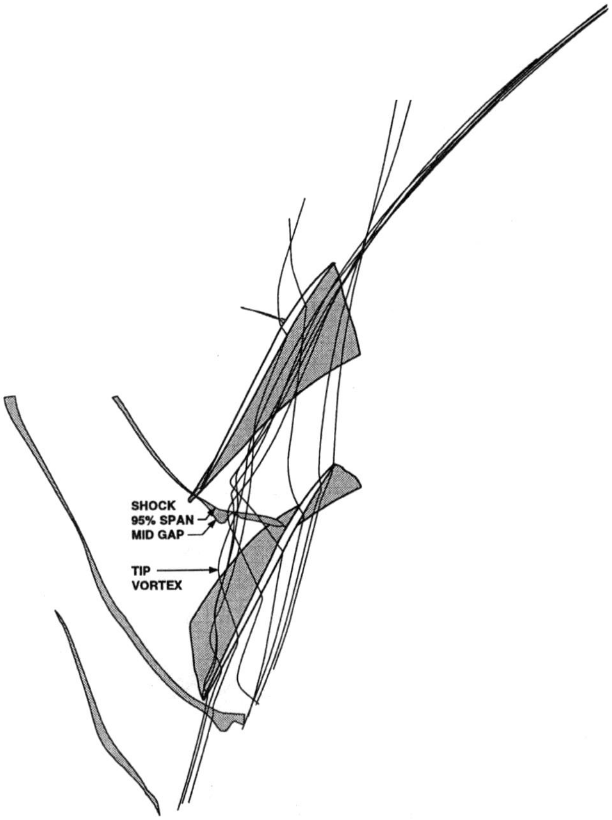

Fig. 10 Shock system above 95 percent span with tip particle traces, peak η

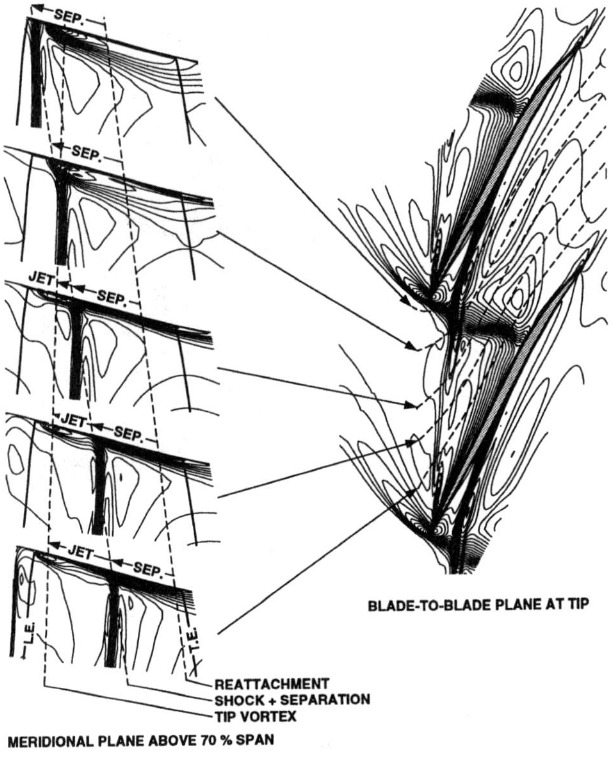

Fig. 11 Mach number contours, peak η, blade-to-blade plane at the tip, five meridional planes above 70 percent span

loaded due to the high relative incidence of the casing boundary layer. The high loading generates a strong tip vortex that moves linearly across the passage and passes through the shock with no obvious change in direction or structure. Particles released in the highly loaded region wrap several times around the vortex.

2. Moderately loaded region (roughly 10 to 70 percent chord). Between the highly loaded region and the shock, the blade is moderately loaded, with most of the loading coming from the shock. Particles leaving the gap in this region move along the casing in a thin wall jet that is highly skewed to the core flow. The wall jet moves upstream axially but downstream relative to the blade surface. When the particles reach the tip vortex they turn abruptly around it, drop down toward the core flow, and continue axially downstream without wrapping around the vortex again.
3. Lightly loaded region (greater than about 70 percent chord). Downstream of the shock the blade is lightly loaded. In this region the clearance flow is basically casing boundary layer flow that is mildly perturbed by the passing blades.

Figure 11 shows the effects of the shock and clearance flow on the casing boundary layer. A blade-to-blade plot of relative Mach number contours at the blade tip is shown at the right of the figure. This close to the casing the shock is highly smeared, and the tip vortex can be followed through the shock to the pressure side of the neighboring blade. Five meridional plots of relative Mach number contours above 70 percent span and at various tangential locations are shown at the left. The tangential locations are along the dashed C-grid lines shown in the blade-to-blade view and are roughly equally spaced blade-to-blade.

The bottom plot is near the suction side of the blade and shows the blade leading and trailing edges for reference. The upstream casing boundary layer is not evident at the far left, partly due to the limited extent of the plot but mostly because the relative Mach number of the casing is high. Plots of axial velocity indicate that the casing boundary layer is about 15 percent span high (half the height of the meridional plots) near the leading edge. The clearance vortex is evident just downstream of the leading edge, followed by a region of low-speed, wake-like flow. The shock is evident at about 60 percent chord, followed by an even larger region of low-speed flow caused by shock-boundary layer interaction.

Arrows above the blade tip indicate regions of reversed flow very near the casing, as determined from vector plots. As discussed previously, a wall jet moves upstream in the region between the shock and the vortex core. When the wall jet reaches the vortex core it turns around the vortex and back downstream, contributing to the shear layer downstream of the clearance vortex. The casing flow separates downstream of the shock and reattaches near the trailing edge.

The locations of the clearance vortex, wall jet, shock, separation, and reattachment are connected by vertical lines in plots moving up the page. The second plot from the top shows the location at which the shock and clearance vortex merge. Here the shock foot bifurcates into a lambda pattern over the vortex core, which was obvious in Fig. 10 as the bend in the shock at midgap. The low-speed rotational flow following the shock flows over the vortex and produces a substantial wake. The top plot shows that the tip vortex is continuous through the shock. It is not clear whether the vortex changes in size when passing through the shock.

Results at an operating point near stall (highlighted point labeled "NS" in Fig. 3) are shown in Figs. 12–16. In Fig. 12 computed and measured contours of normalized axial velocity at 95 percent span are compared. Near stall the shock stands further ahead of the blade and is stronger than at peak efficiency (Fig. 7). The vortex trajectory estimated using the model of Chen et al. [4] is shown by the dashed line. Because the blade is more highly loaded than at peak efficiency, Chen's model gives a steeper angle of 18.8 degrees for the vortex trajectory. Figure 12 shows an angle of about 18 deg for the computations and about 20 deg for the measurements, again in excellent agreement with the model. Since both the shock angle and vortex trajectory are steeper than at peak efficiency, the shock and clearance vortex meet closer to the center of the passage and a larger region of low-momentum fluid follows downstream. The computed contours match the measured contours fairly well except that the computed low-momentum region extends too far downstream, and again the computed wakes decay too slowly.

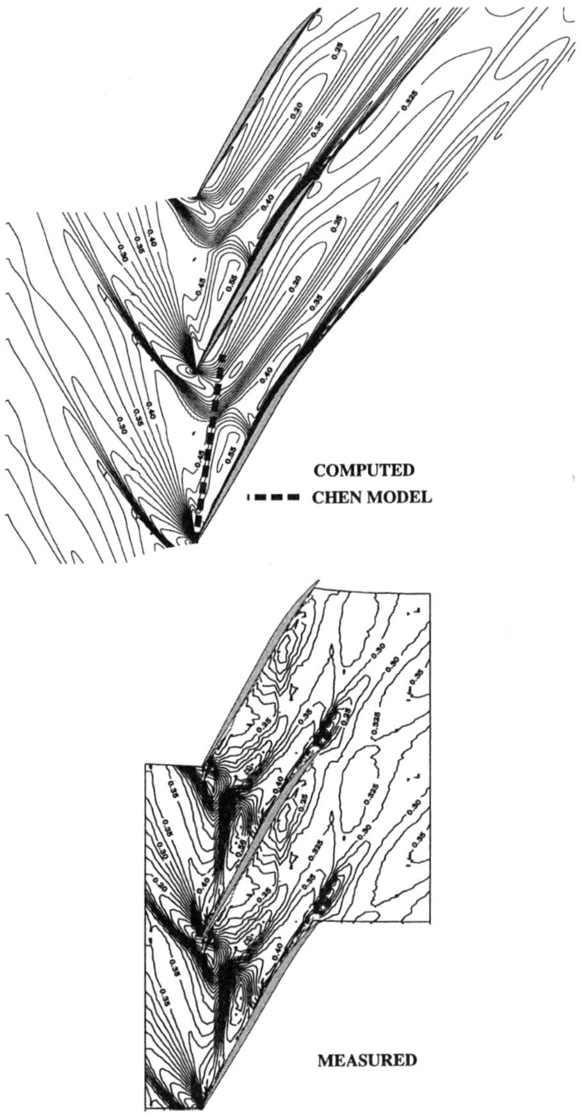

Fig. 12 Contours of normalized axial velocity component at 95 percent span, near stall

Computed blade-to-blade profiles of relative Mach number at 95 percent span are compared to laser data at two axial locations in Figs. 13(*a*) and 13(*b*). Figure 13(*a*) compares profiles at station 2, showing very good agreement between shock location and strength. In Fig. 13(*b*) the laser data show some wake remaining at station 3, but it is more mixed out than the computed wake. The computations also show strong remnants of the low-momentum flow from behind the shock–vortex interaction that is not evident in the measurements.

Figure 14 shows the shock/clearance vortex interaction at the near-stall point. The shock stands much farther ahead of the

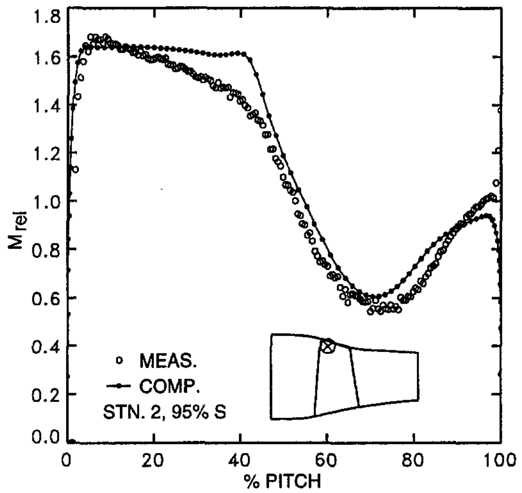

Fig. 13(*a*) Blade-to-blade Mach number, station 2, 95 percent span, near stall

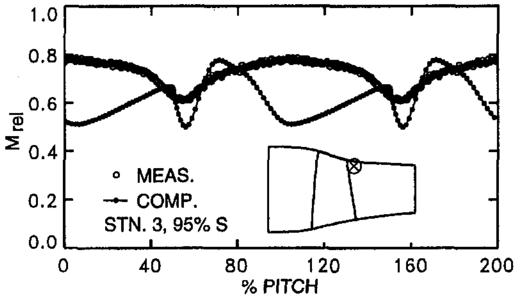

Fig. 13(*b*) Blade-to-blade Mach number, station 3, 95 percent span, near stall

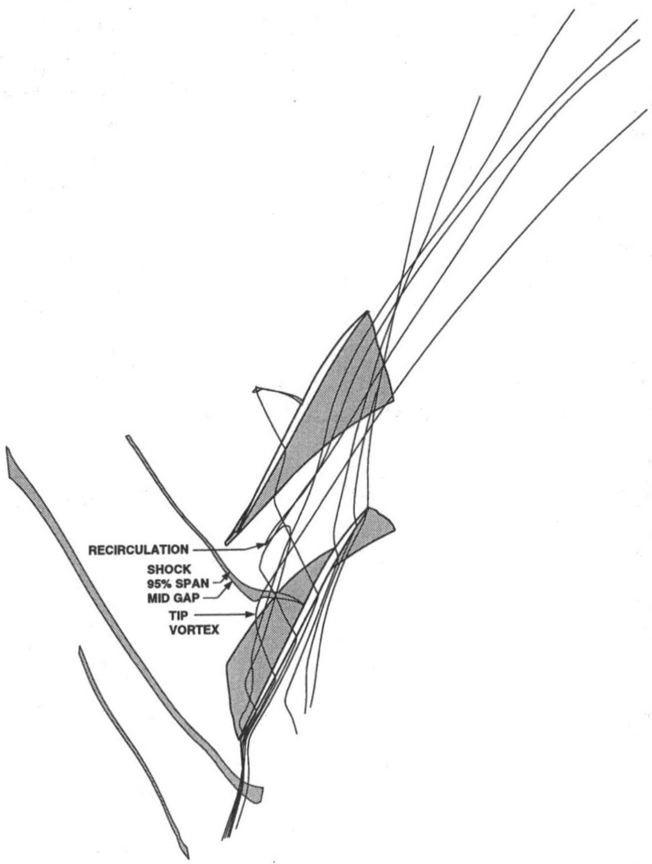

Fig. 14 Shock system above 95 percent span with tip particle traces, near stall

blade than at peak efficiency and intersects the suction surface further upstream. The shock at midgap bends where it intersects the clearance vortex. Again there are three regions of clearance flow: a strong tip vortex region, a wall jet region, and a region of perturbed casing boundary layer. The casing boundary layer separates behind the shock near midpassage, and some of the tip vortex flow is entrained in the separation bubble.

Figure 15 shows the effects of the shock and clearance flow on the casing boundary layer. A blade-to-blade plot of relative Mach number contours at the blade tip is shown at the right of the figure. Near stall the shock stand-off distance is much larger, the clearance vortex is stronger, and the bend in the shock is much more pronounced than at peak efficiency (Fig. 11).

Meridional plots of relative Mach number contours above 70 percent span and along the dashed C-grid lines shown in the blade-to-blade view are shown at the left. The bottom two plots near the suction side of the blade resemble the plots at peak efficiency, except here the shock is farther upstream and the wake-like region behind the tip vortex is stronger. In the middle plot the shock and vortex intersect, forming the lambda shock over the vortex that is visible in the blade-to-blade view. The top three plots show a large recirculating region behind the shock–vortex interaction.

The clearance region includes a strong vortex followed by a wake, a wall jet flowing upstream, and shock-induced separation with reattachment. All of these phenomena are buried in a much deeper casing boundary layer. It is unlikely that the Baldwin–Lomax model can numerically determine a consistent length scale in this region. Moreover, it is unlikely that any algebraic turbulence model can adequately characterize the turbulence in this region with a single length scale. It is thus suspected that inadequacies in the casing turbulence model are responsible for the underprediction of tip efficiencies in Fig. 6 and the predic-

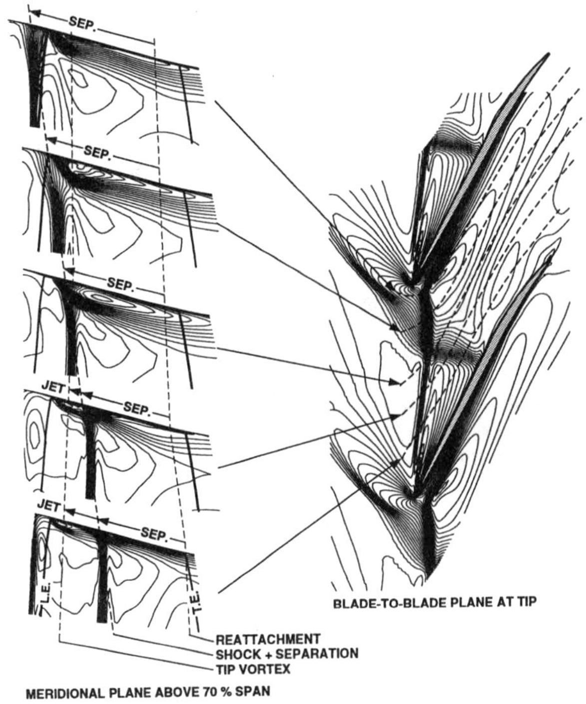

Fig. 15 Mach number contours, near stall, blade-to-blade plane at the tip, five meridional planes above 70 percent span

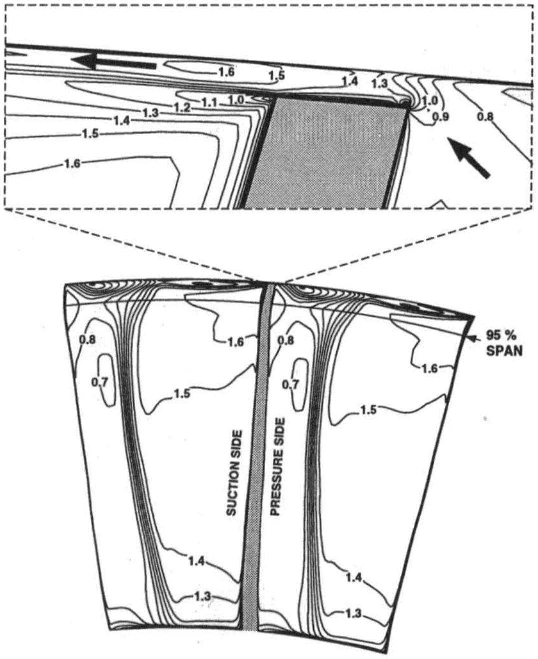

Fig. 16 Contours of M_{rel} on a cross section, 10 percent chord, near stall

tion of low-momentum clearance flow at 95 percent span in the near wake in Fig. 13(*b*).

Relative Mach number contours near stall are shown on a cross section at 10 percent of axial chord in Fig. 16. At this location the tip vortex and shock–boundary layer interaction are distinct and can be seen near the casing. An enlargement of the tip clearance region is shown at the top of the figure. Here the clearance flow originates on the pressure side of the blade at $M_{\mathrm{rel}} \approx 0.8$, then accelerates around the corner of the blade through a Prandtl–Meyer expansion to $M_{\mathrm{rel}} \approx 1.3$, which is roughly the local tip Mach number. The flow accelerates gradually through the gap to $M_{\max} \approx 1.6$, which matches the suction-side Mach number of the core flow, as described by Storer and Cumpsty [19]. The clearance flow is skewed about 50 deg from the core flow (estimated from the particle traces in Fig. 15), and the shear layer between the two flows is obvious in Fig. 16. Several authors have suggested that the mixing of this shear layer causes most of the loss directly attributable to the clearance flow [10, 18, 19].

Figure 16 explains why the simple periodicity clearance model gives the best results using the exact gap height. Since the flow enters the gap through a supersonic expansion fan, there is no separation and the vena-contract model is inappropriate. Calculations by Ameri et al. [1] of a low-speed turbine rotor with a gridded clearance gap have shown the expected edge separation and reattachment. Based on these two calculations it is suggested that the simple periodicity clearance model should be used with the full gap height for blades with clearly supersonic tip speeds. For blades with square corners and subsonic tip speeds, a reduced gap height should probably be used.

Concluding Remarks

Three-dimensional Navier–Stokes calculations were made of the tip clearance flow in a transonic compressor rotor. Tip clearance effects were modeled with a multiblock code by gridding the clearance flow and with a single-block code by using a simple periodicity model across the ungridded gap. The simple model was run with both the full gap height and with half the gap height to simulate a vena-contracta effect. Results were compared to aerodynamic probe data and to laser anemometer data. The following conclusions were drawn:

1 The simple clearance model gave good agreement with the multiblock calculations for performance predictions. The best agreement was obtained when the full gap height was used. The multiblock solution showed that the clearance flow entered the gap through a Prandtl–Meyer expansion with no vena-contracta or separation. This suggests that the simple periodicity clearance model should be used with the full gap height for blades with supersonic tip speeds, but probably with a reduced gap height for subsonic tip speeds.

2 The multiblock calculations agreed fairly well with the laser data at 95 percent span. The agreement was better at peak efficiency than near stall. The agreement was generally good up to the passage shock, but worse after the shock–clearance vortex interaction. This was probably a deficiency of the turbulence model. Computed wake profiles did not decay as quickly as the measured profiles. This may have been due to the turbulence model, but may also have been due to unsteady vortex shedding not modeled by the steady code. Although the computations did not match the data perfectly, it was felt that the results were sufficiently accurate to draw some qualitative conclusions regarding the physics of the clearance flow.

3 Three regions of varying blade loadings along the chord produced three regions of clearance flow with different behaviors. A small, highly loaded region near the leading edge produced a strong clearance vortex. The vortex trajectory agreed very well with the laser measurements and the analytic clearance model of Chen et al. The vortex passed through the passage shock with little change in trajectory. It could not be determined whether the vortex changed in size as it passed through the shock. A large, moderately loaded region between the leading edge and the shock produced a wall jet. The wall jet moved upstream axially, turned abruptly around and under the tip vortex, and continued downstream without joining the tip vortex. A lightly loaded region downstream of the shock passed the clearance flow with little effect.

4 Although the passage shock and clearance vortex are predominantly inviscid phenomena, their impact on the casing flow was highly viscous. The tip vortex acted as an obstacle on the casing that extended across the passage and produced a wake-like structure along its entire length. The wall jet produced a shear layer where it left the clearance gap and another behind the tip vortex. The casing boundary layer separated along the entire length of the passage shock. A lambda shock formed at the shock–vortex intersection. A highly rotational flow followed the shock–vortex interaction, with a large separated region at the operating point near stall. These phenomena were immersed in a much larger casing boundary layer, and strongly suggest the inadequacy of algebraic turbulence models in the clearance region. Many disagreements between the computations and data near the tip are probably due to the turbulence model, although the impact on overall performance predictions was not bad.

References

1 Ameri, A. A., and Steinthorsson, E., 1995, ''Prediction of Unshrouded Rotor Blade Tip Heat Transfer,'' ASME Paper No. 95-GT-142.

2 Adamczyk, J. J., Celestina, M. L., and Greitzer, E. M., 1993, ''The Role of Tip Clearance in High-Speed Fan Stall,'' ASME JOURNAL OF TURBOMACHINERY, Vol. 115, pp. 28–38.

3 Baldwin, B. S., and Lomax, H., 1978, ''Thin-Layer Approximation and Algebraic Model for Separated Turbulent Flows,'' AIAA Paper No. 78-257, Jan.

4 Chen, G. T., Greitzer, E. M., Tan, C. S., and Marble, F. E., 1991, ''Similarity Analysis of Compressor Tip Clearance Flow Structure,'' ASME JOURNAL OF TURBOMACHINERY, Vol. 113, pp. 260–271.

5 Chima, R. V., 1992, ''Viscous Three-Dimensional Calculations of Transonic Fan Performance,'' in: *CFD Techniques for Propulsion Applications*, AGARD Conference Proceedings No. CP-510, AGARD, Neuilly-Sur-Seine, France, Feb. pp. 21-1 to 21-19: also NASA TM-103800.

6 Chima, R. V., Giel, P. W., and Boyle, R. J., 1993, ''An Algebraic Turbulence Model for Three-Dimensional Viscous Flows,'' in: *Engineering Turbulence Modelling and Experiments 2*, Rodi, W., and Martelli, F., eds, Elsevier pub. N.Y., pp. 775–784; also NASA TM-105931.

7 Chima, R. V., and Yokota, J. W., 1990, "Numerical Analysis of Three-Dimensional Viscous Flows in Turbomachinery," *AIAA J.*, Vol. 28, No. 5, pp. 798–806.

8 Chima, R. V., 1996, "A $\kappa-\omega$ Turbulence Model for Quasi-Three-Dimensional Turbomachinery Flows," AIAA Paper No. 96-0248, Jan.

9 Dawes, W. N., 1987, "A Numerical Analysis of the Three-Dimensional Viscous Flow in a Transonic Compressor Rotor and Comparison With Experiment," ASME JOURNAL OF TURBOMACHINERY, Vol. 109, pp. 83–90.

10 Denton, J. D., 1993, "Loss Mechanisms in Turbomachines," ASME JOURNAL OF TURBOMACHINERY, Vol. 115, pp. 621–656.

11 Jameson, A., Schmidt, W., and Turkel, E., 1981, "Numerical Solutions of the Euler Equations by Finite Volume Methods Using Runge-Kutta Time-Stepping Schemes," AIAA Paper No. 81-1259, June.

12 Kirtley, K. R., Beach, T. A., and Adamczyk, J. J., 1990, "Numerical Analysis of Secondary Flow in a Two-Stage Turbine," AIAA Paper No. 90-2356.

13 Kunz, R. F., and Lakshminarayana, B., 1992, "Explicit Navier–Stokes Computation of Cascade Flows Using the $\kappa-\epsilon$ Turbulence Model," *AIAA J.*, Vol. 30, No. 1, Jan. pp. 13–22.

14 Reid, L., Moore, R. D., 1978, "Design and Overall Performance of Four Highly-Loaded, High-Speed Inlet Stages for an Advanced, High-Pressure-Ratio Core Compressor," NASA TP-1337.

15 Reid, L., and Moore, R. D., 1980, "Experimental Study of Low Aspect Ratio Compressor Blading," ASME *Journal of Engineering for Power*, Vol. 102, No. 4.

16 Smith, G. D. J., and Cumpsty, N. A., 1984, "Flow Phenomena in Compressor Casing Treatment," ASME *Journal of Engineering for Gas Turbines and Power*, Vol. 106, July pp. 532–541.

17 Sorenson, R. L., 1980, "A Computer Program to Generate Two-Dimensional Grids About Airfoils and Other Shapes by Use of Poisson's Equation," NASA TM-81198.

18 Storer, J. A., and Cumpsty, N. A., 1991, "Tip Leakage Flow in Axial Compressors," ASME JOURNAL OF TURBOMACHINERY, Vol. 113, pp. 252–259.

19 Storer, J. A., and Cumpsty, N. A., 1993, "An Approximate Analysis and Prediction Method for Tip Clearance Loss in Axial Compressors," ASME JOURNAL OF TURBOMACHINERY, Vol. 116, pp. 648–656.

20 Strazisar, A. J., and Denton, J. D., 1995, "CFD Code Assessment in Turbomachinery—A Progress Report," *IGTI Global Gas Turbine News*, May/June pp. 12–14.

21 Suder, K. L., and Celestina, M. L., 1994, "Experimental and Computational Investigation of the Tip Clearance Flow in a Transonic Axial Compressor Rotor," NASA TM-106711.

22 Suder, K. L., Chima, R. V., Strazisar, A. J., and Roberts, W. B., 1995, "The Effect of Adding Roughness and Thickness to a Transonic Axial Compressor Rotor," ASME JOURNAL OF TURBOMACHINERY, Vol. 117, pp. 491–505.

23 Wisler, D. C., "Loss Reduction in Axial Flow Compressors Through Low-Speed Model Testing," ASME JOURNAL OF TURBOMACHINERY, Vol. 107, pp. 354–363.

Three-Dimensional Flow Calculations of the Stator in a Highly Loaded Transonic Fan

P. R. Emmerson
Defence Evaluation and Research Agency,[1]
Pyestock, Farnborough,
Hampshire, United Kingdom

A three-dimensional viscous solver has been used to model the flow in the stator of a highly loaded single-stage transonic fan. The fan has a very high level of aerodynamic loading at the hub, which results in a severe hub endwall stall. Prediction of the flow at the 100 percent speed, peak efficiency condition has been carried out and comparisons are made with experiment, including stator exit traverses and fixed blade surface pressure tappings and flow visualisation. Comparisons are also made with an analysis of the rotor and stator rows using the DERA S1–S2 method. The three-dimensional predictions show good qualitative agreement with measurements in all regions of the flow field. Quantitatively the flow away from the hub region agreed the best. The general trends of the severe hub endwall stall were predicted, although the shape and size did not match experiment exactly. The S1–S2 system was unable to predict the hub endwall stall, since it arises from fully three-dimensional flow effects.

Introduction

The performance and surge margins of highly loaded, high-speed compressors can be seriously eroded by the complex, unsteady three-dimensional viscous flows in the blade endwall and wake regions. A better understanding of these complex flows is required by using new numerical models, validated by experimental investigation so that the aerodynamic design of axial compressors can be improved, accompanied by reductions in engine weight and cost.

The problem is particularly acute in the highly loaded military style transonic fan, where the demand for high pressure rise per stage leads to high levels of Mach number with strong shocks and severe diffusion requirements. This has particular implications for the first stator hub region where the high deflection, exacerbated by near sonic inlet Mach number, can lead to the condition known as hub stalling. Here the flow separates in the corner regions between the stator suction surface and endwall.

Other workers, such as Jennions and Turner (1993), and Rhie et al. (1994) have modelled a number of different transonic fans using three-dimensional Reynolds-averaged Navier–Stokes solvers with promising results. Previous work has tended to concentrate on modelling the rotor in the fan, studying aerodynamic features such as overtip flow, leading edge bow shocks, normal surface shocks, and shock/boundary layer interactions. This paper concentrates on the stator flow field, particularly the three-dimensional hub stall found in a highly loaded transonic fan. The three-dimensional calculations are supported by extensive experimental measurements.

The Propulsion Department of the Defence Evaluation and Research Agency (DERA Pyestock) is currently engaged in a research program to investigate these problems in a very highly loaded single-stage transonic fan known as C148. Previously extensive experimental work was carried out at DERA Pyestock and this is described by Bryce et al. (1995). Measurements indicated that severe hub stalling occurred in the stator. Preliminary numerical studies using the DERA S1–S2 quasi-three-dimensional method were completed in parallel with the experimental investigations.

The current work described in this paper is aimed at modelling the stator of C148 at the 100 percent speed, peak efficiency condition using a fully three-dimensional Reynolds-averaged Navier–Stokes code, known as the TRANSCode. The calculation process and the preliminary studies into grid dependency and sensitivity to the inlet boundary conditions are described. The predicted results are presented and discussed in reference to the measured flow field and results from the S1–S2 analysis.

C148 Single-Stage Transonic Fan

Design Concept. C148 employed the first stage of an existing Rolls-Royce multistage transonic fan. Table 1 lists the overall design point parameters along with some relevant dimensions. Figure 1 illustrates the radial variation of quantities defining the aerodynamic duty of the stage. It is clear from the above that, although the levels of rotor tip speed, Mach number, and mass flow per unit area are well within current engine experience, the aerodynamic stage loading at the hub is very high and well in advance of present levels. This was a deliberate design intent, setting a very challenging aerodynamic task exemplified by the near-sonic Mach number at inlet to the stator hub and the high diffusion factor (>0.55) and high deflection (>57 degrees turning, relative to axial at stator exit) required.

Fan Test Module. The test module (see Fig. 2) has no inlet guide vanes and has a 0.63 m diameter rotor at inlet. The rotor row is overhung with moderate aspect ratio blades and no snubber. The stators are shrouded, with hub platforms pinned to an inner shroud ring. The running tip clearance of the rotor was less than 1 percent span. The strongly rising hub line and small rotor–stator gap are notable features. The stators have small gaps between the platforms to allow stagger to be varied, but the stagger was fixed at the design value during the work described here. The rig is highly instrumented and has the flexibility of allowing easy insertion and removal of single and twin stator cassettes. These permit various types of on-blade instrumentation to be used. The rig also has provision for detailed traversing of three-dimensional pneumatic probes. Radial traversing can be conducted at rotor exit employing a stator with a cut-back leading edge installed in one of the single stator cassettes. Full area traverses were conducted at stator exit through circumferential traverse slots at 36 and 118 percent of stator axial chord downstream of the trailing edge. Flow

---

[1] Formerly known as the Defence Research Agency (DRA).

Contributed by the International Gas Turbine Institute and presented at the 41st International Gas Turbine and Aeroengine Congress and Exhibition, Birmingham, United Kingdom, June 10–13, 1996. Manuscript received at ASME Headquarters February 1996. Paper No. 96-GT-546. Associate Technical Editor: J. N. Shinn.

Table 1 C148 parameters

Number of rotor blades	25
Rotor pitch/chord ratio (mid-span)	0.65
Number of stator blades	52
Stator pitch/chord ratio (mid-span)	0.55
Corrected mass flow (kg/s)	54.5
Stage pressure ratio	1.807
Stage temperature rise ratio ($\Delta T/T$)	0.214
Stage hub loading ($\Delta H/U^2$)	1.21
Rotor tip speed (m/s)	442
Rotor inlet tip diameter (mm)	633
Stage inlet hub/tip ratio	0.39
Stage exit hub/tip ratio	0.62

visualisation experiments were conducted by painting the surfaces of a twin stator cassette. The hub, casing, pressure, and suction surfaces were painted in different colours, and while still wet the cassette was inserted into the rig and the compressor run up to the desired operating condition. The resulting pattern left on the blades and end surfaces illustrated the major flow features, including the extent of the corner separation and trailing edge separation.

Stator Performance. For results presented in this paper, attention has been concentrated on the operating condition at 100 percent design speed peak efficiency. Test operating conditions were as follows:

Corrected mass flow	53.08	kg/s
Total pressure ratio	1.802	
Total temperature ratio	1.220	
Isentropic efficiency	83.12	percent

The test measurements presented by Bryce et al. (1995) showed that the rotor performance was in reasonable agreement with design intent over most of the span. However, between the hub and 30 percent span, there was a marked disagreement, with the measurements indicating significantly higher pressures than intended. This was attributed to shortcomings in deviation corrections applied when the rotor was designed.

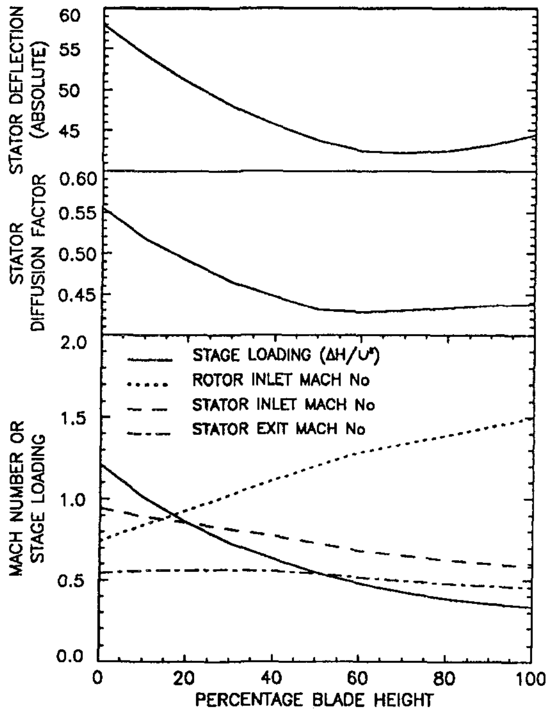

Fig. 1 C148 aerodynamic design parameters

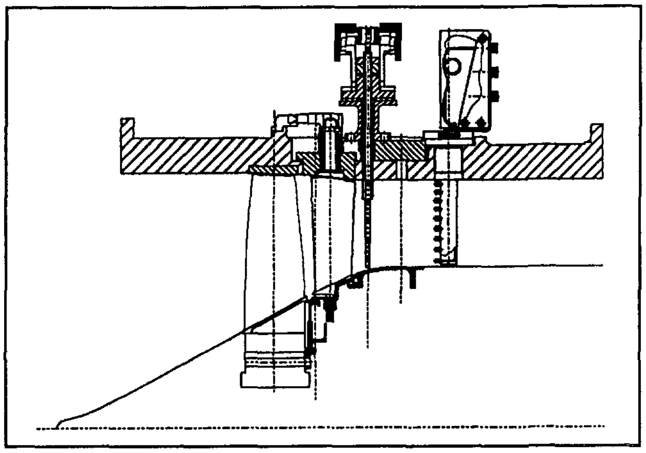

Fig. 2 The C148 single-stage transonic fan

The measurements at stator exit indicated that the stator was operating with a severe endwall corner stall. This produced a high loss (low-pressure) region extending up to 25 percent span; over the rest of the span, the flow was more two dimensional. The high losses in the hub region dissipated the excess pressure generated by the rotor here and the overall stage pressure ratio profile was reasonably close to the design intent.

The S1–S2 analysis carried out by Bryce et al. (1995) produced reasonable predictions of the rotor performance, but it was unable to model the highly three-dimensional flows in the stator hub region. It was concluded that a fully three-dimensional viscous analysis was required, and this led to the present work described here.

Calculation Method

The Code. The CFD code used for the analysis of the C148 stator is based on the three-dimensional viscous flow program BTOB3D written by Dawes (1986). The program known as the TRANSCode has been substantially modified by the Propulsion Department of DERA. These major changes to the program have improved both the accuracy and the level and speed of convergence obtained.

The code solves the Reynolds-averaged Navier–Stokes equations in finite volume form using a multistage explicit time-marching scheme with implicit residual averaging. Convergence acceleration is achieved using local time steps and a multigrid algorithm. Turbulent stresses are treated by an eddy viscosity method, where the eddy viscosities are calculated using an implementation of the mixing length model devised by Baldwin and Lomax (1978). A wall function correction is employed when the near-wall grid point lies outside the laminar sublayer. All calculations assumed that the flow was fully turbulent. Artificial viscosity is implemented based on the combined second and fourth-order schemes of Jameson and Schmidt (1986).

The operating conditions were set to give an inlet mass flow that matched experiment to within 0.5 percent. This was achieved by specifying the exit static pressure at the hub, and using simple radial equilibrium over the remaining annulus height.

The Mesh. The mesh employed by the calculation model is a simple sheared **H** type. A limited grid dependency study was carried out to investigate the effect that the size and distribution of the mesh has on the level of convergence and the predicted overall flow field. Three basic grids were investigated.

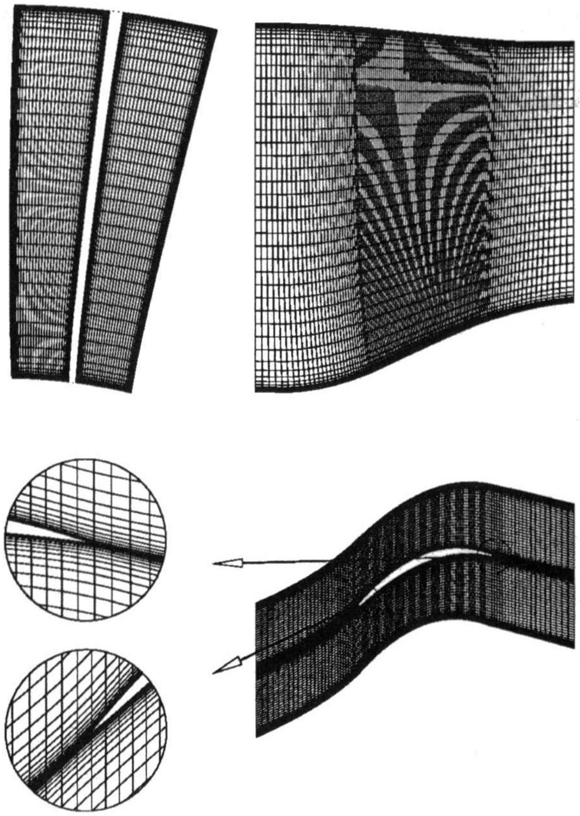

Fig. 3 C148 stator calculation grid

The first was most coarse with 35 pitchwise × 119 axial × 35 radial points, and cusped leading and trailing edges. The second had the same axial grid definition as the first grid, but more points in the pitchwise and radial directions, giving a grid of 41 pitchwise × 119 axial × 45 radial points (see Fig. 3). The third grid modelled the leading and trailing edges more accurately, having additional points packed into these regions, but similar spacing within the blade row as the previous grids. The mesh in the pitchwise and radial directions was kept the same as the second mesh, to give 41 pitchwise × 151 axial × 45 radial points. The predictions given by the three grids were virtually identical over the majority of the flow field. The only differences were seen in the hub region where the size of the hub corner stall was larger for the finer grids, because the first grid did not have sufficient nodal density in this region to capture the phenomenon as accurately.

Parallel grid dependency studies have been conducted on Q3D cascades using the TRANSCode. The results of these studies suggest that it is preferable to model the leading and trailing edge profiles as accurately as possible. However, for the C148, the flow field predicted by the grid with refined leading and trailing edges showed little difference. This is probably because the blade edges on the C148 stator are particularly thin.

A further grid was generated that used an annulus geometry upstream of the blade row that was unaltered from the true geometry (as opposed to the previous grids that are faired out to a constant radius). The inlet conditions specified for this run were calculated (using a throughflow code) to give the same conditions at the leading edge plane. The overall results were little changed from all the previous grids. However, the shape of the high loss region near the hub matched experiment slightly better than the previous grids.

Sensitivity to Inlet Conditions. The inlet boundary conditions required by the code are full profiles of total pressure, total temperature, swirl velocity, and radial angle. Because of the difficulty in defining these inlet conditions, they were derived using both the experimental measurements and the stator inlet conditions from the S1–S2 analysis. The experimental measurements of total pressure were obtained from two sources: a stator leading edge traverse using a four-hole pneumatic wedge probe, and single stator cassettes instrumented with leading edge Pitots. The single stator cassettes were also instrumented with leading edge Kiel thermocouples, to measure total temperature. The yaw angle measurements were taken from the wedge probe. They are compromised by aerodynamic interaction between the probe and the cut back leading edge of the stator, giving an overall shift of approximately −16 degrees in angle. The shift was applied by comparing the probe measurements in the midspan region with S1–S2 values. The experimental measurements at inlet to the stator, together with results from the S1–S2 prediction and profiles corresponding to the "best" TRANSCode solution using cusped leading and trailing edges, are shown in Fig. 4.

Difficulties arise firstly from the fact that the inlet to the grid is almost a chord upstream of the leading edge, where the experimental results were obtained. This means that the input profiles will alter as they approach the leading edge. This is especially true at the endwalls where the boundary layer is developing along the inlet duct. At the hub this problem is compounded by the altered annulus line, which is faired out to a constant radius upstream of the blade row (illustrated by the grid geometry in Fig. 3 as compared with the real test-rig geometry shown in Fig. 2), coupled with the fact that the hub wall does not rotate upstream of the stator in the calculation.

Perhaps more importantly, there is significant uncertainty in the measured values, due to the problems of obtaining accurate measurements in the high Mach number, highly unsteady flow field immediately downstream of the C148 rotor. Because of these uncertainties in the measured stator inlet conditions, particularly near the hub, and the S1–S2 not being expected to model the three-dimensional flow features, it was considered important to assess the sensitivity of the solutions to the inlet boundary conditions.

Five different profiles were run, each with varying degrees of severity of swirl velocity and total pressure within the hub boundary layer region. The maximum increases relative to the datum were 14 percent for the swirl velocity and 6 percent for the total pressure. Each profile assumed a power law variation for rotor exit relative velocity in the hub boundary layer.

Comparing the overall flow fields for the five different inlet boundary conditions, changing the inlet profiles within the hub boundary layer region has little effect on the solution between 30 percent height and the outer wall. There are modest differences in the size and total pressure level of the hub corner stall,

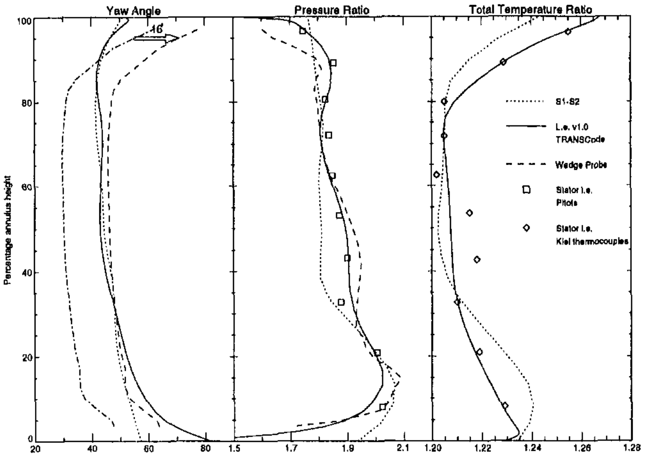

Fig. 4 C148 flow conditions at leading edge

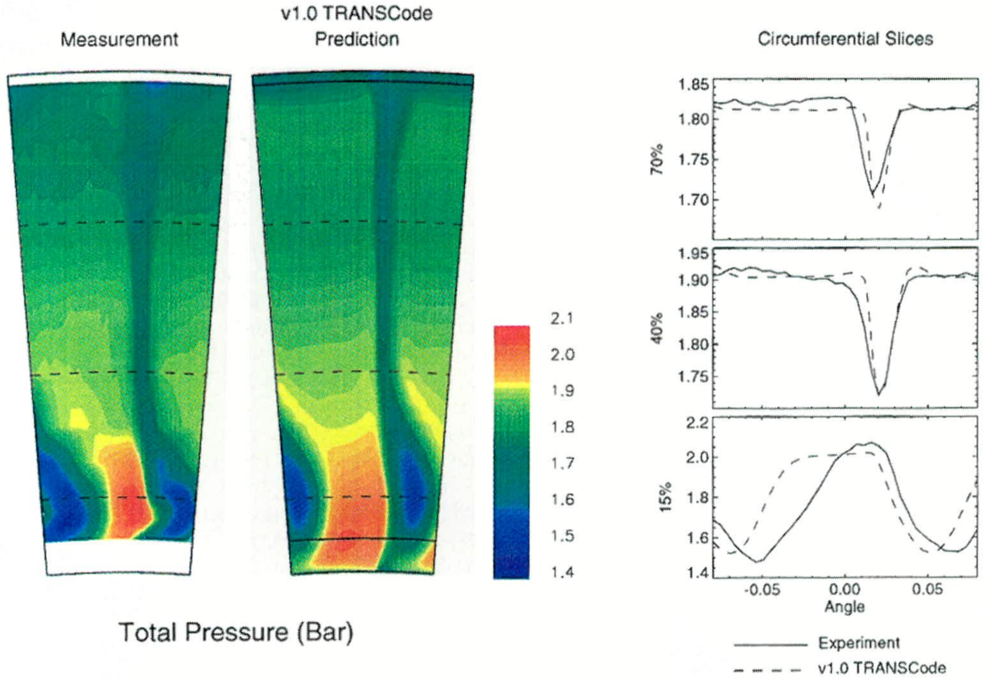

Fig. 5 C148 stator exit total pressure flow field

and in the inviscid region between adjacent loss cores. As the levels of inlet total pressure and swirl velocity near the hub are increased, the size of the loss core decreases in width and height, as does its level. The converse happens for the inviscid region. Using a reduced peak inlet total pressure produces a moderately larger and deeper loss core. However, all of the five different inlet boundary conditions predicted a hub corner stall that qualitatively matched experiment quite well.

Results

The following section compares the final predicted solution with experimental results. This solution was obtained using the second grid from the grid dependency study, with 41 pitchwise × 119 axial × 45 radial points. The level of convergence of this solution, based on either the maximum or the root-mean square (rms) values of the axial momentum residual, is a decrease of about four orders of magnitude.

Exit Total Pressure Field. The predicted exit total pressure flow field at 36 percent of axial chord downstream of the trailing edge is compared in Fig. 5 with the experimental results (taken using a pneumatic four-hole wedge probe). The flow away from the hub region is predicted well compared with experiment. The magnitude and to a lesser extent the width of the wake pressure loss agrees quantitatively; this is confirmed by the circumferential slices taken through the flow field at 40 and 70 percent radial height. The modest difference in the width of the wakes could be explained by different mixing-out rates between the prediction and experiment in the downstream flow.

In the hub region the agreement is not as good, with the predicted total pressure deficit being close to experiment in magnitude, but not in terms of area. The experimental hub loss core occupies 50 percent of pitch, whereas the predicted core covers about 35 percent; both extend to approximately 30 percent of blade span. Sandwiched in between the loss cores from adjacent blade passages exists a high-pressure jet region of inviscid flow. The total pressure level of this inviscid flow agrees well quantitatively, but the area it covers is larger than for experiment, the difference being emphasised in the circumferential slice at 15 percent blade height. The experimental high loss core appears more crescent shaped than the prediction.

The reasons for the differences in the hub region cannot be entirely explained, but an important fact to take into consideration is that the two adjacent measured loss cores are not identical in either magnitude or area, which is probably the result of mechanical tolerances. For the prediction all blades are assumed identical, only a single blade passage is modelled, and any platform leakage effects are ignored. The uncertainty in the rotor exit experimental flow measurements and the possible significant effect of unsteadiness due to rotor passing compound the problem.

Figure 6 plots the radial variation of the total pressure drop across the stator blade for experiment, the TRANSCode prediction, the S1–S2 analysis and design. The total pressure change is non-dimensionalised by the total pressure at the stator inlet. For the experiment and the TRANSCode results, the stator exit total pressures were calculated from a circumferential area-weighted average of the stator exit traverse flow field. The total

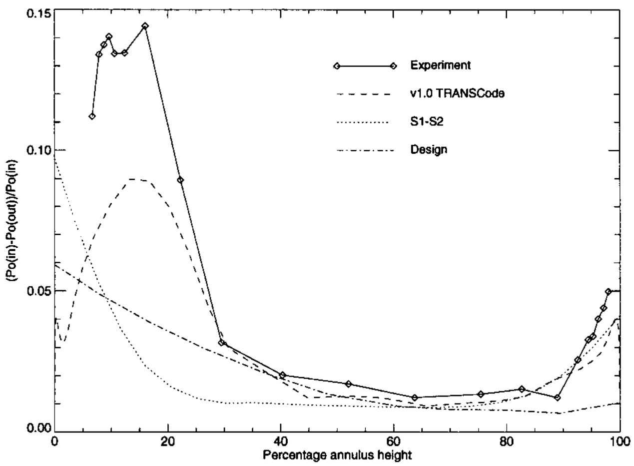

Fig. 6 Pressure drop across the C148 stator

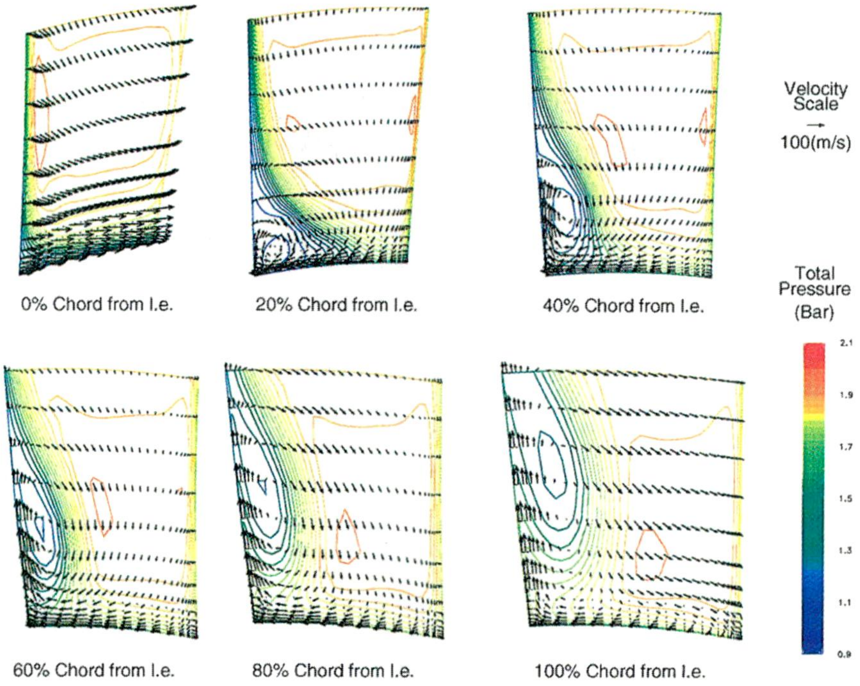

Fig. 7 Predicted secondary velocity vectors and total pressure contours in hub endwall region

pressure drop was assumed to be the difference between the free-stream level at the exit plane and the area-weighted average at each radial position. The design and S1–S2 total pressure drops were calculated by taking the difference between the stator inlet and exit values for each blade-to-blade stream-surface. The experimental results show a large change in total pressure loss in the hub region. The TRANSCode under-predicts this change by about 35 percent, but this is better than S1–S2, which displays only a local rise in total pressure over the inner 20 percent of blade span. For the experimental and TRANSCode results, further increases in loss will occur downstream as the corner stall mixes out and the energy associated with the vortex is dissipated. The design values illustrate that a serious hub endwall stall was not foreseen by the more limited methods available at the time when C148 was designed.

Surface Flow Visualisation. Figure 7 concentrates on the predicted hub endwall flow, illustrating the development of the corner stall through the blade passage as total pressure contours and secondary velocity vectors. In effect the total velocity can be thought of as having a "primary component" along the local grid quasi-streamline plus radial and tangential "secondary components." Sections are shown at six axial planes equispaced from the leading edge to the trailing edge and they extend 25 percent up the blade span.

At the leading edge there is a small concentrated area of low total pressure close to the blade suction surface. The low total pressure area grows rapidly over the first 20 percent of blade chord to reach about one third of the pitch and 10 percent of span. At 20 percent axial chord a small corner vortex with low total pressure is established near the hub platform. Toward the midchord the low-pressure area has moved up the span, elongating along the blade suction surface, narrowing in pitchwise width. The centre of the vortex has moved with the low-pressure region and the magnitude of the velocities near the suction surface has increased. By 80 percent axial chord, the low-pressure region has moved still further up the span, but also extended out from the suction surface to cover about 20 percent of pitch. The centre of the vortex has again moved with the low-pressure region. At the trailing edge the stall region grows further, both in the pitchwise and spanwise directions. Throughout most of the passage, fluid migrates from the inviscid flow down to the hub wall, and then is swept along the platform toward the suction surface. It is subsequently pulled up the suction surface away from the hub. The presence of significant transport along the surfaces near the hub and suction surface corner across the strong gradients of total pressure is indicative of powerful entropy generation in these regions.

The resultant total velocities (i.e., the resultant of axial, tangential, and radial velocity components) near the blade suction surface (two grid points away) are shown in Fig. 8, along with a photograph of a twin stator cassette used in the flow visualisation experiment. In this experiment the blade suction surfaces were coated with a red viscous paint, the pressure surfaces with blue, the hub and tip platforms with green. The cassette was then inserted into the rig while the paint was still wet, and the compressor was run up to design speed, peak

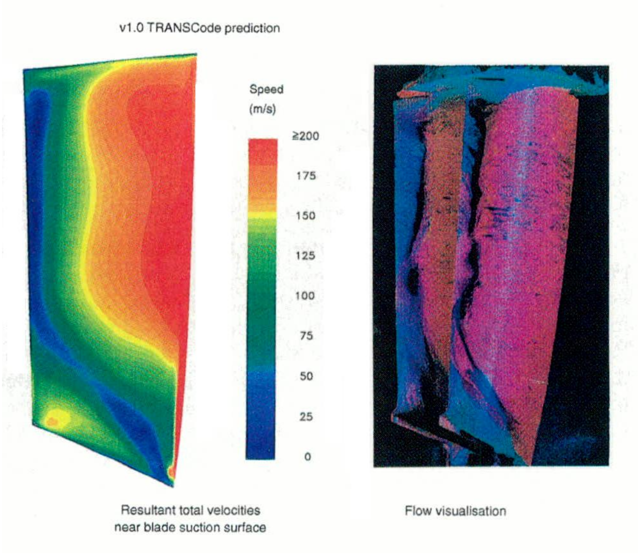

Fig. 8 Comparison between predicted flow near blade suction surface and experimental flow visualisation

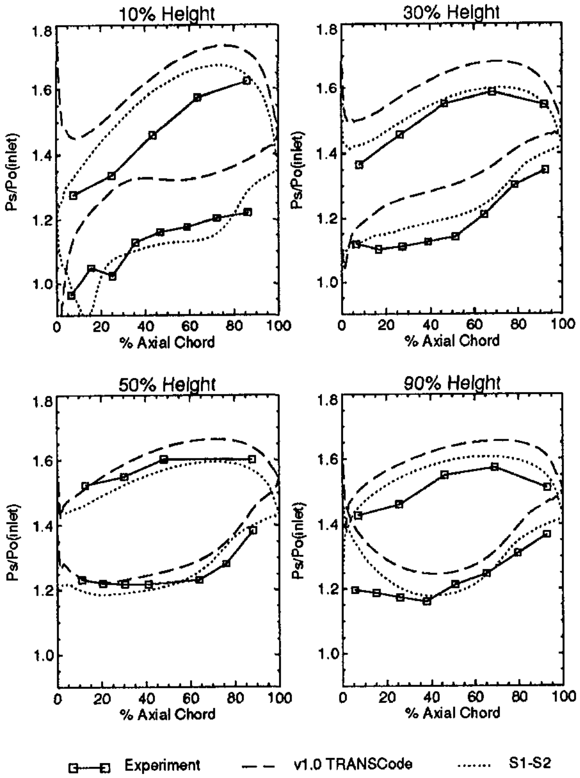

Fig. 9 Blade surface static pressure distributions

efficiency condition. The resulting pattern displays the migration of the fluid up the blade from the hub platform, and vice-versa down the blade from the tip casing. The photograph shows the hub stall appearing to grow steadily and uniformly from the leading edge corner to a maximum of 20 percent span at the trailing edge. A similar, but less severe trend occurs at the casing, with fluid extending uniformly from the casing at the leading edge to cover about 5 percent radial span at the trailing edge. The position at which the free-stream flow detaches from the suction surface is marked on the photograph by a black line, possibly a combination of different paint colours or regions where the paint has been completely scrubbed off the surface. Also present in the free-stream separation are areas of blue paint, which designate regions of reverse flow, the paint having been dragged over from the pressure surface onto the suction surface.

The predicted resultant total velocities show the zone of trailing edge separation in the midspan region and the hub corner stall. These agree qualitatively with the experiment except that the flow visualisation shows less evidence of the stagnant flow region toward the leading edge. There is also good correlation in the complex flow region where the stagnant flow around the hub corner stall merges with the free-stream separation.

Static Pressure Distribution. Figure 9 compares static pressure distributions over the blade surfaces at various radial heights for the TRANSCode and S1–S2 predictions, and experimental measurements taken from instrumented stator cassettes. Results are plotted as a ratio to stage inlet total pressure. This introduces some uncertainty for the TRANSCode solution due to the doubts concerning the inlet total pressure profile. Comparing blade loading levels (i.e., the difference between the levels on the suction and pressure surfaces) the TRANSCode prediction matches experiment quite well, at all selected radial positions. S1–S2 loading levels also agree except near the hub, where a much higher loading is predicted. The actual levels of static pressure ratio vary quite considerably between the three sets of values, particularly at 10 percent radial height. This could be a result of prediction errors, measurement errors, the uncertainty in the stator inlet total pressure, or (most likely) a combination of all three.

Conclusions

This paper has described investigations into the complex, unsteady viscous flows such as stator hub stall that limit the performance of highly loaded transonic compressors.

1 The stator row flow field in the C148 transonic fan has been successfully modelled for the 100 percent speed, peak efficiency condition using the DERA TRANSCode fully three-dimensional viscous solver. The predicted results showed good qualitative agreement with measurements in all regions of the flow field, although the shape and size of the hub endwall stall downstream of the trailing edge did not match the measured results exactly. Experimental flow visualisation on the blade suction surface and measured blade loading distributions showed encouraging agreement with predicted results, although there were some discrepancies.

2 Because of the significant uncertainty in the measured flow conditions at inlet to the stator, the sensitivity of the solution to the inlet conditions was studied, and a limited grid refinement study was also carried out. These indicated that the solutions presented are reasonably grid independent, and not oversensitive to inlet conditions.

3 Modelling of C148 using an S1–S2 flow calculation system did not predict the hub endwall stall. This is as would be expected for a quasi-three-dimensional inviscid–viscous flow solver and exemplifies the need to use a fully three-dimensional viscous solver to predict features that are fundamentally three-dimensional in nature.

4 Sufficient confidence has been gained in TRANSCode to begin to use it as a design tool, with the particular objective of alleviating stator hub endwall stall. This should lead to improved design methodologies for future highly loaded single and multistage fans.

Acknowledgments

The author gratefully acknowledges Mr. W. J. Calvert and Mr. J. D. Bryce for all their technical advice and support throughout the work developing the prediction for the C148 stator.

References

Baldwin, B. S., and Lomax, H., 1978, "Thin Layer Approximation and Algebraic Model for Separated Turbulent Flows," AIAA Paper No. 78-257.

Bryce, J. D., Cherrett, M. A., and Lyes, P. A., 1995, "Three-Dimensional Flow in a Highly Loaded Single-Stage Transonic Fan," ASME JOURNAL OF TURBOMACHINERY, Vol. 117, pp. 22–29.

Dawes, W. N., 1986, "A Numerical Method for the Analysis of Three-Dimensional Viscous Compressible Flow in Turbine Cascades: Application to Secondary Flow in a Cascade With and Without Dihedral," ASME Paper No. 86-GT-145.

Dawes, W. N., 1987, "A Numerical Analysis of the Three-Dimensional Viscous Flow in a Transonic Compressor Rotor and Comparison With Experiment," ASME JOURNAL OF TURBOMACHINERY, Vol. 109, pp. 83–90.

Jameson, A., and Schmidt, W., 1986, "Some Recent Developments in Numerical Methods for Transonic Flows," in: *Computer Methods in Applied Mechanics and Engineering*, North-Holland, Paper No. 51, pp. 467–493.

Jennions, I. K., and Turner, M. G., 1993, "Three-Dimensional Navier–Stokes Computations of Transonic Fan Flow Using an Explicit Flow Solver and an Implicit k-ϵ Solver," ASME JOURNAL OF TURBOMACHINERY, Vol. 115, pp. 261–272.

Rhie, C. M., Zacharias, R. M., Hobbs, D. E., Sarathy, K. P., Biederman, B. P., Lejambre, C. R., and Spear, D. A., 1994, "Advanced Transonic Fan Design Procedure Based on a Navier–Stokes Method," ASME JOURNAL OF TURBOMACHINERY, Vol. 116, pp. 291–297.

A. Arnone
"Sergio Stecco" Department of
Energy Engineering,
University of Florence,
Florence, Italy

R. Pacciani
Nuovo Pignone, S.p.A.,
Florence, Italy

IGV–Rotor Interaction Analysis in a Transonic Compressor Using the Navier–Stokes Equations

A recently developed, time-accurate multigrid viscous solver has been extended to handle quasi-three-dimensional effects and applied to the first stage of a modern transonic compressor. Interest is focused on the inlet guide vane (IGV)–rotor interaction where strong sources of unsteadiness are to be expected. Several calculations have been performed to predict the stage operating characteristics. Flow structures at various mass flow rates, from choke to near stall, are presented and discussed. Comparisons between unsteady and steady pitch-averaged results are also included in order to obtain indications about the capabilities of steady, multi-row analyses.

Introduction

The real flow inside a turbine or compressor is unsteady and strongly influenced by the interaction of pressure waves, shock waves, and wakes between stators and rotors. Three-dimensional, time-accurate simulations of viscous flows are yet to come for practical design purposes. However, designers are trying to arrive at a better comprehension of the multistage environment in order to increase machine performance further.

Unsteady calculations provide realistic simulations, which allow one to gain more insights into the flow physics of component interactions. Moreover, they can be used as target solutions for fine-tuning steady multirow pitch-averaging techniques. The works of Erdos et al. (1977), Rai (1987), Lewis et al. (1987), Jorgenson and Chima (1988), Giles (1988a), and Rao and Delaney (1992) are some examples of basic historical contributions to this topic.

A multigrid Navier–Stokes time-accurate solver (TRAF, Arnone et al., 1993) has recently been extended to the analysis of unsteady rotor–stator interaction. The computational procedure uses fully implicit time discretization. A four-stage Runge–Kutta scheme is used in conjunction with several accelerating techniques typical of steady-state solvers instead of traditional time-expensive factorizations. The capability of the procedure was previously investigated by applying it to a gas turbine stage. In this phase, particular attention was dedicated to grid dependency in space and time as well as to the influence of the number of blades included in the calculation (Arnone et al., 1994; Arnone and Pacciani, 1996).

In this paper, a quasi-three-dimensional release of the TRAF code has been developed and applied to the first stage of a modern transonic compressor. The analysis has been restricted to the inlet guide vane (IGV)–rotor interaction where most of the unsteadiness is to be expected. Several mass flow rates, from choke to near stall, have been analyzed in order to reproduce the stage operating characteristic. The main flow features at various operating conditions are presented and discussed.

Time-averaged results have been compared to steady, pitch-averaged ones. The effects of spurious shock reflections have been investigated by comparing a nonreflective procedure (Giles, 1988a, b) with simple one-dimensional, characteristic boundary treatment. The relative merits of different pitchwise averaging are also discussed.

It has been found that the reflective properties of the boundary conditions represent the first problem that needs to be overcome to obtain reliable steady multistage calculations. Once this problem is addressed, good agreement between time- and pitch-averaged results can be achieved.

Governing Equations and Turbulence Model

The time-accurate release of the TRAF code (Arnone, 1994; Arnone et al., 1994; Arnone and Pacciani, 1996) has been extended to handle quasi-three-dimensional effects. The unsteady, Reynolds-averaged Navier–Stokes equations have been formulated for an axysimmetric blade-to-blade surface and account for both radius and stream-tube thickness variations. The governing equations are written in conservative form in a curvilinear, body-fitted coordinate system and solved for density, absolute momentum components in the axial and tangential directions, and total energy (e.g., Jorgenson and Chima, 1988).

A two-layer algebraic model based on the mixing length concept is used for turbulence closure. In the near-wall region, the mixing length is computed using the Prandtl–Van Driest formula, while in the outer region and on the wake it is kept constant to a fixed fraction of the shear layer thickness δ, according to the standard relation (e.g., Kwon et al., 1988; Vuillot et al., 1993):

$$\ell_{\text{outer}} = 0.085\delta$$

First attempts to determine the outer length scale using methods derived from the Baldwin–Lomax (1978) and Chima et al. (1993) models have led to unsatisfactory results in transonic compressors. For those configurations, large regions with unrealistically high mixing length values and eddy viscosity were noticed. In the rotor row of a transonic compressor, vorticity may be large, even away from the blade boundary layer, due to strong shock systems and incoming wakes from the stator row. In such a situation the vorticity may not decay rapidly away from the wall. As a consequence, the models considered failed to predict a reasonable outer length scale distribution on the blade surface. Valkov and Tan (1995) observed a similar situation in wake–blade interaction computations and proposed a suitable modification of the Baldwin–Lomax model in order to address the problem. In the present work, an algebraic criterion, which resembles the features of both the Baldwin–Lomax

---

Contributed by the International Gas Turbine Institute and presented at the 41st International Gas Turbine and Aeroengine Congress and Exhibition, Birmingham, United Kingdom, June 10–13, 1996. Manuscript received at ASME Headquarters February 1996. Paper No. 96-GT-141. Associate Technical Editor: J. N. Shinn.

(1978) and Chima et al. (1993) models, but which implicitly introduces a cut-off criterion for the vorticity field based on the distance from the wall, is used to estimate the boundary layer thickness. If y denotes the distance normal to the wall, ω the vorticity magnitude, and D the Van-Driest damping factor, the value $y_{\max}$ at which the function:

$$G(y) = \frac{1}{y} \int_0^y y\omega D dy \tag{1}$$

reaches its maximum is assumed as a turbulent length scale. The boundary layer thickness is then obtained from the relationship:

$$\delta = 1.145 y_{\max} \tag{2}$$

which arises from adoption of the Coles wall-wake law to represent turbulent velocity profiles (e.g., Chima et al., 1993; Stock et al., 1987). The proposed model has been assessed in various turbine and compressor configurations and it has proven to be quite effective for steady as well unsteady analyses. The function $G(y)$ can ideally have spurious peaks at grid locations far from the wall, but its absolute maximum has always been found to occur in the outer part of the blade boundary layer, leading to reliable estimates of the mixing length.

Spatial Discretization and Artificial Dissipation

The space discretization is based on a cell-centered finite volume scheme. On each cell boundary, fluxes are calculated after computing the necessary flow quantities at the center of the side. Those quantities are obtained by a simple averaging of adjacent cell-center values of the dependent variables.

The artificial dissipation model used in this paper is basically the one originally introduced by Jameson et al. (1981). In order to minimize the amount of artificial diffusion inside the shear layer, the eigenvalue scalings of Martinelli and Jameson (1988), and Swanson and Turkel (1987) have been implemented to weight these terms (e.g., Arnone and Swanson, 1993).

Boundary Conditions

In cascade-like configurations, there are four different types of boundaries: inlet, outlet, solid wall, and periodicity. In the case of a multistage environment, more than one blade row is taken into consideration, and inlet and outlet refer to the first row inlet and last row exit, while the link between rows must be provided by means of some technique.

According to the theory of characteristics, the flow angle, total pressure, total temperature, and isentropic relations are used at the subsonic-axial first row inlet, while the outgoing Riemann invariant is taken from the interior. At the subsonic-axial last row outlet, the average value of the static pressure is prescribed, and the density and components of velocity are extrapolated.

On the solid walls, the pressure is extrapolated from the interior points, and the no-slip condition and the temperature condition are used to compute density and total energy.

Cell-centered schemes are generally implemented using phantom cells to handle the boundaries. The periodicity is, therefore, easily overimposed by setting periodic phantom cell values. On nonperiodic grids (Arnone et al., 1992; Arnone, 1994), the periodic boundaries do not match and the phantom cells overlap the real ones. Linear interpolations are then used to compute the value of the dependent variables.

The link between rows is handled by means of different techniques in steady or unsteady multiblock computations.

In the unsteady case, stator and rotor grids have a common interface line and the match is provided through appropriate calculation of phantom cell values. For the blade passage under examination, the phantom cells relative to the interface line lie on the adjacent blade passage, and linear interpolations are used to provide the flow variable values. This approach, similar to the one used on periodic boundaries, where grids do not match, is not strictly conservative. However, monitoring of the errors in the conservation of mass, momentum, and energy has indicated a very good level of accuracy. For the practical applications considered up to now, relative errors in conservation were always less then 10^{-4}, which was considered accurate enough.

For steady multirow computations, different methods to transfer informations from one row to the other have been considered in the present work.

A fairly common method of linking rows can be derived by a characteristic one-dimensional approach where quantities are pitch-averaged at the interface lines and transferred between blocks. Total temperatures, total pressures, and flow angles, necessary as inlet conditions, are pitch-averaged on previous blade rows. Static pressures, needed at the outlet boundaries, come from pitch-averaging on successive rows.

Modern state-of-the-art turbine and compressor stages work in transonic regimes and stator and rotors are stacked very close to each other. If inlet and outlet boundaries are located at short distances from the blade rows, the use of the one-dimensional characteristic boundary treatment described above may result in undesired reflections of shock waves (Arnone and Benvenuti, 1994). Moreover, the pitch-averaging process takes place close to the blade passage and, depending on the averaging procedure, the conservation of mass or momentum or energy can be poor if the flow exhibits strong gradients.

One way to overcome such difficulties is to slightly separate the blade rows so that the mixing plane is placed far enough upstream or downstream of the blade rows. Here the flow will result quite uniform in the circumferential direction and the averaging process will be more accurate in conserving mass, momentum, and energy. The major disadvantages of this approach arise from its extension to three dimensions. The bladings of modern compact turbomachines undergo sensible height variation in a single row as well as from row to row in order to accommodate density changes of the flow. As a consequence, endwalls are contoured, and adjustment of the axial gap between rows results in a modification of the meridional channel geometry.

An improved method to deal with the coupling of blade rows in steady multistage calculations, which should allow one to maintain the machine geometry while reducing undesired reflections, is based on the use of nonreflective procedures.

In order to investigate these important issues, the non-reflective treatment proposed by Giles (1988a, b) has been used in the present work as an alternative to the one-dimensional characteristic boundary scheme previously discussed. Following this approach, the time variation of each incoming characteristic variable at the inlet and outlet boundaries is decomposed into a sum of a uniform, pitch-averaged part and a tangentially varying fluctuation. The average time variations of incoming characteristics are set in order to match pitch-averaged flow variables at the interface of two rows. The local time variations are treated according to nonreflective conditions derived from a Fourier analysis of linearized, quasi-three-dimensional Euler equations. The outcoming characteristic changes are extrapolated from the interior of the domain.

Basic Multigrid Steady Solver

The system of governing equations is advanced in time using an explicit four-stage Runge–Kutta scheme. A hybrid scheme is implemented, where, for economy, the viscous terms are evaluated only at the first stage and then frozen for the remaining stages (Arnone and Swanson, 1993).

Three techniques are employed to speed up convergence to the steady-state solution: (1) residual smoothing; (2) local time-stepping; and (3) multigrid.

An implicit smoothing of residuals is used to extend the stability limit and the robustness of the basic scheme. The vari-

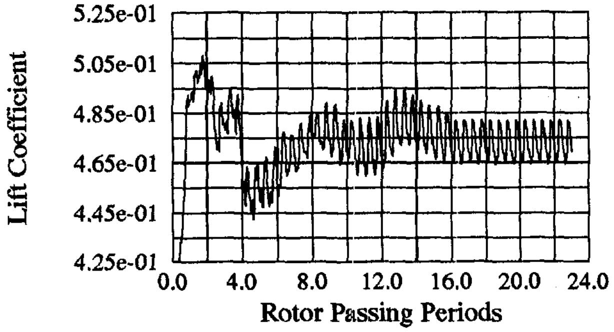

Fig. 1 Unsteady rotor lift evolution

able coefficient formulations of Martinelli and Jameson (1988), and Swanson and Turkel (1987) are used to obtain effective viscous calculations on highly stretched meshes (Arnone and Swanson, 1993). The time step is then locally computed on the basis of the maximum allowable Courant number, typically 5.0, and accounting for both convective and diffusive limitations (Arnone and Swanson, 1993).

The multigrid technique incorporated in the TRAF code is based on the Full Approximation Storage (FAS) schemes of Brandt (1979) and Jameson (1983). A V-type cycle with coarse grid sweeps (subiterations) is used. The turbulent viscosity is evaluated only on the finest grid level and then interpolated on the coarse grids.

On each grid, the boundary conditions are treated in the same way and updated at every Runge–Kutta stage.

Multigrid Time-Accurate Stepping Scheme

Jameson (1991) proposed a method for the time-accurate integration of the Euler equations using time-marching steady-state techniques. Such an approach has become widely popular since its introduction and it has also been successfully applied to the Reynolds-averaged Navier–Stokes equations (i.e., Arnone et al., 1993, 1994; Alonso et al., 1995). By the introduction of dual time-stepping and a fictitious time, a new residual is defined that includes the real time derivatives of the conservative variables as source terms in addition to the convective, diffusive, and artificial dissipation fluxes. Such derivatives are discretized using a three-point backward formula, which results in an implicit scheme that is second-order accurate in time.

Between each time step the solution is advanced in the nonphysical time, and acceleration strategies like local time stepping, implicit residual smoothing, and multigridding are used to speed up the new residual to zero to satisfy the time-accurate equations.

The described method has recently been used by the authors to compute the rotor:stator interaction in a transonic gas turbine stage (Arnone et al., 1993, 1994) and it has indicated up to a 97 percent reduction in the computational effort with respect to classical explicit schemes. By means of the implicit time discretization, stability restrictions are removed, while the efficiency of the explicit approach in addressing high-frequency problems can still be maintained by not performing residual smoothing and multigrid. When the characteristic frequency of the problem decreases, accelerating techniques can be gradually introduced to optimize the computational cost.

Application to a Modern Transonic Compressor Stage

The quasi-three-dimensional release of the TRAF code has been used to study the first-stage transonic blading of an axial compressor under development at the Nuovo Pignone Company (Benvenuti, 1996).

A near-tip section of the stage, where the flow is transonic and important unsteady effects are expected, has been selected for the analysis. The stream-tube thickness and radius distribu-

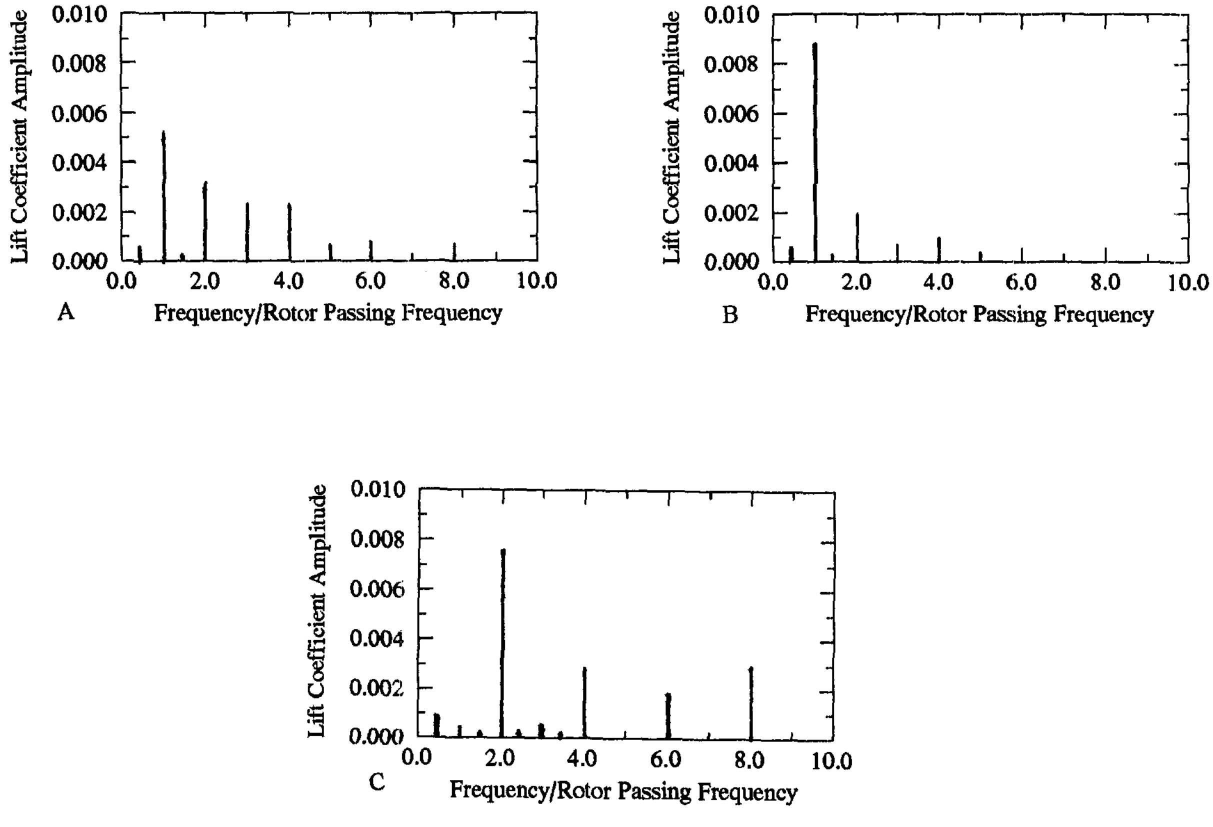

Fig. 2 Frequency spectra of the rotor lift for choke (A), peak efficiency (B), and near-stall (C) conditions

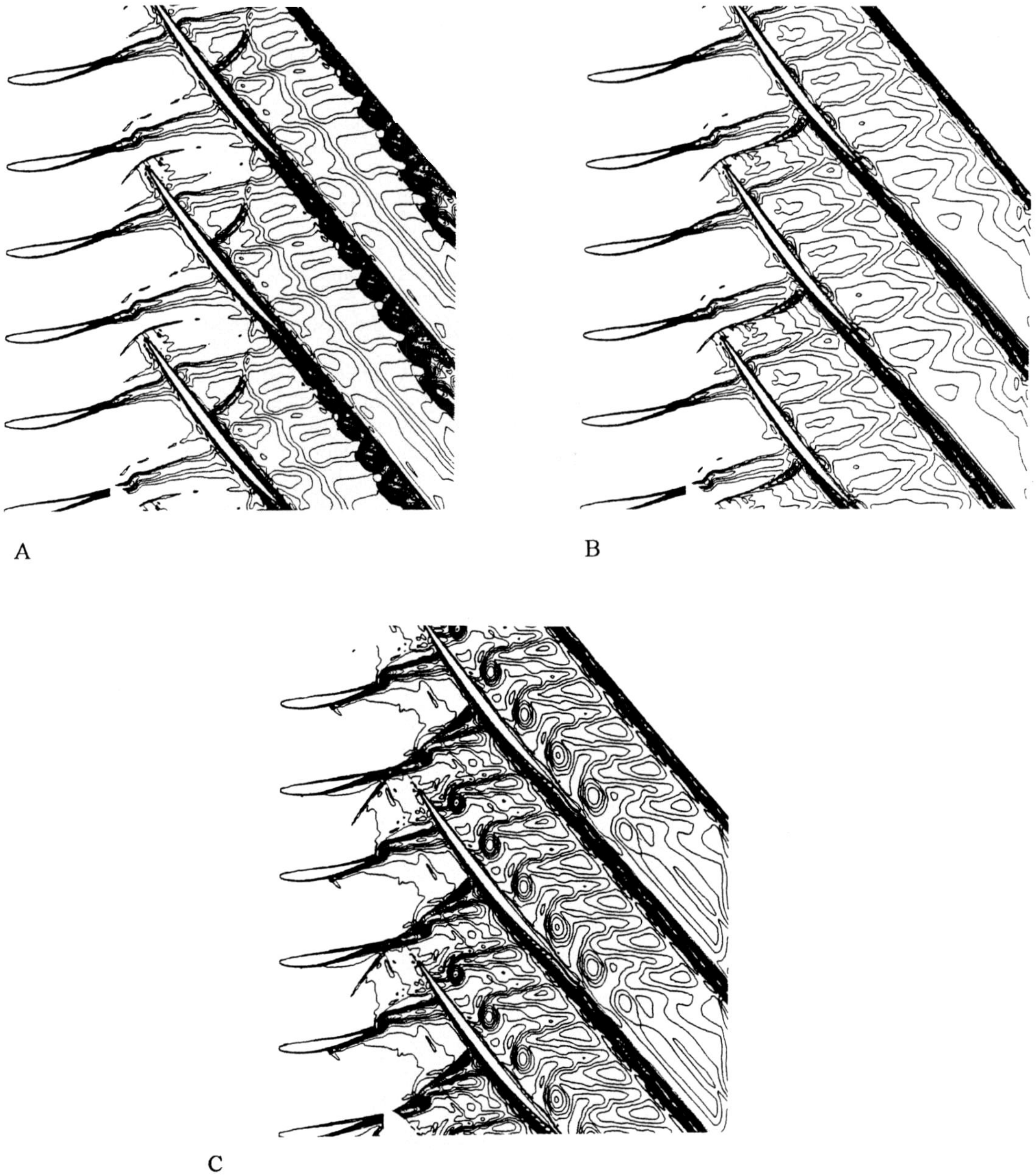

Fig. 3 Instantaneous entropy rise contours for choke (A), peak efficiency (B), and near-stall (C) conditions

tions were established on the base of steady, three-dimensional, viscous stage calculations.

In transonic compressors, like the one under consideration, the flow is supersonic in the relative frame at the rotor inlet. It is common in these industrial compressors to have quite a normal passage shock, which is detached from the leading edge at nominal conditions. The small axial gap between rows allows the shock wave to enter and to be reflected by the inlet guide vanes. Downstream of the rotor throat, the flow is subsonic. Therefore, the unsteady effects experienced by the downstream stator rows are due to pressure waves and wakes from the rotor. Stronger unsteadiness is then to be expected in the inlet guide vanes (IGV)–rotor row interaction.

On the base of such considerations, it was decided to restrict the analysis to the IGV–rotor interaction. The entire operating range of the stage (IGV–rotor), from choke to near-stall conditions, was spanned with nine different mass flow rate values. This extensive analysis was aimed at producing a target solution for the assessment of steady, pitch-averaging techniques as well as to investigate the flow physics of the interaction.

The computational mesh consists of mixed C-type and H-type nonperiodic grids. A C-type grid structure (257 × 65) was selected for the IGV. On the contrary, it was found convenient to use an H-type structure (257 × 161) for the rotor blades. Away from the leading edge, the C-type structure tends to increase the grid size and thus induces a smear of both the incoming wakes and the bow shock. With an H-type structure, it is much easier to control the uniformity and density of the grid before the blade passage. In order to reduce the grid skewness both the C-type and the H-type grids are of the nonperiodic type (i.e., Arnone et al., 1992; Arnone, 1994).

The presentation of results will be split in two parts. The first section will be used to discuss the unsteady calculations, while the second will be dedicated to the comparison of time-averaged results with the predictions of steady pitch-averaging methods.

Unsteady IGV–Rotor Interaction. The first stage under investigation has 30 inlet guide vanes, 18 rotor blades. The first issue to address is how to account for the ratio between the number of IGV and rotor blades. As mentioned before, the

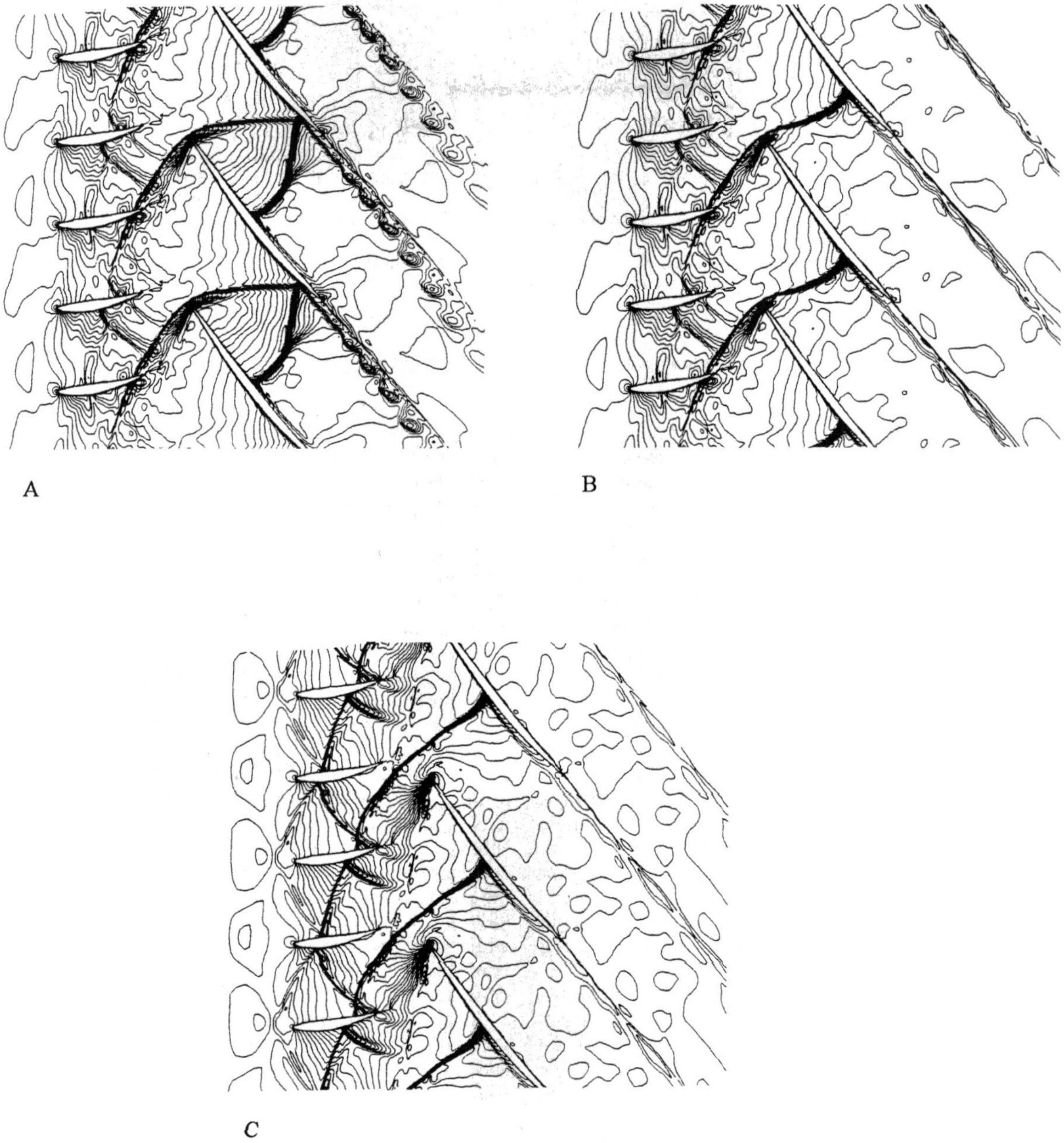

Fig. 4 Instantaneous density contours for choke (A), peak efficiency (B), and near stall (C) conditions

code has been designed to handle more blade passages per row. Periodic conditions are, therefore, applied only between the first and last block of each row. In our case, assuming steady and uniform inlet and outlet stage boundary conditions, the exact combination would be five vanes and three rotors.

It is common in an unsteady rotor–stator interaction analysis to limit the number of blade passages included in the calculation in order to end up with reasonable memory and computer time requirements. Inlight of this, an approximate stage configuration including two vanes and one rotor has been considered.

It must be pointed out that the reduction of the number of blocks included in a row produces a pitch alteration, which can have an impact on the choke mass flow rate and the flow physics (Arnone and Pacciani, 1996). Moreover, an upper limit on the maximum detectable wave length is introduced as

$$\text{max. wave length} = (\text{blade pitch}) \times (\text{No. of blades in a row})$$

This will be reflected in the lowest detectable frequency. For instance, for the rotor row, the lowest detectable frequency will be the one associated with a rotor blade that spans all the inlet guide vanes included in the discretization.

The present stage approximation has been obtained using the exact rotor pitch, while slightly reducing the IGV axial chord to preserve solidity. Such an approach allows one to avoid pitch alterations. Unfortunately in three dimensions, the blade span cannot be adjusted, which results in a modification of the row geometry.

The aspects concerning the limit on the lowest detectable frequency will be discussed later in this section on the basis of a Fourier analysis of the solutions.

A number of 200 temporal divisions within a *cycle* (time that a rotor blade needs to span all the guide vanes included in the discretization) was used. As two vanes are considered in the stage approximation, the time that a rotor blade needs to cross a vane passage (*rotor passing period*) corresponds to 100 time steps.

The nondimensional blade lift coefficient based on pressure distribution was used to monitor unsteadiness. Previous experi-

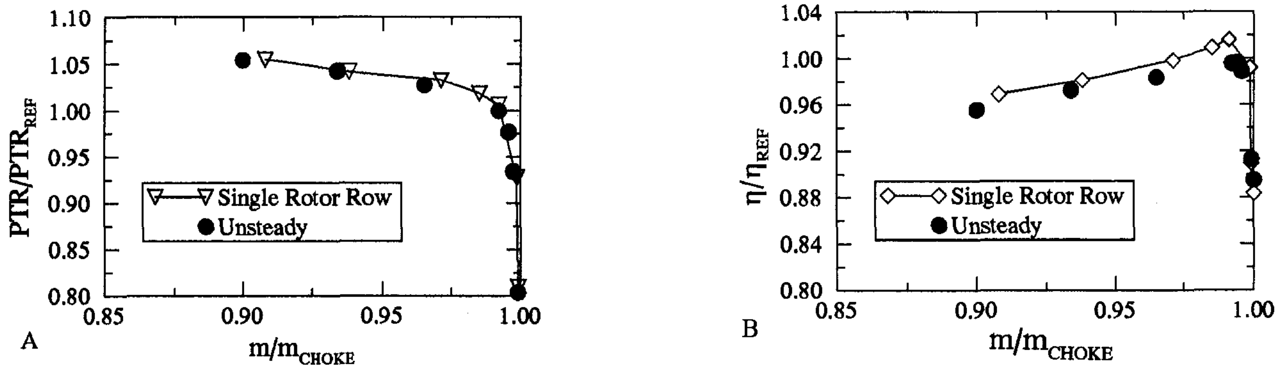

Fig. 5 Comparison between unsteady and steady single rotor row results in terms of total pressure ratio (A), and adiabatic efficiency (B)

ence in unsteady rotor–stator computations (Arnone et al., 1994, 1995) has shown that 100 divisions in a rotor passing period produces a lift evolution, which can be considered reasonably independent from the time discretization for practical purposes.

The rotor lift evolution at peak efficiency is reported in Fig. 1 as a function of time. The calculations were started from an initial steady-state solution accounting for the rotor blade's motion, but without changing the rotor grid position with respect to the guide vanes. As can be noticed, up to 16 rotor passing periods were needed to obtain a periodic solution. Similar times were needed for the other flow conditions.

Figure 2 summarizes the frequency spectra of the lift evolutions for three different mass flow rate values, which refer to choked, peak efficiency, and near-stall flow conditions. It can be noticed how the dominant frequencies are equal to or a multiple of the rotor passing one, while only a small amplitude can be observed at frequency which is half the rotor passing one. For choked flow and peak efficiency conditions, the rotor passing frequency is dominating, while near stall the corresponding amplitude has almost completely disappeared with an increase of the one corresponding to half the rotor passing frequency.

At reduced mass flow rates, low-frequency phenomena become important. The limit on the lowest detectable frequency introduced by the reduction of the number of blocks does not allow for low-frequency phenomena (i.e., rotating stall) to be predicted. Such a limit should not be restrictive away from stall conditions, where high frequencies seems to dominate.

An explanation for the fact that the rotor passing period harmonic disappears as the stage approaches stall, can be attempted assuming that most of the unsteady phenomena are due to the interaction of the leading edge shock with the IGV wakes. Such interaction is depicted in Figs. 3 and 4, where entropy rise and density contours for choked, peak efficiency, and near-stall flow conditions, are reported.

The bow shock interacts with the IGV wake before it is chopped by the passing rotor blades. At high mass flow rates, the wake eventually reaches the passage shock inside the rotor blade channel, once it has been chopped by the rotor blade (choked conditions), or in the throat region (peak efficiency) (Fig. 3). Such effects contribute with a frequency equal to the rotor passing frequency.

As stall is approached, the shock/wake interaction mechanism is quite different. While spanning the vane passage, the bow shock pushes the wake, enters the guide vane, and is reflected by the IGV blade where a sensible thickening of the boundary layer is visible. As a result of this mechanism, quite a large eddy is formed and convected downstream. As shown in Fig. 3(*c*), the passage shock interacts with the eddy before it is ingested into the rotor blade passage. Consequently the shock–wake interaction now has two major contributions. One comes from the bow-shock/wake interaction and the other from the passage-shock/eddy interaction. A frequency that is twice the rotor passing one is then expected to dominate. It is worthwhile to notice traces of the described mechanism also in the configuration of the IGV wake at choke and peak efficiency conditions.

At all flow conditions, important harmonics corresponding to multiples of the rotor passing one are present in the lift spectra (Fig. 2). Some explanations for that are listed in the following:

- Rotor wake instability is present (Fig. 3). Frequencies related to wake instability are well above the rotor passing one. At choked condition (Fig. 4(*a*)), the reflection of the passage shock on the rotor suction side has a λ structure and is located downstream the throat section. As a

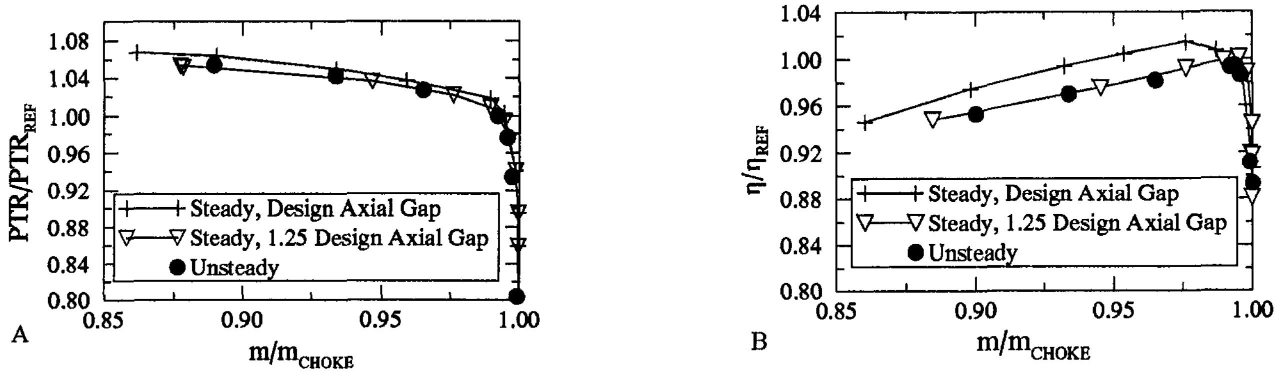

Fig. 6 Effects of the axial gap between rows on steady total pressure ratio (A), and adiabatic efficiency (B) for the one-dimensional characteristic boundary treatment

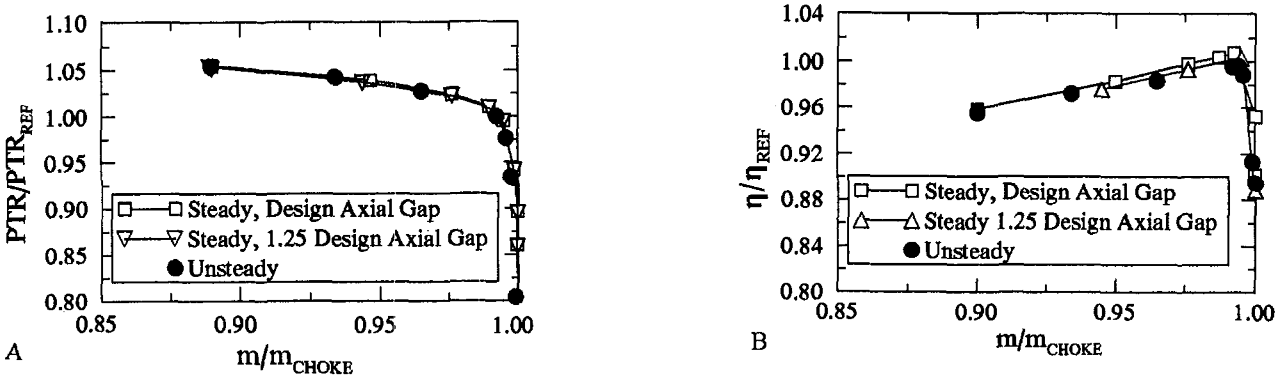

Fig. 7 Effects of the axial gap between rows on steady total pressure ratio (A), and adiabatic efficiency (B) for nonreflective boundary conditions

result of that, a sensible thickening of the blade boundary layer is present on both pressure and suction sides of the rotor blade. It is suspected that such effects are responsible of the evolution of the wake instability in the shedding of vortical spots (Fig. 3(*a*)).

- Although reflections of the bow shock by the guide vanes are much stronger as stall is approached (Fig. 4(*c*)), they can be clearly appreciated even at choked conditions (Fig. 4(*a*), 4(*b*)). Reflections of this shock by the suction side of the IGV impinges back into the rotor row.
- A rotor blade cuts two IGV wakes in a cycle. The parts of the wakes ingested by a rotor row are convected downstream and move with different speeds depending on the compression rate. Pressure and density will increase inside the rotor passage and the motion of these wake parts will progressively lag when decreasing mass flow rate. This situation is quite evident at near-stall conditions (Fig. 3(*c*)), where a large number of eddies chopped from IGV wakes are trapped into the rotor row. Flow unsteadiness related to this phenomenon contributes with frequencies above the rotor passing one.

Steady Pitch-Averaged Analysis. In common industrial practice, it is usual to approach turbomachinery design, by relying on steady predictions. It is then worthwhile to assess how much those predictions can resemble the ones of a realistic, unsteady, multirow computation.

The comparison between steady and time-averaged predictions has been performed in terms of rotor (mass-flow averaged) total pressure ratio and adiabatic efficiency as a function of the flow rate. As usual, the mass flow rates were normalized with their choke value. However, the differences between the various choke flow rates was found to be negligible (less then 0.2 percent).

Figure 5 compares steady rotor row analysis to rotor time-averaged predictions deduced from the stage calculations. Both total pressure ratio (Fig. 5(*a*)) and adiabatic efficiency (Fig. 5(*b*)) are overpredicted in the steady calculations with a slight shift in the peak efficiency point toward lower mass flow rates.

Results for the steady stage calculation are summarized in Figs. 6 to 9.

Figure 6 shows predictions obtained using mixing-plane techniques and one-dimensional characteristic treatment for interface boundaries. Pitch-wise mass-flow averaging was used to handle mixing planes. In the computations performed with the design row axial gap the total pressure ratio is overestimated (Fig. 6(*a*)) and the adiabatic efficiency (Fig. 6(*b*)) is well above the unsteady one with different shape. Also an important disagreement on the peak efficiency position has to be noticed. Such a situation is known to be a consequence of spurious shock system reflections at the interface boundary (Arnone and Benvenuti, 1994). If the axial gap is increased to 1.25 of the design value, no sensible reflections are experienced and the computed characteristic is very similar to the unsteady one. It is assumed that the bow shock lessens in intensity away from the leading edge. As a consequence, when increasing the axial gap, reflections due to boundary conditions decrease. Note that only the inlet part of the rotor grid was increased to reduce reflections. In such a way the IGV wake mixing losses are the same for the two configurations.

When using nonreflective boundary conditions (Fig. 7), the influence of the axial gap is very small. Predicted performance now agrees well with the time-averaged one. The slight differences in the predictions of the two configurations are still the result of weak reflections. The nonreflective procedure used here (Giles, 1988a, b) is based on a linearization of the Euler equations and can produce weak reflections in presence of nonlinear phenomena like shock waves.

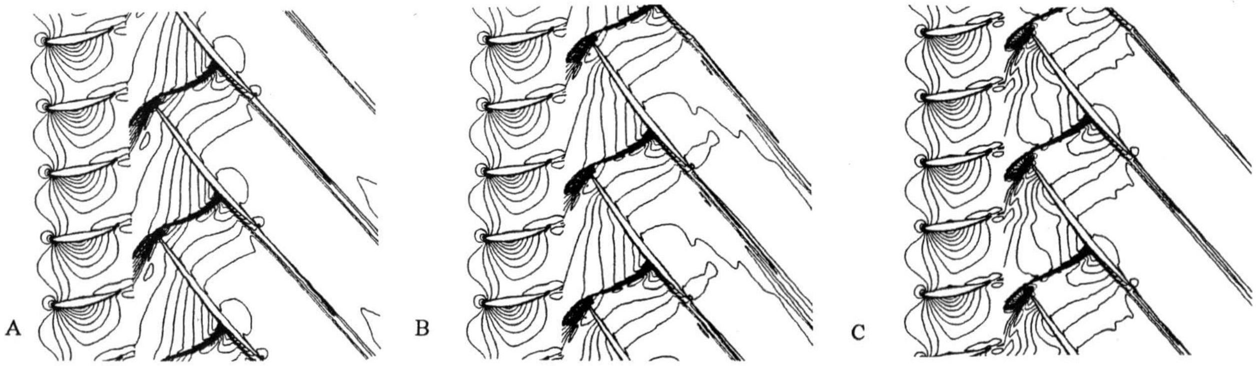

Fig. 8 Density contours for time-averaged solution (A), steady solution with nonreflective boundary conditions (B), and steady solution with one-dimensional characteristic treatment (C)

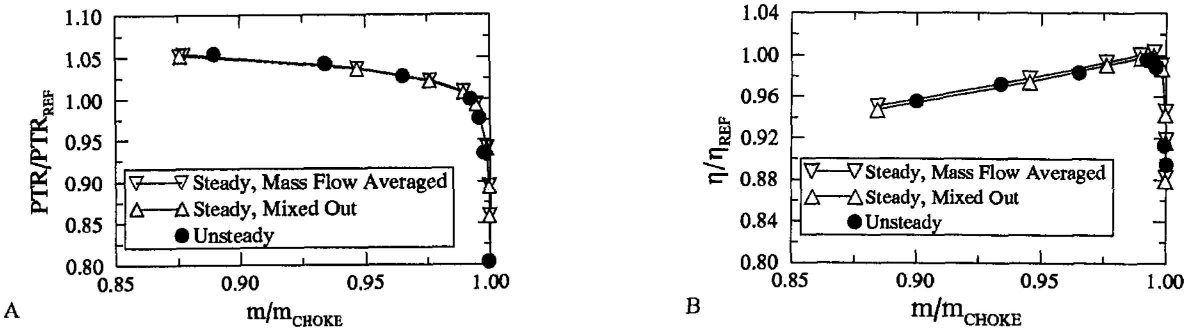

Fig. 9 Effect of the interface pitch-averaging on steady total pressure ratio (A), and adiabatic efficiency (B)

Figure 8 compares density contours for the time-averaged (Fig. 8(*a*)), nonreflective (Fig. 8(*b*)), and one-dimensional characteristic (Fig. 8(*c*)) treatments. Contours obtained with the nonreflective conditions are close to the time-averaged ones, while the previously mentioned reflections of the one-dimensional characteristic approach are clear in Fig. 8(*c*).

It is worthwhile noticing that the method of linking blade rows by matching mass-flow averaged quantities at the interface is not strictly conservative. Despite this fact, all results end up with relative errors in conservation of mass, momentum, and energy at the interface of the order of 10^{-4}.

In order to assess the influence of the pitchwise averaging method, calculations have also been carried out by transferring mixed-out parameters between blade rows. These calculations refer to the original configurations and nonreflective boundary conditions. Results are compared to the mass flow pitch-averaged one in Fig. 9. The transfer of mixed-out quantities at the interface, instead of mass-flow averaged ones, results in a slight decrease in both adiabatic efficiency and total pressure ratio. It is suspected that this is due to the different estimation of the IGV wake losses in the two averaging methods. However, it must be pointed out that the differences arising from different averaging schemes are much smaller than the ones due to spurious reflections (i.e., Fig. 6).

Finally it has to be noticed that in the calculations where the influence of reflections are negligible, the agreement in terms of efficiency tends to improve at low mass flow rate. When approaching stall, most of the losses are expected in the strong leading edge shock and unsteady effects seems to reduce their impact. On the contrary, at high flow rates the shock/wake interactions within the rotor row are not accounted for in the steady analysis and the efficiency is overestimated.

Concluding Remarks

A recently developed quasi-three-dimensional, time-accurate, viscous procedure has been used to study the IGV–rotor interaction in the first stage of a modern transonic compressor. Interaction mechanisms between the rotor shock system and the IGV wakes have been studied for various flow rates.

Unsteady results have been used as a target solution for the comparison with single- and multirow steady calculations. Spurious shock reflections have been found to produce major discrepancies between unsteady and steady predictions. If the blade rows are slightly separated, reflections are reduced and the use of a simple one-dimensional characteristic treatment leads to good predictions. The nonreflective procedure of Giles (1988a, b) has proven to be effective also for closely stacked rows. It would be interesting to extend this procedure to three dimensions. A minor impact of the pitch-averaging method has been observed.

Acknowledgments

The authors would like to express their gratitude to Prof. Ennio Carnevale and to PIN Engineering for providing computational resources for the project. The authors are also indebted to Nuovo Pignone management and particularly to Drs. Erio Benvenuti, Umberto Corradini, and Bruno Innocenti for numerous useful discussions.

References

Alonso, J., Martinelli, L., and Jameson, A., 1995, "Multigrid Unsteady Navier–Stokes Calculations With Aeroelastic Applications," AIAA Paper No. 95-0048.

Arnone, A., and Pacciani, R., 1996, "Rotor–Stator Interaction Analysis Using the Navier–Stokes Equations and a Multigrid Method," ASME JOURNAL OF TURBOMACHINERY, Vol. 118, pp. 679–689.

Arnone, A., Pacciani, R., and Sestini, A., 1994, "Multigrid Computations of Unsteady Rotor–Stator Interaction Using the Navier–Stokes Equations," presented at the 1994 ASME Winter Annual Meeting, Chicago.

Arnone, A., 1994, "Viscous Analysis of Three-Dimensional Rotor Flows Using a Multigrid Method," ASME JOURNAL OF TURBOMACHINERY, Vol. 116, pp. 435–445.

Arnone, A., and Benvenuti, E., 1994, "Three-Dimensional Navier–Stokes Analysis of a Two-Stage Gas Turbine," ASME Paper No. 94-GT-88.

Arnone, A., Liou, M.-S., and Povinelli, L. A., 1993, "Multigrid Time-Accurate Integration of Navier–Stokes Equations," AIAA Paper No. 93-3361-CP.

Arnone, A., and Swanson, R. C., 1993, "A Navier–Stokes Solver for Turbomachinery Applications," ASME JOURNAL OF TURBOMACHINERY, Vol. 115, pp. 305–313.

Arnone, A., Liou, M.-S., and Povinelli, L. A., 1992, "Navier–Stokes Solution of Transonic Cascade Flow Using Non-periodic C-Type Grids," *Journal of Propulsion and Power,* Vol. 8, No. 2, pp. 410–417.

Baldwin, B. S., and Lomax, H., 1978, "Thin Layer Approximation and Algebraic Model for Separated Turbulent Flows," AIAA Paper No. 78-257.

Bevenuti, E., 1996, "Design and Test of a New Axial Compressor for the Nuovo Pignone Heavy Duty Gas Turbines," ASME Paper No. 96-GT-145; ASME *Journal of Engineering for Gas Turbines and Power,* Vol. 119, 1997, pp. 633–639.

Brandt, A., 1979, "Multi-Level Adaptive Computations in Fluid Dynamics," AIAA Paper No. 79-1455.

Chima, R. V., Giel, P. W., and Boyle, R. J., 1993, "Algebraic Turbulence Modeling for Three-Dimensional Viscous Flows," *Proc. Engineering Turbulence Modeling and Experiments* 2, Florence.

Erdos, J. I., Alzner, E., and McNally, W., 1977, "Numerical Solution of Periodic Transonic Flow Through a Fan Stage," *AIAA Journal,* Vol. 115, No. 11.

Fourmaux, A., and Le Meur, A., 1987, "Computation of Unsteady Phenomena in Transonic Turbines and Compressors," *Proc. 4th Symposium on Unsteady Aerodynamics and Aeroelasticity of Turbomachines and Propellers,* Aachen.

Giles, M. B., 1988a, "UNSFLO: A Numerical Method For Unsteady Inviscid Flow in Turbomachinery," GTL Report #195.

Giles, M. B., 1988b, "Non-Reflecting Boundary Conditions for the Euler Equations," *AIAA Journal,* Vol. 28, No. 12.

He, L., and Denton, J. D., 1994, "Three-Dimensional Time-Marching Inviscid and Viscous Solutions for Unsteady Flows Around Vibrating Cascades," ASME JOURNAL OF TURBOMACHINERY, Vol. 116, pp. 469–476.

Jameson, A., 1983, "Transonic Flow Calculations," MAE Report 1651, MAE Department, Princeton University, July.

Jameson, A., 1991, "Time Dependent Calculations Using Multigrid With Applications to Unsteady Flows Past Airfoils and Wings," AIAA Paper No. 91-1596.

Jameson, A., Schmidt, W., and Turkel, E., 1981, "Numerical Solutions of the Euler Equations by Finite Volume Methods Using Runge–Kutta Time-Stepping Schemes," AIAA Paper No. 81-1259.

Jorgenson, P. C. E., and Chima, R., 1988, "An Explicit Runge–Kutta Method for Unsteady Rotor/Stator Interaction," AIAA Paper No. 88-0049.

Kwon, O. K., Pletcher, R. H., and Delaney, R. A., 1988, "Calculation of Unsteady Turbulent Boundary Layers," ASME JOURNAL OF TURBOMACHINERY, Vol. 110, pp. 195–201.

Lewis, J. P., Delaney, R. A., and Hall, E. J., 1987, "Numerical Prediction of Turbine Vane-Blade Interaction," AIAA Paper No. 87-21419.

Martinelli, L., and Jameson, A., 1988, "Validation of a Multigrid Method for the Reynolds Averaged Equations," AIAA Paper No. 88-0414.

Rai, M. M., 1987, "Unsteady Three-Dimensional Navier–Stokes Simulations of Turbine Rotor Stator Interactions," AIAA Paper No. 87-2058.

Rao, K. V., and Delaney, R. A., 1992, "Investigation of Unsteady Flow Through a Transonic Turbine Stage, Part I, Analysis," AIAA Paper No. 90-2408.

Stock, H. W., and Haase, W., 1987, "The Determination of Turbulence Length Scales in Algebraic Turbulence Models for Attached as Slightly Separated Flows Using Navier–Stokes Equation," AIAA Paper No. 87-1302.

Swanson, R. C., and Turkel, E., 1987, "Artificial Dissipation and Central Difference Schemes for the Euler and Navier–Stokes Equations," AIAA Paper No. 87-1107.

Valkov, T., and Tan, C. S., 1995, "Control of the Unsteady Flow in a Stator Blade Row Interacting With Upstream Moving Wakes," ASME JOURNAL OF TURBOMACHINERY, Vol. 117, pp. 97–105.

Vuillot, A. M., Couallier, V., and Liamis, N., 1993, "3-D Turbomachinery Euler and Navier–Stokes Calculations With a Multidomain Cell-Centered Approach," presented at the AIAA/SAE/ASME/ASEE 29th Joint Propulsion Conference and Exhibit, Monterey, CA, June 28–30.

Aspirating Probe Measurements of the Unsteady Total Temperature Field Downstream of an Embedded Stator in a Multistage Axial Flow Compressor

N. Suryavamshi

B. Lakshminarayana

J. Prato

Center for Gas Turbines and Power,
The Pennsylvania State University,
University Park, PA 16802

The results from the area traverse measurements of the unsteady total temperature using a high-response aspirating probe downstream of the second stator of a three-stage axial flow compressor are presented. The measurements were conducted at the peak efficiency operating point. The unsteady total temperature data are resolved into deterministic and unresolved components. Hub and casing regions have high levels of unsteadiness and consequently high levels of mixing. These regions have significant levels of shaft resolved and unresolved unsteadiness. Comparisons are made between the total temperature and the total pressure data to examine the rotor 2 wake characteristics and the temporal variation of the stator exit flow. Isentropic efficiency calculations at the midpitch location show that there is about a 4 percent change in the algebraically averaged efficiency across the blades of the second rotor and if all the rotor 2 blades were behaving as a "best" blade, the improvement in efficiency would be about 1.3 percent. An attempt is made to create a composite flow field picture by correlating the unsteady velocity data with temperature and pressure data.

Introduction

Knowledge of both steady and unsteady temperature in turbomachinery is essential for accurate assessment, analysis, and design. One of the approaches suggested for multistage turbomachinery design and analysis is based on the average passage equations of Adamczyk (1985). Several other approaches are still evolving. The apparent heat-flux terms that are analogous to turbulent heat-flux terms in the energy equation of the average passage system of Adamczyk (1985) are responsible for redistribution and spanwise mixing in multistage turbomachinery. These terms are presently either neglected or modeled with ad-hoc constants. The purpose of the research at Penn State is to acquire unsteady temperature data in a multistage axial flow compressor and through analysis provide a scientific basis for the modeling of these terms, which can then be incorporated into the Navier–Stokes design or analysis codes.

Time-resolved measurement of fluid total temperature in a turbomachinery environment has always been a very difficult task. Conventional thermocouples have a frequency response less than 1 kHz, while compensated thermocouples are yet to be demonstrated. Constant current hot-wire techniques are also limited to low frequencies unless the fluctuations are small compared to the mean. Electronically compensated, thin-wire resistance thermometers operated at very low overheat ratios have been used to measure temperature at 5 to 10 kHz. However, these techniques are not easily extendable to high-speed compressible flows with high dynamic pressure such as those found in turbomachinery configurations. Ng and Epstein (1983) reported the development of a piggy-backed high-frequency total temperature probe (aspirating probe) for use in unsteady compressible flows. Kotidis and Epstein (1991) and Alday et al. (1993) have used the aspirating probe to measure the time-resolved total temperature and pressure in transonic compressors. Van Zante et al. (1995) improved the original design of the aspirating probe of Ng and Epstein (1983) by using platinum–iridium alloy hot-wires and spreading the calibration space to measure both the instantaneous total temperature downstream of a transonic axial flow compressor rotor. The main advantage of this probe over the earlier ones is that data from the two hot-wires alone are used to obtain the total temperature, which reduces the size of the probe and consequently the blockage. It is this configuration with tungsten hot-wires that is used in the present investigation. The main objective of the research reported in this paper is to understand the nature of the unsteady total temperature field downstream of an embedded stator of a multistage axial flow compressor.

Test Facility, Instrumentation, and Data Acquisition System

The test compressor is a three-stage axial flow compressor consisting of an inlet guide vane row and three stages of rotor and cantilevered stator blading with a rotating hub drum. Table 1 gives the general specifications of the research compressor. The test facility is equipped with a stepper motor driven area traverse mechanism. This traverse has three degrees of freedom: radial, circumferential, and probe rotation. The probes are inserted into the compressor casing through teflon shoes and the chamber is sealed to prevent flow from recirculating through the slots. The motors are controlled by an IBM compatible 486 personal computer. Approximately 185 percent of the stator 2 blade pitch can be traversed at each radial location (only 100

Contributed by the International Gas Turbine Institute and presented at the 41st International Gas Turbine and Aeroengine Congress and Exhibition, Birmingham, United Kingdom, June 10–13, 1996. Manuscript received at ASME Headquarters February 1996. Paper No. 96-GT-543. Associate Technical Editor: J. N. Shinn.

Table 1 General specifications of test compressor

Number of Stages	3
Tip Diameter	0.6096 m
Hub Diameter at inlet	0.5075 m
Hub Diameter at exit	0.5232 m
Blade Count (rotor)	70, 72, 74
Blade Count (stator)	71, 73, 75
Design Corrected Rotor speed	5410 rpm
Design Corrected Mass Flow	8.609 kg/s
Design Overall Total Pressure Ratio	1.354
Mass Averaged Peak Efficiency at 100% Corrected Speed (Torque Based)	90.65%
Blade Tip Mach Number	0.5
Average Reynolds Number (Based on Stator 3 chord length and axial velocity)	2.448×10^5
Average Hub-Tip Ratio	0.843
Diffusion factor (avg)	0.438
Average Stage Flow Coefficient (V_x/U_t)	0.509
Reaction (avg)	0.570
Space Chord Ratio (avg)	0.780
Aspect Ratio (avg)	1.500
Average Rotor Tip Clearance (static)	1.328 mm
Average Rotor Tip Clearance (dynamic)	0.667 mm
Average Stator Hub Clearance (static)	0.686 mm

percent of the stator 2 pitch was traversed for this case). The traverse can be axially moved such that area traverses can be conducted downstream of stators 2 and 3 and rotor 3. Lakshminarayana et al. (1994) and Suryavamshi et al. (1994) give a complete description of the test compressor, associated instrumentation, operating characteristics, blade profile geometries, and area traverse locations. All the measurements reported in this paper were acquired at the *peak efficiency* operating condition.

The high-speed data were acquired using the Metrabyte DAS-50 system. The DAS-50 system was triggered using the once-per-rev pulse from an encoder mounted on the compressor shaft. A signal based upon the resolution of the rotor 2 blade passage (20 points per blade passage) obtained from a disk mounted on the same encoder is used to provide the clock frequency (approximately 130 kHz for this traverse) for the data acquisition system. At each location approximately 3.37 seconds (300 rotor revolutions) of data was acquired. Also a continuous stream of data was acquired at a few locations at a frequency of 200 kHz to conduct a spectral analysis of the data. A 19 by 17 mesh (19 tangential nodes and 17 radial nodes) across one blade passage at stator 2 exit (5.6 percent chord downstream of the stator trailing edge) with clustering in the endwall and the wake regions was employed to resolve the flow field. At each radial location the aspirating probe was rotated to align it in the direction of the mean flow as measured by a pneumatic five hole probe.

Aspirating Probe. The principle of operation involves operating two coplanar hot-wires at different overheat ratios (different wire temperatures) in a channel of a choked orifice. Detailed description of the working of the probe is given by Ng and Epstein (1983) and Van Zante et al. (1995). The governing equation of the aspirating probe is given by:

$$E_i^2 = \left[C_i\left(\frac{P_0}{\sqrt{T_0}}\right)^{n_i}\right](T_{wi} - rT_0) \qquad (1)$$

The design of the aspirating probe was obtained from Dr. Ng (1990). This was scaled down to reduce interference effects in the multistage compressor environment. The final channel diameter and the choked orifice diameter were then scaled such that the Mach number at the wire plane during operation (with the orifice choked) would be approximately 0.40 (the average Mach number of the flow in the compressor). The schematic drawing of the aspirating probe is shown in Fig. 1. The spectrum of the hot-wire voltages shows that eight harmonics of rotor blade passing frequency (all three rotors) were captured and the combined frequency response was about 40 kHz (Suryavamshi, 1996).

A static calibration of the aspirating probe is considered adequate since the frequency response of the probe is high. The calibration requires measurement of the dc output voltage from each hot-wire for a range of pressures and temperatures of the pressure and temperature-controlled tank. The calibration is performed at a constant temperature of the tank at various tank

Nomenclature

C and n = hot-wire calibration constants
C_{pt} = total pressure coefficient = $(\overline{\overline{P_o}} - \overline{\overline{P_{s1}}})/(\overline{\overline{P_{o1}}} - \overline{\overline{P_{s1}}})$
$DS2$ = downstream of stator 2
E = hot-wire output voltage
N_b = number of blades per rotor
N_{pb} = resolution of a blade passage
N_{rev} = number of revolutions of data acquired
P_o = total pressure
P_r = total pressure ratio
P_s = static pressure
PS = pressure side
r = recovery factor for hot-wire
rms = root mean square value
SS = suction side
T = rotor blade passing period
T_o = total temperature of flow
T_{or} = total temperature rise
T_{orijk} = instantaneous total temperature rise
$(T_{orjk})_s$ = ensemble-averaged total temperature rise
T'_{orijk} = unresolved component of total temperature rise
$\overline{T_{or}}$ = time-averaged total temperature rise
$(T_{orjk})_{BA}$ = blade aperiodic component of total temperature rise
$(T_{ork})_{BP}$ = blade periodic component of total temperature rise
$(T_{orj})_{RA}$ = revolution aperiodic component of total temperature rise
$(T_{orjk})_{RP}$ = revolution periodic component of total temperature rise
T_r = total temperature ratio
T_{wi} = hot-wire temperature
U_t = blade tip speed
V = denotes velocity
γ = ratio of specific heats
η_{isen} = isentropic efficiency
τ = fraction of rotor blade passing period

Subscripts

1 = inlet to IGV
i = indicates number of hot-wire; also ensemble-averaging index indicating rotor revolution
j = ensemble-averaging index indicating rotor blade count
k = ensemble-averaging index indicating position in rotor blade passage
l = indicates local value
r = denotes radial component
x = denotes axial component
θ = denotes tangential component

Superscripts

$-$ = denotes time average
$=$ = denotes passage average

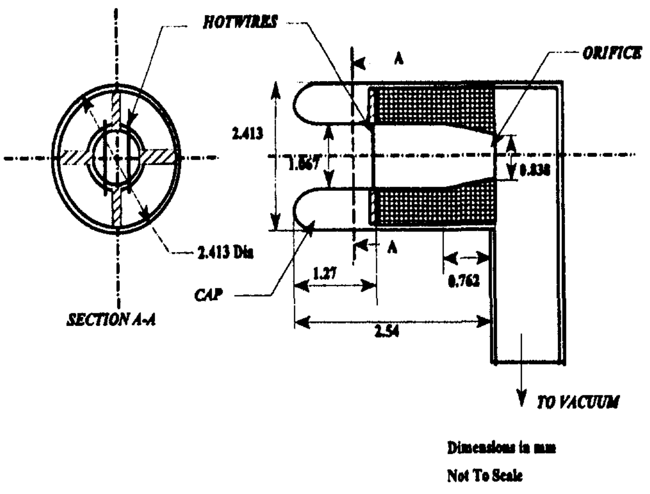

Fig. 1 Schematic drawing of the aspirating probe

pressures, and at each point, the pressure, temperature and the two hot-wire voltages are recorded. The data are reduced and the calibration constants (C_1, C_2, n_1, and n_2) are calculated. The wire overheat ratios were set at 1.5 and 1.8 (to spread the calibration space), which gave pulse responses of 50.0 and 83.2 kHz, respectively. The probe was calibrated through a range of temperatures consistent with the approximate range of the compressor operating point. The calibration constants are a function of temperature and this functionality (a linear regression model) was used in the iteration loop to solve for the unknowns. The calibration space is shown in Fig. 2. The calibration shows good pressure and temperature sensitivity and the temperature resolution is approximately 0.04 K, which is much lower than the uncertainty of temperature measurement which is around 0.5 K.

Equating total pressure from the two wires of Eq. (1) we get:

$$\left[\frac{E_1^2}{C_1(T_{w1} - rT_o)}\right]^{1/n_1} = \left[\frac{E_2^2}{C_2(T_{w2} - rT_o)}\right]^{1/n_2} \tag{2}$$

A Newton–Raphson iteration technique was used to solve Eq. (2). The levels of total pressure unsteadiness derived from the measurement in the multistage compressor were almost twice that derived from a traverse of the semi-conductor kulite probe at the same location. Until this discrepancy is resolved, it was decided that the aspirating probe would be used to measure total temperature and the kulite probe to measure total pressure.

Decomposition of Instantaneous Signal

Each discrete measurement of total temperature is presented as an instantaneous total temperature rise T_{orijk}:

$$T_{orijk} = (T_{oijk} - \overline{T_{o1}}) \tag{3}$$

Here subscripts i, j, and k represent indices in ensemble averaging (i indicates the index of revolution, j the index of the blade in the row, and k the index of the point in the blade passage). Following the description of Suder et al. (1987) and Suryavamshi et al. (1994), the instantaneous total temperature is then decomposed into a shaft-resolved (ensemble average, $(T_{orjk})_s$) and an unresolved component (T'_{orijk}):

$$T_{orijk} = (T_{orjk})_s + T'_{orijk} \tag{4}$$

where the ensemble average is given by:

$$(T_{orjk})_s = \frac{1}{N_{\text{rev}}} \sum_{i=1}^{N_{\text{rev}}} (T_{or})_{ijk} \tag{5}$$

and

$$T'_{orijk} = T_{orijk} - (T_{orjk})_s \tag{6}$$

This shaft-resolved component has contributions from viscous and inviscid rotor–stator interaction effects, which repeats every revolution. The shaft-resolved component is further decomposed into a time average ($\overline{T_{or}}$), a revolution periodic ($(T_{orjk})_{RP}$) and a revolution aperiodic ($(T_{orj})_{RA}$) component as shown in Fig. 3.

$$(T_{orjk})_s = \overline{T_{or}} + (T_{orj})_{RA} + (T_{orjk})_{RP} \tag{7}$$

$$\overline{T_{or}} = \frac{1}{N_{\text{rev}} \times N_b \times N_{pb}} \sum_{i=1}^{N_{\text{rev}}} \sum_{j=1}^{N_b} \sum_{k=1}^{N_{pb}} T_{orijk} \tag{8}$$

$$(T_{orj})_{RA} = \frac{1}{N_{pb}} \sum_{k=1}^{N_{pb}} [(T_{orjk})_s - \overline{T_{or}}] \tag{9}$$

$$(T_{orjk})_{RP} = [(T_{orjk})_s - \overline{T_{or}} - (T_{orj})_{RA}] \tag{10}$$

The time-averaged component describes the steady-state flow field, which is the same in each blade passage of the blade row. The revolution periodic component describes the temporal fluctuations due to the relative motion between the blade rows and the revolution aperiodic component (which is a passage-to-passage average) arises from different blade count in successive stages (rotor or stator). For a single-stage machine or a multistage machine with the same blade count in successive stages, the revolution aperiodic component identically goes to zero. The revolution aperiodic component generally represents the asymmetry about the circumference in the rotor frame of reference with a time constant of one rotor 2 blade passing period. During analysis of the total pressure data acquired it was found that there are variations in the periodic fluctuations between blades in the same row due to various causes (geometric, incidence variations, loading changes, etc.). Since most of

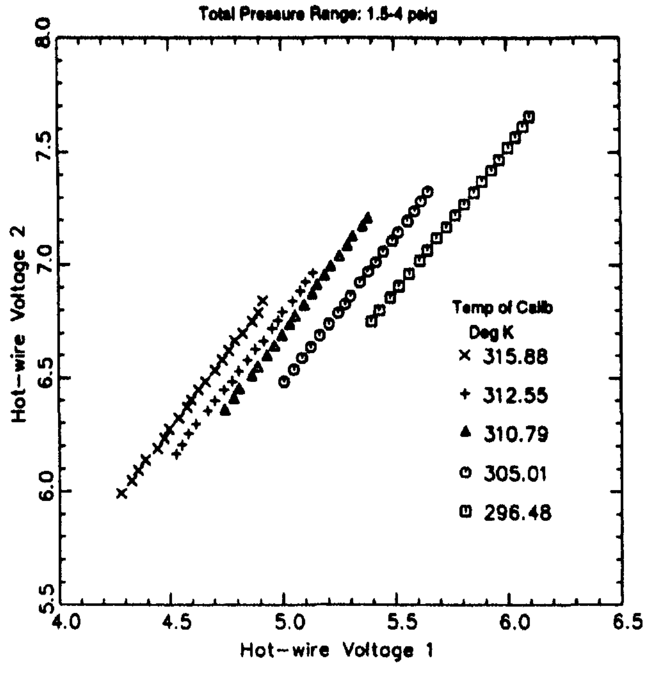

Fig. 2 Calibration space of aspirating probe

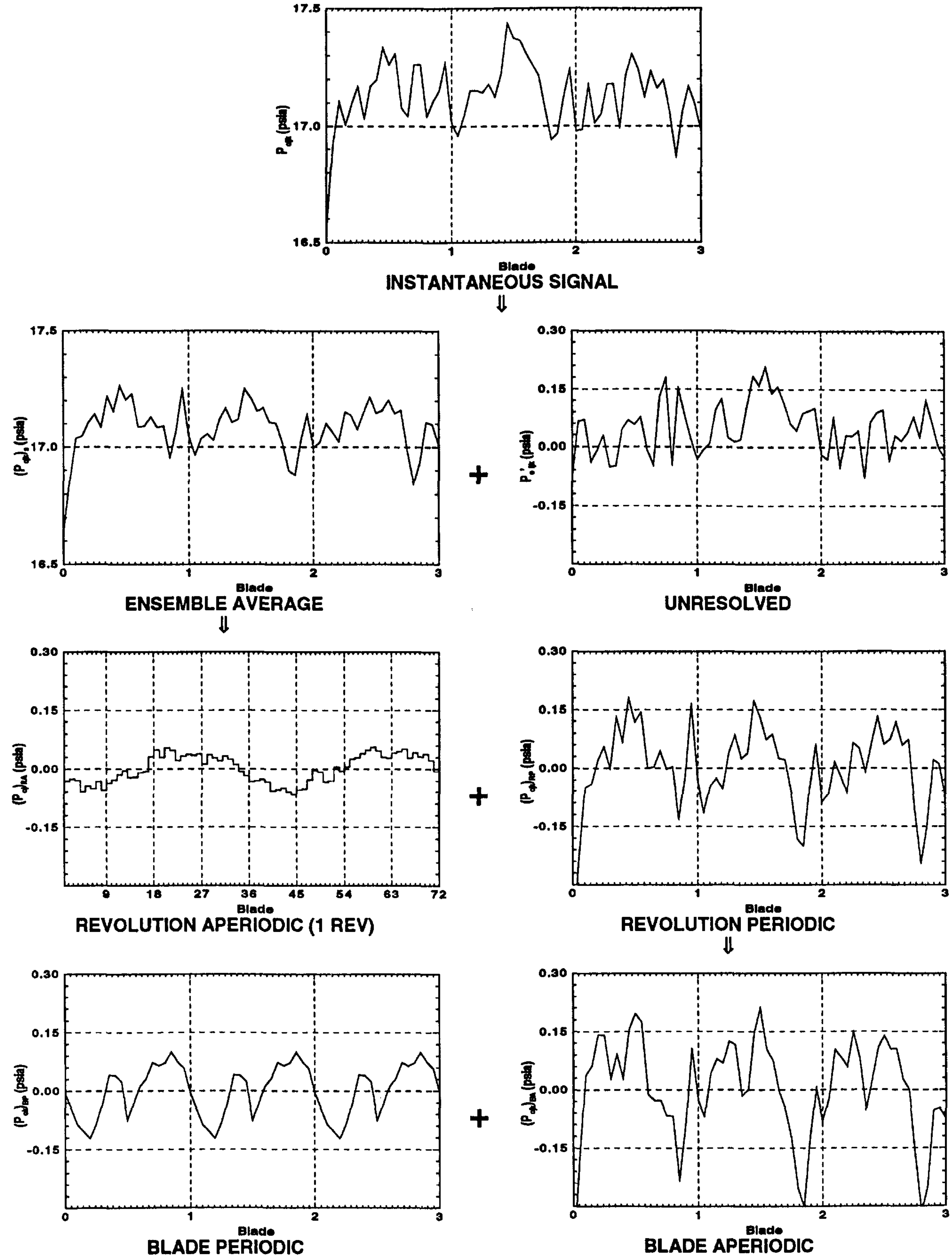

Fig. 3 Schematic of decomposition of instantaneous data: actual total pressure data

the design principles are based on solving the flow equations for one blade passage, it is essential to determine the periodic unsteadiness for the average rotor passage. This average passage is termed the "blade periodic unsteadiness" and the difference between the revolution periodic and the blade periodic is the "blade aperiodic unsteadiness":

$$(T_{orjk})_{RP} = (T_{ork})_{BP} + (T_{orjk})_{BA} \tag{11}$$

$$(T_{ork})_{BP} = \frac{1}{N_b}\sum_{j=1}^{N_b} [(T_{orjk})_{RP}] \tag{12}$$

$$(T_{orjk})_{BA} = [(T_{orjk})_{RP} - (T_{ork})_{BP}] \tag{13}$$

The blade periodic component $((T_{ork})_{BP})$ generally represents the fluctuations of the total pressure field over an "average" rotor 2 blade passing period. The blade aperiodic component $((T_{orjk})_{BA})$ generally represents the asymmetry about the circumference in the rotor frame of reference with a time constant of the sampling period. Since the decomposition of the original signal has already filtered the asymmetries with a time constant on the order of a rotor 2 blade passing period (revolution aperiodic), this component includes short-term asymmetries synchronized to the passage of the individual rotor 2 blades. Full details of the decomposition (including the equations used to derive the various components) are given in Suryavamshi et al. (1994) and shown in Fig. 3 for the total pressure signal. While this decomposition is mathematically rigorous (i.e., the unsteady signal can be reconstructed by summing each of the components), it is premised upon the idealized assumption that all of the deterministic structure is synchronized to the shaft rotation. Measurement of the unsteady total temperature field resulting from some deterministic physical phenomena, such as vortices originating in the stationary frame of reference, will be included in the unresolved component. Additionally, variations in the magnitude of the velocity deficit, width, and spatial positions of the rotor wakes between rotor revolutions, which are clearly shaft-synchronized physical phenomena, contribute to the unresolved component. As a consequence, the magnitude of the shaft-resolved and unresolved components of the unsteady temperature signals cannot be explicitly defined as the respective contributions to the total unsteadiness of the deterministic structures and random turbulence. However, these data can be used to identify in which regions of the flow field each of these components make significant contributions to the total unsteadiness and consequently mixing in the compressor.

Time-Averaged Data

Figure 4 shows the blade-to-blade variation of time-averaged total temperature rise near the hub, midspan, and casing locations. Also shown in this figure are the hub to casing distributions of mass-weighted passage-averaged values of time-averaged total temperature and pressure. The total pressure was acquired using a high-frequency total pressure probe. The details of this measurement are given in Suryavamshi et al. (1994). Higher temperatures seen on the pressure side of the stator wake are consistent with the analysis of Kerrebrock and Mikolajczak (1970). This is due to the rotor wake accumulation on the pressure side of a downstream stator. The average variation of temperature between the stator core flow to the stator wake is about 1.0 K, which is about 10 percent of the rotor temperature rise except around 22 percent span where the variation is around 5.0 K. The endwall flow region with lower pressures and higher temperature, near the casing extends to 70 percent span while the region near the hub extends to about 15 percent of the span. The presence of endwall flow as well as interaction with the rotor leakage flow contributes to much lower efficiency in the casing endwall region. Consequently higher temperatures and lower pressures are recorded compared with the hub region.

Figure 5 shows the contours of the time-averaged quantities (total pressure coefficient, total temperature rise, and isentropic efficiency). The isentropic efficiency is calculated using the following equation:

$$\eta_{\text{isen}} = \frac{P_r^{(\gamma-1)/\gamma} - 1}{T_r - 1} \tag{14}$$

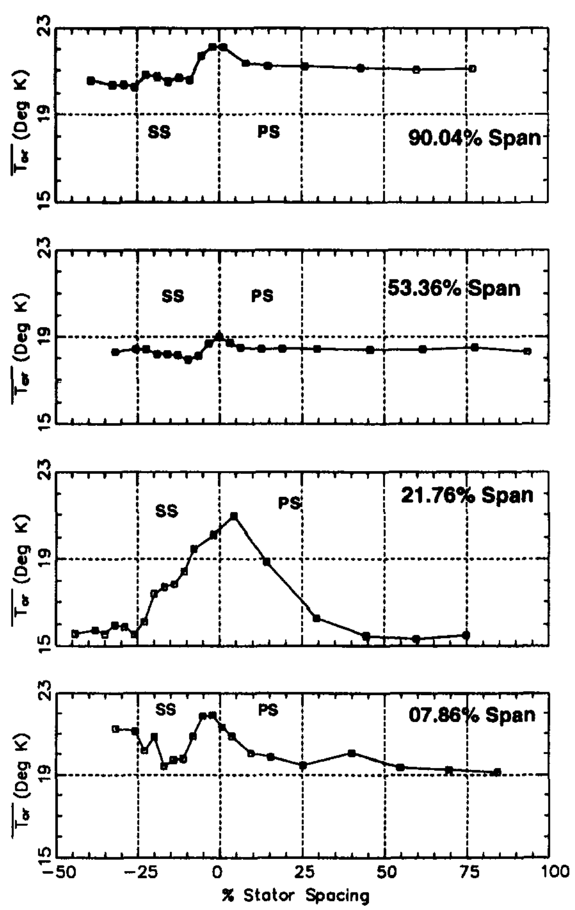

(a) Blade to Blade Distribution

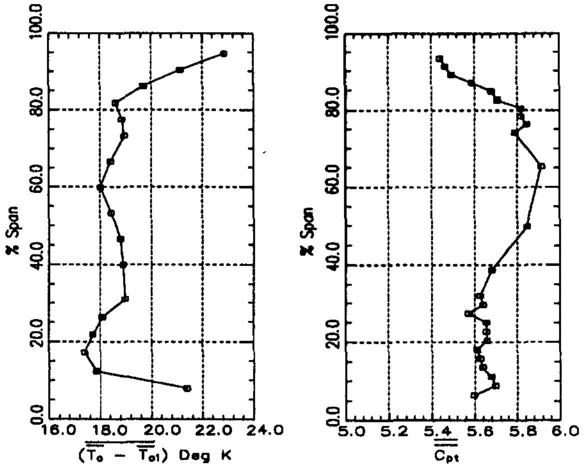

(b) Hub to Tip Variation

Fig. 4 Blade-to-blade and hub-to-tip variation of time-averaged quantities

where

$$P_r = \frac{P_{ol}}{\overline{P}_{o1}}, \quad T_r = \frac{T_{ol}}{\overline{T}_{o1}} \tag{15}$$

Let us focus on the important features of the flow: the presence of the stator wakes, effect of the secondary flow, and the thickening of the boundary layer near the suction surface corner in the casing region. The measurement grid in the endwall regions is denser for the total pressure measurement due to a smaller

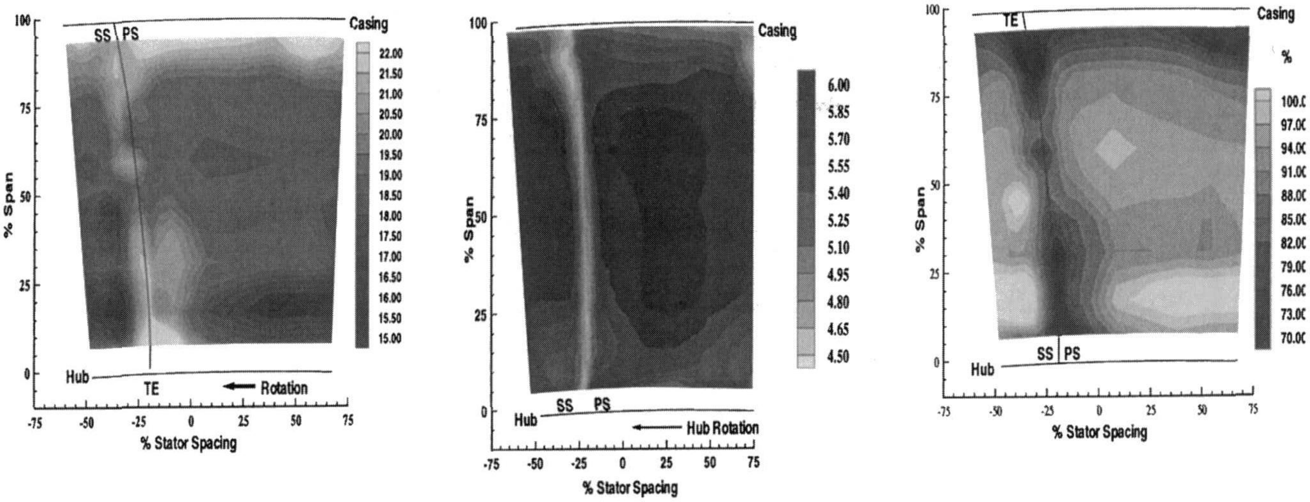

(a) Total Temperature($\overline{T_{or}}$ (Deg K)) **(b) Total Pressure ($\overline{C_{pt}}$)** **(c) Isentropic Efficiency ($\overline{\eta_{isen}}$)**

Fig. 5 Contours of time-averaged total quantities: temperature, pressure, and isentropic efficiency

size of the kulite probe. As a result the radial contouring is smoother for the pressure compared with the temperature data. The interaction of the stator wake flow with the endwall flow features and rotor tip clearance flow causes intense mixing, which results in much thicker wakes and very low efficiency in the endwall regions compared with the midspan region. Similar distributions have been measured by Howard et al. (1994). The suction surface-casing endwall corner region of low total pressure due to probable corner stall, inlet skew, and casing corner flow does not show much variation in the time-averaged total temperature across the passage. This is, however, a region of low efficiency and high unresolved unsteadiness (as will be seen later). In the casing endwall region, intense mixing caused by interaction of the rotor tip leakage flow and the casing endwall boundary layer gives rise to almost uniform distribution of pressures, temperatures and efficiency across the blade pitch from 85 to 95 percent span (last measurement location). Blade-to-blade nonuniformities are observed only near the stator wake regions.

On the pressure side of the stator wake, around 25 percent span, there is a region of low efficiency, low pressure rise, and high temperature rise. This region is probably caused by the accumulation of hubwall boundary layer fluid due to the scraping effect of the blade caused by hub rotation as well as migration of upstream rotor flow toward the pressure surface. This region at its largest almost spans $\frac{1}{3}$ of the blade spacing. This could also be caused by the accumulation of fluid due to radial outward transport of the low-momentum rotor 2 hubwall corner flow toward midspan by the radial outward velocity at the exit of the rotor. Near the suction side of the stator wake close to the hub, low temperatures, moderate pressure rise, and high efficiency are observed. This is probably caused by leakage flow from the hub region augmented by hub rotation washing away the corner separation region. This is also the region of intense flow mixing. This may account for high efficiency observed almost across the entire passage.

Unsteady Data

In this section the unsteady total temperature field is presented and analyzed. Unsteadiness at the exit of the stator exists due to interaction of at least three different mechanisms: the presence of rotor 2 wakes being convected through the stator passage, which have not fully mixed out, the shedding of vorticity from the stator trailing edge due to a time-varying stator circulation or loading caused by the passage of the rotor wakes over the stator surface, and the presence of the rotor 3 potential field. By analyzing the stator exit data, it is possible to determine which of these mechanisms are dominant contributors to the unsteadiness. Care must be taken when interpreting the unsteady data because of the frequency response limitations of the aspirating probe. The most apparent limitation of these measurements is the resolution of the random turbulent fluctuations included in the unresolved component of total temperature. Assuming a mean velocity of 100 m/s, the smallest length scale measured by the probe is given by $100/40{,}000 = 2.5 \times 10^{-3}$ m. Hence energy in turbulent eddies with length scales smaller than this is not measured by the instrument. Therefore, the instrument measures all the features associated with frequencies less than 40 kHz (blade passing, shaft frequency, and substantial part of random turbulence). For deterministic structure associated with the rotor blades (blade passing frequency of 6.5 kHz for the second rotor), this instrumentation can measure the first six harmonics. Although finer details of the structure may be contained in higher harmonics, beyond the measurement capability of the probe, the majority of the energy content is included in these lower harmonics. 250 revolutions of rotor locked data were used for ensemble averaging. The appropriate number of ensembles to process was determined by examining the differences between averaged signals at the suction surface casing endwall corner region comprised of 10, 20, 50, 100, 150, 200, 250, and 300 revolutions. Assuming exponential decay of difference as a function of number of ensembles, it was estimated that the bias introduced by averaging 125 ensembles was a small fraction of the measurement uncertainty.

The ensemble-averaged flow is viewed from three different perspectives in this paper. First, attention is focused on the rms flow field. This gives an overall picture of the unsteady flow field as frozen in time downstream of the stator. Both pressure and temperature plots are used to explain this flow. Then, attention is focused on the temporal variation of the stator exit flow at each instant of rotor passage time. This gives the complete picture of how the flow field downstream of the stator is changing with passage of the rotor. For this perspective 6 frames of ensemble-averaged and rms unresolved unsteadiness in total temperature are used. Each frame represents one rotor 2 location with respect to the stator and 20 frames represent one blade passage (only six are shown for the sake of brevity). A movie version of this description is available on the world wide web.

The access URL is http://members.iquest.net./~nsurya/movie.html. This represents the description from the perspective of one rotor blade only. Ensemble-averaged total temperature and rms unresolved unsteadiness in total temperature are used to describe the flow. Comparisons are made to the total pressure field similarly described in Suryavamshi et al. (1994). The results from this description are useful in determining the influence of the stator on the inlet flow to the downstream rotor. Finally, blade-to-blade distributions of the unsteady pressures and temperatures at the midspan, midpitch location are correlated with the unsteady velocity field obtained at the same location using a slanted hot-film probe to derive the composite flow field.

The RMS Flow Field. In this section the hub-to-tip contours of rms values of the unsteady components of total temperature are presented and analyzed. For each of the unsteady components, the rms values are calculated by averaging the square of the unsteadiness over their respective time periods (one revolution for revolution periodic and blade aperiodic components, one blade passage for blade periodic, all the blades of rotor 2 for revolution aperiodic and all 250 revolutions for the unresolved component) and normalizing it by the local time-averaged total temperature rise. (Similar unsteadiness numbers are expressed for the total pressure data as well.) The rms total unsteadiness is calculated by squaring and adding the rms values of the individual components and taking the square root.

Figure 6 shows the blade-to-blade variation of rms unsteadiness in total temperature across the stator pitch at three typical radial locations. This figure shows that the unresolved unsteadiness is much higher than the deterministic unsteadiness in the endwall regions (almost three times near the hub (not shown)) but is only marginally higher than the deterministic unsteadiness in the midspan–midpitch region. In the stator wake region, the unsteadiness level is much higher than in the core region of the flow. The width of the stator wake can be clearly seen in these data. A large increase in the unresolved unsteadiness in the stator wake is probably due to the increase in unsteadiness in the stator wake and its interaction with the rotor wake. Similar distributions are seen in the total pressure kulite data and in the slanted hot-film data. As one progresses from hub to casing, there is very little change in the width of the core region on the suction surface, but a significant decrease is seen in the casing endwall region, as the unsteadiness increases in the suction surface casing endwall region, even though the total temperature does not significantly change in this region. The deterministic unsteadiness as seen earlier has been broken down into revolution periodic and aperiodic unsteadiness. The revolution aperiodic unsteadiness, which is a measure of the rotor–rotor interaction, is almost constant across the pitch at all three radial locations and is much smaller than the revolution periodic unsteadiness at every location. This indicates that the influence of potential field of rotor 3 on the stator exit data is probably very small at this axial station downstream of the second rotor. Further measurements are probably necessary to quantify this much more clearly. The revolution periodic unsteadiness, which is a measure of the periodic rotor wake fluctuations, behaves much like the unresolved unsteadiness in that the wakes show higher periodic fluctuations than in the core flow. The pressure side of the stator wake shows higher fluctuations and larger region affected by rotor–stator interaction than on the suction side except in the casing endwall region. This could be due to the accumulation of the rotor wake fluid on the pressure side of the downstream stator as well as unsteady loading of the stator causing shed vorticity. Similar distributions were also observed in the total pressure data as well.

Figure 7(*a*)–(*f*) shows the hub to tip contours of total, unresolved, and revolution periodic unsteadiness in total temperature compared with the respective rms values in total pressure coefficient. Let us start with the total unsteadiness distributions (Fig. 7(*a*) and (*b*)) and then proceed to the components: unresolved (Fig. 7(*c*) and (*d*)) and revolution periodic (Fig. 7(*e*) and (*f*)). Low levels of total unsteadiness in both pressure and temperature are seen in the core region. In addition, the stator wake has higher unsteadiness than the core region, and this is caused by upstream rotor wake, the resulting unsteady stator blade boundary layer, and the turbulence in the stator wake. In the casing endwall region on the suction surface, a zone of high unsteadiness is seen in both the plots. This is due

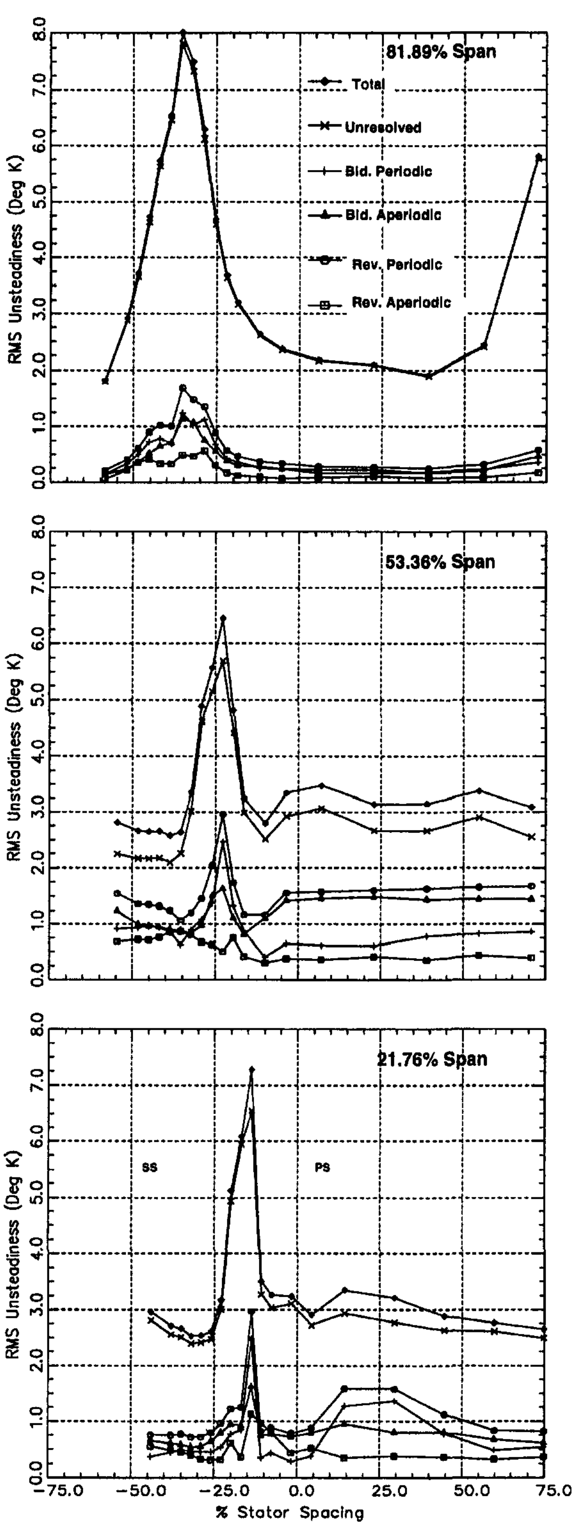

Fig. 6 Blade-to-blade variation of time averaged rms unsteadiness in total temperature rise (K)

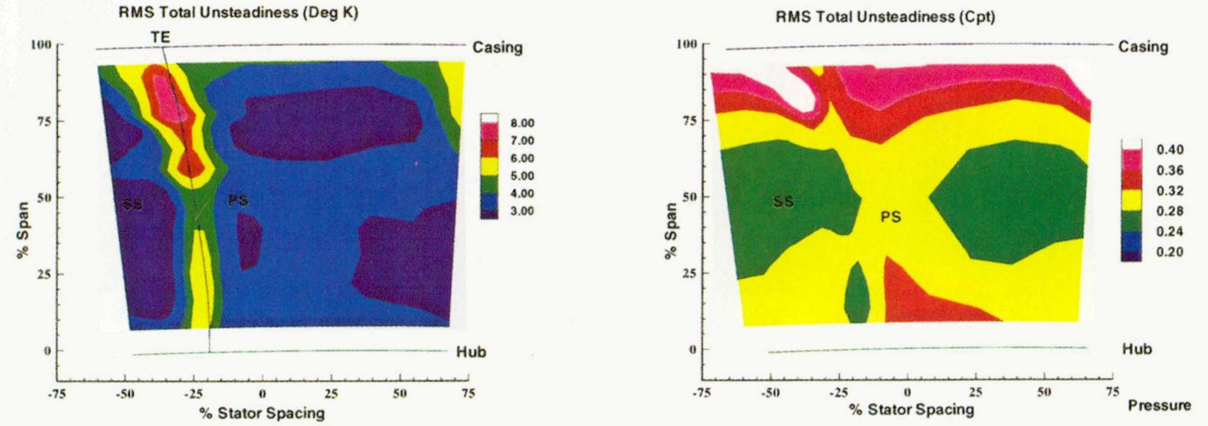

(a) RMS Total Unsteadiness (Deg K)

(b) RMS Total Unsteadiness (Cpt)

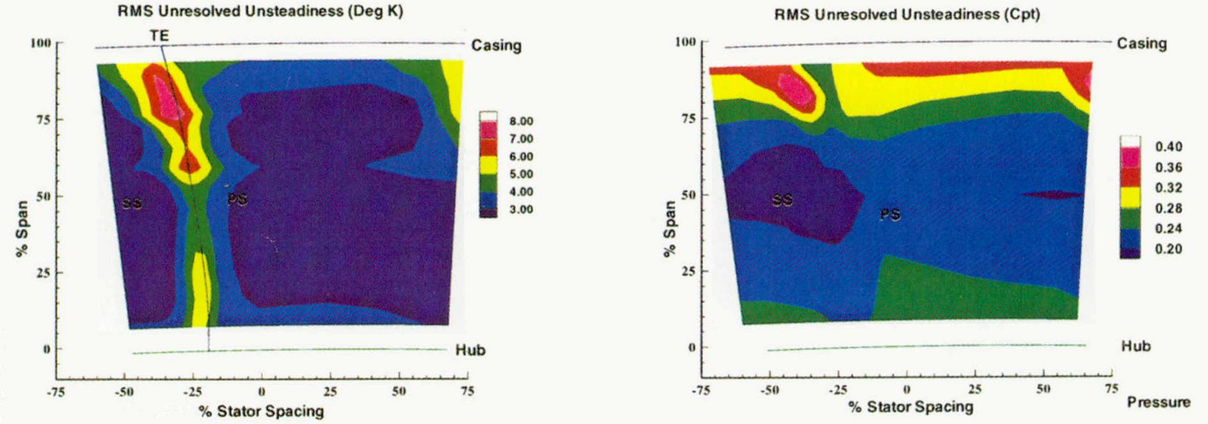

(c) RMS Unresolved Unsteadiness (Deg K)

(d) RMS Unresolved Unsteadiness (Cpt)

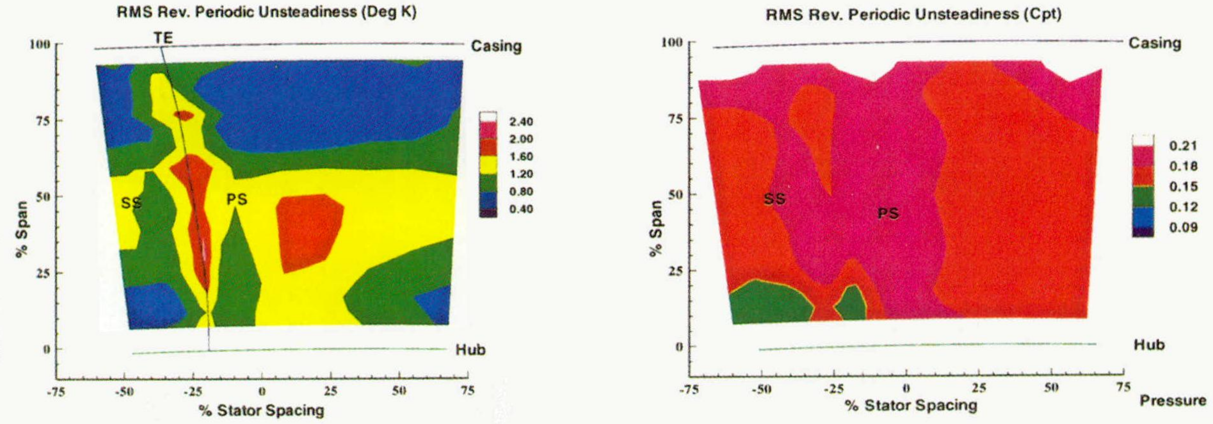

(e) RMS Revolution Periodic Unsteadiness (Deg K)
Total Temperature

(f) RMS Revolution Periodic Unsteadiness (Cpt)
Total Pressure (Cpt)

Fig. 7 Contours of rms unsteadiness in total temperature compared with total pressure (Cpt)

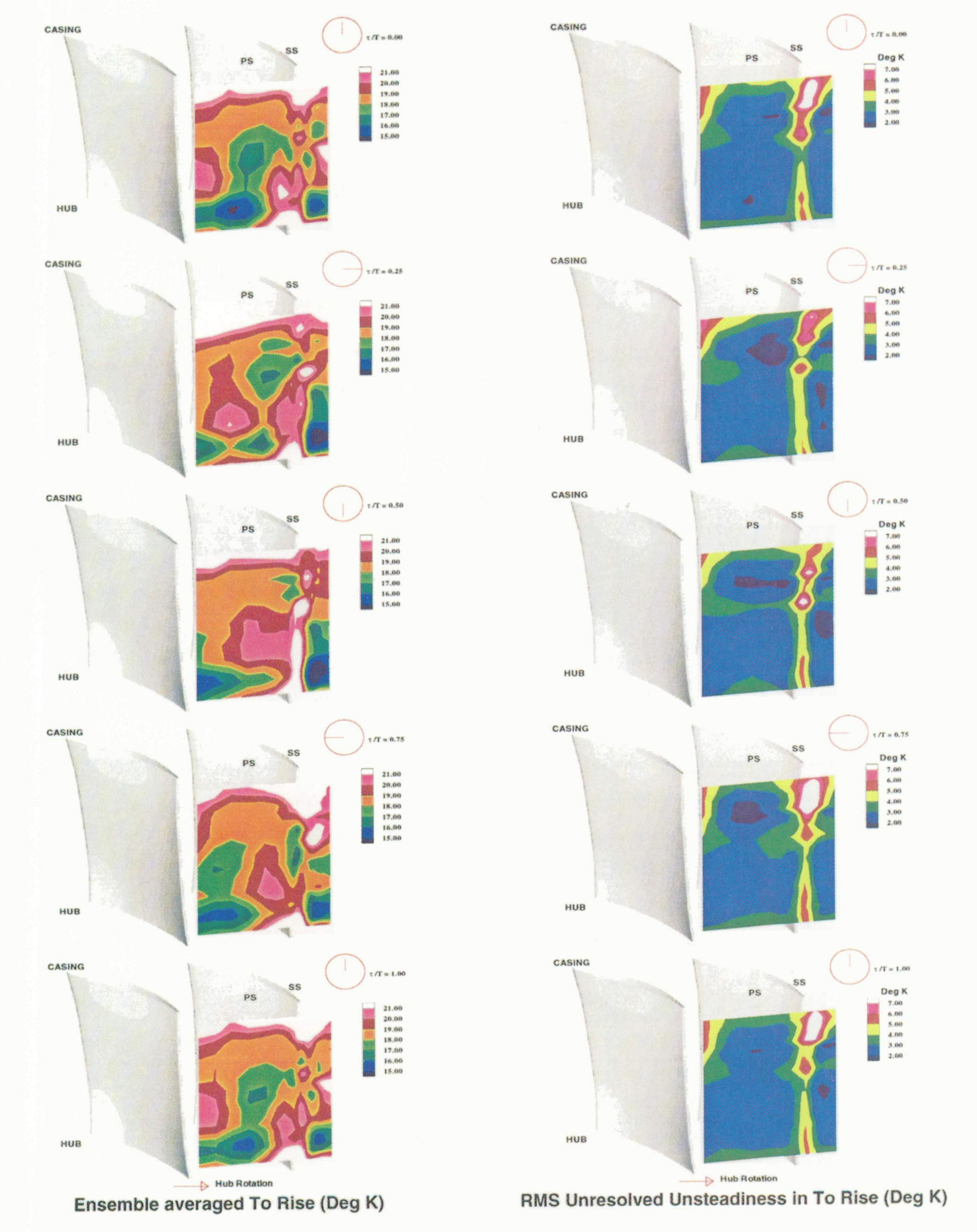

Ensemble averaged To Rise (Deg K)

RMS Unresolved Unsteadiness in To Rise (Deg K)

Fig. 8 Temporal variation of stator exit flow

to the high levels of mixing present as a result of interaction between the annulus wall boundary layer, secondary flow, and the low-momentum region on the suction surface endwall corner and the leakage flow from the upstream rotor. The location of this region with respect to the blade passage is almost the same in both plots; however, the width of this region is different. The total temperature shows a slightly larger region of unsteadiness compared to the pressure data. This could be due to the relatively sparse grid used for the temperature measurement. It is now interesting to progress from the total unsteadiness distribution into the deterministic and the unresolved components. Figures 7(*c*), (*d*), (*e*), and (*f*) show the deterministic and unresolved unsteadiness distributions for the total temperature and total pressure, respectively. The deterministic unsteadiness is represented by the revolution periodic component (which is a combination of both blade periodic and blade aperiodic components). By comparing Figs. 7(*a*) through (*f*), bulk of the unsteadiness in the endwall regions is unresolved in nature. However, in the core regions of the flow, both deterministic and unresolved unsteadiness are of similar magnitude. The suction surface casing endwall corner zone is mainly unresolved in nature; both the temperature and pressure data seem to confirm this. The deterministic unsteadiness distributions do not show many changes in the wake except on the pressure side of the wake, where slightly higher total temperature and much higher total pressure unsteadiness is seen. This tends to confirm the theory that the rotor wake (which has high levels of periodic unsteadiness) accumulates on the pressure side of the downstream stator. This is not seen very clearly in the temperature, possibly because of very low temperature unsteadiness compared with the total pressure at this location. The aspirating probe may not have much sensitivity to resolve such a low temperature difference. The total temperature rise of the second stage is approximately only 10 K, whereas the total pressure rise is approximately 1.6 psia. In addition, the wake in the hub region has higher unsteadiness. This is probably caused by transport of both the rotor wake and the stator boundary layer toward the hub, caused by radial pressure gradient.

In the casing endwall region, the temperature distribution shows a drop in the periodic unsteadiness (from the core region) but no such change is seen in the total pressure data. This could be due to a much faster decay of the total temperature unsteadiness in the casing endwall region due to interactions with the annulus wall boundary layers and rotor leakage flow/vortex or it could be due to a smearing of the rotor leakage flow by the stator passage. Also the uncertainty band on the total temperature is much higher than that on the total pressure. In the unresolved unsteadiness distribution, a clear wake is seen in the total temperature data but not in the total pressure data. Possibly due to the larger surface area of averaging on the kulite total pressure probe, the unsteadiness levels are lower in the total pressure than in the total temperature measurement. The suction surface casing corner endwall region is seen in both the pressure and temperature data. The width of the region is much larger in the temperature data compared to the pressure data. Comparing the deterministic and unresolved unsteadiness distributions, it is clear that the unsteadiness in the suction surface casing endwall corner region is mainly unresolved in nature.

It is interesting to compare Fig. 7 with Fig. 5(*c*). Regions of high levels of total unsteadiness are regions of very low efficiency (suction surface casing endwall corner region and the stator wake regions). This seems to indicate that higher unsteadiness is associated with mixing of the wakes, leakage flow, and secondary flow due to the upstream rotor, essentially a viscous phenomena. Associated with this are losses due to viscous and turbulent dissipation. This results in higher temperature rise, lower pressure rise, and lower efficiency. Thin stator wakes and elimination of the casing endwall corner flow regions are the key to increasing the efficiency of the compressor.

Temporal Variation of Stator Exit Flow. The temporal variation of the stator exit flow is discussed in this section. For the sake of brevity, the following discussion is limited to the ensemble-averaged and unresolved unsteadiness results only. Figure 8 contains several perspectives of the stator exit measurements "frozen" at the same instant in time within the rotor revolution, but derived by averaging over 250 consecutive rotor revolutions. Six frames from the passage of the first rotor blade across the stator passage are shown but the interpretation is based on the analysis of 20 frames (the first blade in the revolution). A clock in the upper right-hand corner of each picture shows the passage of the rotor blade across the stator passage (from $\tau/T = 0.0$ to $\tau/T = 1.0$). Here τ represents the fraction of blade passing period T. These times are arbitrary as the location of the rotor blade with respect to stator is not known. The location of the trigger is the same with respect to all locations in the stator passage. Three regions of the flow are focused on in this discussion: (1) the stator wake region away from the casing endwall; (2) the casing endwall corner region (blade suction surface and casing endwall corner); and (3) hub endwall flow region.

Stator Wake Region Away From the Casing Endwall. As the rotor passes across the stator passage, there is a change in the behavior of the stator wakes away from the casing endwall. This is best seen in the unresolved unsteadiness distribution. Different behaviors are seen at different radii. Near the hub, the width of the wake decreases from $\tau/T = -0.25$ (not shown) to about $\tau/T = 0.25$ and then starts increasing again. The width is the highest at $\tau/T = 0.75$ and then slowly decreases, until $\tau/T = 1.25$ (not shown). The wake is also the deepest (defined by the increase in the rms value of the unresolved unsteadiness) at $\tau/T = 0.75$ and the shallowest at $\tau/T = 0.25$. The depth of the wake decreases from $\tau/T = -0.25$ to $\tau/T = 0.25$ and then increases until $\tau/T = 0.75$. At mid span, however, the width of the wake is almost constant as the rotor passes by. The stator wake depth at midspan shows almost the opposite behavior. The wake is deepest at $\tau/T = 0.25$ and the shallowest at $\tau/T = 0.75$. However, the change in the maximum values of the unresolved unsteadiness in the wake between the two time periods is small. So one can almost say that the wake depth at midspan does not change very much. This time step ($\tau/T = 0.75$) is termed the "*maximum interaction time.*" On the pressure side of the stator the width of the wake (unresolved unsteadiness) is always greater than on the suction side. This is because the rotor wake is being transported toward the pressure side as the rotor passes the stator.

Casing Endwall Corner Region. Like the wake region, this region also changes significantly with rotor passing. This region pulses (increases and decreases in size) as the rotor passes. Similar behavior was observed by Cherrett et al. (1995) in the hub corner flow region downstream of a stator of a single-stage transonic fan. The region starts decreasing in size as the time increases from $\tau/T = 0.0$ and is the smallest at $\tau/T = 0.5$ and then starts increasing, rapidly reaching a maximum at the maximum interaction time. As time further increases, the region starts decreasing once again in size. This is true for both the ensemble average as well as the unresolved unsteadiness. Cherrett et al. (1995) theorize that this is due to the rotor moving in front of the stator leading edge. The stator wake as we saw earlier was the thickest at $\tau/T = 0.75$. As the region grows in size from $\tau/T = 0.5$ to 0.75, the region is no longer confined to the suction surface region. It slowly spreads to the pressure surface and at $\tau/T = 0.75$, the region is almost the same size on either of side of the stator blade. It is also interesting to see that the corner region is seen to be "feeding" the flow in the casing region away from the endwalls as the blade passes by. This is seen very clearly in the unresolved unsteadiness distribution but not in the ensemble-averaged plots.

Hub Endwall Flow Region. This region can be best explained using both the unresolved unsteadiness and the ensemble-averaged temperature distributions. Slightly higher levels of unsteadiness seen between the stator blades very close to the hub are indicative of this region. At $\tau/T = 0.0$ the region is spread out almost across the entire passage and as the rotor moves across the stator blade, the clearance flow grows in size in the spanwise direction while shrinking in the circumferential direction and starts moving across the passage probably transporting some of the hubwall boundary layer flow toward the pressure surface of the stator blade. This can be verified by the appearance of higher levels of unsteadiness on the pressure surface of the blade. It was supposed earlier that there is scraping of the hubwall boundary layer and a presence of scraping vortex (see Prato et al., 1996). The appearance of high unsteadiness on the pressure surface away from the hub seems to substantiate this notion. And as the rotor blade continues further, the hub clearance region starts decreasing in size in the spanwise direction and starts spreading across the stator passage. The rotor passing has indeed triggered this type of behavior and certainly needs to be modeled for accurate prediction of the stator exit flow fields in a multistage compressor.

From this discussion it can very clearly remarked that the stator exit flow is controlled by not only the rotor passing but also by the relative location of the rotor with respect to the stator. Very consistent information like the appearance of thick stator wakes and a large casing corner endwall region when the rotor trailing edge is in front of the stator leading edge characterizes the maximum interaction phenomena as well.

Rotor 2 Exit Field at Midpitch. In this section, the blade-to-blade distribution of the rotor 2 field at the exit of the stator at the midpitch location (32.7 percent pitch at midspan) is presented. The ensemble-averaged data acquired at the midpitch location of the area traverse are used to explain this flow field. Contour plots of the ensemble-averaged total temperature and unresolved unsteadiness in total temperature compared with the ensemble-averaged and unresolved unsteadiness in total pressure derived from the high-frequency total pressure probe are shown in Figs. 9(*a*)–(*d*), respectively. Four blade passages are shown in each plot and the same blade passages are shown in all the plots. For each of these plots, the rotor wake location is identified by the higher total temperature and pressure as well as by the higher unresolved unsteadiness. There seems to be a phase shift between the pressure and temperature wakes. This is possibly due to slight variations in the trigger locations since these measurements were taken a year apart or due to differential probe lengths, which will change the local flow around the probes. In any case by shifting the data relative to each other (a constant shift for the entire revolution), the wakes can be made to align. Comparing the ensemble-averaged results, it is clear that both total temperature and total pressure wakes are present at this axial location. Since the data are at midpitch, the interaction of the rotor 2 wake with the stator is minimal. Consequently a very clear wake is seen. The flow is also fairly periodic from blade to blade. A complete revolution plot of these data (not shown in this paper) showed a typical two nodes per revolution pattern consistent with the difference in blade count between rotors 2 and 1. The wakes are much thicker in the casing endwall region than in the hub region. Also the temperature wakes and pressure wakes have different thickness across the span. This could be due to differential decay rates for the temperature and pressure, respectively. Another interesting phenomenon is that the rotor wake in the casing endwall region has decayed substantially as indicated in both the temperature and pressure distribution. The rotor wake width is lowest in the tip, increasing to very high values near the hub. The rotor wake is distorted as it passes through the stator passage due to differing convection velocity. The wakes are the thickest (as evidenced by the ensemble-averaged data) near the hub, possibly due to radial inward transport of the rotor wake by the stator flow field due to imbalance between the centrifugal forces and the pressure gradient. The core flow is more clearly seen in the temperature distribution than in the pressure signature for the ensemble average and in the pressure than in the temperature signature for the unresolved unsteadiness. In the unresolved unsteadiness distribution, a much larger total pressure core is seen as opposed to the total temperature distribution. Higher levels of unresolved unsteadiness in the casing endwall region are probably a manifestation of the clearance flow.

Isentropic Efficiency Distribution. Isentropic efficiency has been calculated using Eq. (14) for the ensemble-averaged pressure and temperature distribution (one rotor revolution each) at the midpitch location. This is the location away from the endwalls downstream of the stator, which has the least influence on the rotor flow. Instantaneous efficiency cannot be calculated since the pressure and temperature measurements have been made at different times. It has to be remembered here that the efficiency calculated in this section is for two stages and is not calculated on a streamline. As a result, the efficiency numbers could be higher than 100 percent. The overall efficiency calculated using the mass-averaged total temperature and pressure downstream of stator 2 referenced to the compressor inlet conditions is 89.5 percent compared with the overall isentropic efficiency of 89.3 percent. The uncertainty in the computed efficiency is about ±0.25 percent. An algebraic averaged (across the passage) efficiency (at each radial location) was calculated for each blade passage in the revolution and Fig. 10(*a*) shows the radial variation of this average efficiency for each blade passage. This picture depicts the bandwidth of efficiency variation across the rotor revolution. There is significant variation in the efficiency of each of the rotor blades. The average bandwidth is about 5 percent with the maximum variation being around 10 percent. The possible reasons for the change in efficiency across the rotor revolution are: different incidences, loading changes, influence of the aperiodicity brought about by the differing blade count (seen in the complete rotor revolution contours), etc. Low-efficiency numbers are present in the hub and casing endwall regions. The presence of rotor tip clearance flow and stator hub clearance flow and their mixing is probably the main cause of drop in efficiency in these regions. From the designer's viewpoint, it would be desirable to have all the blades perform with the same efficiency. By radially averaging the efficiency for each blade passage, it is possible to look at the best, worst, and average blade. For this compressor, if all the blades in rotor 2 behaved as the "best" blade, there would be an improvement in efficiency by about 1.3 percent. It should also be mentioned that the best blade was about 2.5 percent more efficient than the worst blade. The radial variation of efficiency for the best, worst, and average blade is shown in Fig. 10(*b*). The efficiency of the best blade is better than the average blade at almost all radial locations except close to the endwalls, where the efficiencies are almost the same.

Blade-to-blade distributions of ensemble-averaged and blade periodic isentropic efficiency calculated from the temperature and pressure distributions at the midpitch circumferential location are shown in Fig. 10(*c*) and (*d*), respectively. For both the distributions, three radial locations are shown and at each location four blade passages are shown for the ensemble average and one blade passage for the blade periodic efficiency, respectively. The locations of the rotor wake can be easily identified as those that have low efficiency. The efficiency distributions are fairly periodic from blade to blade but they do change substantially in the radial direction. The efficiency is very low near the casing. This is partly due to the use of a mass-averaged total pressure and total temperature at the inlet and partly due to the large flow mixing that is occurring in the casing endwall region due to the rotor clearance flow.

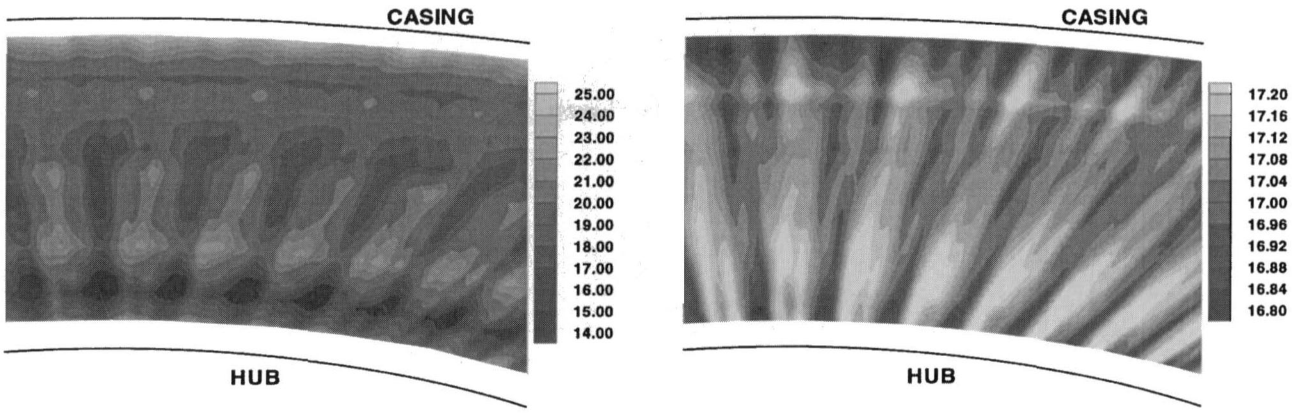

(a) Ensemble Average (Deg K) **(b) Ensemble Average (Psia)**

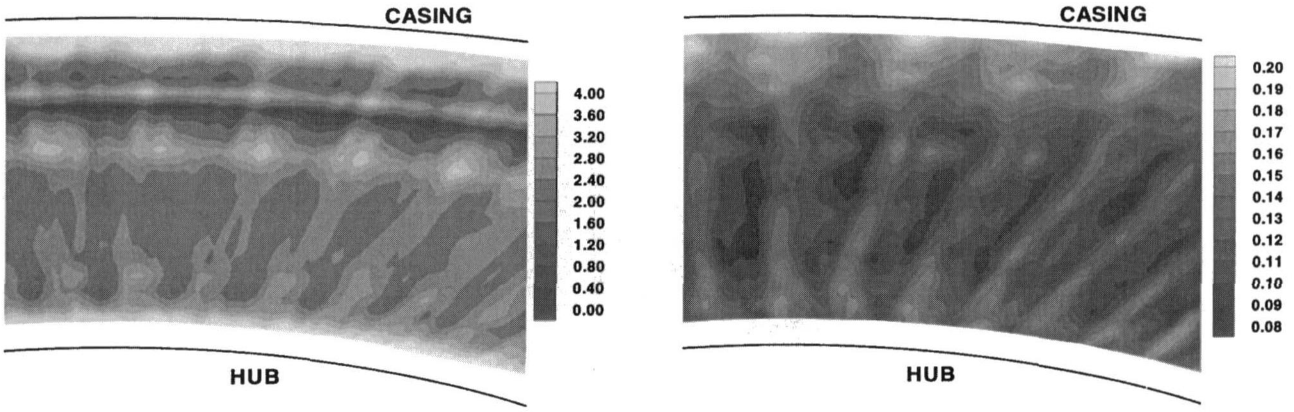

(c) RMS Unresolved Unsteadiness (Deg K) **(d) RMS Unresolved Unsteadiness (Psia)**

Fig. 9 Contours of ensemble-averaged and rms unresolved unsteadiness: rotor 2 exit flow at midpitch

Composite Flow Field. An attempt was made to determine the composite picture of the rotor exit flow field downstream of stator 2 at the midspan, midpitch location by correlating the unsteadiness in total temperature distribution with the unsteady total pressure data acquired using the kulite probe and the unsteady velocity distributions acquired using the slanted hot-film probe with four rotations. Details of the hot-film measurement are given in Prato (1996). Blade-to-blade distributions of ensemble-averaged, blade periodic properties and rms unresolved unsteadiness in total pressure and temperature are shown in Fig. 11. Six blade passages of an ensemble-averaged revolution are shown for the ensemble average and unresolved unsteadiness and one blade passage for the blade periodic distribution. For the rotor exit flow in the absolute frame of reference, the wake is defined as the region that has lower axial velocity, higher absolute tangential velocity and higher radial velocity. Depending on the velocity triangles, the total pressure could be higher or lower in the wake. At the location shown, the velocity triangles indicate that the total pressure and total temperature are higher in the wake as the absolute tangential velocity is higher in the wake. In each of these figures, the location of the wake for each of the blade passages is also shown. Since the data are acquired with respect to the trigger on the compressor shaft, it is expected that the ensemble average does indeed show the same wake location. There seem to be small discrepancies in the location of the wake (within 5 percent of the blade passage) between the velocity, pressure, and temperature data. This seems acceptable considering the data have been acquired at different times and the pitchwise resolution of each of these probes is different (hot-film has the best resolution whereas the kulite has the worst). From these figures it is clear that the rotor wake is visible in all the data sets. The axial location of measurement is 130 percent chord downstream of the rotor. Hence, it is reasonable to expect that the rotor wake has decayed and widened considerably. Larger interpassage oscillations are found in the total pressure data than in the either the velocity or temperature data sets. This is possibly due to a much higher frequency response of the kulite probe compared with the aspirating and hot-film probes and differing measuring techniques. The wake widths from each of the measurements are approximately the same (approximately 60 percent of the passage). This is surprising considering the pitchwise resolution of these instrumentation are different. The pressure and suction surfaces of the wake are marked on the temperature data. In all the data sets a sharper wake is seen on the pressure side and a broader wake on the suction side. This is one more piece of evidence regarding the ability of the aspirating probe to measure total temperature fluctuations and wake widths very accurately.

Concluding Remarks

Some remarks based on the area traverse of an aspirating probe downstream of second stator are:

1 Higher total temperatures and higher levels of deterministic unsteadiness on the pressure side of the stator confirm the transport of rotor exit flow to the pressure side of the downstream stator.
2 The suction surface casing endwall corner region has high levels of unresolved unsteadiness and is also a region of

low efficiency, which is probably due to corner stall, inlet skew, and casing corner flow as well as intense mixing of the rotor leakage flow, rotor wake, and stator endwall flow.

3 The unresolved unsteadiness levels are much higher than the deterministic unsteadiness in the endwall regions and only marginally higher than the deterministic unsteadiness at midspan.

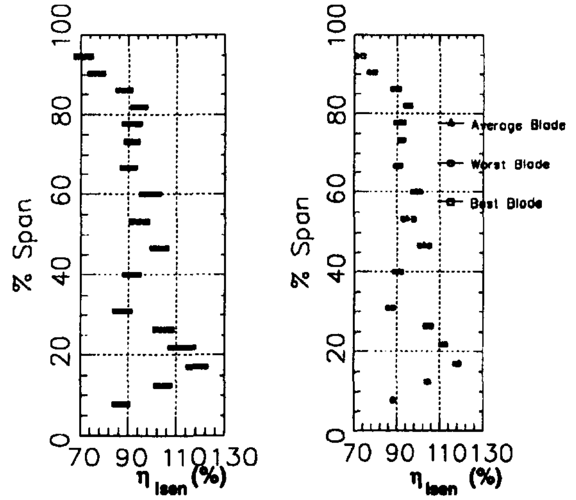

(a) Bandwidth of Efficiency **(b) Best, Worst and Average Blade**

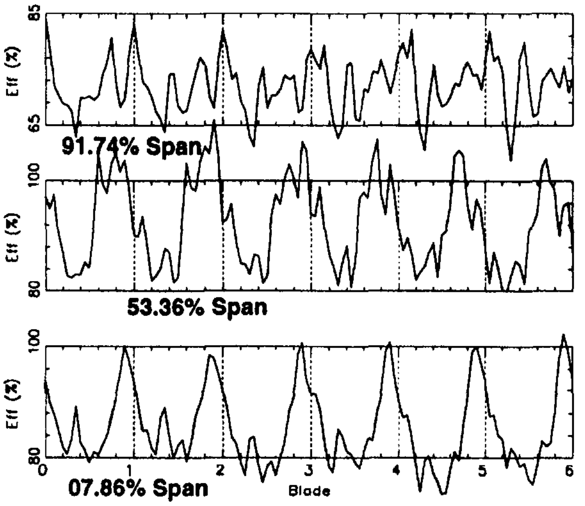

(c) Ensemble Average

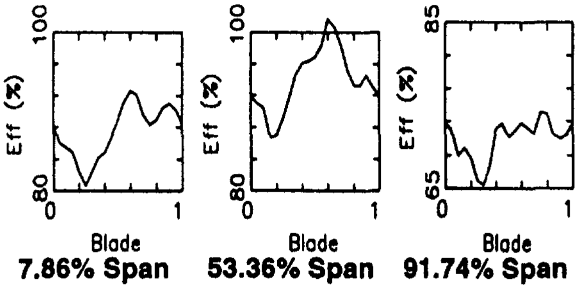

(d) Blade Periodic

Fig. 10 Isentropic efficiency distribution at midpitch

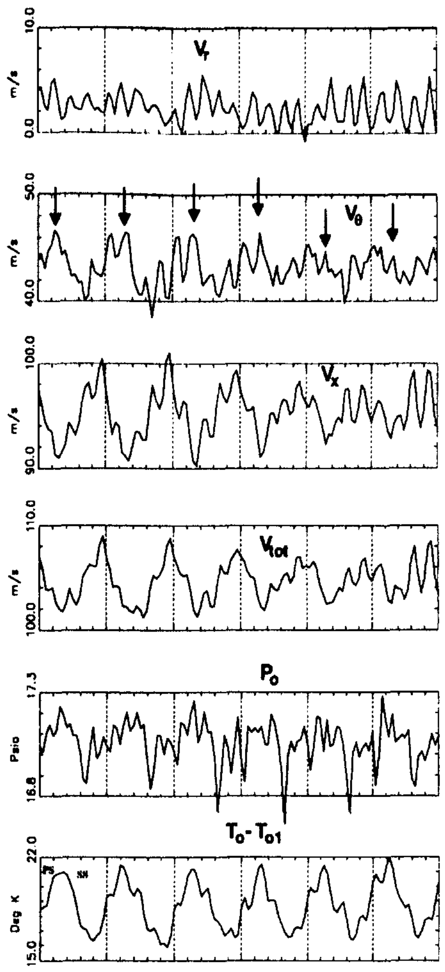

Ensemble Average

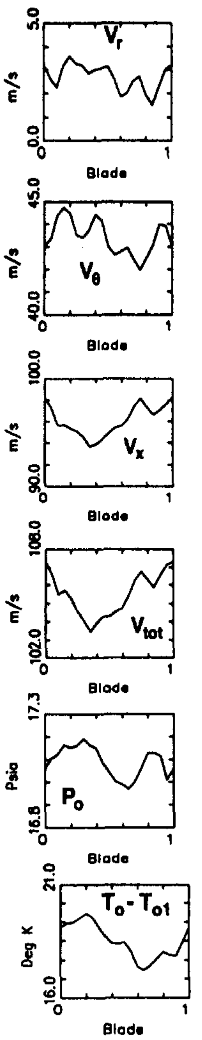

Blade Periodic

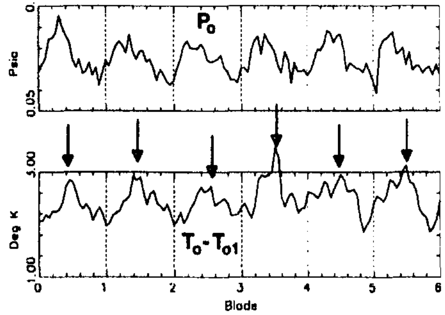

Unresolved Unsteadiness

Fig. 11 Composite flow field at the midspan, midpitch location: blade-to-blade distribution

4 Regions of high levels of total unsteadiness (stator wakes and casing endwall regions) are also regions of very low efficiency. Thin stator wakes and elimination of casing endwall corner flow regions are the keys to increasing the efficiency of the compressor.

5 Thickening of the rotor wakes near the hub was possibly due to radial inward transport of the rotor wake by the stator flow field due to imbalance between the centrifugal forces and the pressure gradient.

6 At the midpitch location of measurement downstream of the stator, if all the rotor blades were behaving as a "best" blade, the improvement in isentropic efficiency of the compressor would be about 1.3 percent.

7 As the rotor passes across the stator passage, there are dramatic changes in the flow behavior. They are summarized below:
   - The presence of thick stator wakes and the largest extent of the casing endwall corner region is an indication of the maximum interaction time.
   - As the rotor passes the stator leading edge, the stator wakes start increasing in size and the corner region starts reducing in size. The hub leakage flow region starts contracting in the circumferential direction and starts moving radially. Some of the stator hub wall flow is then transported across the stator passage and deposited on the pressure surface of the stator.

From this study it is clear that significant levels of unsteadiness exist downstream of an embedded stage and that majority of this is due to interaction of rotor 2 wakes with the stator flow field. The interaction of rotor wakes that have both deterministic and unresolved unsteadiness with the stator exit flow, which is mainly unresolved in nature (shedding of vorticity from the stator trailing edge due to a time-varying circulation on the stator caused by the passage of the rotor wake flow over the stator surfaces) tends to overshadow the interaction between the rotor 2 wake flow and the rotor 3 potential field as evidenced by the low values of the revolution aperiodic unsteadiness (a measure of the rotor/rotor interaction). Development of computational tools that solve the combined stator rotor flow fields are what is needed for the design of future compressors.

Acknowledgments

This project was supported by a grant from NASA Lewis Research Center (NAG3-1222 with Dr. A. J. Strazisar as technical monitor), Rolls Royce plc (Mr. M. A. Howard), Rolls Royce Inc. (Mr. R. Moritz), and the Allison engine company (Dr. J. R. Fagan). Helpful suggestions and discussions by these personnel are acknowledged. The authors wish to acknowledge Dr. Wing Ng of VPISU for having provided the design of the aspirating probe and for the helpful suggestions and discussions, Mr. Dale Van Zante of Iowa State for providing useful suggestions and the methodology of measurement, and Mr. H. Houtz of Penn State for having fabricated the aspirating probe. The authors also wish to acknowledge United Technologies Research Center (UTRC)/Pratt & Whitney Aircraft Division of United Technologies Corporation for donating the multistage compressor facility to Penn State.

References

Adamczyk, J. J., 1985, "Model Equation for Simulating Flows in Multistage Turbomachinery," ASME Paper No. 85-GT-226.

Alday, J., et al., 1993, "Flow Randomness and Tip Losses in Transonic Rotors," ASME Paper No. 93-GT-189.

Cherrett, M. A., et al., 1995, "Unsteady Three-Dimensional Flow in a Single-Stage Transonic Fan: Part II—Unsteady Stator Exit Flow Field," ASME JOURNAL OF TURBOMACHINERY, Vol. 117, pp. 514–521.

Howard, M. A., et al., 1994, "Endwall Effects at Two Tip Clearances in a Multistage Axial Flow Compressor With Controlled Diffusion Blading," ASME JOURNAL OF TURBOMACHINERY, Vol. 116, pp. 635–647.

Kerrebrock, J. L., and Mikolajczak, A. A., 1970, "Intra-Stator Transport of Rotor Wakes and Its Effect on Compressor Performance," ASME *Journal of Engineering for Power,* 92, pp. 359–368.

Kotidis, P. A., and Epstein, A. H., 1991, "Unsteady Radial Transport in a Transonic Compressor Stage," ASME JOURNAL OF TURBOMACHINERY, Vol. 113, pp. 207–218.

Lakshminarayana, B., et al., 1994, "Experimental Investigation of Flow Field in a Multistage Axial Flow Compressor," ASME Paper No. 94-GT-455.

Ng, W. F., 1990, private communication.

Ng, W. F., and Epstein, A. H., 1983, "High Frequency Temperature and Pressure Probe for Unsteady Compressible Flows," *Review of Scientific Instruments,* Vol. 54, No. 12, pp. 113–124.

Prato, J. P., et al., 1996, "Experimental Investigation of the Mean Flow Field at the Exit of an Embedded Stator in a Multistage Axial Flow Compressor," *AIAA J. of Propulsion and Power,* Vol. 13, No. 2, pp. 169–177.

Prato, J. P., 1996, "Steady and Unsteady Flow in an Embedded Stator Stage of a Multistage Axial Flow Compressor," PhD thesis, The Pennsylvania State University.

Suder, K. L., et al., 1987, "Measurements of the Unsteady Flow Fields Within the Stator Row of a Transonic Axial Flow Fan, Part I: Measurement and Analysis Technique," ASME Paper No. 87-GT-226.

Suryavamshi, N., et al., 1994, "Unsteady Total Pressure Field Downstream of an Embedded Stator in a Multistage Axial Flow Compressor," *Unsteady Flows in Aeropropulsion,* ASME AD-Vol. 40, pp. 61–76; to be published in ASME *J. Fluids Engineering,* 1998.

Suryavamshi, N., 1996, "Unsteady Flow, Spanwise Mixing and Rotor-Stator Interaction in Multistage Axial Flow Compressors," PhD thesis, The Pennsylvania State University.

Van Zante, D. E., et al., 1995, "An Improved Aspirating Probe for Total-Temperature and Total-Pressure Measurements in Compressor Flows," ASME JOURNAL OF TURBOMACHINERY, Vol. 117, pp. 642–649.

Laser-Doppler-Velocimetry Measurements in a Cascade of Compressor Blades at Stall

G. V. Hobson

A. J. H. Williams

H. J. Ganaim Rickel

Department of Aeronautics
and Astronautics,
Turbopropulsion Laboratory,
Naval Postgraduate School,
Monterey, CA 93943

Compressor stall was simulated in the Low-Speed Cascade Wind Tunnel at the Turbopropulsion Laboratory of the Naval Postgraduate School. The test blades were of controlled-diffusion design with a solidity of 1.67, and stalling occurred at 10 deg of incidence above the design inlet air angle. All measurements were taken at a flow Reynolds number, based on chord length, of 700,000. Laser-sheet flow visualization techniques showed that the stalling process was unsteady and occurred over the whole cascade. Detailed laser-Doppler-velocimetry measurements over the suction side of the blades showed regions of continuous and intermittent reverse flow. The measurements of the continuous reverse flow region at the leading edge were the first data of their kind in the leading edge separation bubble. The regions of intermittent reverse flow, measured with laser-Doppler velocimeter, corresponded to the flow visualization studies. Blade surface pressure measurements showed a decrease in normal force on the blade, as would be expected at stall. Data are presented in a form that characterizes the unsteady positive and negative velocities about their mean, for both the continuous reverse flow regions and the intermittent reverse flow regions.

Introduction

The continuing effort to predict off-design performance and stalling behavior of compressor blades during the design phase has prompted studies to characterize the flow in and around leading edge separation bubbles of blades in cascade. One of the earliest studies of stall in a two-dimensional cascade was performed by Sovran (1959). He obtained measurements and used smoke flow visualization to study rotating stall in an axial-flow compressor and in a cascade of seven blades. He also produced a movie of the stalling process in the cascade for low-Reynolds-number flow. Yocum and O'Brien (1993) presented flow visualization and time-mean velocity measurements of stalled flow in a cascade. They also presented a good historical perspective of earlier cascade studies as an introduction to their measurements. Experimental studies have attempted to map viscous flow development in specific geometries. Recently Hobson and Shreeve (1993) reported detailed two-component laser-Doppler-velocimetry (LDV) measurements of the flow through the same set of controlled-diffusion (CD) compressor blades in cascade at a high incidence angle prior to stall.

A laminar leading-edge separation bubble was observed, which reattached turbulent within 5 percent of a chord length from the the leading edge. Consistent with measurements at lower incidence angles, the reattached suction surface boundary layer remained turbulent and attached over the rear part of the blade. Since boundary layer separation had not been achieved, the next step was to increase the incidence angle further, to a value of 10 deg above design, in an attempt to stall the blades.

The intention was to determine the maximum turning or lift generated by the blades, and to determine the way in which the suction-side boundary layer would separate. In others words, would the leading-edge separation bubble grow or would separation begin from the trailing edge where the boundary layer was fully turbulent? Two-component LDV measurements were taken in the pitchwise or blade-to-blade direction upstream, on the suction side, and across the wake, at most of the stations measured by Hobson and Shreeve (1993). Blade surface static pressure measurements were recorded and laser-sheet flow visualization studies were performed for comparison with the LDV data.

Experimental Apparatus

The Low-Speed Cascade Wind Tunnel test facility is shown in Fig. 1. A thorough description of the facility, test section, and controlled-diffusion blading was presented by Sanger and Shreeve (1986). The figure also shows the position where seed particles were introduced into the tunnel for LDV measurements. The cascade had 20 blades, the flow Reynolds number, based on chord length, was approximately 700,000, and the inlet air angle was 50 deg.

Blade surface static pressure measurements were recorded with a 48-channel Scanivalve. The instantaneous horizontal and vertical velocities of one micron (1 μm) sized oil mist particles were measured with a two-component LDV system, which consisted of standard optics and was powered by a 4W argon-ion laser. Laser sheet flow visualization was performed with a 300 mW argon-ion laser, which directed its beam into a fiber optic cable. This cable directed the beam into a series of standard optics which produced the laser sheet. The schematic of the system and the laser sheet is also shown in Fig. 1.

Experimental Procedure

The initial pitchwise survey at station 1 (Fig. 2) was conducted over three passage widths to determine inlet flow uniformity. All subsequent inlet pitchwise surveys were traversed over a distance, spanning 133 percent of the blade spacing, which corresponded to the region of maximum seeding. Figure 2 shows the exact vertical location, horizontal distance, and step size (in parentheses after the station number as a percentage of blade pitch) of each inlet and exit survey.

Measurements were only taken on the suction side within the blade passage, over a pitchwise distance covering 67 percent of blade spacing. Figure 2 also shows the positions for the passage surveys and each point on the figure represents a mea-

---

Contributed by the International Gas Turbine Institute and presented at the 41st International Gas Turbine and Aeroengine Congress and Exhibition, Birmingham, United Kingdom, June 10–13, 1996. Manuscript received at ASME Headquarters February 1996. Paper No. 96-GT-484. Associate Technical Editor: J. N. Shinn.

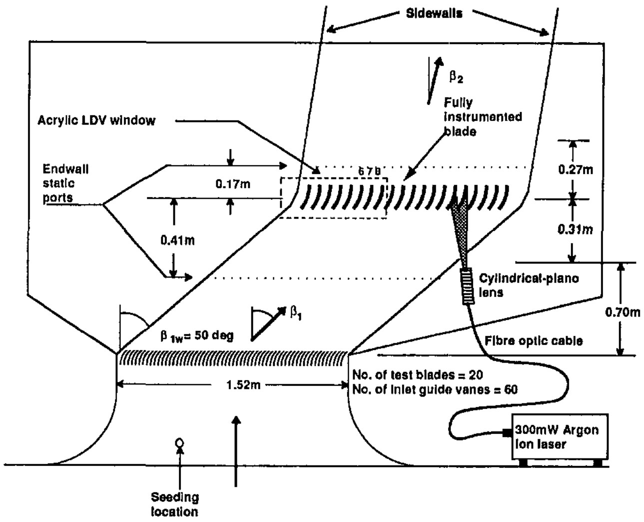

Fig. 1 Schematic of the cascade wind tunnel and laser sheet flow visualization system

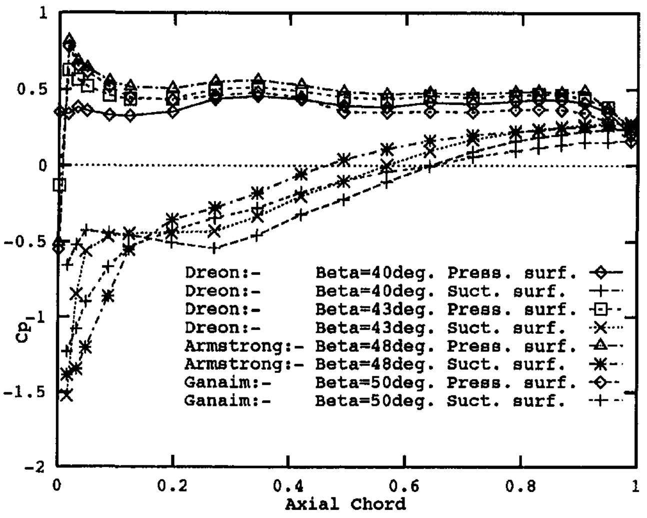

Fig. 3 Blade surface pressure distribution for increasing inlet flow angle

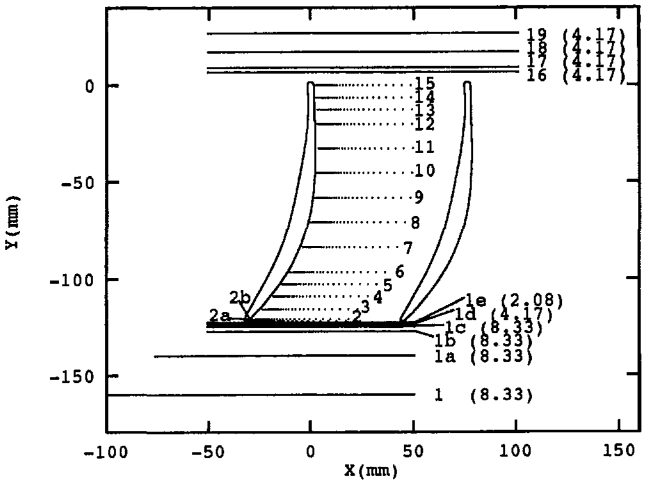

Fig. 2 LDV survey locations (numbers in parenthesis denote traverse size in percent pitch)

surement location. These points were stretched away from the surface to approximate a boundary layer survey. The wake surveys were conducted with the same LDV optics configuration specified for the inlet surveys. The LDV was horizontal and perpendicular to the tunnel for stations 16 to 19 and the surveys were performed over two passage widths.

All LDV measurements presented in this study were averaged over 3000 data points. The presentation of mean flow velocity distributions was without any editing of the histograms. Specific editing was used to distinguish positive and negative velocity distributions, and these will be described in detail in the next section. Time between data points was recorded so that subsequent Fourier analyses could be performed on the data to determine the frequency of the unsteady stalling process. Editing based on plus or minus 2 standard deviations for the histogram was performed to determine the edge of the separation and reverse flow regions.

The flow visualization was carry out by projecting a laser sheet from the bottom left of the cascade to blade number 14, and while the tunnel was operated at a flow Reynolds number of 700,000, fog was introduced into the tunnel through one of the endwalls. This process was filmed with an 8 mm video camera, which operated at 30 frames per second.

Results and Discussion

Blade Surface Pressure Measurements. Figure 3 shows the blade surface pressure distribution measured by Dreon (1986) at 40 and 43 deg, Armstrong (1990) at 48 deg, and the present measurements at 50 deg (Ganaim Rickel, 1994, and Williams, 1995). The integration of the area within the pressure distributions for each angle gave the normal force coefficient. Figure 4, which is a plot of the normal force coefficient versus inlet flow angle, shows the drop-off in force, or lift, at 50 deg and that the cascade had entered into stall.

Inlet Surveys. A periodic disturbance, of approximately 5 percent, in the inlet total velocity profiles was evident at station 1. This disturbance corresponded to the spacing of the blades and thus the presence of the blades was felt, 30 percent of an axial chord, ahead of the leading edges. The magnitude of upstream disturbance was not as significant at lower inlet air angles. The final inlet profile showed a variation in total velocity of 40 percent across the leading edges. This variation was less than that previously measured (Hobson and Shreeve, 1993) at

Nomenclature

Cp = coefficient of pressure
Re_c = Reynolds number based on chord length
Tu = pitchwise, or tangential, turbulence intensity = $\sqrt{\overline{u'^2}}/V_{ref}$
Tv = axial turbulence intensity = $\sqrt{\overline{v'^2}}/V_{ref}$
U = pitchwise, or tangential, mean velocity component
U_{tot} = total mean velocity = $\sqrt{U^2 + V^2}$
u' = pitchwise, or tangential, fluctuating velocity component
V = axial mean velocity component
V_{ref} = upstream reference total mean velocity
v' = axial fluctuating velocity component
X = pitchwise, or tangential, direction
Y = axial direction
β = inlet flow angle from the axial direction

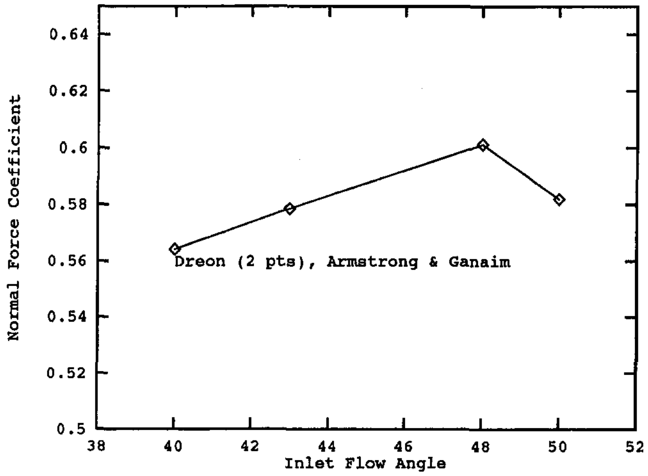

Fig. 4 Normal force coefficient versus inlet flow angle

48 deg inlet air angle (which showed more than a 50 percent variation), and this too was an indication that stall had occurred.

Passage Surveys (Station 3). Mean velocity distributions are presented in Fig. 5 for station 3, and the turbulence intensities for the respective velocity components are presented in Fig. 6. The turbulence intensity for the two components showed anisotropic behavior near the blade surface. However, the shapes of both profiles were initially similar, then the tangential turbulence fell to a minimum at 20 percent pitch. Beyond 50 percent pitch the turbulence became isotropic in the inviscid region, as the levels of turbulence corresponding to the *U* and *V* velocity components were comparable. The data were presented as turbulence intensities, yet because the flow field was intermittent, the standard deviation of the histograms did not represent the turbulence in the flow. Rather, these should be considered as a measure of the unsteadiness in the flow, which was a combination of the random turbulence and intermittent reverse flow.

Figure 7 separates the mean total velocity components into its respective positive and negative modes. The velocity histograms for each point across the passage were specially edited such that only negative velocities were retained and averaged to create a negative velocity distribution and, likewise, only positive velocities were retained and averaged at each point to create a positive velocity distribution. Thus the weighted average of the negative and positive distributions would make up the mean distribution for each velocity component. The reverse flow region was confined to within 10 percent of a blade pitch from the suction surface.

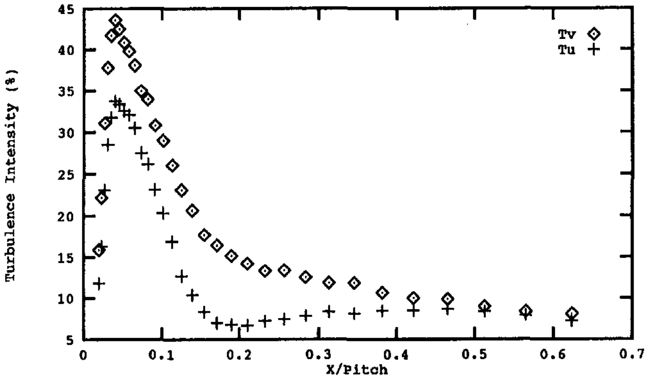

Fig. 6 Turbulence intensity at station 3

This analysis showed more of the character of the intermittent reverse flow than did a plot of the mean velocity. What occurred in the unsteady stalling process was not the arithmetic mean; however, the flow spent most of its time close to the positive and negative modes. Since the data were taken in coincidence mode, one disadvantage of this form of presentation was that during editing of the positive *U* velocity component data, all of its negative points were discarded, as well as the corresponding *V* velocity component data. The opposite but equivalent process occurred during editing of the *V* velocity component data; such that all the data that were left were the velocity components in the first quadrant of a flow that was oscillating through all four quadrants.

An expanded analysis of station 3 (Fig. 7) includes three points chosen from the 32 during the survey based on the changing nature of the flow across the passage. Point 1 was located 0.5 mm off the blade surface. This was inside the leading-edge separation bubble as was evident by the negative mean velocities of all the data points in the histograms (Fig. 8). The second location was point 7 at 2.5 percent pitch. This point was within the intermittent reverse flow region, as indicated by the bimodal velocity histograms. The third location was point 20, at 17 percent pitch, and this point was outside the region of intermittent reverse flow.

The progression from a negative mean velocity to a positive mean velocity was apparent with the crossover distinctly evident in the bimodal histogram at point 7. Since editing of the data to provide the average positive and negative velocities eliminated the second and fourth quadrant velocity vectors of a unsteady rotating velocity vector, Fig. 9 provided an alternate view of the data by plotting the tangential and axial velocity components on a *U*–*V* velocity correlation plot.

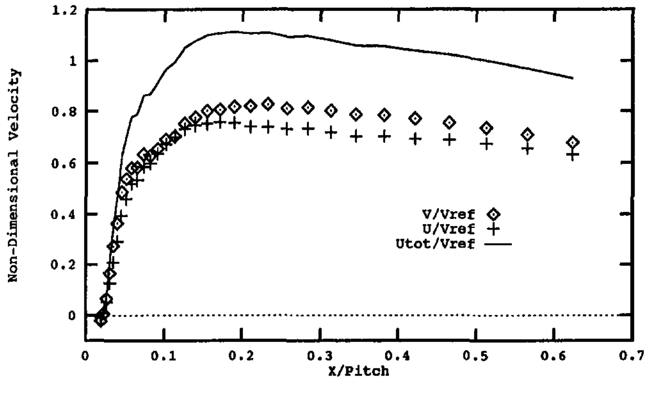

Fig. 5 Mean velocity survey at station 3

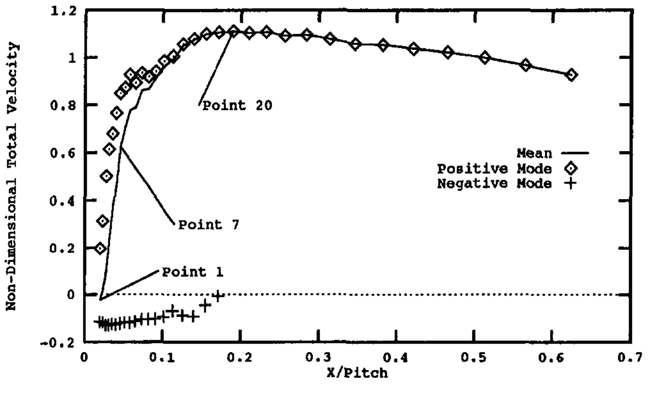

Fig. 7 Station 3: total velocity mean and mode components

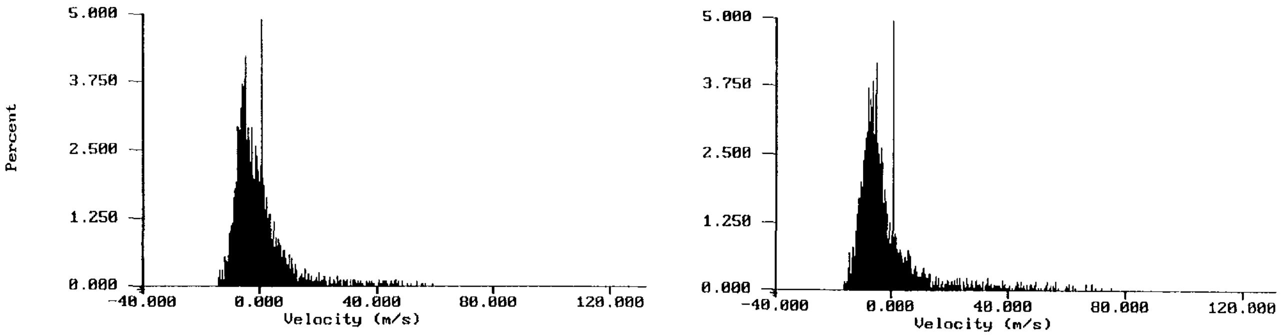

Point 1: Tangential velocity Axial velocity

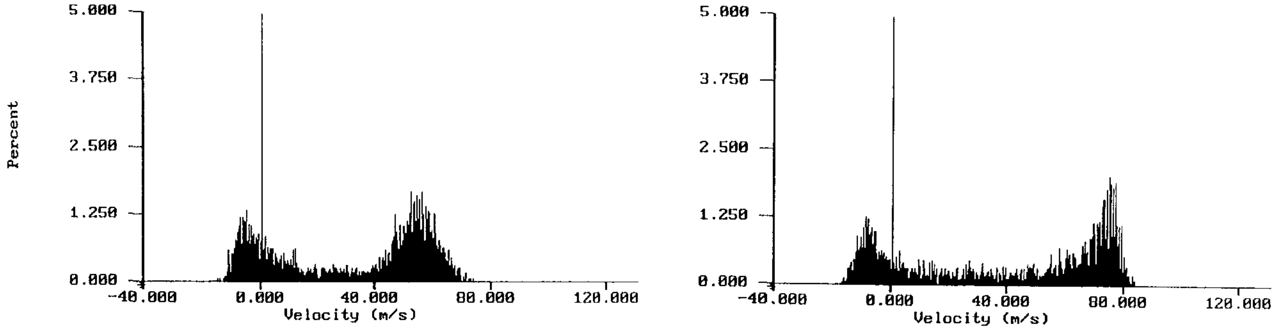

Point 7: Tangential velocity Axial velocity

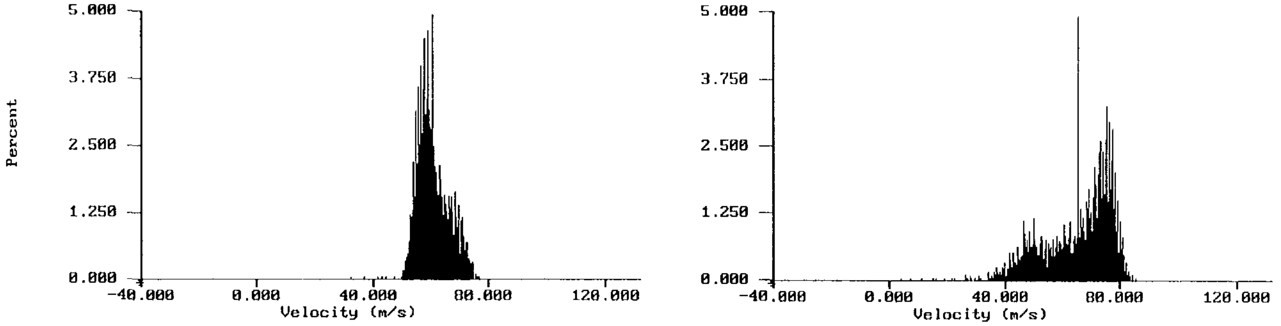

Point 20: Tangential velocity Axial velocity

Fig. 8 Velocity histograms at station 3

Station 7. Mean velocity distributions are presented in Fig. 10 for station 7, and the turbulence intensity for the respective velocity components are presented in Fig. 11. The turbulence intensity for the two components showed anisotropic behavior near the blade surface until about 50 percent pitch. Beyond this point the turbulence became isotropic in the inviscid region, as the levels of turbulence corresponding to the *U* and *V* velocity components were comparable. Of interest to note is the high level of unsteadiness in the axial velocity direction resulting in a peak turbulence intensity of 40 percent.

As with Fig. 7, the total velocity component is separated into its respective positive and negative mean values in Fig. 12 for station 7. At this location almost half of the passage width experienced some form of reverse flow particles, which is indicative of the extent of the separation region on the aft portion of the blades.

Wake Survey (Station 19). The final wake survey, performed at 22 percent of an axial chord downstream of the trailing edge, is shown in Figs. 13 and 14. Both the mean flow and turbulence intensity/unsteadiness show good periodicity of the asymmetric wakes that formed after the blade surface boundary layers coalesced. Once again the turbulence profiles (Fig. 14) showed anisotropy in the wake, which became isotopic in the core flow region. Figure 15 is the result of the special editing as outlined for stations 3

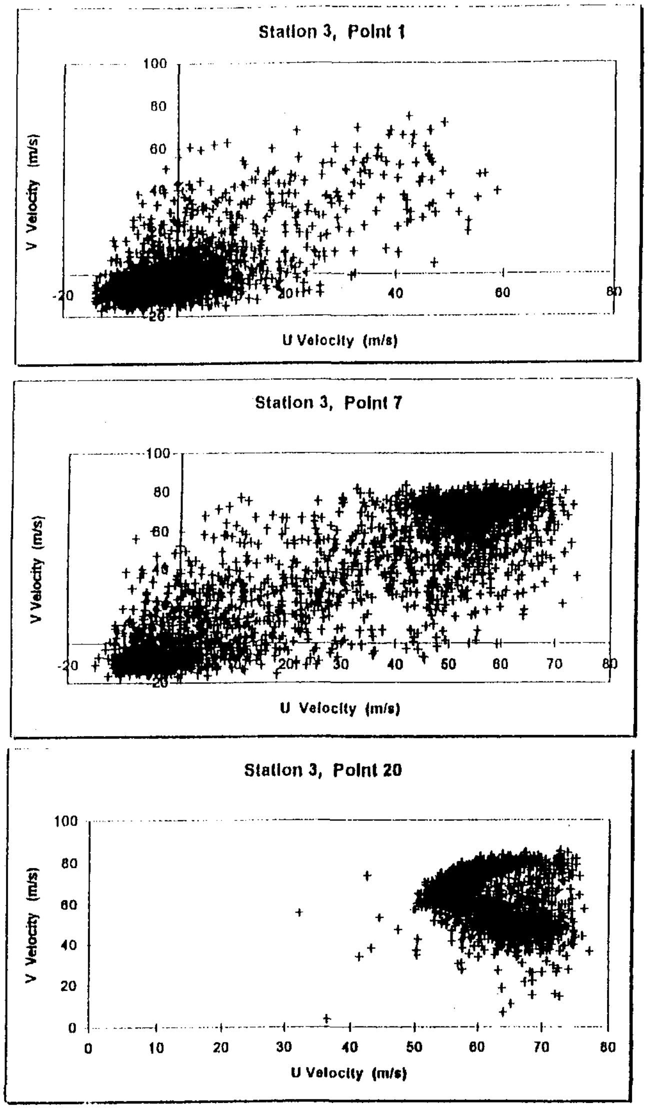

Fig. 9 *U–V* velocity correlation plots

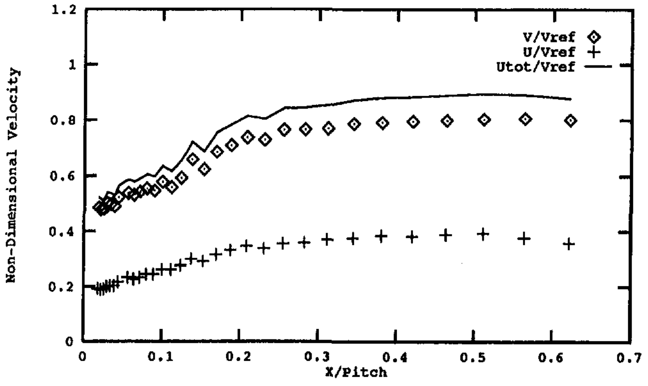

Fig. 10 Mean velocity survey at station 7

and 7, in Figs. 7 and 12. It was of interest to note that the reverse flow velocity component was of the same magnitude as the reverse flow velocities at station 7.

Power Spectrum Analysis. Power spectral density analyses (Yocum and O'Brien, 1993) were performed at various locations within the blade passage. The only point of recur-

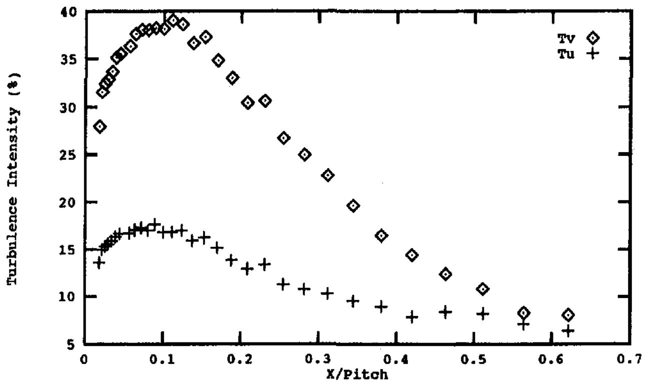

Fig. 11 Turbulence intensity at station 7

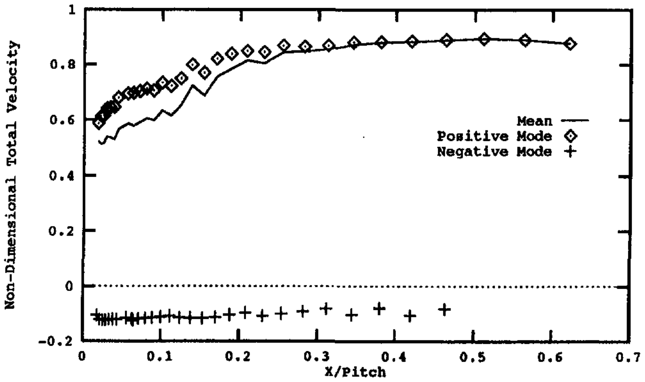

Fig. 12 Station 7: Total velocity mean and mode components

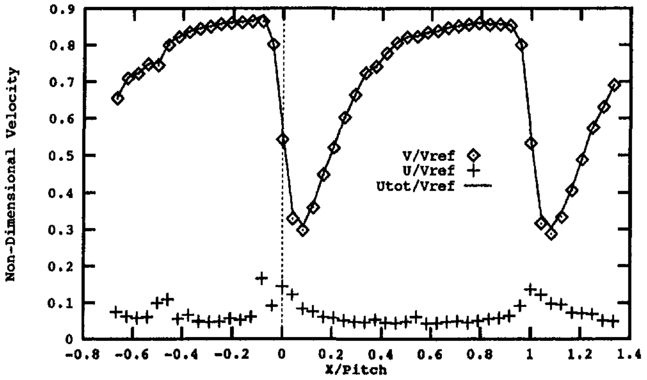

Fig. 13 Mean velocity survey at station 19

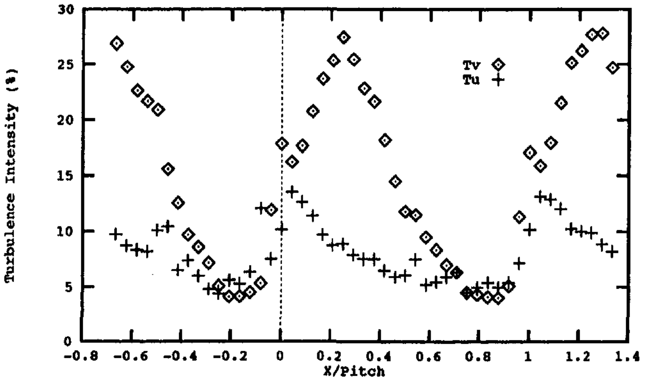

Fig. 14 Turbulence intensity at station 19

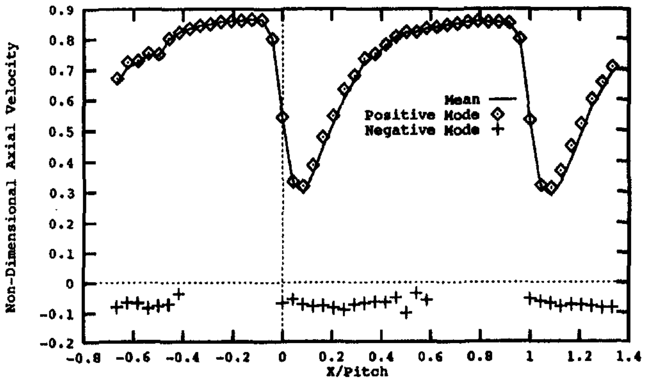

Fig. 15 Station 19: total velocity mean and mode components

ring significance throughout the power spectrum plots was the region between 20–25 Hz as shown in Fig. 16 for the third point from the blade at station 3. Any interpretation of these results must be tempered with the realization that the data are discretely sampled and that they arrive randomly within the probe volume. Time history data were recorded to allow for the above-mentioned Fourier analysis. As this seemed to be the frequency at which the tunnel was pulsating during operation, then it is felt that the 20–25 Hz range represents the frequency of passage of the stall cells in the cascade.

LDV and Flow: Comparison. Propagating stall was evident along the length of the cascade, as could be determined qualitatively with the use of tufts on adjacent blades. Unfortunately no quantitative measurements of the size of the stall cells could be made, even with repeated attempts to strobe the flow while videotaping the cascade.

Figure 17 contains a sequence of digitized images from the videotape of the laser flow visualization performed at midchord of the blade. The images cover 0.3 s of filming at $\frac{1}{30}$ of a second per frame. The brightest curved image represents the curvature of the blade. This image is of the fog undergoing instantaneous reverse flow at approximately midchord. The trace of fluid particles on the left-hand side of the burst shows the fluid that adhered to the blade surface.

Once all the histograms from each station were analyzed (with editing of plus or minus two standard deviations), the boundary of the region of intermittent reverse flow (last point of negative velocity at a station) was plotted for each station 2 through 19. This is also shown in Fig. 17 with dotted lines. Also shown in this figure, with the solid line,

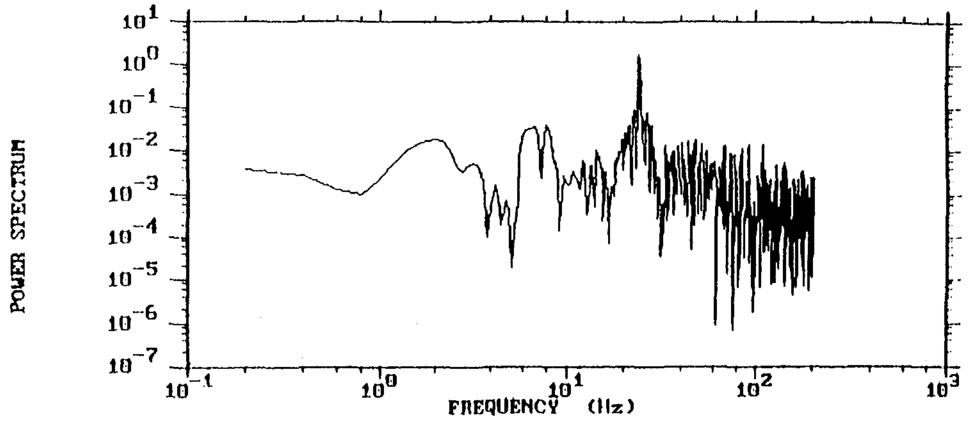

Tangential (U) velocity component

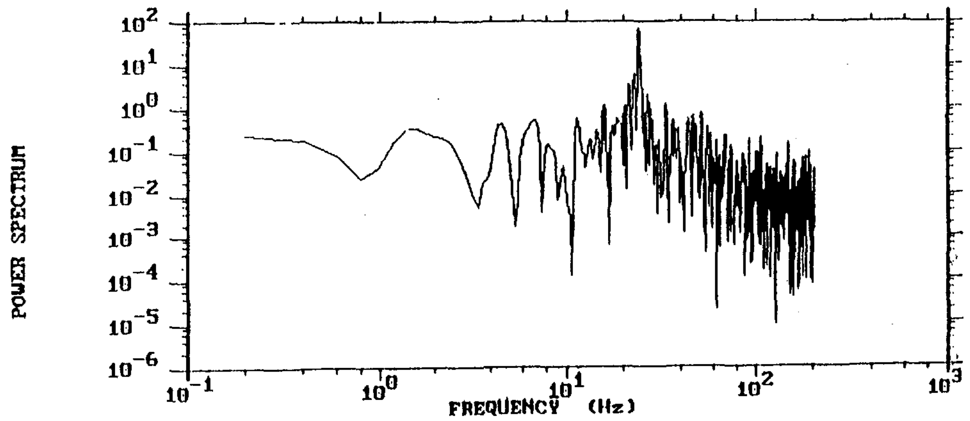

Axial (V) velocity component

Fig. 16 Power spectrum analysis of point 3, station 3

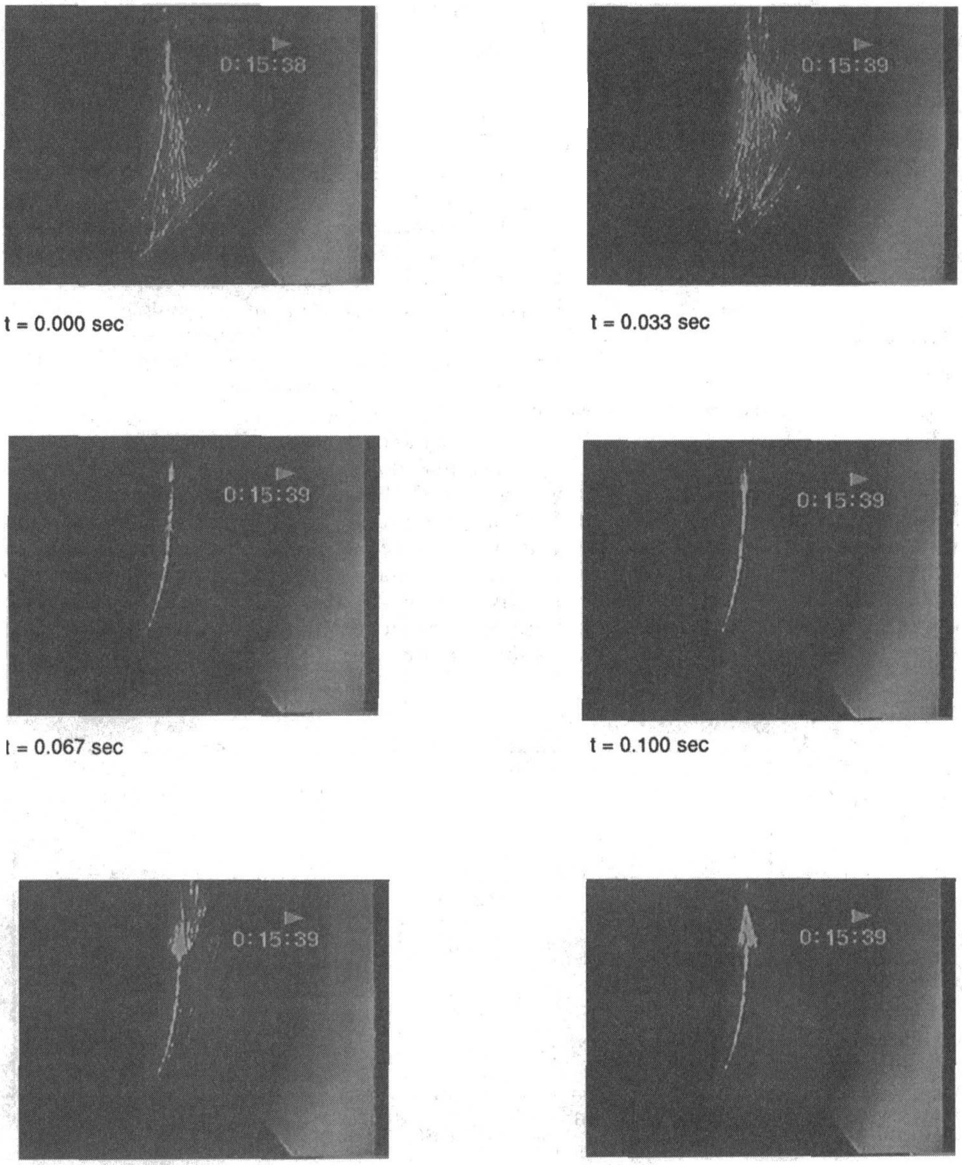

t = 0.000 sec

t = 0.033 sec

t = 0.067 sec

t = 0.100 sec

t = 0.133 sec

t = 0.167 sec

Fig. 17 Laser sheet flow visualization at midchord, and summary of LDV surveys in the passage and the wake

is the region of reverse flow as determined by a negative mean velocity. This line represented the reverse flow region of the leading edge separation bubble, which had been observed with flow visualization techniques. It was postulated that the reason reverse flow was measured in this region was that the flow was unsteady and that seed particles were entrained into the leading edge separation bubble. This was not possible at lower inlet air angles because the flow was relatively steady compared to the present study.

Flow visualization also confirmed the two distinct regions of intermittent reverse flow, as shown by the two regions of dotted lines, the lower region being associated with the leading edge separation bubble and the upper region represented the turbulent separation that occurred aft of midchord. This shows a continuous laminar separation bubble (with unsteady bypass flow) at the leading edge and intermittent stall of the turbulent boundary layer aft of midchord. The remarkable coincidence between these two images shows the extent of the intermittent reverse flow region, which originated from the aft section of the blade. The real-time video showed that the intermittent reverse flow was repeatable, however random, as could be expected from turbulent flow separation.

Conclusions

The lack of experimental data of compressor cascades at or near stall has been improved with the current set of detailed measurements. The successful stalling of the controlled diffusion cascade was initially confirmed with the blade surface pressure measurements, which showed that for 50 deg the normal force on the blade had decreased. Flow visualization techniques (both tufting and laser sheet with fog) also confirmed that the blades had stalled.

It was possible to measure both mean reverse flow and intermittent reverse flow with the LDV. With the appropriate use of frequency shifting, it was possible to make these measurements with the certainty that the results from the histograms were correctly representing negative or positive velocities. The regions of reverse flow were plotted. With the information obtained from each histogram at each station, it was possible to plot regions of intermittent reverse

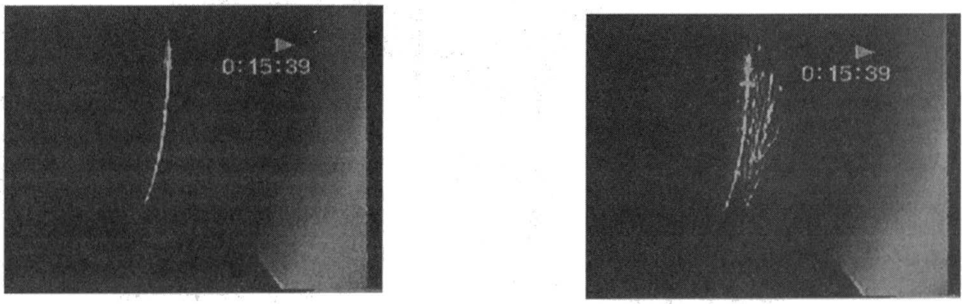

t = 0.200 sec

t = 0.233 sec

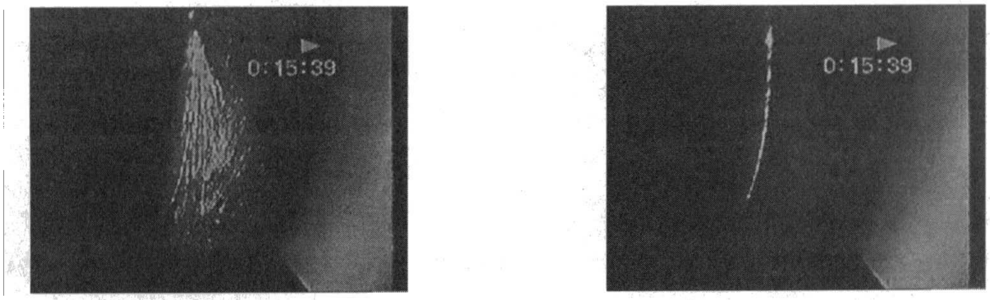

t = 0.267 sec

t = 0.300 sec

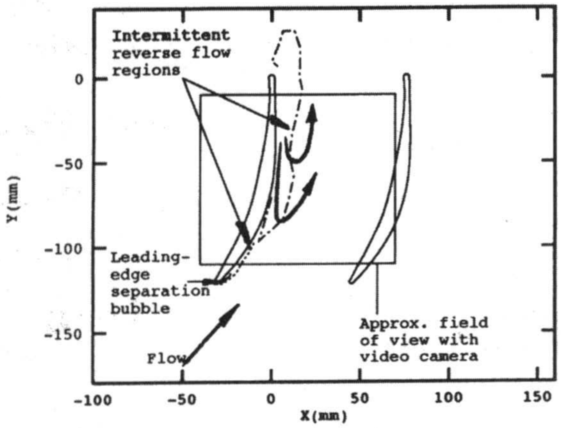

Fig. 17 (Continued)

flow and also a region of leading-edge reverse flow. These measurements could be qualitatively compared with flow visualization results.

It was possible, for the first time, to take mean reverse flow LDV measurements inside the leading edge separation bubble.

This paper also distinguished between the large-scale unsteadiness or intermittent stall at a frequency of about 20–25 Hz, resulting in bimodal histograms of the LDV data, and smaller scale turbulence depicted by the broadening of the histograms about their modes. The levels of unsteadiness have been quantified and the overall flow physics was verified qualitatively with flow visualization techniques at a realistic Reynolds number, based on chord length, of 700,000.

Acknowledgments

This work was sponsored by the Naval Air Warfare Center (Patuxent River), as part of a Fan and Compressor Stall Project. Mr. Stoney McAdams was technical monitor for the project, and his support is greatly appreciated.

References

Armstrong, J. H., 1990, ''Near-Stall Loss Measurements in a *C–D* Compressor Cascade With Exploratory Leading Edge Flow Control,'' Master of Science in Engineering, Thesis, Naval Postgraduate School, Monterey, CA.

Dreon, J. W., 1986, ''Controlled Diffusion Compressor Blade Wake Measurements,'' Master of Science in Engineering, Thesis, Naval Postgraduate School, Monterey, CA.

Ganaim Rickel, J., 1994, ''Laser-Doppler Velocimetry Measurements and Flow Visualization in a Cascade of Controlled-Diffusion Compressor Blades at Stall,'' Master of Science in Engineering, Thesis, Naval Postgraduate School, Monterey, CA.

Hobson, G. V., and Shreeve, R. P., 1993, ''Inlet Turbulence Distortion and Viscous Flow Development in a Controlled-Diffusion Compressor Cascade at Very High Incidence,'' *AIAA Journal of Propulsion and Power*, Vol. 9, No. 3, pp. 397–407.

Sanger, N. L., and Shreeve, R. P., 1986, "Comparison of Calculated and Experimental Cascade Performance for Controlled-Diffusion Compressor Stator Blading," ASME JOURNAL OF TURBOMACHINERY, Vol. 108, pp. 42–50.

Sovran, G., 1959, "The Measured and Visualized Behaviour of Rotating Stall in an Axial-Flow Compressor and in a Two-Dimensional Cascade," *Trans. ASME*, Vol. 81, pp. 24–34.

Williams, A. J. H., 1995, "Laser Doppler Velocimetry and Viscous Flow Computation of the Flow Through a Compressor Cascade Near Stall," Master of Science in Engineering, Thesis, Naval Postgraduate School, Monterey, CA.

Yocum, A. M., and O'Brien, W. F., 1993, "Separated Flow in a Low-Speed Two-Dimensional Cascade: Part I—Flow Visualization and Time-Mean Velocity Measurements," ASME JOURNAL OF TURBOMACHINERY, Vol. 115, pp. 409–420.

Investigation of Hydrodynamic Forces on Rotating and Whirling Centrifugal Pump Impellers

R. Fongang
University of Kaiserslautern,
Kaiserslautern,
Federal Republic of Germany

J. Colding-Jørgensen
Ødegaard & Danneskiold-Samsøe AS,
Copenhagen, Denmark

R. Nordmann
Technical University of Darmstadt,
Darmstadt, Federal Republic of Germany

A two-dimensional fluid model is developed to investigate the hydrodynamic forces exerted on a rotating impeller caused by the impeller–fluid–volute interaction in a centrifugal pump. In this model, the impeller periphery and the volute contour are replaced by a distribution of unsteady vortices. The impeller center is assumed to execute a whirling motion about the rotor center. This is an improvement of the earlier quasi-steady flow model of Colding-Jørgensen (1980) where the impeller was taken as a single vortex source point. The forces can be presented as a sum of a steady and an unsteady part. The rotordynamic coefficients are deduced from the unsteady forces decomposed into radial and tangential components relative to the orbit described by the impeller center. In comparison to most of the theoretical and experimental results found in the literature, the model seems to give good prediction. It appears clearly from this analysis that, under certain operating conditions, the fluid forces on the impeller have a destabilizing effect on the pump rotor.

Introduction

The rotordynamic behavior of a centrifugal pump (Fig. 1) is strongly influenced by the forces acting on its shaft due to the fluid–structure interaction. These are bearing and seal forces as well as fluid forces acting on the impeller due to the impeller–volute interaction. Among these, hydrodynamic bearing and seal forces have been the subject of intensive studies, as attested by many papers presented in workshops on rotordynamic instability problems. Their effects and evaluation are well known. Hydrodynamic forces on the impeller contribute largely to the destabilization of the pump rotor under certain operating conditions, as demonstrated theoretically (Colding-Jørgensen, 1980, 1989; Allaire et al., 1982; Adkins and Brennen, 1988; Tsujimoto et al., 1988) and experimentally (Chamieh et al., 1982; Jery et al., 1984; Ohashi and Shoji, 1987; Adkins and Brennen, 1988), but their predictions are still a problem.

As indicated by Adkins and Brennen, the fluid forces on the impeller are a sum of the shroud forces caused by the pressure on the external surface of the impeller shrouds, and of the lateral forces, also called impeller forces (Colding-Jørgensen, 1980) due to the pressure and momentum exchange in the impeller. The goal of the present work is to suggest a method of investigation of the impeller forces, usually described in rotordynamics by the following equation:

$$\underline{F} = \underline{\bar{F}} + [A]\underline{\epsilon} \tag{1}$$

or in more detailed form as:

$$\underline{F} = \underline{\bar{F}} - ([K]\underline{\epsilon} + [C]\underline{\dot{\epsilon}} + [M]\underline{\ddot{\epsilon}}) \tag{2}$$

$\underline{\bar{F}}$ represents the mean or steady impeller forces resulting from the impeller-volute interaction when the impeller center coincides with the volute center. $\underline{\epsilon}$ is the eccentricity of the impeller or rotor center relative to the volute or stator center.

Previously, studies on hydrodynamic impeller–volute interaction were focused on the steady impeller forces. The papers of Iversen et al. (1960), Biheller (1960), and Csanady (1962) present some of them. They all noted the existence of a flow rate, the design flow rate, for which these forces are minimal. Domm and Hergt (1970) and Hergt and Krieger (1969–1970) first demonstrated the dependency of the impeller forces on the rotor center eccentricity. Since that time, fluid forces acting on a rotating and whirling impeller have become the subject of intensive research.

Colding-Jørgensen (1980) developed a quasi-steady fluid model based on the singularity theory, replacing the impeller by a single vortex source point and the volute by a set of vortex segments. Then he calculated the impeller forces, taking into account the impeller center eccentricity and velocity and deduced for the first time the stiffness and damping coefficients.

Shoji and Ohashi (1987) introduced an unsteady potential flow theory, substituting the diffuser vanes by a set of steady vortices and the impeller blades by a distribution of unsteady vortices. They considered the influence of free vortices shed from the trailing edge of the impeller blades in their flow calculations. They then determined the complete lateral fluid forces on the impeller presented into tangential and radial components relative to the orbital motion of the impeller center.

To examine the effect of the fluid on the behavior of the pump rotor in the impeller–volute domain, Adkins and Brennen (1988) proposed an unsteady flow analysis. They assumed the impeller to have a very large number of thin blades guiding perfectly the flow. They then used a bulk flow description of the flow in the volute to determine the flow disturbance in the impeller discharge.

Tsujimoto et al. (1988) assimilated the impeller to an actuator disk to define a two-dimensional flow field in the impeller–volute domain. Their complete flow field tangential to the impeller blades at the outlet was calculated by replacing the volute by a set of unsteady vortices and by assuming the tangential flow conditions on the volute contour. They also made use of shed free vortices.

Allaire et al. (1982) and Colding-Jørgensen (1989) oriented their analysis on an impeller rotating and whirling without the volute, assuming also that the impeller had a very large number of infinitely thin vanes.

Apart from Shoji and Ohashi, who noted the damping effect of the impeller forces on the pump rotor, all these theoretical analyses concluded that the impeller forces have a destabilizing effect on the pump rotor for forward whirling motion of the impeller center with small whirl speed ratio Ω/ω.

Contributed by the International Gas Turbine Institute and presented at the 41st International Gas Turbine and Aeroengine Congress and Exhibition, Birmingham, United Kingdom, June 10–13, 1996. Manuscript received at ASME Headquarters February 1996. Paper No. 96-GT-18. Associate Technical Editor: J. N. Shinn.

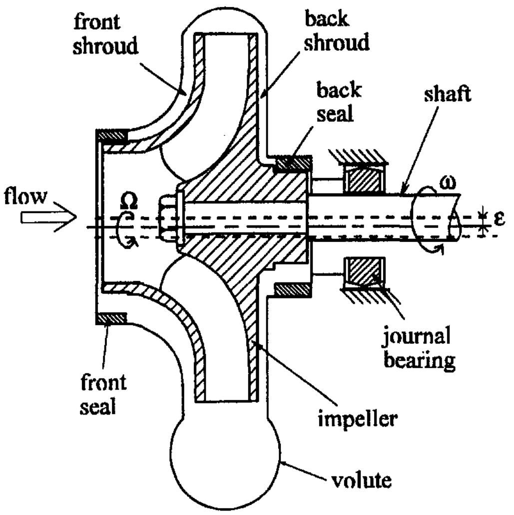

Fig. 1 Centrifugal pump

This conclusion was confirmed by some experimental studies of lateral fluid forces on the impeller. Chamieh et al. (1982) made measurements of quasi-steady impeller forces and determined the stiffness matrix. His work was extended to the determination of the damping and mass matrices by Jery et al. (1984) who then got the first complete measurements of the impeller forces. The test facility of Chamieh et al. and Jery et al. was modified by Adkins and Brennen (1988). They isolated the impeller–volute interaction from the external influences (pressure force on the external surface of shrouds) to measure the impeller forces. The authors of the three papers observed the contribution of the impeller forces to the pump rotor destabilization under the conditions mentioned above.

Ohashi and Shoji (1987) also made measurements of lateral fluid forces on the impeller. They noted, like the others and unlike their own theory, destabilizing fluid forces at lower flow coefficients for slow forward impeller center whirl motion.

The present paper proposes a different method of impeller forces analysis. A two-dimensional fluid model is developed to study the flow in the impeller–volute domain of a centrifugal pump. In this model, the impeller periphery and the volute contour are replaced by a set of unsteady vortices. This is an improvement of the earlier quasi-steady flow model of Colding-Jørgensen (1980) mentioned above. The hydrodynamic forces acting on the rotating and whirling impeller are then determined and presented in terms of rotordynamic coefficients. A comparison with most of the theoretical and experimental results found in the literature is performed.

Assumptions

The analysis follows the same route as in some previous studies (Allaire et al., 1982; Adkins and Brennen, 1988; Tsujimoto et al., 1988). The impeller, which is supposed to have a very large number of infinitely thin blades perfectly guiding the flow, is substituted by an actuator disk. As indicated by Tsujimoto et al., the goal of this assumption is to eliminate the unsteadiness due to the rotation of the impeller blades and then, for simplification, to consider only the unsteadiness due to the whirling motion of the rotor center.

The impeller rotates at a constant angular speed ω. Its center whirls on a concentric orbit around the volute center with a constant angular speed Ω and a small eccentricity ϵ ($\epsilon \ll r_2$). Since the unsteady or dynamic part of the impeller forces (second term of second member of Eq. (1)) is proportional to the eccentricity, the procedure of calculation for elliptical or any motion of the rotor center with small eccentricity consists of using the concentric whirling motion $\underline{\epsilon} = \epsilon e^{i\Omega t}$ to get the hydrodynamic force matrix $[A]$. Then $[A]$ and the real rotor center motion are used to determine the impeller forces.

The following conditions are also assumed:

1 Incompressible, inviscid, and irrotational flow in the absolute coordinate system with constant flow rate.
2 Volute and impeller blades replaced by spirals with a constant spiral angle (λ and β respectively). Constant impeller and volute width.
3 Tangential flow conditions for the absolute flow on the volute surface and for the relative flow on the impeller blades surface. This last assumption is the basis of the present theory, since the goal is to determine a flow field satisfying both conditions.

Fluid Model

The model is based on the unsteady potential flow theory, as mentioned above and annotated in Fig. 2:

The volute is replaced by an unsteady vortex distribution.

Since the impeller is substituted by an actuator disk, we replace its periphery by a set of unsteady vortices. This vortex distribution at the impeller outlet characterizes the change of the circulation around the impeller due to the perturbation $\underline{\epsilon} = \epsilon e^{i\Omega t}$, the volute asymmetry, and the variation of the flow rate.

A source Q and a circulation Γ are put at the impeller center to model the flow rate and the prerotation. Γ is chosen to satisfy

Nomenclature

$[A] = [A_{ij}]$ $(i = x, y; j = x, y)$ = hydrodynamic force matrix
b = impeller width
$[C] = [C_{ij}]$ $(i = x, y; j = x, y)$ = damping matrix
$\underline{c}_\infty = (c_{\infty x}, c_{\infty y})$-induced velocity
$\underline{c} = (c_x, c_y)$ = absolute velocity
$\underline{F} = (F_x, F_y)$ = lateral force acting on the impeller
$\bar{F} = (\bar{F}_x, \bar{F}_y)$ = steady impeller force
i = imaginary unit ($i^2 = -1$)
$[K] = [K_{ij}]$ $(i = x, y; j = x, y)$ = stiffness matrix
$[M] = [M_{ij}]$ $(i = x, y; j = x, y)$ = mass matrix
$\underline{n}_1, \underline{n}_2$ = vector normal to s_1, vector normal to s_2

o, o' = volute center, impeller center
Q, Q_n = flow rate, design flow rate
Q_{rel} = relative flow rate = Q/Q_n
r_1, r_2 = inner and outer radius of the impeller
r_t = tongue radius
s_1, s_2 = volute contour, impeller periphery
t = time
$\underline{w} = (w_x, w_y)$ = velocity relative to the impeller
$z = re^{i\theta}$ complex position of a point in (o, x, y) frame
$z' = r'e^{i\theta'} = z - \epsilon e^{i\Omega t}$ = complex position of a point in (o', x', y') frame with its axes parallel to those of (o, x, y)

β = impeller blade angle
ϵ = eccentricity
Γ = circulation of the prerotation
λ = spiral angle
ρ = flow density
ϕ = flow coefficient = $Q/2\pi b\omega r_2^2$
ω = angular velocity of the impeller
Ω = whirl speed of the impeller center

Superscript

$'$ = refers to the frame (o', x', y')

Subscripts

r = radial relative to the whirl orbit
t = tangential relative to the whirl orbit

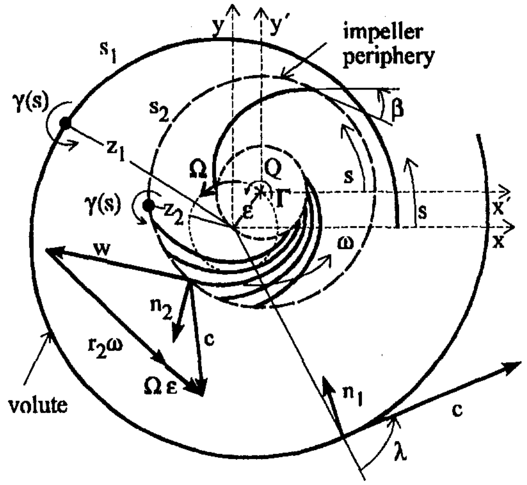

Fig. 2 Two-dimensional centrifugal pump model

the tangential flow condition at the impeller outlet for an unbound impeller.

Flow Field

(a) Region Downstream of the Impeller. According to the fluid model definition above, the absolute flow in the region downstream of the impeller can be described by the following equation:

$$c_x - ic_y = \int_{s_1} \frac{i\gamma(s)ds}{2\pi(z - z_1(s))} + \int_{s_2} \frac{i\gamma(s)ds}{2\pi(z - z_2(s))} + \frac{Q - i\Gamma}{2\pi b(z - \epsilon e^{i\Omega t})} - i\epsilon\Omega e^{-i\Omega t} \quad (3)$$

with the prerotation given by

$$\Gamma = 2\pi r_2^2 b\omega - \frac{Q}{\tan \beta} \quad (4)$$

In Eq. (3), $\gamma(s)ds$ is the strength of a vortex point on s_1 of frame $z_1(s)$ or on s_2 of frame $z_2(s)$. In this expression, γ is unknown and must be determined to satisfy the flow tangential conditions mentioned in assumption (3). In other words, the normal component of the absolute flow must vanish on the volute contour:

$$\underline{c} \cdot \underline{n}_1|_{s_1} = 0 \quad (5)$$

and the velocity relative to the rotating impeller must be tangential to the blade at the impeller periphery. That means its component normal to the blade must vanish:

$$\underline{w} \cdot \underline{n}_2|_{s_2} = 0 \quad (6)$$

where $\underline{w}$ is given by:

$$w_x - iw_y = c_x - ic_y + ir_2\omega e^{-i\theta'} + i\epsilon\Omega e^{-i\Omega t} \quad (7)$$

The combination of Eq. (3) with Eqs. (5) and (6) will give rise to two integral equations in which $\gamma(s)$ is unknown as mentioned above. These integral equations can be solved numerically. This consists of replacing the contours s_1 and s_2 by a set of discrete vortex points j (N_1 points for s_1 fixed to (o, x, y) and N_2 points for s_2 fixed to (o', x', y')) of strength $\gamma_j ds_j$ put at frame z_j. Then one must choose on each contour a set of control points k (N_1 points for s_1 fixed to (o, x, y) and N_2 points for s_2 fixed to (o', x', y')) of frame z_k, each different from z_j (Fig. 3). This gives rise to a system of $N_1 + N_2$ linear equations with $N_1 + N_2$ unknowns.

The vector normal to s_1 at point k being

$$\underline{n}_{1k} = (-\sin(\theta_k + \lambda), \cos(\theta_k + \lambda)) \quad (8)$$

and the vector normal to the blade at point k of s_2

$$\underline{n}_{2k} = (\cos(\theta'_k + \beta), \sin(\theta'_k + \beta)) \quad (9)$$

that system can be presented as follows:

for $k \in s_1$:

$$-\sin(\theta_k + \lambda)c_{xk} + \cos(\theta_k + \lambda)c_{yk} = 0 \quad (10)$$

for $k \in s_2$:

$$\cos(\theta'_k + \beta)w_{xk} + \sin(\theta'_k + \beta)w_{yk} = 0 \quad (11)$$

where

$$c_{xk} - ic_{yk} = \sum_j^{N_1} \frac{i\gamma_j ds_j}{2\pi(z_k - z_j)} + \sum_j^{N_2} \frac{i\gamma_j ds_j}{2\pi(z_k - z_j)} + \frac{Q - i\Gamma}{2\pi b(z_k - \epsilon e^{i\Omega t})} - i\epsilon\Omega e^{-i\Omega t} \quad (12)$$

and

$$w_{xk} - iw_{yk} = \sum_j^{N_1} \frac{i\gamma_j ds_j}{2\pi(z_k - z_j)} + \sum_j^{N_2} \frac{i\gamma_j ds_j}{2\pi(z_k - z_j)} + \frac{Q - i\Gamma}{2\pi b(z_k - \epsilon e^{i\Omega t})} + ir_2\omega e^{-i\theta'} \quad (13)$$

As $\epsilon \ll r_2$, the system can be linearized by neglecting all the terms of second or higher order of ϵ and by taking

$$\gamma_j = \overline{\gamma}_j + \epsilon\gamma_{jc} \cos \Omega t + \epsilon\gamma_{js} \sin \Omega t \quad (14)$$

Then the system can be divided into a steady part of order ϵ^0 with $\overline{\gamma}_j$ as unknown and an unsteady part of order ϵ^1 with γ_{jc} and γ_{js} as unknowns. The steady system must first be solved independently of the unsteady one. Then $\overline{\gamma}_j$ obtained must be used to solve the unsteady system. After determining γ_j and using Eq. (3), the flow in the considered domain can be calculated and written in the following form:

$$\underline{c} = \underline{\overline{c}} + \epsilon\underline{c}_c \cos \Omega t + \epsilon\underline{c}_s \sin \Omega t \quad (15)$$

(b) Region Between the Inlet and Outlet of the Impeller. The fluid through the impeller has been assumed to be perfectly guided by the vanes. For this purpose, the continuity equation

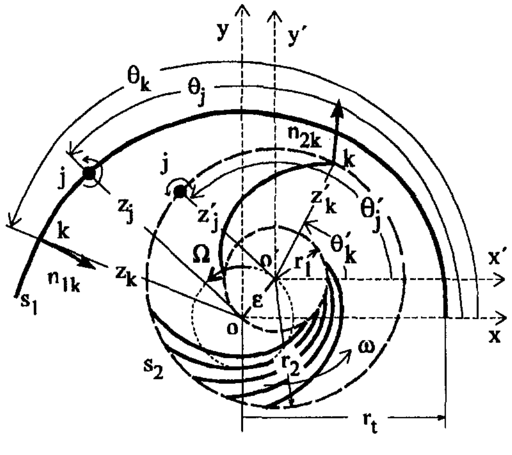

Fig. 3 Discrete vortex and control points configuration

can be applied to determine the radial component of the flow at any point of the region between the inlet and outlet of the impeller. Making use of the relative flow tangential condition on the impeller blades, one can also get the tangential component. These both conditions are expressed by the following equations:

Continuity equation:

$$r' c_{r'}(r', \theta') = r_2 c_{r'}(r_2, \theta_2') \tag{16}$$

Flow tangential condition:

$$c_{\theta'}(r', \theta') = \omega r' - \frac{c_{r'}(r', \theta')}{\tan \beta} \tag{17}$$

In Eqs. (15) and (16), θ_2' is the angular position of any impeller blade tip, while $\theta' = \theta_2' + (1/\tan \beta) \ln (r_2/r')$ is the angular position of the point of radius r' of the same blade.

Impeller Forces

The hydrodynamic forces on the impeller are a sum of the momentum forces due to the momentum exchange between the impeller and the fluid and of the pressure forces acting on the impeller as expressed by Allaire et al. (1982):

$$\underline{F} = -\frac{\partial}{\partial t}\int_V \rho \underline{c} dv - \oint_K \rho \underline{c}(\underline{c} \cdot d\underline{K}) - \oint_K p d\underline{K} \tag{18}$$

where V is the control volume of length b delimited by the inlet and outlet of the impeller, K the inlet and outlet surface of the impeller and p the pressure.

The impeller has been assimilated to an actuator disk. Then we can calculate these forces the same way as Colding-Jørgensen (1980). We consider the impeller to be a cylindrical body possessing a circulation Γ in the presence of the source Q. It is assumed that the induced velocity in the impeller center has the same effect as a parallel stream $\underline{c}_\infty$. Then the unsteady Bernoulli equation can be written as follows:

$$\int \frac{\partial \underline{c}}{\partial t} \cdot d\underline{s} + \frac{p}{\rho} + \frac{\underline{c}^2}{2} = \frac{p_\infty}{\rho} + \frac{\underline{c}_\infty^2}{2} \tag{19}$$

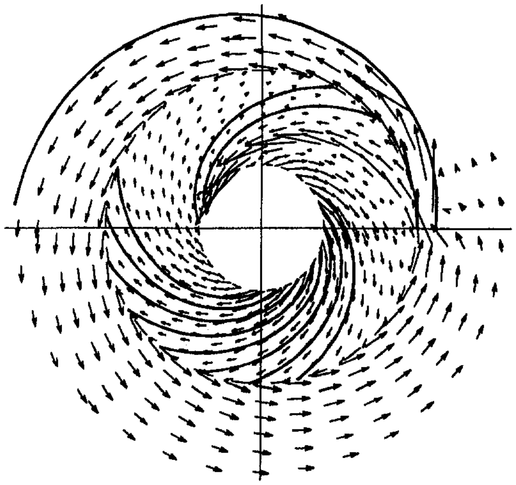

Fig. 4 Absolute flow downstream of the impeller and relative flow inside the impeller for $Q_{rel} = 0.4$

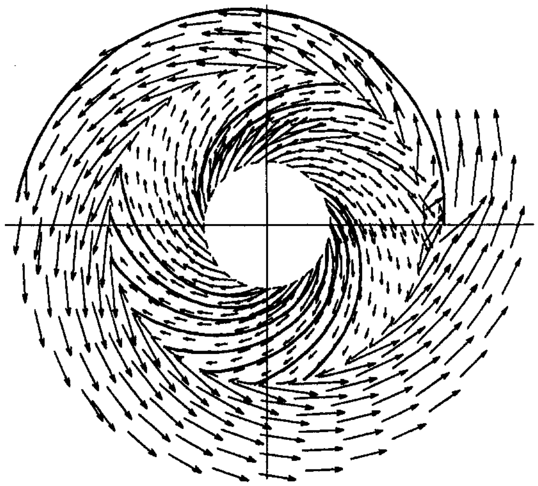

Fig. 5 Absolute flow downstream of the impeller and relative flow inside the impeller for $Q_{rel} = 1.3$

Making use of this equation and integrating Eq. (18) according to the above assumption, one will get:

$$\frac{\underline{F}}{\rho} = \pi b \frac{\partial \underline{c}_\infty}{\partial t}(r_2^2 - r_1^2) + \underline{c}_\infty Q + \underline{\hat{c}}_\infty \Gamma + \pi b \frac{\partial \underline{c}_\infty}{\partial t}(r_2^2 - r_1^2) \tag{20}$$

where $\underline{c}_\infty$ is the velocity induced in the impeller center by the volute given as:

$$c_{\infty x} - i c_{\infty y} = \sum_j^{N_1} \frac{-i\gamma_j ds_j}{2\pi(\epsilon e^{i\Omega t} - z_j)} + i\epsilon\Omega e^{-i\Omega t} + \sum_j^{N_2} \frac{-i\gamma_j ds_j}{2\pi(z_j - \epsilon e^{i\Omega t})} \tag{21}$$

and

$$\underline{\hat{c}}_\infty = (c_{\infty y}, -c_{\infty x}) \tag{22}$$

Equation (20) is an extension of the Kutta–Jokowski theorem used by Colding-Jørgensen (1980) in the force calculation. This expression takes into account the impeller geometry and the unsteady part of the flow, not considered in the earlier model.

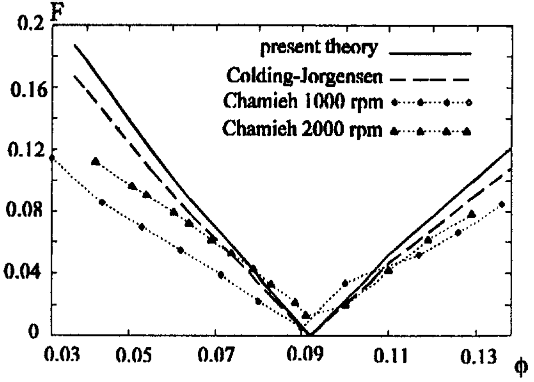

Fig. 6 Dimensionless steady fluid force (normalized by $\rho \pi b \omega^2 r_2^3$) as a function of the flow coefficient

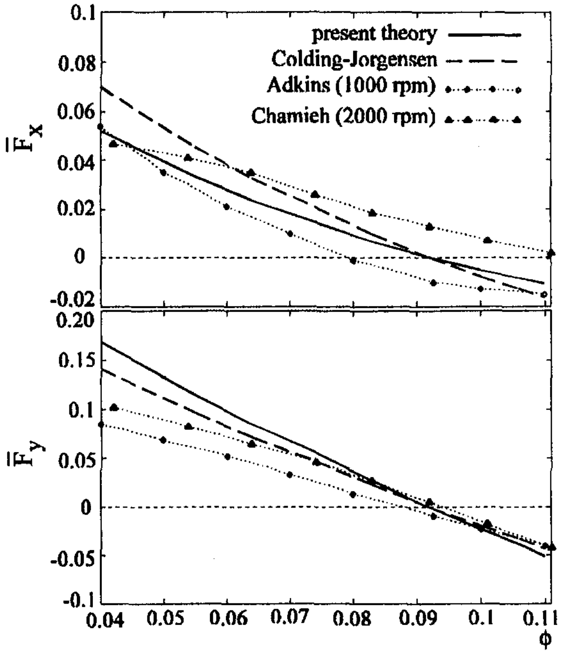

Fig. 7 Dimensionless x and y components of the steady impeller force (normalized by $\pi\rho b\omega^2 r_2^3$) as a function of the flow coefficient

Radial Force, Tangential Force, and Rotordynamic Coefficients

Since $\epsilon \ll r_2$, the impeller forces can also be linearized and expressed as follows:

$$\underline{F} = \begin{bmatrix} \bar{F}_x \\ \bar{F}_y \end{bmatrix} + \begin{bmatrix} F_{cx} & F_{sx} \\ F_{cy} & F_{sy} \end{bmatrix} \begin{bmatrix} \epsilon \cos \Omega t \\ \epsilon \sin \Omega t \end{bmatrix} \tag{23}$$

A comparison of this equation with Eq. (1) gives rise to the hydrodynamic force matrix $[A]$.

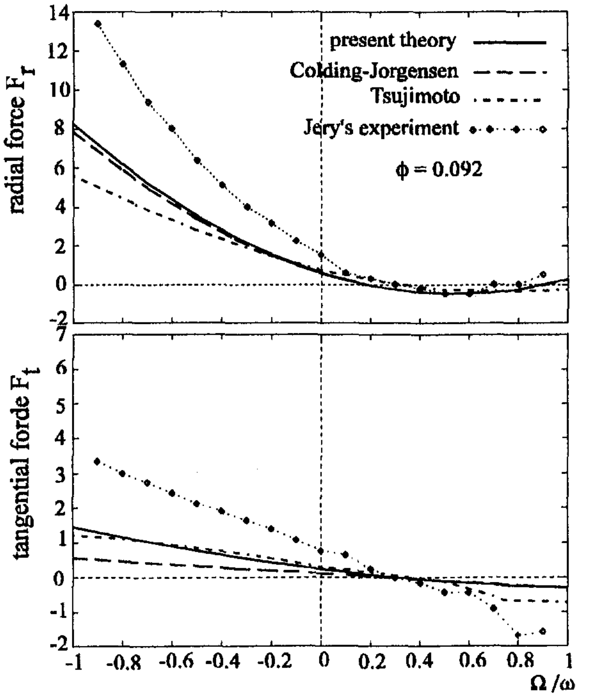

Fig. 8 Dimensionless radial and tangential force (normalized by $\pi\rho b\omega^2 r_2^2\epsilon$) as a function of the speed ratio at design flow coefficient

The unsteady part of the impeller forces can be decomposed into radial and tangential components relative to the orbit described by the impeller center movement. The mean values of these both components have an important significance in rotordynamics as clearly explained by Shoji and Ohashi (1987). The natural bending frequencies of the shaft are influenced by the bending moment exerted by the radial component F_r, while the tangential component F_t has either a destabilizing or a damping effect on the shaft: If F_t and the whirling motion have the same sense, F_t will promote the whirling motion, which will destabilize the shaft. Alternatively, if they are in opposite sense, F_t will tend to reduce the kinetic energy of the whirling rotor and exert a stabilizing or damping effect. As indicated by Jery et al., F_r and F_t are given by:

$$\begin{bmatrix} F_r \\ F_t \end{bmatrix} = \frac{\epsilon}{2} \begin{bmatrix} A_{xx} + A_{yy} \\ A_{yx} - A_{xy} \end{bmatrix} \tag{24}$$

Comparing Eq. (1) to Eq. (2), one will get the stiffness, damping, and inertia coefficients written as:

$$\begin{bmatrix} A_{xx} & A_{xy} \\ A_{yx} & A_{yy} \end{bmatrix}$$

$$= - \begin{bmatrix} K_{xx} + \Omega C_{xy} - \Omega^2 M_{xx} & K_{xy} - \Omega C_{xx} - \Omega^2 M_{xy} \\ K_{yx} + \Omega C_{yy} - \Omega^2 M_{yx} & K_{yy} - \Omega C_{yx} - \Omega^2 M_{yy} \end{bmatrix} \tag{25}$$

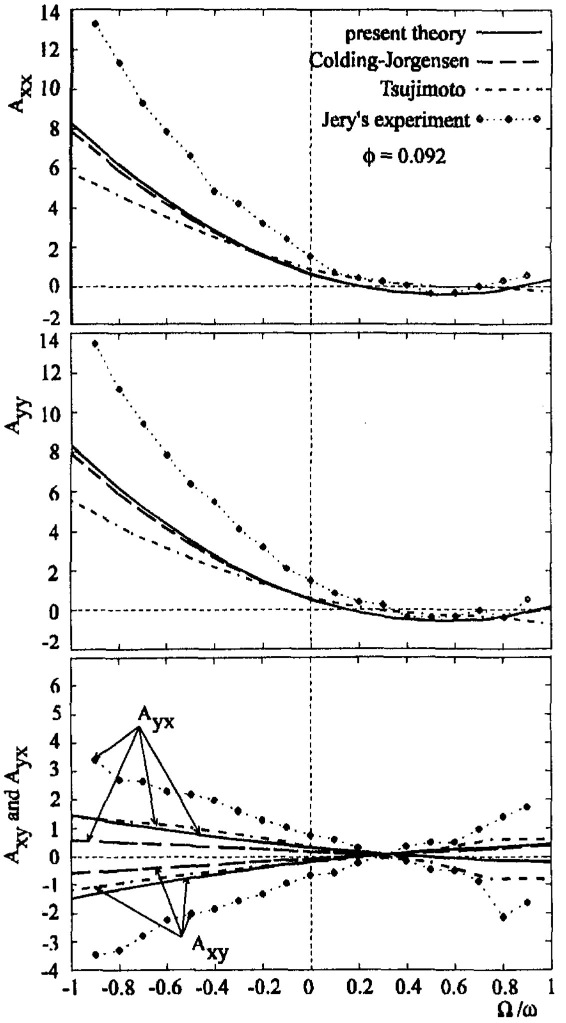

Fig. 9 Dimensionless generalized hydrodynamic force coefficients (normalized by $\pi\rho b\omega^2 r_2^2$) as a function of the speed ratio at design flow coefficient

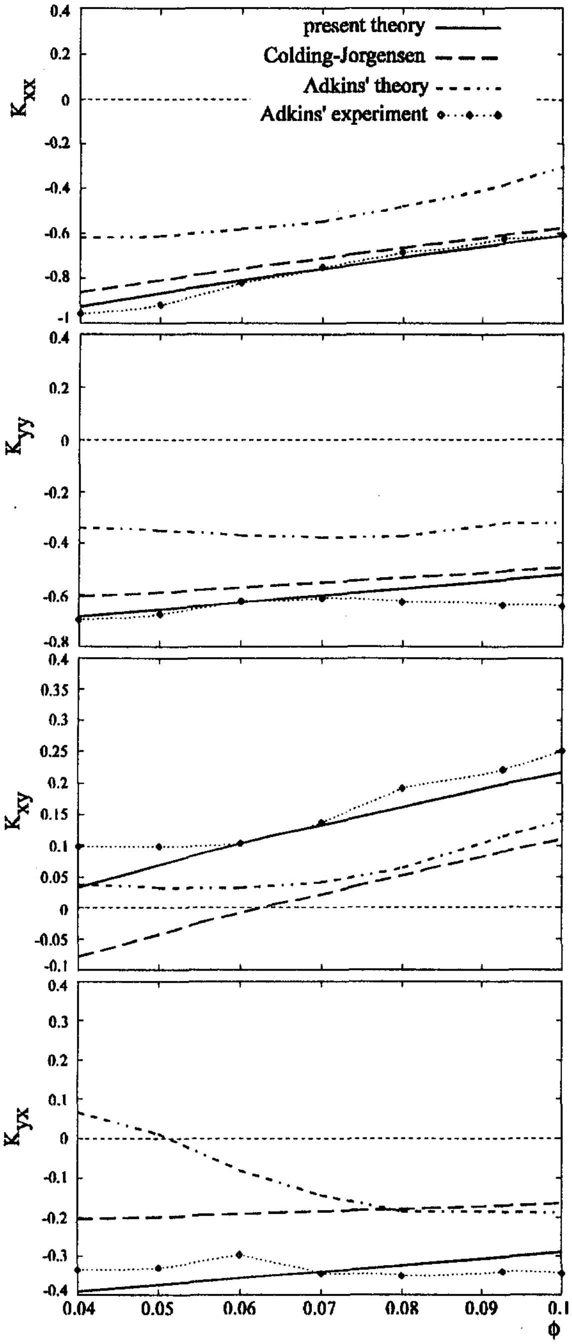

Fig. 10 Dimensionless stiffness coefficients (normalized by $\pi\rho b\omega^2 r_2^2$) as a function of the flow coefficient

The principle of calculation of these coefficients consists of determining the impeller forces for any three different values of Ω and to deduce from Eqs. (23) and (25) each rotordynamic coefficient.

Results and Discussion

In order to make a comparison with the experimental and theoretical results given in the literature, the calculations are performed for the following centrifugal pump geometry (data of Tsujimoto et al. (1988)): $\lambda = 83.462$ deg, $\beta = 25$ deg, $r_1/r_2 = 0.4$, $r_t/r_2 = 1.123$. The volute is modeled by $r/r_2 = 1.123e^{\theta/\tan\lambda}$ with $0 \le \theta \le 380$ deg. It results in a design flow coefficient of $\phi = 0.092$. N_1 and N_2 are chosen equal to 100.

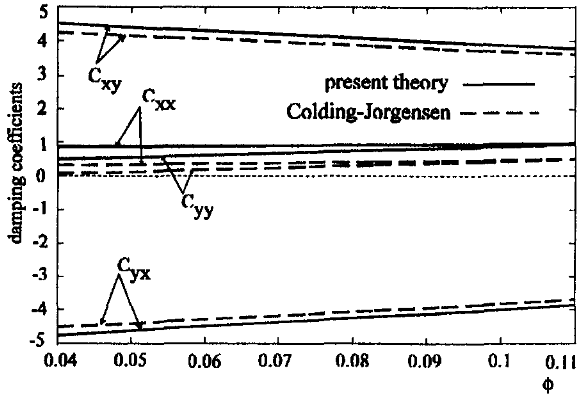

Fig. 11 Dimensionless damping coefficients (normalized by $\pi\rho b\omega r_2^2$) as a function of the flow coefficient

Curves named "Colding-Jorgensen" are calculated with these pump data using the source vortex representation of the impeller and replacing the spiral volute by a distribution of vortex points as introduced by Colding-Jørgensen (1980). The impeller forces are determined by making use of the unsteady forces formula presented by Eq. (20). Then the unsteady hydrodynamic forces on the impeller can be expressed in terms of radial and tangential components relative to the impeller center orbit (Figs. 8 and 9) for that model.

Figures 4 and 5 present the steady flow distribution around and inside the impeller for $Q_{\mathrm{rel}} = 0.4$ and $Q_{\mathrm{rel}} = 1.3$, respectively, the impeller center coinciding with the volute center. As predicted by Hergt and Krieger (1984) and shown in Fig. 4, the pressure at the tongue region is so high that the flow tends to return inside the impeller for off-design flow rate. Then the impeller receives a part of energy from the flow and works in that region like a turbine impeller. For higher flow rates, the pressure in that region is very weak and the flow speed becomes higher.

The dimensionless steady hydrodynamic forces acting on the impeller as a function of the flow coefficient are shown in Fig. 6 and their components in the x and y directions in Fig. 7. Results of the present calculations are compared to those of the model of Colding-Jørgensen (1980) and to the measurements of Chamieh et al. (1982) and Adkins and Brennen (1988) with the same pump exhibiting $\beta = 25°$, $\phi_n = 0.092$, and $r_t/r_2 = 1.13$. It appears that the present theory is close to that of Colding-Jørgensen (1980) and both agree with the measurements around the design flow coefficient.

Figure 8 presents the dimensionless radial and tangential force for $\phi = 0.092$, while the generalized hydrodynamic force

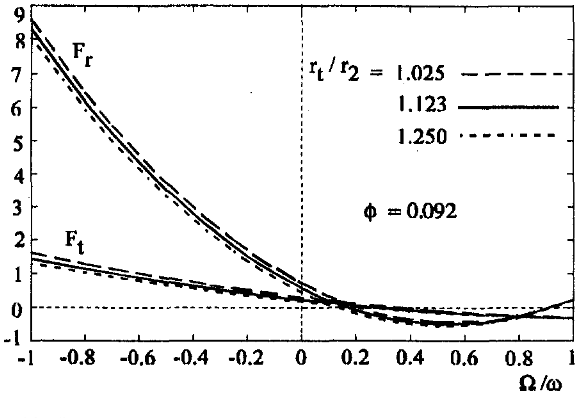

Fig. 12 Dimensionless radial and tangential force (normalized by $\pi\rho b\omega^2 r_2^2\epsilon$) as a function of the speed ratio; variation with the radius ratio

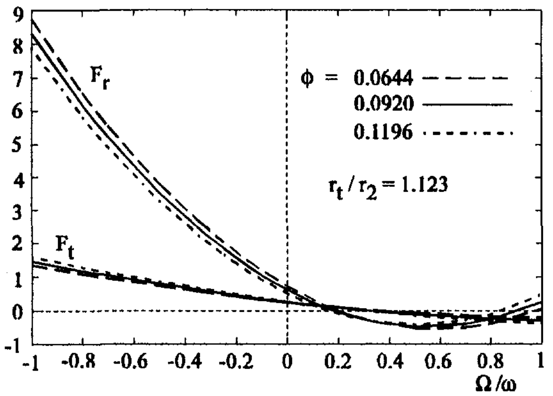

Fig. 13 Dimensionless radial and tangential force (normalized by $\pi\rho b\omega^2 r_2^2\epsilon$) as a function of the speed ratio; variation with the flow coefficient

coefficients are shown in Fig. 9 for the design flow coefficient. The comparison of our results is made with Colding-Jørgensen's prediction calculated as indicated above, theory of Tsujimoto et al. (1988), and measurements of Jery et al. (1984) at 1000 rpm with the same pump as that of Adkins and Brennen (1988). As explained by Adkins and Brennen (1988) and Tsujimoto et al. (1988), the forces measured by Jery et al. (1984) are a sum of the lateral fluid forces due to the impeller–volute interaction and of the pressure forces acting on the external surface of the shrouds. This is probably the cause of the difference between the theory and the measurement of Figs. 8 and 9.

According to Fig. 8, the tangential force F_t and the whirl speed Ω are both positive for $0 \leq \Omega/\omega \leq 0.3$ for our model. That means, in this domain, the lateral fluid forces on the impeller have a destabilizing effect on the pump rotor. The impeller forces become stabilizing when one moves from that interval of the whirl speed ratio.

The rotordynamic coefficients are presented in Figs. 10 and 11. The inertia coefficients have not been represented graphically because they remain constant relative to the flow rate and equal to

$$\frac{[M]}{\rho\pi b r_2^2} = \begin{bmatrix} 3.67 & -0.32 \\ 0.33 & 3.70 \end{bmatrix}$$

These inertia terms are of a considerable magnitude and deserve a comment. In some pumps, they can be larger than the impeller mass and hence be very important for the correct rotor modeling as indicated by Childs in his book *Turbomachinery Rotordynamics* (1993).

The stiffness coefficients were measured and calculated by Adkins and Brennen (1988). Their results are compared to those of our theory and that of Colding-Jørgensen (1980) in Fig. 10. As one can note, the present model simulates better the experimental measurements of Adkins and Brennen (1988). Figure 11 presents the damping coefficients compared to those of Colding-Jørgensen (1980). The actual model seems to give larger damping coefficients than the calculations of Colding-Jørgensen due to the impeller geometry, which was not considered in the earlier model.

Figure 12 presents the variation of the radial and tangential forces with r_t/r_2. As expected, the impeller forces increase when this ratio decreases for backward whirl. The destabilizing region of the whirl velocity expands with decreasing r_t/r_2.

The last figure shows the variation of the forces with the flow coefficient. It is noted that, for $\Omega/\omega \leq 0$, F_r decreases with increasing ϕ, while F_t increases with increasing ϕ. The destabilizing region of the whirl velocity expands with the decrease in the flow coefficient. This agrees with the results of the theory of Tsujimoto et al. (1988) and of the measurements of Jery et al. (1984).

Conclusion and Suggestion

A simple model based on the singularity theory in which the impeller periphery is replaced by a distribution of unsteady vortices has been developed to calculate the forces acting on a rotating and whirling impeller of centrifugal pumps. The calculated results have shown a stalled angular region in the impeller due to the volute asymmetry at off-design flow. In comparison to most of the theoretical and experimental results found in the literature, the model seems to give good prediction. The destabilizing effect of the impeller forces on the pump rotor for small forward whirl has been observed. The destabilizing region of this whirl velocity expands with decreasing r_t/r_2 and with the decrease in the flow coefficient ϕ. The next step of the analysis will consist of checking the influence of free shed vortices on the results.

Acknowledgments

This research was supported by the AG Maschinendynamik of the University of Kaiserslautern, Germany. R. Fongang would like to thank the German Academic Exchange Service (DAAD) for the financial support of his stay in the Federal Republic of Germany for his post-graduate studies. He would also like to express his gratitude to Prof. Dr.-Ing. H. Hellmann for his invaluable contribution to this work and to his colleagues of AG Maschinendynamik for their help in the preparation of the present paper.

References

Adkins, D. R., and Brennen, C. E., 1988, "Analyses of Hydrodynamic Radial Forces on Centrifugal Pump Impellers," ASME *Journal of Fluids Engineering*, Vol. 110, pp. 20–28.

Allaire, P. E., Branagan, L. A., and Kocur, J. A., 1982, "Aerodynamic Stiffness of an Unbound Eccentric Whirling Centrifugal Impeller With an Infinite Number of Blades," NASA CP. 2250, pp. 323–343.

Biheller, H. J., 1960, "Radial Force on the Impeller of Centrifugal Pumps With Volute, Semivolute and Concentric Casings," ASME *Journal of Engineering of Power*, Vol. 82, pp. 319–323.

Chamieh, D. S., Acosta, A. J., Brennen, C. E., Caughey, T. K., and Franz, R., 1982, "Experimental Measurements of Hydrodynamic Radial Forces and Stiffness Matrices for a Centrifugal Pump-Impeller," NASA CP 2250, pp. 382–390.

Colding-Jørgensen, J., 1980, "Effect of Fluid Forces on Rotor Stability of Centrifugal Compressors and Pumps," NASA CP 2133, pp. 249–266.

Colding-Jørgensen, J., 1989, "Fluid Induced Rotordynamic Instability of a Rotor With an Unbound Centrifugal Impeller," *Rotating Machinery Dynamics*, ASME DE-Vol. 18-1, pp. 63–69.

Csanady, G. T., 1962, "Radial Forces in a Pump Caused by Volute Casing," ASME *Journal of Engineering for Power*, Vol. 84, pp. 337–340.

Domm, V., and Hergt, P., 1970, "Radial Forces on Impeller of Volute Casing Pumps," *Flow Research on Blading*, Elsevier Pub. Co., pp. 305–321.

Hergt, P., and Krieger, P., 1969-1970, "Radial Forces in Centrifugal Pumps With Guide Vanes," *Proc. Inst. of Technical Engineers*, Vol. 184, Part 3N, pp. 101–107.

Hergt, P., and Krieger, P., 1984, "Theoretische und Experimentelle Bestimmung der Instationären Hydrodynamischen Kräfte auf die Laufschaufelenden," KSB Technische Berichte 18, pp. 5–9.

Iversen, H. W., Rolling, R. E., and Carlson, J., 1960, "Volute Pressure Distribution, Radial Force on the Impeller and Volute Mixing Losses of a Radial Flow Centrifugal Pump," ASME *Journal of Engineering for Power*, Vol. 82, pp. 136–144.

Jery, B., Acosta, A. J., Brennen, C. E., and Caughey, T. K., 1984, "Hydrodynamic Impeller Stiffness, Damping and Inertia in the Rotordynamics of Centrifugal Flow Pumps," NASA CP 2338, pp. 137–160.

Ohashi, H., and Shoji, H., 1987, "Lateral Fluid Forces on Whirling Centrifugal Impeller (2nd Report: Experiment in Vaneless Diffuser)," ASME *Journal of Fluids Engineering*, Vol. 109, pp. 100–106.

Shoji, H., and Ohashi, H., 1987, "Lateral Fluid Forces on Whirling Centrifugal Impeller (1st Report: Theory)," *Journal of Fluids Engineering*, Vol. 109, pp. 94–99.

Tsujimoto, Y., Acosta, A. J., and Brennen, C. E., 1988, "Theoretical Study of Fluid Forces on a Centrifugal Impeller Rotating and Whirling in a Volute," ASME *Journal of Vibration, Acoustics, Stress, and Reliability in Design*, Vol. 110, No. 3, pp. 263–269.

T. F. Fric

R. Villarreal

R. O. Auer

General Electric Company,
Corporate Research & Development,
1 Research Circle,
Niskayuna, NY 12309

M. L. James

D. Ozgur

T. K. Staley

General Electric Company,
Power Systems,
1 River Road,
Schenectady, NY 12345

Vortex Shedding From Struts in an Annular Exhaust Diffuser

Results from scale-model experiments and industrial gas turbine tests show that strut vortex shedding in an annular exhaust diffuser can effectively be modified by adding tapered chord to the struts. The struts are bluff bodies at full-speed, no-load conditions, when inlet swirl is close to 60 deg. Data from wind tunnel tests show that wake Strouhal number is 0.47, larger than that expected for an isolated cylinder wake. This value of Strouhal number agrees with those measured in full-scale exhaust diffusers. Wind tunnel tests showed that a strut with tapered chord most effectively reduced wake amplitudes and shifted shedding frequency. The tapered strut was also effective in reducing shedding amplitude in a scale-model diffuser. Finally, gas turbine tests employing a tapered strut showed significant reductions in unsteady pressure and noise. A major benefit of strut taper is a reduction of noise by uncoupling of vortex shedding from acoustic resonant response.

Introduction

A typical exhaust diffuser of an industrial gas turbine is annular with structural members, called struts, in the flow path. The struts extend radially from the inner to the outer annulus wall. Struts are optimized for baseload operation, where flow from the turbine into the exhaust diffuser is axial or nearly so. By orienting the struts axially, incidence angle to the oncoming flow is small at baseload. However, at full-speed, no-load (FSNL) conditions swirl exiting the last turbine blade row can be large, up to 60 deg relative to axial. At high incidence angles the struts act as bluff bodies and consequently cause unsteady wakes.

GE gas turbine tests of exhaust diffusers have shown relatively higher levels of unsteady pressure and noise at FSNL operating points than at baseload. Data show that unsteady pressure amplitudes of up to 2 psi (peak-to-peak) can occur. Typically the highest unsteady pressures are measured near the struts, with amplitudes decreasing both upstream and downstream of them. Unsteady pressure spectra show a dominant frequency. The sharpness of spectral peaks and acoustic data from FSNL tests suggest that an acoustic resonance of the diffuser flow path is excited. One possible acoustic stimulus is vortex shedding from struts when the swirl angle is large. It is conjectured that unsteady pressures are highest when vortex shedding frequency couples with an acoustic frequency of the flow path.

Excitation of acoustic modes by vortex shedding is not an uncommon phenomenon. Parker and Stoneman (1989) review occurrences of vortex shedding excitation of acoustic oscillations in internal flow systems with flat plates. The acoustic mode excited is a function of the characteristic vortex shedding Strouhal frequency. For flow aligned with the flat plates, the acoustic response can be affected by subtleties of the plate geometry such as leading and trailing-edge shape. Parker and Stoneman also recognize that vortex shedding characteristics, such as frequency, can be altered by acoustic response. The pressure amplitudes created when an acoustic resonance is excited are significantly larger than those from vortex shedding alone. An example of severe damage that can occur from acoustic resonances in diffusers is described by Rizk and Seymour (1964).

In order to understand and reduce diffuser dynamics encountered at FSNL conditions, a test program was initiated. The program involved three test phases: the first two with scale models and the third with a full-scale gas turbine. Since strut vortex shedding was considered as a possible stimulus, the first test was designed to observe and measure vortex shedding from a baseline strut and to allow for screening of modified struts to change vortex shedding. In order to screen new struts quickly, the first phase of experiments was performed in a three-strut, "component" two-dimensional wind tunnel, with strut aspect ratio and midspan pitch scaled from the annular diffuser. Three struts were considered to provide sufficient interaction effects, with the central strut's wake being most representative. The second phase of testing was performed in a scale-model annular exhaust diffuser. Tests in an annular model allowed for verification of strut vortex shedding performance in a three-dimensional geometry. The first two phases of testing were laboratory experiments designed to study strut vortex shedding. Since gas turbine Mach numbers were not matched, resonance between vortex shedding and acoustics could not be investigated. The third test phase, gas turbine tests at FSNL conditions, was run in order to measure the effects of strut design in an environment with correct acoustics.

New strut designs screened in the three-strut component tests were chosen based on their probability of modifying wake shedding and on their ease of implementation into exhaust diffuser hardware. Strut designs that had a potential to change dominant wake frequencies or significantly reduce the amplitude of wake fluctuations, or ideally both, were considered. Manipulation of bluff-body vortex shedding has been studied extensively. One class of techniques often employed involves the addition of plates near the bluff body. As examples, splitter plates in the

---

Contributed by the International Gas Turbine Institute and presented at the 41st International Gas Turbine and Aeroengine Congress and Exhibition, Birmingham, United Kingdom, June 10–13, 1996. Manuscript received at ASME Headquarters February 1996. Paper No. 96-GT-475. Associate Technical Editor: J. N. Shinn.

near wakes of circular cylinders affect wake frequencies and drag (Roshko, 1955), a spoiler plate attached to one side of an airfoil affects predominant shedding frequencies (McLachlan and Karamcheti, 1985), and the addition of a tandem bluff body either upstream or downstream from the original can influence the collective vortex shedding and drag (Lesage and Gartshore, 1987). Although these techniques are effective methods to reduce wake dynamics and drag, they are typically useful only over a small angle-of-attack range. An essential requirement for a strut modification is that it is effective over a large range of swirl angles (0 through 60 deg). A new design should not improve dynamics at FSNL at the expense of reduced performance at base load operation. Cimbala and Garg (1991) tested a splitter plate attached to the trailing side of a cylinder with the additional feature that the splitter plate is hinged, allowing it to float as dictated by the flow. Although such a floating splitter may be effective over a wider range of swirl, implementation of a hinged splitter in an annular geometry, particularly in a high-temperature environment, may be difficult. The above-listed techniques generally require that additional objects be introduced, adding complexity to the mechanical design of the flow path.

Another class of techniques to control wakes is the addition of vortex generators. Vortex generators effectively keep flow attached, but only up to moderate angles of attack. Larger-scale vortex generators, which introduce streamwise vorticity and break up dominant spanwise structure, can be effective in reducing vortex shedding amplitudes but are not necessarily effective in changing shedding frequency (Gulati, 1990). Higuchi and Takahashi (1989) studied the aerodynamic characteristics of vented bluff bodies. Their results showed that vents, in the form of slots in the bluff body, can change vortex shedding strength and drag. The vents act as wake fillers, and alter the communication between separations from each edge of the bluff body.

For the tests reported on here, quantitative data are presented in the form of amplitude spectra from unsteady pressure transducers in the vicinity of struts. Peak frequencies are nondimensionalized as Strouhal number St based on strut chord and total velocity. Data from FSNL gas turbine tests show that resonance occurred at St = 0.47 at swirl angles near 60 deg. The three-strut component and scale-model annular tests produced vortex shedding at St = 0.47 and 0.38, respectively. These St values are sufficiently close to real machine values at resonant conditions to suggest that vortex shedding is a component of exhaust diffuser dynamics.

Five strut concepts were screened in the three-strut component wind tunnel. The five concepts are called baseline, vortex generator, tapered chord, long chord, and vented. The vortex generator, tapered chord, and long chord designs are relatively simple modifications to the existing struts. The vented design involves a more significant modification since air paths through the struts are required. Each of the four new strut designs showed some improvement in wake dynamics. However, the tapered chord clearly performed the best; it significantly shifted wake frequency and reduced peak vortex shedding amplitudes. Since the tapered strut performed best in the screening tests, this design was tested in the annular scale-model test. The tapered strut was again effective in reducing peak vortex shedding amplitude and shifting frequency. Tapered struts were then installed in a full-scale exhaust diffuser. Gas turbine tests with the tapered strut showed significant unsteady pressure amplitude and noise level reductions, relative to the baseline design.

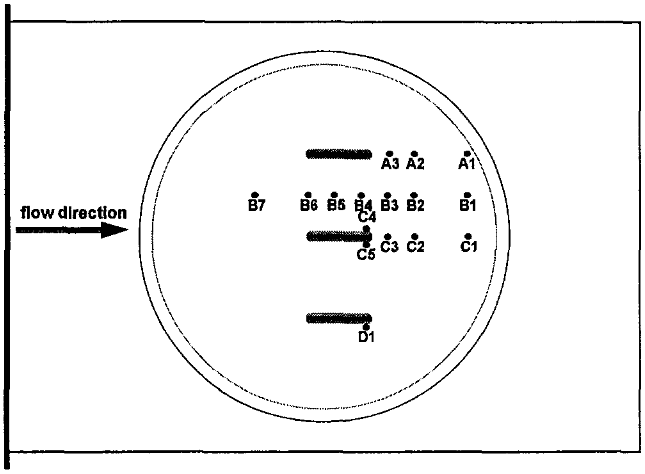

Fig. 1 Test section for three-strut component wind tunnel (drawn to scale). Struts are shown at α = 0 deg.

Test Setups: Phases 1, 2, and 3

1 Three-Strut Component Wind Tunnel. The test section of the three-strut component wind tunnel is shown in Fig. 1. Three unstaggered struts were mounted in the test section. The baseline struts were $\frac{1}{6}$ scale of gas turbine size with a chord of 12.4 cm (4.9 in.) and a spacing of 15.7 cm (6.2 in.), equivalent to the midspan radial struts' pitch. The rectangular test section, 122 cm (48 in.) in length, 82.3 cm (32.4 in.) in height, and 14.6 cm (5.75 in.) in width, was supplied by a rectangular nozzle from a 122 cm (48 in.) diameter plenum. The three struts were mounted on a rotatable disk, which was centered on the rear side wall. "Swirl" could be varied by rotating the disk to the desired angle. Although the tests focused on the α = 60 deg case, lower swirl angles of 45, 30, and 0 deg were also looked at. Unsteady pressure data were obtained at 16 locations on the disk, and these are shown in Fig. 1. Unsteady pressure transducers (PCB model 103A02) were mounted on the 16 pressure taps. Test section velocity u_{tot} was 30.5 m/s (100 ft/s), and the velocity at the inlet was spatially uniform to within ±1.25 percent. Test section frequency spectra were flat with no discernible peaks, when no struts were installed.

Unsteady pressure data were acquired with a 486 personal computer. Signals from each transducer were filtered and amplified (gain = 10) by a Krohn-Hite model 3944 multichannel filter. Transducer signals were low-pass filtered at 500 Hz, sampling rate was 1500 Hz, and sampling time was 2 s. Data are presented in the form of amplitude spectra of the unsteady pressure signal. In order to smooth spectral fluctuations, each 3000 point sample was partitioned into ten 512 point rectangular windows with overlap. Each spectrum shown is an ensemble average of the ten 512 point FFTs. Smoothing in this manner allowed for improved spectral peak determination at the expense of frequency resolution. The spectral amplitudes shown are in arbitrary units on a linear scale.

Nomenclature

$A_{\max}$ = maximum spectral amplitude among transducers
c = strut chord (minimum chord for tapered struts)
f = frequency of peak spectral amplitude
M = Mach number = u_{tot}/a
Re = strut Reynolds number = $u_{\text{tot}}c/\nu$
St = wake Strouhal number = fc/u_{tot}
u_{tot} = radially averaged total velocity at strut leading edge plane
α = nominal swirl angle at diffuser inlet plane

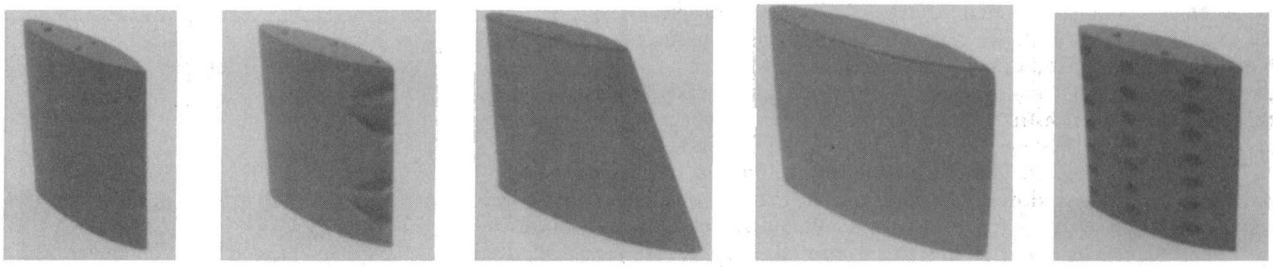
(a) Baseline (b) Vortex generators (c) Tapered-1.5 (d) Long chord (e) Vented

Fig. 2 Photographs of five strut designs

Five strut designs, shown in Fig. 2, were screened. The following describes the five designs in detail.

Baseline. The baseline strut is a $\frac{1}{6}$-scale model of the exhaust diffuser strut. The strut profile is a NACA 16 with a maximum thickness of 2.6 cm (1.0 in.) and a chord c of 12.4 cm (4.9 in.).

Vortex Generators. Four vortex generator tabs are mounted on the pressure side of the baseline strut near its trailing edge (Fig. 2(b)). The vortex generators are oriented at 20 deg relative to the axial direction. The tabs' axial lengths are 3.73 cm (1.47 in.), and their height at the strut trailing edge is 1.15 cm (0.45 in.).

Tapered. To test the effects of varying a characteristic length scale, a tapered strut, with variable chord along its span, was tested. Based on initial promising tests, several variations of the tapered strut were tested. The tapered strut shown in Fig. 2(c) is identified as ''tapered-1.5.'' ''Tapered'' indicates that the strut chord (and thickness) varies linearly along its span. The strut profile remains the same at all cross sections. ''1.5'' indicates the amount of chord taper; the chord at one end is always fixed at 1× (12.4 cm, 4.9 in.), and the chord at the other end of the strut is 1.5× (18.6 cm, 7.35 in.). Smaller amounts of taper, 1.38 and 1.25, were also tested. In each case taper was added to the strut trailing edge.

Long Chord. The long chord design also uses a NACA 16 strut profile, with a chord 1.5× larger (18.6 cm, 7.35 in.) than the baseline. The long chord effectively increases the solidity of the flow path at high swirl angles. The long chord was tested to help distinguish between the solidity and nonuniform chord effects of the tapered strut.

Vented. The baseline vented strut has three rows of holes, each row with seven 0.95 cm (0.38 in.) holes. The holes are angled at 45 deg relative to the chord line, such that at $\alpha = 45$ deg the holes are in line with the flow direction.

2 $\frac{1}{6}$-Scale Annular Exhaust Diffuser Model. The $\frac{1}{6}$-scale model of the annular exhaust diffuser is shown in Fig. 3. The diffuser outer wall expansion (half) angle is approximately 6 deg, and the centerbody is of uniform diameter. Ten equally spaced radial struts of chord 12.4 cm (4.9 in.) are located one chord length from the diffuser inlet plane. Inlet swirl is provided by a radial swirler. Inlet total velocity u_{tot} was 43.9 m/s (144 ft/s) with a radial variation of ±4.6 m/s (15 ft/s). Nominally $\alpha = 60$ deg, but α dips to 50 deg near the centerbody. Unsteady pressure instrumentation and the data acquisition system were like those used in the three-strut component tests. Pressure transducers (locations B1 through B7 and C1 through C5 only) were mounted on the diffuser outer wall at equivalent positions relative to a selected strut as those shown in Fig. 1.

Two strut designs, the baseline and tapered chord, were tested. The tapered chord strut was selected from the screening tests to be the most effective in vortex shedding amplitude reduction and frequency shift. Two variations of a tapered strut were investigated. The first had 1.5 taper at the strut trailing edge. The second design tested was one with 1.65 overall taper, consisting of 1.4 trailing-edge taper and 1.25 leading-edge taper. In both cases maximum chord was mounted at the root.

3 Full-Scale Gas Turbine. Full-scale tests at full-speed, no-load (FSNL) gas turbine conditions were run in order to compare the performance of the tapered strut with that of the baseline design. The tapered design tested was the tapered-1.65, which performed best in annular scale-model tests. Inlet guide vane (IGV) settings were changed in order to measure exhaust diffuser dynamics under varying mass flow rate and exhaust temperatures, anticipating that exhaust temperature would affect diffuser acoustics. Instrumentation included 18 transducers on the outer wall of the exhaust diffuser. Six transducers were circumferentially located one-half chord length aft of the diffuser inlet plane. The remaining transducers were positioned in the vicinity of a selected strut. The flow conditions for the gas turbine exhaust diffuser at FSNL are compared with those for the laboratory tests in Table 1.

Results and Discussion

1 Three-Strut Component Wind Tunnel. Figure 4 shows smoke-wire flow visualization of the baseline strut wake at $\alpha = 60$ deg. The wakes contain vortical structure, seen most clearly at the center strut's trailing edge. Flow separates from the leading and trailing edges, and the wake of a strut strongly interacts with the adjacent strut. Visualization for $\alpha = 45$ deg is similar to that shown here. At $\alpha = 30$ deg interactions be-

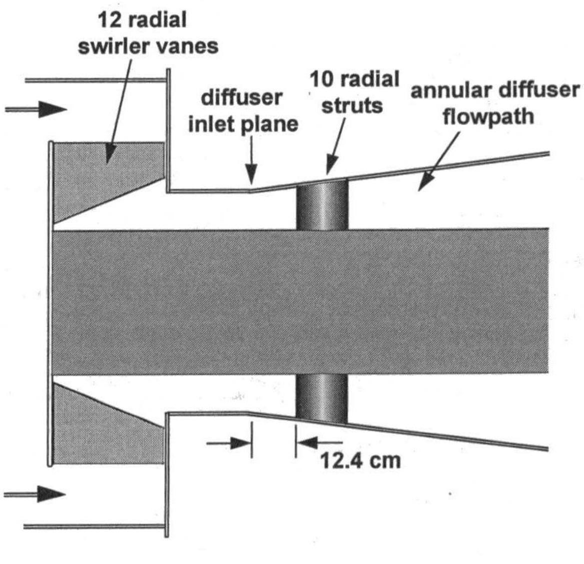

Fig. 3 $\frac{1}{6}$-scale model of the annular exhaust diffuser

Table 1 Comparison of flow conditions among tests

Test	α	*M*	*Re*
Full-scale gas turbine (FSNL)	60°	.45	3,000,000
1/6-scale annular model	60°	.11	400,000
3-strut component	60°	.09	300,000

tween wakes and struts are weaker, and at $\alpha = 0$ deg small isolated wakes exist, but flow remains attached over most of each strut.

Figure 5 shows amplitude spectra for the five strut designs at $\alpha = 60$ deg. The spectra shown are for those transducer locations that resulted in maximum peak amplitude for each design. Maximum amplitudes $A_{\max}$ for the baseline and vortex generators designs are 15.1 and 10.5, respectively. Peak frequencies are similar for both designs, as indicated by St values of 0.47 and 0.50, respectively. Table 2 shows $A_{\max}$, transducer location corresponding to $A_{\max}$, and St for five designs and three α. The long chord and vented struts shifted the dominant frequency higher, to St = 0.57 in both cases. Peak amplitudes are 10.9 and 14.7 for the long chord and vented designs, respectively. The tapered-1.5 design shifted the dominant frequency even higher to St = 0.67 and reduced the peak amplitude significantly to 6.71. (The tapered results shown are for the case where the short chord is at the tunnel side-wall with the transducers.) Clearly at $\alpha = 60$ deg the greatest amplitude reduction and frequency shift was obtained by the tapered strut. Tapered strut results with varying amounts of taper will be discussed later. Data from all transducers uniformly indicate that the tapered strut performed best.

Values of St measured here are considerably larger than those expected for isolated airfoils at high incidence angles or for classical cylinder wakes. Data for isolated airfoils at $\alpha = 60$ deg show values of St to be in the range of 0.17 to 0.24 (Fung, 1955). Data from the three-strut component tests show that baseline St = 0.47. To check consistency between our tests and those presented by Fung, the test section was modified so that only the central strut was installed. Peak amplitude in the wake of an isolated baseline strut occurred at St = 0.25, close to the values of Fung. However, wake frequencies measured by Cenedese et al. (1981) for a single airfoil at $\alpha = 60$ deg yielded St $\approx$ 0.46, a value close to that measured in the three-strut test. An important aspect of the setup of Cenedese et al. is that although they studied an isolated airfoil, the wind tunnel test section height was only about twice the airfoil chord. At high incidence angles blockage due to the airfoil was therefore large.

One possible explanation to resolve such discrepancies in St is that closely spaced struts redistribute wake structure so that transducers detect vortices shed from both edges of each strut, creating an apparent frequency doubling. Similarly, a transducer located in the central portion of a circular cylinder wake records vortices shed from both sides. However, the reason for the high values of St may be more fundamental. Flow visualization such as that shown in Fig. 4 reveals "jets" at the strut trailing edge, from the pressure side. As flow accelerates in the narrowing passage between the leading-edge separation streamline and the pressure side of the "downstream" strut, a locally higher velocity is created where separation from the strut trailing-edge occurs. The locally higher velocity at the trailing edge would likely result in higher wake frequencies and therefore high values of Strouhal number that are based on incoming free-stream velocity. A similar argument could be made for the geometry studied by Cenedese et al., where wind tunnel blockage would create locally higher velocities at the separation lines.

Fig. 4 Smoke-wire flow visualization of baseline strut: $\alpha = 60$ deg

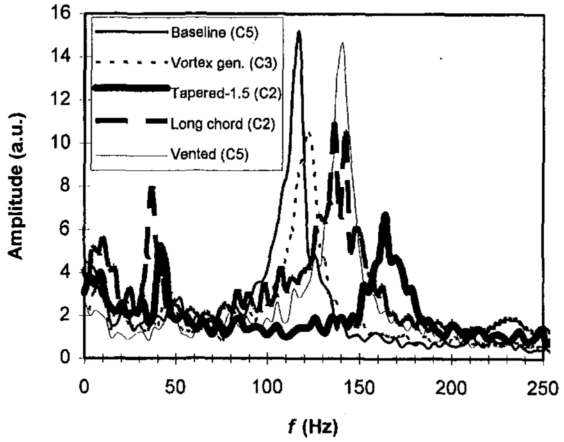

Fig. 5 Amplitude spectra for five strut designs: $\alpha = 60$ deg

Figure 6 shows sample pressure versus time traces comparing the baseline and tapered struts. The time trace for the baseline case clearly shows a strong periodic fluctuation, which matches the 115 Hz peak of its spectrum (Fig. 5). The time trace for the tapered-1.5 design shows a significantly reduced fluctuating component. Figure 7 shows a sample flow visualization of the tapered-strut wake. Although the visual differences between the wakes are more subtle than differences between spectra, less large-scale vortical structure appears in the tapered-strut wakes than in the baseline wakes.

Data for the five strut designs at $\alpha = 45$ and 30 deg are shown in Table 2. Three observations are noteworthy. First, the tapered-1.5 strut reduced peak amplitude from 13.4 to 4.31 and shifted peak St from .47 to 0.52 at $\alpha = 45$ deg. Second, amplitudes are comparable at $\alpha = 60$ and 45 deg but drop off considerably at $\alpha = 30$ deg. Third, the vented strut did extremely well

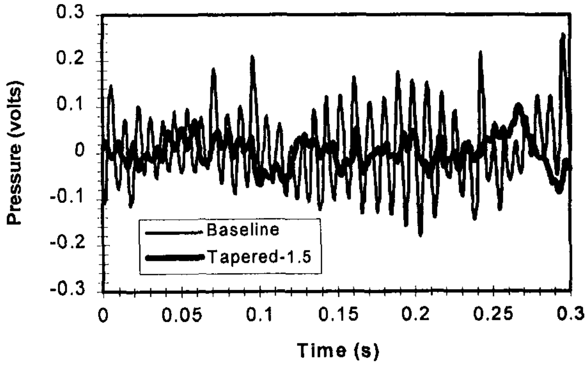

Fig. 6 Sample pressure versus time traces comparing baseline and tapered-1.5 designs: $\alpha = 45$ deg

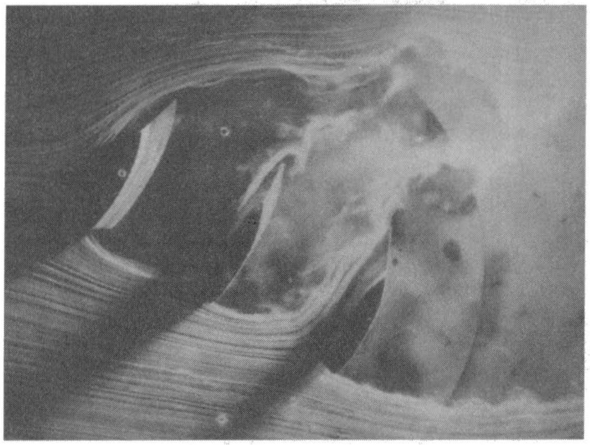

Fig. 7 Smoke-wire flow visualization of tapered-1.5 strut at $\alpha = 45$ deg

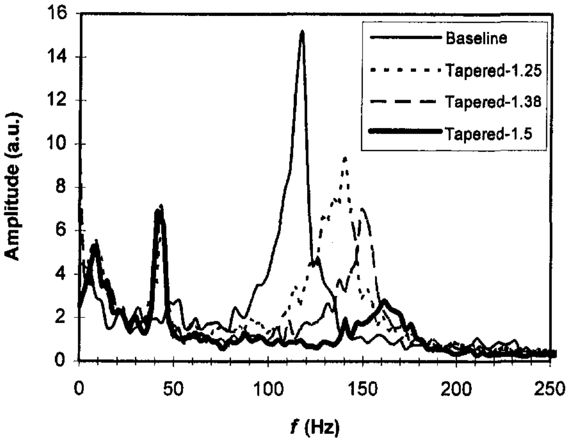

Fig. 8 Amplitude spectra comparing tapered struts with baseline strut. $\alpha = 60$ deg. Location is C5.

at $\alpha = 45$ deg, where no discrete peak was found. Recalling that the vented strut did not reduce peak amplitudes at $\alpha = 60$ deg, it appears that the success of the vented design is highly dependent on the relative angle between in the incident flow and holes comprising the vents.

Additional Tapered Strut Results. Data from the three-strut component tests indicate that the tapered-1.5 strut is overall most effective in reducing unsteady pressure amplitudes and in shifting wake frequencies. Varying strut chord along its span was motivated by the fact that the characteristic wake frequency of a bluff body scales with its diameter or, equivalently in this case, with its chord. This information is implicit in the definition of Strouhal number; frequency is inversely proportional to length scale. By varying the characteristic length scale along the strut's span, wake formation is disrupted since a single dominant frequency is not apparent anymore. The flow doesn't have a single length scale by which to set its frequency. Earlier it was conjectured that the higher than expected wake frequencies were perhaps caused by flow acceleration in between struts. If this is the case, the appropriate length scale that sets wake frequencies may in fact be the effective gap distance in between struts. It follows then that tapering has a similar disruptive effect since the distance between struts also varies in the spanwise direction.

Further tests were conducted in order to investigate the effect of amount of taper on amplitude reduction and frequency shift. Trailing-edge tapers of 1.25 and 1.38 were investigated. Figure 8 shows amplitude spectra for various amounts of taper. Amplitude decreases with increasing trailing-edge taper. The results show that amplitudes decrease from 15.1 to 9.37, 6.91, and 6.71 as trailing-edge taper is increased by amounts of 1.25, 1.38, and 1.5, respectively. Also, peak amplitudes shift to higher frequencies as the amount of taper increases. Although the amplitude reduction realized with different tapers varied somewhat with transducer location, the shift of peak frequency with increasing taper was consistently observed at all transducers.

Perhaps the best measure of taper effectiveness is to compare $A_{\max}$ for each taper design at $\alpha = 60$ and 45 deg. This comparison is shown in Table 3. Percent reductions in $A_{\max}$ relative to baseline, peak frequency f, and percent increases in f are also indicated in Table 3. The data show that taper was also effective at $\alpha = 45$ deg. Each amount of taper, even 1.25, essentially eliminated vortex shedding peaks. The data suggest, therefore, that the effectiveness of taper is higher for $\alpha = 45$ deg than for $\alpha = 60$ deg; the amount of taper required to reduce vortex shedding amplitude by a prescribed amount is less than that required for $\alpha = 60$ deg.

2 $\frac{1}{6}$-Scale Annular Exhaust Diffuser Model. Figure 9 shows amplitude spectra for the baseline strut and two versions of the tapered strut as tested in the $\frac{1}{6}$-scale annular model. Spectra shown correspond to the location for which maximum amplitude for the baseline strut was recorded. The spectral peak for the baseline strut is now relatively broader than that for the three-component tests. St = 0.38, somewhat lower than that measured in the three-strut tests. This difference may be attributed to three-dimensional effects such as nonuniform inlet velocity and swirl profiles, a diffusing endwall, and varying strut pitch.

The tapered-1.5 strut produced an amplitude reduction of 1.43 to 1.11 (22 percent) with a corresponding St shift from 0.38 to 0.42 (11 percent). Although these shifts are not as large as those measured in the three-component tests, an amplitude reduction and shift to higher frequency were both realized. A strut with combined leading and trailing-edge taper was also tested. With a net taper of 1.65, this strut resulted in a larger amplitude reduction. Figure 9 shows that an amplitude reduction from 1.43 to .87 (39 percent) and a St reduction from 0.38 to 0.24 (37 percent) were obtained by the dual tapered design. This result counters those in Fig. 8, which suggested that more taper shifts wake frequencies to higher levels, and perhaps the addition of leading-edge taper is instrumental.

Table 2 $A_{\max}$, transducer location corresponding to $A_{\max}$, and St. $\alpha = 60$, 45, and 30 deg. $u_{\text{tot}} = 30.5$ m/s (100 ft/s).

	α = 60°		α = 45°		α = 30°	
STRUT DESIGN	A_{max} (location)	*St*	A_{max} (location)	*St*	A_{max} (location)	*St*
Baseline	15.1 (C5)	.47	13.4 (C5)	.47	4.06 (C5)	.68
Vortex generators	10.5 (C3)	.50	7.75 (C3)	.50	2.35 (B2)	.67
Tapered-1.5	6.71 (C2)	.67	4.31 (B4)	.52	no discrete peaks	---
Long chord	10.9 (C2)	.57	9.07 (B2)	.56	no discrete peaks	---
Vented	14.7 (C5)	.57	no discrete peaks	---	did not test	---

Table 3 Effectiveness of trailing-edge taper on maximum amplitudes and frequencies: α = 60 and 45 deg

	$\alpha = 60°$				$\alpha = 45°$			
Design	A_{max} (location)	ΔA_{max} %	f Hz	Δf %	A_{max} (location)	ΔA_{max} %	f Hz	Δf %
1.00	15.1 (C5)	-	117	-	13.6 (C5)	-	111	-
1.25	9.37 (C5)	-38	141	+21	3.11 (C3)	-77	129	+16
1.38	6.91 (C5)	-54	149	+27	3.24 (C2)	-76	161	+45
1.5	6.71 (C2)	-56	164	+40	4.31 (B4)	-68	132	+19

3 Full-Scale Gas Turbine. Since the dual-tapered strut with 1.65 total taper performed best in annular scale-model tests, it was selected to be tested in the full-scale FSNL gas turbine test stand. First, to establish the baseline strut behavior of the exhaust diffuser at real conditions, consider the data in Figs. 10(*a*), 11, and 12. Figure 10(*a*) shows exhaust diffuser amplitude spectra for inlet guide vane (IGV) settings of 54 and 74. These spectra are for those transducer locations that resulted in maximum peak amplitude for each IGV setting. The characteristic behavior of the baseline exhaust diffuser is that unsteady pressure amplitudes and noise increase as IGVs are opened from 54 to 84 at FSNL. For example, two low amplitude peaks at f = 134 Hz. and 157 Hz. become one high amplitude peak at f = 127 Hz. for the higher IGV setting (Fig. 10(*a*)). Figure 11 clearly shows the trend of increasing dynamics with opening IGV setting.

For baseline full-scale tests at high IGV settings St = 0.47. This value is the same as that measured in the three-strut component tests and somewhat higher than the value of 0.38 from the annular scale model. The degree of agreement of St among these tests is sufficient to suggest that vortex shedding phenomena is relevant to the full-scale dynamics.

That unsteady pressure signals increased rapidly and appeared to lock into a preferred frequency suggests that an acoustic resonance was excited. At no load and constant rotor speed, as the IGVs are opened, mass flow through the diffuser increases and temperature decreases. The effects of this are twofold; changes in velocity affect vortex shedding frequency and a decrease in temperature affects acoustic frequency. Shifting of these values could collectively act to enhance coupling of vortex shedding and acoustics, creating a resonance. The six circumferentially positioned pressure transducers located forward of the struts allowed for determining the mode shape of resonance for baseline struts. The relative phases among signals from these transducers are plotted in Fig. 12(*a*). The linear fit to these phases, showing 1080 deg (3 × 360 deg) accumulated phase around the circumference of the diffuser, suggests that the acoustic wave is a nodal diameter $n = 3$ circumferentially traveling (spinning) wave. That an $n = 3$ wave is a traveling wave is consistent with the observations of Parker and Pryce (1974), who found that for annular passages traveling waves are common when the number of half-waves is not equal to the number of struts. The approximately uniform amplitude among these transducers is also consistent with a spinning wave (Fig. 12(*b*)).

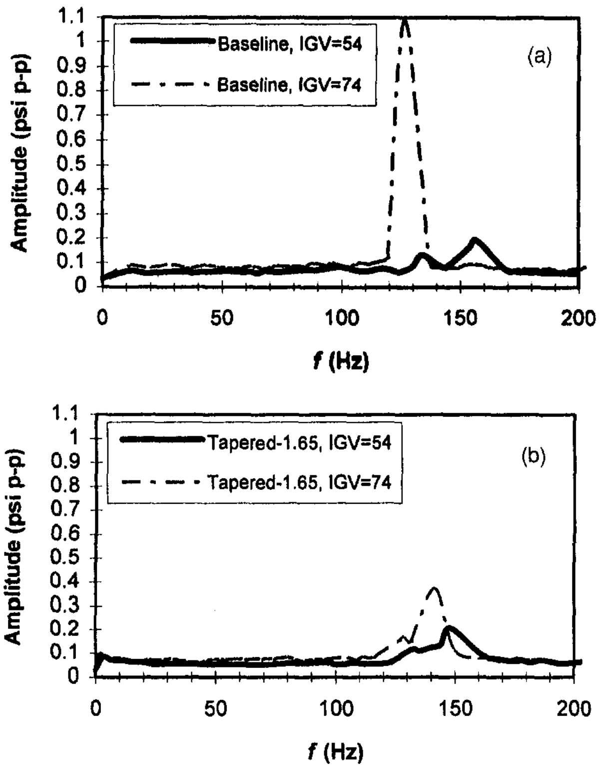

Fig. 10 FSNL gas turbine exhaust diffuser spectra: (*a*) baseline strut, (*b*) tapered-1.65 strut

The tapered-1.65 struts were then installed, and data from this test are shown in Figs. 10(*b*) and 11. Equivalent forward diffuser data, like those shown in Fig. 12, could not be resolved since amplitudes were too low, less than 0.02 psi *p-p*. Figure 10(*b*) shows that an amplitude similar to that for the baseline strut was measured at IGV = 54. However, as the IGV setting was increased, amplitudes stayed relatively low (Fig. 10(*b*)). Figure 11 shows the improvement in unsteady pressure levels at all IGV settings for the tapered strut. Furthermore, near-field

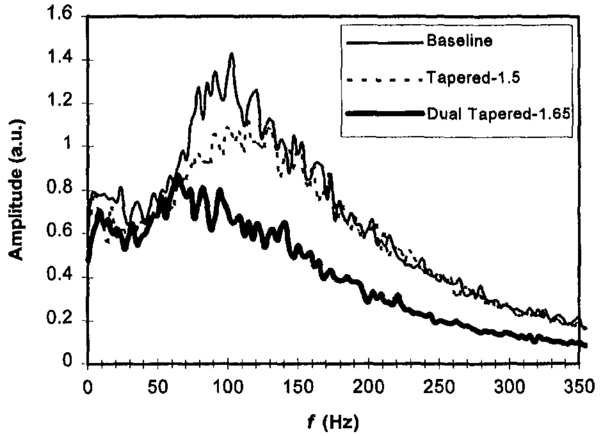

Fig. 9 Spectra comparing tapered struts with baseline in $\frac{1}{6}$-scale annular exhaust diffuser. Location is B3.

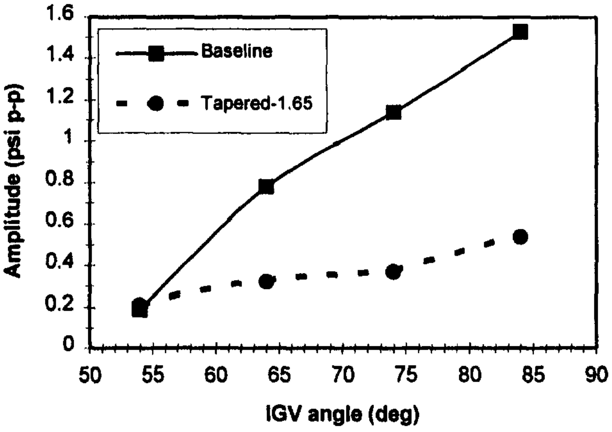

Fig. 11 FSNL exhaust diffuser unsteady pressure amplitudes with varying IGV setting

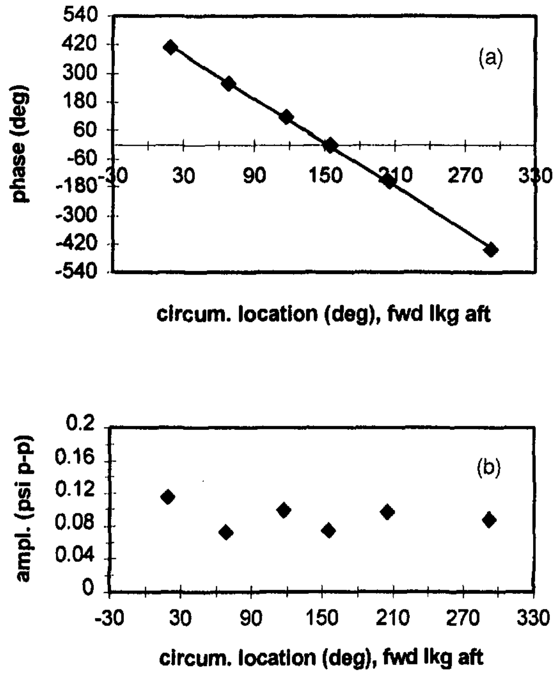

Fig. 12 FSNL baseline diffuser acoustic signature. Data were obtained from 6 transducers forward of struts. (*a*) phase, (*b*) amplitude.

sound meters showed that broad-band noise from the exhaust frame decreased by 1 to 5 dB, depending on IGV setting.

Since it is not possible to separate the exhaust diffuser's acoustic response from strut vortex shedding in the full-scale tests, the precise mechanism by which the tapered strut improved dynamics cannot be known for certain. Scale-model test data suggest that one effect of tapered struts is to shift vortex shedding frequency and reduce its amplitude. If vortex shedding is the excitation source for the acoustic resonance in the baseline case and if vortex shedding was sufficiently altered by tapering the struts, then a decoupling of excitation from the acoustic resonance response occurred. In fact, if the tapered struts were totally effective in eliminating vortex shedding amplitude, this excitation source is totally eliminated. However, it is also a possibility that the effect of tapered struts is to alter the acoustic nature of the diffuser. Given that a spinning wave can couple with oscillatory (acoustic) flows between struts (Alford, 1966), tapering the struts could also have a direct effect on acoustic modes. This effect, if present, could not be diagnosed in the low Mach number laboratory experiments.

Summary

Scale-model tests and a full-scale gas turbine test were used to diagnose and reduce relatively high levels of unsteady pressures in an industrial gas turbine exhaust diffuser operating at full-speed, no-load conditions. Past experience suggested that the source of high dynamics may have been radial struts near the forward portion of the annular diffuser. Since swirl can be as high as 60 deg at FSNL operation, efforts were first focused on vortex shedding from the axially oriented struts. Wind tunnel tests established a vortex shedding Strouhal number of 0.47, based on strut chord and total velocity. This St value matched that measured in a full-scale diffuser operating at FSNL.

Given this match in St, four new strut designs were tested in the laboratory in order to achieve vortex shedding amplitude reduction and frequency shift. If vortex shedding was the stimulus for the diffuser resonance, perhaps changing vortex shedding would eliminate the resonance. Results from the three-strut component screening suggest that vortex shedding modification is possible with passive control techniques such as a tapered chord, vortex generators, and vented struts. Of these the tapered strut was the only design that reduced vortex shedding amplitude, shifted peak frequency, and remained effective over a large range of swirl ($\alpha = 30$ through 60 deg).

In order to establish the effectiveness of a tapered strut design in a three-dimensional diffuser geometry before going to full-scale testing, two tapered strut designs were tested in a scale-model annular diffuser. The design with 50 percent chord taper at its trailing edge reduced vortex shedding amplitude and shifted peak frequency, but by amounts less than in the three-strut component tests. In addition, a baseline St value of 0.38 was measured, somewhat lower than those recorded in the three-strut tests and in full-scale tests. These differences can perhaps be attributed to three-dimensional effects that are not necessarily matched among the three experiments. The scale-model annular diffuser tests suggested that a strut with combined leading and trailing-edge taper, with a net chord taper of 65 percent, is most effective in the annular geometry. Therefore, this dual taper design was chosen for gas turbine testing.

Full-scale tests at full-speed, no-load conditions employing a tapered strut with combined leading and trailing-edge taper resulted in approximately factors of three reductions in unsteady pressure amplitudes. Baseline strut tests at FSNL conditions showed that a spinning wave exists in the exhaust diffuser. The presence of an acoustic wave and the consistency of Strouhal numbers among the laboratory and gas turbine tests indicate that a coupling between vortex shedding and acoustics exists for a diffuser with baseline struts. The results suggest tapered struts decouple vortex shedding excitation and acoustic response of the diffuser.

Acknowledgments

This work benefited from the collaborative efforts of many at GE Power Systems in Schenectady, NY and Greenville, SC and at GE Corporate Research and Development. Specifically, the leadership and support of Dave Foland and Al McCallum (Greenville) during the gas turbine tests is appreciated. Data reduction by Ralph Bush is recognized. The work benefited greatly from insights into the acoustics of the problem provided by Rich Loud (Schenectady), Bob Hedeen, Graham Holmes, Z. Hu, Ramani Mani (CR&D), and Joe Alford (GE Aircraft Engines). The contribution of Chris Wilkes to the three-component tests is also recognized.

References

Alford, J. S., 1966, "Protecting Turbomachinery From Unstable and Oscillatory Flows," ASME Paper No. 66-WA/GT-13, pp. 145–166.

Cenedese, A., Cerri, G. and Iannetta, S., 1981, "LDV Analysis of Wakes Behind Circular Cylinders and Airfoils," *Meccanica*, Dec., pp. 220–231.

Cimbala, J. M., and Garg, S., 1991, "Flow in the Wake of a Freely Rotatable Cylinder With Splitter Plate," *AIAA Journal*, Vol. 29(6), pp. 1001–1003.

Fung, Y. C., 1955, *An Introduction to the Theory of Aeroelasticity*, Wiley, London.

Gulati, A., 1990, "Passive Control of Combustion-Induced Instabilities," General Electric Company—CRD Report 90CRD093.

Higuchi, H., and Takahashi, F., 1989, "Flow Past Two-Dimensional Ribbon Parachute Models," *J. Aircraft*, Vol. 26(7), pp. 641–649.

Lesage, F., and Gartshore, I. S., 1987, "A Method of Reducing Drag and Fluctuating Side Force on Bluff Bodies," *Journal of Wind Engineering and Industrial Aerodynamics*, Vol. 25, pp. 229–245.

McLachlan, B. G., and Karamcheti, K., 1985, "An Experimental Study of Airfoil-Spoiler Aerodynamics," NASA-CR-177328.

Parker, R., and Pryce, D. C., 1974, "Wake Excited Resonances in an Annular Cascade: An Experimental Investigation," *Journal of Sound and Vibration*, Vol. 37(1), pp. 247–261.

Parker, R., and Stoneman, S. A. T., 1989, "The Excitation and Consequences of Acoustic Resonances in Enclosed Fluid Flow Around Solid Bodies," *Proc. Instn. Mech. Engrs*, Vol. 203, pp. 9–19.

Rizk, M. A., and Seymour, D. F., 1964, "Investigations Into the Failure of Gas Circulators and Circuit Components at Hinkley Point Nuclear Power Station," *Proc. Instn Mech. Engrs*, Vol. 179(1), No. 21, pp. 627–703.

Roshko, A., 1955, "On the Wake and Drag of Bluff Bodies," *Journal of Aeronautical Sciences*, Vol. 22(1), pp. 124–132.

H.-S. Dou[1]
Visiting Associate Professor.
Mem. ASME

S. Mizuki
Professor.
Mem. ASME

Department of Mechanical Engineering,
College of Engineering,
Hosei University,
Koganei-city, Tokyo 184, Japan

Analysis of the Flow in Vaneless Diffusers With Large Width-to-Radius Ratios

The flow in vaneless diffusers with large width-to-radius ratios is analyzed by using three-dimensional boundary-layer theory. The variations of the wall shear angle in the layer and the separation radius of the turbulent boundary layer versus various parameters are calculated and compared with experimental data. The effect of the separation point on the performance of vaneless diffusers and the mechanism of rotating stall are discussed. It is concluded that when the flow rate becomes very low, the reverse flow zone on the diffuser walls extends toward the entry region of diffusers. When the rotating jet-wake flow with varying total pressure passes through the reverse flow region near the impeller outlet, rotating stall is generated. The influences of the radius ratio on the reverse flow occurrence as well as on the overall performance are also discussed.

Introduction

Centrifugal compressors are widely used for many industrial purposes. They commonly display two kinds of unstable flow phenomena when they operate at flow rates substantially below the design points. The vaneless diffusers are widely used for them because of the advantage for the wide operation range with higher efficiency. However, sometimes they might be the components leading to machine breakdown into rotating stall and surge. Over the past thirty years, much research has been carried out both theoretically and experimentally to explore their essential flow mechanisms and to try to predict the flow behaviors. But because of the complexity of the flow, there seem to be some contradictions among the open literature (see Greitzer, 1981; Van den Braembussche, 1984, 1985; Japikse, 1984; Cumpsty, 1989; Pampreen, 1993, and Japikse and Baines, 1994), and further work is needed.

There are currently reported three kinds of analytical methods for the flow in vaneless diffusers. One is the method using the momentum integral equations of the boundary layer (Jansen, 1964b; Senoo et al., 1977; Schumann, 1986; Dou and Cheng, 1986). The second is to study the stability of the inviscid axisymmetric flow in the diffuser or the interaction of the inviscid core with the boundary layer for predicting rotating stall (Jansen, 1964a; Abdelhamid, 1980; Frigne and Van den Braembussche, 1985; Moore, 1991). The third method is to supply a method for predicting the flow losses and the performance of diffusers (Johnston and Dean, 1966; Bammert et al., 1978; Dou, 1989).

Jansen (1964a, b) first proposed a method to predict the rotating stall by using two-dimensional inviscid theory and a method to analyze the axisymmetric boundary-layer. Concerning the more practical approach, Senoo et al. (1977) developed a theory to analyze the asymmetrical flow relative to the width between the walls. This method has shown good agreements with experimental data in a few cases. Tsurusaki et al. (1987) made some corrections to this method and accounted for the influence of the width. Then, he used a correlation with experimental data and gave an empirical formula to calculate the critical inlet flow angle for rotating stall. However, the influence of the relative width on the critical inlet flow angle for the initiation of rotating stall is opposite to that by Jansen's model. The Jansen and Senoo methods both assumed the occurrence of reverse flow prior to rotating stall. However, Cumpsty (1989) showed that the presence of reverse flow on one of the diffuser walls is not an indicator of stall. Dou (1991) found that Senoo's method is only valid for narrow and moderate width diffusers. Rodgers (1977) proposed a criterion to judge the initiation of rotating stall in terms of a stability index. This model is proved to be an indicator of losses in the diffusers increasing with the decreasing flow rate. Recently, Moore (1991) developed a two-dimensional theory, which is applicable to diffusers with infinite width. Abdelhamid and Bertrand (1979) investigated the effect of diffuser width-to-radius ratio in the unstable flow and found that the effect of radius ratio on the flow behavior for different widths is different. Dou (1994) also showed that the factors affecting the stability of flow are different for narrow and wide diffusers.

The above-mentioned results have been controversial and confusing. Thus, the mechanisms for rotating stall and surge are still obscure. Therefore, further researches to clarify these problems are important. In this paper, the flow in diffusers with large width is investigated by using three-dimensional boundary-layer theory. The momentum integral equations of the boundary-layer need not be solved. The wall shear angle in the boundary layer is calculated by using Johnston's "triangular model," and the direction of limiting streamline on the wall is calculated for various flow conditions, and the variations of the separation point on diffuser walls are also presented. Then, the analytical results are compared with experimental data. The effect of the radius ratio between diffuser exit and inlet and the width-to-radius ratio on the diffuser performance is discussed. In this way, the mechanism of the generation of rotating stall in vaneless diffusers is clarified.

Theory

The flow in the vaneless diffusers of centrifugal compressors is highly complex. This type of flow is known to be three dimensional, turbulent, and unsteady at the entrance region. The flow in the diffuser varies with the inlet flow conditions as well. A three-dimensional boundary layer exists on the walls (skewed). This type of boundary layer is the same as the one Maskell (1955) described. The existence of a three-dimensional boundary layer makes it possible for flow separation to occur,

---

[1] Permanent address: Department of Hydraulic Engineering, Tsinghua University, Beijing 100084, People's Republic of China.

Contributed by the International Gas Turbine Institute and presented at the 41st International Gas Turbine and Aeroengine Congress and Exhibition, Birmingham, United Kingdom, June 10–13, 1996. Manuscript received at ASME Headquarters February 1996. Paper No. 96-GT-389. Associate Technical Editor: J. N. Shinn.

and hence a reverse flow zone is generated. Although there are some theories using the inviscid analysis for vaneless diffusers, only the employment of three-dimensional boundary layer theory can clarify a few phenomena and mechanisms in physical sense. This is just as Cumpsty (1989) stated, that the analysis using the three-dimensional turbulent boundary layer theory would be a more complete description. Since it is difficult to determine the flow condition at the impeller exit (diffuser inlet), some assumptions for the inlet condition have been generally made in the analyses. In the present analysis, the following assumptions are introduced:

1. The flow is steady, incompressible, and axisymmetric.
2. The velocity vector distribution at diffuser inlet is uniform.
3. The boundary layer on diffuser walls is fully turbulent.
4. The boundary layer at two diffuser walls does not merge in the passage and an inviscid flow core is present.

As is well known, the inviscid core of flow in parallel-walled vaneless diffusers traces a logarithmic spiral. The boundary layer on the walls is skewed owing to the pressure gradient and the streamline curvature. The fluid particles near the walls flow along the path with larger curvature than the logarithmic spiral, as shown in Fig. 1. The velocity vector in the boundary layer gradually deviates from the main-flow direction from the outer edge of the layer to the wall surface. The direction of wall-limiting streamline deviates from the primary streamline by an angle γ_w (Fig. 2). The angle γ_w increases along the radius downstream. When the direction of the wall-limiting streamline coincides with the tangential direction, a three-dimensional separation occurs. This type of separation can be described by the model of Maskell (1955). The wall-limiting streamline becomes perpendicular to the direction of local pressure gradient at the separation point. Therefore, it is possible to predict the separation point by calculating the variation of the direction of wall-limiting streamline.

Thus, during the calculation of three-dimensional turbulent boundary layer, the value of the angle γ_w indicates the condition of turbulent boundary layer approaching separation. Because the separation of boundary layer results in the formation of reverse flow zone and, hence, may further induce rotating stall, it is important to predict the wall shear angle γ_w.

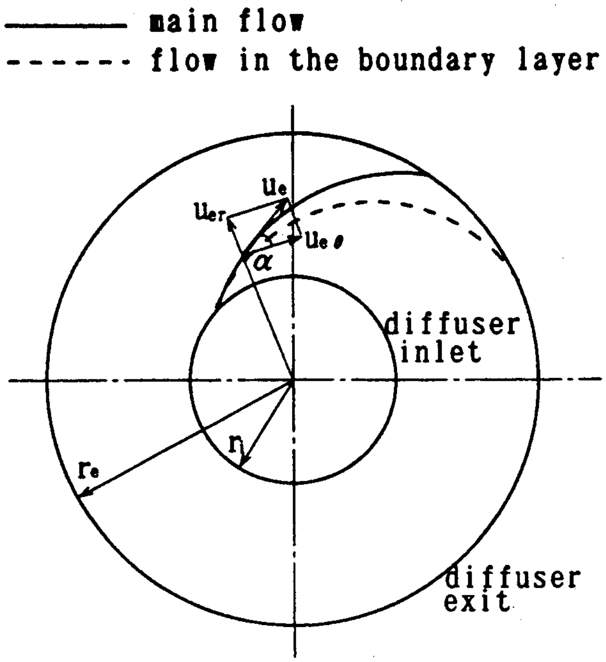

Fig. 1 Flow in vaneless diffuser

For this type of pressure-driven three-dimensional turbulent boundary layer, a lot of research has been carried out (see White, 1974; Olcmen and Simpson, 1992). If the wall shear angle γ_w is not very large and the lateral flow is not bidirectional, Johnston's triangular model gives the best approximation (White, 1974). This model has been widely used in many engineering problems (Cumpsty and Head, 1967; Smith, 1972; Swafford and Whitfield, 1985). The law of wall in the three-dimensional turbulent boundary layer based on this model by Johnston is still one of the best in many related models up to present (Olcmen and Simpson, 1992).

Johnston (1960) studied the nature of the boundary layer on a flat wall under the influence of a turning main flow. He stated

Nomenclature

A = parameter in the "triangular model"
b = diffuser width, m
b/r_i = diffuser width-to-radius ratio
$C_p = (p - p_i)/(\rho_i u_{ei}^2/2)$ = static pressure recovery coefficient
c_{fx} = component of local skin friction coefficient in the main-flow direction
K = constant in Eq. (14)
p = static pressure, N/m^2
$\mathrm{Re}_{r_i} = u_{ei} r_i / \nu_i$ = Reynolds number at diffuser inlet
r = radius, m
r_e/r_i = exit-to-inlet radius ratio, radius ratio between the exit and the inlet of diffusers
$\bar{r} = r/r_i$ = radius ratio
$\bar{r}_{\mathrm{sep}}$ = position of separation point
u = velocity component in the main flow direction in the boundary layer, m/s
u_2 = tip speed of impeller, m/s
w = velocity component in crossflow direction in boundary layer, m/s
x = coordinate in streamwise direction, m
y = distance in direction normal to walls, m
z = coordinate in the direction normal to streamwise, m
α = flow angle of main flow, measured from the tangential direction, deg
α_c = turning angle of main flow, measured relative to the direction of velocity vector at the diffuser inlet, rad
$\alpha_w = \alpha - \gamma_w$ = flow angle at wall, the limiting streamline direction measured from the tangential direction, deg
γ_w = wall shear angle, angle between the direction of the wall limiting streamline and the external streamline direction of boundary layer, deg
δ = thickness of boundary layers, m
δ^* = displacement thickness of boundary layers, m
θ = angle in Fig. 5, rad
μ = dynamic viscosity, Pa·s
ν = kinematic viscosity, m^2/s
ρ = density, kg/m^3
τ = shear stress, N/m^2

Subscripts

e = diffuser exit; external of the boundary layer
i = diffuser inlet
p = apex of "triangular model," Fig. 3
r = radial component
w = at walls
x = component in the direction of main flow
z = component in the direction of crossflow
θ = tangential component

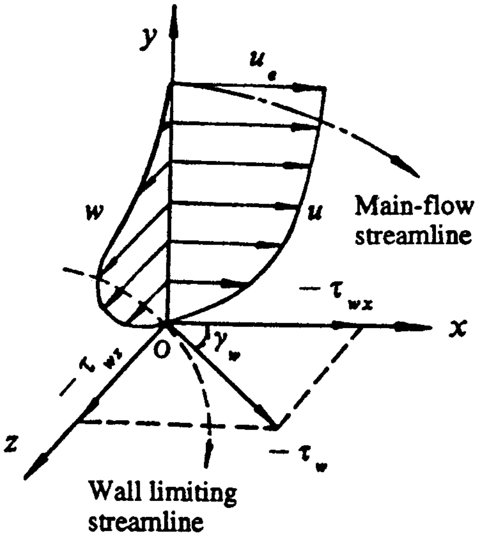

Fig. 2 Velocity component profiles in three-dimensional boundary layer

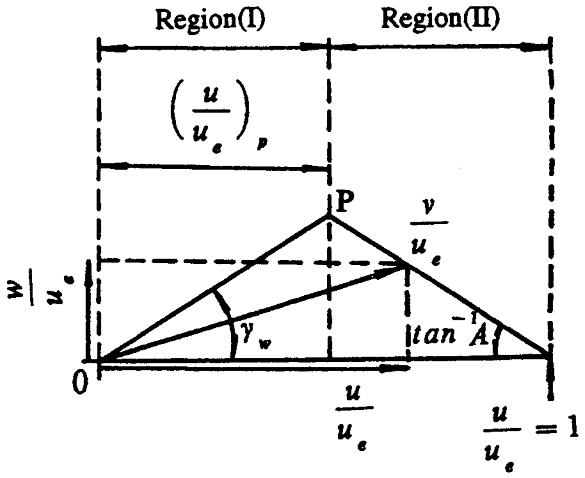

Fig. 3 Triangular model by Johnston

that this type of boundary-layer problems is commonly described as secondary-flow problems because the three-dimensional perturbations in the layer are caused by the radial pressure gradient imposed on the layer by the curvature of the main flow. The effect generally observed is a skewing of the boundary-layer velocity vectors toward the center of curvature of the main flow. The type of boundary layer in vaneless diffusers is the same as that described by Johnston. Thus, the theory developed by Johnston can be used to analyze the boundary layer in vaneless diffusers.

Johnston divided the turbulent boundary layer into two regions in the direction of boundary layer thickness. He assumed that a collateral region near the wall exists and the direction of the velocity vector at this region is coincident with the shear stress vector. This region is called the inner region of the boundary layer. In the outer region, the behavior of flow is primarily dominated by the outer inviscid flow. According to this model, the crossflow velocity profile of the boundary layer can be expressed as follows (see Fig. 3):

$$\left.\begin{aligned} \frac{w}{u_e} &= \tan\gamma_w \frac{u}{u_e} \quad \text{for} \quad \frac{u}{u_e} \le \left(\frac{u}{u_e}\right)_p \\ \frac{w}{u_e} &= A\left(1 - \frac{u}{u_e}\right) \quad \text{for} \quad \frac{u}{u_e} \ge \left(\frac{u}{u_e}\right)_p \end{aligned}\right\} \tag{1}$$

where γ_w is the angle between the wall limiting streamline and the external streamline, $(u/u_e)_p$ is the streamwise velocity ratio at the apex of the triangle. If the variation of the direction of external flow is known, the direction of the wall limiting streamline can be calculated by evaluating the angle γ_w.

From Eq. (1) and Fig. 3, the following expression is obtained:

$$\tan\gamma_w = A\left[\left(\frac{u}{u_e}\right)_p^{-1} - 1\right] \tag{2}$$

It can be seen that the parameters A and $(u/u_e)_p$ must be determined for the calculation of γ_w.

Johnston (1960) expressed the parameter A as a function of the parameters of the main flow. For the cases in which a pressure gradient exists along the main streamline direction ($\partial p/\partial x \neq 0$) and the turning angle varies in the normal direction of mainflow ($\partial \alpha_c/\partial z \neq 0$), he derived the following equation:

$$A = 2[u_e(r)]^2 \int_0^{\alpha_c} \frac{d\alpha_c}{[u_e(r)]^2} \tag{3}$$

where u_e is the velocity at the outer edge of the boundary layer, α_c is the turning angle of main flow and is measured relative to the main flow direction at the beginning of the turn of main flow streamline.

In terms of the second assumption in this paper, the value of the angle γ_w at the diffuser inlet is assumed to be zero. Allow that the value of α_c at diffuser inlet is set to zero, i.e., the main flow begins to turn at the inlet, the turning angle α_c of main flow in the vaneless diffuser means an angle that the velocity vector at any radius in vaneless diffusers deviates from the velocity vector at diffuser inlet. This implies that $\alpha_c = 0$ and $\theta = 0$ at diffuser inlet $r/r_i = 1$, $\alpha_c = \theta$ at any radius position in the diffuser (Fig. 4). When the boundary layers on the diffuser walls do not merge in the passage, an inviscid core exists in the diffuser. As the trace of the inviscid flow in the diffuser is logarithmic spiral, the flow angle α of main flow is invariant along the radius (see Fig. 4).

According to the conservations of mass flow and angular momentum, the velocity components of the inviscid core in the circumferential direction and the radial direction are expressed as follows:

$$u_{e\theta} = \frac{r_i}{r} u_{e\theta i} \tag{4}$$

$$u_{er} = \frac{\rho_i}{\rho} \frac{b}{b - 2\delta^*} \frac{r_i}{r} u_{eri} \tag{5}$$

Thus the velocity u_e and the flow angle α of the core flow are, respectively, expressed as follows:

$$u_e = \sqrt{\left(\frac{r_i}{r} u_{e\theta i}\right)^2 + \left(\frac{\rho_i}{\rho} \frac{b}{b - 2\delta^*} \frac{r_i}{r} u_{eri}\right)^2} \tag{6}$$

$$\tan\alpha = \frac{u_{er}}{u_{e\theta}} = \frac{\rho_i}{\rho} \frac{b}{b - 2\delta^*} \tan\alpha_i \tag{7}$$

Here, the vaneless diffuser with large width (see Fig. 5), i.e., $2\delta^* \ll b$, is considered. Because the density increases along the radius, $\rho > \rho_i$, it tends to compensate for the influence of δ^*, and the variation of the values of u_e is almost opposite to that of the radius ratio. Thus, the flow angle α of the inviscid core almost does not change along the radius. So in the following we assume α to be a constant. By these relations, the velocity u_e in Eq. (6) can be written as follows:

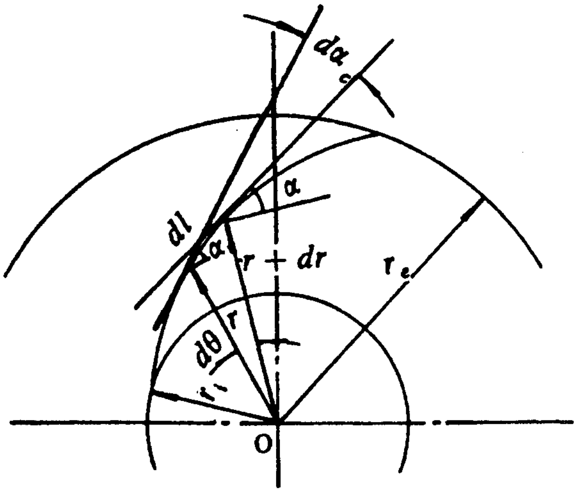

Fig. 4 Potential flow in vaneless diffusers

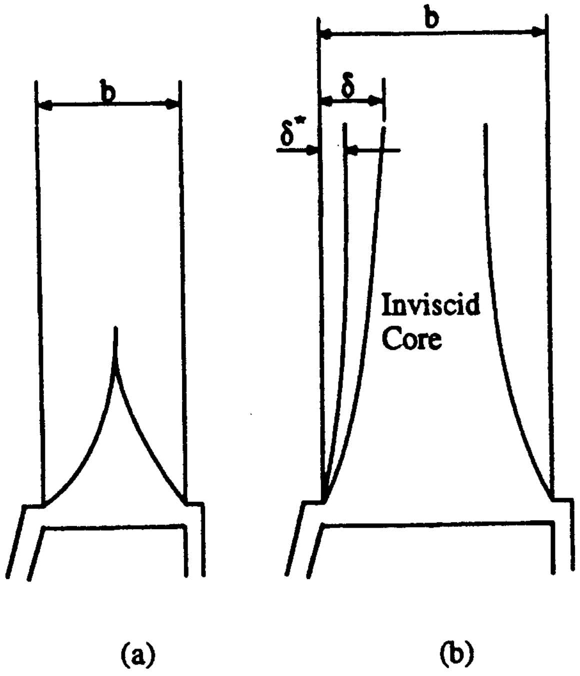

Fig. 5 Boundary layers in vaneless diffusers: (*a*) the boundary layers merge (narrow diffuser); (*b*) an inviscid core exists throughout the diffuser (wide diffuser)

$$u_e = \frac{r_i}{r} u_{ei} = \frac{1}{\bar{r}} u_{ei} \tag{8}$$

where $\bar{r} = r/r_i$.

Taking an element of length dl on the main streamline, which relates to a radial increment dr and an angular increment $d\theta$, the increment of the turning angle of main flow becomes $d\alpha_c$. From Fig. 4, we can find

$$d\alpha_c = d\theta \tag{9}$$

and

$$\tan\alpha = \frac{dr}{r d\theta} \tag{10}$$

From Eqs. (9) and (10),

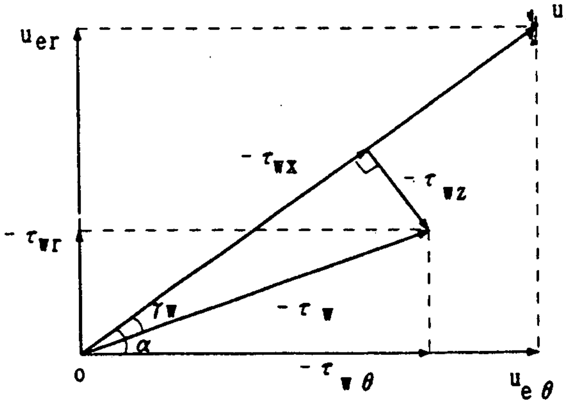

Fig. 6 Components of wall shear stresses

$$d\alpha_c = \frac{1}{\tan\alpha} \frac{d\bar{r}}{\bar{r}} \tag{11}$$

Introducing Eqs. (8) and (11) into Eq. (3), then integrating and simplifying, Eq. (12) can be solved

$$A = \frac{1}{\tan\alpha}\left(1 - \frac{1}{\bar{r}^2}\right) \tag{12}$$

The parameter $(u/u_e)_p$ is expressed as (Johnston, 1960; Smith, 1972)

$$\left(\frac{u}{u_e}\right)_p = \bar{y}_p \sqrt{\frac{\rho_e}{\rho_w} \frac{c_{fx}\cos\gamma_w}{2}} \tag{13}$$

where $\bar{y}_p = (y_p/\nu_w)\sqrt{\tau_w/\rho_w}$, and c_{fx} is the component of the skin friction coefficient in the direction of main flow. The density ratio ρ_w/ρ_e can be calculated from the energy equation for compressible flow. For incompressible flow, $\rho_w/\rho_e = 1$ is used. The relations of wall shear stresses are shown in Fig. 6.

By the physical relationship for the three-dimensional boundary layer, the value of y_p is related to the conditions of boundary layers. From the test data at low speed, $y_p = 12{\sim}16$ (Johnston, 1960), and $y_p = 14.0$ is employed here as in Johnston (1960) and Smith (1972).

The local skin friction coefficient toward the streamline direction in vaneless diffusers was obtained by Dou (1989):

$$c_{fx} = K\left(\frac{\mathrm{Re}_{ri}}{\sin\alpha_i}\right)^{-1/5} f(\bar{r}) \tag{14}$$

$$f(\bar{r}) = \bar{r}^{-1/2}(1 - \bar{r}^{-5/2})^{-1/5} \tag{15}$$

where K is a constant and amounts to 0.07. $\mathrm{Re}_{r_i} = u_{ei}r_i/\nu_i$ is the Reynolds number at diffuser inlet. The function $f(\bar{r})$ is shown in Fig. 7. It can be seen that c_{fx} is only a function of α_i, Re_{r_i}, and $\bar{r}$.

Substituting Eqs. (12) and (13) into Eq. (2), the following equation can be derived:

$$\tan\gamma_w = \frac{1}{\tan\alpha}\left(1 - \frac{1}{\bar{r}^2}\right)\left(\frac{0.10}{\sqrt{\frac{\rho_e}{\rho_w} c_{fx}\cos\gamma_w}} - 1\right) \tag{16}$$

Using Eqs. (14)–(16), the variation of γ_w along the radius ratio $\bar{r}$ can be calculated for given flow angle α_i and Re_{r_i} at the diffuser inlet. Then, the flow angle $\alpha - \gamma_w$ on the wall along the radius ratio $\bar{r}$ can be evaluated. When the flow angle at the wall becomes $\alpha - \gamma_w = 0.0$, the separation of the three-dimensional boundary layer is considered to occur as was shown

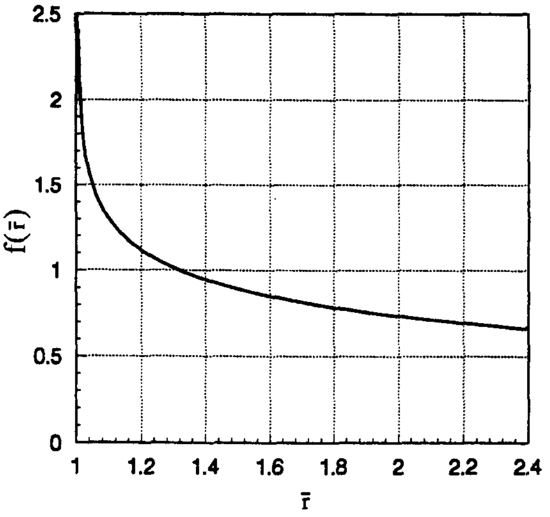

Fig. 7 Function $f(\bar{r})$ versus the radius ratio $\bar{r}$ (Dou, 1989)

by Maskell (1955). The radial component of the shear stress on the wall is zero at the separation point. When the surface friction force line becomes perpendicular to the direction of the local pressure gradient, the separation line is obtained. The separation line is a circular separation ring formed at the separation radius because of the axisymmetry of the flow. Similar calculations can be carried out for various inlet conditions. The flow pattern in vaneless diffusers is shown in Fig. 8, which was described by Senoo and Kinoshita (1978) and Pampreen (1993).

The position of separation point can also be directly evaluated by using Eq. (17). Substituting the criterion for separation occurrence $\alpha - \gamma_w = 0.0$ into Eq. (16), and simplifying, one obtains

$$\bar{r}_{sep} = \left\{ 1 - \tan^2 \alpha \left[\frac{\sqrt{\frac{\rho_e}{\rho_w}}\, c_{fx} \cos \alpha}{0.10 - \sqrt{\frac{\rho_e}{\rho_w}}\, c_{fx} \cos \alpha} \right] \right\}^{-1/2} \qquad (17)$$

It can be seen that the separation point only depends on α and c_{fx} for incompressible flow.

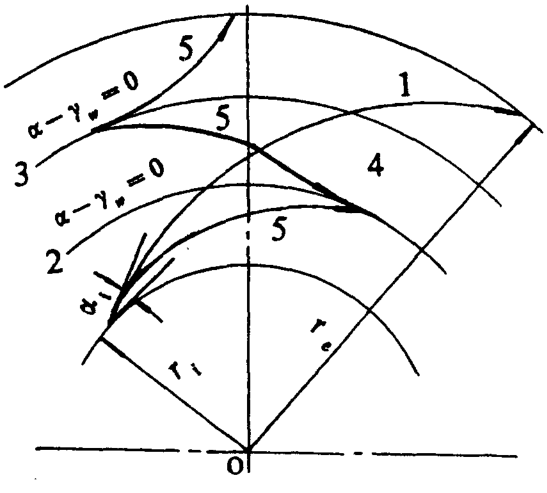

Fig. 8 Flow pattern in radial vaneless diffusers: (1) main flow streamline; (2) separation line; (3) reattachment line; (4) reverse flow region; (5) wall limiting streamline

Results and Discussion

Comparison of the Wall Shear Angle With Experimental Data. Cham and Head (1970) cited the experimental data by Gardow (1958). The test model by Gardow is a parallel walled vaneless diffuser. The component of the velocity in circumferential direction at the inlet is generated by a rotating screen. The ratio of the diffuser width to the inlet radius is $b/r_i = 0.144$. Another reference (Cham and Head, 1970) quoted about three sets of test data, where the inlet flow angles are 44.8, 39.4, and 35.5 deg, respectively. The comparison of the present calculation with Gardow's test data is shown in Fig. 9, in which the calculated results by Cham and Head are also indicated, which employs the momentum integration equation method. It can be seen that the present results show good agreements with the test data for $\bar{r} < 1.80$, and more accurate for all the radius ratios at all of three flow conditions. When $\bar{r} > 1.80$, the flow angle $\alpha - \gamma_w$ on the wall of the experimental data does not decrease as the predicted values. For $\alpha_i = 35.5$ deg, the value of $\alpha - \gamma_w$ somewhat increases with the increasing radius, while the predicted values decrease. It may be interpreted in such a way that the boundary layers on the two walls merged in the flow passage and the thickness of the boundary layers does not increase any more at larger radius ratio. The momentum thickness also does not increase and the skin friction coefficient does not drop. Thus, the present theory is not valid due to the difference of the considered condition. In the case of $\alpha_i = 35.5$ deg, the separated boundary layer reattaches at $\bar{r} = 2.1$.

In the present theory, when there exists an inviscid core in the vaneless diffusers, the separation point can be predicted accurately. However, when the width-to-radius ratio is large enough to merge the two boundary layers on the walls at a large radius ratio, the separation point occurs at a position before the merging station for the small inlet flow angle of α_i. Therefore, the position of separation point can be calculated by this theory in such condition. As shown in Fig. 9(c), the predicted separation point, denoted by the letter "S," coincides well with the experimental data. These results show the validity of the present model for vaneless diffusers with large width.

Variation of Separation Point With Various Parameters. In the real diffusers of radial machines, because of the high turbulence intensity and the flow irregularity, the friction coefficient is much larger than that from the ordinary friction coefficient formula. Senoo et al. (1977) found that the friction coefficient is about 1.33 times that of the flat plate formula by measuring the flow in a vaneless diffuser for a radial blower. According to this fact, we used a factor $K = 0.07 \times 1.33$ for Eq. (14) and calculated a few of results for further discussion. These results are shown in the Figs. 10–12.

The calculated results of the flow angle $\alpha - \gamma_w$ on the wall versus the radius ratio for various Re_{r_i} numbers are shown in Fig. 10, in which the inlet flow angle α_i is given to be 30 deg. The value of $\alpha - \gamma_w = 0.0$ indicates the separation points. It can be seen that the position of separation point is more near the inlet of diffuser with the increasing Re_{r_i}. The flow angle $\alpha - \gamma_w$ on the wall versus the radius ratio is shown in Fig. 11 for different inlet flow angle of α_i, in which Re_{r_i} is the same for all cases. The position of separation point moves toward the diffuser inlet from the outer part with decreasing inlet flow angle. The variation of the separation point versus the inlet flow angle is shown in terms of Re_{r_i} in Fig. 12. It can be seen that the effect of Re_{r_i} is strong when α_i is large, while the effect is very small when α_i become small. The separation point is located in the range of $\bar{r} = 1.07 \sim 1.13$ at $\alpha_i = 14.0$ deg for $\mathrm{Re}_{r_i} = 5 \times 10^5 \sim 3 \times 10^6$. This range of Reynolds number covers all the possible Reynolds numbers at impeller exit for ordinary centrifugal compressors. We noticed that even at such a large flow angle as 30 deg, the position of the separation

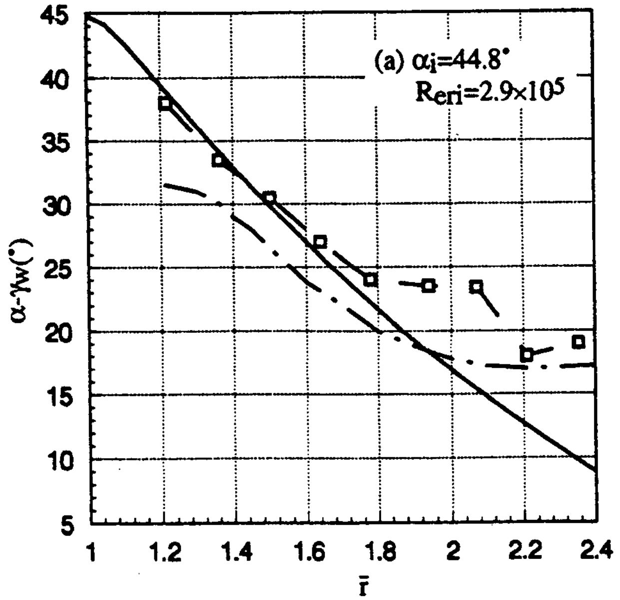

Fig. 9(*a*)

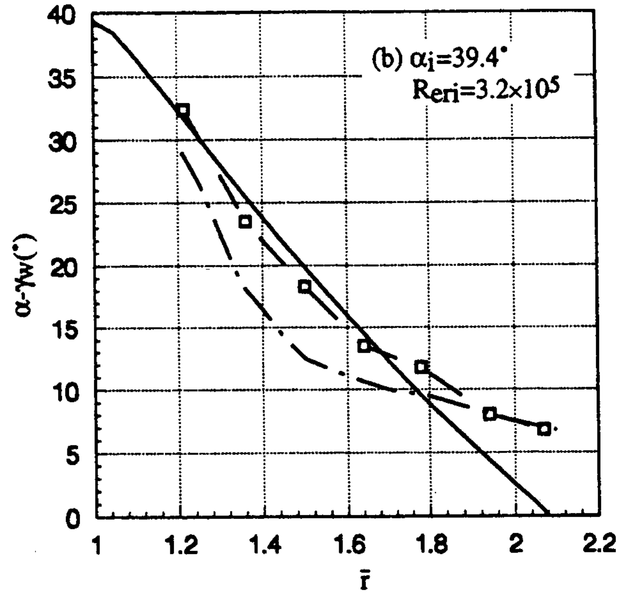

Fig. 9(*b*)

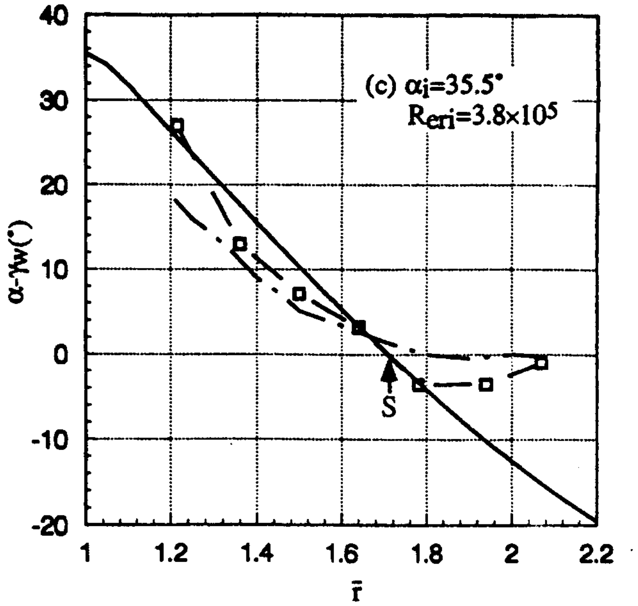

Fig. 9(*c*)

Fig. 9 Flow angle at the wall versus the radius ratio: —□— Gardow's test data; — — — Cham and Head method; —— present method

points is located within the range of $\bar{r} < 1.70$. It must be pointed out that the reverse flow formed by this separation at such high flow angle will be limited within the very thin layer near the wall due to the swirling role of the main flow and the equilibrium of the pressure across the boundary layer.

For a given diffuser geometry, the flow behavior in it is primarily determined by the inlet flow angle. The variation of the value of Re_{r_i} at the diffuser inlet in real centrifugal compressors is very limited, and the value is almost constant as the flow rate is reduced. This can be shown by the velocity triangle at impeller exit. Therefore, as discussed above, at small flow rate, a reverse flow zone first formed in the rear part of the diffuser. When the flow rate is very low, the inlet flow angle becomes very small and the reverse flow zone tends to appear in the entry region of the diffuser.

Physical Mechanism of Inception for Rotating Stall. The mechanism of occurrence for rotating stall is not understand so far as stated in the introduction. Although many researchers considered that the existence of reverse flow preceding rotating stall, it is not known how rotating stall is initiated from the separation ring (Pampreen, 1993).

The mechanism of occurrence for rotating stall could be explained by the present results as follows. When $\alpha_i = 14.0$ deg, the reverse flow zone reaches $\bar{r} = 1.07 \sim 1.13$. In this range of radius ratio, the jet-wake pattern discharged from impellers generally still remains clear. When the rotating jet-wake flow with varying total pressure passes through this reverse flow region near the impeller outlet, the rotating stall is generated (Fig. 13). In Fig. 13(*a*), although there exists a reverse flow zone on the diffuser wall in the outlet part at some flow rate, because it is far away from the jet-wake mixing region, this reverse flow zone will not suffice to lead to rotating stall. As

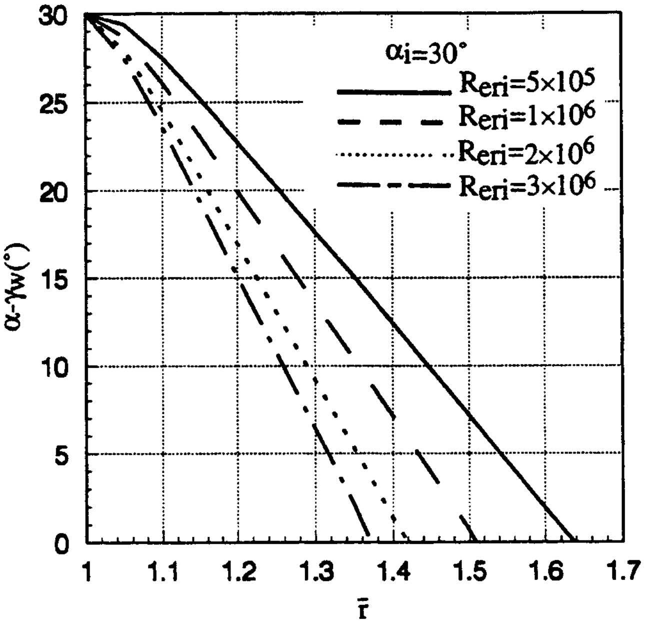

Fig. 10 Effect of Re_{r_i} on the flow angle at wall

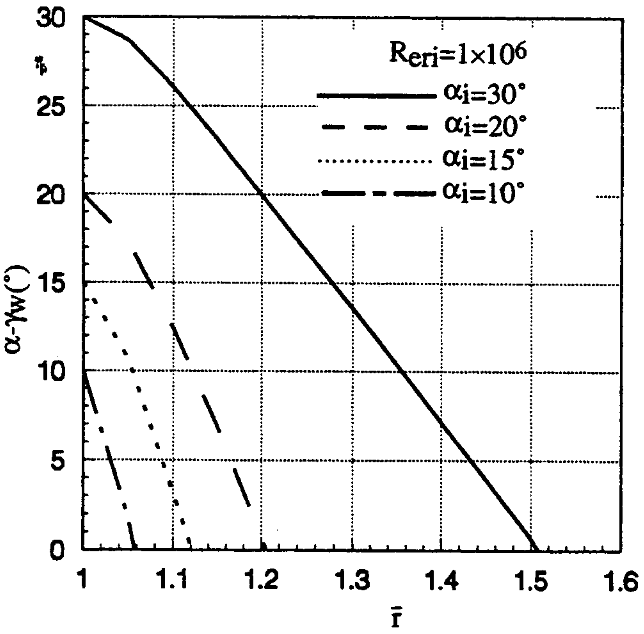

Fig. 11 Effect of inlet flow angle on the flow angle at wall

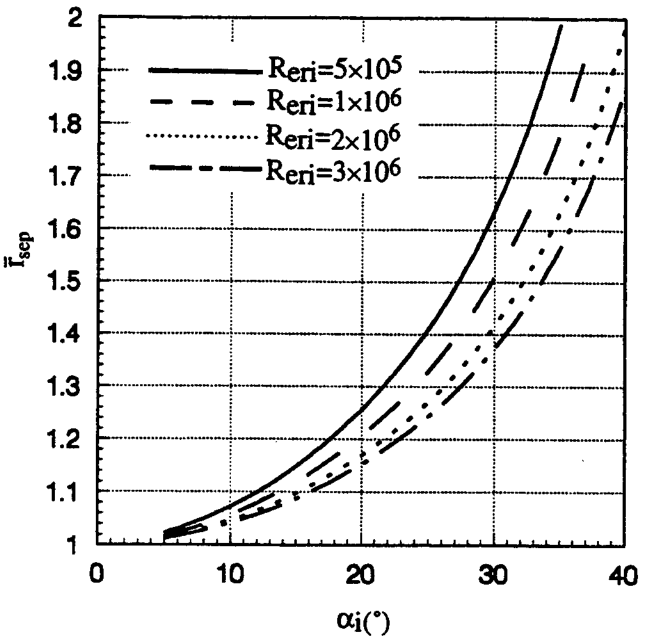

Fig. 12 Separation point versus inlet flow angle

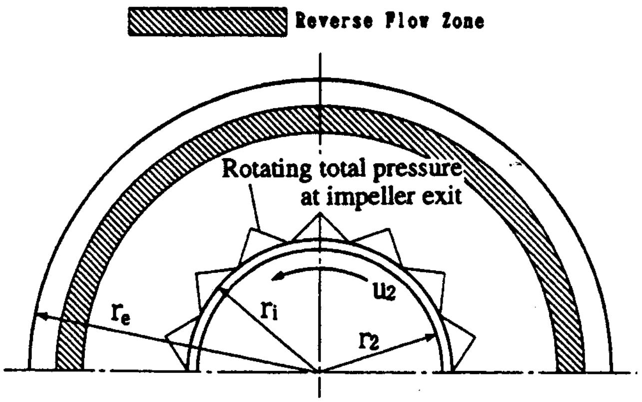

(a) Rotating stall does not occur(at higher flow rate)

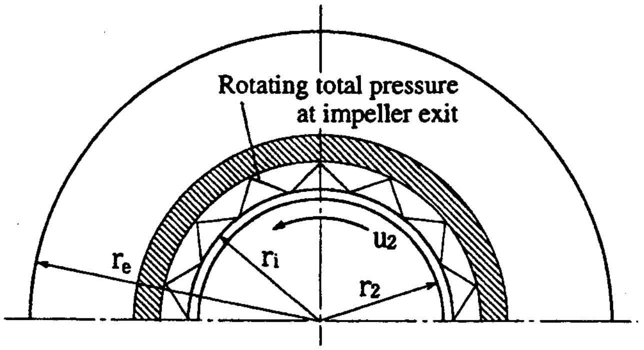

(b) Rotating stall occurs(at lower flow rate)

Fig. 13 Rotating stall model in vaneless diffusers

the flow rate is further reduced, this reverse flow zone moves to the inlet part of the diffuser. When it reaches the intense jet-wake region (for example, $\bar{r} < 1.20$), rotating stall will be generated due to the interaction of the rotating jet-wake pattern and the reverse flow zone on the wall. The condition for rotating stall to occur is governed by many factors because the flow discharged from impellers is very complicated. Therefore, there is much difference among the experimental data for the critical inlet flow angle of the rotating stall in the literature. The critical value $\alpha_i = 14.0$ deg accords well with many experiments (see Jansen, 1964b; Dean, 1971; Kinoshita and Senoo, 1985; Dou, 1991), especially for wide diffusers.

The mixing of the jet-wake pattern from impellers is generally finished at $\bar{r} = 1.15 \sim 1.20$ (Dean and Senoo, 1960; Johnston and Dean, 1966; and Cumpsty, 1989), even extremely distorted jet-wake patterns became uniform at $\bar{r} = 1.20$ (Senoo and Ishida, 1975). Therefore, the interaction between the reverse flow on the diffuser walls and the mixing of the jet-wake pattern in this range plays an important role in governing the flow instability of centrifugal compressors. Mizuki et al. (1985) have shown that the interaction of the mixing of jet-wake with the diffuser inlet flow has important effect on the flow instability and losses in vaneless diffusers.

The recent experiments by Ishida et al. (1993) and Watanabe et al. (1994) also show that rotating stall could occur when the reverse flow appears in the diffuser inlet. The flow discharged from the impeller is always nonuniform over the width of the diffuser at small flow rate. The reverse flow first formed on one wall. Then, it is alternately present on the two walls. At the diffuser entry region, there is a pressure difference between the two walls owing to the reverse flow existing on one wall. Bando et al. (1993) show that the rotating stall could be predicted by measuring the pressure difference at the inlet on two diffuser walls.

Jansen (1964b) and Senoo et al. (1977) all considered that the appearance of the reverse flow indicates the beginning of rotating stall. Senoo and Kinoshita (1978) took $\alpha_r = 0.88\alpha_t$ as the critical inlet flow angle of rotating stall, i.e., the reverse flow developed to a sufficient large extent leads to rotating stall. Here, α_t is the critical inlet flow angle for the separation. In this paper, we consider that the reverse flow reaching the diffuser inlet region as the flow rate decreases will result in rotating stall. The first appearance of the reverse flow zone on diffuser walls in early stage of appearance will not necessarily lead to rotating stall. However, the effect of wall pressure fluctuation exists. As pointed out by Cumpsty (1989), the presence of reverse flow on one of the walls of the diffuser is not an indicator of diffuser stall. Only when the reverse flow reaches to the diffuser inlet region (the intense jet-wake region) will the generation of rotating stall become possible.

However, the process of stall cell generation is not yet elucidated in the present study. The mechanism is quite complicated by the severe unsteady flow with the interaction between the annulus reverse flow and the jet-wake pattern. This problem should be clarified by taking into account the parameters related to the strong nonlinearity of the time-dependent flow in the future.

Effect of Exit-to-Inlet Radius Ratio on the Performance. Senoo's theory shows that the occurrence of rotating stall is almost irrespective of the exit-to-inlet radius ratio r_e/r_i. However, Abdelhamid's experiments (Abdelhamid, 1981; Abdelhamid and Bertrand, 1979; Abdelhamid et al., 1979) show that the radius ratio has significant effect on the initiation of the flow oscillation in diffusers, especially, for large b/r_i value. Rodgers' (1979) semi-empirical relation also indicates a strong effect of radius ratio on the performance stability.

Practically, the influence of r_e/r_i on the occurrence of reverse flow is relevant to the value of the width-to-radius ratio b/r_i. When b/r_i is very large, there exists an inviscid flow core in the diffuser. As shown in Fig. 12, the critical inlet flow angle to separate the boundary layer is larger for large value of r_e/r_i. Thus, the radius ratio r_e/r_i has an important effect on the appearance of the reverse flow, as well as on the fluctuation of wall pressure. When b/r_i is small, two boundary layers merge in the diffuser channel and the inviscid core does not exist anymore. The interaction of two boundary layers delays the separation. The critical inlet flow angle to separate the boundary layer is irrelevant to the value of r_e/r_i. Therefore, the effect of r_e/r_i on the occurrence of the reverse flow as well as on the wall pressure fluctuation is very small. This is just the case as Senoo et al. (1977) predicted.

In other words, if an inviscid core flow exists throughout the diffuser channel when the separation occurs, increasing r_e/r_i will make the critical inlet flow angle increase. If the inviscid core does not exist when the separation occurs, increasing r_e/r_i will give no effect on the critical flow angle. The radius ratio r_e/r_i does not affect the initiation of rotating stall, because the rotating stall is mainly caused by the presence of reverse flow in diffuser entry.

However, no matter what the magnitude of b/r_i, the influence of r_e/r_i on the losses is predominant. The increasing of r_e/r_i will generate high losses owing to the long flow path, increase the slope of the pressure recovery coefficient versus flow rate (or inlet flow angle), and hence affect the stability of the overall performance of the stage. This can be shown by Fig. 14. Generally, the static pressure recovery coefficient C_p versus the radius ratio $\bar{r}$ for various flow angles is as that shown in Fig. 14(a) (Johnston and Dean, 1966; Dou, 1994). For large α_i, the increase of $\bar{r}$ in a certain range makes C_p increase. But for small α_i, a large $\bar{r}$ will result in large losses, and not make C_p increase any more. If one designs a few diffusers with different radius ratios r_e/r_i for a given width-to-radius ratio b/r_i, their behavior of the static pressure recovery versus the inlet flow angle α_i can be expressed as those shown in Fig. 14(b), which is converted from Fig. 14(a). It can be seen that the increase of the exit-to-inlet radius ratio r_e/r_i makes the value of $dC_p/d\alpha_i$ increase for a given inlet flow angle, i.e., increase the slope of the static pressure recovery coefficient C_p versus the flow rate, which will lead to the overall performance of stage more unstable according to Dean's stability criterion (see Japikse and Baines, 1994).

The analytical method in this paper is applicable to parallel walled vaneless diffusers with large width-to-radius ratios, as long as an inviscid core flow exists throughout the diffuser. This means that $2\delta_e < b$ should be required, where δ_e is the thickness of the boundary layer at the diffuser exit.

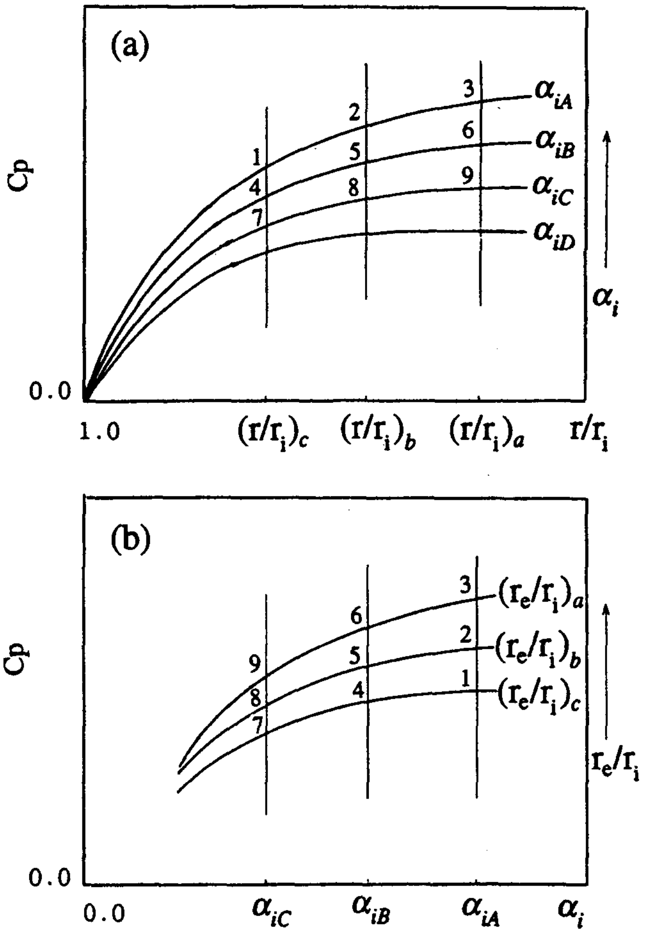

Fig. 14 Influence of radius ratio on the pressure recovery

Conclusions

In this paper, a theoretical model to analyze the three-dimensional turbulent boundary layer in vaneless diffusers with large b/r_i is developed based on Johnston's "triangular model." Although this model is simple, it explains a few of the physical phenomena and mechanisms. The prediction of γ_w by this model yielded good agreements with experimental data for diffusers with large width.

The radial location of separation point is primarily dependent on the inlet flow angle and the Reynolds number Re_{r_i}. The smaller the flow angle and the higher the Reynolds number Re_{r_i}, the nearer the separation point to the diffuser inlet.

For a diffuser with large b/r_i, a reverse flow zone exists on the walls even at high flow angle. But this reverse flow zone, if appearing at the rear part of the diffuser, does not generate rotating stall. Rotating stall is generated only when the reverse flow extends close to the entry region.

The mechanism of rotating stall is explained as follows: When the flow rate becomes very low, the reverse flow zone on the diffuser walls extends to the entry region of diffusers. When the rotating jet-wake flow pattern with varying total pressure passes through the reverse flow region near the impeller outlet, rotating stall is generated.

The influence of the exit-to-inlet radius ratio r_e/r_i on the flow in vaneless diffusers depends on the width-to-radius ratio. Concerning the overall performance, the increase of the radius ratio makes the stage more unstable because the increase of r_e/r_i increases the losses. Thus the slope of the pressure recovery versus the flow rate increases.

Generally, the flow in the entry region of vaneless diffusers in real centrifugal compressors is highly fluctuating and generating high losses. This will play a decisive role for the flow instability. The flow mechanism of stall cell generation is very complicated. This problem should be clarified in the future.

References

Abdelhamid, A. N., 1981, "Effects of Vaneless Diffuser Geometry on Flow Instability in Centrifugal Compression System," ASME Paper No. 81-GT-10.

Abdelhamid, A. N., 1980, "Analysis of Rotating Stall in Vaneless Diffusers of Centrifugal Compressors," ASME Paper No. 80-GT-184.

Abdelhamid, A. N., and Bertrand, J., 1979, "Distinctions Between Two Types of Self Excited Gas Oscillations in Vaneless Radial Diffusers," ASME Paper No. 79-GT-158.

Abdelhamid, A. N., Colwill, W. H., and Barrows, J. F., 1979, "Experimental Investigation of Unsteady Phenomena in Vaneless Radial Diffusers," ASME *Journal of Engineering for Power,* Vol. 101, pp. 52–60.

Bammert, K., Rautenberg, M., and Wittekindt, W., 1978, "Vaneless Diffuser Flow With Extremely Distorted Inlet Profile," ASME Paper No. 78-GT-47.

Bando, K., Miyake, Y., Adachi, Y., and Otsuki, A., 1993, "Correlation of Surge Inception of Compressor and Pressure Difference Between Two Walls of Vaneless Diffuser Inlet," *Proc. 4th Asian International Conference on Fluid Machinery,* Suzhou, China, pp. 24–29.

Cham, T.-S., and Head, M. R., 1970, "Calculation of the Turbulent Boundary-Layer in a Vortex Diffuser," ARC 31237.

Cumpsty, N. A., 1989, *Compressor Aerodynamics,* Wiley, New York, pp. 266–309.

Cumpsty, N. A., and Head, M. R., 1967, "The Calculation of Three-Dimensional Turbulent Boundary-Layers, Part 1: Flow over the Rear of an Infinite Swept Wing," *The Aeronautical Quarterly,* Vol. 18, No. 1, pp. 55–84.

Dean, R. C., Jr., and Senoo, Y., 1960, "Rotating Wakes in Vaneless Diffusers," ASME *Journal of Basic Engineering,* Vol. 82, No. 3, pp. 563–574.

Dean, R. C., Jr., 1971, "On the Unsolved Fluid Dynamics of the Centrifugal Compressor," in: *Advanced Centrifugal Compressors,* Dean, R. C., ed., ASME.

Dou, H.-S., and Cheng, X.-D., 1986, "Calculation of Three-Dimensional Turbulent Boundary-Layers in the Vaneless Diffuser of a Centrifugal Compressor," *Journal of Northeast University of Technology,* Vol. 7, No. 4, pp. 39–48.

Dou, H.-S., 1989, "A Method of Predicting the Energy Losses in Vaneless Diffusers of Centrifugal Compressors," ASME Paper No. 89-GT-158.

Dou, H.-S., 1991, "Investigation of Prediction of Losses in Radial Vaneless Diffusers," ASME Paper No. 91-GT-323.

Dou, H.-S., 1994, "The Stability Regimes of Radial Vaneless Diffusers," *Journal of Engineering Thermophysics,* Vol. 15, No. 2, pp. 166–169.

Frigne, P., and Van den Braembussche, R., 1985, "A Theoretical Model for Rotating Stall in the Vaneless Diffusers of a Centrifugal Compressor," ASME *Journal of Engineering for Gas Turbines and Power,* Vol. 107, No. 2, pp. 507–513.

Gardow, E. B., 1958, "The Three-Dimensional Turbulent Boundary Layer in a Free Vortex Diffuser," Massachusetts Institute of Technology, Gas Turbine Laboratory Report No. 42.

Greitzer, E. M., 1981, "The Stability of Pumping Systems—The 1980 Freeman Scholar Lecture," ASME *Journal of Fluids Engineering,* Vol. 103, pp. 193–242.

Ishida, M., Ueki, H., Sakaguchi, D., and Surana, T., 1993, "Unstable Flow Measurement in a Centrifugal Blower by Semiconductor Laser 2-Focus Velocimeter," *Proc. 4th Asian International Conference on Fluid Machinery,* Suzhou, China, pp. 77–82.

Jansen, W., 1964a, "Rotating Stall in a Radial Vaneless Diffuser," ASME *Journal of Basic Engineering,* Vol. 86, pp. 750–758.

Jansen, W., 1964b, "Steady Fluid Flow in a Radial Vaneless Diffuser," ASME *Journal of Basic Engineering,* Vol. 86, pp. 607–619.

Japikse, D., 1984, "A Critical Evaluation of Stall Concepts for Centrifugal Compressor and Pumps—Studies in Component Performance, Part 7," *Proc. ASME Conference on Stall and Surge in Compressors and Pumps,*

Japikse, D., and Baines, N. C., 1994, *Introduction to Turbomachinery,* Concepts ETI, Inc. and Oxford University Press, pp. (9-1)–(9-28).

Johnston, J. P., 1960, "On the Three-Dimensional Turbulent Boundary Layer Generated by Secondary Flow," ASME *Journal of Basic Engineering,* Vol. 82, No. 1, pp. 233–248.

Johnston, J. P., and Dean, R. C., Jr., 1966, "Losses in Vaneless Diffusers of Centrifugal Compressors and Pumps," ASME *Journal of Engineering for Power,* Vol. 88, No. 1, pp. 49–62.

Kinoshita, Y., and Senoo, Y., 1985, "Rotating Stall Induced in Vaneless Diffusers of Very Low Specific Speed Centrifugal Blowers," ASME *Journal of Engineering for Gas Turbines and Power,* Vol. 107, pp. 514–521.

Maskell, E. C., 1955, *Flow Separation in Three Dimensions,* RAE Report No. 2625.

Mizuki, S., Park, C. W., and Deckker, B. E. L., 1985, "Unstable Flows in the Vaneless Diffuser of a Centrifugal Compressor at Low Flow Rates," ASME Paper No. 85-IGT-7.

Moore, F. K., 1991, "Theory of Finite Disturbances in a Centrifugal Compression System With a Vaneless Radial Diffuser," ASME Paper No. 91-GT-082.

Olcmen, M. S., and Simpson, R. L., 1992, "Perspective: On the Near Wall Similarity of Three-Dimensional Turbulent Boundary Layers," ASME *Journal of Fluids Engineering,* Vol. 114, pp. 487–495.

Pampreen, R. C., 1993, *Compressor Surge and Stall,* Concepts ETI, Inc., Norwich, pp. (2-86)–(2-103).

Rodgers, C., 1977, "Impeller Stalling as Influenced by Diffusion Limitation," ASME *Journal of Fluids Engineering,* Vol. 99, pp. 84–79.

Schumann, L. F., 1986, "A Three-Dimensional Axisymmetric Calculation Procedure for Turbulent Flows in a Radial Vaneless Diffuser," ASME *Journal of Engineering for Gas Turbines and Power,* Vol. 108, pp. 118–124.

Senoo, Y., and Ishida, M., 1975, "Behavior of Severely Asymmetric Flow in a Vaneless Diffuser," ASME *Journal of Engineering for Power,* Vol. 97, pp. 375–387.

Senoo, Y., and Kinoshita, Y., 1978, "Limits of Rotating Stall and Stall in Vaneless Diffusers of Centrifugal Compressors," ASME Paper No. 78-GT-19.

Senoo, Y., Kinoshita, Y., and Ishida, M., 1977, "Asymmetric Flow in Vaneless Diffusers of Centrifugal Blowers," ASME *Journal of Fluids Engineering,* Vol. 99, pp. 104–114.

Smith, P. D., 1972, "An Integral Prediction Method for Three Dimensional Compressible Turbulent Boundary Layer," RAE 72228.

Swafford, T. W., and Whitfield, D. L., 1985, "Time-Dependent Solution of Three-Dimensional Compressible Turbulent Integral Boundary-Layer Equations," *AIAA Journal,* Vol. 23, No. 7, pp. 1005–1013.

Tsurusaki, H., Imaichi, K., and Miyake, R., 1987, "A Study on the Rotating Stall in Vaneless Diffusers of Centrifugal Fans," *JSME International Journal,* Vol. 30, No. 260, pp. 279–287.

Van den Braembussche, R., 1984, "Surge and Stall in Centrifugal Compressors," VKI Lecture Series, 1984-07.

Van den Braembussche, R., 1985, "Design and Optimization of Centrifugal Compressors," in: *Thermodynamics and Fluid Mechanics of Turbomachinery,* Ucer, A. S., et al., eds., Vol. II, Martinus Nijhoff Publishers, Dordrecht, pp. 829–885.

Watanabe, H., Konomi, S., and Ariga, I., 1994, "Transient Process of Rotating Stall in Radial Vaneless Diffusers," ASME Paper No. 94-GT-161.

White, F. M., 1974, *Viscous Fluid Flow,* McGraw-Hill, New York, pp. 542–558.